Edited by
Hartmut Yersin

WILEY-VCH

Highly Efficient OLEDs with Phosphorescent Materials

Highly Efficient OLEDs with Phosphorescent Materials

Edited by
Hartmut Yersin

Related Titles

Schwoerer, M., Wolf, H.C.

Organic Molecular Solids

2007
ISBN 978-3-527-40540-4

Heinzel, T.

Mesoscopic Electronics in Solid State Nanostructures

2007
ISBN 978-3-527-40638-8

Müllen, K., Scherf, U. (eds.)

Organic Light Emitting Devices

Synthesis, Properties and Applications

2006
ISBN 978-3-527-31218-4

Brütting, W. (ed.)

Physics of Organic Semiconductors

2005
ISBN 978-3-527-40550-3

Highly Efficient OLEDs with Phosphorescent Materials

Edited by
Hartmut Yersin

Contents

Preface

For nearly a hundred years, the properties of organo-transition metal compounds have fascinated chemists and physicists from a scientific point of view. Although the enormous potential of these materials for opto-electronic applications was evident since long, a break-through came only about fifteen years ago after the demonstration that these compounds are well suited as emitters in highly efficient OLEDs (organic light emitting diodes). This is due to the specific properties of these materials with regard to the electroluminescent processes. In OLEDs, light emission proceeds via a recombination of electrons and holes leading to the formation of 25% singlet and 75% triplet excitons. The 75% triplet excitons are transferred into heat and hence are lost for the generation of light, unless spin-orbit coupling (SOC) induced by a transition metal ion opens a radiative path for the emission from the excited triplet to the singlet ground state. SOC induces also an efficient transfer from the populated 25% singlets to the emitting triplets. Thus, the total excitation energy is transferred to the emitting triplet states. This process is called *triplet harvesting*. In particular, due to these effects, OLEDs which contain organo-transition metal triplet emitters (phosphorescent emitters) can reach a four times higher efficiency than OLEDs built with purely organic singlet emitters (fluorescent emitters). Therefore, this book focuses on phosphorescent emitter materials, their photophysical properties, and their applications in OLEDs.

OLEDs have already started to be commercially applied in small and bright displays and entered the market which hitherto is governed by LCD or other technologies. Lighting by OLEDs comes also into the focus of commercial interests, since efficient and thin large-area lighting sources will become available in near future. The development of these new technologies is characterized by an exceptional interdisciplinary research in the fields of physics, chemistry, and material sciences. Thus, basic research meets applied sciences and industrial interests. Vice versa, the interplay in this field strongly stimulates basic sciences and fundamental material research. Hence, it can be expected that a number of fascinating new materials will be developed in the near future.

In this volume, leading scientists present comprehensive reviews, which provide insight into the emission properties of organo-metallic triplet emitters, the mecha-

nisms of electroluminescence, the development of new emitter and host materials, and the improvement of OLED efficiencies by optimizing the emitter materials and the device architectures. The different contributions are written in a style which enables researchers from related fields and industrial laboratories as well as graduate students to follow the highly informative presentations. I am convinced that the contributions demonstrate the attractiveness and the great potential of the compounds and that further studies towards a better understanding of optoelectronic properties and mechanisms are induced. This will not only open large-scale applications of OLED displays and lighting systems, but will also stimulate the research and development of future applications in organic electronics, such as electrically pumped lasers or highly efficient and inexpensive organic solar cells.

Regensburg, Germany
August, 2007   Hartmut Yersin

List of Contributors

Detlef Berner
CFG Microelectronic
Avenue de Lonay 2-2bis
1110 Morges
Switzerland

Zu-Qiang Bian
Beijing National Laboratory for
    Molecular Sciences
State Key Laboratory of Rare Earth
    Materials Chemistry and
    Applications
Peking University
Beijing, 100871
P.R. China

Herbert Börner
Royal Philips Electronics
Philips Research Europe – Aachen
Weisshausstrasse 2
52066 Aachen
Germany

Klemens Brunner
Royal Philips Electronics
Philips Research Europe –
    Eindhoven
High Tech Campus 4
5654 AE Eindhoven
The Netherlands

Wai Kin Chan
Department of Chemistry
The University of Hong Kong
Pokfulam Road
Hong Kong
P.R. China

Chi-Ming Che
Department of Chemistry and HKU-
    CAS Joint Laboratory on New
    Materials
The University of Hong Kong
Pokfulam Road
Hong Kong
P.R. China

Yun Chi
Department of Chemistry
National Tsing Hua University
101, Section 2, Kuang Fu Road
Hsinchu, 30013
Taiwan

Pi-Tai Chou
Department of Chemistry
National Taiwan University
1, Section 4, Roosevelt Road
Taipei, 10617
Taiwan

Addy van Dijken
Royal Philips Electronics
Philips Research Europe—Eindhoven
High Tech Campus 4
5654 AE Eindhoven
The Netherlands

Peter I. Djurovich
Department of Chemistry
University of Southern California
840 W. 36th Place/Downey Way
Laird J. Stabler Labs, Room 368
Los Angeles, CA 90089
USA

Walter J. Finkenzeller
Institut für Physikalische Chemie
Universität Regensburg
Universitätsstr. 31
93040 Regensburg
Germany

Michael Grätzel
Laboratory for Photonics and
    Interfaces
Institute of Chemical Sciences and
    Engineering
School of Basic Sciences
Swiss Federal Institute of
    Technology
1015 Lausanne
Switzerland

Chun-Hui Huang
Beijing National Laboratory for
    Molecular Sciences
State Key Laboratory of Rare Earth
    Materials Chemistry and
    Applications
Peking University
Beijing, 100871
P.R. China

Frank Jaiser
Physik weicher Materie
Universität Potsdam
Am Neuen Palais 10
14469 Potsdam
Germany

Cedric Klein
Laboratory for Photonics and Interfaces
Institute of Chemical Sciences and
    Engineering
School of Basic Sciences
Swiss Federal Institute of Technology
1015 Lausanne
Switzerland

P. T. Lai
Department of Electrical and Electronic
    Engineering
The University of Hong Kong
Pokfulam Road
Hong Kong
P.R. China

Siu-Wai Lai
Department of Chemistry and HKU-
    CAS Joint Laboratory on New
    Materials
The University of Hong Kong
Pokfulam Road
Hong Kong
P.R. China

Bea M. W. Langeveld
TNO Science and Industry
De Rondom 1
5600 HE Eindhoven
The Netherlands

John M. Lupton
Department of Physics
University of Utah
115 South 1400 East
Salt Lake City
UT 84112-0830
USA

Chris Shuk Kwan Mak
Department of Chemistry
The University of Hong Kong
Pokfulam Road
Hong Kong
P.R. China

Mohammad K. Nazeeruddin
Laboratory for Photonics and
    Interfaces
Institute of Chemical Sciences
    and Engineering
School of Basic Sciences
Swiss Federal Institute of
    Technology
1015 Lausanne
Switzerland

Dieter Neher
Physik weicher Materie
Universität Potsdam
Am Neuen Palais 10
14469 Potsdam
Germany

Shinjiro Okada
Leading-Edge Technology
    Development Headquarters
Canon Inc.
5-1 Morinosato-Wakamiya
Atsugi-shi
Kanagawa 243-0193
Japan

Isao Tanaka
NHK (Japan Broadcasting
    Corporation)
Osaka Broadcasting Station
Technical and Engineering Division
Otemae, Chuo-ku
540-8501 Osaka
Japan

Mark E. Thompson
Department of Chemistry
University of Southern California
840 W. 36th Place/Downey Way
Laird J. Stabler Labs, Room 368
Los Angeles, CA 90089
USA

Shizuo Tokito
NHK (Japan Broadcasting Corporation)
Science and Technical Research
    Laboratories
Materials Science and Advanced
    Devices
Kinuta, Setagaya-ku
157-8510 Tokyo
Japan

Akira Tsuboyama
Leading-Edge Technology Development
    Headquarters
Canon Inc.
5-1 Morinosato-Wakamiya
Atsugi-shi
Kanagawa 243-0193
Japan

Kazunori Ueno
Leading-Edge Technology Development
    Headquarters
Canon Inc.
5-1 Morinosato-Wakamiya
Atsugi-shi
Kanagawa 243-0193
Japan

Manfred J. Walter
Photonics & Optoelectronics Group
Physics Department and CeNS
Ludwig-Maximilians-Universität
    München
Amalienstr. 54
80799 München
Germany

Hai-Feng Xiang
Department of Chemistry and HKU –
   CAS Joint Laboratory on New
   Materials
The University of Hong Kong
Pokfulam Road
Hong Kong
P.R. China

Xiao-Hui Yang
Arizona State University
School of Materials and Flexible
   Display Center
7700 South River Parkway
Tempe, AZ 85284
USA

Hartmut Yersin
Institute of Physical Chemistry
University of Regensburg
Universitätsstr. 31
93040 Regensburg
Germany

Libero Zuppiroli
Laboratoire d'Optoélectronique
   desMatériaux Moléculaires
Institut des Matériaux
Ecole Polytechnique Fédérale
1015 Lausanne
Switzerland

1
Triplet Emitters for Organic Light-Emitting Diodes: Basic Properties

Hartmut Yersin* and Walter J. Finkenzeller

1.1
Introduction

Within the past decade, organo-transition metal compounds consisting of triplet emitters have become highly attractive, in particular, due to their applicability in electro-luminescent devices such as organic light-emitting diodes (OLEDs). With this new technology, efficient light-emitting systems are evolving. For example, in the future it will become possible to fabricate large and brilliant flat panel displays at a moderate price, to prepare illuminating wallpapers, and micro displays for all types of application. One important requirement for all of these applications is low power consumption and high efficiency of the light-emitting devices. Here, the organo-transition metal compounds offer a great advantage. The maximum obtainable efficiency may be a factor of *four* higher than for purely organic emitter materials. Thus, many research groups, both from academic and industrial laboratories, have become interested in this challenging scientific- and application-driven field [1–40].

Organo-transition metal compounds, such as the famous $Ir(ppy)_3$ or $[Ru(bpy)_3]^{2+}$ complexes,[1] represent triplet emitters. This means, they exhibit an emission – a phosphorescence – from the lowest excited electronic triplet state to the electronic singlet ground state. Although this electronic transition is formally forbidden, it may become sufficiently allowed by spin–orbit coupling (SOC) induced by the central metal. Depending on the specific compound, the emission can show widely differing properties. Its wavelength can lie in the spectral range from blue to red, or even from ultraviolet to infrared. Normally, at ambient temperature, the spectra are not resolved line emissions, but rather are broad and often exhibit an undesirably low color purity. The emission decay time ranges from shorter than $1\,\mu s$ to as long as several milliseconds, and the photoluminescence quantum yield may be almost 100%, or unattractively low. The desire

---

* Author for correspondence.
1) Chemical structures are shown in Fig. 1.12.

to understand these and many other photophysical properties developed as the focal point of several research groups, and led to the investigation of these luminescent materials in greater detail. Indeed, the main subject of this chapter is to present the background for an understanding of these emission properties. This will be achieved first by discussing some relatively simple – and, with respect to the number of the involved states, sometimes even slightly oversimplified – models, in order to help to introduce also non-specialists to this field. In later sections, a more detailed description of the photophysics of the triplet state is developed. The discussion of these models, and their relationship to the observed properties, will be outlined in rather elementary terms, and illustrated by examples related to OLED emitter materials. In this respect, references relating to further studies will be given.

This chapter is organized in the following manner. Following a very brief introduction into the working principle of an OLED, exciton formation and the process of electron–hole recombination are addressed. There follows a discussion of the process leading to the population of higher excited singlet and triplet states of the doped emitter molecules, and it is shown, how finally the excitation energy is harvested in the emitting triplet state (Section 1.2). Usually, the same state can be populated either directly or indirectly by photoexcitation; therefore, electroluminescence and photoluminescence spectra result from the same electronic state(s) and thus are normally almost equal, at least for doped triplet emitters in the absence of host emission. Consequently, detailed photoluminescence studies can be applied to explore also the electro-luminescence properties of OLEDs. In Section 1.3, the different types of electronic HOMO–LUMO transitions[2] are introduced, which are important for organo-transition metal complexes. In particular, ligand-centered (LC), metal-centered (MC), and metal-to-ligand charge transfer (MLCT) transitions are discussed. Models that are based merely on these transitions, however, do not display energy states, such as singlets and triplets. It is possible to show, in a very simple approach, how these states and the related splittings can be deduced from experimentally supported "rules of thumb". More accurate approaches and models, which include SOC, will also be discussed. The emitting triplet state splits almost in any case into three substates. The extent of this splitting – the zero-field splitting (ZFS) – may serve as a very useful parameter for a classification of the corresponding compound, also with respect to its suitability for OLED application. Especially, it will be shown that the magnitude of ZFS depends on the MLCT character in the emitting state, and is governed by SOC. Interestingly, the SOC routes are distinctly different for quasi-square planar as compared to quasi-octahedral complexes. These differences have direct influences on the properties of the emitting triplet state, and thus also on OLED applications. In Section 1.4, an ordering scheme is presented for triplet emitters based on the amount of ZFS, and trends are discussed, how photophysical properties are

---

2) HOMO = highest occupied molecular orbital; LUMO = lowest unoccupied molecular orbital.

related to the magnitude of the ZFS. In Sections 1.5 and 1.6 it is shown, in a number of case studies applied to Pt(thpy)$_2$ and Ir(ppy)$_3$, how triplet energy level schemes and the emission decay times of the individual triplet substates can be elucidated from highly resolved and broadband emission spectra, respectively. Phosphorescence dynamics and the effects of spin–lattice relaxation (SLR) are addressed in Section 1.7. The influence of high external magnetic fields on the triplet state splitting and the decay dynamics is discussed in Section 1.8, again as a case study focusing on Ir(btp)$_2$(acac). In Section 1.9, the importance of vibronic coupling is discussed – that is, the origin of the vibrational satellite structure – which is induced by Franck–Condon (FC) and/or Herzberg–Teller (HT) activity, and which usually determines the form and width of an emission spectrum. Finally, in Sections 1.10 and 1.11, environmental effects on the triplet state energy, splitting and decay dynamics are addressed, and spectral broadening by inhomogeneous as well as by homogeneous effects are discussed. The latter effect leads to the unresolved spectral band structure at ambient temperature. These discussions are again based on case studies applied to Pt(thpy)$_2$ and Ir(btp)$_2$(acac). At higher temperatures, the emission generally represents a thermalized decay from the different triplet substates. In particular in Section 1.11, it is shown that it is possible to simulate the ambient temperature broadband luminescence spectra by use of the well-resolved, low-temperature spectra simply by taking basic spectral broadening mechanisms into account. The chapter is completed with a short conclusion (Section 1.12).

1.2
Electro-Luminescence and the Population of Excited States

In this section, we first present the basic principle of an OLED. Following this short introduction, attention is focused on the energetics and dynamics of electron–hole recombination in the emission layer (EML). Here, the main interest is in those processes which take place within the vicinity of the emitting center. In this context, we explain concepts of exciton formation, spin-statistics, intersystem crossing, and population of the lowest triplet substates, which is often referred to as triplet harvesting.

1.2.1
Multilayer Design of an OLED

Figure 1.1 shows a typical and well-established set-up of an OLED. It consists of a number of thin layers which are either solution-processed or vacuum-deposited, for example, on a glass substrate. In operation, holes are injected from a transparent anode, mostly consisting of a non-stoichiometric composite of SnO$_2$ (10–20%) and In$_2$O$_3$ (90–80%), called "indium tin oxide" (ITO). Adjacent to this anode layer, a hole injection/transport layer (HTL) is normally applied to allow for a well-
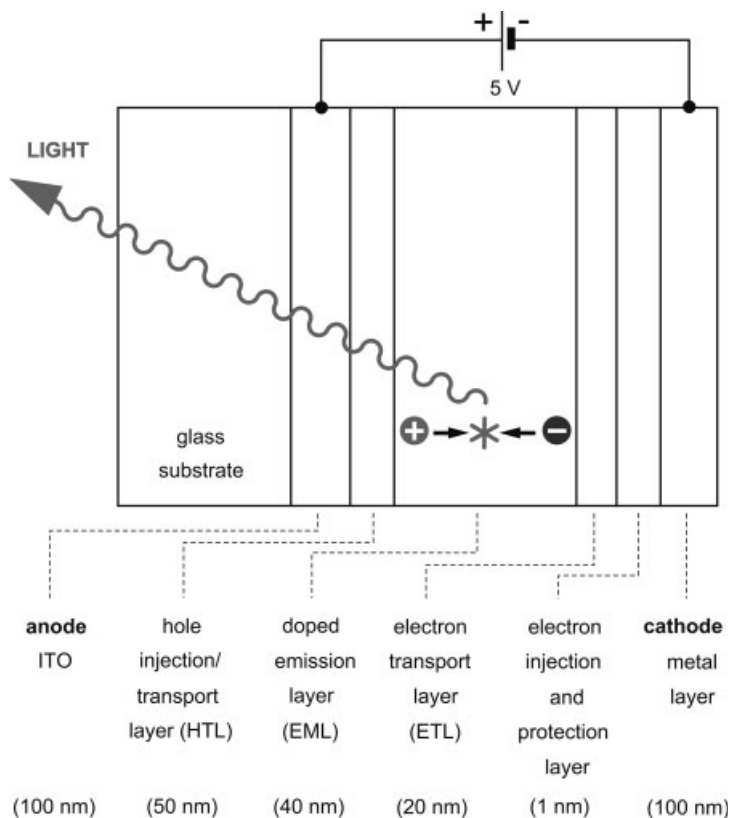
Fig. 1.1 Basic set-up of an organic light-emitting diode (OLED). The different layers are not drawn to scale. Examples of materials used for a realization of an OLED device are given in Fig. 1.2. Within the scope of this chapter, interest is mainly focused on the process of electron(–)–hole(+) recombination and the triplet state population of the emitter molecule (depicted as a star). Further optimized OLEDs contain additional hole and/or electron blocking layers (e.g., see Ref. [42]).

balanced hole[3] transport into the EML. At the opposite side, a metal-cathode with a suitably chosen work function injects electrons into an electron transport layer (ETL). It has been shown that an additional, very thin layer of LiF or CsF (0.5 to

---

3) Note that the "hole" represents a model particle which is physically based on the movement (hopping) of an electron. The HOMO of a neutral organic molecule is usually populated with two electrons. If one electron is extracted, for example, by transferring it to the anode, a positively charged molecule is left. Subsequently, the empty electron position in the HOMO can be populated by an electron from the HOMO of a neighboring molecule. Thus, the positive charge has moved to the neighbor. An equivalent process occurs involving the next nearest neighbor, and so on. Thus, the positive charge – called a "hole" – moves from molecule to molecule into direction of the cathode. Such a hole has properties of a particle, it carries a positive charge, a spin (the one of the residual electron) and it can move in the HOMOs with a specific hole mobility. For two molecules with different HOMO energies, the electron hops downwards, and this corresponds formally to an upwards hopping of the hole.

1 nm) strongly reduces the injection barrier and also protects the ETL from chemical reactions with the cathode material [41]. Clearly, although electron transport from the cathode to the EML must be efficient, it is also important that the electron current is well balanced with the hole current in order to avoid ohmic losses. Such losses can be minimized by introducing a hole-blocking layer (e.g., [8, 42]) between the EML and the ETL and/or an electron blocking layer (e.g., [43]) between the HTL and the EML. These additional layers (which are not shown in the diagram) prevent holes/electrons from crossing and leaving the EML without electron–hole recombination. As result, the device efficiency can be distinctly increased. However, such blockings may lead to the build-up of high charge densities at the interfaces, with unfavorable consequences for the device lifetime [44].

The materials used for an OLED device must fulfill a series of requirements, such as suitability for a specific fabrication procedure (e.g., spin-coating, inkjet printing, vacuum deposition), good film-forming properties, sufficiently high glass transition temperature to avoid crystallization of the layer material within the desired lifetime of the device, and chemical and photochemical stability. Moreover, hole and electron injection barriers must be low, and the mobilities as well as HOMO and LUMO energies must match for neighboring layers. A further requirement is that the lowest triplet state of the host material used for the EML lies significantly higher (i.e., about $3000\,cm^{-1}$ or approximately $0.4\,eV$) than the triplet of the emitting complex. Otherwise, the triplet of the host can be populated, and subsequently the excitation energy can easily diffuse to quenching sites, or can be quenched at the host itself. (Compare also the other contributions to this volume [9, 10]). In particular, for high-energy blue emitters, specific matrix materials must be chosen, or even must still be developed.

Figure 1.2 illustrates one example of a device realized according to the structure depicted in Fig. 1.1. This example (which is adapted from Ref. [45]) is built up by the use of small-molecule, vacuum-depositable materials. The figure depicts the corresponding HOMO und LUMO levels in the absence of an electrical bias, as well as the chemical structures of the materials applied. The diagram shows that energy barriers occur since the hopping of holes upwards (in energy) and of electrons downwards to the EML do not seem to be favored, although this would be advantageous. The energy barriers can be overcome, however, by level shifts due to the external potential, and additionally by thermal activation processes. Level shifts induced by the external potential are not shown in Fig. 1.2. Such a device was first reported by the Forrest and Thompson groups [45] in 2001. It exhibits a relatively high external quantum efficiency of 19% and a luminous power efficiency of $60\,lm\,W^{-1}$. These values are obtained only at low current densities. With increasing currents, the efficiency gradually decreases due to a growing influence of different quenching effects [46], of which triplet–triplet annihilation is regarded as being of particular importance [45–47]. In more recent developments, much higher efficiencies have been obtained with modified devices. For example, by p-doping of the HTL and n-doping of the ETL and additionally by introducing a double emission layer (D-EML), the Leo group [48] obtained with the green-emitting Ir(ppy)$_3$ a luminous power efficiency of $77\,lm\,W^{-1}$ and an external quantum
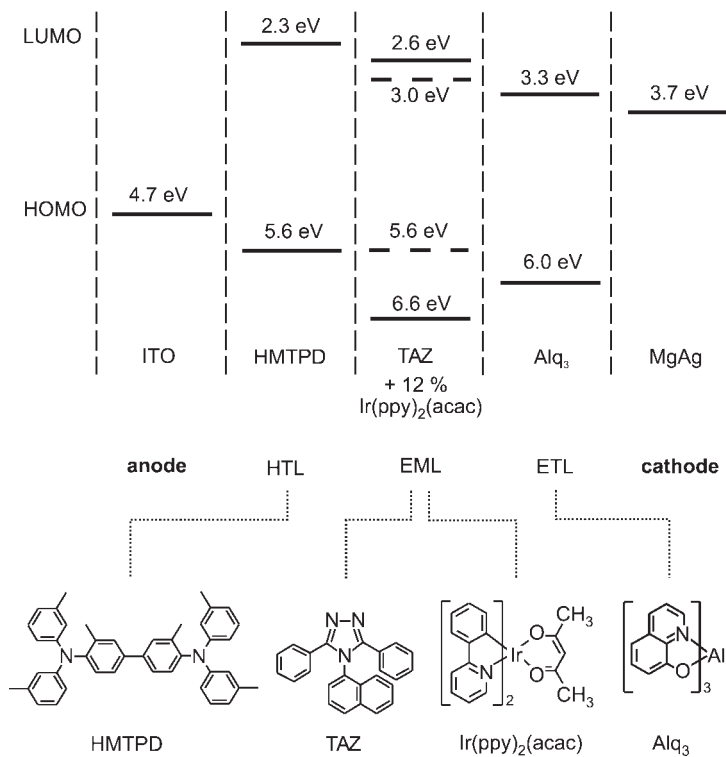
Fig. 1.2 HOMO-LUMO diagram and materials of an OLED device similar to the one shown in Fig. 1.1. The HOMO/LUMO values are given relative to the vacuum level, and therefore are negative. Values and materials are taken from Ref. [45]. For the emission layer (EML), the oxidation and reduction potentials are given for the host (TAZ, solid line) and the emitter (Ir(ppy)$_2$(acac), dashed line).

efficiency of more than 19% at $100\,cd\,m^{-2}$ at an operating voltage of only 2.65 V. Also applying the Ir(ppy)$_3$ complex, the authors of Ref. [49] obtained a luminous power efficiency of $79\,lm\,W^{-1}$ and a current efficiency of $81\,cd\,A^{-1}$ by use of a transparent silver anode. This device structure features an enhanced hole injection, and also allows for more efficient outcoupling of light due to a microcavity structure. In Ref. [50], values of $110\,lm\,W^{-1}$ at $10^3\,cd\,m^{-2}$ were communicated. By use of a microcavity, two-unit tandem device, efficiencies as high as $200\,cd\,A^{-1}$ at $10^3\,cd\,m^{-2}$ were reported recently [51]. Interestingly, efficiencies which can be reached today with OLEDs are as high as – or even higher than – those of highly efficient inorganic LEDs.

Although, in this chapter, we do not aim to discuss further progress in the field of OLED device architectures, it is referred to some interesting recent developments reported in the literature [51–60].

1.2.2
Electron–Hole Recombination, Relaxation Paths, and Light Emission

In order to gain some general understanding of the processes in the EML, Fig. 1.3 displays a simplified model of electron–hole recombination. This layer consists of a host material (matrix) which is doped with a suitable triplet emitter complex at low concentration. For the subsequent discussion, it is assumed that both charge carriers – electron and hole – are already present in the EML. Different steps of electron–hole recombination – that is, exciton formation and population of the emitting triplet state – can take place. For example, the exciton can be formed and trapped on the host molecule with subsequent energy transfer to the triplet emitter. In an alternative process, one of the charge carriers is directly trapped on the emitter dopant itself and the recombination occurs on this molecule. This has been proposed specifically for efficient devices containing Ir(III) emitter complexes [45, 61, 62], but also for PtOEP [63], that the hole is trapped first on the emitter complex. The electron – or, more exactly, the negatively charged polaron[4)] [64] – experiences a Coulomb attraction and the formation of the overall neutral exciton starts. This process of hole trapping as a first step can occur, if the oxidation potential of the emitter complex fits well to the HOMO energy of the hole transport material (HTL) (compare Ref. [45]). Presumably, this process of charge carrier trapping directly on the emitter molecule will usually result in a more efficient OLED device than by indirect excitation of the emitter molecule by energy transfer [5]. In part, alternative approaches for the description of exciton formation processes are discussed in Refs. [5, 65, 66].

For the model depicted in Fig. 1.3, it is assumed (as mentioned above) that the hole is already trapped at the emitter molecule. In our simple approach, it is supposed that the reorganization energy after oxidation of the emitter (hole trapping) sitting in the relatively rigid host environment is small. Subsequently, we discuss the electron dynamics until the emitting triplet state is populated. With an external potential ΔV, the electron will migrate through the host material towards the anode. Under normal conditions, this process additionally requires thermal activation energy to overcome energy sinks due to inhomogeneities and due to host reorganization effects related to the polaronic properties of the electron. Electron trapping is avoided if the energies of the sink depths are less than, or on the order of, the thermal energy $k_B T$, where k_B is the Boltzmann constant and T the absolute temperature.

When the electron is still far from the trapped hole, it will migrate towards the anode independently from the hole. Thus, the hole and electron are neither bound nor correlated (see left-hand side of the diagram, Fig. 1.3). However, when the electron migrates further into a region given by a critical electron–hole separation R_C, the positively charged hole (h) will attract the electron (e). This distance is

---

4) Electron (or hole) hopping is normally connected with a polarization of the matrix. Therefore, the corresponding negatively (positively) charged particle coupled to matrix distortions represents a polaron. For background information see, for example Ref. [64].
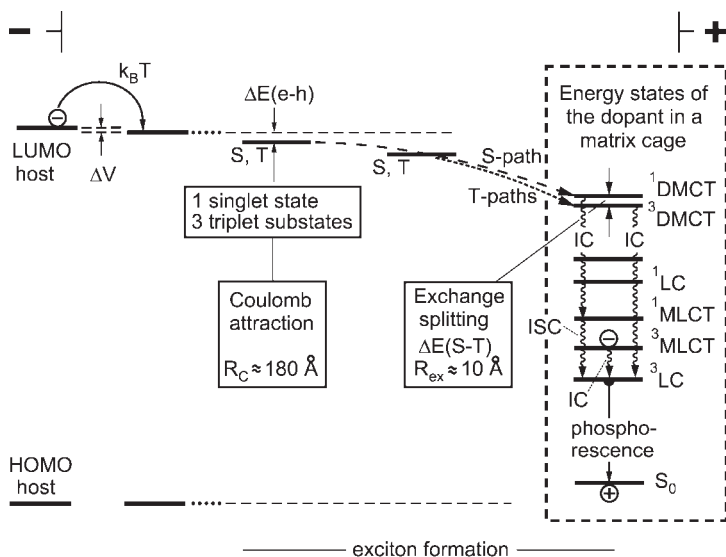
Fig. 1.3 Dynamics of exciton formation. In this model, the exciton formation is induced by Coulomb attraction between electron and hole and starts already at a separation of 150 to 180 Å. The exciton trapping on the emitter complex, which is doped into a host material, occurs via charge transfer states [5, 69]. The wavefunctions of these [1,3]**DMCT** states extend over 10 to 15 Å, and thus involve the triplet emitter itself and the nearest-neighbor host molecules. The exciton trapping processes lead finally to the population of the lowest excited triplet state(s) of the emitter molecule via internal conversion (IC) and intersystem crossing (ISC). The lower-lying states depicted in the dashed frame represent electronic states of the doped emitter molecule itself. Note, this energy level diagram is strongly simplified.

reached when the energy of Coulomb attraction $\Delta E(e-h)$ is of similar size as the thermal energy $k_B T$. Thus, for an estimate of R_C, we can write

$$\Delta E(e-h) = \frac{e^2}{4\pi\varepsilon_0\varepsilon R_C} = k_B T \tag{1}$$

wherein e is the electron charge and ε_0 and ε represent the dielectric constants of the vacuum and the host material, respectively. If a dielectric constant of $\varepsilon = 3$ is assumed, a value of $R_C \approx 180$ Å is obtained for $T = 300$ K. This means that the electron experiences the hole potential even when it is still far from the trapped hole. Both particles are already bound, although a relatively large number of host molecules lies between electron and hole. These two attracting particles may already be called "exciton". However, at this electron–hole separation, the exciton can easily dissociate thermally.

For the further discussion, it is required to take also the spins of both electron and hole into account. The spin of the hole is given by the spin of the residual electron at the emitter molecule. In a quantum mechanical treatment, in which

the bound electron–hole states must be described by four antisymmetrized wave-functions, the spins are coupled and *four* new combined states are obtained – that is, *one* singlet state and *one* triplet state. The triplet consists of *three* substates. These substates differ from each other mainly by their relative spin orientations. An energy splitting between the resulting singlet and triplet states may be neglected at large electron–hole separations. Therefore, the corresponding exciton state – being four times quasi-degenerate – is shown in Fig. 1.3 (middle) just by one energy level, designated as **S, T**. In a statistical limit, all *four* substates of this exciton state will be formed (populated) with equal probability. Consequently, a *population ratio of one to three* of singlet to triplet substates is obtained. For a more detailed discussion concerning the statistically determined population ratio, see Refs. [67, 68].

Driven by the long-range electron–hole Coulomb attraction, the electron moves further on matrix molecules towards the trapped hole. When the electron reaches a distance of 10 to 15 Å – that is, when the electron is approximately located in the first coordination sphere of the emitter dopant – the wavefunctions of electron and hole (or that of the residual electron) begin to overlap slightly [5, 69]. Consequently, the exchange interaction must be taken into account. This quantum mechanical interaction, based on the electron–electron interaction, is responsible for a split-ting $\Delta E(S-T)$ of the singlet state **S** and the triplet state **T** by about twice the exchange integral. In this situation of small wavefunction overlap, $\Delta E(S-T)$ depends approximately exponentially on the electron–hole separation R

$$\Delta E(S-T) \sim \exp(-aR) \tag{2}$$

where a is a constant which depends on the individual wavefunctions of the emitter dopant and the nearest neighbor host molecules. Due to the still relatively large electron–hole separation of 10 to 15 Å with respect to the extension of the wavefunctions, the singlet–triplet splitting is expected to be very small, i.e. much smaller than is typically found for singlet–triplet splittings in molecules.

In the subsequent discussion, we follow further the model first presented by Yersin [5, 69]. According to this approach, it is suitable to analyze the above-described situation also from a slightly different viewpoint. Let us focus only on the emitter complex, the dopant (D), and its first coordination sphere of matrix (M) molecules. In this relatively large dopant–matrix–cage unit, the hole is located in the HOMO of the dopant and the electron resides on the LUMO of a matrix molecule. This situation corresponds to a charge transfer excitation. The corre-sponding states represent dopant-to-matrix charge transfer (DMCT) states. When the spin of the remaining electron in the HOMO of the dopant (D) and the spin of the electron in the LUMO of the matrix (M) molecule as well as the electron–electron interaction are taken into account, ^{1}**DMCT** and ^{3}**DMCT** states are obtained.[5] The corresponding splitting is relatively small due to the weak overlap

---

5) In Section 1.3, we will discuss in more detail, how singlet and triplet states are deduced from HOMO–LUMO excitations.

of the involved molecular orbitals. Clearly, these two states correspond to those exciton states **S** and **T** which are realized at a small electron–hole separation (Fig. 1.3).

The discussion presented above allows us to relate the exciton states with states of a larger molecular unit which consists of the dopant and its matrix cage. This molecular unit exhibits the **¹DMCT** and **³DMCT** states as well as a number of lower-lying states which are largely confined to the dopant (triplet emitter) itself, such as $^{1,3}\pi\pi^*$, ^{1,3}**dd***, ^{1,3}**MLCT** states or adequate mixtures of these (see also Section 1.3).[6] The resulting energy level diagram is depicted in the dashed frame of Fig. 1.3.

Interestingly, on the basis of this energy level scheme, one obtains also information about the relaxation paths from the exciton charge transfer states **¹DMCT** and **³DMCT** to the lower-lying states which largely belong to the emitting center. In particular, the relaxation from the **¹DMCT** state to lower states will be faster within the system of singlet states than making a spin-flip first. This is due to the fact that SOC in organic host molecules (matrix) is relatively small and, thus, intersystem crossing (ISC) is not favored. As consequence, a fast singlet path (internal conversion) is obtained that finally populates the lowest singlet state (Fig. 1.3). Subsequently, the population of this lowest singlet will be followed by ISC processes to the lowest triplet substates. In case of significant singlet–triplet mixing due to SOC, the difference between ISC and internal conversion (IC) might be lost. An initial population of the **³DMCT** state is similarly followed by a very fast relaxation (IC) within the system of triplet states down to the lowest triplet state (Fig. 1.3). The beginning of these relaxation processes corresponds to the singlet and triplet paths in the exciton trapping model, as shown in Fig. 1.3 (compare Refs. [5, 69].) The relaxation times within the singlet and triplet system, respectively, are of the order of 1 ps or faster, while the ISC processes can be slower or of similar time, depending on the importance of SOC and the resulting perturbation of the lowest triplet by singlet admixtures. In a favorable situation, which is usually realized for the organo-transition metal triplet emitters, the ISC rate is very high (order of 10^{12} to $10^{13}\,\mathrm{s^{-1}}$) [70, 71]. Thus, relaxation processes to the lowest triplet state occur mostly with a yield of 100%. This means that all originally formed singlet excitons (25%) and triplet excitons (75%) finally relax into the lowest triplet state of the doped emitter molecule. This process is called *triplet harvesting*. Therefore, under suitable conditions a fourfold larger electro-luminescence efficiency for triplet emitters can be obtained compared to purely organic singlet emitters.[7]

---

6) Within this simple model, it is assumed that the energy states of the matrix (host) molecules lie at relatively high energies and thus do not interfere significantly with the lower-lying states of the dopant (triplet emitter).

7) For purely organic molecules, the radiative triplet–singlet transition rates are, at ambient temperature, orders of magnitude smaller than the corresponding non-radiative rates. Therefore, any excitation energy is converted into heat and the triplets do not emit.

1.3
Electronic Excitations and Excited States

In general, photoluminescence properties are largely determined by the nature of those molecular orbitals (MOs), which are mainly responsible for the electronic ground state and the lowest excited state. These are called "frontier orbitals". Here, the aim is to focus on organo-transition metal complexes, such as Ir(ppy)$_3$, Ir(ppy)$_2$(CO)(Cl), Ir(btp)$_2$ (acac), Pt(thpy)$_2$, [Pt(bpy)$_2$]$^{2+}$, Re(phen)(CO)$_3$(Cl), [Ru(bpy)$_3$]$^{2+}$, [Os(bpy)$_3$]$^{2+}$, etc. For such compounds, different excitations between various MOs have to be taken into account.[8] Specifically, there are

- ligand-centered (LC) excitations, e.g., of π-π* character
- metal-centered (MC) excitations, e.g., of d-d* character
- metal-to-ligand charge transfer (MLCT) excitations, e.g., of d-π* character.

In these descriptions, the asterisk refers to an excited (i.e., a non-occupied) MO.

However, it is not sufficient to restrict the discussion only to HOMO ↔ LUMO transitions. Energetically nearby lying orbitals can also dominate emission properties. Thus, HOMO-1, HOMO-2, LUMO+1, LUMO+2, etc. have also to be included in the set of frontier orbitals. In this section, we discuss properties of the above-mentioned excitations and trends concerning the resulting electronic states, such as singlet and triplet states. These are many-electron states and can be significantly mixed by SOC. This presentation will initially be carried out using rather simple models, although more detailed descriptions are also presented later on to illustrate the nature of the set of low-lying states and the importance of SOC.

1.3.1
Ligand-Centered (LC) Transitions: States and Splittings

In a series of compounds, the lowest excited states are determined dominantly by MOs which can be well described by the π-HOMO and the π*-LUMO of the organic ligands, since MOs of other than π and π* character lie at significantly lower and higher energies, respectively. Thus, it is suitable to confine a first-order approach only to the HOMO-LUMO excitation(s) of the ligand(s). Clearly, these orbitals and their energies are somewhat altered by coordination of the ligand(s) to the positively charged metal. Usually, this leads to a red shift (i.e., a shift to lower energy) of the corresponding transitions of the order of 10^3 cm^{-1} (≈0.12 eV).[9] Of course, the metal induces further changes, and in particular changes which

---

8) For completeness, also ligand-to-metal-charge-transfer (LMCT) excitations, e.g., of π-d* character, are mentioned. However, for the compounds of interest in this chapter the corresponding excited states exhibit relatively high energies and therefore, are not discussed at this point.

9) 1 eV ≙ 8068 cm^{-1}.

HOMO-LUMO diagram   **Energy state diagram**
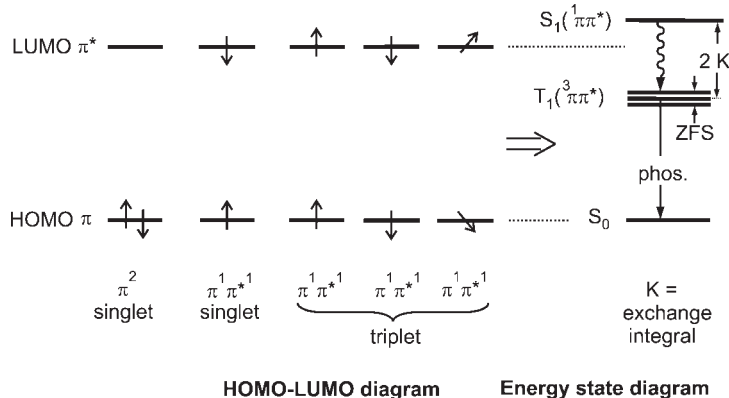
Fig. 1.4 Comparison of a HOMO-LUMO diagram to an energy state description. The configuration π^2 leads to the ground state S_0, while the configuration $\pi^1\pi^{*1}$ gives four different excited states, one singlet S_1 and one triplet T_1 which consists of three substates. By taking the change of electron–electron interaction for both configurations into account, usually a significant $\Delta E(S_1 - T_1)$ splitting is obtained. For ligands which are in the focus of this contribution, $\Delta E(S_1 - T_1)$ can be as large as $10^4\,cm^{-1}$. The three triplet substates of T_1 exhibit a splitting, the zero-field splitting (ZFS). The corresponding value can be used to assess a triplet emitter compound for its application in an OLED. (See Section 1.4 and Fig. 1.11.)

result from SOC, such as changes of radiative and non-radiative rates as well as of energy splittings. (These important effects will be discussed later in Sections 1.3.3.3 and 1.4.2.) For completeness, it should be mentioned that, for this class of compounds, the lowest excited state (the triplet state) is largely localized on one ligand (compare Refs. [72–74] and Section 1.4.2).

For most molecules, which are of interest here, the HOMO is occupied by two electrons and the compound is diamagnetic. Thus, the two electrons carry opposite spins (α and β spins). This situation is described by an electron configuration of π^2. The resulting state, the ground state, is a spin singlet S_0 ($^1\pi^2$) (Fig. 1.4, left). When, after a HOMO–LUMO excitation the spins are also taken into account, one obtains for the excited state configuration $\pi^1\pi^{*1}$ four different situations (Fig. 1.4, middle). An excitation without a spin flip gives an excited singlet, while an excitation with a spin flip gives a triplet due to three different possible spin orientations. This description is similar to the one discussed in Section 1.2.2. Again, in a quantum mechanical treatment, four different (antisymmetrized) wavefunctions must be formulated to describe the resulting singlet and the three triplet states (compare , for example, Ref. [75], p. 163).

In the simple HOMO–LUMO model, all four states, which result from the $\pi^1\pi^{*1}$ configuration, still have the same energy and are degenerate. However, from spectroscopic investigations it is known that the splitting between the excited singlet state and the excited triplet state is usually significant. For example, for the ligands discussed in this chapter, it can be as large as $10^4\,cm^{-1}$ ($\approx 1.24\,eV$). There-

fore, the HOMO–LUMO model must be improved, specifically, by taking changes of the electron–electron interaction into account which are connected with the HOMO–LUMO excitation. This results in the energy state diagram (or the many electron state diagram) as depicted in Fig. 1.4 (right-hand side). A quantum mechanical consideration shows that the triplet state T_1 (or $^3\pi\pi^*$), consisting of three substates, is stabilized by an energy given by a difference of Coulomb integrals, while the singlet state S_1 (or $^1\pi\pi^*$) is destabilized relative to the triplet state by twice the exchange integral

$$K = const \times \left\langle \pi(r_1)\pi^*(r_2) \left| \frac{1}{r_{12}} \right| \pi(r_2)\pi^*(r_1) \right\rangle \tag{3}$$

wherein π and π^* are the HOMO and LUMO wavefunctions, r_1 and r_2 represent the electron coordinates, and r_{12} the separation between the two electrons (compare, for example, Ref. [75], p. 174). The exchange interaction is a quantum mechanical effect which takes the spin correlation into account. This means that two electrons with opposite spin orientations (in the singlet state) have a larger probability of being found near to each other than two electrons with the same spin orientation (the triplet state). In the latter situation, the two electrons have the tendency to avoid each other. Hence, the average electron–electron repulsion is smaller and thus the triplet has a lower energy than the singlet state (Fig. 1.4).

The exchange integral – as displayed in Eq. (3) in a shortened notation (compare, for example Ref. [76]) – is given in this elementary chapter, since it permits important qualitative conclusions to be reached by considering the overlap of the involved wavefunctions. The following conclusions fit to the spin correlation model discussed above. First, with an increasing conjugation length of the π and π^* orbitals, the exchange integral K becomes smaller. For example, in purely organic molecules, the singlet-triplet splitting $\Delta E(^1\pi\pi^* - {}^3\pi\pi^*)$ decreases in the series of benzene, naphthalene, anthracene from $\approx 18\,000\,cm^{-1}$ ($\approx 2.2\,eV$) [77], to $12\,300\,cm^{-1}$ ($\approx 1.5\,eV$) [78], and to $10\,500\,cm^{-1}$ ($\approx 1.3\,eV$) [78]. Second, when the MOs are mainly confined to different spatial regions of the molecule, the MO overlap can become very small, and consequently so also can the integrals. For example, for n-HOMO to π^*-LUMO excitations, which are relevant for organic molecules with heteroatoms, such as benzophenone, the singlet-triplet splitting $\Delta E(^1n\pi^* - {}^3n\pi^*)$ amounts to only $1750\,cm^{-1}$ ($\approx 0.22\,eV$) [79]. Equivalent considerations apply also to states of organo-transition metal complexes. Small admixtures of metal d-orbital or MLCT character to the ligand-centered states will increase the spatial extension of the wavefunctions and thus reduce the exchange integral – that is, the singlet–triplet splitting between the perturbed $^1LC(^1\pi\pi^*)$ and $^3LC(^3\pi\pi^*)$ states. For example, $\Delta E(^1\pi\pi^* - {}^3\pi\pi^*)$ of the free ligand H(2-thpy) is of the order of $10^4\,cm^{-1}$ (1.24 eV), as can be estimated from the data given in Ref. [80], whereas for Pd(thpy)$_2$ (doped into n-octane) $\Delta E(^1LC - {}^3LC)$ is significantly smaller and amounts only to $5418\,cm^{-1}$ [70]. This tendency becomes even more obvious for $^1MLCT - {}^3MLCT$ splittings.

The triplet state is always split into three substates, at least, if the symmetry of the molecule is sufficiently low.[10] This is valid for most organo-transition metal compounds that are of interest for OLED applications. The splitting occurs also at zero magnetic field, and is therefore referred to as zero-field splitting (ZFS) (Fig. 1.4). For $^3\pi\pi^*$ states of organic molecules, the ZFS is mainly induced by spin–spin interactions of the two unpaired electrons in the triplet state (compare, for example, Refs. [77, 81, 82]). This interaction leads to ZFS-values of the order of $0.1\,cm^{-1}$ ($\approx 1.2 \times 10^{-5}\,eV$). For largely ligand-centered ^{3}**LC** states of organo-transition metal complexes, the value of ZFS lies in the same order of magnitude. For example, for $[Rh(bpy)_3]^{3+}$, the total ZFS has been determined as $0.125\,cm^{-1}$ ($\approx 1.55 \times 10^{-5}\,eV$) [83, 84], and for $Pd(qol)_2$ to about $0.25\,cm^{-1}$ ($\approx 3.1 \times 10^{-5}\,eV$) [85]. However, SOC carried by metal d-orbitals can drastically increase the magnitude of ZFS, as found for ^{3}**MLCT** states. (Compare especially Sections 1.3.3, 1.4, and Refs. [5, 70, 72–74].) In this situation, the small contribution from spin–spin interactions can be neglected.

For completeness it is mentioned that, although the ZFS values of only slightly perturbed ^{3}**LC**($^3\pi\pi^*$) states of organo-transition metal compounds are of similar size, as found for purely organic molecules, the metal can manifest itself already drastically by increasing radiative and/or non-radiative rates. This is a consequence of a relatively small but still very effective SOC. For instance, the population of the triplet from an excited singlet state by ISC becomes orders of magnitude faster. Thus, the quantum efficiency of ISC reaches 100%. For example, for $Pd(thpy)_2$ [70] and $Pt(qol)_2$ [86], which both emit from ^{3}**LC** states, we determined ISC relaxation times of $\tau(ISC) = 800\,fs$ and $500\,fs$, respectively. Moreover, the radiative $T_1 \rightarrow S_o$ rate also becomes orders of magnitude larger than are found for purely organic molecules. Thus, mostly the triplet substates can easily be excited resonantly [87, 88].[11] This implies that the increased radiative rate can dominate over the non-radiative deactivation. As a consequence, even high-emission quantum yields can occur. For example, for $Re(phbt)(CO)_4$ – a ^{3}**LC**($^3\pi\pi^*$) emitter with a ZFS much smaller than $1\,cm^{-1}$ – the photoluminescence quantum yield ϕ_{PL} amounts to 27% at ambient temperature in ethanol (Ar saturated) [88]. However, the emission decay time of $\tau(300\,K) = 21\,\mu s$ is still relatively long, and therefore the compound is probably not well suited for OLED applications [88] but probably well suited as an oxygen sensor molecule. It will be shown below that the size of ZFS represents a good measure of the importance of MLCT character in the lowest triplet state and that, for the most efficient OLEDs, emitter compounds are used which exhibit

---

10) Molecules which belong to a point group symmetry lower than C_3 do not exhibit any state degeneracies (apart from Kramer's degeneracies of molecules with uneven numbers of electrons).

11) For several compounds only two of the three triplet substates of dominant ^{3}**LC** character

can be excited directly from the ground state, while the transition to the third substate is still largely forbidden. This has, for example, been shown for $Pd(thpy)_2$ [70], $Pt(qol)_2$ [71], $Ir(ppy)_2(CO)(Cl)$ [87], and $Re(phbt)(CO)_4$ [88].

ZFS-values of about $10 \, cm^{-1}$ or larger ($1.2 \times 10^{-3} \, eV$). (Compare Sections 1.3.3, 1.4, and Refs. [5, 70, 72–74].)

1.3.2
Metal-Centered Transitions and States

A large number of compounds is known, for which the absorption and luminescence properties are determined by metal-centered (MC) excitations. For example, complexes or doped materials of main-group metal ions with s^2 ground state and sp excited state configurations have low-lying MC excitations (e.g., $[PbCl_4]^{2-}$) [89–91]. Lanthanide compounds with f-f excitations also exhibit MC transitions (e.g., Eu^{3+}, Tb^{3+} compounds; see e.g., Refs. [92–96]). A short summary of compounds which exhibit different types of MC transitions is found in Ref. [91]. However, within the scope of the present chapter, we are interested in properties of d-d* excitations and related states. Well-known compounds with optical properties dominated by such MC excitations include ruby (Cr^{3+} in Al_2O_3) [97, 98]) and $[Cr(urea)_6]^{3+}$ [99–101], both with $3d^3$ configurations. The latter compound is among the first synthesized transition metal complexes with organic ligands. Further examples include $[MnCl_4]^{2-}$ [102], $[Co(CN)_6]^{3-}$ [103, 104], and $[PtCl_4]^{2-}$ [104, 105], in which the metal centers have $3d^5$, $3d^6$, and $5d^8$ configurations, respectively.

The d-orbitals and d-d* transitions are indirectly of importance for OLED materials. This is due to two different effects. On the one hand, the quantum mechanical mixing of d-orbitals of open-shell transition metal ions, such as Pt^{2+}, Ir^{3+}, or Os^{2+}, can induce the required SOC to make the formally forbidden triplet–singlet transitions sufficiently allowed (see next section). On the other hand, states which result from d-d* excitations often quench the emission efficiently, and therefore should not lie in a thermally accessible energy range of the emitting states (see below).

Usually, a description of dd* states is carried out by use of group theory and the symmetry of the complex. An introduction to ligand field or crystal field theory is found in most inorganic chemistry textbooks (e.g., see Refs. [106, 107]), whilst more detailed descriptions are found in Refs. [108, 109]. At this point, we present only a brief illustration of excitations (in particular of HOMO–LUMO excitations), provide some comments regarding the resulting states, and highlight the relevance of these states for triplet emitters in OLEDs. In this section, only those compounds having central metal ions with a d^6 configuration, such as Ir^{3+}, Ru^{2+}, Os^{2+}, Re^+, and W^0, will be discussed as examples. These metals/ions tend to prefer a sixfold coordination which includes, for example, three bidentate chelates. In a first-order approach, the complexes can be described in an octahedral symmetry (symbol: O_h) of the first coordination-sphere around the central metal. In this symmetry, the d-orbitals split into two sets of orbitals (Fig. 1.5). The magnitude of splitting is given by the ligand field strength, and amounts to Δ which is – for historic reasons – often named 10 Dq. The Dq parameter varies with the ligand according to the spectrochemical series (compare , for example Refs. [107], p. 221, and [108], p. 84):

$$J^- < Br^- < S^{2-} < Cl^- \approx \underline{S}CN^- < N_3^- < (C_2H_5O)_2PS_2^- < NO_3^- < F^-,$$
$$< (C_2H_5)_2NCS_2^- < (NH_2)_2C\underline{O}\,(urea) < OH^- < C_2O_4^{2-} < H_2\underline{O} < \underline{N}CS^- <$$
$$NH_3 < C_5H_5N < NH_2-CH_2-CH_2-NH_2 \approx SO_3^{2-} < NH_2OH < bpy <$$
$$phen < NO_2^- < PPh_3 < CH_3^- \approx C_6H_5^- < ppy^- < carbene^- < CN^- < CO$$
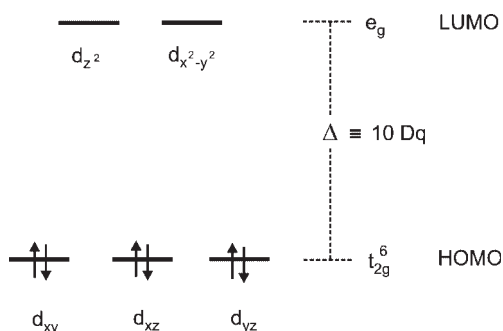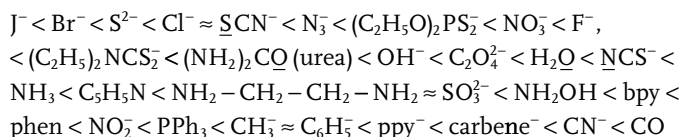
Fig. 1.5 Splitting of d-orbitals in an octahedral ligand field with O_h symmetry. For a high ligand field (large Δ or Dq value), the ground state configuration is t_{2g}^6.

This series gives the approximate ordering of the Dq parameter.[12] In particular, ligands found on the left-hand side induce a small ligand field splitting (they are called "weak" ligands), while those on the right-hand side of the series are "strong" ligands with large ligand field splittings. These splittings depend also on the central metal ion. For OLED applications, one is usually interested in compounds with large ligand field splittings to avoid emission quenching processes at ambient temperature (see below). Consequently, it is useful to have some rules of thumb for the development of efficient triplet emitters. Such rules should help to estimate changes of Dq values with chemical variations. Indeed, if a reference compound is available, then specific trends can be given (Ref. [108], p. 83):

1. Compounds with the same ligands and the same central metal ion exhibit a 40–80% Dq increase, when the metal oxidation changes from 2+ to 3+.

2. Compounds with the same ligands experience an increase of Dq by 30–40%, when the metal of the first row of transition metal ions in the Periodic Table is replaced by one of the second row, and similarly if a second-row metal ion is replaced by one of the third row.

3. For compounds with mixed ligands (heteroleptic compounds), the Dq value can be estimated from the average ligand field strength.

12) According to different binding properties in different complexes, the sequence of the ligands in the spectrochemical series may slightly vary. In particular, the positions of (ppy)$^-$ and carbenes$^-$ are given only tentatively.

From Fig. 1.5 it is clear that compounds with a d^6 electron configuration and a large ligand field splitting have a t_{2g}^6 ground state configuration (in an O_h parent group approach). Thus, the t_{2g} sub-shell is filled. This leads to a low-spin compound with a (totally symmetric) diamagnetic ground state ($^1A_{1g}$ in O_h). From the excitations $t_{2g}^6 \rightarrow t_{2g}^5 e_g^1$ and $t_{2g}^6 \rightarrow t_{2g}^4 e_g^2$ etc., the excited states can be determined by taking electron–electron interaction into account (e.g., see Refs. [108, 109]). Usually, this is carried out by use of group theoretical methods. For example, for the $t_{2g}^5 e_g^1$ configuration, two triplets and two singlets are obtained. In a group theoretical notation (in the O_h group), the terms ordered according to increasing energy are $^3\mathbf{T_{1g}}$, $^3\mathbf{T_{2g}}$, $^1\mathbf{T_{1g}}$, and $^1\mathbf{T_{2g}}$. Further excitations such as $t_{2g}^6 \rightarrow t_{2g}^3 e_g^3$ lead to a number of additional energy states. All of the resulting states are summarized in the well-known Tanabe–Sugano diagrams, which are found in many inorganic textbooks (e.g., see Ref. [106], p. 1189, and Ref. [107], p. 683).

It is an important property that all of these excited states have distinctly larger metal–ligand bond lengths than the ground state. This can simply be deduced by visualizing the effects of the HOMO–LUMO excitation of $t_{2g}^6 \rightarrow t_{2g}^5 e_g^1$. It corresponds to a population of an anti-bonding e_g orbital from a non-bonding t_{2g} orbital. Therefore, the metal–ligand bond lengths increase, and additionally the potential surfaces become less stiff (smaller force constants). Consequently, the potential surfaces of the ground and of the excited states can cross at relatively low energies. These changes can have significant effects on non-radiative deactivation processes. This is due to a resulting distinct overlap of lower-lying vibrational wavefunctions of the excited electronic state with high-energy vibrational wavefunctions of the electronic ground state. Accordingly, the corresponding Franck–Condon factors which govern the rate of the radiationless deactivation from the excited state to the ground state, increase (compare , for example, Refs. [78], p. 71 and [110], p. 129). As consequence, the radiationless deactivation rate can become significantly larger than the radiative rates, and an emission is prevented ("quenched").

In summary, a population of the excited $^{1,3}\mathbf{dd^*}$ states of transition metal compounds with a d^6 configuration often leads to emission quenching at ambient temperature. Although, for OLED applications, the $^{1,3}\mathbf{dd^*}$ states do not have to be characterized in detail, it is still required to take care of these quenching states. Energetically, they should not lie too close to the emitting states of, for example, ^{3}LC/^{3}MLCT character (compare next section). An energy difference of 3000 to 4000 cm^{-1} (0.37 to 0.50 eV) is required to obtain a sufficiently small Boltzmann factor, and thus a sufficiently small population of the quenching state, at ambient temperature. Note that arguments similar to those developed for central metal ions with a d^6 configuration also hold for compounds with a d^8 configuration, such as Pt(II) or Ir(I) complexes.

However, a strategy which aims to maximize the ligand field strength in order to shift the $^{1,3}\mathbf{dd^*}$ states to an energy as high as possible will fail. For a very high Dq value, the occupied d-orbitals may be stabilized too much. This can have the consequence that a necessary MLCT admixture to the emitting triplet becomes too small and that the resulting compound turns into a less effective ^{3}**LC** emitter. Exactly this behavior is observed for Re(I) complexes. Re(phen)(CO)$_3$(Cl) shows a

relatively good OLED performance [111, 112] which is related to a large ZFS of 50 cm^{-1} and thus to a large MLCT perturbation of the emitting triplet. For Re(phbt)(CO)$_4$, on the other hand, with ligands of an on-average much higher Dq value, the emitting state turns out to be a ^{3}**LC** state (ZFS << 1 cm^{-1}) [88]. For this latter material, only a very weak OLED performance was observed [88]. Obviously, a good balance between MLCT character of the emitting state and a high energy separation of the quenching state must be found.

1.3.3
Metal-to-Ligand Charge Transfer/Ligand-Centered Transitions: States in Organo-Transition Metal Triplet Emitters

In the two previous sections, we have discussed well-seizable models with respect to the frontier orbitals and the resulting energy states. The situation becomes a little more complicated, when additionally MLCT transitions are taken into account. In particular, the interplay – that is, the quantum mechanical mixing between ^{3}**LC**, ^{1}**LC**, ^{3}**MLCT**, and ^{1}**MLCT** states – determines the properties of the lowest triplet state and thus also the applicability of an emitter material in an OLED. For example, a compound with an almost "pure" ^{3}**LC** emitting state would presumably not be well suited as an OLED emitter, whereas a complex with a mixed emitting ^{3}**LC**/^{3}**MLCT** state might be a very good candidate. Such mixtures can occur, for instance, for a d-orbital admixture to the HOMO of mainly π character, that is, for πd → π* transitions. (Compare the examples given at the end of Section 1.3.2 with those later in this section.) The inherent reason is SOC which, for the compounds under consideration in this contribution, is carried by the metal 5d-orbitals.

It is the subject of this section, to illustrate how many-electron states result from frontier orbitals, such as HOMO-1, HOMO, LUMO, LUMO+1, etc., and to discuss the properties of electronic states, the MLCT character, SOC routes, triplet state splittings, and radiative rates. In a first step (see Section 1.3.3.1.), a very simple model is presented with a strongly restricted number of MOs. Yet, this model is well suited for describing some trends. In a second step (see Section 1.3.3.2.), it will be shown that a more realistic model requires the inclusion of a larger number of active frontier orbitals, and a very large number of states in the optical energy range is obtained. Finally, in Section 1.3.3.3, the important effects induced by SOC are discussed.

1.3.3.1 Introductory MO Model and Energy States
Figure 1.6 illustrates a strongly simplified MO diagram for an organo-transition metal compound, and how the MOs relate to the energy states. In this model, one single ligand π-orbital (HOMO-1) and one d-orbital (HOMO) are considered as the occupied frontier orbitals. Both of these are occupied with two electrons. The lowest unoccupied orbital is given by a single π*-MO. An additional unoccupied d*-orbital, also displayed in the figure, is not further discussed, as it is assumed that its energy and those of the resulting states are sufficiently high and thus have no importance for this introduction (but compare Section 1.3.2). In summary, this
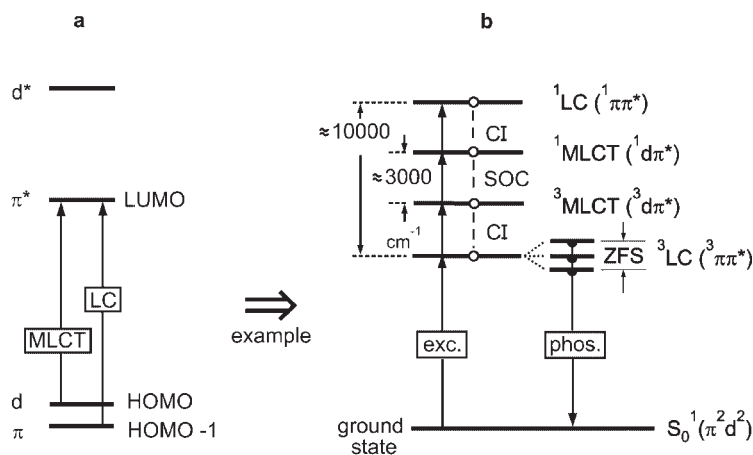
HOMO-LUMO model   Simplified energy state model

Fig. 1.6 (a) Introductory MO model for a compound with single π, d, and π* orbitals and the respective MLCT and LC transitions. It is assumed that the d*-orbital lies at a significantly higher energy and that it does not lead to low-lying energy states. (b) From the two MLCT and LC transitions eight energy states are obtained: two singlets **¹LC** and **¹MLCT**, three **³LC**, and three **³MLCT** substates. The states can experience substantial quantum mechanical mixings due to configuration interaction (CI) and spin–orbit coupling (SOC). SOC induces the zero-field splitting (ZFS). After these quantum mechanical mixings, the terms singlet, triplet, LC, MLCT can no longer be regarded as "pure" classifications. For details, see Section 1.3.3.3. Here, we illustrate a situation in which the order of the d- and π-orbital does not necessarily lead to the same sequence of the corresponding triplets. It is remarked that the SOC path is only symbolized in (b), realistic requirements are discussed later (compare Fig. 1.9).

three-orbital model is characterized by just two excitations: one MLCT and one LC transition between the corresponding MOs (Fig. 1.6a).

In Section 1.3.1, it has been shown that each of these excitations results in one singlet and one triplet state. The electronic ground state is a singlet (Fig. 1.6b). Furthermore, according to the distinct spatial differences of the respective electron distributions in the involved orbitals, the exchange interactions – and thus the singlet–triplet splittings – differ strongly [see Eq. (3)]. For the π- and π*-orbitals of the ligands which are in the focus of this chapter, $\Delta E(^1\pi\pi^* - {}^3\pi\pi^*)$ is of the order of $10^4\,cm^{-1}$ (1.24 eV). On the other hand, $\Delta E(^1MLCT - {}^3MLCT)$ is much smaller, as the electron–electron interaction of the two electrons being distributed over the d-orbital and the spatially separated π*-orbital, respectively, is weaker. According to Ref. [70], $\Delta E(^1MLCT - {}^3MLCT)$ is about $3000\,cm^{-1}$ (0.37 eV), or even smaller. With this information, an energy level diagram is obtained as depicted in Fig. 1.6b.

Although the model for organo-transition metal compounds as presented in Fig. 1.6 is greatly simplified, it may still be used for an orientation and some general conclusions or helpful rules of thumb:

- In general, a HOMO/LUMO model does not contain singlet or triplet states.
- The relative positions of HOMO-1 and HOMO do not allow to predict the energy sequence of the corresponding triplet states directly. Figure 1.6 shows that **³LC** can be the lowest state, although the HOMO–HOMO-1 sequence may suggest that **³MLCT** might be the lowest state. This behavior is related to the difference in energy between HOMO and HOMO-1, which may be small in comparison to the energy difference between the exchange integrals.
- The number of states is quite large, even for this simple model. Eight states are obtained, two singlets (**¹LC, ¹MLCT**) and $2 \times 3 = 6$ triplet substates (**³LC, ³MLCT**) (neglecting double excitations, for example, to $d^2(\pi^*)^2$ configurations).
- The eight states can mix quantum mechanically induced by electron–electron interaction between the different configurations (configuration interaction, CI) and by SOC.[13] Especially, SOC between **¹MLCT** and **³MLCT** and CI between **³MLCT** and **³LC** will alter the properties of the lowest triplet state (see Section 1.3.3.3). A splitting of the zero-order **³LC** state into substates (ZFS) will result, the transitions between these and the ground state will become more allowed, the emission decay time will decrease, the photoluminescence quantum yield is mostly increased, and the spectra change, etc. (see Section 1.4.2. and Refs. [5, 70, 73, 74]).

1.3.3.2 Extended MO Model and Energy States

The simple model as discussed in Section 1.3.3.1 will certainly not be applicable for describing experimental results with sufficient quantitative precision. In particular, the number of electronic states is far from being realistic. This message is illustrated in Fig. 1.7 on the basis of two approaches, applied to discuss the example of Ir(ppy)$_3$. In a first introductory step, the discussion is restricted only to MLCT transitions; this approach is displayed in the inner frame of Fig. 1.7. Some group theory will help to find the number of d- and π^*-orbitals and, subsequently, the number of resulting energy states. In the electronic ground state, Ir(ppy)$_3$ has C$_3$ point group symmetry [113] and probably also in the lowest triplet state [114, 115].[14] In C$_3$ symmetry, the 5d-orbitals of t$_{2g}$ representation split into

---

13) SOC is particularly important for third row transition metal complexes with open 5d shells. It increases approximately with Z^4, Z being the atomic number.

14) In Refs. [70, 73, 74, 114] it has been shown by low-temperature investigations that in homoleptic organo-transition metal compounds the lowest triplet state is

delocalized over the three ligands and the metal. However, this result is only valid for a sufficiently large metal-induced ligand–ligand coupling. This coupling increases with a growing MLCT character of the lowest triplet state. A measure for this property represents the amount of ZFS (see also Sections 1.3.3.3 and 1.4). For example,
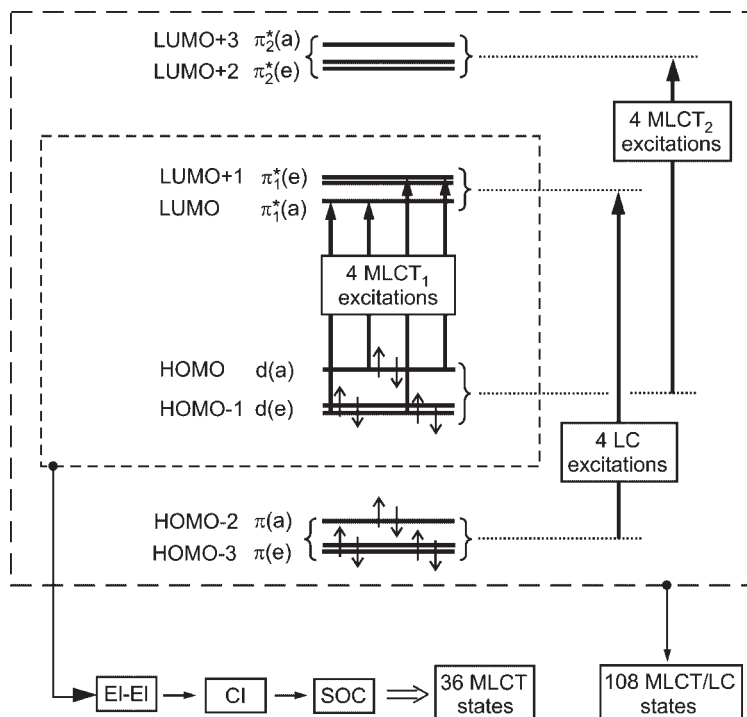
Fig. 1.7 Frontier orbitals, MLCT, and LC excitations and resulting number of states. Inner frame: In a simple model system for an organo-transition metal compound, such as Ir(ppy)$_3$ with a C$_3$ symmetry, the four MLCT$_1$ excitations lead to 36 states. Outer frame: An extension of the number of frontier orbitals by additional inclusion of four LC and four MLCT$_2$ transitions results in 108 states. About 70 states are expected to be within 8000 cm^{-1} (1 eV), just above the lowest triplet state [124].

two sets of d-orbitals – that is, a non-degenerate *a* and a doubly degenerate *e* representation. Due to the 5d^6 configuration of Ir^{3+}, these orbitals are occupied by two and four electrons, respectively, giving the HOMO and HOMO-1 (Fig. 1.7, inner frame). The adequate, symmetry-adapted lowest unoccupied MOs result from the π_1^*-orbitals of the three (ppy)-ligands. Combinations of these lead, similarly, to one MO of *a* and two MOs of *e* representation, giving the LUMO and LUMO+1. It should be noted that these group theoretical considerations do not allow determination of the sequence of the respective MOs, as shown in Fig. 1.7. The energy ordering of the MOs has been adopted from Ref. [116]. It should be

for Pt(thpy)$_2$ and [Ru(bpy)$_3$]$^{2+}$ with ΔE(ZFS) = 16 cm^{-1} [70] and 61 cm^{-1} [73, 74], respectively, we have shown that the excited state is delocalized, whereas for [Pt(bpy)$_2$]$^{2+}$ or [Rh(bpy)$_3$]$^{3+}$ with ΔE(ZFS) <1 cm^{-1}, we found ligand-centered localized situations [73, 74]. For Ir(ppy)$_3$, ΔE(ZFS) amounts to 83 cm^{-1} [115]. According to this large value – and thus very large MLCT character – the assumption of having a delocalized triplet is well justified. Consequently, the C$_3$ symmetry is probably maintained for the lowest excited triplet.

further mentioned that a similar model was presented more than 20 years ago for $[Ru(bpy)_3]^{2+}$ (compare Refs. [117, 118] and Ref. [74], p. 174).

According to the four different MOs shown in the inner frame of Fig. 1.7, four $MLCT_1$ transitions are obtained.[15] The effects of electron–electron interaction give the excited states (see Sections 1.3.1 and 1.3.3.1). For example, the HOMO–LUMO transition of type $d(e)^4 d(a)^2 \rightarrow d(e)^4 d(a)^1 \pi_1^*(a)^1$ leads to one singlet and one triplet – that is, to four states including triplet substates. Similarly, the three other $MLCT_1$ transitions $d(e)^4 d(a)^2 \rightarrow d(e)^4 d(a)^1 \pi_1^*(e)^1$, $d(e)^4 d(a)^2 \rightarrow d(a)^2 d(e)^3 \pi_1^*(a)^1$, and $d(e)^4 d(a)^2 \rightarrow d(a)^2 d(e)^3 \pi_1^*(e)^1$ result in an additional 32 states (including sub-states and counting doubly degenerate states twice). The resulting states of same symmetry will interact quantum mechanically due to CI, which is a consequence of electron–electron interaction. Moreover, SOC between singlets and triplets, as well as between different triplets, will lead to further energy shifts and splittings. This quantum mechanical mixing strongly alters the photophysical properties of the triplet substates, and is also the origin of the ZFS. As a consequence of these mixings, assignments as singlets or triplets (e.g., as ^{1}**MLCT** or ^{3}**MLCT**) might not be fully adequate, especially if extensive mixings, such as in third period transition metal compounds, occur. However, the triplet character of the very lowest substate is usually almost maintained (see Section 1.3.3.3).

The total number of states, which result from the four $MLCT_1$ electron transitions, is 36. For Ir(ppy)$_3$, if having a C$_3$ symmetry, 12 states would be doubly degenerate (representation E) and 12 would be non-degenerate (representation A). (Compare the situation described for $[Ru(bpy)_3]^{2+}$ in Ref. [74], p. 175.) If, on the other hand, Ir(ppy)$_3$ sits, for example, in a host cage which allows only a lower symmetry than C$_3$ – as would be expected for a complex doped into an amorphous matrix – the doubly degenerate **E** states will split. A splitting of **E** states would also be expected, if the complex were to be distorted in the excited state to a lower symmetry. This can occur due to polarization effects. Such distortions may be dissimilar for different excited states of the same complex. The 36 states are expected to lie within an energy range of about 4500 cm^{-1} (0.56 eV) (compare Ref. [116], Table 1.3). In this context, reference should also be made to the valuable model calculation carried out by Kober and Meyer [118] for $[Ru(bpy)_3]^{2+}$.

Clearly, chemical intuition tells us that the model presented above (the inner frame of Fig. 1.7) will not lead to a successful description of organo-transition metal compounds. Specifically, their properties are extensively influenced or even dominated by ligand-centered contributions (compare , for example, Refs. [71–74, 82–88, 116–134]). These LC components are also very important for Ir(ppy)$_3$ [116, 123, 124]. Hence, the lower-lying occupied π-MOs and the higher-lying unoccupied π*-MOs must also be taken into account. Combinations of the respective ligand orbitals lead to occupied $\pi(a)$ and $\pi(e)$ as well as to unoccupied $\pi_2^*(e)$ and $\pi_2^*(a)$-MOs (Fig. 1.7, outer frame). The inclusion of the π_2^*-MOs is justified by estimates

---

15) These MLCT transitions can be described by the configuration $d^6 \rightarrow d^5(\pi^*)^1$. Transitions of the type of $d^6 \rightarrow d^4(\pi^*)^2$ lie at much higher energy, and are not taken into account in this model.

carried out for $[Ru(bpy)_3]^{2+}$, for which the corresponding π_2^*-MOs lie only about $6000\,cm^{-1}$ (0.74 eV) above the π_1^*-MOs (see Refs. [117, 118, 132] and [74], p. 175). Consequently, a more realistic model is extended by several additional frontier orbitals and the respective electron transitions. Beside the four $MLCT_1$ transitions, shown in the inner frame of Fig. 1.7, the extended model additionally provides four LC and four $MLCT_2$ transitions. Following the quantum mechanical procedures outlined above, $3 \times 36 = 108$ states are obtained. For completeness, it should be noted that 36 of these states are doubly degenerate E states, which split into 72 substates, if $Ir(ppy)_3$ does not sit on a strict C_3 site. Interestingly, Nozaki's [124] theoretical approach can only achieve results which are comparable to experimental values, by taking as many as 50 singlets and 50 triplets (200 states) into account. Thus, the large number of states within a relatively small energy range, giving a high density of states, is a property that is characteristic of the systems under consideration.

Obviously, the total number of states depends on the number of chromophoric ligands. For example, for $Ir(ppy)_2(LL)$ with only two chromophoric (ppy) ligands, one obtains only 64 non-degenerate electronic states in an equivalent model and energy range (2×24 MLCT and 16 LC states). In general, one electronic excitation between two non-degenerate MOs gives one singlet and one triplet state with three substates – that is, four states. Thus, the number of resulting states can easily be determined, if the number of frontier orbitals is increased.

It should be emphasized that the resulting states are mostly quantum mechanically mixed. For example, the lowest triplet substates contain triplet and singlet admixtures of higher-lying states, of which the singlets carry the allowednesses of the transitions to the electronic ground state. These admixtures determine ZFSs, radiative rates, emission quantum yields, and spectral forms (see Sections 1.3.3.3 and 1.4.2).

Although the model presented has not been quantitatively applied to organo-transition metal compounds, it has the advantage of fitting well to the intuition of organo-metal chemistry. It offers good insight into the different MOs involved, their spatial distributions, and the resulting states. Thus, trends may be identified and can be used to predict changes in photophysical properties according to chemical variations, such as the effects of electron-donating or -withdrawing substitutions, variations of conjugation lengths, influence of the ligand field strength, variation of the oxidation and reduction potentials (compare, for example, Ref. [133]). Even predictions of SOC routes are possible (compare Sections 1.3.3.3 and 1.4.2). However, for quantitative descriptions, the current research is mainly based on *ab-initio* methods, such as time-dependent density functional theory (TDDFT) [116, 120–128] or CASSCF/CASPT2 [119]. Although the predictions of transition energies, singlet–triplet oscillator strengths, number of low-lying triplet states, and ZFS energies are mostly not very reliable, or may even not be determined at all, the calculated results are still helpful in understanding certain photophysical trends. However, the predictions become much more realistic when SOC effects are taken into account, and this point forms the subject of the next section.

1.3.3.3 **Spin–Orbit Coupling, Triplet Substates, Zero-Field Splitting, and Radiative Decay Rates**

The emission properties of an organo-transition metal complex are largely determined by the individual characteristics of the three substates of the lowest triplet term T_1. The substates do not represent "pure" states, but contain contributions from singlets and triplets of other configurations due to CI and SOC. In particular, the mixed-in singlet components provide the required radiative rates and allowednesses of the optical transitions to the electronic singlet ground state. Further, specific interactions with higher-lying states lead to individual, but different, energy stabilizations of the substates. Thus, a splitting of the T_1 state, the ZFS, results.[16] It is subject of the subsequent considerations to develop some insight into the quantum mechanical description of these effects [82, 122, 124, 134–136].

The energies of the triplet substates can be calculated – at least in principle – by use of second order spin–orbit perturbation theory. The zero-order wavefunctions ϕ_{S_n}, ϕ_{T_n} and energies E_{S_n}, E_{T_n} of singlet and triplet states are considered as known before inclusion of spin–orbit interaction. They are, for example, determined by DFT calculations [122, 127, 128, 134]. The energies $E(i)$ of the resulting (perturbed) triplet substates of T_1 with i = I, II, III can be expressed by:[17),18)]

$$E(i) = E_{T_1} + \sum_{S_n} \frac{\left|\left\langle \phi_{S_n}\left|\hat{H}_{SO}\right|\phi_{T_1(i)}\right\rangle\right|^2}{E_{T_1} - E_{S_n}} + \sum_{T_n} \frac{\left|\left\langle \phi_{T_n(j)}\left|\hat{H}_{SO}\right|\phi_{T_1(i)}\right\rangle\right|^2}{E_{T_1} - E_{T_n}} \qquad (4)$$

wherein $\hat{H}_{SO}$ is the SOC Hamiltonian. S_n and $T_n(j)$ refer to those singlet states and triplet substates j, which have the same symmetry representation as the individual substate **I**, **II**, and **III**, respectively. Otherwise, the matrix elements of Eq. (4) vanish.[19)]

The energies $E(I)$, $E(II)$, and $E(III)$ of the individual triplet substates **I**, **II**, and **III** will energetically be stabilized, though differently, depending on the magnitudes of the respective matrix elements. Distinct shifts of $E(I)$, $E(II)$, and $E(III)$ can only occur, if SOC between the involved states is significant. This is only possible, if ^{1,3}MLCT (^{1,3}dπ*) contributions are present in the respective wavefunctions. The resulting differences of the energy shifts give ΔE(ZFS). In other words, an experimentally determined value of a relatively large ΔE(ZFS) displays directly the importance of ^{1,3}MLCT (^{1,3}dπ*) components in the wavefunction of the corresponding

---

16) The small effects of spin–spin coupling, giving splittings of the order of $0.1\,\text{cm}^{-1}$, are neglected here.

17) Note that the DFT calculations do not yield the exact states of the systems including full configuration interaction (CI) before taking SOC into account; hence, additional CI may lead to further mixing and energy shifts.

18) We simplify the notation in view of the fact that one has to use degenerate perturbation theory. Also note that first-order contributions are vanishing.

19) The matrix elements can only be non-zero, if the grouptheoretical product of all components contains the totally symmetric representation. Since $\hat{H}_{SO}$ is totally symmetric, the two interacting states have to belong to the same representation. For experts, it should be noted that we refer here to representations of the double group.

triplet state.[20] Clearly, this is connected with all other photophysical implications, which are induced by the involved MLCT character, such as an increase in the radiative rate and the photoluminescence quantum efficiency, and/or changes of the emission spectra (see below and Section 1.4.2). "Relatively large" in this context means $\Delta E(\mathrm{ZFS}) \gtrsim 2\,\mathrm{cm}^{-1}$ – that is, the ZFS is more than one order of magnitude larger than splittings induced by spin–spin interactions.

The radiative rate constant $k^{\mathrm{r}}(i)$ of the transition from triplet substate i, with i = I, II, III, to the electronic ground state represents a crucial quantity for the luminescence of an organometallic compound. The rate can be expressed by use of perturbation theory as [77, 134].

$$k^{\mathrm{r}}(\mathrm{i}) = \mathrm{const} \times \bar{\nu}^3 \times \left| \sum_{\mathrm{S_n}} \frac{\left\langle \phi_{\mathrm{S_n}} \middle| \hat{\mathrm{H}}_{\mathrm{SO}} \middle| \phi_{\mathrm{T_1(i)}} \right\rangle}{E_{\mathrm{T_1}} - E_{\mathrm{S_n}}} \times \left\langle \phi_{\mathrm{S_0}} \middle| e\mathbf{r} \middle| \phi_{\mathrm{S_n}} \right\rangle \right|^2 \qquad (5)$$

where $\bar{\nu}$ is the transition energy in cm^{-1} and $e\mathbf{r}$ the electric dipole operator. The zero-order wavefunctions $\phi_{\mathrm{S_n}}$ and the zero-order energies $E_{\mathrm{T_1}}$, $E_{\mathrm{S_n}}$ have been defined above. Similarly as discussed before, the wavefunction $\phi_{\mathrm{S_n}}$ of a higher-lying singlet state must have the same symmetry representation as the respective triplet substate **I, II,** or **III**. Otherwise $\left\langle \phi_{\mathrm{S_n}} \middle| \hat{\mathrm{H}}_{\mathrm{SO}} \middle| \phi_{\mathrm{T_1(i)}} \right\rangle$ vanishes, and mixing between the corresponding states does not occur.

The radiative rate $k^{\mathrm{r}}(i)$ depends not only on the values of the matrix elements $\left\langle \phi_{\mathrm{S_n}} \middle| \hat{\mathrm{H}}_{\mathrm{SO}} \middle| \phi_{\mathrm{T_1(i)}} \right\rangle$ – that is, the spin–orbit interactions of the respective triplet substate with higher-lying singlets – but also on the allowednesses of the transitions from $\mathbf{S_0}$ to the interacting singlet states $\mathbf{S_n}$. The corresponding transition dipole moments can be calculated by using DFT approaches [122, 123, 128].

With an increase of the radiative decay rate k^{r}, usually also an increase of the photoluminescence quantum yield ϕ_{PL} is found, according to

$$\phi_{\mathrm{PL}} = \frac{k^{\mathrm{r}}}{k^{\mathrm{r}} + k^{\mathrm{nr}}} \qquad (6)$$

wherein k^{r} can be expressed for one specific triplet substate by use of Eq. (5). k^{nr} is the non-radiative decay rate, which depends on the energy gap between the emissive triplet state and the electronic ground state (the "energy gap law"), the number of coupling and deactivating vibrational modes, and on the coupling strength of the corresponding modes. For further information, see Refs. [78, 79].

In Section 1.3.3.2 it was shown that a very large number of excited states exists in an adjacent small energy range. In principle, these can all contribute to the lowest triplet substates via spin–orbit interaction, if the corresponding symmetries

20) It should be noted that small $\Delta E(\mathrm{ZFS})$ values might, hypothetically, result also from large, but near-equal energy shifts of all three substates due to significant ^{1,3}MLCT components in each case. Corresponding mixings to the sublevels of $\mathbf{T_1}$, at least of singlet character, would, for example, directly be displayed in shortening of the emission decay times (at low temperature). However, such a situation has never been found experimentally [5, 70, 73, 74].

fit. However, many of these SOC routes contribute little, and they can be neglected compared to a few dominating spin–orbit interactions. Interestingly, in a series of investigations, relatively simple rules for important SOC routes have been elucidated [82, 122, 136] and recently summarized by K. Nozaki et al. [122]. These considerations are based on estimating the magnitudes of matrix elements. In particular, if they do not involve one-center integrals on the transition metal center, the magnitudes are small.[21] [137] For example, SOC between ^{3}**LC($^3\pi\pi$*)** and ^{1}**MLCT(^{1}dπ*)** states involves only two-center integrals on the metal. Consequently, SOC between these states is small and therefore, cannot be responsible for the relatively large effects of SOC found in organo-transition metal compounds [82, 136] (Fig. 1.8a). On the other hand, one-center SOC integrals can induce effective SOC between ^{1}**MLCT(^{1}dπ*)** and ^{3}**MLCT(^{3}dπ*)** states [82, 136], as is symbolized in Fig. 1.8b. (Note that additional requirements have to be taken into account, see Fig. 1.9.)

From experimental investigations it is known, however, that many organo-transition metal complexes have (perturbed) ^{3}**LC($^3\pi\pi$*)** states as lowest triplets which exhibit relatively high radiative transition rates to the electronic ground state. Obviously, these triplets involve significant ^{1}MLCT(^{1}dπ*) components (compare, for example, Refs. [5, 70, 73, 74]). Therefore, another mechanism must be effective. Indeed, according to Miki et al. [82, 122, 136], an important indirect SOC mixing route is efficient. It is proposed that the ^{1}**MLCT(^{1}dπ*)** state interacts by SOC with the ^{3}**MLCT(^{3}dπ*)** state which on its part interacts by CI with the ^{3}**LC($^3\pi\pi$*)** state (CI results from electron–electron interaction). According to Nozaki's investigations [122, 124], this indirect coupling route is the dominant mechanism for the intense photoluminescence of many complexes. The corresponding SOC route is shown in Fig. 1.8c, and was depicted earlier in Fig. 1.6b.

To summarize, an effective SOC between triplet substates and higher-lying states can lead to significant magnitudes of the matrix elements $\langle \phi_{S_n} | \hat{H}_{SO} | \phi_{T_1(i)} \rangle$, for example, and thus lead to appreciable ΔE(ZFS) values [Eq. (4)] and radiative rates k^r (i) to the ground state [Eq. (5)], in contrast to zero-order ^{3}**LC($^3\pi\pi$*)** states.

With regards to the discussed SOC route between ^{3}**MLCT(^{3}dπ*)** and ^{1}**MLCT(^{1}dπ*)** (Fig. 1.8b), a restriction must be accounted for. Again, based on the arguments of the dominance of one-center integrals, a ^{3}**MLCT** state only couples effectively with a ^{1}**MLCT** state, if the configurations of both states involve the *same π*- orbital*, but *different d-orbitals* [137]. For quasi-octahedral d^6 complexes, these d-orbitals belong to the t$_{2g}$ manifold. This additional requirement for an effective SOC is illustrated

---

21) From the usual rules for evaluating matrix elements of one-electron operators between Slater determinants (see Ref. [137], Table 2.3), one may conclude that single excitations $\psi_1 \rightarrow \psi_2^*$ and $\psi_3 \rightarrow \psi_4^*$ can only lead to non-vanishing contributions of SOC (approximated as a one-electron operator), when $\psi_1 = \psi_3$ or $\psi_2^* = \psi_4^*$. Thus, for example, SOC between states resulting from d $\rightarrow \pi$* and $\pi \rightarrow$ d* vanishes. On the other hand, for d $\rightarrow \pi$* and $\pi \rightarrow \pi$* excitations to the same π* orbital, matrix elements of the form $\langle d | \hat{H}_{SO} | \pi \rangle$ are obtained, while for d$_1 \rightarrow \pi$* and d$_2 \rightarrow \pi$* excitations, integrals of the form $\langle d_1 | \hat{H}_{SO} | d_2 \rangle$ occur. The former is at least a two-center integral and, hence, small, while the latter is a one-center integral and can be large. Note, that diagonal matrix elements of the type $\langle d_1 | \hat{H}_{SO}(\text{metal}) | d_1 \rangle$, involving the same d$_1$ orbital, vanish.
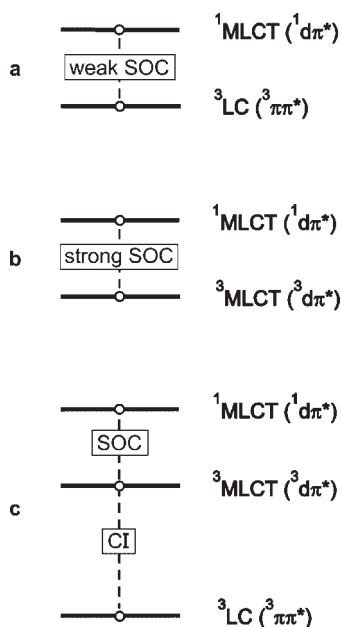
Fig. 1.8 Spin–orbit coupling (SOC) routes. (a) SOC between ^{3}**LC($^3\pi\pi^*$)** and ^{1}**MLCT(^{1}dπ^*)** does not involve one-center integrals on the transition metal center, and is therefore weak. (b) SOC between ^{3}**MLCT(^{3}dπ^*)** and ^{1}**MLCT(^{1}dπ^*)** states can be strong under specific conditions, which are discussed in Fig. 1.9. (c) Indirect SOC mixing routes can be efficient, if the ^{1}**MLCT(^{1}dπ^*)** state interacts with the ^{3}**MLCT(^{3}dπ^*)** state, which couples with ^{3}**LC($^3\pi\pi^*$)** by configuration interaction (CI). Compare also the Refs. [82, 122, 136].

in Fig. 1.9. For complexes with a distorted O_h symmetry, the three t_{2g}-orbitals can split and three MLCT transitions are obtained, if we consider in this simplifying illustration only one π^*-orbital, for example of a compound with just one chromophoric ligand (Fig. 1.9a) These transitions lead to three ^{1}**MLCT** and three ^{3}**MLCT** states (12 substates; compare Section 1.3.3.1). In Fig. 1.9b, the states are depicted in separate diagrams to illustrate the required coupling routes. According to footnote 21 and to Ref. [122], SOC between states of the same configuration is weak, while it can be significant between singlets and triplets of different configurations.[22]

Theoretical studies of phosphorescence properties of organo-transition metal compounds require a thorough inclusion of effects of SOC, in particular with respect to the lowest triplet states. A recent investigation by Nozaki [124] approaches this challenge by using – as an example – a strongly simplified model system for

---

22) It should be noted again that SOC between the corresponding states is only possible, if they belong to the same irreducible representation (same symmetry). Often, the point group symmetry of a complex is only slightly distorted to C_1. In this case, however, symmetry restrictions of the parent group might still be valid.
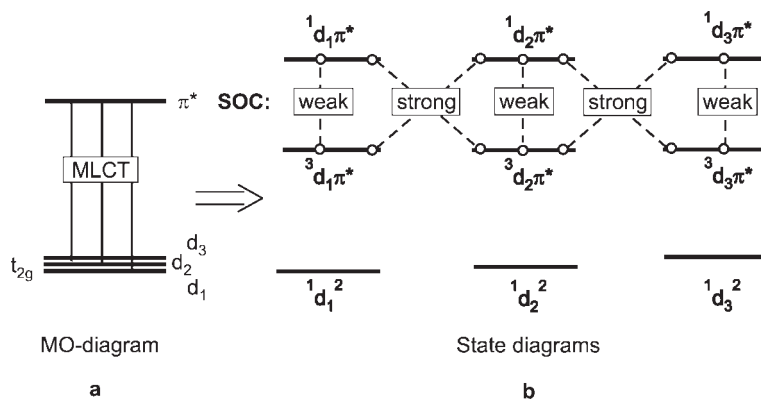
Fig. 1.9 Spin–orbit coupling (SOC) between ^{3}**MLCT**(^{3}dπ*) and ^{1}**MLCT**(^{1}dπ*) states. SOC can be effective under specific conditions; that is, it can be strong, if the same π*-orbital but different d-orbitals are involved, otherwise SOC is weak. These considerations are based on estimates of SOC matrix elements (see Refs. [82, 122, 136] and Footnote 21). Note that, in addition to the depicted coupling routes, strong SOC can also occur between ^{3}d$_3\pi$* and ^{1}d$_1\pi$* states. This illustration is greatly simplified, as only one π*-orbital is taken into account in this model.

Ir(ppy)$_3$. In these studies, zero-order wavefunctions and energies were obtained from TDDFT calculations. Subsequently, spin–orbit interactions were included as perturbation. The evaluation of the SOC matrix elements was carried out by considering only one-center spin–orbit integrals in the scope of the arguments presented above and depicted in Figs. 1.8 and 1.9. The resulting description of properties of the three lowest-lying triplet substates fits in several respects to experimental observations. From the very long emission decay time of substate **I** of $\tau_I = 145\,\mu s$, this state can be assigned to be an almost pure triplet [115]. Indeed, according to Ref. [124], substate **I** consists of about 92% of the T_1 contribution (which carries very high MLCT character) and of components of higher-lying triplets (T_4: ≈5% and T_6: ≈2%) but – in the scope of this approximation – of no singlet character.

It seems to be a more general property of organo-transition metal compounds that the lowest triplet substate **I** represents an almost pure triplet. This has been observed experimentally for many compounds (compare the reviews in Refs. [5, 70, 73, 74]), and also found by *ab-initio* calculation for [Ru(bpy)$_3$]$^{2+}$, [Os(bpy)$_3$]$^{2+}$, and Ir(ppy)$_3$ [124]. Presumably, this behavior is indicative of an energetically proximate higher-lying triplet, which is responsible for stabilizing substate **I**, obviously without providing singlet character.

The situation concerning singlet admixtures is different for the two higher-lying substates **II** and **III** of Ir(ppy)$_3$ [124]. These represent also mainly T_1 substates (**II**: ≈92% and **III**: ≈94%), and have different contributions of admixed higher-lying triplet components (**II**: ≈5% T_4, **III**: ≈2% T_6). However, the substates **II** and **III** contain in addition small admixtures of higher-lying singlets. Specifically, these

admixtures provide the required allowednesses for efficient emission ($II \approx 2\%$ S_4, III: $\approx 1\%$ S_5). The calculated prediction of the sequence of radiative rates $k^r(I) < k^r(II) < k^r(III)$ is also in accordance with the experimentally determined emission decay rates. We found $k(I) = 6.9 \times 10^3\,s^{-1}$, $k(II) = 91 \times 10^3\,s^{-1}$, and $k(III) = 1330 \times 10^3\,s^{-1}$ (compare Section 1.6 and Ref. [115]). The fact that $k^r(III) > k^r(II)$ in spite of a somewhat larger singlet admixture in substate II can be explained by a larger oscillator strength (allowedness) of the transition $S_0 \rightarrow S_5$ in comparison to $S_0 \rightarrow S_4$ (see Fig. 1.3 of Ref. [124]).

Calculations as carried out in Ref. [124] led also to interesting conclusions concerning the number of states, which was the subject of discussion in Section 1.3.3.2. For example, according to Ref. [124], an "accurate" calculation requires the inclusion of up to 200 states (50 singlets and 50 triplets). Further, for the example of Ir(ppy)$_3$, it has been found [124] that about 70 states lie within a range of $8000\,cm^{-1}$ (1 eV) above the emitting triplet. This corresponds to a range from $\approx 20\,000\,cm^{-1}$ (500 nm) to $28\,000\,cm^{-1}$ (357 nm).

For the application of an organo-transition metal compound in an OLED, it is required that the radiative rate of the transition from the lowest triplet state to the singlet ground state is large. This is connected with a short emission decay time and – if non-radiative deactivation is not dominating – with a high photoluminescence quantum yield. From this requirement, it can be concluded that SOC routes to the lowest triplet state – i.e. to the specific triplet substates – have to be as effective as attainable. Presumably, when paying attention to the relatively simple rules for efficient SOC routes (Figs. 1.8 and 1.9), and when applying adequate chemical engineering, it might be possible to obtain compounds with distinctly improved efficiencies. This subject is re-addressed in Section 1.4.2.

1.4
Zero-Field Splitting (ZFS) of the Emitting Triplet, Photophysical Trends, and Ordering Scheme for Organo-Transition Metal Compounds

The emission of organo-transition metal compounds discussed in the scope of this chapter occurs from the lowest excited triplet state T_1 to the electronic ground state S_0. Without including spin–orbit coupling, this transition is strictly forbidden. However, for third row transition metal compounds, SOC to the lowest triplet can be very important and can induce drastic effects, such as substantial splittings of the triplet into substates and an increase of radiative decay rates. Due to this latter effect, the phosphorescence quantum yields may reach almost 100%. Several other photophysical properties of the compounds will also be altered distinctly (see below). In Section 1.3.3.3, we have already illustrated SOC routes which are responsible for these effects. In particular, changes of the radiative rates of transitions from the three T_1 substates I, II, and III to the electronic ground state S_0 **(0)** can be calculated using Eq. (5), whilst splitting of the T_1 state (ZFS) can be determined using Eq. (4). However, sufficiently accurate quantum mechanical calculations, which include SOC, remain difficult to perform. Thus, an empirical ordering

scheme can be helpful for assessing the materials' properties. We have shown that especially the size of the total ZFS [ΔE(ZFS)] represents a valuable parameter to assess or even predict the important photophysical properties of organometallic compounds [5, 70, 74, 114]. According to Eq. (4) and the subsequent discussions, ΔE(ZFS) displays directly the importance of ^{1,3}MLCT (^{1,3}dπ*) components in the corresponding triplet state. In other words, a value of ΔE(ZFS) of more than 1–2 cm^{-1} is connected with ^{1,3}dπ* components in the wavefunctions of the triplet substates. In particular, significant ΔE(ZFS) values are representative of significant ^{1,3}MLCT components in the corresponding triplet state. Usually, states with very large MLCT character (very large ΔE(ZFS) values) are termed as MLCT states, although it is generally known that substantial π *and* π* character of the ligand(s) is also involved. These considerations are summarized schematically in Fig. 1.10.
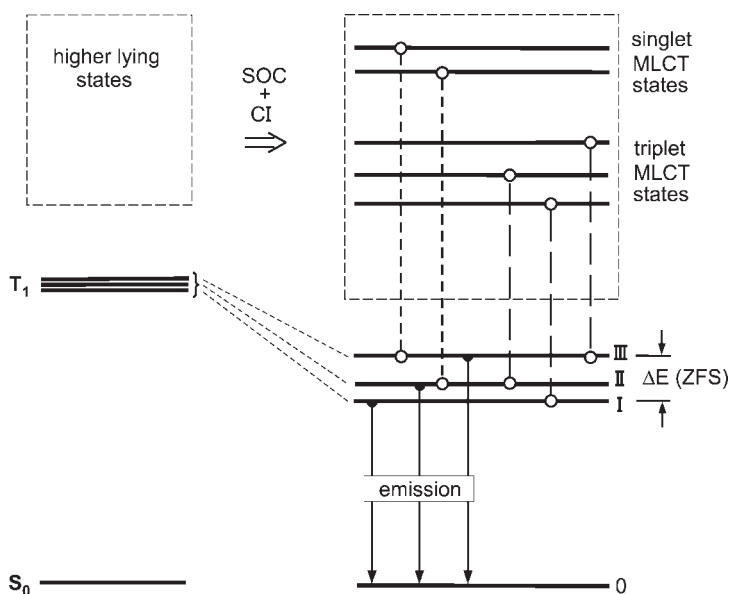
Fig. 1.10 Schematic diagram showing that spin–orbit coupling (SOC) and configuration interaction (CI) of the three triplet substates **I**, **II**, and **III** with higher-lying states result in energy shifts, splittings ΔE(ZFS) of the lowest triplet **T$_1$** state – also at zero magnetic field – and changes of the **T$_1$** $\leftrightarrow$ **S$_0$** transition probabilities. Rules for the required mixings are discussed in Sections 1.3.3.3 and 1.4.2. Specifically, the allowedness of a transition between a triplet substate and the electronic ground state is governed by an admixture of ^{1}MLCT character to the corresponding substate according to Eq. (5). Consequently, the magnitudes of the radiative rates are determined by the significance of the ^{1}MLCT admixtures and by the involved (admixed) singlet state – that is, its transition probability to the electronic ground state. Frequently, the very lowest triplet substate does not contain distinct singlet components and therefore is usually an almost pure triplet and hence long-lived (compare Refs. [5, 70, 73, 74, 124]).

1.4.1
Ordering Scheme

Figure 1.11 summarizes a series of compounds which are arranged according to an increasing ΔE(ZFS) of the emissive triplet state; the corresponding chemical

211	$[Os(bpy)_3]^{2+}$	[156]
186	$[Os(phen)_3]^{2+}$	[155]
cm^{-1}		
83	Ir(ppy)$_3$	[115]
67	Ir(4,6-dFppy)$_2$(pic)	[143]
66	Ir(piq)$_2$(acac)	[154]
64	$[Os(phen)_2(dppee)]^{2+}$	[153]
61	$[Ru(bpy)_3]^{2+}$	[151, 152]
50	Re(phen)(CO)$_3$(Cl)	[150, 111]
38	Pt(bhq)$_2$	[149]
32	Ir(piq)$_3$	[154]
32	Pt(ppy)$_2$	[148]
28	Pt(ph-salen)	[145]
25	Ir(btp)$_2$(acac)	[147]
19	Pt(ONN-t-Bu)Cl	[145]
17.5	Pt(dphpy)(CO)	[146]
17	Pt(Me$_4$-salen)	[145]
16	Pt(thpy)$_2$	[70, 144]
8	Pt(4,6-dFppy)(acac)	[143]
6.4	Pt(ppy)(CO)(Cl)	[142]
3.8	Pt(thpy)(CO)(Cl)	[141]
1.0	Ir(ppy)$_2$(CO)(Cl)	[87]
	Pt(qtl)$_2$	[140]
	Re(phbt)(CO)$_4$	[88, 111]
	Pt(qol)$_2$	[71]
	Pd(thpy)$_2$	[70, 139]
	Pd(qol)$_2$	[85]
	$[Pt(bpy)_2]^{2+}$	[139]
0.1	$[Rh(bpy)_3]^{3+}$	[83, 138]

Left axis labels: Increasing MLCT contribution in the emitting triplet state; ^{3}MLCT states; ^{3}LC($\pi\pi^*$) – ^{3}MLCT states; ^{3}LC($\pi\pi^*$) states; ΔE (ZFS)

Fig. 1.11 The compounds are arranged according to an increasing splitting of the emitting triplet state into substates (zero-field splitting, ZFS). The splitting reflects the ^{1,3}MLCT character in the corresponding wavefunctions. The related structure formulae are shown in Fig. 1.12. The listed references refer to reports in which the corresponding ΔE(ZFS) values have been provided. Note that the size of ZFS can also depend on the individual environment of the emitter compound (compare Section 1.10). For most emitters the positions of compounds with ΔE(ZFS) ≤ 1 cm^{-1} are only roughly estimated.

$[Rh(bpy)_3]^{3+}$ $\qquad$ $[Pt(bpy)_2]^{2+}$ $\qquad$ $Pd(qol)_2$ $\qquad$ $Pd(thpy)_2$

$Pt(qol)_2$ $\qquad$ $Re(phbt)(CO)_4$ $\qquad$ $Pt(qtl)_2$

$Ir(ppy)_2(CO)(Cl)$ $\qquad$ $Pt(thpy)$ $(CO)(Cl)$ $\qquad$ $Pt(ppy)$ $(CO)(Cl)$ $\qquad$ $Pt(4,6\text{-}dFppy)$ $(acac)$

$Pt(thpy)_2$ $\qquad$ $Pt(Me_4\text{-}salen)$ $\qquad$ $Pt(dphpy)(CO)$
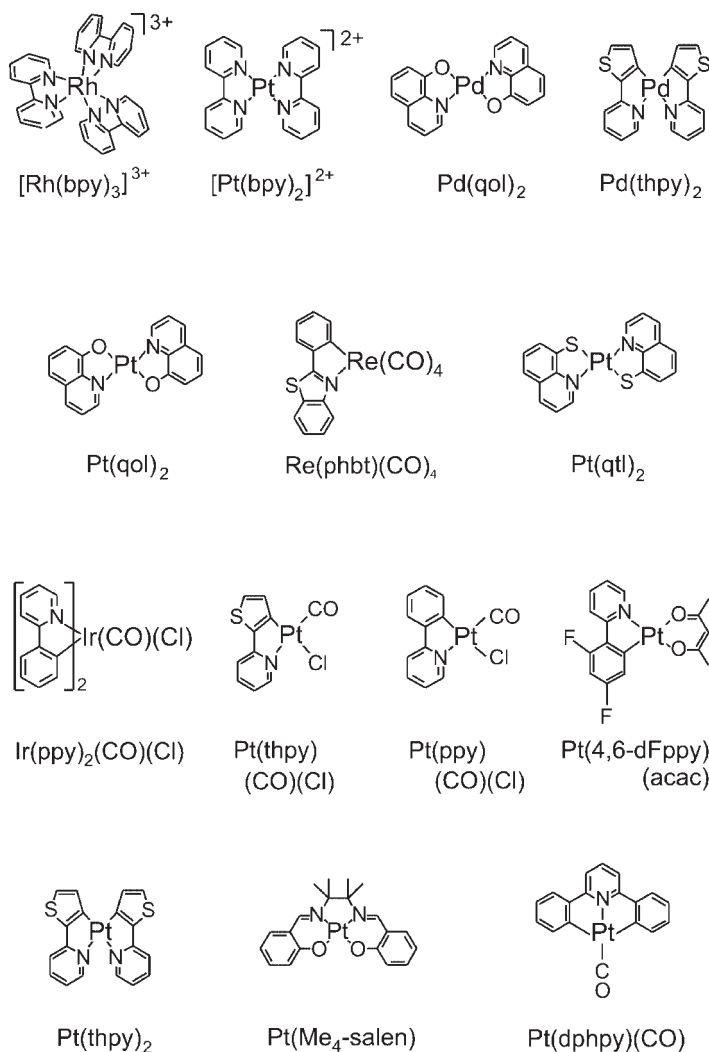
Fig. 1.12 Structure formulae of emitter compounds shown in Fig. 1.11 and discussed in this chapter.

structures are illustrated in Fig. 1.12. The ΔE(ZFS) values have been determined mostly by use of optical high-resolution spectroscopic methods. A representative example, of how this procedure is carried out, is discussed in Section 1.5 for $Pt(thpy)_2$ with an intermediate magnitude of ZFS. On the other hand, compounds with very small ΔE(ZFS) values of much less than $1\,cm^{-1}$, such as $[Rh(bpy)_3]^{2+}$ [83, 84, 138], $Pd(qol)_2$ [85], and $Pd(thpy)_2$ [139] have been investigated by using double-resonance methods, in particular optically detected magnetic resonance (ODMR). Details of the procedure are provided elsewhere (e.g., [83] and references therein.)

Pt(ONN-t-Bu)Cl   Ir(btp)₂   Pt(ph-salen)   Pt(ppy)₂
                       (acac)

Ir(piq)₃   Pt(bhq)₂   Re(phen)   [Ru(bpy)₃]²⁺
                                (CO)₃(Cl)

[Os(phen)₂   Ir(piq)₂(acac)   Ir(4,6-dFppy)₂(pic)
(dppee)]²⁺

Ir(ppy)₃   [Os(phen)₃]²⁺   [Os(bpy)₃]²⁺
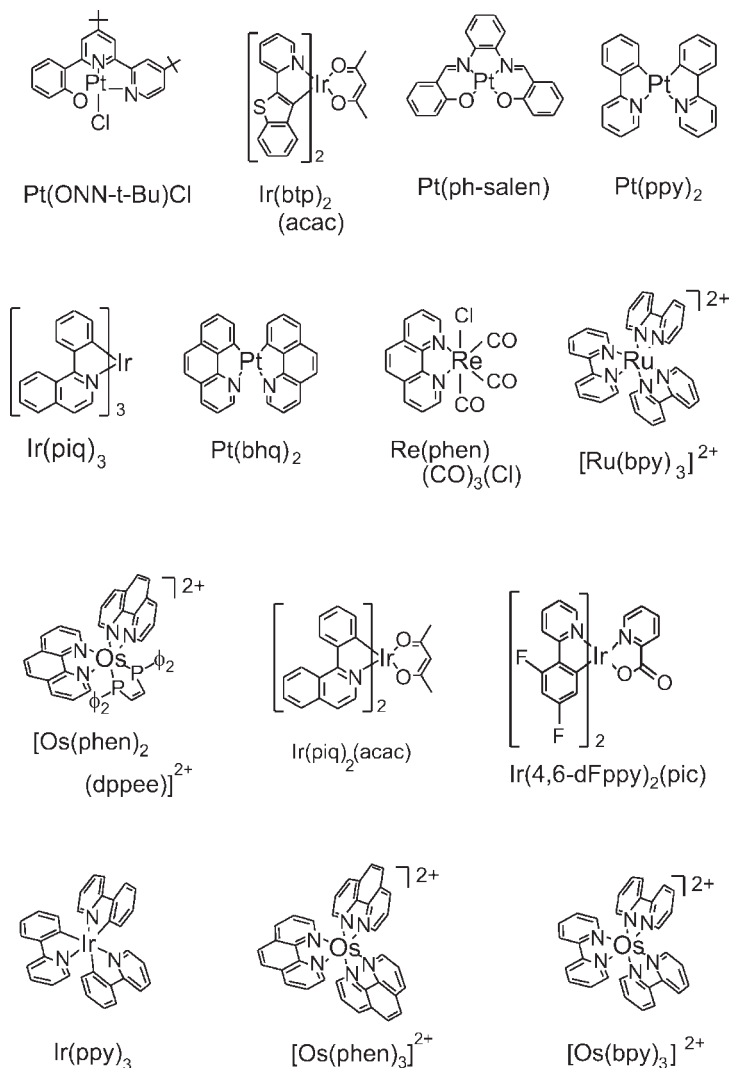
Fig. 1.12 *Continued*

In several cases, however, it is not possible to obtain highly resolved spectra, despite the ZFS being large. This behavior is connected to a relatively large inhomogeneity of the emitter compound in the applied host and/or to a large electron–phonon coupling of the singlet–triplet transition (compare Section 1.11). In these cases, an indirect method of determining the temperature dependence of the emission decay time was applied, and from a fit of these data valuable information concerning the triplet state can be obtained. A corresponding example is presented in Section 1.6, illustrating the properties of Ir(ppy)₃.

According to the discussions presented above, an increasing ZFS of the emitting triplet state, as shown in the ordering scheme of Fig. 1.11, is connected with an increasing MLCT component in this triplet state. Compounds with ΔE(ZFS) values of less than ≈1 cm^{-1} exhibit largely ligand-centered **^{3}LC($^3\pi\pi^*$)** emitting states. The triplets of complexes in the intermediate range cannot be regarded as pure **^{3}LC** states. The **^{3}LC($^3\pi\pi^*$)** character is significantly perturbed by ^{1,3}dπ^* admixtures. Those emitters with larger ΔE(ZFS) values 50 cm^{-1} than about are normally termed and assigned as **^{3}MLCT** emitters. Extensive literature concerning MLCT assignments is available, for example for [Ru(bpy)$_3$]$^{2+}$ [117, 118, 124, 132, 157, 158], Ir(ppy)$_3$ [115, 116, 123, 124], and [Os(bpy)$_3$]$^{2+}$ [70, 74, 124, 125, 159].

1.4.2
Photophysical Properties and ZFS

The magnitude of the ZFS parameter increases in the range shown in Fig. 1.11 by more than a factor of 2000. This is a result of essential changes of the wavefunctions of the lowest triplet substates due to increasing SOC of $^3\pi\pi^*$ states with ^{1,3}dπ^* states. The effectiveness of this coupling is given by specific SOC routes which are discussed in Section 1.3.3.3.

An interesting trend is found, when inspecting the ordering scheme of Fig. 1.11, which shows that large ΔE(ZFS) values (e.g., >40 cm^{-1}) have not yet been found for quasi-square planar organometallic Pt(II) compounds, whereas for quasi-octahedral Re(I), Os(II), Ir(III) – and even for second row transition metal compounds, such as Ru(II) complexes – much larger ΔE(ZFS) values are not unusual. This behavior can be explained on the basis of the SOC considerations carried out in Section 1.3.3.3. For *quasi-octahedral complexes*, it follows from Fig. 1.9 (middle) that the lowest **^{3}MLCT(^{3}dπ^*)** state can experience strong SOCs with **^{1}MLCT(^{1}dπ^*)** states (and other **^{3}MLCT(^{3}dπ^*)** states, not depicted in Fig. 1.9) which involve different d-orbitals of the t$_{2g}$ manifold. For compounds with distorted O$_h$ symmetry, the resulting orbital energies are still rather proximate. On the other hand, for *quasi-square planar* Pt(II) complexes, the lowest **^{1}MLCT** and **^{3}MLCT** states result from the same $d_{z^2} \rightarrow \pi^*$ excitation. Therefore, SOC between these states can be neglected, since for an effective SOC, the involvement of different d-orbitals is required (see Section 1.3.3.3). For square-planar complexes, the corresponding candidates would be the d$_{xz}$, d$_{yz}$ orbitals; however, these are energetically significantly separated from the d_{z^2} orbitals. Estimates of the orbital energies lead to differences of about 4000 cm^{-1} (0.5 eV) or more for ligands with high D$_q$ values [160, 161]. Accordingly, the energy denominator, which also governs the effectiveness of SOC [see Eqs. (4) and (5)], is significantly larger than for octahedral compounds. These considerations are summarized schematically in the upper part of Fig. 1.13, specified as MLCT range, for ^{1,3}**MLCT** states of octahedral and square planar complexes, respectively.

For many compounds, however, the lowest triplet is largely of LC($\pi\pi^*$) parentage. This is found, for example, for Pt(thpy)$_2$ (see Refs. [70, 119] and Section 1.5) and for Ir(btp)$_2$(acac) (see Ref. [147] and Section 1.8). Again schematically, this
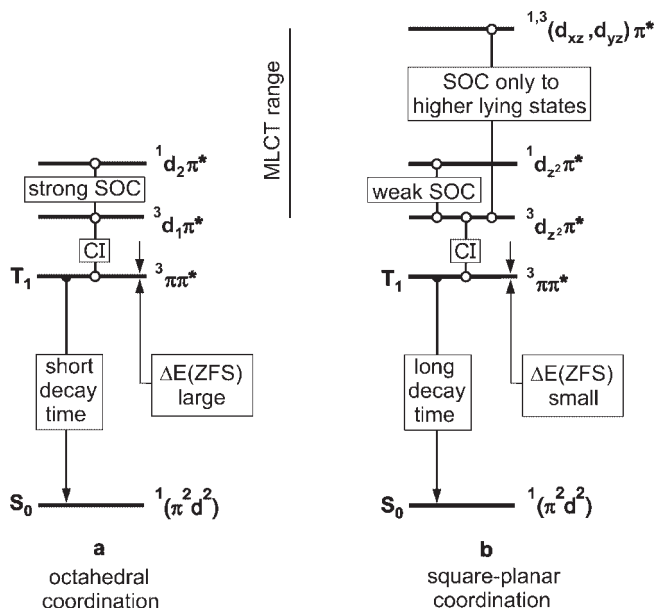
Fig. 1.13 Schematic and simplified comparison of quasi-octahedral to quasi-square planar triplet emitter compounds. The spin–orbit coupling (SOC) routes are different and thus can result in distinctly different zero-field splittings ΔE(ZFS) and radiative emission decay rates. These considerations apply to ^{3}**MLCT**(^{3}**dπ***) states (higher-lying states specified by the MLCT range) as well as to ^{3}**LC**(^{3}**$\pi\pi$***) states. The ^{3}**LC**(^{3}**$\pi\pi$***) states mix with ^{3}**MLCT**(^{3}**dπ***) states by configuration interaction (CI), and thus are *indirectly* altered by changes of SOC routes.

situation is taken into account in Fig. 1.13 by introducing a low-lying ^{3}**LC**(^{3}**$\pi\pi$***) state. Although, for this state, SOC to ^{1,3}**MLCT** states is negligible (no one-center integrals on the metal; Section 1.3.3.3), CI – representing an electron–electron interaction – can induce mixing of ^{3}**MLCT**(^{3}**dπ***) and ^{3}**LC**(^{3}**$\pi\pi$***) states. Hence, this mixing modifies the lowest states of ^{3}**$\pi\pi$*** parentage and induces a ^{1}**dπ*** admixture indirectly.

Thus, the differences of the SOC routes of quasi-octahedral compared to quasi-square planar complexes refer not only to the ^{3}**MLCT**(^{3}**dπ***) manifolds but also to the ^{3}**LC**(^{3}**$\pi\pi$***) states. From these considerations it follows that the magnitudes of ΔE(ZFS) and of the radiative decay rates can be larger for quasi-octahedral than for quasi-square planar complexes. These specific coupling routes often lead to relatively short emission decay times of quasi-octahedral emitters. Therefore, quasi-octahedral complexes might, in several cases, be better suited as OLED emitters than quasi-square planar compounds. In particular, this can be important if the OLEDs are operated at high current densities. These considerations explain – in part – the attractiveness of Ir(III) complexes for application in OLED devices.

The effectiveness of SOC is – as outlined above – very important for the photophysical properties of the emitting compounds. At this point it becomes instructive to discuss the further consequences of an increasing perturbation by comparing two structurally similar compounds, $Pd(thpy)_2$ and $Pt(thpy)_2$, which exhibit strongly different MLCT character of the T_1 states. This is, in part, due to the different values of SOC constants of the involved $4d\pi^*$ and $5d\pi^*$ perturbations of the Pd(II) and the Pt(II) compound, respectively. The properties of these compounds are further compared to those of a typical small purely organic molecule with low-lying $^3\pi\pi^*$ and $^1\pi\pi^*$ states. For these states, SOC is of minor importance. Such molecules have already been investigated in great detail (e.g., see Refs. [77–79]).

In the subsequent comparison, trends are illustrated which are connected with an increasing perturbation of the $^{1,3}\pi\pi^*$ states by $^{1,3}d\pi^*$ states (compare Fig. 1.14).

1.4.2.1 Singlet–Triplet Splitting

Organic molecules of the type of ligands which are of interest in this investigation usually exhibit singlet–triplet splittings $\Delta E(S_1 - T_1)$ of the order of typically $10^4\,cm^{-1}$ (1.24 eV). This splitting is mainly given by the exchange interaction, which is
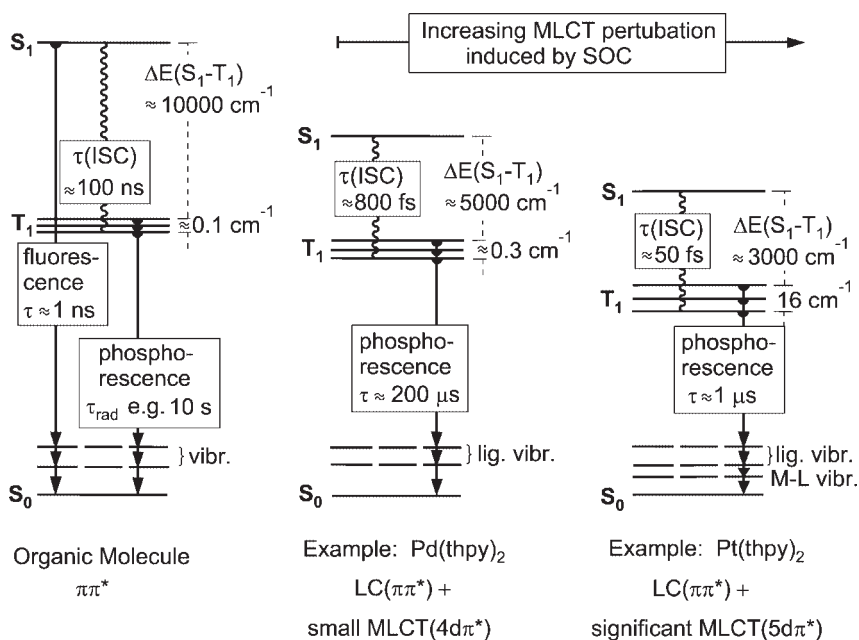
Fig. 1.14 Photophysical properties of two organo-transition metal emitters compared to those of a representative purely organic molecule. The emissive triplets of $Pd(thpy)_2$ and $Pt(thpy)_2$ exhibit small and significant MLCT admixtures to the $LC(\pi\pi^*)$ states, respectively. The positions of the compounds in the ordering scheme and the molecular structures are found in Figs. 1.11 and 1.12. The properties of $Pd(thpy)_2$ and $Pt(thpy)_2$ are discussed and compared in detail in Ref. [70]. lig. vibr.=ligand vibrations; M-L vibr.=metal–ligand vibrations.

essentially determined by the extensions and overlap of the involved wavefunctions (see Section 1.3.1). For the organometallic Pd(thpy)$_2$, a value of $5418 \, cm^{-1}$ is found [70].[23] The emissive triplet of this compound has been classified – based on experimental investigations [70, 139, 162, 163] and later also by CASPT2 *ab-initio* calculations [119] – as being mainly of LC($\pi\pi^*$) character with small MLCT($4d\pi^*$) admixtures. Therefore, the compound is found in the lower range of the ordering scheme of Fig. 1.11. On the other hand, for Pt(thpy)$_2$ with significant MLCT($5d\pi^*$) admixtures to the ^{3}**LC($\pi\pi^*$)** state [70, 144], the amount of $\Delta E(S_1 - T_1)$ is reduced to $3278 \, cm^{-1}$ (Fig. 1.14) [70].[23] Obviously, enhancing the metal character in the corresponding wavefunctions increasingly reduces the $\Delta E(S_1 - T_1)$ value. Due to the higher MLCT character, the electronic wavefunctions extend over a larger spatial region of the complex involving, in the case of Pt(thpy)$_2$, both ligands and the metal [114]. This is connected to an on average larger spatial separation between the interacting electrons. Thus, electron–electron interactions – and especially the exchange interaction – are reduced. This explains both the reduction of $\Delta E(S_1 - T_1)$ and the lowering of the S_1 state for compounds with higher metal character (Fig. 1.14).

1.4.2.2 Intersystem Crossing Rates

After excitation of the singlet state S_1, either optically or by electron-hole recombination, an organic molecule can exhibit an efficient fluorescence ($S_1 \rightarrow S_0$ emission) with a time constant of the order of 1 ns. In competition to this process, ISC can at least principally depopulate the S_1 state. However, the time constant of τ(ISC) is often much larger (order of 100 ns or even more) than the radiative decay time of the S_1 state, and hence ISC does not effectively quench the fluorescence (Fig. 1.14). On the other hand, in organo-transition metal complexes, the ISC time is drastically reduced due to singlet–triplet mixing induced by SOC, and due to the reduction of the energy separation $\Delta E(S_1 - T_1)$. According to this latter effect, the number of vibrational quanta, which are needed for the relaxation process, is reduced and thus the ISC probability becomes higher. For example, already for a compound, such as Pd(thpy)$_2$, with a relatively small MLCT perturbation in the wavefunction of the T_1 state and a halved $\Delta E(S_1 - T_1)$ value, ISC is by five orders of magnitude faster (800 fs [70]) than in typical organic compounds with $^1\pi\pi^*$ and $^3\pi\pi^*$ states. For Pt(thpy)$_2$ with a higher metal purturbation, the process is again much faster (τ(ISC) at $\approx$50 fs [70]) (Fig. 1.14). It should be noted that the term "intersystem crossing" loses its specific meaning, if SOC is large and effectively mixes singlet and triplet states. In this situation, IC and ISC cannot be discriminated.

In conclusion, the process of ISC in organometallic compounds with transition metal ions is fast and efficient for all compounds shown in Fig. 1.11. The quantum efficiency for this process is usually almost one (e.g., see Ref. [164]). Therefore, an emission from the S_1 state is not observable – a property which is the basis of the triplet harvesting effect, as discussed in Section 1.2.2.

---

23) This value refers to the specific site of M(thpy)$_2$ investigated in *n*-octane.

1.4.2.3 Emission Decay Time and Photoluminescence Quantum Yield

In purely organic molecules, the $S_0(\pi^2) \leftrightarrow T_1 (\pi\pi^*)$ transition is strongly forbidden, and the radiative decay time can be of the order of 10 s [78]. On the other hand, non-radiative processes are in general much faster, and consequently phosphorescence from the T_1 state is totally quenched at ambient temperature. With increasing SOC, the radiative decay time of the $T_1 \rightarrow S_0$ transition is reduced and thus the radiative path can compete with the non-radiative one [compare Eq. (5)]. Interestingly, already a relatively small singlet admixture to the $^3LC(^3\pi\pi^*)$ state – or, more exactly, to the respective triplet substate – increases the radiative transition probability drastically (see Section 1.3.3.3). For example, for Pd(thpy)$_2$ the emission decay time may be as short as $\tau_{mean} = 235 \mu s$ (τ_{mean} is the mean decay time for the three triplet substates with $\tau_I = 1200 \mu s$, $\tau_{II} = 235 \mu s$, and $\tau_{III} = 130 \mu s$ [163]). For Pt(thpy)$_2$, with a significant MLCT admixture to the lowest ^3LC state, the decay time is even reduced by six to seven orders of magnitude as compared to a purely organic emitter, and an emission decay time of the order of 1 μs is found (Fig. 1.14) [70].[24]

In summary, for organometallic compounds the radiative decay rates between the states T_1 and S_0 can be tuned by several orders of magnitude as compared to organic emitters. This is induced by an increase of SOC of the triplet substates to higher-lying singlets. Particularly short decay times are found, if effective SOC occurs to singlets S_n, which exhibit high transition probabilities of the transitions $S_0 \rightarrow S_n$ [Eq. (5)]. Thus, for such compounds, the radiative processes can well compete with or even exceed the non-radiative ones [compare Eq. (6)]. Consequently, organo-transition metal compounds can exhibit efficient emission (phosphorescence) with high ϕ_{PL} values. Therefore, these compounds are well suited as emitter materials for OLEDs.

1.4.2.4 Zero-Field Splitting – Summarizing Remarks

Triplet states split generally into substates, and this is also valid for purely organic molecules. However, for these one finds only small values of ZFS of the order of 0.1 cm^{-1} (1.2×10^{-5} eV) which result from spin–spin couplings between the electrons in the π and π^* orbitals, respectively (e.g., see Refs. [77, 82–84]). On the other hand, in organo-transition metal compounds SOC will modify the properties of the emitting triplet state by mixing in higher-lying states of singlet and triplet character. Yet, small admixtures may have drastic consequences: For example, increase of the ISC rate and of the phosphorescence decay rate (see the previous subsections) by orders of magnitude are found, whereas the ZFS is not drastically altered by small MLCT perturbations. Well-studied examples of this behavior are [Rh(bpy)$_3$]$^{3+}$ and Pd(qol)$_2$ [72, 83, 85]. However, larger MLCT perturbations due to stronger SOCs lead to appreciable ZFSs, as was discussed in Section 1.3.3.3 [Eq. (4)] and depicted in Fig. 1.11. For the example of Pt(thpy)$_2$, we find $\Delta E(\text{ZFS}) = 16$ cm^{-1}, which lies in the intermediate range.

24) The emission decay behavior of emitter compounds is of crucial importance for an understanding of the triplet state properties and the compounds' applicability in OLEDs. Therefore, decay properties will be discussed later in detail (see Sections 1.6, 1.7, 1.8, 1.9.2.3, and 1.10.3).

Importantly, the individual triplet substates **I, II**, and **III** can have very different photophysical properties with regard to radiative decay rates, vibronic coupling, coupling to the environment, emission quantum yields, population and relaxation dynamics due to spin–lattice relaxation (SLR), and sensitivity with respect to symmetry changes (see also the following sections). At ambient temperature, the individual properties are largely smeared out, and in general only an averaged behavior is identified. Nevertheless, the individual triplet substates still determine the overall emission properties (compare Section 1.11). It should be noted that the magnitude of ΔE(ZFS) and the properties of the substates are not independent of the environment or the matrix cage in which the emitter complex is situated. This behavior is discussed in more detail in Section 1.10.

1.4.2.5 Emission Band Structures and Vibrational Satellites

At ambient temperature, the phosphorescence of organo-transition metal compounds usually consists of superimposed spectra, which stem from the different triplet substates (see Section 1.9). An individual spectrum which results from only one specific substate is normally composed of a transition at the electronic origin (0-0 transition), a large number of vibrational satellites, and of in part overlapping low-energy satellites which – due to electron–phonon coupling – involve low-energy vibrations of the complex in its environment (lattice cage). Moreover, all of these individual transitions are masked by homogeneous broadening effects, and consequently at ambient temperature only a broadband emission normally results (compare Section 1.11). On occasion, residual, moderately resolved structures occur, which stem from overlapping vibrational satellites (not necessarily from progressions). Interestingly, at low temperature and under suitable conditions, these structures can often be well resolved and characterized (compare Section 1.9). Based on this type of investigation, it follows that the vibrational satellite structure is also influenced by the MLCT component in the electronic states [165]. Specifically, the spectra of compounds with electronic transitions of mainly LC($\pi\pi^*$) character (small MLCT perturbation) are largely determined by satellites corresponding to ligand vibrations (fundamentals, combinations, progressions). However, with increasing MLCT character, low-energy vibrational satellites of metal–ligand character become more important (up to about $600\,cm^{-1}$ from the electronic origin) [165] (Fig. 1.14). Thus, the emission spectrum (at ambient temperature) becomes less resolved and the maximum of the emission shifts away from the electronic 0-0 transition towards the metal–ligand vibrational satellites.

To summarize, metal participation (i.e. MLCT purturbation) in the emitting state leads to a slight shift of the unresolved emission maximum as compared to an LC-based spectrum with the same 0-0 transition energy. This is due to the occurrence of additional low-energy metal–ligand vibrational satellites which causes also a further smearing out of the spectrum.

1.4.2.6 Localization/Delocalization and Geometry Changes in the Excited Triplet State

The singlet–triplet transitions of compounds with small MLCT character (as shown in the lower part of Fig. 1.11) are usually confined to one of the ligands,

even if the formal symmetry of the complex would allow a delocalization over all of the ligands. This has been proven for $[Rh(bpy)_3]^{3+}$ [72] and $[Pt(bpy)_2]^{2+}$ [74] by use of the method of deuteration labeling [74, 114]. In contrast, for compounds with emissive ^{3}**MLCT** states such as $[Ru(bpy)_3]^{2+}$ [166] and $[Os(bpy)_3]^{2+}$ [167], it has been shown that the excited state is delocalized over the three ligands and the metal. This is even valid for Pt(thpy)$_2$, in which the triplet state is largely of LC($\pi\pi^*$) character, but for which the metal orbital admixture induces sufficient coupling between the ligands to result in a delocalization of the lowest excited state [70, 114]. It should be noted that these results were obtained at low temperature for compounds doped into rigid matrices. (For a detailed discussion of this subject, see Ref. [74].)

Moreover, since the metal character or MLCT component in the triplet state – if sufficiently large – can induce a ligand–ligand coupling which delocalizes the excited state wavefunction, the metal contribution will also affect the geometry change that follows an excitation. This is indicated by the values of the Huang–Rhys parameters. For the localized situation in the above-mentioned compounds, a maximum Huang–Rhys parameter [70] of $S = 0.3$ is found, whilst for compounds with delocalized triplets with larger (!) MLCT components this characteristic parameter is smaller by a factor of three to four [70, 74]. The description of S and the corresponding background information are presented in Section 1.9 [Eq. (21), see below]. Interestingly, geometry changes or reorganization effects which occur upon excitation of the emissive triplet states are small for almost all investigated complexes (in rigid matrices).

In conclusion, we point to an interesting observation. The organo-transition metal emitters, which have been applied in *efficient* OLEDs, exhibit ΔE(ZFS) values greater than $\approx 10\,cm^{-1}$ ($1.2 \times 10^{-3}\,eV$). It is indicated that for splittings above this magnitude, components of higher-lying singlet states in the emitting triplet substates can be large enough to induce the required radiative allowednesses, short emission decay times, and sufficiently high photoluminescence quantum yields.

1.5
Characterization of the Lowest Triplet State Based on High-Resolution Spectroscopy: Application to Pt(thpy)$_2$

Pt(thpy)$_2$ has been used as emitter dopant in OLEDs [168–170] and for generation of chemiluminescence [171], albeit less frequently than Ir(ppy)$_3$ (Section 1.6) or Ir(btp)$_2$(acac) (Section 1.8). Nevertheless, Pt(thpy)$_2$ represents a highly illustrative example to demonstrate, how the triplet T_1 substates can be characterized by high-resolution spectroscopy. At this point, initially a survey is provided. Figure 1.15a shows the absorption spectrum below $\approx 50\,000\,cm^{-1}$ (6.2 eV) and the emission spectrum, both measured at ambient temperature (compare Refs. [172–174]). The features in absorption are typical structures which are related to strongly mixed MLCT/LC states (compare the CASPT2 treatment of Ref. [119]). The low-energy weak absorption peak near $\approx 580\,nm$, which overlaps with the emission, corre-
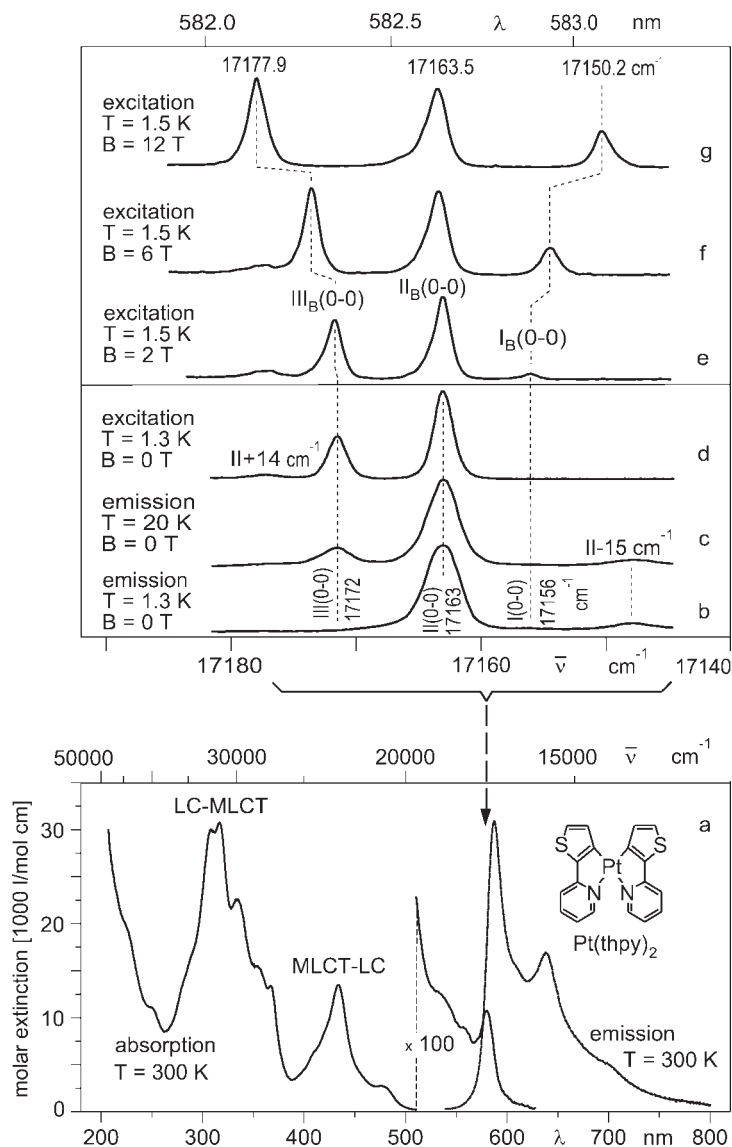
Fig. 1.15 Emission, excitation, and absorption of Pt(thpy)$_2$ at various temperatures and magnetic fields. (a) Compound dissolved in *n*-octane, λ_{exc}=457.9 nm. (b–g) Pt(thpy)$_2$ dissolved in *n*-octane, ca. ≈10^{-5} mol L^{-1}. For experimental details, see Ref. [70].

sponds to the lowest triplet state **T$_1$**. Already from this investigation, carried out at ambient temperature and showing the "allowedness" of the **S$_0$** → **T$_1$** transition, it is expected that the **T$_1$** state contains MLCT admixtures and is distinctly split into substates. Accordingly, it is within the focus of this section to illustrate, how

the ZFS can be determined and the substates as well as the corresponding electronic transitions to the ground state can be characterized. Clearly, the total emission spectrum from a triplet term consists almost generally not only of electronic 0-0 transitions, but additionally of vibrational and lattice mode satellites. In this section, attention is focused on the purely electronic 0-0 transitions, whereas in Section 1.9 the vibrational satellite structures will be discussed.

1.5.1
Highly Resolved Electronic Transitions

The transitions corresponding to the triplet substates **I**, **II**, and **III** can be well resolved by applying the methods of high-resolution and site-selective Shpol'skii[25] spectroscopy at low temperatures. However, for Pt(thpy)$_2$, the three electronic transitions $0 \leftrightarrow$ **I** (I(0-0)), $0 \leftrightarrow$ **II** (II(0-0)), and $0 \leftrightarrow$ **III** (III(0-0)) cannot be observed in the same spectrum (Fig. 1.15b–g). At $T = 1.3$ K, the emission from substate **III** is frozen out and the transition **I** $\leftrightarrow$ **0** at the electronic origin I(0-0) is largely forbidden. Thus, only the electronic origin II(0-0) at $17\,163$ cm^{-1} is found (Fig. 1.15b). Interestingly, this emission cannot be frozen out due to the relatively slow thermalization between the substates **I** and **II**. This behavior is a consequence of a long spin-lattice relaxation (SLR) time of $\tau_{SLR} = 720$ ns at $T = 1.3$ K (see Section 1.7). With a temperature increase, for example to $T = 20$ K, substate **III** is populated and the III(0-0) emission grows in (Fig. 1.15c). On the other hand, an excitation spectrum measured at low temperature shows the two electronic transitions $0 \leftrightarrow$ **II** and $0 \leftrightarrow$ **III**, but again, $0 \leftrightarrow$ **I** is too weak to be detectable (Fig. 1.15d). However, the position of substate **I** can be located indirectly by a comparison of energies of infrared-active vibrations with energies of the vibrational satellites which are well resolved in the $T = 1.3$ K emission spectrum (see Section 1.9). It is shown that the vibrational satellites fit well, if the position of the electronic origin of substate **I** is set to $17\,156$ cm^{-1}. Indeed, a careful inspection of the 1.3 K emission spectrum shows that a very weak transition occurs at exactly this energy. The forbiddenness of this transition is displayed also in the long emission decay time of $\tau_I = 110$ μs [70].

An independent confirmation of the position of this origin I(0-0) is obtained, when a high magnetic field is applied. With increasing field strength, the electronic origin line I$_B$(0-0) grows in due to a B-field-induced Zeeman interaction of substate **I** with higher-lying triplet substates (Fig. 1.15e–g). Distinct Zeeman shifts of the lines I$_B$(0-0) and III$_B$(0-0) are also observed. The interpretation of this behavior is straightforward, as a similar behavior has been observed for [Os(bpy)$_3$]$^{2+}$ and has been thoroughly discussed in Refs. [74] (p. 223) and [177]. In particular, an extrapolation from high magnetic fields to zero field clearly allows one to confirm the position of $17\,156$ cm^{-1} for the energy of the I(0-0) transition.

25) Alkanes, such as hexane, heptane, and octane, crystallize at low temperature as so-called Shpol'skii matrices [175, 176]. For many neutral molecules, these matrices represent relatively inert hosts. The guest molecules, doped at low concentrations of 10^{-4} to 10^{-5} mol L^{-1}, substitute host molecules. In suitable situations, one obtains highly resolved spectra also of organo-transition metal compounds [70–72, 85, 86, 139–144, 162, 163].
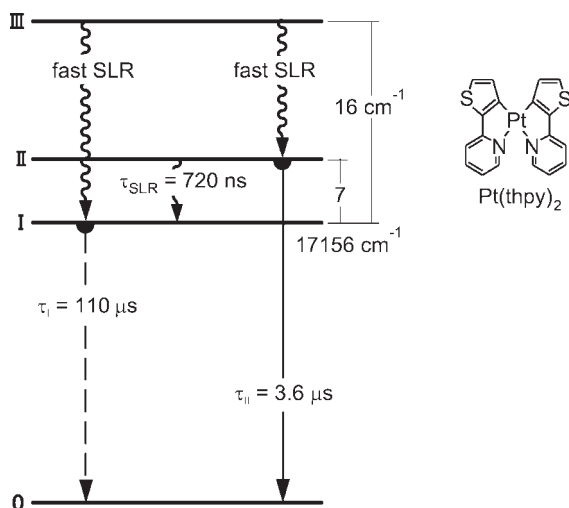
Fig. 1.16 Energy level diagram and decay times of the T_1 substates of Pt(thpy)$_2$ dissolved in *n*-octane. The energy values and splittings result from highly resolved spectra, as discussed in Section 1.5. The decay properties are discussed in Section 1.7. SLR = spin-lattice relaxation.

In summary, using the methods of high-resolution emission and excitation spectroscopy at various temperatures and under the application of high magnetic fields, allows identification of the three triplet substates of the T_1 term. In particular, an observation of the Zeeman effects confirms that the observed origins do not belong to different sites of the emitter in the host, but represent substates of the same T_1 parent term. The magnetic field effects will be discussed in more detail in a case study applied to Ir(btp)$_2$(acac) in Section 1.8.

Figure 1.16 displays the resulting energy level diagram for Pt(thpy)$_2$; several specific decay times taken from Ref. [70] are also given (compare Section 1.7). In particular, it is found that the total ΔE(ZFS) amounts to $16\,\mathrm{cm}^{-1}$. Thus, according to Section 1.4 and Fig. 1.11, it can be concluded that Pt(thpy)$_2$ belongs to the group of compounds with an emitting ^{3}**LC** state which, however, is significantly perturbed by MLCT admixtures.

1.5.2
Symmetry and Grouptheoretical Considerations

The crystal structure determination [178] has shown that the point group symmetry of Pt(thpy)$_2$ deviates from a C_{2v} symmetry, because the molecule is not planar. Also, a geometry optimization based on a density functional theory (DFT) calculation resulted in a structure which deviates from the C_{2v} symmetry. However, the calculations showed also that the corresponding energy minimum is shallow and

that the C_{2v} structure has only a slightly higher energy (1.7 kcal mol^{-1}, ≈600 cm^{-1} or 0.074 eV) [119]. This energy is so small, however, that intermolecular forces between the matrix cage and the Pt(thpy)$_2$ compound can easily have an effect on the geometry of the doped molecule. In particular, Pt(thpy)$_2$ might also become planar. This hypothesis is indicated due to the following considerations:

- Matrix cages consisting of *n*-octane or other *n*-alkanes host planar molecules with preference [175, 176, 179].
- The electronic forbiddenness of the transition **0 ↔ I** is unusually pronounced (Fig. 1.15b), if compared to other compounds; this indicates that the transition is spin and symmetry forbidden.
- After a relatively fast cooling rate of Pt(thpy)$_2$ dissolved in *n*-octane, the corresponding transition is found to be more allowed and thus well observable at *T* = 1.3 K; this indicates that the forbiddenness of the transition **0 ↔ I** depends on the specific cage geometry.
- Unsymmetric vibrations induce distinct radiative deactivation paths (appearance of strong "false origins"; compare Section 1.9.2.1).

Hence, it is assumed that Pt(thpy)$_2$ is flattened under the experimental situation, at which the spectrum of Fig. 1.15b has been measured, and that Pt(thpy)$_2$ adopts a C_{2v} symmetry. Under this assumption, an illustrative grouptheoretical consideration can be carried out. It is a specific property of the C_{2v} symmetry group[26] that only one representation exists – the A_2 representation – for which the transition to the electronic ground state of A_1 symmetry is electric dipole forbidden [180] and therefore is very sensitive to symmetry-breaking processes. Accordingly, we assign the triplet substate **I** to an A_2 representation. Thus, with the additional spin–flip-forbiddenness of the triplet–singlet transition, one can understand, why the transition **I ↔ 0** is so weak and almost non-observable at zero magnetic field.

Ab-initio calculations of Ref. [119] lead to an assignment of the lowest triplet (with a calculated transition energy of ≈18 200 cm^{-1}) to $^3A_1$ (in C_{2v}). From this representation it follows under SOC (not included in Ref. [119]) that in the C_{2v} double group the triplet splits into the three substates A_2, B_1 and B_2 (compare Ref. [180]). Thus, if the assignment of Ref. [119] holds, one obtains just one sublevel with the symmetry A_2 for state **I**, while the two other triplet substates **II** and **III** have B_1 and B_2 representations, respectively. An individual assignment of these two other states is not yet possible. Both transitions between the ground state A_1 and these triplet substates B_1 and B_2 are formally dipole-allowed [180].[27]

---

26) The subsequent classification is carried out in the C_{2v} double group which takes into account orbital and spin symmetries [108, 180].

Indeed, the experiment shows that both substates **II** and **III** can directly be excited from the ground state (Fig. 1.15d). Moreover, the ambient temperature absorption spectrum (Fig. 1.15a) indicates that the corresponding electronic 0-0 transitions together exhibit an absorption coefficient of $\approx 90\,L\,mol^{-1}\cdot cm$. Thus, the transitions to the two triplet substates **II** and **III** are considerably allowed.

The model presented above can be discussed further with respect to the radiative rates $k^r(i)$ (with i = I, II, III) as expressed by Eq. (5). Specifically, the T_1 substates **II** and **III** of Pt(thpy)$_2$ – exhibiting B_1 and B_2 symmetry, respectively – couple with higher-lying singlets also of $B_1(^1B_1)$ and $B_2(^1B_2)$ representation. Thus, these two transitions between the substates **II** and **III** and the electronic ground state **0** borrow their allowednesses from the $^1B_1 \leftrightarrow {}^1A_1$ and $^1B_2 \leftrightarrow {}^1A_1$ transition, respectively ($\langle \phi_{S_0}|e\mathbf{r}|\phi_{S_n}\rangle$ term of Eq. (5)). On the other hand, the transition between the electronic ground state and a higher-lying $^1A_2$ state is dipole-forbidden and thus cannot provide transition probability to the transition **I** $\leftrightarrow$ **0**.

It is expected that the considerations discussed in relation to a planar C_{2v} symmetry remain at least approximately valid for a slightly distorted geometry.

In conclusion, for most of the organo-transition metal compounds it has been found that the lowest triplet substate **I** represents an almost pure triplet – that is, SOC to higher-lying singlets is unimportant (compare Section 1.3.3.3). Hence, the SOC matrix elements $\langle \phi_{S_n}|\hat{H}_{SO}|\phi_{T_1(I)}\rangle$ representing the first term of Eq. (5), are very small. This is also valid for substate **I** of Pt(thpy)$_2$. In addition, the second term of Eq. (5) vanishes in a strict C_{2v} symmetry (or is very small in a slightly distorted symmetry) due to the dipole forbiddenness of the intensity-providing transition between the singlets. Consequently, the model proposed above allows an understanding of why the transition between the T_1 substate **I** and the electronic ground state **0** is difficult to detect.

1.6
Characterization of the Lowest Triplet State Based on Decay Time Measurements: Application to Ir(ppy)$_3$

Ir(ppy)$_3$ represents a well-known and efficient OLED emitter; therefore, it is of great interest to characterize the emitting triplet state of this and related compounds in detail. Until now, however, it has not been possible to obtain highly resolved and thus highly informative emission or excitation spectra, even when

27) Due to the restricted accuracy of the CASPT2 calculations [119], it is not excluded that the substates of a different triplet term, namely of $^3B_2$, can become the lowest ones under inclusion of spin-orbit coupling. $^3B_2$ would lead to A_1, A_2, and B_1 substate symmetries in C_{2v}. In this case, we would also assign substate **I** to the A_2 symmetry. The corresponding transition between the ground state A_1 and the sublevel of symmetry A_2 would again be forbidden, while transitions to the substates **II** and **III** of A_1 and B_1 representations, respectively, would formally be dipole allowed.
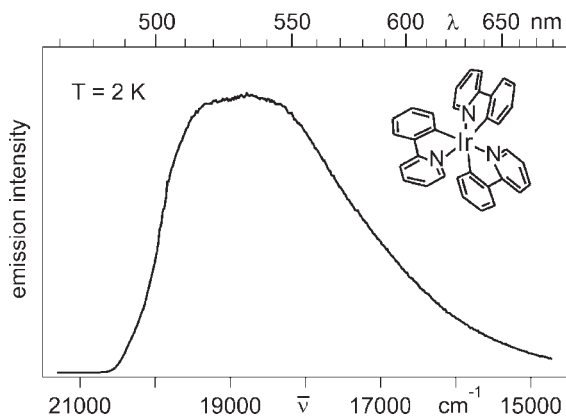
Fig. 1.17 Emission spectrum of Ir(ppy)$_3$ in tetrahydrofuran ($\approx 10^{-5}$ mol L^{-1}) at $T = 2$ K, $\lambda_{exc} = 363.8$ nm (compare Ref. [115]).

investigating the compound at low temperature. This may be due to the fact that, until now, a suitable host material for Ir(ppy)$_3$ has not been found.

Figure 1.17 shows an emission spectrum of Ir(ppy)$_3$ doped into tetrahydrofuran (THF). Although the temperature is as low as $T = 2$ K, the spectrum is still very broad (compare also Section 1.11). Therefore, indirect methods must be applied to gain sufficient information for a successful characterization of the emitting states. A determination of the ZFS values and the *individual* decay times of the T_1 substates is possible, if the *thermalized* emission decay times are available for a larger temperature range. This method will be explained by applying it to Ir(ppy)$_3$, although it has also been successfully used to characterize many other compounds [150, 153, 181–184].

The emission at $T = 1.2$ K stems from the lowest triplet substate **I**. From the relatively long decay time of $\tau_I = 145$ μs (Fig. 1.18), it follows that the corresponding transition to the ground state is largely forbidden. Therefore – and according to the spectral features as discussed for Ir(ppy)$_3$ in Ref. [115] – the radiative processes stemming from substate **I** have been assigned to be vibronically induced. From this behavior, it is indicated again that substate **I** represents a relatively pure triplet and that the transition to the ground state is symmetry forbidden. With temperature increase to T = 4 K, the emission decay time is drastically reduced, whereby the emission quantum yield remains high. This behavior shows clearly that higher-lying emitting states are thermally populated.

The temperature dependence of the emission decay time, as displayed in Fig. 1.18, allows the evaluation of an energy level diagram for the spectroscopically active states involved in the emission processes. Under assumption of a fast thermalization – as given for Ir(ppy)$_3$ – the occupation dynamics of excited states is governed by the expression (e.g., compare Ref. [181]):
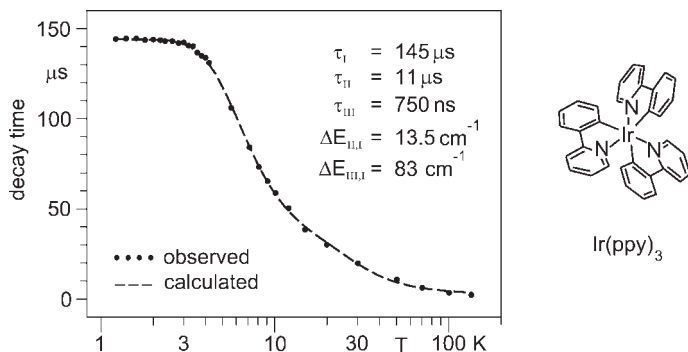
Fig. 1.18 Emission decay time of Ir(ppy)$_3$ dissolved in tetrahydrofuran (10^{-5} mol L^{-1}) versus temperature measured after excitation at 337.1 nm. The decay curves are monoexponential over the whole temperature range, at least after the experimental limit of the equipment of ≈ 300 ns. From a fit of Eq. (8), one obtains the zero-field splitting energies and the decay times, which are also given. $\Delta E_{II,I}$ and $\Delta E_{III,I}$ are the energy differences between the respective triplet substates (compare Fig. 1.19).

$$\frac{\mathrm{d}N}{\mathrm{d}t} = -k_{\mathrm{therm}}N = -\sum_i k(\mathrm{i})n_{\mathrm{i}} \tag{7}$$

wherein n_{i} denotes the Boltzmann occupation number of state i, and $k(\mathrm{i})$ is the total rate constant for depopulation of state i. N is the total number of occupied excited states and $k_{\mathrm{therm}} = 1/\tau_{\mathrm{therm}}$ the rate constant for depopulation of the equilibrated (thermalized) system of excited states or the inverse of the measured decay time. The introduction of Boltzmann factors and the assumption of three emitting states with i = I, II, and III lead to the expression (e.g., compare Refs. [181–185]):

$$k_{\mathrm{therm}} = \frac{k(\mathrm{I}) + k(\mathrm{II})\mathrm{e}^{-\Delta E_{II,I}/k_B T} + k(\mathrm{III})\mathrm{e}^{-\Delta E_{III,I}/k_B T}}{1 + \mathrm{e}^{-\Delta E_{II,I}/k_B T} + \mathrm{e}^{-\Delta E_{III,I}/k_B T}} \tag{8}$$

All constants and symbols have been explained above, and this equation can be applied for a fit to the measured lifetime data in dependence of the sample temperature, as shown in Fig. 1.18. The fitting procedure leads to $\Delta E_{II,I} = 13.5$ cm^{-1}, $\Delta E_{III,I} = 83$ cm^{-1}, $\tau_{II} = 11$ µs, $\tau_{III} = 750$ ns. The fit was carried out with the fixed value of $\tau_I = 145$ µs, which is the emission decay time at 1.2 K, when only state **I** emits. The accuracy of the fit parameters is better than 10% if the model of just three emitting substates holds.[28] These data are summarized in the energy level diagram shown in Fig. 1.19.

It should be noted that a fit based on a simplified Eq. (8) involving only two excited states cannot describe the observed temperature behavior. On the other hand, it cannot be ruled out definitely that more than three states are involved in

---

28) It should be noted that the value $\Delta E_{III,I}$ depends critically on the decay time data in the temperature range of (30 ± 10) K. Thus, the error of the $\Delta E_{III,I}$ value presumably exceeds 10% [186].
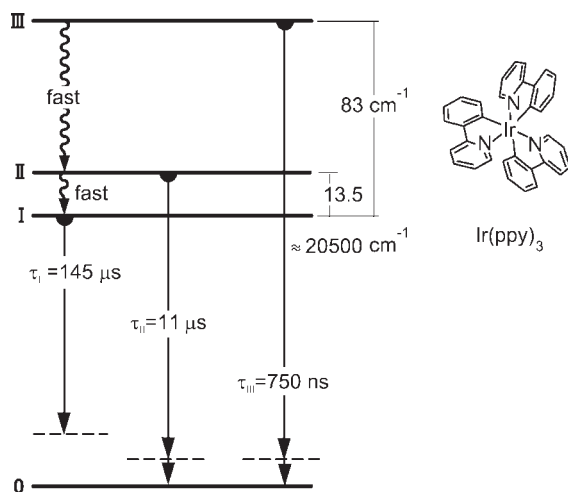
Fig. 1.19 Energy level diagram and decay times of Ir(ppy)$_3$ dissolved in tetrahydrofuran. The data are determined from broadband emission spectra by use of the temperature dependence of the emission decay time (compare Fig. 1.18 and Ref. [115]). The dashed lines represent vibrational energy levels.

the emission process, for example proximate higher-lying triplets. Further, the data obtained do not provide any reliable information about degeneracies or near degeneracies which might occur in the case that Ir(ppy)$_3$ maintains (nearly) the C$_3$ symmetry, as the fitting procedure does not allow the deduction of any grouptheoretical assignment. Therefore, Eq. (8) is given for the simplest model of three non-degenerate substates.

Further, determination of the emission decay time for $T = 300$ K is also possible by use of Eq. (8). If the parameters obtained from the fitting procedure are used, a value of $\tau_{therm} = 2.6$ μs is found, which corresponds well to the measured decay time at higher temperatures. The value measured for Ir(ppy)$_3$ in THF at 130 K is 2 μs, in degassed acetonitrile at 300 K it is 1.9 μs [187], and in degassed toluene 2 μs [188].

In conclusion, the emission decay behavior of Ir(ppy)$_3$ can be well modeled by three triplet substates with a total ZFS of $\Delta E(ZFS) = 83$ cm^{-1}. This value is much larger than that found for Pt(thpy)$_2$ with $\Delta E(ZFS) = 16$ cm^{-1}, or even for [Ru(bpy)$_3$]$^{2+}$ ($\Delta E(ZFS) = 61$ cm^{-1}), which is regarded as a typical ^{3}**MLCT** emitter. Therefore, and especially according to Section 1.4 (Fig. 1.11), we assign the lowest triplet **T$_1$** of Ir(ppy)$_3$ as being largely of MLCT parentage (compare also Ref. [189].) A corresponding interpretation results also from *ab-initio* calculations [116, 123, 124]. For completeness, the reader is referred to Section 1.3.3.3, where the magnitudes of singlet admixtures to the three triplet substates according to the calculations by Nozaki [124] are discussed. The two short-lived triplet substates **II** and **III** have singlet admixtures of the order of 1%, whilst substate **I** is largely a pure triplet, as predicted from the long emission decay time of $\tau_I = 145$ μs.

1.7
Phosphorescence Dynamics and Spin–Lattice Relaxation: Background and Case Study Applied to Pt(thpy)$_2$

1.7.1
Processes of Spin–Lattice Relaxation

The population dynamics of the different triplet substates, emission decay properties, and even emission spectra are, at low temperature, usually essentially determined by the times of relaxation between the substates. These times can be very long (e.g., the order of many µs), if the energy separations between the substates are of the order of several wavenumbers. This behavior is connected to the property that the excess energy of a higher-lying triplet substate is not easily transferred to the lattice due to the small density of states of lattice vibrations (phonons) in this energy range, and due to the requirement of spin-flips for transitions between the substates. This type of relaxation is known as spin–lattice relaxation (SLR). Although, it has been known for decades that such slow processes are of significant importance for the emission behavior (e.g., see Refs. [98, 190–198]), the almost general importance for organometallic compounds also has not yet been fully recognized. Within the literature, different mechanisms have been discussed which may induce a spin-flip due to an interaction of phonons with the triplet substates of a molecule. The phonon modes can cause fluctuations of molecular properties, such as intramolecular distances, and thus can modulate electronic charge distributions, SOC, and mixing coefficients between different states. It is beyond the scope of this chapter, however, to discuss these mechanisms in greater detail (see Refs. [98, 190–200]).

Usually, SLR is described by considering three different processes, namely the *direct*, the *Orbach*, and the *Raman process* [98, 193–198]. These are illustrated in Fig. 1.20 (compare also Refs. [70, 74, 182, 185, 201]). The three electronic states **I**, **II**, and **III** represent, for example, the three triplet substates of an organometallic compound with energy separations of several cm^{-1}. It is assumed that one of the higher-lying states – for example state **II** – is populated by a relaxation from a still higher-lying state or by a resonant excitation of just this electronic state.

These three SLR processes and the temperature dependences of the corresponding rates are briefly introduced in the following sections.

1.7.1.1 **The Direct Process**
A relaxation from state **II** to state **I** may occur by emission of one phonon with the energy $\Delta E_{\text{II,I}}$, which is transmitted to the lattice (Fig. 1.20a). This process is called the *direct process* of SLR. The corresponding rate $k_{\text{II,I}}^{\text{SLR}}$ (direct) dominates the rates of other processes of SLR at low temperature T. For higher temperatures, the absorption of a phonon can also take place, and thus represents a back process from state **I** to state **II**. Both up and down processes give rise to the *direct process*. For the net rate, one obtains (e.g., compare Refs. [74, 98, 182, 193, 195, 201]):
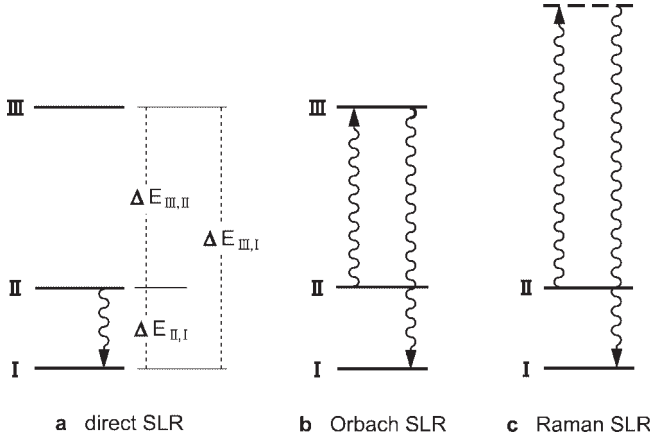
a direct SLR **b** Orbach SLR **c** Raman SLR

Fig. 1.20 Schematic diagram to illustrate the different processes of spin–lattice relaxation (SLR). The states **I**, **II**, and **III** represent, for example, triplet substates of organo-transition metal compounds. The energy separations are given by the zero-field splittings (ZFS) (compare also Table 1.1).

$$k_{II,I}^{SLR}(\text{direct}) = \frac{3}{2\pi\hbar^4\rho v^5}\cdot|\langle II|V|I\rangle|^2\cdot(\Delta E_{II,I})^3\cdot\coth(\Delta E_{II,I}/2k_B T) \tag{9}$$

where ρ is the mass density of the matrix material, v the (average) velocity of sound in the matrix, and k_B the Boltzmann constant. *V* represents the perturbation caused by lattice modes (phonons) which couple the electronic states **I** and **II**. The *direct process* exhibits only a weak temperature dependence.

1.7.1.2 The Orbach Process

At higher temperatures, the relaxation may also proceed indirectly by the two-phonon *Orbach process* (Fig. 1.20b). Schematically, in this process one phonon of the energy $\Delta E_{III,II}$ is absorbed, while a second phonon of the energy $\Delta E_{III,I}$ is emitted. The inverse process can also occur. The rate of this process has been determined only recently also for a general pattern of ZFS states, which are often found for the compounds being of interest here. The corresponding approximation, representing an *extended Orbach process*, was derived in Refs. [182, 201]. A slightly simplified expression is given by the following equation [182, 185]:

$$k_{II,I}^{SLR}(\text{Orbach}) = \frac{C_{III,II}C_{III,I}(e^{\Delta E_{III,II}/k_B T} + e^{\Delta E_{III,I}/k_B T})}{C_{III,I}e^{\Delta E_{III,I}/k_B T}(e^{\Delta E_{III,II}/k_B T} - 1) + C_{III,II}e^{\Delta E_{III,II}/k_B T}(e^{\Delta E_{III,I}/k_B T} - 1)} \tag{10}$$

with the abbreviations

$$C_{III,I} = \frac{3}{2\pi\hbar^4\rho v^5}\cdot|\langle III|V|I\rangle|^2\cdot(\Delta E_{III,I})^3$$

$$C_{III,II} = \frac{3}{2\pi\hbar^4\rho v^5}\cdot|\langle III|V|II\rangle|^2\cdot(\Delta E_{III,II})^3 \tag{11}$$

The used parameters and matrix elements correspond directly to the definitions given above. The energy separations are specified in Fig. 1.20. From the more general equation [Eq. (10)], the original *Orbach expression* can be obtained. It is derived under the assumption of specific energy differences, namely of $\Delta E_{\mathrm{III,I}} \approx \Delta E_{\mathrm{III,II}} = \Delta E$ (compare Refs. [98, 194, 195, 198]:

$$k_{\mathrm{II,I}}^{\mathrm{SLR}}(\text{Orbach}) \approx \frac{2C_{\mathrm{III,II}}C_{\mathrm{III,I}}}{(C_{\mathrm{III,I}} + C_{\mathrm{III,II}})} \cdot \frac{1}{e^{\Delta E/k_{\mathrm{B}}T} - 1} \tag{12}$$

This expression can further be simplified for $\exp(\Delta E/k_{\mathrm{B}}T) \gg 1$ or for $\Delta E \gg k_{\mathrm{B}}T$. Thus, one obtains the famous and simple approximation for the *Orbach process*

$$k_{\mathrm{II,I}}^{\mathrm{SLR}}(\text{Orbach}) \approx \text{const} \cdot (\Delta E)^3 \cdot e^{-\Delta E/k_{\mathrm{B}}T} \tag{13}$$

This approximation has – together with the expression for the *direct process* according to Eq. (9) – been used successfully to fit the temperature dependence of the SLR rate of $[\mathrm{Ru(bpy)_3}]^{2+}$ doped into $[\mathrm{Zn(bpy)_3}](\mathrm{ClO_4})_2$ up to $T \approx 10\,\mathrm{K}$ [74]. However, application of the approximations given in Eqs. (12) and (13) to the experimental data obtained for $\mathrm{Pt(thpy)_2}$ does not lead to a successful fit, as the condition described above – assuming $\Delta E_{\mathrm{III,I}} \approx \Delta E_{\mathrm{II,I}}$ does not hold for the specific ZFS pattern of this complex (see Fig. 1.16.). In contrast, a good fit is obtained, if Eq. (10) is used (see Ref. [201] and below). For completeness, it should be noted that the rate according to the *Orbach process* vanishes for $T \to 0\,\mathrm{K}$, and also for $\Delta E \to 0\,\mathrm{cm}^{-1}$.

1.7.1.3 The Raman Process

A relaxation between the states **II** and **I** can also proceed by a two-phonon Raman scattering process, according to Fig. 1.20c. The temperature dependence of the corresponding rate is usually approximated by

$$k_{\mathrm{II,I}}^{\mathrm{SLR}}(\text{Raman}) = \mathrm{R} \cdot T^n \tag{14}$$

with a constant R and with n equal to 5 or 7 (for non-Kramers compounds [196]). For the organo-transition metal complexes hitherto studied, the T^5 dependence fits to the experimental observations much better than the T^7 dependence. [185, 202]. It should be noted that the *Raman process* is usually less effective than the *Orbach process*, if a higher-lying electronic state is present, such as state **III** in Fig. 1.20b. If not, however, the *Raman process* becomes important. For example, for $\mathrm{Pt(thpy)(CO)(Cl)}$ with an energy level diagram similar to that shown in Fig. 1.20c, it has been found that the *Raman process* with a T^5 dependence must be taken into account for $T \gtrsim 5\,\mathrm{K}$. Its rate exceeds the one of the *direct process* above $T = 9\,\mathrm{K}$ [185].

1.7.2
Population and Decay Dynamics of the Triplet Substates of Pt(thpy)₂

The emission rise and decay properties of the three triplet substates have been well studied for $\mathrm{Pt(thpy)_2}$. Therefore, this complex represents a good example to
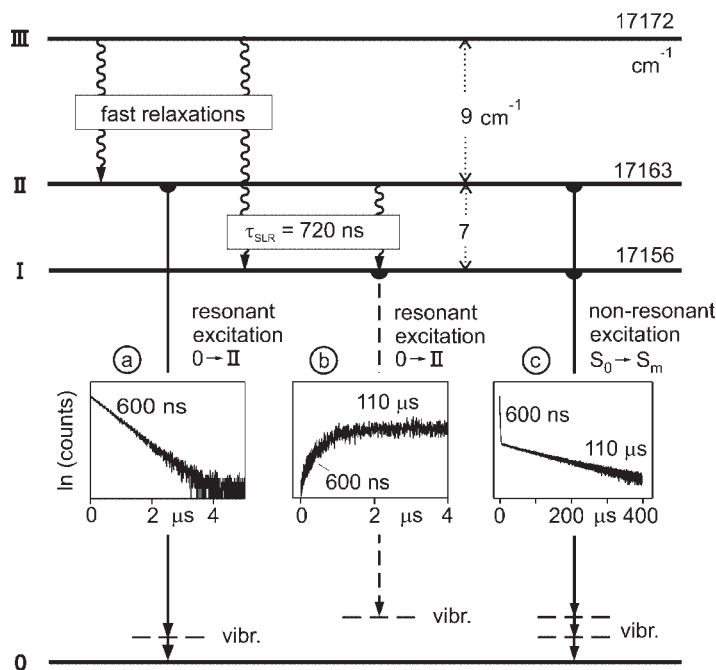
Fig. 1.21 Triplet substates of Pt(thpy)$_2$ and dynamic processes of spin–lattice relaxation at $T = 1.3$ K. Pt(thpy)$_2$ is dissolved in *n*-octane at a concentration of $\approx 10^{-5}$ mol L^{-1}. (a) Resonant excitation at the electronic origin II (0–0) (17 163 cm^{-1}) and detection of the emission of state II at the 653 cm^{-1} vibrational satellite at 16 510 cm^{-1}. (b) Same excitation as in (a), but detection of the emission of state I at the 531 cm^{-1} satellite at 16 625 cm^{-1}. (c) Excitation into a higher-lying singlet (e.g., $\lambda_{exc} = 337.1$ nm), detection at 16 444 cm^{-1} with a bandwidth of ≈ 5 cm^{-1}. Thus, the emissions from substate I on the 713 cm^{-1} vibrational satellite and from substate II on the 718 cm^{-1} satellite, are monitored (compare Section 1.9 and Refs. [182, 185]).

illustrate the importance of SLR between the triplet substates of organo-transition metal compounds. Figure 1.21 reproduces the energy level diagram of Pt(thpy)$_2$ (as already presented in Fig. 1.16), and summarizes the dynamical emission properties observed at $T = 1.3$ K. Interestingly, at low temperature they depend on the excitation as well as on the detection energy. Such behavior is rather typical for organo-transition metal compounds if they exhibit similar splitting patterns and magnitudes of ΔE(ZFS). The properties will be explained by use of the insets shown in Fig. 1.21 [182, 185].

- After an excitation with a laser pulse of triplet substate **III** at 17 172 cm^{-1}, one finds a fast SLR to the two lower-lying substates **II** and **I**. At $T = 1.3$ K, the *Orbach* and the *Raman processes* are negligible, and the SLR is governed by the *direct process*. Due to the relatively large energy separation of $\Delta E_{III,I} = 16$ cm^{-1} and the $(\Delta E_{III,I})^3$ dependence [Eq. (9)], the SLR

rate according to this process will be large, as depicted in Fig. 1.21.

- The emission decay behavior of substate **II** is of specific interest. After a pulsed and resonant excitation of the **0 → II** transition at $17\,163\,cm^{-1}$, a strictly monoexponential decay with a decay constant of $600 \pm 10\,ns$ is observed (for more than five lifetimes), if the emission is detected selectively on a vibrational satellite that corresponds to the emission of substate **II** (Fig. 1.21a). For example, the $653\,cm^{-1}$ satellite is well suited (compare Fig. 1.32, below). The corresponding decay rate is $k_{exp} = 1/600\,ns = 1.67 \times 10^6\,s^{-1}$. This decay is mainly determined by the *direct process* of SLR from state **II** to state **I** (for a slight correction see Eq. (15) below). Again at $T = 1.3\,K$, the other two SLR processes are inefficient. Later in this section, we will discuss the temperature dependence of the rate of SLR between these two substates **II** and **I**. An increasing importance of the *Orbach* and the *Raman processes* at higher temperatures will be demonstrated below.

- After substate **II** is excited selectively, substate **I** will be populated indirectly by the SLR process. Indeed, a corresponding rise is observed (Fig. 1.21b). For this experiment, the excitation is maintained as before, but the emission is detected on a vibrational satellite which belongs selectively to the state **I** emission. The $531\,cm^{-1}$ satellite represents such a specific satellite (compare Fig. 1.31, below). After the emission rise, the population of substate **I** decays with the usual emission decay time of substate **I** of $\tau_I = 110\,\mu s$ [185].

- It is also instructive to discuss the decay behavior, in case Pt(thpy)$_2$ is excited non-selectively by exciting a singlet (**S$_0$ → S$_m$**), for example, and by applying a non-selective detection. These conditions correspond to a usual experimental situation. In this case, the two decay components of $600\,ns$ and $110\,\mu s$ are found, since by the relaxation both substates **I** and **II** are initially populated and both states exhibit their individual relaxation and emission decay behavior (compare Fig. 1.21c and Refs. [182, 185]).

The experimentally determined decay time of the higher-lying triplet substate **II** of $\tau_{exp} = 600\,ns$ ($= 1/k_{exp}$) does not directly represent the SLR time, since the decay of substate **II** is given by two processes – that is, by the usual decay from this substate **II** to the ground state **0**, $k_{II,0} = 1/\tau_{II}$, and by the SLR rate from substate **II** to substate **I**, $k_{II,I}^{SLR}$. Thus, the SLR rate is obtained by [182, 185]:

$$k_{II,I}^{SLR} = k_{exp} - k_{II,0} \qquad\qquad (15)$$

Although the emission decay time $\tau_{II} = 1/k_{II,0}$ of substate **II** cannot be measured directly, it can be determined from the temperature dependence of the emission decay time of the thermally equilibrated system of the triplet substates. This procedure, as described in Section 1.6, has been carried out for Pt(thpy)$_2$ in Ref. [182], where $k_{II,0} = 2.78 \times 10^5 \, s^{-1}$ ($\tau_{II} = 3.6 \, \mu s$) is obtained. (Compare Fig. 1.16.) By use of Eq. (15) with $k_{exp} = 1.67 \times 10^6 \, s^{-1}$ ($\tau_{exp} = 600 \, ns$), the values $k_{II,I}^{SLR} = 1.39 \times 10^6 \, s^{-1}$ or $\tau_{SLR} = 720 \, ns$ are found (compare Fig. 1.21).

The SLR observed at $T = 1.3 \, K$ is given by the *direct process*. However, with temperature increase, the other processes also become important and will dominate at higher temperature; this behavior is illustrated in Fig. 1.22. The SLR rate is determined from the measured decay times $\tau_{exp}(T) = 1/k_{exp}(T)$, according to the inset in Fig. 1.22, and by applying the correction expressed by Eq. (15). The resulting data of $k_{II,I}^{SLR}(T)$ can be fitted well (Fig. 1.22), when the three processes, illustrated in Fig. 1.20, are taken into account. Thus, application of the expressions for the *direct process* $k_{II,I}^{SLR}(\text{direct})$ [Eq. (9)], the *extended Orbach process* $k_{II,I}^{SLR}(\text{Orbach})$ [Eq. (10)], and the *Raman process* $k_{II,I}^{SLR}(\text{Raman})$ [Eq. (14)], leads to

$$k_{II,I}^{SLR} = k_{II,I}^{SLR}(\text{direct}) + k_{II,I}^{SLR}(\text{Orbach}) + k_{II,I}^{SLR}(\text{Raman}) \tag{16}$$

This expression describes the temperature dependence of the SLR rate from state **II** to state **I** of Pt(thpy)$_2$, and is used for the fitting procedure (compare Refs. [182, 185, 201]). Equation (16) contains six parameters after insertion of Eqs. (9), (10), and (14). However, these are reduced to only two free fit parameters, as all energy separations are known from highly resolved spectra
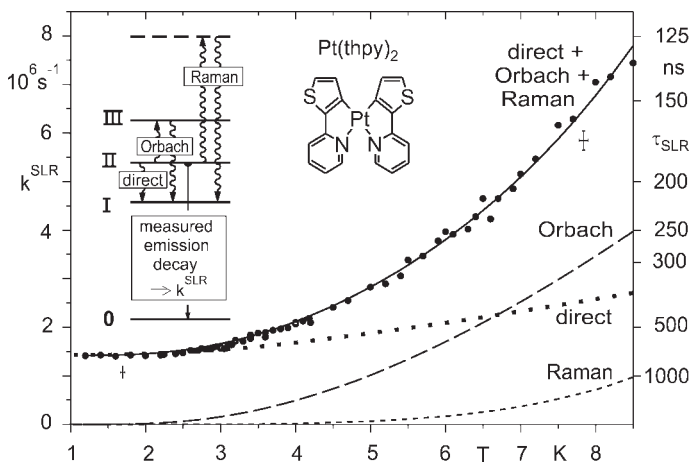
Fig. 1.22 Temperature dependence of the rate $k_{II,I}^{SLR}$ (= k^{SLR} as displayed in the figure) and time τ_{SLR} of spin–lattice relaxation of state **II** of Pt(thpy)$_2$ dissolved in *n*-octane. The experimental data (points) result from emission decay times of state **II**, corrected according to Eq. (15). The solid line represents a fit according to Eq. (16), while the broken and dotted lines give the contributions of the respective processes. The inset shows the triplet substates and depicts schematically the three different processes of spin–lattice relaxation (compare Ref. [185]).

(Fig. 1.21), the ratio $C_{III,I}/C_{III,II}$ is determined as ≈ 1.2 [182] from time-resolved excitation spectra, $C_{II,I}$ is equal to the low-temperature limit of the SLR with $k_{II,I}^{SLR}$(direct, $T = 1.3$ K) $= 1/\tau_{SLR} = 1.39 \times 10^6$ s^{-1} (see above), and the exponent of Eq. (14) can be set to $n = 5$. Thus, the fitting procedure leads to the two unknown parameters and produces the solid line in Fig. 1.22 (for further details, see Ref. [182]).

The results obtained are also used to illustrate graphically the relative magnitudes of the three different processes that give the total rate of SLR $k_{II,I}^{SLR}(T)$. For the temperature range between 1.3 K $\leq T \leq 3$ K, the total rate $k_{II,I}^{SLR}$ is nearly exclusively determined by the *direct process*. Above $T \approx 3$ K and above ≈ 6 K, the *Orbach* and the T^5 *Raman process*, respectively, become important. Although, the *Raman process* is less significant than the two other processes, its inclusion with R $= (10 \pm 3)$ K^{-5} s^{-1} improves the fit.

In conclusion, the times of relaxation between different triplet substates can be relatively long, such as 720 ns for Pt(thpy)$_2$ at $T = 1.3$ K. As a consequence, the emission of higher-lying states cannot be frozen out. Therefore, the usually monitored time-integrated, low-temperature emission spectra often represent superimposed spectra which stem from different excited states. (Compare also the results discussed for Ir(btp)$_2$(acac), Fig. 1.34, below.) Moreover, in this situation, the emission decay behavior depends on the excitation and the detection energy. At very low temperature, the *direct process* of SLR dominates for compounds with ZFSs of the triplet state of a few cm^{-1}, while with temperature increase the SLR becomes distinctly faster due to growing in of the *Orbach* and/or the *Raman processes*. The specific temperature dependence of the SLR rate and the importance of an individual process is essentially determined by the magnitude and pattern of ZFS of the lowest triplet. In particular, when a real electronic state (such as substate **III**) is present (see Fig. 1.20b), the *Orbach process* will dominate the *Raman process*. On the other hand, the latter process will govern the temperature dependence of SLR, when the third state is absent [182, 185]. For completeness, it should be noted that the processes of SLR are very fast at ambient temperature, and a thermalized decay time of the three substates is observed.

The pattern and magnitude of ZFS is chemically tunable, as is depicted schematically in Fig. 1.11. Thus, the effective SLR can also be varied chemically. Several emitter/matrix combinations, for which highly resolved spectra as well as SLR properties have been investigated, are summarized in Table 1.1. The τ_{SLR} values given in the table refer to the low temperature ($T = 1.3$ K) at which the *Orbach* and *Raman processes* can be neglected. Only the *direct process* of SLR is important. The data in the table show that the effects of SLR are quite general, with the SLR times mostly in the range of several 100 ns to some µs, when the energy separation between the two involved states is of the order of 10 cm^{-1}, or less. The value found for site **H** of Ir(btp)$_2$(acac) in CH$_2$Cl$_2$ with $\tau_{SLR} = 22$ µs is, at first sight, remarkably long. However, the energy separation of $\Delta E_{II,I} = 2.9$ cm^{-1} is, compared to the one of Pt(thpy)$_2$ in *n*-octane, relatively small. Thus, if one takes the $(\Delta E_{II,I})^3$ dependence of the corresponding rate $k_{II,I}^{SLR}$ into account [Eq. (9)] and calculates formally the expected time of τ_{SLR} for an assumed $\Delta E_{II,I}$ value of 7 cm^{-1}, a hypothetical SLR time

Table 1.1 Photophysical data of several organo-transition metal compounds arranged according to an increasing spin–lattice relaxation time due to the direct process of SLR.

Compound, Matrix	Lowest triplet substate I[1] (cm^{-1})	ZFS		Decay times		Remarks, References
		$\Delta E_{II,I}$ [1] (cm^{-1})	$\Delta E_{III,I}$ [1] (cm^{-1})	τ_I [2] (μs)	τ_{SLR} (II → I) [1),2)] (μs)	
$[Ru(bpy)_3]^{2+}$ in $[Zn(bpy)_3](ClO_4)_2$	17 684	8.7	61	230	0.22	74
$Pt(ppy)_2$ in n-octane	19 571	6.5	32	70	0.39	70, 148
$Pt(thpy)_2$ in n-octane	17 156	7	16	110	0.72	182, 185
$Pt(thpy)(CO)(Cl)$ in n-octane	18 012.5	0.055	3.8	120	3	182, 141, SLR between the substates III and I/II
$Pt(4,6-dFppy)_2$ in n-octane	20 629	4	31	55	3.7	204
$Ir(btp)_2(acac)$ in CH_2Cl_2 (site H)	16 268	2.9	25	150	22	147, 203

1) Determined from highly resolved spectra.
2) Measured at $T = 1.3\,K$.

of $\approx 1.5\,\mu s$ would be obtained. This value is only by a factor of about two longer than that found for $Pt(thpy)_2$. Such a deviation might easily result from different values of the prefactors, the velocity of sound, and/or the matrix element, in Eq. (9) (compare also Section 1.10.3 and Ref. [203]).

Finally, an interesting implication of the occurrence of a slow SLR should be noted which opens the possibility of investigating the emission properties of the higher-lying substate **II** also at $T = 1.3\,K$, as the corresponding emission cannot be frozen out. Therefore, access is obtained to the highly informative low-temperature emission spectrum of this higher lying state. This favorable situation is applied in Section 1.9.2.3 to study the highly resolved vibrational satellite structure of the emission of substate **II** of $Pt(thpy)_2$.

1.8
The Triplet State Under Application of High Magnetic Fields: Properties of Ir(btp)₂(acac)

The triplet substates and the related transitions of a specific organometallic compound exhibit distinct differences with respect to photophysical properties, such as radiative rates, energy separations, SLR dynamics, vibronic coupling (see below, Section 1.9), and emission and excitation spectra. Many studies have shown that these properties can distinctly be altered under the application of large external magnetic fields (compare Fig. 1.15 and Refs. [74, 85, 115, 147, 163, 177, 185, 202,

204–215]). In this section, we will illustrate how the application of magnetic fields alters the properties of the three triplet substates and of the corresponding electronic 0-0 transitions. For this, we have chosen Ir(btp)$_2$(acac) [147, 203], as it represents a very efficient red-emitting OLED material. Consequently, many photophysical and OLED related investigations were carried out with this complex [215–236], although the influence of magnetic field application has (apart from Ref. [147]) not yet been discussed.

Ir(btp)$_2$(acac) was first synthesized and studied spectroscopically by Thompson et al. [227]. The emitter exhibits a high photoluminescence quantum yield of $\phi_{PL} = 21\%$ in solution, and a decay time of 5.8 µs. [227] In a 4,4′-bis(carbazol-9-yl)biphenyl (CBP) film, a ϕ_{PL} value as high as 50% has been reported [216].

Figure 1.23 shows emission spectra of Ir(btp)$_2$(acac) dissolved in CH_2Cl_2, and the spectral changes upon cooling. The host material crystallizes as a Shpol'skii-like matrix, and therefore, at $T = 4.2$ K line spectra are observable. The lines represent electronic 0-0 transitions of a large number of different sites, which are characterized by dissimilar interactions of the dopants with their respective environments or matrix cages (compare Section 1.10). It will be shown below that these electronic transitions occur between the respective triplet substate **II** and the elec-
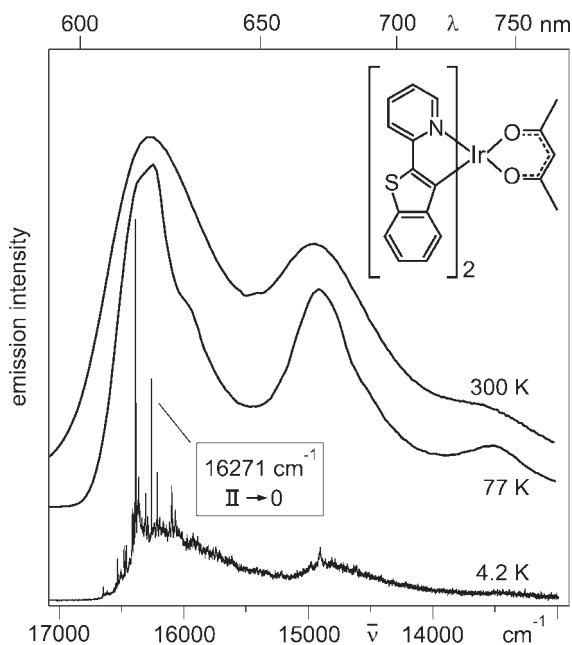
Fig. 1.23 Emission spectra of Ir(btp)$_2$(acac) in CH_2Cl_2 (ca. $\approx 10^{-5}$ mol L^{-1}) at different temperatures. The emission structure at $T = 4.2$ K consists mainly of 0-0 lines (triplet substate **II** to the electronic ground state **0**) of a large number of discrete sites and a broad inhomogeneous background. In this section, properties of the site at 16 271 cm^{-1} (specified as site **H** in Section 1.10) are investigated in detail. Other sites are discussed in Section 1.10.

tronic ground state S_0 (**0**). In the 4.2 K spectrum of Fig. 1.23, the **II** $\leftrightarrow$ **0** transition at 16 271 cm^{-1} of one specific site is marked (in Section 1.10 and Ref. [147] this site is specified as site **H**). This site can be selectively excited with a tunable laser and studied individually.

Within the scope of this section, we want to focus on the electronic transitions between the T_1 substates and the ground state S_0. The emission line spectra of the corresponding energy range are reproduced in Fig. 1.24. One can clearly identify the three 0-0 transitions from the three triplet substates **I**, **II**, and **III**, though only at different temperatures. At $T = 1.35$ K, a very weak peak at 16 268 cm^{-1} is detected, and is assigned to the purely electronic **I** $\rightarrow$ **0** transition (I(0-0)). At $T = 4.2$ K, the **II** $\rightarrow$ **0** emission (II(0-0)) at 16 271 cm^{-1} dominates and represents almost the only 0-0 emission line. With temperature increase, the triplet substate **III** is also populated according to a Boltzmann distribution, and the corresponding 0-0 transition (III(0-0)) at 16 293 cm^{-1} grows in [147]. These data reveal that the substates **I** and **II** are separated by (2.9 ± 0.2) cm^{-1}, whereas the splitting of substates **I** and **III**, representing the total ZFS, amounts to (25.0 ± 0.5) cm^{-1}. From the intensity distribution and its temperature dependence, it can be concluded that the radiative transition from the lowest substate **I** to the ground state **0** is largely forbidden,
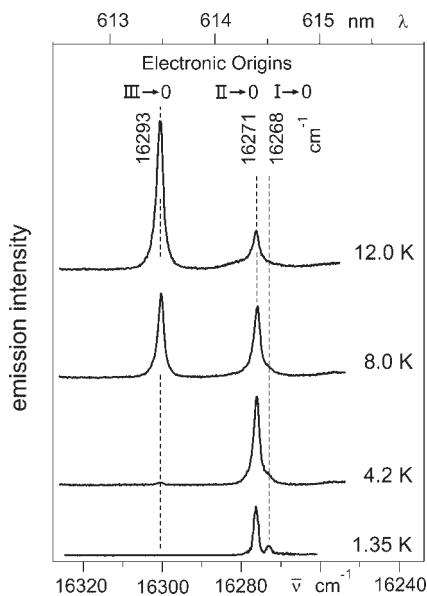
Fig. 1.24 Emission spectra at different temperatures of a selected site of Ir(btp)$_2$(acac) dissolved in CH$_2$Cl$_2$ at a concentration of $\approx 10^{-5}$ mol L^{-1}. In Section 1.10, this site is specified as site **H**. Only the region of the electronic origins is reproduced. The specific site was excited at 16 742 cm^{-1} (449 cm^{-1} vibrational satellite of the **0** $\rightarrow$ **III** transition at 16 293 cm^{-1}). The intensities of the different spectra are comparable. The spectrum at $T = 1.35$ K was measured with a higher resolution to obtain the energy difference of $\Delta E_{II\text{-}I} = 2.9$ cm^{-1} sufficiently accurate (compare Section 1.9.3 and Ref. [147]).

while the transitions from the two higher-lying substates **II** and **III** to the ground state are significantly more allowed. This can also be verified by decay time measurements, which reveal individual decay times of the T_1 substates of $\tau_I = 150\,\mu s$, $\tau_{II} = 58\,\mu s$, and $\tau_{III} = 2\,\mu s$ [203]. The ZFS and decay time values are summarized in an energy level diagram given in Fig. 1.27 (see below). Mainly due to the magnitude of $\Delta E(\text{ZFS}) = 25\,\text{cm}^{-1}$, it can be concluded from Sections 1.3.3.3 and 1.4 that the triplet T_1 parent term has to be assigned as a $^3\text{LC}(^3\pi\pi^*)$ term which, however, is significantly perturbed by an $^{1,3}\text{MLCT}$ admixture according to the coupling routes presented in Fig. 1.13a.

The forbiddenness of the transition from substate **I** to the singlet ground state **0** and the long emission decay time allows one to conclude that the lowest triplet substate **I** represents an almost pure triplet. A similar conclusion holds also for the lowest triplet substates of Ir(ppy)_3, Pt(thpy)_2, $[\text{Ru(bpy)}_3]^{2+}$, $[\text{Os(bpy)}_3]^{2+}$, and many other organo-transition metal compounds.

For completeness, it should be noted that the data given above refer only to the specific site investigated. Other sites exhibit different ZFSs, decay times of the substates, SLR times, etc. [147, 203]; these properties are discussed in Section 1.10.

The application of external magnetic fields significantly alters the splitting pattern and the intensity distribution of the three electronic origin lines. Figure 1.25 reproduces the corresponding trends for the field range of $B = 0\,\text{T}$ to $B = 8\,\text{T}$. Figure 1.25a shows the spectra measured at $T = 8\,\text{K}$ for the complete spectral range of the three electronic origins. The relatively high temperature was chosen to provide sufficient population of the higher-lying substate **III**. Figure 1.25b reproduces only the region of the electronic origins $I \rightarrow 0$ and $II \rightarrow 0$. The spectra are monitored at $T = 2.8\,\text{K}$ in order to obtain a better resolution; the population of substate **III** is frozen out at this temperature.

With an increase of the magnetic field strength, distinct Zeeman shifts of the transition energies are observed. Transition III(0-0) is shifted to higher energy from $16\,293\,\text{cm}^{-1}$ ($B = 0\,\text{T}$) to $\approx 16\,295\,\text{cm}^{-1}$ ($B = 8\,\text{T}$), while transition I(0-0) is shifted to lower energy from $16\,268\,\text{cm}^{-1}$ ($B = 0\,\text{T}$) to $\approx 16\,265.5\,\text{cm}^{-1}$ ($B = 8\,\text{T}$). The energy of II(0-0) at $16\,271\,\text{cm}^{-1}$ ($B = 0\,\text{T}$) is only slightly increased by $\approx 0.5\,\text{cm}^{-1}$ up to $B = 8\,\text{T}$. Figure 1.26 summarizes the magnetic field-induced energy shifts of the three electronic origins. Clearly, the Zeeman shifts are asymmetric. This is qualitatively understood, since the B-field induced mixings between the corresponding states depend on their energy separations at zero field (energy denominators) which are strongly asymmetric for $\text{Ir(btp)}_2(\text{acac})$.

It should further be noted that the Zeeman shifts are usually different for molecules with different orientations relative to the magnetic field vector. This applies also to polycrystalline samples, as the molecules have different orientations in different micro-crystals. Therefore, the observed Zeeman pattern corresponds to an averaged orientational distribution of molecules.

A further important magnetic field-induced effect becomes apparent in the spectra of Fig. 1.25b. At $B = 0\,\text{T}$, the transition from substate **I** to the ground state **0** is very weak, even at lowest temperature applied. With an increase of the field
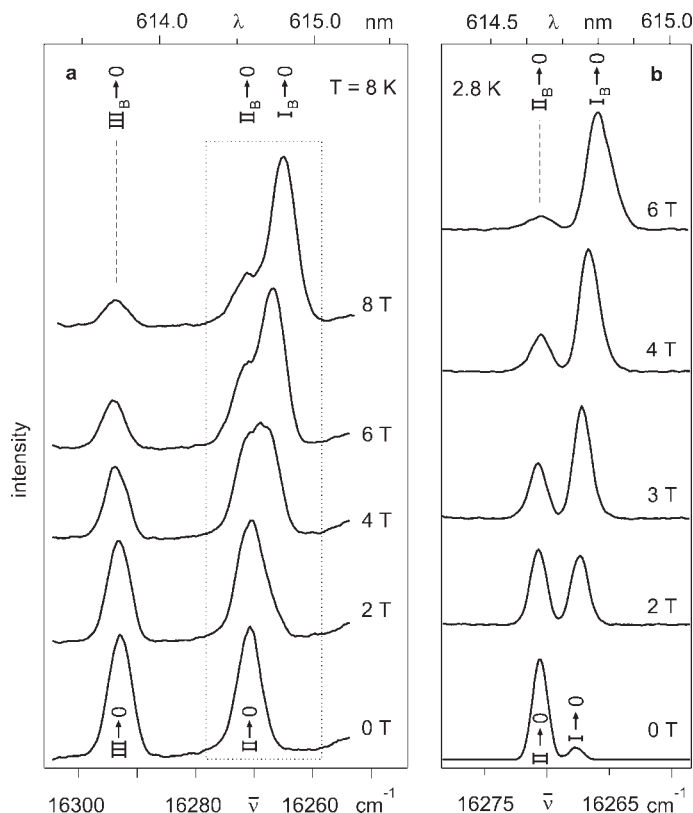
Fig. 1.25 Emission spectra of Ir(btp)$_2$(acac) in CH$_2$Cl$_2$ at ≈10^{-5} mol L^{-1} in the energy range of the electronic 0-0 transitions at different magnetic fields. The spectra refer to the specific site which is investigated in this section (site **H** in Section 1.10). (a) The spectra were monitored at *T*=8 K to obtain sufficient thermal population of substate **III** ($\bar{\nu}_{exc}$ = 26810 cm^{-1}, non-selective excitation). (b) Selectively excited emission spectra for the energy range of the two lowest transitions **I** → **0** and **II** → **0**, *T*=2.8 K, $\bar{\nu}_{exc}$ = 16293 cm^{-1} (**0** → **III**). For further experimental details, see Ref. [147].

strength, this transition gains intensity. This effect becomes obvious already for *B* <1 T (not shown). At *B*=2 T and *T*=2.8 K, the intensity stemming from the perturbed state **I**$_B$ is almost equal to the intensity resulting from substate **II**$_B$. At *B*=6 T, for example, the intensity of transition **I**$_B$ → **0** dominates clearly. For an explanation of this effect, three factors are important [147] (compare Fig. 1.27). First, the magnetic field-induced mixing of the wavefunction of substate **I** with the wavefunctions of the two higher states renders transition **I**$_B$ → **0** more allowed. Second, due to the increased splitting between substates **I** and **II** under the magnetic field, the Boltzmann factor for population of state **II** (relative to state **I**) is significantly smaller. Third, SLR between the triplet substates becomes considerably faster with increasing field-induced energy separation between the
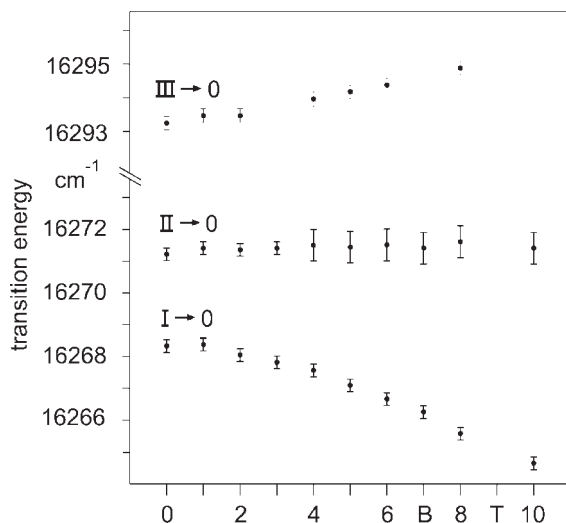
Fig. 1.26 Magnetic field-induced shifts of the **T₁** substates **I**, **II**, and **III** of Ir(btp)₂(acac) in CH₂Cl₂. For experimental details, see Fig. 1.25 and Ref. [147].
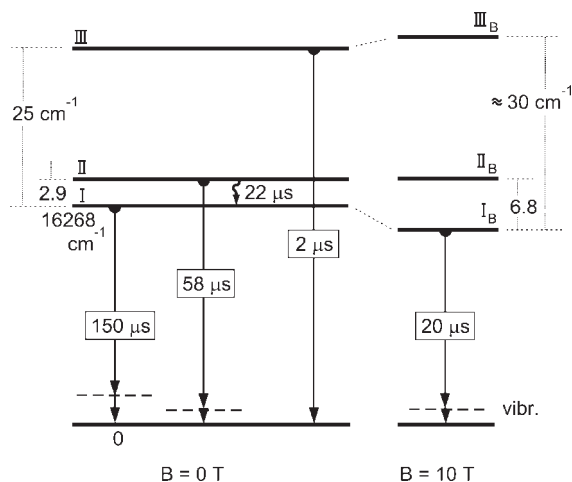
Fig. 1.27 Energy level diagram and photophysical data for the lowest triplet state **T₁** of Ir(btp)₂(acac) without and with an external magnetic field, respectively. The state is classified as **³LC** (³ππ*), which is significantly MLCT perturbed. The values given apply to the individual site under investigation in this section (specified as site H in Ref. [147] and in Section 1.10). Other sites exhibit different spectroscopic properties (compare Section 1.10). The decay times of the **T₁** substates and the spin–lattice relaxation time of 22 μs (at $T=1.5$ K) referring to zero magnetic field have been determined in Ref. [203], while the data at $B=10$ T ($T=1.7$ K) are taken from Ref. [147].

Fig. 1.28 Emission decay time of Ir(btp)$_2$(acac) in CH$_2$Cl$_2$ for different magnetic flux densities B at T=1.7 K and under selective excitation of **T$_1$** substate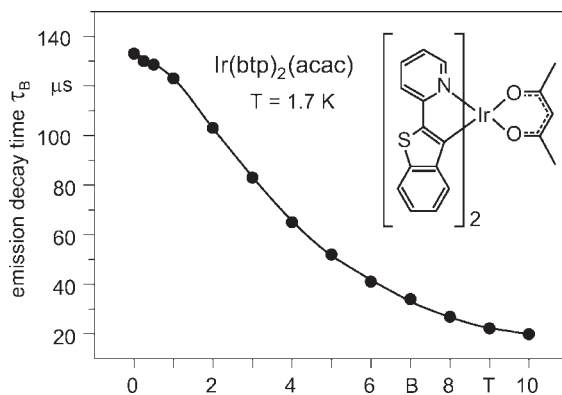 **III**. The decay is monoexponential over the whole range $0 \leq B \leq 10$ T; detection at the transition **I$_B$ → 0**.

corresponding states (compare Section 1.7).[29] Accordingly, the Boltzmann distribution is established faster and thus the non-equilibrated fraction of the emission resulting from the higher-lying substate **II$_B$** is strongly reduced.

The increased allowedness of transition **I$_B$ → 0** under the application of a magnetic field is also reflected in the emission decay time of the perturbed substate **I$_B$**. In particular, the almost pure and long-lived triplet substate **I** is expected to experience a distinct reduction of the emission decay time, when mixing with shorter-lived substates. Indeed, Fig. 1.28 shows that a drastic effect is observed. At T=1.7 K, the decay time decreases from $\tau_I (B=0\,\text{T}) = 133\,\mu\text{s}$ to $\tau_I (B=10\,\text{T}) = 20\,\mu\text{s}$. The measurements were carried out with detection at the respective Zeeman shifted electronic origin (for B=0 T at 16 268 cm^{-1} and for B=10 T at 16 264.7 cm^{-1}). Comparable measurements are often interpreted by the use of a simple first-order perturbation model which takes into account only mixing of the two lowest strongly interacting substates. Such a model is valid, if the energy separation between the substates **I** and **II** and the corresponding Zeeman shifts are small compared to the energy separation to substate **III**. This situation has been found, for example, for Ir(ppy)$_3$ [115], [Ru(bpy)$_3$]$^{2+}$ [205], and [Os(bpy)$_3$] [177, 206, 207]. For Ir(btp)$_2$(acac), however, the data show clearly that this simple approach is not successful, as the decay time of **I$_B$** at B=10 T is, with τ_B=20 μs, much shorter than the decay time of **II** at B=0 T (τ_{II} =58 μs). Therefore, it must be concluded that the Zeeman mixing occurs between all three substates. In particular, the singlet component of substate **III** is responsible for the drastic shortening of the emission decay time of the lowest substate by the applied magnetic field.

29) Magnetic-field induced changes of SLR times have been investigated with Pt(thpy)$_2$ [185]. These studies support the assignment given above.

In conclusion, the magnetic field experiments are very helpful for the characterization of an organo-transition metal complex, as they allow a more thorough interpretation of obtained data. For Ir(btp)$_2$(acac), the Zeeman behavior as described demonstrates that the three states involved represent indeed substates of one triplet parent term. An assignment of the three electronic origins to different sites can thus be excluded.

1.9
Vibrational Satellite Structures: Case Studies Applied to Pt(thpy)$_2$ and Ir(btp)$_2$(acac)

Usually, the emission from an electronic state takes place as purely electronic transition, for example, from a substate of the lowest triplet state T_1 to the electronic ground state S_0 with involvement of vibrational modes. At low temperature, these latter transitions occur at the low-energy side of the purely electronic transition. Generally, many different vibrations – having different energies – are active in the radiative processes from the emitting state of an organo-transition metal compound. Thus, an energetically widespread distribution of vibrational satellites is obtained. In suitable cases, the corresponding lines can be well resolved. With temperature increase, these vibrational satellites are smeared out and result in broad vibrational side bands (compare Section 1.11). The sidebands can comprise a substantial part of the total emission intensity, and this can have significant consequences, for example, on the color purity of an emitter applied in an OLED. In particular, a compound, of which the purely electronic 0-0 transition lies in the deep blue region of the visible spectrum, can still be a blue-green or turquoise emitter, if the vibrational satellite bands extend with significant intensity into the green region of the spectrum. This is due to the wavelength dependence of the human eye sensitivity, being highest for green. On the other hand, vibrational sidebands of red emitters frequently extend into the near-infrared region. This part is lost for the visual efficiency of an OLED.

Clearly, it is very important to study the mechanisms which lead to the occurrence of vibrational satellites, and to understand the corresponding spectral features. This will be addressed in the next sections, while broadening mechanisms including effects induced by temperature increase are discussed in Section 1.11.

1.9.1
Vibrational Satellites: Background

An electronic transition is usually accompanied by vibrational satellites which are found in absorption or excitation spectra, and also in emission spectra. Within this chapter, attention is focused on emission properties. The satellite lines result from different vibrational activities, namely from the well-known Franck–Condon activity and the less frequently discussed Herzberg–Teller (HT) activity. Here, we introduce details of both mechanisms.

1.9.1.1 **Franck–Condon Activity**

Vibrational satellites according to Franck–Condon activity can only occur, if the involved purely electronic transition between the ground state **0** and an electronically excited state **1** carries allowedness. In this situation, progressions can result. The occurrence of a progression is always connected with a geometry change between the two electronic states with respect to the vibrational coordinate of the progression forming mode. A useful measure for the extent of such a geometry variation is the Huang–Rhys parameter, *S*. In the following sections an introduction to these properties and to the spectroscopic implications is given (compare Refs. [98] (p. 200),and [70, 237, 238]).

Figure 1.29a depicts the harmonic potentials for a model system with only one vibrational coordinate *Q* in the electronic ground state **0** and the excited state **1**. It is assumed that the potentials are (nearly) equal, but are shifted by ΔQ with respect to each other – that is, the vibrational frequencies of both states are also (nearly) equal. Generally, the wavefunctions of electronic-vibrational states depend on both, the coordinates of the electrons and nuclei, and thus the wavefunctions are
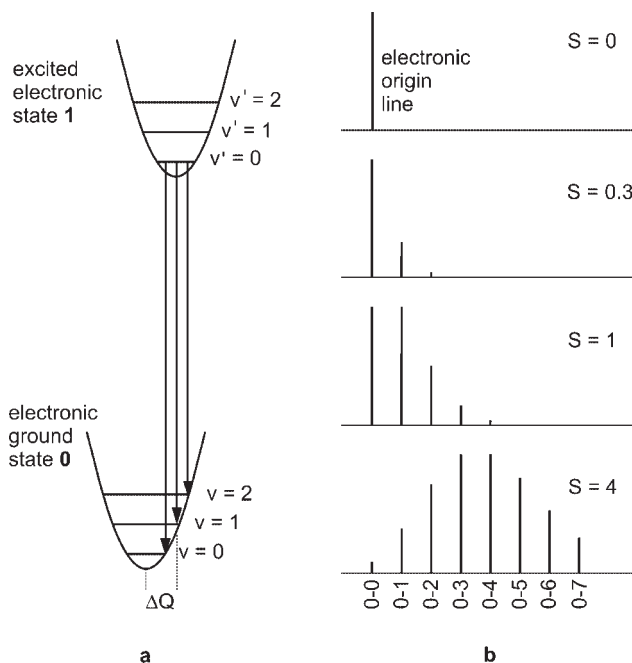
Fig. 1.29 Franck–Condon progressions. (a) The equilibrium positions of the potential surfaces of the excited state **1** and the ground state **0** are shifted by ΔQ. This leads to a progression in the emission spectrum, if the dipole moment of the transition between the states **1** and **0** is non-zero. The progression is characterized by vertical transitions that are depicted for a low-temperature emission. (b) The intensity distribution of a progression of vibrational satellites depends on the Huang–Rhys parameter, *S*, which is proportional to $(\Delta Q)^2$ [see Eq. (21)]. The examples given in (b) are calculated according to Eq. (22). The peaks of highest intensity are normalized for the different diagrams.

very difficult to handle. However, taking into account that the electronic motion is much faster than the vibrational motion, one can factorize the vibrational and the electronic part of the wavefunction. This leads to the Born–Oppenheimer approximation with the

$$\text{ground state } \mathbf{0}: \psi_0(v) = \phi_0 \cdot \chi_0(v) \tag{17}$$
$$\text{and the excited state } \mathbf{1}: \psi_1(v') = \phi_1 \cdot \chi_1(v')$$

wherein ϕ_0 and ϕ_1 are the electronic wavefunctions and $\chi_0(v)$ and $\chi_1(v')$ are harmonic oscillator functions with vibrational quantum numbers v and v' for the electronic ground state $\mathbf{0}$ and the excited state $\mathbf{1}$, respectively. The harmonic oscillator functions are similar sets of wavefunctions, but they are defined with respect to different zero-positions of the variable Q.

The desire is to apply this model to study low-temperature emission spectra. The corresponding intensity distribution is proportional to the square of the electronic transition dipole moment involving the two states. When applying the approximation [Eq. (17)], the intensity of a transition from the zero-point vibrational level ($v' = 0$) of the excited state $\mathbf{1}$ to a level v of the electronic ground state $\mathbf{0}$ can be expressed by (Fig. 1.29a):

$$I_{1,0}(v' = 0, v) \sim |\langle \phi_1 | \mathbf{er} | \phi_0 \rangle|^2 \cdot |\langle \chi_1(v' = 0) | \chi_0(v) \rangle|^2 \tag{18}$$

where $\mathbf{er}$ is the usual electric dipole operator. The first term of the right-hand side of Eq. (18) represents the squared electronic dipole matrix element, and specifies the intensity of the purely electronic transition. The second term is the Franck–Condon factor, which is discussed in more detail below. This leads to the well-known Franck–Condon progression of vibrational satellites that progress in the spectrum by the energy $\overline{v}_Q$ of the vibrational mode under consideration.

The total emission intensity, I_{tot}, of all transitions with the different vibrational quantum numbers v can be summed up, and one obtains

$$I_{\text{tot}} \sim |\langle \phi_1 | \mathbf{er} | \phi_0 \rangle|^2 \tag{19}$$

This result means that the total emission intensity – that is, the intensity of the electronic 0-0 transition and the complete Franck–Condon progression – depends only on the purely electronic transition dipole moment. Thus, the electronic allowedness represents the source of intensity which is distributed according to the Franck–Condon factor to the different vibrational satellites of the progression.

The Franck–Condon factor is given by the squared overlap integral of displaced harmonic oscillator functions.[30] It can be related ([109], p. 113) to the so-called Huang–Rhys parameter, S, according to

---

30) The Franck–Condon factor can only be non-zero for totally symmetric modes, as the vibrational ground state $\chi_1(v'=0)$ is totally symmetric.

$$|\langle\chi_1(v'=0)|\chi_0(v)\rangle|^2 = \frac{e^{-S}S^v}{v!} \tag{20}$$

This parameter S is directly connected with the shift ΔQ of the equilibrium positions of the involved electronic states (Fig. 1.29a). According to Ref. [109] (p. 112), one obtains

$$S = \frac{\pi c M \bar{v}_Q}{\hbar}(\Delta Q)^2 \tag{21}$$

wherein c is the velocity of light and M is the effective mass (=reduced mass) of the vibration Q. The value of M is usually not known, unless a normal coordinate analysis is available.

From Eq. (20), and by use of Eqs. (18) and (19), an expression can be derived, which is very useful for the characterization of geometry shifts of an excited state as compared to the ground state. For the intensity ratio of successive vibrational satellites of a Franck–Condon progression one finds, using the abbreviation $I_v = I_{1,0}$ (v'=0, v) for v≠0:

$$\frac{I_v}{I_{v-1}} = \frac{S}{v} \tag{22}$$

The intensity at the electronic origin (0-0 transition), I_0, can be expressed by

$$I_0 = I_{tot} \cdot e^{-S} \tag{23}$$

From the above equations it is seen that for $S=0$ the total intensity is contained in the purely electronic origin line [Eq. (23)] and the displacement between the two electronic states **1** and **0** is zero [Eq. (21)]; that is, there is no geometry change connected with the electronic transition. With an increase of the displacement ΔQ (Fig. 1.29a), and thus an increase of the Huang–Rhys parameter S, the intensity of the electronic 0-0 line decreases and the vibrational satellites of the Franck–Condon progression gain intensity [Eq. (22)]. This behavior is illustrated in Fig. 1.29b for several different values of S. Thus, the satellites gain intensity only by borrowing it from the electronic origin line. If the electronic transition is forbidden, Franck–Condon satellites also do not occur. This situation is found, for example, for the **0** ↔ **I** transition of Pt(thpy)$_2$ (see Fig. 1.15b). The consequences of the vibrational satellite structure being connected with such a forbiddenness will be discussed in the next section, and also in Sections 1.9.2 and 1.9.3.

The S-value represents a characteristic parameter, in particular, when different compounds are compared [70]. Hence, it is possible to characterize changes of the binding situation that occur between excited electronic states and ground states for different types of electronic transitions. For example, for the $T_1 \rightarrow S_0$ transitions of a large number of organo-transition metal compounds, the maximum S-values

lie between 0.3 and 0.08 (compare Ref. [70] and Sections 1.9.2 and 1.9.3). From this it follows that the geometry changes between the ground and excited triplet state are small. Moreover, the S parameters are found to be significantly smaller for compounds with large (!) MLCT admixtures to the excited triplet states than for compounds with emitting ^{3}LC states. This behavior is ascribed to the enlarged spatial extensions of the electronic wavefunctions with an increasing MLCT admixture. In this situation, an electronic transition results in a smaller charge density change per ligand, and thus has less influence on the specific binding separation (small ΔQ values) [70, 165].

1.9.1.2 Herzberg–Teller Activity

In the preceding section, it was shown that Franck–Condon-induced satellites or progressions can only occur if the electronic transition carries allowedness, which may then be distributed to the vibrational satellites. However, in many cases, the electronic transition is largely forbidden. Nevertheless, a rich vibrational satellite structure is observed. This situation is frequently found for organo-transition metal compounds, for which the transition probability from the lowest triplet substate **I** to the singlet ground state **0** is very small due to the almost pure triplet character of substate **I** (compare Sections 1.5, 1.6, and 1.8). Clearly, a different process – the vibronic or Herzberg–Teller coupling – must be taken into account. In particular, this mechanism must provide singlet character to the triplet substate via spin–orbit coupling in order to induce radiative allowedness to the vibronic transition.

As the corresponding vibronic mechanisms are discussed comprehensively elsewhere in the literature [206, 239–243], only a brief discussion of a specific mechanism – the *spin-vibronic coupling* – is given here. It has been shown that such a mechanism can indeed provide the required transition probability [70, 206]. This coupling route is illustrated schematically in Fig. 1.30.

For purely organic compounds the mechanism of spin-vibronic coupling is usually neglected due to the small value of the SOC constant. In contrast, for compounds of the platinum metal group, this mechanism can be very important. Specifically, vibrations of the central-metal ion – that are connected with variations of electron density of d-character in the spatial region of the organic ligands – can induce significant changes in the effective SOC. Good candidates for such vibrations are metal–ligand vibrations. Such a coupling route is shown schematically in Fig. 1.30. $\hat{H}_{SO}$ is the SOC Hamiltonian, **I** represents the unperturbed lowest triplet substate, and $\mathbf{S_m}$ is a higher lying singlet. The matrix element given in Fig. 1.30 signifies that the vibration with the (normal) coordinate Q modulates the SOC operator. This mechanism induces intensity to the specific vibrational satellite with the energy $\bar{v}_Q$ relative to the forbidden electronic origin, but it does not provide any intensity to the purely electronic 0-0 transition. Clearly, this vibronic mechanism can be effective for a large number of different vibrational modes Q. In this case, usually different intensity-providing higher-lying singlets $\mathbf{S_m}$ are involved. The corresponding vibrational satellites are frequently called "false origins".
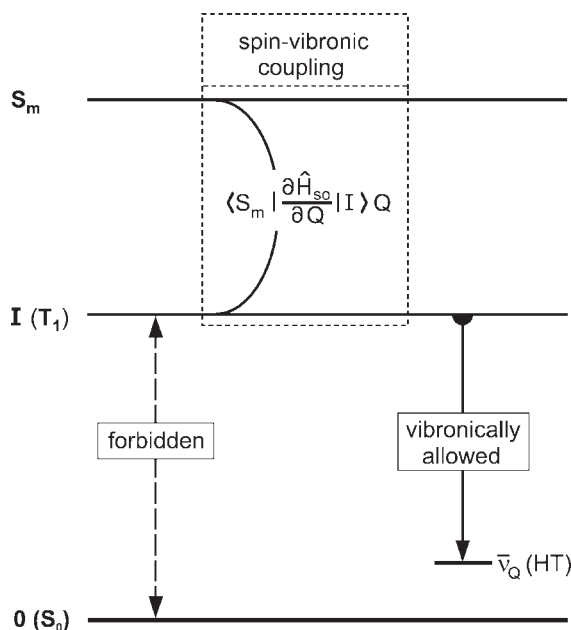
Fig. 1.30 Schematic illustration of the spin-vibronic coupling route (Herzberg–Teller coupling). This mechanism can become important, when the purely electronic **I** ↔ **0** transition is forbidden. The matrix element expresses schematically that a vibration, specified by a coordinate Q, changes the spin–orbit coupling (SOC) and thus induces an admixture of a higher-lying singlet state $\mathbf{S}_m$ to the triplet substate **I**. This mechanism can provide intensity to a vibrational satellite, but not to the electronic 0-0 transition. Note that HT coupling usually occurs with many HT active modes to different higher-lying singlets. Hence, a rich vibrational satellite structure results. For further explanation, see the text.

In Sections 1.9.2.1 and 1.9.3, we will demonstrate that HT coupling is indeed important for the low-temperature emission of Pt(thpy)$_2$ and Ir(btp)$_2$(acac). The importance of the HT coupling has also been shown for many other organo-transition metal compounds [70, 71, 73, 74, 115, 163, 177, 206].

1.9.2
Pt(thpy)$_2$ Emission: Temperature- and Time-Dependence of the Vibrational Satellite Structure

The vibrational satellite structures in the emission of Pt(thpy)$_2$ display triplet substate properties in a characteristic manner. In particular, the emission from substate **I** features a completely different vibrational satellite structure than the emission from the substates **II** and **III**. This behavior will be illustrated by presenting spectra, which are measured at different temperatures and at different delay times after an exciting laser pulse, respectively.

1.9.2.1 Herzberg–Teller-Induced Emission from Substate I: The 1.3 K Spectrum

Figure 1.31 shows the emission spectrum of Pt(thpy)$_2$ measured at $T = 1.3$ K. The rich vibrational satellite structure seems to belong to the electronic 0-0 transition at $17\,163$ cm^{-1}, which represents the **II → 0** transition (see Figs. 1.15 and 1.16). However, all vibrational energies as determined relative to this 0-0 transition do *not* match the vibrational energies available from IR measurements [70], and they cannot be related to vibrational energies found for Pd(thpy)$_2$ [70, 163]. On the other hand, by setting the electronic origin for these satellites to the position of the transition **I ↔ 0** at $17\,156$ cm^{-1} which, however, does not carry any intensity, an excellent correspondence of the satellite energies to those of known vibrational modes is obtained. This procedure allows us to determine the position of a missing electronic origin line. Indeed, as discussed in Section 1.5.1, the I(0-0) line can be observed directly under application of a magnetic field of $B \gtrsim 1$ T (see Fig. 1.15e). Interestingly, none of the satellites that is clearly identified in the 1.3 K time-integrated emission spectrum belongs to the electronic origin II(0-0) at $17\,163$ cm^{-1}, apart from a 15 cm^{-1} phonon satellite (Fig. 1.15b) and some spectral background.

The vibrational satellites observed in Fig. 1.31 correspond in most cases to fundamentals. Modes which occur up to ≈ 100 cm^{-1} relative to the electronic origin
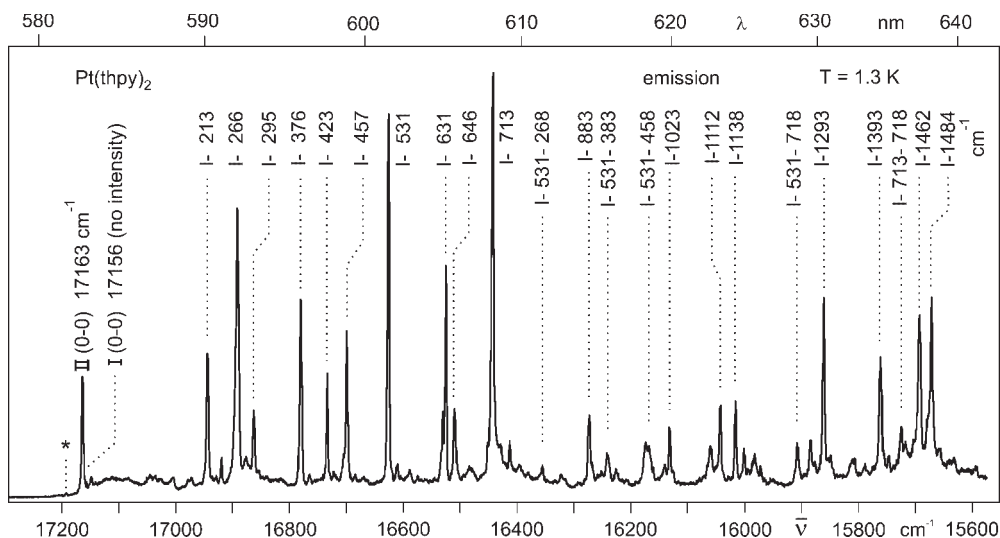

Fig. 1.31 Emission spectrum of Pt(thpy)$_2$ dissolved in *n*-octane and monitored at $T = 1.3$ K. Concentration $\approx 10^{-5}$ mol L^{-1}; $\lambda_{exc} = 457.9$ nm. The vibrational satellites are characterized by their energy separations from the electronic origin I(0-0) at $17\,156$ cm^{-1}. The asterisk denotes an electronic origin of a different site. The region of the electronic origins is shown in Fig. 1.15, on an enlarged scale.

have significant lattice or chromophore-cage mode character. It should even be taken into account that a mixing of complex vibrations with cage modes is still obvious up to $\approx$150 cm^{-1} [244]. Overlapping with this energy range up to 500/600 cm^{-1}, one finds metal–ligand (M-L) vibrations, which can, for example, be identified by a comparison of vibrational energies of Pt(thpy)$_2$ to those of Pd(thpy)$_2$ [70].[31] Fundamentals with energies higher than $\approx$600 cm^{-1} represent internal ligand vibrations. It should be noted that many vibrational satellite lines are accompanied by weak phonon satellites at their low-energy side.

The structure of the 1.3 K emission of Pt(thpy)$_2$ (Fig. 1.31) is characterized by the absence of the electronic I(0-0) transition, but by an occurrence of intense vibrational satellites. Since: (i) the satellites do not show any distinct progression; and (ii) the electronic origin does not show any intensity, it can be concluded that the satellites do not result from Franck–Condon activity (compare Section 1.9.1.1). All satellites that correspond to fundamentals are vibronically (Herzberg–Teller) induced, and hence represent so-called "false origins".

In Section 1.9.1.2 and Fig. 1.30, a mechanism has been proposed, which can provide intensity to the vibrational satellites (false origins), even when the electronic transition is spin-forbidden. In particular, for low-energy vibrations below $\approx$600 cm^{-1}, which exhibit pronounced metal–ligand character, such as the 266, 295, 376, 531 cm^{-1} modes (Fig. 1.31), it is very probable that the vibrating platinum ion can induce spin-vibronic coupling.

Presumably, this specific mechanism should be extended to describe also the occurrence of satellites of high-energy fundamentals, such as the 1023, 1138, 1293, 1393, and 1462 cm^{-1} vibrations (Fig. 1.31).[32] A corresponding mechanism has been treated theoretically with respect to organic molecules [239–243], and proposed to be of importance also for organo-transition metal compounds, such as Pt(thpy)$_2$ [70] and [Os(bpy)$_3$]$^{2+}$ [206]. It is based on a two-step coupling route, which involves the usual vibronic coupling of state **I** to a higher-lying triplet substate that experiences on its part effective SOC.

1.9.2.2 Franck–Condon Activity in the Emissions from Substates II and III: The 20 K Spectrum

With a temperature increase, for example to $T = 20$ K (Fig. 1.32), the electronic 0-0 transitions II(0-0) and III(0-0) at 17 163 cm^{-1} and 17 172 cm^{-1} grow in strongly. This is attributed to the thermal population of the two higher-lying states. Also, the vibrational satellite structure changes and satellites that correspond to fundamen-

---

31) Due to the largely ligand-centered transition in Pd(thpy)$_2$, its emission spectrum exhibits only very weak vibrational satellites of M-L mode character.

32) It should also be pointed out that for most of the intense false origins combinations are also observed, such as (531 + 1484), (713 + 1400), (1462 + 718) cm^{-1}, etc. (not all are shown in Fig. 1.31, but see Refs. [70, 144]). The second member of the combination represents a vibrational mode which is not Herzberg–Teller active, but shows Franck–Condon activity and corresponds to a totally symmetric mode (see next section). It is remarked that the 1484 cm^{-1} mode seems to be HT and FC active, presumably, two vibrational modes of different symmetry have nearly the same energy.
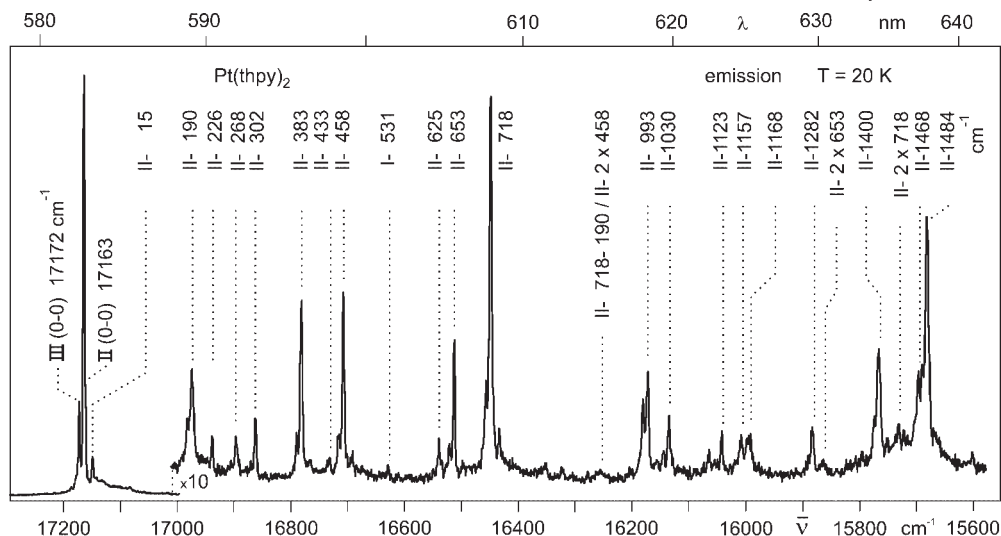
Fig. 1.32 Emission spectrum of Pt(thpy)$_2$ dissolved in *n*-octane and monitored at $T = 20$ K. Concentration $\approx 10^{-5}$ mol L^{-1}; $\lambda_{exc} = 457.9$ nm. The vibrational satellites are characterized by their energy separations from the electronic origin II(0-0) at 17 163 cm^{-1}, apart from the weak 531 cm^{-1} satellite which belongs to the emission of substate **I**. The region of the electronic origins is reproduced in Fig. 1.15, on an enlarged scale.

tals different from those found in the 1.3 K emission spectrum, grow in; thus, the emission spectrum changes drastically (compare Figs. 1.31 to 1.32). Moreover, those satellites which dominate at $T = 1.3$ K, such as the 531 cm^{-1} satellite, become weak at higher temperature. Further, in the 20 K emission spectrum, the electronic origin lines II(0-0) and III(0-0) are the dominating peaks. In contrast to the situation of the electronic 0-0 transition **I** $\leftrightarrow$ **0**, they carry significant allowedness. This is evidenced, for example, by the possibility of exciting the substates **II** and **III** directly (see Fig. 1.15a and 1.15d)

The vibrational satellites in the 20 K emission spectrum are observed as vibrational doublets. These all exhibit the same energy separation of 9 cm^{-1}, like the two electronic origins II(0-0) and III(0-0). Thus, the same vibrational modes are active in the radiative processes of both electronic states **II** and **III**. In Fig. 1.32, only satellites of origin II(0-0) (at 17 163 cm^{-1}) are specified by marking the vibrational energies.

The 20 K emission spectrum exhibits vibrational satellites due to the activity of fundamentals (e.g., 190, 383, 458, 718, 1400, 1484 cm^{-1}, etc.; see Fig. 1.32), of combinations of these fundamentals [e.g., (190 + 1484), (383 + 1400), (458 + 1484), (718 + 1400), (718 + 1484) cm^{-1}, etc.], and for the most intense satellites, also the second members of progressions (e.g., 1×718 cm^{-1}, 2×718 cm^{-1}, 1×1484 cm^{-1}, 2×1484 cm^{-1}) are also observed. Some of these satellites are not displayed in Fig. 1.32 (but see Refs. [70, 144]). These results can be rationalized, when all vibrational satellites with significant intensity are assigned to correspond to totally symmetric fundamentals. This assignment is also in accordance with the observation that the

same fundamentals are built upon the false origins occurring in the 1.3 K emission spectrum. An assignment to an alternative symmetry would not allow us to explain the very distinct differences of vibrational activities found in the emission from the states **I** and **II**, respectively.

Moreover, these totally symmetric fundamentals are assigned to be Franck–Condon active (compare Section 1.9.1.1) and indeed, for the most intense satellites weak overtone satellites are also found. By use of Eq. (22), the corresponding Huang–Rhys parameters S can be estimated. For the most "pronounced" progressions of the 718 and the 1484 cm^{-1} modes, a value of $S \approx 0.08$ is obtained. The occurrence of other progressions, namely of the fundamentals of 383, 458, and 653 cm^{-1} is also indicated (Fig. 1.32). However, progressions are not observed for each totally symmetric fundamental. These might exhibit still smaller S parameters, although even for a similar Huang–Rhys parameter of $S \approx 0.08$, most of the corresponding overtone satellites would be hidden in the noise of the spectrum.

The occurrence of only small Huang–Rhys parameters means that the shifts of the equilibrium positions for all vibrational coordinates is small – that is, the triplet geometry of $Pt(thpy)_2$ is only slightly perturbed with respect to the electronic ground state, at least for the applied rigid low-temperature matrix. An equivalent conclusion can be drawn for almost all triplet emitters hitherto studied by our group [70]. This result implies, indirectly, that the coupling of the excited state(s) of the emitter molecule to its host environment is small. It should be noted that this property may depend on the applied host material; hence, care must be taken when selecting adequate matrix–emitter combinations.

1.9.2.3 Time-Resolved Emission and Franck–Condon/Herzberg–Teller Activities

In Section 1.7.2 and Fig. 1.21 it was shown that the emission of $Pt(thpy)_2$ decays at $T = 1.3$ K biexponentially, with time constants of 600 ns and 110 µs, when the compound is excited non-selectively, for example in the ultraviolet. This behavior is a consequence of a population of substate **II** by very fast ISC processes and of the depletion of this state **II** with a time constant of 600 ns. This decay is mainly determined by the SLR from substate **II** to substate **I**. State **I** is also populated directly by the fast ISC routes and emits with its intrinsic decay time of 110 µs. Thus, during the first about two microseconds after the laser pulse, substate **II** is still populated, and superimposed emissions stemming from both states **I** and **II** with strongly different decay times are obtained. According to the large difference of these time constants, discrimination of the two emission spectra will be possible by applying time-resolved spectroscopy.

Indeed, this is successful, and has been demonstrated in Ref. [245]; the results are illustrated in Fig. 1.33. Figure 1.33a reproduces the emission spectrum detected immediately after the exciting laser pulse ($\lambda_{exc} = 337.1$ nm, pulse width 0.5 ns) with no time delay ($t = 0$ ns) and integrated during a time window of $\Delta t = 500$ ns. Hence, the *fast* and non-delayed emission spectrum which predominantly results from substate **II** is obtained. A totally different spectrum results, when the emission is monitored after a time being long compared to the decay time of 600 ns. For example, with a delay of $t = 10$ µs after the laser pulse and an integration time of
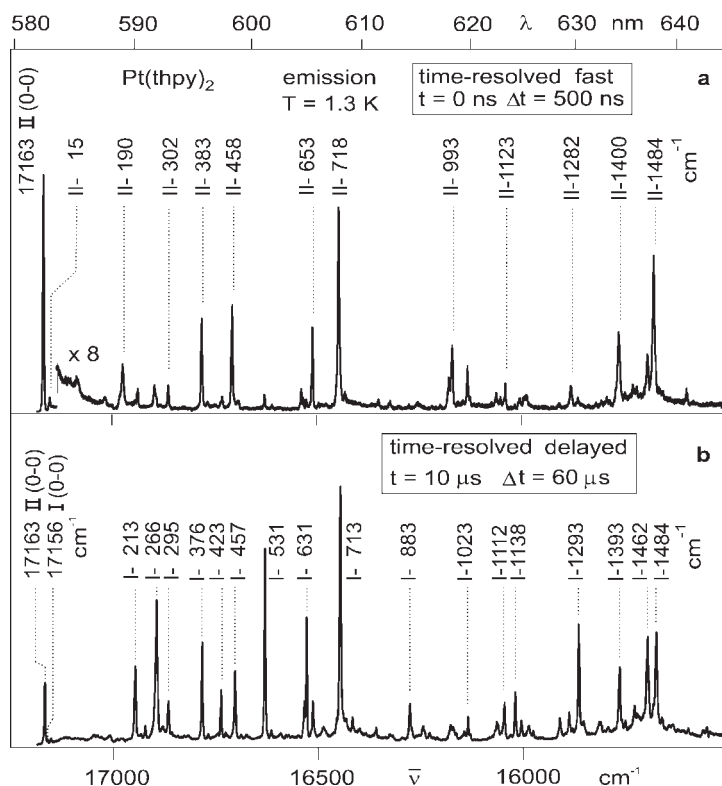
Fig. 1.33 Time-resolved emission of Pt(thpy)$_2$ dissolved in *n*-octane (ca. ≈10^{-5} mol L^{-1}) and monitored at T=1.3 K. Excitation: λ_{exc}=337.1 nm; pulse width ≈0.5 ns; repetition rate 100 Hz. (a) The emission is detected without any delay and integrated over Δt=500 ns. (b) Detection of the emission after a delay of t=10 μs and integrated over Δt=60 μs. The energies of the vibrational satellites are given in cm^{-1} relative to the electronic origin II(0-0) (a) and origin I(0-0) (b), respectively (compare Ref. [245]).

Δt=60 μs (time window), the emission spectrum as reproduced in Fig. 1.33b, is obtained. This spectrum represents the emission of substate **I**.

The delayed emission spectrum is very similar to the time-integrated emission spectrum measured at T=1.3 K (compare Fig. 1.33b and Fig. 1.31.) Therefore, this delayed spectrum is similarly assignable, as described in Section 1.9.2.1. In particular, all vibrational satellites that are marked in Fig. 1.33b represent false origins, and their intensities are vibronically (Herzberg–Teller) induced. Also, this delayed emission spectrum does not reveal any intensity at the position of the electronic 0-0 transition from **I → 0**.[33]

33) The occurrence of the electronic origin II(0-0) in the time-delayed spectrum (Fig. 1.33b) is not expected at first sight. However, its appearance is a consequence of a thermal repopulation of substate **II**, according to a Boltzmann distribution which applies after a sufficiently long delay time and according to the relatively large transition probability of the **II → 0** transition.

The fast and non-delayed emission spectrum (Fig. 1.33a) shows nearly the same structure as the time-integrated spectrum measured at $T = 20$ K (Fig. 1.32). However, the satellites that result from substate **III** ($9 \, cm^{-1}$ higher-lying peaks of the "doublet" structure in the 20 K emission spectrum) do not occur in the fast spectrum. Obviously, at $T = 1.3$ K, an emission of substate **III** is not observed. This is due to very fast SLR processes from substate **III** to the lower lying substates **II** and **I** (compare also Section 1.7). Thus, the fast spectrum represents the non-thermalized emission spectrum of state **II**. The Boltzmann distribution does not apply immediately after the excitation pulse, as the thermal equilibration is relatively slow. (This behavior has been studied in detail also for $[Ru(bpy)_3]^{2+}$; compare Refs. [74, 185].) The emission spectrum displayed in Fig. 1.33a (fast spectrum) is assigned similarly as discussed in Section 1.9.2.2. In particular, the electronic 0-0 transition **II** $\rightarrow$ **0** (origin II(0-0)) strongly dominates the spectrum (note the factor of 8 in Fig. 1.33a), and very probably almost all vibrational satellites are induced by Franck–Condon active vibrations.

In conclusion, it is possible for Pt(thpy)$_2$, to separate the emission spectra which are superimposed in time-integrated spectra by time-resolved emission spectroscopy. It is important that a low-temperature (1.3 K) emission spectrum from a higher-lying state with the corresponding high spectral resolution can be obtained. This possibility is a consequence of the relatively slow SLR. Vice versa, as the monitored time-resolved emission spectra are clearly assignable to different triplet substates, these results nicely support the concept of a slow SLR, as developed above. Moreover, the results presented clearly reveal the triplet substate selectivity with respect to Franck–Condon and Herzberg–Teller vibrational activity.

To summarize, the vibronic properties are related to the different allowednesses of the purely electronic transitions. The 0-0 transitions from substates **III, II** to the ground state **0** are (sufficiently) allowed. Thus, Franck–Condon activity becomes possible. On the other hand, substate **I** represents an almost pure triplet, and therefore, the 0-0 transition to the singlet ground state is forbidden. Moreover, the specific symmetry of substate **I** of Pt(thpy)$_2$ probably leads additionally to a symmetry forbiddenness (see Section 1.5.2). Nevertheless, radiative deactivation can occur due to the action of molecular vibrations (i.e., due to vibronic coupling). Such a coupling route can provide the adequate symmetry and SOC, and thus can open the vibrational satellite channels. It should be noted that the 0-0 transition still remains forbidden. This model is strongly supported by investigations under the application of high magnetic fields. Due to the field-induced mixing of the wavefunctions of the three triplet substates, the *B*-field-perturbed lowest triplet substate **I$_B$** gains relatively high radiative allowedness of the 0-0 transition to the electronic ground state (see Fig. 1.15g). Accordingly, Franck–Condon activity should become possible. Indeed, this behavior of tuning in Franck–Condon activity has been demonstrated in particular for $[Os(bpy)_3]^{2+}$ [74, 177, 206, 207], for Pt(thpy)$_2$ [149], Ir(btp)$_2$(acac) [246], and indirectly for several other compounds, such as Ir(ppy)$_3$ [115] and $[Ru(bpy)_3]^{2+}$ [205] (compare also Refs. [247–249]).

1.9.3

Ir(btp)₂(acac) Emission: Low-Temperature Vibrational Satellite Structure

In this section, the aim is to discuss the low-temperature vibrational satellite structure of the Ir(btp)₂(acac) emission. Figure 1.34 shows the 1.5 K spectrum of the selectively excited site, which is in the focus of Section 1.8 (site H in Section 1.10). The frame on the left-hand side displays the two electronic 0-0 transitions I(0-0) and II(0-0) separated by $\Delta E_{II-I} = 2.9\,\text{cm}^{-1}$. The II(0-0) transition strongly dominates, due to the much higher transition probability of $II \leftrightarrow 0$ as compared to $I \leftrightarrow 0$ and due to the very slow SLR time of $\tau_{SLR} = 22\,\mu s$ between the two substates (see Section 1.7.2 and Table 1.1). As consequence of this property, the emission from substate **II** cannot be frozen out (compare Fig. 1.24 and Ref. [203]). Accordingly, both substates emit, and thus the usual (time-integrated) emission spectrum is superimposed of two spectra. However, as depicted in Fig. 1.34, the different vibrational satellites can still be specified with respect to the corresponding electronic origins. This is possible by use of three independent methods:

- Substate **II** and **I**, respectively, exhibit different decay times at low temperature due to the effect of SLR. Thus, time-resolved spectroscopy allows separation of the different spectra in the regions of the electronic origins and the vibrational satellites, in a similar manner as described for Pt(thpy)₂ in Section 1.9.2.3 [246].
- With a temperature increase to $T = 4.2\,\text{K}$, the emission results dominantly from substate **II**, and vibrational
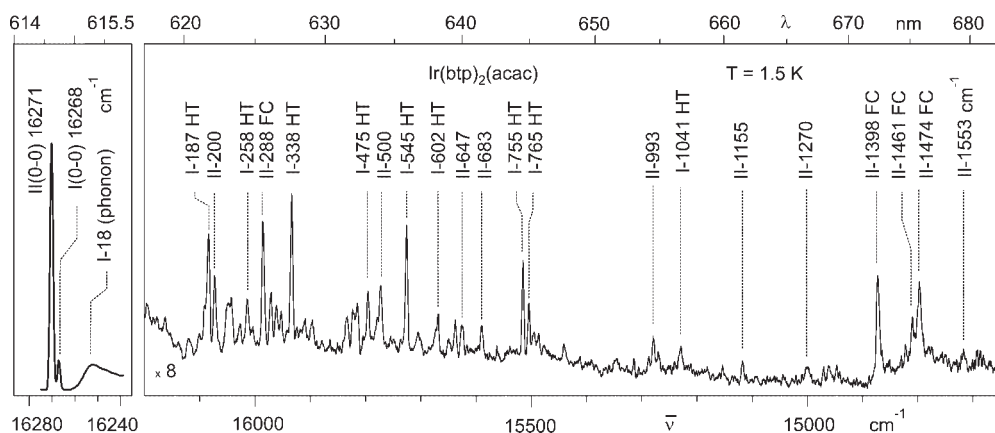

Fig. 1.34 Emission spectrum of site **H** of Ir(btp)₂(acac) doped into CH₂Cl₂ (ca. ≈10⁻⁵ mol L⁻¹). The frame on the left-hand side shows the region of the two lowest electronic 0-0 transitions on an enlarged scale (compare Fig. 1.24). The spectra were monitored at $T = 1.5\,\text{K}$ under selective excitation of substate **III** with an energy of 16 293 cm⁻¹. The vibrational satellite lines are labeled according to the electronic origins I(0-0) and II(0-0), and are assigned with respect to the Herzberg–Teller (HT) or Franck–Condon (FC) activity of the corresponding vibrational mode.

satellites from substate **I** become less important (compare
the 4.2 K spectrum in Fig. 1.24).

- Under the application of high magnetic fields, and according
to the field-induced admixtures of wavefunctions of the
substates **II** and **III** to substate **I**, the resulting perturbed
substate I_B changes its properties significantly. In particular,
it gains allowedness for the I_B(0-0) transition. The resulting
emission spectrum at a high magnetic field, for example at
$B = 10$ T, corresponds largely to the spectrum of the
perturbing states **II** and **III**. Consequently those vibrational
satellites, which grow in with B-field increase, correspond to
vibrational modes which are active in the radiative
deactivation of substate **II** at zero magnetic field [147, 246].

Interestingly, also for Ir(btp)$_2$(acac) the different vibrational modes exhibit different activities with respect to the vibronic mechanisms. *All* vibrational satellites, which belong to the substate **I** emission, are induced by Herzberg–Teller activity. This conclusion is possible, as the electronic origin transition I(0-0) carries only very little oscillator strength and since no progression is found in the emission spectrum of substate **I**. On the other hand, for several vibrational satellites, which belong to the substate **II** emission, also the second members of Franck–Condon progressions are observed, for example for the 288, 1398, 1461, and 1474 cm^{-1} modes. The largest Huang–Rhys parameter for these progressions is estimated by use of Eq. (22) to $S = 0.08$. Presumably, almost all other vibrational satellites found in the emission spectrum of substate **II** are also FC induced, though with smaller Huang–Rhys parameters. In many cases, the second members of vibrational progressions may be hidden in the noise of the spectrum.

In conclusion, the vibrational satellite structure of the Ir(btp)$_2$(acac) emission can be described in accordance to the behavior of Pt(thpy)$_2$. In particular, it is found also for Ir(btp)$_2$(acac) (in a rigid low-temperature matrix) that the geometry of the lowest triplet state T_1 is only very slightly perturbed with respect to the geometry of the electronic ground state S_0.

1.10
Environmental Effects on Triplet State Properties: Case Studies Applied to Ir(btp)$_2$(acac)

In the preceding sections, we have introduced to photophysical properties of organo-transition metal compounds without addressing specifically the differences of the individual sites – that is, the influence of the specific matrix cage on the electronic behavior of the emitter molecule. Studies show that important properties can be dissimilar, such as transition energies, ZFSs, emission decay times, SLR times, and vibrational satellite structures. These properties vary over specific ranges, which depend on the individual energy state of the emitter and its

host environment. In the following sections, the aim is to outline these dissimilarities on the example of different sites of Ir(btp)$_2$(acac) doped into a low-temperature CH$_2$Cl$_2$ matrix.

1.10.1
Energy Distribution of Sites

Figure 1.35 shows the low-temperature emission spectrum of Ir(btp)$_2$(acac) in CH$_2$Cl$_2$ in the region of the electronic 0-0 transitions. This spectrum, which corresponds to the 4.2 K spectrum shown in Fig. 1.23, is characterized by several narrow lines of halfwidths of a few cm^{-1} and a broad background. Both the narrow lines as well as the background can be explained by taking into account that the Ir(btp)$_2$(acac) dopants experience dissimilar interactions with their respective environments in the host. Different orientations of the dopants within the host cage and/or a different number of host molecules that are replaced cause dissimilar shifts of the electronic states, splittings, and couplings to the matrix. Since specific energy minima exist for the dopants, discrete sites result and narrow lines occur. Almost each of the narrow lines is related to one specific site. On the other hand, a large number of dopants is inhomogeneously distributed. This leads to the broad background in the emission spectrum (compare also Section 1.11.1).

The different discrete sites of Ir(btp)$_2$(acac) are labeled with capital letters in Fig. 1.35. The distribution of sites spans over a width of about 450 cm^{-1}, the most

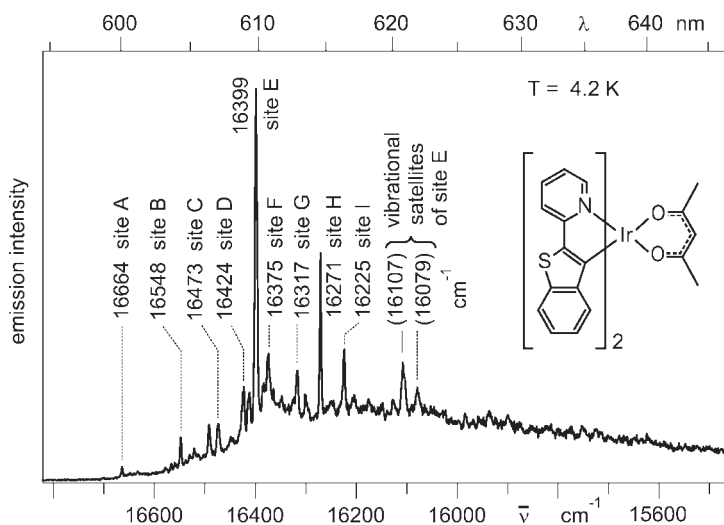**Fig. 1.35** Emission of Ir(btp)$_2$(acac) in CH$_2$Cl$_2$ in the region of the electronic origins, monitored under UV excitation at T=4.2 K. The spectrum consists of resolved electronic 0-0 lines (**II → 0**) of the different sites and of an inhomogeneous background. The different sites are labeled with capital letters.

Table 1.2 Transition energies and zero-field splittings (ZFS) for various sites of Ir(btp)$_2$(acac) doped into CH$_2$Cl$_2$ and n-octane, respectively, and for single crystals of Ir(btp)$_2$(acac). Properties of the sites **E** and **H** are discussed in detail (see text).

Matrix	Site	Relative intensity	Spectral position (cm^{-1})			ZFS (cm^{-1})	
			I	II	III	$\Delta E_{\text{II-I}}$	$\Delta E_{\text{III-I}}$
CH$_2$CH$_2$	A	0.03	–	16 664	–	–	–
	B	0.09	–	16 548	16 566	–	≈21
	C	0.08	16 470	16 473	16 488	3.2 ± 0.5	17.5 ± 1
	D	0.14	16 422	16 424	16 445	2.2 ± 0.5	23.0 ± 0.5
	E	**1**	**16 396**	**16 399**	**16 411**	**2.9 ± 0.2**	**14.8 ± 0.5**
	F	0.12	–	16 375	≈16 395	–	≈23
	G	0.12	16 314	16 317	16 333	3.7 ± 1	19 ± 3
	H	**0.49**	**16 268**	**16 271**	**16 293**	**2.9 ± 0.2**	**25.0 ± 0.5**
	I	0.19	16 221	16 225	16 247	3.6 ± 0.3	26.5 ± 1
n-Octane	A	0.89	16 198	16 201	16 224	2.5 ± 0.2	25.3 ± 0.5
Single crystal	–	–	16 293	16 296	16 312	3.4 ± 0.4	19 ± 1

dominant site being located at 16 399 cm^{-1} (site **E**). Sites with weaker intensities are found at higher energies than the main site at least up to 16 664 cm^{-1}, and lower energies at least down to 16 225 cm^{-1}, respectively (Table 1.2).

Most of the lines represent electronic 0-0 transitions from substate **II** of the lowest triplet state **T$_1$** to the ground state **O(S$_0$)**. This has been confirmed by detailed investigations under selective excitation, variation of temperature, and the application of high magnetic fields (compare Fig. 1.24 and Refs. [147, 203]).

It should be noted that the distribution of transition energies of the different sites due to dissimilar dopant–matrix interactions is a well-known phenomenon in the spectroscopy of organic molecules doped into Shpol'skii or Shpol'skii-like matrices [175, 176, 179]. Organo-transition metal compounds have also been investigated in this respect, though less frequently. For example, different sites were studied of Pt(thpy)$_2$ [144], Pd(thpy)$_2$ [244], Pt(II)-phthalocyanines [250, 251], and of the related compounds [Ru(bpy)$_3$]$^{2+}$ [74, 252] and [Os(bpy)$_3$]$^{2+}$ [74, 177, 253].

1.10.2
Zero-Field Splittings at Different Sites

The investigation of an individual site can be achieved by site-selective spectroscopy. For Ir(btp)$_2$(acac) in CH$_2$Cl$_2$, emission and excitation spectra have been monitored under selective excitation and detection, respectively. Additionally, variation of temperature and high magnetic field have been applied to ensure a
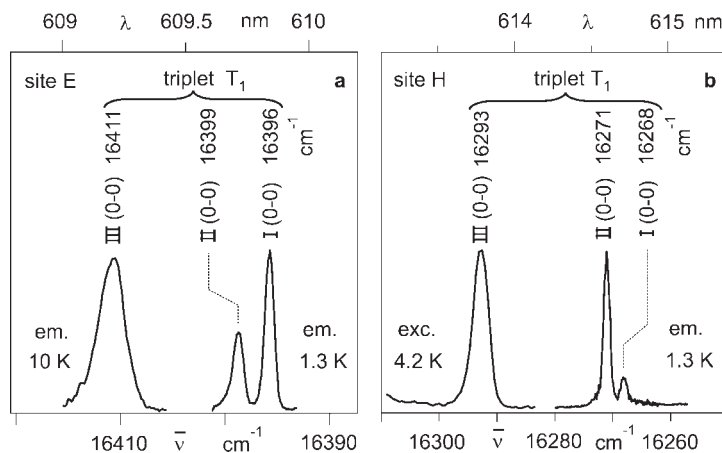
Fig. 1.36 Region of the electronic origins (0-0 transitions) of two major sites **E** and **H** of Ir(btp)$_2$(acac) in CH$_2$Cl$_2$, as specified in Fig. 1.35. The emission spectra of site **E** and **H** were obtained by exciting into the vibrational satellite of substate **III** at 16 775 cm^{-1} (16 411 cm^{-1} + 364 cm^{-1}) and at 16 742 cm^{-1} (16 293 cm^{-1} + 449 cm^{-1}), respectively. The excitation spectrum of site **H** was measured by detection at the electronic origin II(0-0) at 16 271 cm^{-1}. Note that the intensity ratio of the lines II(0-0) to I(0-0) is significantly different for the two sites (compare Ref. [203]). This is mainly a consequence of different spin–lattice relaxation times between substates **II** and **I** (see Section 1.10.3).

reliable interpretation of the observed data. Figure 1.36 shows site-selective spectra of the regions of electronic origins for the two specific sites **E** and **H** (Table 1.2). These sites are especially suited for detailed studies due to the high intensities of the corresponding lines compared to the broad background.

The obtained data clearly show that the two sites exhibit distinctly different total zero-field splittings of the **T$_1$** substates. The total ZFS $\Delta E_{\text{III-I}}$ amounts to 14.8 cm^{-1} for site **E** and to 25.0 cm^{-1} for site **H**. The splitting $\Delta E_{\text{II-I}}$ between the two lower substates of 2.9 cm^{-1} is identical for these specific sites, but – as shown in Table 1.2 – this is not the general case. A study of the ZFSs of sites **A** to **I** of Ir(btp)$_2$(acac) in CH$_2$Cl$_2$ reveals that the total ZFS $\Delta E_{\text{III-I}}$ is distributed from 14.8 cm^{-1} to 26.5 cm^{-1}. Additional investigations of Ir(btp)$_2$(acac) in *n*-octane and as a single crystal result in $\Delta E_{\text{III-I}}$ values of 25.3 cm^{-1} and 19 cm^{-1}, respectively. The splitting $\Delta E_{\text{II-I}}$ varies from 2.2 cm^{-1} to 3.7 cm^{-1} for the different sites and matrices. A correlation to the $\Delta E_{\text{III-I}}$ variation does not exist. The ZFS values are summarized in Table 1.2, together with the relative intensities of the lines corresponding to the different sites.

The variation of ΔE(ZFS) by almost 100% indicates a strong influence of the host on the **T$_1$** state. In Section 1.4, it was shown that the ZFS may be regarded as a measure of the MLCT character of the emitting **T$_1$** state. Presumably, the amount of MLCT admixture to the **T$_1$** state is susceptible to the environment of the complex.

1.10.3
Emission Decay and Spin–Lattice Relaxation Times

Investigations of the decay dynamics between the three substates of T_1 and from the substates to the ground state S_0 show again distinct differences for the different sites of Ir(btp)$_2$(acac) doped into CH$_2$Cl$_2$. By using site-selective spectroscopy and varying the temperature, it is possible to determine the emission decay times of the transitions from the substates **I**, **II**, and **III** to the ground state. This procedure is carried out similarly as described in Section 1.6. Whilst for site **H** the values amount to $\tau = 150\,\mu s$, $\tau_{II} = 58\,\mu s$, and $\tau_{III} = 2\,\mu s$, one finds for site **E** $\tau_I = 62\,\mu s$, $\tau_{II} = 19\,\mu s$, and $\tau_{III} = 3\,\mu s$ [203]. These dissimilarities can result from different radiative allowednesses of the respective transitions and/or from different radiationless deactivation rates to the ground state. The radiative rate might be altered due to different singlet admixtures to the T_1 substates, while the non-radiative deactivation might vary according to different coupling strengths of the electronic states to the lattice. Further studies in this respect are necessary.

The times of SLR between the substates **I** and **II** are, at $T = 1.5\,K$, $\tau_{SLR} = 4\,\mu s$ and $22\,\mu s$ for sites **E** and **H**, respectively (compare Section 1.7 and Ref. [203]). This different relaxation behavior manifests itself also in the emission spectra at $T = 1.5\,K$. As seen in Fig. 1.36, the emission of site **E** is dominated by the transition from the lowest triplet substate **I** to the ground state, while the emission of site **H** stems mainly from substate **II**. For site **H**, substate **II** is only depopulated *slowly* into substate **I** and therefore, a more intense emission stems from **II** [203].

Furthermore, the temperature dependence of the SLR rate is different for the two sites. For site **E**, the SLR rate increases significantly faster with temperature, than for site **H** (not depicted). This is due to the fact that the energy separation $\Delta E_{III\text{-}II}$ is distinctly smaller for site **E** ($12\,cm^{-1}$) than for site **H** ($22\,cm^{-1}$). Therefore, the *Orbach process* of SLR, which depends on this energy separation, has its onset at lower temperature for site E (see Section 1.7 and Ref. [203]).

The data in Table 1.3 summarize the decay times of the T_1 substates and the SLR times at 1.5 K for the two major sites **E** and **H** of Ir(btp)$_2$(acac) in CH$_2$Cl$_2$,

Table 1.3 Decay times of the T_1 substates **I**, **II**, and **III** and spin–lattice-relaxation times determined for Ir(btp)$_2$(acac) at different sites in CH$_2$Cl$_2$, in n-octane, and in a neat single crystal.

Matrix	Site	τ_I (µs)	τ_{II} (µs)	τ_{III} (µs)	τ_{SLR}[1] (µs)
CH$_2$Cl$_2$	E	62	19	3	4
	H	150	58	2	22
n-Octane	A	105	51	–	57
Single crystal	–	140	–	–	–

1) T = 1.5 K.

and also provides decay times for the complex in *n*-octane and in a single crystal.

In conclusion, photophysical properties of organo-transition metal complexes can distinctly depend on the individual environment or matrix cage which hosts the emitter complex. The specific interactions between the complex and the environment lead to a variation of the transition energy, the emission decay times, and the ZFSs. It is the subject of further investigations to study the importance of the environmental influence on triplet emitters doped into amorphous polymeric matrices by use of the spectroscopic method of hole burning [254]. It is also intended to analyze to what extent the spread of photophysical properties, as studied at low temperature, survives when the material is used as emitter at ambient temperature and applied in an OLED.

1.11
Emission Linewidths and Spectral Broadening Effects

Detailed information about photophysical properties of the lowest excited states of organo-transition metal compounds can usually only be obtained at cryogenic temperatures, when highly resolved spectra can be recorded. However, in all OLED applications, the compounds are used at ambient temperature. In this situation, the spectral information is smeared out and only broad absorption or emission spectra can be measured. Nevertheless, the photophysical properties determined at low temperature from highly resolved spectra also often govern the emission behavior under ambient conditions. In this section, the aim is to discuss spectral broadening effects which are already present at low temperature, and those broadening effects which occur with temperature increase. Further, it will be shown that emitters with large MLCT character of the triplet state experience specific emission broadening effects.

1.11.1
Inhomogeneous Linewidths

Molecules doped into a solid matrix are always influenced by inhomogeneous interactions with their environments. This occurs also at low temperature in both crystalline and amorphous hosts though usually to a different extent. The electronic and vibrational states of the dopants experience dissimilar shifts, which depend on the individual matrix cage, i.e. – for a given matrix – on the position and orientation of the dopant and the number of matrix molecules in the environment. Consequently, the spectra are shifted with respect to each other, and this results in superimposed spectra. Especially in amorphous matrices such as glasses, the resulting inhomogeneous distribution (which is usually Gaussian-like) is very broad and can reach hundreds of wavenumbers. The width of such a distribution is not easily predictable, as several mechanisms of host–guest interaction can

take effect [255]. On the other hand, the inhomogeneous Gaussian-like width can become relatively small for dopants in crystalline or polycrystalline matrices, such as Shpol'skii matrices. In these hosts, inhomogeneous linewidths may be as small as only 1 or $2\,cm^{-1}$ (compare Sections 1.5, 1.8, and 1.9). In many cases, specific minima exist for dopants in the crystalline hosts, and these give rise to the formation of discrete sites. This leads to the specific lines with the small halfwidths. Often, many different discrete sites are present, as found for $Ir(btp)_2(acac)$ doped into CH_2Cl_2 (see Table 1.2). Additionally, for the example of the $Ir(btp)_2(acac)$/CH_2Cl_2 combination, many dopants are quasi-continuously distributed over a large number of only slightly different minima. This results in a broad background with a halfwidth of about $400\,cm^{-1}$ (Fig. 1.25). In other dopant/matrix combinations, one specific site can dominate clearly. For example, for $Pt(thpy)_2$ doped into an *n*-octane Shpol'skii matrix, one site carries 98% of the line emission (see Section 1.5.1 and Ref. [144]).

Importantly, for the situations discussed above it is often possible to measure highly resolved spectra of individual sites by applying the well-established methods of site-selective spectroscopy (e.g., see Sections 1.5 and 1.7–1.10), of luminescence line-narrowing (e.g., see Refs. [256, 257]), and of spectral hole burning (e.g., see Ref. [258]), respectively. The application of these methods will, however, only be successful, if the homogeneous line broadening effects do not dominate.

1.11.2
Homogeneous Linewidths

The Heisenberg uncertainty principle correlates an energy uncertainty to the lifetime of a state. This energy uncertainty is identified by the so-called homogeneous linewidth $\Delta\bar{v}_{hom}$ (often referred as Γ_{hom}). It can be expressed by [259, 260]:

$$\Delta\bar{v}_{hom} = \frac{1}{2\pi c\tau_2} \tag{24}$$

wherein c is the velocity of light, and τ_2 is the full dephasing time

$$\frac{1}{\tau_2} = \frac{1}{2\tau_1} + \frac{1}{\tau_2^*} \tag{25}$$

where τ_1 is the excited state lifetime, which for an emission process, is determined by *all* radiative and non-radiative depopulation processes. Therefore, τ_1 is often called *population* or *energy relaxation time*. τ_2^* represents the *pure dephasing time*; this is strongly temperature-dependent and can become very large when zero temperature is approached (see below). In this situation, pure dephasing can be neglected and the homogeneous halfwidth $\Delta\bar{v}_{hom}$ can easily be estimated. (For a

further discussion of τ_2^*, see below.) For example, for an emission decay time of $\tau_1 = 1\,\mu s$, a homogeneous linewidth of $\Delta\bar{\nu}_{\mathrm{hom}} = 2.6 \times 10^{-6}\,\mathrm{cm}^{-1}$ is obtained. This value is about six orders of magnitude smaller than the inhomogeneous widths found for highly resolved spectra discussed in this contribution.

It should be noted that Eq. (24) is derived under the assumption of an infinite lifetime of one of the involved states. Thus, the presented estimate is well applicable to purely electronic 0-0 transitions. On the other hand, a transition which involves a vibrationally excited state as final state (e.g., a vibrational or phonon satellite line) usually exhibits homogeneous linewidths which are several orders of magnitude larger than those of purely electronic transitions of triplet emitters. This is due to the fast depopulation of the vibrational state, being of the order of 1 ps; consequently, it results an additional uncertainty of the transition energy. Indeed, the vibrational satellite lines of highly resolved emission or excitation spectra exhibit, at low temperature, homogeneous halfwidths of typically 3 to $5\,\mathrm{cm}^{-1}$ and even up to $10\,\mathrm{cm}^{-1}$ for vibrational combinations and higher members of progressions. Thus, these linewidths are substantially broader than the inhomogeneously broadened purely electronic origin lines of triplet emitters in suitable hosts or at suitable sites.

With temperature increase, the homogeneous linewidth of a *purely electronic transition* broadens significantly due to the involvement of phonons. In particular, processes of pure dephasing become important [compare τ_2^* in Eq. (25)]. These processes induce phase shifts of the wavefunction of an involved (populated) state, and result in a so-called dephasing of the originally excited situation [98, 261]. Thus, τ_2^* becomes shorter and $\Delta\bar{\nu}_{\mathrm{hom}}$ increases. If, for example, a Raman scattering process of phonons is taken into account, it can be derived that τ_2^* increases with a T^7 temperature dependence [98, 262]. Further, for triplet substates with thermally accessible higher-lying substates, the Orbach process is also expected to be of importance. (In this context, it is referred to elastic up-and-down processes that involve the same two energy substates.) In general, such processes can occur not only by scattering of phonons, but also by interactions of any other kind of elementary excitations with the dopant [259].

The above discussion refers only to the homogeneous broadening of a purely electronic 0-0 line – that is, the electronic zero-phonon line (ZPL). However, important homogeneous broadening effects result additionally from the involvement of specific phonons, for example, of low-energy vibrations or librations[34] of the dopant in its lattice cage (local phonons) in the optical transition. This leads to the occurrence of phonon satellites, which lie in a range of less than about $100\,\mathrm{cm}^{-1}$ from the electronic origin [compare Fig. 1.15b,c (Section 1.5.1) and Fig. 1.31 (Section 1.9.2.1)]. In several cases, some of these local phonon satellites, with phonon energies of 15 or $18\,\mathrm{cm}^{-1}$, for example, are resolvable for organo-transition metal complexes dissolved in crystalline matrices. However, mostly only unresolved phonon wings or *phonon sidebands* are found [98]. At low temperature, the phonon sidebands are

---

34) Librations are hindered rotational motions of the dopant molecule in the cage of the surrounding matrix.

situated at the low energy side of the electronic ZPL. The structure and width of a phonon sideband depend on the local situation – that is, on the number of coupling (local) phonons and on the coupling strength of the electronic transition to the phonons, the so-called electron-phonon coupling.

These latter properties are directly related to the effects of the Franck–Condon activity of a specific mode (see Section 1.9.1.1). For example, a large geometry change with respect to a local phonon coordinate according to an electronic transition (large electron–phonon coupling) leads to a large ΔQ(phonon) value and thus to a large Huang–Rhys parameter S(phonon) for the specific local phonon mode [Eq. (21)]. This results in a distinct phonon progression and a shift of the emission intensity from the purely electronic line (ZPL) to the local phonon satellites (compare Fig. 1.29). As discussed above, the phonon satellites have homogeneous linewidths, which are orders of magnitude broader than those of the electronic ZPL. Furthermore, usually different local phonon modes of different energies couple to the electronic transition. All of the resulting phonon satellites overlap and lead to the broad phonon sidebands.

With temperature increase, an emission can also occur from a thermally populated higher-lying phonon state, and this leads to an energetically higher lying sideband (anti-Stokes phonon sideband). As consequence, the intensity of an emission spectrum is redistributed. It is moved from the ZPL to its phonon sideband mainly at the anti-Stokes side (Fig. 1.37). If the temperature dependence of nonradiative relaxation processes can be neglected, the total intensity of ZPL and sideband is constant. At higher temperatures – mostly already below 77 K (but see the exception of Pt(thpy)$_2$; Section 1.11.3) – the emission intensity is found only in the phonon sideband and no longer in the ZPL (the spectrum at the right-hand side of Fig. 1.37).

For completeness, it should be noted that the considerations presented above for the purely electronic transitions and their coupling properties to local phonon modes, apply similarly to all vibrational satellites of metal–ligand or ligand vibrational character (compare Section 1.9). In this sense, the vibrational satellite lines
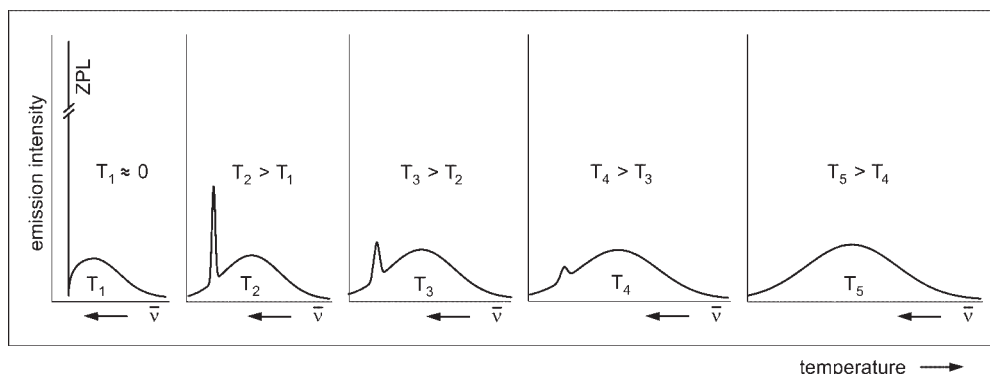

Fig. 1.37 Temperature dependence of a zero-phonon line (ZPL) and the accompanying phonon sideband in emission (compare Ref. [259]).

represent ZPL. The intensity of the phonon side–band is given by the individual coupling of the respective vibrational satellite transition to the local phonons.

1.11.3
Line Broadening Effects on the Example of Pt(thpy)$_2$

Here, the aim is to illustrate the temperature-broadening effects of the purely electronic origin (electronic ZPL) of Pt(thpy)$_2$ doped into *n*-octane. At $T = 10$ K, the dominating emission line at $17\,163$ cm^{-1} represents the purely electronic transition from triplet substate **II** to the electronic ground state **0** (Fig. 1.38a). Weak lines corresponding to a local phonon satellite of 15 cm^{-1} and the purely electronic III(0-0) line are also observed in this spectral range (compare also Fig. 1.15). The line II(0-0) is inhomogeneously broadened to about 3 cm^{-1}. With a temperature increase to 77 K, the halfwidth of the electronic ZPL is broadened to ≈ 20 cm^{-1}, and the intensity is reduced and distributed to the associated phonon sideband. With further temperature increase, the ZPL becomes even weaker, and above ≈ 130 K can no longer be distinguished from the phonon sideband. The integrated intensity stays largely constant from 10 K to 90 K, and decreases only slightly above 90 K.

At a temperature higher than ≈ 90 K, the width of the observed phonon sideband is of the order of 100 cm^{-1} (Fig. 1.38b). Thus, it becomes clear that high-resolution spectroscopy is only possible at low temperatures, usually below 30 to 40 K in the case of Shpol'skii matrices. Below this temperature, homogeneous broadening is weak then and the spectra are dominated by electronic and vibrational satellite ZPLs. This is especially important for organo-transition metal compounds, for which the vibrational satellite lines lie close in energy, with an average separation below 50 to 100 cm^{-1}. Therefore, the appearance of phonon sidebands at higher temperatures leads to a smearing out of the spectrum and to a loss of information.

In general, it is not predictable at which temperature the homogeneous line broadening becomes dominant. For Pt(thpy)$_2$ in *n*-octane, even at 110 K a weak ZPL is observable and, due to the occurrence of only one single site, comparatively
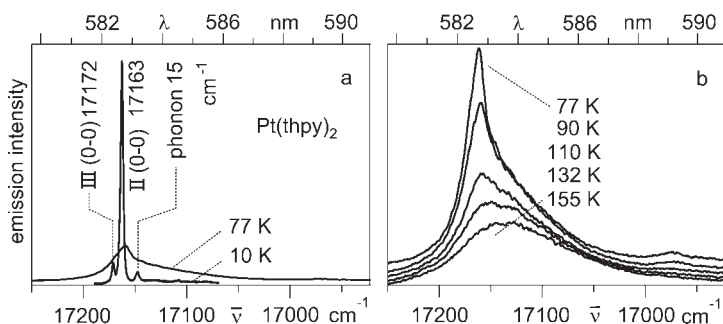

Fig. 1.38 Emission spectra in the region of the electronic origins of Pt(thpy)$_2$ in *n*-octane (ca. $\approx 10^{-5}$ mol L^{-1}) at different temperatures. Excitation at 355 nm. Upon increase of temperature, a decrease of the ZPL intensity and an intensity distribution to the broad phonon sideband is observed.

well-resolved spectra can be obtained. However, mostly – also in Shpol'skii matrices – spectra of several discrete sites will occur. The spectra will be superimposed and then smeared out due to the homogeneous effects. Depending on the importance of homogeneous and inhomogeneous broadenings and the extent of site distributions, a broad and unresolved or a well structured spectrum, as in the case of Pt(thpy)$_2$, can result.

To summarize, at low temperature, a typical emission spectrum of an organo-transition metal compound consists of a purely electronic transition (electronic ZPL) which is accompanied by phonon satellites or, if smeared out, by phonon sidebands. Further, the electronic transition is also associated with vibrational satellites (vibrational satellite ZPL) which are also accompanied by phonon sidebands. In case of an occurrence of different sites and/or of an inhomogeneous distribution, a number of spectra will be superimposed. However, by use of the methods of site-selective spectroscopy or of luminescence line-narrowing, a well defined site can still be investigated. However, if electron–phonon coupling is large [large phonon Huang–Rhys parameter S(phonon)], the ZPLs might no longer be detectable. In this situation, the spectrum is homogeneously broadened and application of high-resolution methods is unsuccessful, even at low temperature.

When the temperature is increased, homogeneously broadened phonon sidebands gain intensity, and the electronic as well as the vibrational satellite ZPLs disappear (Fig. 1.37) and consequently the whole spectrum becomes broad. High-resolution methods would not be applicable successfully in this situation. The corresponding temperature at which any resolution is lost lies at about 60 K for Ir(btp)$_2$(acac) in CH$_2$Cl$_2$ and at 110 K for Pt(thpy)$_2$ in *n*-octane (see above).

At this point, attention should be drawn to an interesting broadening mechanism which especially applies to compounds with emitting triplet states of high MLCT character. These compounds are of special attraction for OLED applications. At low temperature, the emission spectra can often be very well resolved, even for a typical MLCT emitter such as [Os(bpy)$_3$]$^{2+}$ [177, 253]. The emission spectra are characterized by the occurrence of many particularly pronounced vibrational satellites of metal–ligand vibrational character. These modes have energies below ≈600 cm^{-1}, and thus the corresponding ZPLs lie between the ZPLs of the ligand modes and the ZPL of the purely electronic transition. With temperature increase, the homogeneous broadening mechanisms become effective and smear out the whole spectrum. Consequently, the spectra are usually much broader than those corresponding to typical ligand-centered transitions.

1.11.4
Phenomenological Simulation of Spectral Broadening

At very low temperature, it is frequently possible to obtain highly resolved spectra of organo-transition metal complexes and to elucidate photophysical properties. The question arises, however, of whether these properties remain relevant for the emission behavior at 77 K or even at 300 K; that is, for example, for a complex, which is incorporated in an OLED. This question is addressed here simply on a

spectral basis; that is, it is checked whether it is possible to simulate the high-temperature spectra from the low-temperature, highly resolved spectra. The corresponding spectral modifications can, in principle, be accomplished by performing a convolution of the highly resolved line spectrum with the shape function determined by the different mechanisms of temperature broadening. However, the physically relevant function which takes into account overlapping spectra of different sites and homogeneous broadening effects cannot be given. Thus, as a simple approach, it makes sense to apply a Gaussian function, i.e. to convolve the highly resolved spectra with a broadening Gaussian distribution function of a halfwidth of $\Delta\bar{\nu}(FWHM) = 2.35\sigma$, wherein σ represents the well-known Gaussian σ. (FWHM: full width at half maximum) The parameter σ has to be adapted to reproduce the measured spectra.

Figure 1.39 shows that this procedure is successful, when applied to the highly resolved 4.2 K spectra of Pt(thpy)$_2$. By using a Gaussian width of 65 cm^{-1} (FWHM),
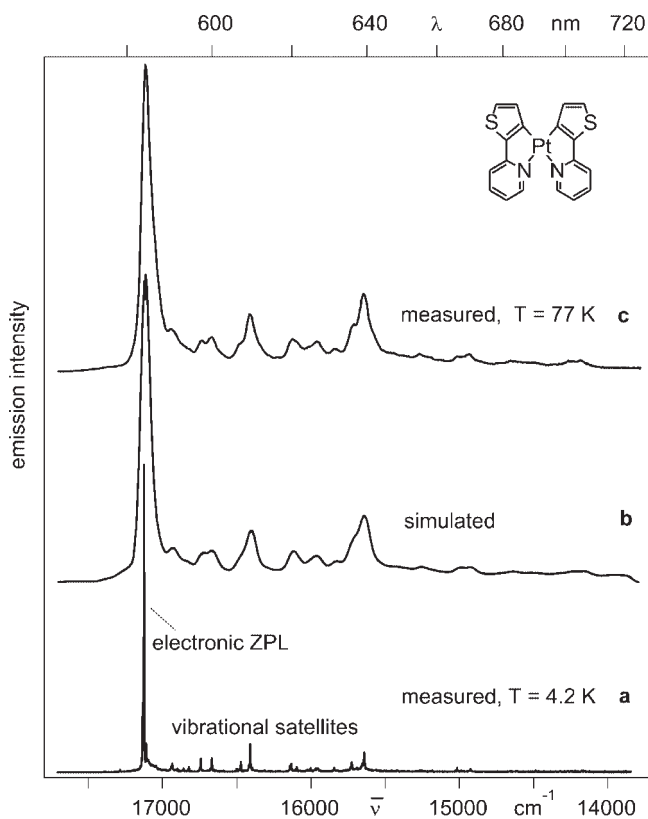
Fig. 1.39 Emission spectra of Pt(thpy)$_2$ in *n*-octane. (a) Spectrum measured at *T*=4.2 K under non-selective excitation at 457.9 nm. The spectrum has been red-shifted by 43 cm^{-1} to be able to simulate also the spectral position of the 77 K spectrum. (b) Simulated spectrum using a Gaussian distribution function with $\Delta\bar{\nu} = 65$ cm^{-1} (σ=27.6 cm^{-1}). (c) Spectrum measured at *T*=77 K, excitation wavelength as in (a).

the procedure simulates the measured 77 K spectrum nicely. All spectral features are reproduced, and even the relative intensities of the simulated bands match closely to those of the measured spectrum.

The simulation can also be carried out to obtain a 300 K spectrum. In a physical model, additional line broadenings due to dynamic effects in the liquid solvent must be considered. The phenomenological simulation, however, takes these effects into account simply by using a Gaussian width of $\Delta\bar{v}(\text{FWHM}) = 500\,\text{cm}^{-1}$. The resulting simulation shows a very good agreement with the measured 300 K emission spectrum (Fig. 1.40). This fitting procedure reflects the enormous broadening of the spectrum, even when compared to the 77 K spectrum. In the resulting spectrum, only three bands are recognized: the maximum at $17\,100\,\text{cm}^{-1}$ represents mainly the broadened phonon sideband of the electronic origin, while the two features at $15\,710\,\text{cm}^{-1}$ and $14\,220\,\text{cm}^{-1}$ correspond to overlapping (sidebands of) vibrational satellites, which result from combinations and progressions of modes lying in the 1400 to $1500\,\text{cm}^{-1}$ range.

In conclusion, the high-temperature spectra of many organo-transition metal compounds, and in particular of Pt(thpy)$_2$, can be traced back to low-temperature, highly resolved spectra. Consequently, the information elucidated for the emitting
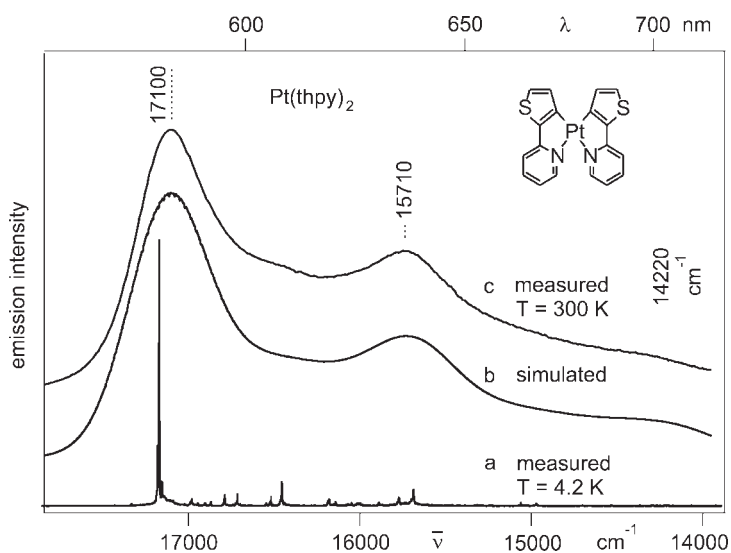
Fig. 1.40 Emission spectra of Pt(thpy)$_2$ in *n*-octane. (a) Spectrum measured at $T = 4.2\,\text{K}$ (for further data, see Fig. 1.39). (b) Simulated spectrum using a Gaussian distribution function with $\Delta\bar{v} = 500\,\text{cm}^{-1}$ ($\sigma = 213\,\text{cm}^{-1}$). (c) Spectrum measured at $T = 300\,\text{K}$.

states at low temperatures retains relevance also for emission properties at ambient temperature.

1.12
Conclusions

For many years, a deeper understanding of the triplet state properties of organo-transition metal compounds has been in the focus of fundamental research. However, within the past decade these activities have been greatly stimulated by the beginning application of these compounds as OLED emitters. Nonetheless, many questions remain unanswered. Clearly, OLEDs are applied at ambient or higher temperatures, but even when the technical application is in the focus of interest, the required detailed characterization and insight into the compound's properties cannot be obtained by using only high-temperature studies. This is due to the fact that the emission processes are always averaged or smeared out and, as a consequence, much information is lost. Therefore, it is required to investigate these emitter materials down to low temperature, for example to $T = 1.3$ K. Indeed, such studies reveal that the emitting triplet (usually) splits into three substates, and thus access to the individual substate emission becomes possible. In particular, information is obtained regarding the magnitude of the splitting (the ZFS), emission decay dynamics and decay times, radiative deactivation paths as purely electronic transitions or under involvement of internal vibrations and/or low-energy phonon modes, geometry changes of the emitter compound due to excitation of the triplet state, etc.. Most of these properties also show a dependence on the direct environment of the complex. Of particular interest are the discovered trends between the magnitude of ZFS and the photophysical properties of the emitter materials. Thus, the amount of ZFS represents a very valuable parameter.

One of these trends is of particular concern for OLED applications. This is due to the fact that the magnitude of ZFS is determined by SOC to higher-lying singlet and triplet MLCT states. Specifically, the occurrence of a significant ZFS indicates pronounced admixtures of ^{1}MLCT components to the triplet substates. Such singlet admixtures usually lead to short emission decay times and can result in high photoluminescence quantum yields; also quenching effects of triplet-triplet annihilation can become less important. It is well known that these properties are crucial for emitters applied in OLEDs. As a rule of thumb, it is found that emitter materials, which are successfully applied in OLEDs, have ZFSs of not less than about 10 cm^{-1}. However, those emitters which are employed at high current densities in high-brightness applications, should exhibit even larger ZFSs and strong singlet admixtures to further reduce the emission decay time. Interestingly, it has been shown that the relevant SOC routes can be significantly more efficient in quasi-octahedral than in quasi-square planar compounds. For example, whilst large ZFSs (i.e., >40 cm^{-1}) have not yet been observed for quasi-square planar Pt(II) compounds, but frequently occur in Ir(III), Os(II), or even Ru(II) complexes. Clearly, the success of the quasi-octahedral Ir(ppy)$_3$ as OLED emitter material is related to this trend.

In particular, these latter results show that detailed studies of the emission processes in organo-transition metal complexes can indeed lead to a better understanding of the correlation between molecular structures and photophysical properties which are of interest for a specific application as emitter material, for example in an OLED.

Acknowledgements

References

1 J. Shinar (Ed.), *Organic Light-Emitting Devices*, Springer, AIP Press, Berlin, **2004**.

2 Z. H. Kafafi (Ed.), *Organic Electroluminescence*, Taylor and Francis, CRC Series, Boca Raton, **2005**.

3 K. Müllen, U. Scherf (Eds.), *Organic Light-Emitting Devices – Synthesis, Properties, and Applications*, Wiley-VCH, Weinheim, **2006**.

4 J. Kalinowski, *Organic Light-Emitting Diodes: Principles, Characteristics, and Processes*, CRC Press, Boca Raton, **2004**.

5 H. Yersin, *Top. Curr. Chem.* **2004**, *241*, 1.

6 R. C. Evans, P. Douglas, C. J. Winscom, *Coord. Chem. Rev.* **2006**, *250*, 2093.

7 K. Walzer, B. Maenning, M. Pfeiffer, K. Leo, *Chem. Rev.* **2007**, *107*, 1233.

8 A. Tsuboyama, S. Okada, K. Ueno, this volume, pp. 163.

9 A. van Dijken, K. Brunner, H. Börner, B. M. W. Langeveld, this volume, pp. 311.

10 X.-H. Yang, F. Jaiser, D. Neher, this volume, pp. 221.

11 D. Tanaka, H. Sasabe, Y.-J. Li, S.-J. Su, T. Takeda, J. Kido, *Jap. J. Appl. Phys.* **2007**, *46*, L10.

12 S. Watanabe, N. Ide, J. Kido, *Jap. J. Appl. Phys.* **2007**, *46*, 1186.

13 T. Sajoto, P. I. Djurovich, A. Tamayo, M. Yousufuddin, R. Bau, M. E. Thompson, R. J. Holmes, S. R. Forrest, *Inorg. Chem.* **2005**, *44*, 7992.

14 Y. Sun, N. C. Giebink, H. Kanno, B. Ma, M. E. Thompson, S. R. Forrest, *Nature* **2006**, *440*, 908.

15 C. Borek, K. Hanson, P. I. Djurovich, M. E. Thompson, K. Aznavour, R. Bau, Y. Sun, S. R. Forrest, J. Brooks, L. Michalski, J. Brown, *Angew. Chem. Int. Ed.* **2007**, *46*, 1109.

16 S. C. F. Kui, I. H. T. Sham, C. C. C. Cheung, H.-W. Ma, B. Yan, N. Zhu, C.-M. Che, W.-F. Fu, *Chem. Eur. J.* **2007**, *13*, 417.

17 Y.-Y. Lin, S.-C. Chan, M. C. W. Chan, Y.-J. Hou, N. Zhu, C.-M. Che, Y. Liu, Y. Wang, *Chem. Eur. J.* **2003**, *9*, 1263.

18 Y. Ma, H. Zhang, J. Shen, C.-M. Che, *Synth. Met.* **1998**, *94*, 245.

19 C.-H. Yang, Y.-M. Cheng, Y. Chi, C.-J. Hsu, F.-C. Fang, K.-T. Wong, P.-T. Chou, C.-H. Chang, M.-H. Tsai, C.-C. Wu, *Angew. Chem. Int. Ed.* **2007**, *46*, 2418.

20 P.-T. Chou, Y. Chi, *Chem. Eur. J.* **2007**, *13*, 380.

21 E. B. Namdas, A. Ruseckas, I. D. W. Samuel, S.-C. Lo, P. L. Burn, *J. Phys. Chem. B* **2004**, *108*, 1570.

22 R. N. Bera, N. Cumpstey, P. L. Burn, I. D. W. Samuel, *Adv. Funct. Mater.* **2007**, *17*, 1149.

23 J. Ding, J. Gao, Y. Cheng, Z. Xie, L. Wang, D. Ma, X. Jing, F. Wang, *Adv. Funct. Mater.* **2006**, *16*, 575.

24 L. Chen, H. You, C. Yang, D. Ma, J. Qin, *Chem. Commun.* **2007**, *1352*.

25 R. Meerheim, K. Walzer, M. Pfeiffer, K. Leo, *Appl. Phys. Lett.* **2006**, *89*, 061111.

26 G. Schwartz, K. Fehse, M. Pfeiffer, K. Walzer, K. Leo, *Appl. Phys. Lett.* **2006**, *89*, 083509.

27 Y. Kawamura, K. Goushi, J. Brooks, J. Brown, H. Sasabe, C. Adachi, *Appl. Phys. Lett.* **2005**, *86*, 071104.

28 X. H. Yang, F. Jaiser, S. Klinger, D. Neher, *Appl. Phys. Lett.* **2006**, *88*, 021107.

29 F.-I. Wu, X.-H. Yang, D. Neher, R. Dodda, Y.-H. Tseng, C.-F. Shu, *Adv. Funct. Mater.* **2007**, *17*, 1085.

30 A. J. Wilkinson, H. Puschmann, J. A. K. Howard, C. E. Foster, J. A. G. Williams, *Inorg. Chem.* **2006**, *45*, 8685.

31 M. Cocchi, D. Virgili, V. Fattori, D. L. Rochester, J. A. G. Williams, *Adv. Funct. Mater.* **2007**, *17*, 285.

32 M. S. Lowry, S. Bernhard, *Chem. Eur. J.* **2006**, *12*, 7970.

33 E. L. Williams, K. Haavisto, J. Li, G. E. Jabbour, *Adv. Mater.* **2007**, *19*, 197.

34 T. Tsuzuki, S. Tokito, *Adv. Mater.* **2007**, *19*, 276.

35 E. Holder, B. M. W. Langeveld, U. S. Schubert, *Adv. Mater.* **2005**, *17*, 1109.

36 K. Brunner, A. van Dijken, H. Börner, J. J. A. M. Bastiaansen, N. M. M. Kiggen, B. M. W. Langeveld, *J. Am. Chem. Soc.* **2004**, *126*, 6035.

37 G. Zhou, W.-Y. Wong, B. Yao, Z. Xie, L. Wang, *Angew. Chem.* **2007**, *119*, 1.

38 X. Wang, J. Li, M. E. Thompson, J. I. Zink, *J. Phys. Chem. A* **2007**, *111*, 3256.

39 C.-H. Fang, Y.-L. Chen, C.-H. Yang, Y. Chi, Y.-S. Yeh, E. Y. Li, Y.-M. Cheng, C.-J. Hsu, P.-T. Chou, C.-T. Chen, *Chem. Eur. J.* **2007**, *13*, 2686.

40 L.-L. Wu, C.-H. Yang, I.-W. Sun, S.-Y. Chu, P.-C. Kao, H.-H. Huang, *Organometallics* **2007**, *26*, 2017.

41 R. Schlaf, B. A. Parkinson, P. A. Lee, K. W. Nebesny, G. Jabbour, B. Kippelen, N. Peyghambarian, N. A. Armstrong, *J. Appl. Phys.* **1998**, *84*, 6729.

42 X. Ren, J. Li, R. J. Holmes, P. I. Djurovich, S. R. Forrest, M. E. Thompson, *Chem. Mater.* **2004**, *16*, 4743.

43 Y.-H. Niu, M. S. Liu, J.-W. Ka, A. K.-Y. Jen, *Appl. Phys. Lett.* **2006**, *88*, 093505.

44 M. E. Thompson, private communication.

45 C. Adachi, M. A. Baldo, M. E. Thompson, S. R. Forrest, *J. Appl. Phys.* **2001**, *90*, 5048.

46 M. A. Baldo, C. Adachi, S. R. Forrest, *Phys. Rev. B* **2000**, *62*, 10967.

47 (a) S. Reineke, K. Walzer, K. Leo, *Phys. Rev. B* **2007**, *75*, 125328; (b) W. Staroske, M. Pfeiffer, K. Leo, M. Hoffmann, *Phys. Rev. Lett.* **2007**, *98*, 197402.

48 G. He, M. Pfeiffer, K. Leo, M. Hofmann, J. Birnstock, R. Pudzich, J. Salbeck, *Appl. Phys. Lett.* **2004**, *85*, 3911.

49 H. J. Peng, X. L. Zhu, J. X. Sun, X. M. Yu, M. Wong, H. S. Kwok, *Appl. Phys. Lett.* **2006**, *88*, 033509.

50 T. Canzler, A. G. Novaled, Oral Presentation at: *Photonics China*, Shanghai, **2005**.

51 T.-Y. Cho, C.-L. Lin, C.-C. Wu, *Appl. Phys. Lett.* **2006**, *88*, 111106.

52 H. Peng, J. Sun, X. Zhu, Y. Yu, M. Wong, H.-S. Kwok, *Appl. Phys. Lett.* **2006**, *88*, 073517.

53 J. Y. Lee, *Appl. Phys. Lett.* **2006**, *88*, 073512.

54 Q. Huang, K. Walzer, M. Pfeiffer, V. Lyssenko, G. He, K. Leo, *Appl. Phys. Lett.* **2006**, *88*, 113515.

55 Y. Y. Yuan, S. Han, D. Grozea, Z. H. Lu, *Appl. Phys. Lett.* **2006**, *88*, 093503.

56 B. C. Krummacher, V.-E. Choong, M. K. Mathai, S. A. Choulis, F. So, F. Jermann, T. Fiedler, M. Zachau, *Appl. Phys. Lett.* **2006**, *88*, 113506.

57 S. W. Kim, J. H. Park, S. S. Oh, D. Y. Kim, E. H. Choi, G. S. Cho, Y. H. Seo, S. O. Kang, B. Park, Y. Saito, N. Watanabe, H. Takezoe, J. Watanabe, *App. Phys. Lett.* **2006**, *89*, 213511.

58 K. Fehse, K. Walzer, G. He, M. Pfeiffer, K. Leo, W. Loevenich, A. Elschner, *Proc. SPIE (Organic Optoelectronics and Photonics II) Vol. 6192*, **2006**, 61921Z.

59 J. H. Park, S. S. Oh, S. W. Kim, E. H. Choi, B. H. Hong, Y. H. Seo, G. S. Cho, B. Park, *Appl. Phys. Lett.* **2007**, *90*, 153508.

60 X. Yang, D. C. Müller, D. Neher, K. Meerholz, *Adv. Mater.* **2006**, *18*, 948.

61 S. Lamansky, R. C. Kwong, M. Nugent, P. I. Djurovich, M. E. Thompson, *Org. Electron.* **2001**, *2*, 53.

62 X. Gong, W. Ma, J. C. Ostrowski, G. C. Bazan, D. Moses, A. J. Heeger, *Adv. Mater.* **2004**, *16*, 615.

63 P. A. Lane, L. C. Palilis, D. F. O'Brien, C. Giebeler, A. J. Cadby, D. G. Lidzey, A. J. Campbell, W. Blau, D. D. C. Bradley, *Phys. Rev. B* **2001**, *63*, 235206.

64 K.-H. Hellwege, *Einführung in die Festkörperphysik*, Springer-Verlag, Berlin, p. 509, **1976**.

65 J. Kalinowski, in: Z. H. Kafafi (Ed.), *Organic Electroluminescence*, Taylor and Francis, CRC Series, Boca Raton, **2005**, p. 23.

66 M Schott, *C. R. Acad. Sci. Paris*, tome 1, Série IV, **2000**, *381*.

67 M. J. Walter, J. M. Lupton, this volume, p. 99.

68 M. Reufer, J. J. Walter, P. G. Lagoudakis, A. B. Hummel, J. S. Kolb, H. G. Roskos, U. Scherf, J. M. Lupton, *Nature Mater.* **2005**, *4*, 340.

69 H. Yersin, *Proc. SPIE 5214*, 124, 2004 Oral presentation at the SPIE conference 5214, San Diego, August, **2003**.

70 H. Yersin, D. Donges, *Top. Curr. Chem.* **2001**, *214*, 81.

71 D. Donges, J. K. Nagle, H. Yersin, *Inorg. Chem.* **1997**, *36*, 3040.

72 W. Humbs, H. Yersin, *Inorg. Chem.* **1996**, *35*, 2220.

73 H. Yersin, W. Humbs, J. Strasser, *Coord. Chem. Rev.* **1997**, *159*, 325.

74 H. Yersin, W. Humbs, J. Strasser, *Top. Curr. Chem.* **1997**, *191*, 153.

75 M. Klessinger, *Elektronenstruktur organischer Moleküle*, Verlag Chemie, Weinheim, **1982**.

76 C. Cohen-Tannoudji, B. Diu, F. Laloë, *Quantum Mechanics*, Vol. I, p. 109, Wiley, New York, **1977**.

77 S. P. McGlynn, T. Azumi, M. Kinoshita, *Molecular Spectroscopy of the Triplet State*, Prentice-Hall, Englewood Cliffs, New Jersey, **1969**.

78 N. J. Turro, *Modern Molecular Photochemistry*, Benjamin-Cummings, Menlo Park, Calif. p. 31, **1978**.

79 N. Mataga, T. Kubota, *Molecular Interactions and Electronic Spectra*, Marcel Dekker, New York, p. 187, **1970**.

80 M. Maestri, D. Sandrini, V. Balzani, L. Chassot, P. Jolliet, A. von Zelewsky, *Chem. Phys. Lett.* **1985**, *122*, 375.

81 N. E. Geacintov, C. E. Swenberg, in: M.D. Lumb (Ed.), *Luminescence Spectroscopy*, Academic Press, London, p. 239, **1978**.

82 T. Azumi, H. Miki, *Top. Curr. Chem.* **1997**, *191*, 1.

83 M. Glasbeek, *Top. Curr. Chem.* **2001**, *213*, 96.

84 Y. Komada, S. Yamauchi, N. Hirota, *J. Phys. Chem.* **1986**, *90*, 6425.

85 H. Yersin, D. Donges, J. K. Nagle, R. Sitters, M. Glasbeek, *Inorg. Chem.* **2000**, *39*, 770.

86 D. Donges, J. K. Nagle, H. Yersin, *Inorg. Chem.* **1997**, *36*, 3040.

87 W. J. Finkenzeller, P. Stössel, H. Yersin, *Chem. Phys. Lett.* **2004**, *397*, 289.

88 R. Czerwieniec, A. Strasser, A. Starukhin, T. Hofbeck, A. Wedel, W. Finkenzeller, H. Yersin, submitted, First results have been presented at the SPIE Optics and Photonics, Conference 5937, San Diego (USA), August, **2005**.

89 A. Vogler, H. Nikol, *Comments Inorg. Chem.* **1993**, *14*, 245.

90 G. Blasse, *Progr. Solid State Chem.* **1988**, *18*, 79.

91 A. Vogler, H. Kunkely, *Top. Curr. Chem.* **2001**, *213*, 143.

92 G. H. Dieke, *Spectra and Energy Levels of Rare Earth Ions in Crystals*, Interscience Publishers, New York, **1968**.

93 D. R. Gamelin, H. U. Güdel, *Top. Curr. Chem.* **2001**, *214*, 1.

94 H. Yersin, D. Trümbach, J. Strasser, H. H. Patterson, Z. Assefa, *Inorg. Chem.* **1998**, *37*, 3209.

95 Z.-Q. Bian, C.-H. Huang, this volume, pp. 391.

96 J. Yu, L. Zhou, H. Zhang, Y. Zheng, H. Li, R. Deng, Z. Peng, Z. Li, *Inorg. Chem.* **2005**, *44*, 1611.

97 P. Kiliuk, C. A. Moore, *Phys. Rev.* **1967**, *160*, 307.

98 B. Henderson, G. F. Imbusch, *Optical Spectroscopy of Inorganic Solids, Oxford Science Publ.*, Clarendon Press, Oxford, **1989**.

99 G. B. Porter, H. L. Schäfer, *Z. Phys. Chem. (NF)* **1963**, *37*, 109.

100 R. Dingle, *J. Chem. Phys.* **1969**, *50*, 1952.

101 H. Yersin, P. Huber, G. Gietl, D. Trümbach, *Chem. Phys. Lett.* **1992**, *199*, 1.

102 M. Wrighton, D. Ginley, *Chem. Phys.* **1974**, *4*, 295.

103 G. A. Crosby, *Acc. Chem. Res.* **1975**, *8*, 231.

104 H. Yersin, H. Otto, J. I. Zink, G. Gliemann, *J. Am. Chem. Soc.* **1980**, *102*, 951.

105 W. Tuszynski, G. Gliemann, *Z. Naturforsch.* **1979**, *34a*, 211.

106 F. A. Cotton, G. Wilkinson, *Anorganische Chemie*, Verlag Chemie, Weinheim, **1980**.

107 D. F. Shriver, P. W. Atkins, C. H. Langford, *Inorganic Chemistry*, Oxford University Press, Oxford, **1991**.

108 H. L. Schläfer, G. Gliemann, *Einführung in die Ligandenfeldtheorie*, Akademische Verlagsgesellschaft Frankfurt/Main, **1967**.

109 C. J. Ballhausen, *Molecular Electronic Structures of Transition Metal Complexes*, McGraw-Hill, New York, **1979**.

110 A. Gilbert, J. Baggot, *Essentials of Molecular Photochemistry*, Blackwell Scientific Publications, Oxford, **1991**.

111 R. Czerwieniec, W. Finkenzeller, T. Hofbeck, X. H. Yang, D. Neher, A. Starukhin, A. Wedel, H. Yersin, XXII International Conference on Organometallic Chemistry, Zaragoza, Spain Vol. *2*, p. 882, **2006**.

112 F. Li, M. Zhang, G. Cheng, J. Feng, Y. Zhao, Y. Ma, S. Liu, J. Shen, *Appl. Phys. Lett.* **2004**, *84*, 148.

113 J. Breu, P. Stößel, S. Schrader, A. Starukhin, W. J. Finkenzeller, H. Yersin, *Chem. Mater.* **2005**, *17*, 1745.

114 H. Yersin, W. Humbs, *Inorg. Chem.* **1999**, *38*, 5820.

115 W. J. Finkenzeller, H. Yersin, *Chem. Phys. Lett.* **2003**, *337*, 299.

116 P. J. Hay, *J. Phys. Chem. A* **2002**, *106*, 1634.

117 A. Ceulemans, L. G. Vanquickenborne, *J. Am. Chem. Soc.* **1981**, *103*, 2238.

118 E. M. Kober, T. J. Meyer, *Inorg. Chem.* **1982**, *21*, 3967.

119 K. Pierloot, A. Ceulemans, M. Merchán, L. Serrano-Andrés, *J. Phys. Chem. A* **2000**, *104*, 4374.

120 Z. Abedin-Siddique, Y. Yamamoto, T. Ohno, K. Nozaki, *Inorg. Chem.* **2003**, *42*, 6366.

121 L. Yang, A.-M. Ren, J.-K. Feng, X.-D. Liu, Y.-G. Ma, H.-X. Zhang, *Inorg. Chem.* **2004**, *43*, 5961.

122 S. Obara, M. Itabashi, F. Okuda, S. Tamaki, Y. Tanabe, Y. Ishii, K. Nozaki, M. Haga, *Inorg. Chem.* **2006**, *45*, 8907.

123 E. Jansson, B. Minaev, S. Schrader, H. Ågren, *Chem. Phys.* **2007**, *333*, 157.

124 K. Nozaki, *J. Chinese Chem. Soc.* **2006**, *53*, 101.

125 K. Nozaki, K. Takamori, Y. Nakatsugawa, T. Ohno, *Inorg. Chem.* **2006**, *45*, 6161.

126 M.-F. Charlot, Y. Pellegrin, A. Quaranta, W. Leibl, A. Aukauloo, *Chem. Eur. J.* **2006**, *12*, 796.

127 T. Liu, B.-H. Xia, X. Zhou, H.-X. Zhang, Q.-J. Pan, J.-S. Gao, *Organometallics* **2007**, *26*, 143.

128 A. V. Vlček, S. Záliš, *Coord. Chem. Rev.* **2007**, *251*, 258.

129 M. G. Colombo, A. Hauser, H. U. Güdel, *Inorg. Chem.* **1993**, *32*, 3088.

130 M. G. Colombo, T. C. Brunold, T. Riedener, H. U. Güdel, M. Förtsch, H.-B. Bürgi, *Inorg. Chem.* **1994**, *33*, 545.

131 M. G. Colombo, A. Hauser, H. U. Güdel, *Top. Curr. Chem.* **1994**, *171*, 143.

132 G. Calzaferri, R. Rytz, *J. Phys. Chem.* **1995**, *99*, 12141.

133 P. I. Djurovich, M. E. Thompson, this volume, pp. 131.

134 Z. Abedin-Siddique, T. Ohno, K. Nozaki, *Inorg. Chem.* **2004**, *43*, 663.

135 T. Yutaka, S. Obara, S. Ogawa, K. Nozaki, N. Ikeda, T. Ohno, Y. Ishii, K. Sakai, M. Haga, *Inorg. Chem.* **2005**, *44*, 4737.

136 H. Miki, M. Shimada, T. Azumi, J. A. Brozik, G. A. Crosby, *J. Phys. Chem.* **1993**, *97*, 11175.

137 A. Szabo, N.S. Ostlund, *Modern Quantum Chemistry*, McGraw-Hill, **1989**.

138 J. Westra, M. Glasbeek, *Chem. Phys. Lett.* **1991**, *180*, 41.

139 M. Glasbeek, R. Sitters, E. van Veldhoven, A. von Zelewsky, W. Humbs, H. Yersin, *Inorg. Chem.* **1998**, *37*, 5159.

140 D. Donges, J. K. Nagle, H. Yersin, *J. Luminescence* **1997**, *72–74*, 658.

141 H. Yersin, D. Donges, W. Humbs, J. Strasser, R. Sitters, M. Glasbeek, *Inorg. Chem.* **2002**, *41*, 4915.

142 K. P. Balashev, D. Donges, P. C. Ford, W. Humbs, M. M. Mdleleni, J. Strasser, H. Yersin, *12th International Symposium on the Photochemistry and Photophysics of Coordination Compounds*, Vermont, USA, Book of Abstracts, P 97, **1997**.

143 H. Yersin, A. F. Rausch, P. I. Djurovich, M. E. Thompson, *SPIE Optics and Photonics*, San Diego, USA, August, **2007**.

144 H. Wiedenhofer, S. Schützenmeier, A. von Zelewsky, H. Yersin, *J. Phys. Chem.* **1995**, *99*, 13385.

145 S. W. Lai, C.-M. Che, W. J. Finkenzeller, A. F. Rausch, H. Yersin, submitted.

146 C. Kratzer, M. Koulikowa, H. Yersin, *14th International Symposium on the Photo-chemistry and Photophysics of Coordination Compounds*, Veszprém, Hungary, Book of Abstracts p. 83, **2001**.

147 W. J. Finkenzeller, T. Hofbeck, M. E. Thompson, H. Yersin, *Inorg. Chem.* **2007**, *46*, 5076.

148 H. Wiedenhofer, PhD Thesis, Universität Regensburg, **1994**.

149 H. Yersin et al., unpublished results.

150 D. R. Striplin, G. A. Crosby, *Coord. Chem. Rev.* **2001**, *211*, 163.

151 H. Yersin, D. Braun, *Chem. Phys. Lett.* **1991**, *179*, 85.

152 M. Kato, S. Yamauchi, N. Hirota, *Chem. Phys. Lett.* **1989**, *157*, 543.

153 D. Pentlehner, I. Grau, T. Hofbeck, H. Yersin, *Chem. Phys. Lett.*, submitted.

154 T. Fischer, R. Bauer, R. Fortte, J. Schwaiger, J. Kroeber, M. Holbach, H. Vestweber, H. Yersin, in preparation.

155 H. Backert, Diplomarbeit, Universität Regensburg, **1996**.

156 H. Yersin, E. Gallhuber, G. Hensler, *Chem. Phys. Lett.* **1987**, *140*, 157.

157 A. Juris, V. Balzani, F. Barigelletti, S. Campagna, P. Belser, A. von Zelewsky, *Coord. Chem. Rev.* **1988**, *84*, 85.

158 C. Daul, E. J. Baerends, P. Vernooijs, *Inorg. Chem.* **1994**, *33*, 3538.

159 E. M. Kober, T. J. Meyer, *Inorg. Chem.* **1984**, *23*, 3877.

160 T. Ziegler, J. K. Nagle, J. G. Snijders. E. J. Baerends, *J. Am. Chem. Soc.* **1989**, *111*, 5631.

161 T. Schönherr, private communication about angular overlap model calculations, University of Düsseldorf, **2007**.

162 H. Yersin, S. Schützenmeier, H. Wiedenhofer, A. von Zelewsky, *J. Phys. Chem.* **1993**, *97*, 13496.

163 J. Schmidt, H. Wiedenhofer, A. von Zelewsky, H. Yersin, *J. Phys. Chem.* **1995**, *99*, 226.

164 J. N. Demas, B. A. De Graff, *Coord. Chem. Rev.* **2001**, *211*, 317.

165 H. Yersin, P. Huber, H. Wiedenhofer, *Coord. Chem. Rev.* **1994**, *132*, 35.

166 D. Braun, P. Huber, J. Wudy, J. Schmidt, H. Yersin, *J. Phys. Chem.* **1994**, *98*, 8044.

167 P. Huber, H. Yersin, *J. Phys. Chem.* **1993**, *97*, 12705.

168 M. Cocchi, V. Fattori, D. Virgili, C. Sabatini, P. DiMarco, M. Maestri, J. Kalinowski, *Appl. Phys. Lett.* **2004**, *84*, 1052.

169 M. Cocchi, D. Virgili, C. Sabatini, V. Fattori, P. DiMarco, M. Maestri, J. Kalinowski, *Synth. Met.* **2004**, *147*, 253.

170 S. Lamansky, R. C. Kwong, M. Nugent, P. I. Djurovich, M. E. Thompson, *Organic Electronics* **2001**, *2*, 53.

171 S. Bonafede, M. Ciano, F. Bolletta, V. Balzani, L. Chassot, A. von Zelewsky, *J. Phys. Chem.* **1986**, *90*, 3836.

172 M. Maestri, D. Sandrini, V. Balzani, L. Chassot, P. Jolliet, A. von Zelewsky, *Chem. Phys. Lett.* **1985**, *122*, 375.

173 V. Balzani, M. Maestri, A. Melandri, D. Sandrini, L. Chassot, C. Cornioley-Deuschel, P. Jolliet, U. Maeder, A. von Zelewsky, In: H. Yersin, A. Vogler (Eds.), *Photochemistry and Photophysics*, Springer-Verlag, Berlin, **1987**.

174 M. Maestri, V. Balzani, C. Deuschel-Cornioley, A. von Zelewsky, *Adv. Photochem.* **1992**, *17*, 1.

175 E. V. Shpol'skii, *Sov. Phys. Usp. (Engl. Transl.)* **1960**, *3*, 372.

176 Ph. Garrigues, H. Budzinski, *Trends Anal. Chem.* **1995**, *14*, 231.

177 H. Yersin, C. Kratzer, *Coord. Chem. Rev.* **2002**, *229*, 75.

178 J. Breu, K.-J. Range, A. von Zelewsky, H. Yersin, *Acta Crystallogr. C53*, 562, **1997**.

179 R. N. Nurmukhametov, *Russian Chemical Reviews* **1969**, *38*, 180.

180 J. A. Salthouse, M. J. Ware, *Point group character tables and related data*, Cambridge University Press, London.

181 R. W. Harrigan, G. A. Crosby, *J. Chem. Phys.* **1973**, *59*, 3468.

182 J. Strasser, H. H. H. Homeier, H. Yersin, *Chem. Phys.* **2000**, *255*, 301.

183 D. R. Striplin, G. A. Crosby, *Chem. Phys. Lett.* **1994**, *221*, 426.

184 T. Azumi, C. M. O'Donnel, S. P. McGlynn, *J. Chem. Phys.* **1966**, *45*, 2735.

185 H. Yersin, J. Strasser, *Coord. Chem. Rev.* **2000**, *208*, 331.

186 T. Hofbeck, PhD thesis, Universität Regensburg; in preparation.

187 K. Dedeian, P. I. Djurovich, F. O. Garces, G. Carlson, R. J. Watts, *Inorg. Chem.* **1991**, *30*, 1685.

188 K. A. King, P. J. Spellane, R. J. Watts, *J. Am. Chem. Soc.* **1985**, *107*, 1431.

189 M. G. Colombo, T. C. Brunhold, T. Riedener, H. U. Güdel, M. Förtsch, H.-B. Bürgi, *Inorg. Chem.* **1994**, *33*, 545.

190 I. Waller, *Z. f. Physik* **1932**, *79*, 370.

191 R. L. de Kronig, *Physica* **1939**, *6*, 33.

192 J. H. van Vleck, *Phys. Rev.* **1940**, *57*, 426.

193 P. L. Scott, C. D. Jeffries, *Phys. Rev.* **1962**, *127*, 32.

194 A. A. Manenkov, R. Orbach, *Spin-Lattice-Relaxation in Ionic Solids*, Harper & Row, New York, **1966**.

195 A. Abragam, B. Bleaney, *Electron Paramagnetic Resonance of Transition Ions*, Clarendon Press, Oxford, **1970**.

196 M. B. Walker, *Can. J. Phys.* **1968**, *46*, 1347.

197 M. B. Walker, *Phys. Rev. Lett.* **1967**, *162*, 199.

198 R. Orbach, M. Blume, *Phys. Rev. Lett.* **1962**, *8*, 478.

199 V. A. Andreev, Y. I. Prilutskii, *Phys. Solid State* **1993**, *35*, 1624.

200 V. A. Andreev, Y. I. Prilutskii, *Sov. Phys. Solid State (engl. Translation)* **1992**, *34*, 1178.

201 H. H. H. Homeier, J. Strasser, H. Yersin, *Chem. Phys. Lett.* **2000**, *316*, 280.

202 T. Hofbeck, Diplomarbeit, Universität Regensburg, **2007**.

203 W. J. Finkenzeller, M. E. Thompson, H. Yersin, *Chem. Phys. Lett.* **2007**, *444*, 273.

204 A. Rausch, T. Hofbeck, W. J. Finkenzeller, M. E. Thompson, H. Yersin, in preparation.

205 E. Gallhuber, G. Hensler, H. Yersin, *J. Am. Chem. Soc.* **1987**, *109*, 4818.

206 D. Braun, G. Hensler, E. Gallhuber, H. Yersin, *J. Phys. Chem.* **1991**, *95*, 1067.

207 H. Yersin, C. Kratzer, *Chem. Phys. Lett.* **2002**, *362*, 365.

208 G. Gliemann, *Comments Inorg. Chem.* **1986**, *5*, 263.

209 G. Gliemann, 31st International Congress Pure Applied Chemistry (Proceedings) Sofia, Bulgaria, Pergamon Press, Oxford, p. 11, **1987**.

210 D. C. Baker, G. A. Crosby, *Chem. Phys.* **1974**, *4*, 428.

211 G. A. Crosby, K. R. Kendrick, *Coord. Chem. Rev.* **1998**, *171*, 407.

212 N. van Dijk, M. Noort, S. Voelker, G. W. Canters, J. H. Van der Waals, *Chem. Phys. Lett.* **1980**, *71*, 415.

213 W.-H. Chen, K. E. Rieckhoff, E.-M. Voigt, *Molecular Physics* **1987**, *62*, 541.

214 A. Zilian, H. U. Güdel, *J. Luminescence* **1992**, *51*, 237.

215 A. P. Marchetti, J. C. Deaton, R. H. Young, *J. Phys. Chem. A* **2006**, *110*, 9828.

216 Y. Kawamura, K. Goushi, J. Brooks, J. J. Brown, H. Sasabe, C. Adachi, *Appl. Phys. Lett.* **2005**, *86*, 071104.

217 A. Tsuboyama, H. Iwawaki, M. Furugori, T. Mukaide, J. Kamatani, S. Igawa, T. Moriyama, S. Miura, T. Takiguchi, S. Okada, M. Hoshino, K. Ueno, *J. Am. Chem. Soc.* **2003**, *125*, 12971.

218 I. Tanaka, Y. Tabata, S. Tokito, *Jap. J. Appl. Phys.* **2004**, *43*, L1601.

219 J. Thompson, V. Arima, F. Matino, S. Berkebile, G. Koller, F. P. Netzer, M. G. Ramsey, R. Cingolani, R. I. R. Blyth, *Synth. Met.* **2005**, *153*, 233.

220 N. R. Evans, L. S. Devi, C. S. K. Mak, S. E. Watkins, S. I. Pascu, A. Köhler, R. H. Friend, C. K. Williams, A. B. Holmes, *J. Am. Chem. Soc.* **2006**, *128*, 6647.

221 Y. Kawamura, J. Brooks, J. J. Brown, H. Sasabe, C. Adachi, *Phys. Rev. Lett.* **2006**, *96*, 17404.

222 M. Sudhakar, P. I. Djurovich, T. E. Hogen-Esch, M. E. Thompson, *J. Am. Chem. Soc.* **2003**, *125*, 7796.

223 B. W. D'Andrade, M. E. Thompson, S. R. Forrest, *Adv. Mater.* **2002**, *14*, 147.

224 S. Tokito, T. Iijima, T. Tsuzuki, F. Sato, *Appl. Phys. Lett.* **2003**, *83*, 2459.

225 V. Maiorano, E. Perrone, S. Carallo, A. Biasco, P. P. Pompa, R. Cingolani, A. Croce, R. I. R. Blyth, J. Thompson, *Synth. Met.* **2005**, *151*, 147.

226 J.-H. Jou, M.-C. Sun, H.-H. Chou, C.-H. Li, *Appl. Phys. Lett.* **2005**, *87*, 043508.

227 S. Lamansky, P. I. Djurovich, D. Murphy, F. Abdel-Razzaq, H.-E. Lee, C. Adachi, P. E. Burrows, S. R. Forrest, M. E. Thompson, *J. Am. Chem. Soc.* **2001**, *123*, 4304.

228 F.-C. Chen, Y. Yang, M. E. Thompson, J. Kido, *Appl. Phys. Lett.* **2003**, *80*, 2308.

229 C. Adachi, M. A. Baldo, S. R. Forrest, S. Lamansky, M. E. Thompson, R. C. Kwong, *Appl. Phys. Lett.* **2001**, *78*, 1622.

230 S. Lamansky, P. I. Djurovich, F. Abdel-Razzaq, S. Garon, D. Murphy, M. E. Thompson, *J. Appl. Phys.* **2002**, *92*, 1570.

231 D. G. Moon, R. B. Pode, C. J. Lee, J. I. Han, *Mater. Sci. Eng. B* **2005**, *121*, 232.

232 F.-C. Chen, S.-C. Chang, G. He, S. Pyo, Y. Yang, M. Kurotaki, J. Kido, *J. Pol. Sci. B* **2003**, *41*, 2681.

233 S. Tokito, M. Suzuki, F. Sato, M. Kamachi, S. Shirane, *Org. Electr.* **2003**, *4*, 105.

234 X. Chen, J.-L. Liao, Y. Liang, M. O. Ahmed, H.-E. Tseng, S.-A. Chen, *J. Am. Chem. Soc.* **2003**, *125*, 636.

235 S. Tokito, M. Suzuki, F. Sato, *Thin Solid Films* **2003**, *445*, 353.

236 A. J. Sandee, C. K. Williams, N. R. Evans, J. E. Davies, C. E. Boothby, A. Köhler, R. H. Friend, A. B. Holmes, *J. Am. Chem. Soc.* **2004**, *126*, 7041.

237 T. C. Brunhold, H. U. Güdel, in: E. I. Solomon, A. B. P. Lever (Eds.), *Inorganic Electronic Structure and Spectroscopy*, Wiley, Vol. *1*, 259, **1999**.

238 E. I. Solomon, *Comments Inorg. Chem.* **1984**, *3*, 225.

239 A. C. Albrecht, *J. Chem. Phys.* **1963**, *38*, 358.

240 G. Fischer, *Vibronic Coupling*, Academic Press, London, **1984**.

241 C. D. Flint (Ed.), *Vibronic Processes in Inorganic Chemistry*, NATO ASI Series C, Vol. *288*, Kluwer Academic Publishers, Dordrecht, **1989**.

242 R. M. Hochstrasser, *Molecular Aspects of Symmetry*, Benjamin Inc., WA, New York, Amsterdam, **1966**.

243 N. Mataga, T. Kubota, *Molecular Interactions and Electronic Spectra*. Marcel Decker Inc., New York, **1970**.

244 D. Becker-Donges, H. Yersin, A. von Zelewsky, *Chem. Phys. Lett.* **1995**, *235*, 490.

245 J. Schmidt, J. Strasser, H. Yersin, *Inorg. Chem.* **1997**, *36*, 3957.

246 W. Finkenzeller, PhD Thesis, Universität Regensburg, in preparation.

247 L. Bär, G. Gliemann, *Chem. Phys. Lett.* **1984**, *108*, 14.

248 R. Dillinger, G. Gliemann, *Chem. Phys. Lett.* **1985**, *122*, 66.

249 G. Gliemann, H. Yersin, *Structure and Bonding*, Springer Berlin, *62*, 87, **1985**.

250 T.-H. Huang, K. E. Rieckhoff, E. M. Voigt, *Chem. Phys.* **1979**, *36*, 423.

251 T.-H. Huang, K. E. Rieckhoff, E. M. Voigt, *J. Chem. Phys.* **1982**, *77*, 3424.

252 D. Braun, H. Yersin, *Inorg. Chem.* **1995**, *34*, 1967.

253 J. Breu, C. Kratzer, H. Yersin, *J. Am. Chem. Soc.* **2000**, *122*, 2548.

254 R. Bauer, W. J. Finkenzeller, U. Bogner, M. E. Thompson, H. Yersin, submitted.

255 I. Renge, *J. Phys. Chem. A* **2001**, *105*, 9094.

256 W. M. Yen, P. M. Selzer (Eds.), *Laser Spectroscopy of Solids, Springer Berlin*, Topics in Applied Physics, Vol. *49*, **1981**.

257 R. I. Personov, in: V. R. Agronovich, R. M. Hochstrasser (Eds.), *Spectroscopy and Excitation Dynamics of Condensed Molecular Systems*, North Holland, Amsterdam, p. 555, **1983**.

258 W. E. Moerner (Ed.), *Persistent Spectral Hole Burning: Science and Applications*, Springer, Berlin, **1988**.

259 K. K. Rebane, in: O. Sild, K. Haller (Eds.), *Zero-Phonon Lines and Spectral Hole Burning in Spectroscopy and Photochemistry*, Springer, Berlin, **1988**.

260 H. Riesen, *Coord. Chem. Rev.* **2006**, *250*, 1737.

261 W. H. Hesseling, D. A. Wiersma, *J. Chem. Phys.* **1980**, *73*, 648.

262 D. E. McCumber, M. D. Sturge, *J. Appl. Phys.* **1963**, *34*, 1682.

2
Spin Correlations in Organic Light-Emitting Diodes

Manfred J. Walter and John M. Lupton

A particular characteristic of organic materials used in light-emitting diodes is that they are predominantly composed of carbon and therefore only exhibit a very weak spin–orbit coupling. Electrically injected electrons and holes each carry spin 1/2 so that recombination can occur in a total of four spin combinations. It is an important question whether interconversion between the spin states can occur during electrostatic carrier capture prior to the formation of the ultimate excited state on the individual molecule, the singlet or the triplet exciton. Conjugated polymers containing minute quantities of spin–orbit enhancing heavy metal atoms open a unique window to spin dynamics in organic light-emitting diodes by enabling optically or electrically generated triplets to decay radiatively without impacting dramatically on the actual generation mechanism of triplets through excited state intersystem crossing. We show that optically generated singlet excitons can be electrically stabilized to prevent recombination. Storage of the charge carrier pair for tens of microseconds does not reveal a preference for delayed recombination in the lower energy triplet channel, suggesting that spin conversion in the charge carrier pair precursor state to exciton formation is rather inefficient. The message of this basic study of spin-lattice relaxation in excited states of organic films to device engineers is that correlations between the spins of electrostatically bound carrier pairs are intrinsically remarkably stable. In the absence of a strong external mixing channel such as a heavy metal atom as in organometallic dopants it is expected that the dominant recombination in an organic light-emitting diode occurs in nonradiative triplets, forming a serious loss channel in actual devices.

2.1
Introduction

The most significant difference between organic, carbon-based semiconductors and inorganic crystalline materials lies in the properties of the electron spin and the exchange interaction. Due to the low atomic order number of carbon, spin is

referred to as a good quantum number in organic molecules. Furthermore, the highly localized, tightly bound molecular excitations are subject to exceptional exchange interactions, which can lead to a splitting of up to 1 eV between the singlet and triplet excited state spin manifold of the molecule. The weak spin–orbit coupling and strong exchange splitting generally imply that a molecule excited in the triplet manifold cannot simply return to the ground state – typically a singlet – by emission of a photon. It rather has to choose a nonradiative relaxation pathway, which is generally highly inefficient and therefore very slow and naturally not desirable in a device designed to emit light. The emission from radiative, spin-forbidden transitions from the triplet excited state to the ground state is referred to as phosphorescence. Even at low temperatures, this is typically extremely weak in pure hydrocarbon materials and often unobservable, particularly in high molecular weight organic semiconductor molecules such as conjugated polymers.

Simple spin statistics suggest that electrons and holes, which are injected at the cathode and anode of the device, respectively, and both carry spin 1/2 can combine in a total of four different spin combinations, summarized in Fig. 2.1. Three of these spin combinations are symmetric, whereas only one is antisymmetric. The symmetric spin wavefunction is referred to as a triplet, whereas the antisymmetric spin wavefunction describes the singlet state. While most of the contributions of this book deal with the question of how to harvest energy from the spin symmetric excitations by using efficient phosphors such as organometallic triplet emitters, we would like to summarize some of the recent research efforts into spin-dependent recombination processes in organic semiconductors. These efforts have spurred the development of exploitation of the triplet state in electrophosphorescence.

One of the most fundamental questions in the field of organic LEDs is the process describing the final transformation step of the isolated charge carriers injected into the material by the electrodes to a molecular excitation. The scale of the problem is readily exemplified by considering the terminology involved. The
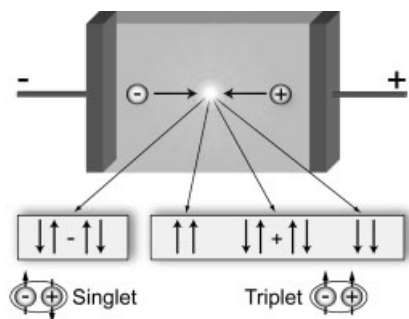
Fig. 2.1 Elementary operation principle of an organic light-emitting diode. Charge carriers can combine to form excitations either in the singlet or in the triplet manifold of the molecule.

reader will be acquainted with the concept of mobile electrons in a semiconducting solid, describing negative charges, and mobile holes, describing positive charges or vacant electron states. As organic semiconductors are intrinsically molecular in nature it is helpful to draw a link to the terminology of electrochemistry. Rather than being delocalized over many sites as Bloch electrons are in a semiconductor crystal, charges are generally localized to individual molecular sites. An individual molecule can therefore acquire either a positive or a negative charge, making it a radical cation or anion, respectively. As a net charge, positive or negative, on the molecule will change the intramolecular interatomic binding, it will also lead to a conformational change, that is, a lattice distortion. In the terminology of conventional semiconductors, the high degree of coupling of charge to lattice distortions is taken into account by referring to a polaron. Effectively, these three terminologies of electron/hole, anion/cation, and negative/positive polaron are equivalent, as they all describe a net charge of negative or positive sign which possesses a spin of 1/2.

It is fairly straightforward to picture these charges diffusing and drifting under an applied electric field through the active layer of the device by hopping from one polymer chain to the other. It is less trivial to come up with a microscopic description of this migration process, and a review of progress made in this area is beyond the scope of this chapter. Each net positive charge exerts a Coulombic attraction on each net negative charge. Once this attractive potential grows larger than the thermal energy of the single carrier, positive and negative charge carriers are said to be Coulombically bound. The respective maximum spatial separation of charge carriers is referred to as the Onsager limit. Figure 2.2 summarizes the different regimes of carrier correlation entered as a function of distance [1].

The degree of Coulombic electron–hole correlation is described in terms of a binding energy. For distant Coulombically bound pairs, the exchange interaction is irrelevant so that the four conceivable spin configurations are of equal energy, i.e., degenerate. As the carriers approach each other, however, and the wavefunctions begin to overlap, the exchange interaction becomes relevant and the degeneracy between singlet and triplet states is lifted. This intermediate region of charge separation can be thought of as a charge transfer state. It can be either monomolecular or bimolecular in nature. Once an electron and a hole reside on the same molecule, a molecular excitation is formed, either in the singlet or in the triplet manifold. Due to the constituent nature of this excitation formed by an electron and a hole it is often referred to as an exciton whose singlet and triplet states are split energetically due to the strong electronic correlation. A typical value for the singlet–triplet exchange splitting in conjugated polymers is 0.7 eV. This final step in carrier recombination is the most intriguing, as it is here that the analogy to semiconductor physics breaks down. After all, one would not consider describing a photoexcitation on a rhodamine molecule in solution, for example, as a Coulombically bound electron–hole pair. The problem is somewhat relaxed in conjugated polymers, as it has been shown that the conjugation length of an electronically active segment on the chain can by far exceed the spatial delocalization of the molecular excited state [2], i.e., the exciton can move within the conjugated
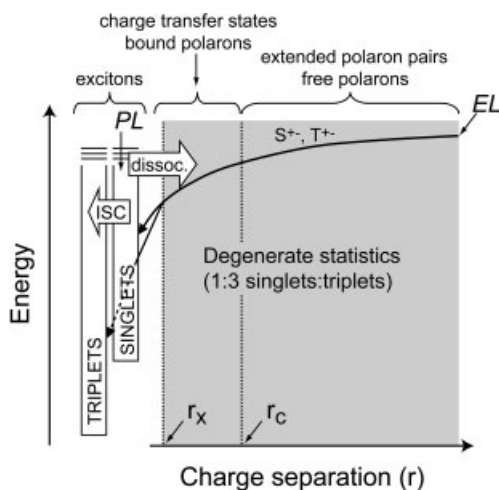
Fig. 2.2 Binding energy of electrons and holes as a function of spatial separation. At a large separation, the two spin states of electrons and holes injected into the organic semiconductor are degenerate. The two characteristic length scales r_c and r_x describe the distances for which the Coulombic and exchange interactions become relevant, respectively. Once an electron and a hole are bound Coulombically, a charge transfer state is formed which can ultimately lead to the population of a molecular excitation. Adapted from [1].

segment. Experimentally, this is seen by the fact that well-defined oligomers and polymers can have the same emission and absorption properties, but differ in terms of oscillator strength of the transitions [2]. Nevertheless, it is this final transition from a close polaron pair [3, 4] or charge transfer state to a molecular excitation – equivalent in energy and transition lifetime to a photoexcitation – which has caught the interest of researchers over the past years. This step determines the ultimate electron to photon conversion efficiency achievable with organic LEDs and is the subject of the present discussion.

Following this introduction to the topic we will review the history of research on spin-dependent recombination in conjugated polymers. We will outline how important spin-mixing channels between the singlet and triplet manifold of the molecule are to break the spin-statistical limit of the OLED efficiency. We will then discuss the experimental technique and material system used to test the degree of spin mixing during charge carrier recombination. Using transient (gated) electroluminescence spectroscopy, a lower limit for the triplet formation rate is derived. This is then used to evaluate electric field modulation of singlet and triplet emission under optical excitation, where the electric field controls the transition from the charge transfer, polaron pair or radical pair state to the final molecular excitation. After comparison with further results in the literature and discussing the influence of magnetic fields on the recombination dynamics we conclude that spin mixing is absent in organic semiconductors and the maximum OLED efficiency

in the absence of phosphorescent triplet emission is therefore given by the spin-statistical limit of 25%.

While it appears that the spins of Coulombically bound charge carriers are strongly correlated and thus spin-mixing is very weak in organic semiconductors, the implications for real devices are not necessarily detrimental. The problem of spin statistics can be overcome by using phosphorescent, triplet-emitting acceptors in the organic semiconductor. The spin degree of freedom, however, opens a whole new array of application potential of organic semiconductors such as in giant magnetoresistive sensors for magnetic memory media and spin valves for information processing, which is only just becoming visible [5, 6].

2.2
Spin-Dependent Recombination of Charge Carriers and Spin-Lattice Relaxation

Absolute quantum efficiencies are fairly straightforward to determine under optical [7] and electrical excitation [8, 9]. The problem is that a direct comparison of the two in an LED structure is not that trivial. Charge carrier recombination typically occurs in a narrow region of the LED, whereas photon absorption leads to a continuous profile of excitations following Lambert–Beer's law. It is then hard to assure that absolute measurements of the optical and electrical quantum efficiency are carried out in exactly the same region of a device structure. Such an experiment is further complicated by interference effects and interactions with surface plasmons in the metallic electrode, which can either quench or enhance the emission and introduce a particular sensitivity to the substantial birefringence characteristic of one-dimensional conjugated polymers [9, 10]. A few initial comparisons of optical and electrical quantum yields [8, 11] suggested that the ratio of the two could substantially exceed the spin-statistical limit of $1:3$ in conjugated polymers, whereas similar experiments in OLEDs based on small molecules such as aluminum-tris-(8-hydroxyquinoline) confirmed the 25% ratio [1, 12]. However, the quantum efficiencies of the devices studied remained substantially below 10%, whereas at the same time over twice the efficiency was being achieved with OLEDs incorporating triplet-harvesting phosphors [13].

Prompted by the surprising suggestion that the spin-statistical limit could be broken in fluorescent OLEDs [8, 9, 11, 14–25], a number of models were devised to explain this discrepancy. Nevertheless, a concluding picture concerning the singlet–triplet ratio has not yet evolved and the topic remains controversial (e.g., [1, 26–31]). To follow this line of thought, we need to realize that the transition rates from the charge transfer or polaron pair state to the final exciton or molecular excitation could differ, depending on the final spin configuration. That is, the rate for triplet formation k_T could differ from the rate for singlet formation k_S, as illustrated schematically in Fig. 2.3. While it is not immediately obvious why this should be the case [1], a number of quantum chemical and analytical calculations suggest this [22, 24, 25, 32]. The driving argument is that if the charge transfer states of singlet or triplet configuration are nearly degenerate, substantially more
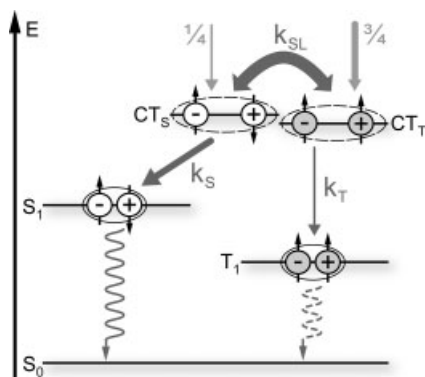
Fig. 2.3 Interplay between exchange splitting and molecular level population. Singlets are populated from the charge transfer (CT) states (the bound electron–hole pairs) at a rate of k_S, whereas triplets are created at a rate of k_T. The fundamental question is whether a conversion of the spin configuration can occur in the charge transfer state. If such a conversion occurs due to spin-lattice relaxation (k_{SL}) (also referred to as intersystem crossing within the CT state) with associated conservation of energy through absorption or emission of phonons, then the ultimate quantum efficiency of the device can exceed the spin-statistical limit of 25% assuming that singlet formation occurs faster than triplet formation [19].

energy has to be dissipated to relax the intermolecular charge transfer state to an intramolecular excitation of the lower lying triplet configuration rather than the singlet configuration. In short, $E_{CT} - E_T \gg E_{CT} - E_S$. This relaxation requires multiple phonon emission, which may be a problem due to the existence of a phonon bottleneck [21, 23], although we note in passing that energy dissipation in organic molecules is generally very efficient and even intramolecular energy transfer does not appear to suffer from such a bottleneck phenomenon [33]. This is particularly relevant as the intrinsic Stokes shift (i.e., the energy dissipated upon geometric relaxation under excitation) has been shown to be miniscule (<70 cm^{-1} [34]). The second argument relates to the symmetry of the exciton precursor and the final exciton states. Whereas the charge transfer or polaron pair state as the relevant intermediate to exciton formation is highly polar and delocalized, the triplet state is strongly bound, symmetrical, unpolar and can be thought of as being supported by a covalent bond. The bond holding together a singlet exciton, in turn, is more ionic in nature, and thus resembles the exciton precursor much more in terms of local symmetry properties. This imbalance may increase k_S with respect to k_T [19, 24].

It is important to realize that an imbalance in formation rates is actually irrelevant to device performance if there is no spin-mixing channel, that is, if the spin configuration of the precursor state cannot change with time. More rapid singlet than triplet formation will only influence the singlet to triplet ratio in a device if a transition between spin states of the precursor carrier pair can occur. There are a number of ways to think of such a spin-mixing channel, the most instructive

possibly being the spin-lattice interaction which leads to a spin flip of the single particle (electron or hole). If the spin-lattice relaxation rate k_{SL} substantially exceeds the triplet formation rate k_T, then preferential singlet exciton formation can occur provided the transition from carrier pairs to molecular excitations is biased in favor of singlets, that is $k_S > k_T$. It is this spin-mixing rate which is the focus of this chapter and has previously been hard to assess experimentally and impossible to determine theoretically.

Besides the detailed theoretical investigations of the problem of the final charge carrier recombination step [21–25], there have been three main directions of experimental work to address this problem (see also the following reviews: [1, 35, 36]). The first is based on electron spin resonance in combination with photoluminescence and photoinduced absorption [19, 20]. This technique allows a direct measurement of the spin multiplicity of species associated with features identified in optical spectroscopy. In particular, it can be used to measure the transition rates from nongeminate charge carriers to exciton states directly. Whereas nongeminate (i.e., free, unbound) carriers carry spin 1/2, the exciton has a spin of 1 (triplet) or 0 (singlet) so that transitions can be followed by the spin resonance signature. Strictly speaking, as these are basically static measurements, it is the formation cross sections rather than the formation rates which are measured. Detailed investigations along this line showed that not only is there a marked bias toward recombination in the singlet channel (i.e., $k_S > k_T$), but this ratio also exhibits a marked dependence on the particular material system studied [19]. Interestingly, studies on a series of oligomers pointed toward a chain length dependence of the ratio of formation cross sections [20, 22, 23, 37]. Whereas short molecules apparently follow spin statistics, longer molecules show a deviation with a bias toward singlet recombination. The problem with these results is that the immediate relevance to LEDs is not apparent as no information on the spin-mixing rate k_{SL} is available. In fact, the technique of electron spin resonance actually induces spin mixing. Furthermore, there are considerable methodological problems which arise because of the requirement of optical carrier generation. This is achieved by photo-oxidation of the sample [20], a process which could clearly modify the physics of the material. We note that the technique itself is also highly debated [1], and a recent extension of the method to shorter timescales in the frequency domain claimed to observe no deviation from spin statistics [38–40].

The second method is based on a comparison of fluorescence and phosphorescence in a working LED configuration. Initial studies on small molecular systems pointed toward a spin-statistical ratio [12], whereas subsequent investigations on model oligomer and polymer compounds containing heavy metal atoms required to activate the radiative triplet channel pointed toward a substantial deviation from spin statistics as the size of the molecular system increases [11]. The problem hereby is that the model systems contain metal atoms in every repeat unit, which induce strong spin mixing so that singlet and triplet are no longer pure states. In a simple microscopic picture, the heavy metal atoms induce spin crossovers between singlet and triplet by the spin-orbit coupling, both in the exciton state and in any exciton precursor state. While these results therefore again point toward a

chain length dependence of the exciton formation cross section, they provide no immediate insight into the competing mechanism of spin-lattice relaxation.

The third technique is not dissimilar to the first as it principally relies on induced absorptions arising from optical and electrical excitation and a direct quantification of the triplet density [14, 41, 42]. Whereas the singlet density can be measured from the photoluminescence intensity, the triplet absorption ($T_1 \rightarrow T_n$) provides a measure of the triplet density. The problem hereby is to disentangle the triplet absorption from the polaron absorption feature or even from absorptions of other unidentified species [42]. While this is possible at low temperatures, where the transitions are narrow, it becomes very hard at elevated temperatures. Furthermore, a conversion of the triplet absorption into a number for the triplet density requires accurate knowledge of the triplet absorption cross section. This number is hard to assess experimentally and is typically estimated from quantum chemical calculations [43]. A further complication is the absence of accurate knowledge of the intrinsic inter-system crossing efficiency from an excited singlet state to the excited triplet. Values in the range of a few percent have been reported for this [44], but it is not at all clear whether this really is the intrinsic value relevant to the individual molecular S_0–S_1–T_1 three-level system. After all, singlet excitons are rather mobile in a polymer film and can diffuse over more than 1nm. As the spin–orbit coupling scales with Z^4, a single impurity such as an oxygen atom will enhance intersystem crossing locally by a factor of about 3 compared to carbon atoms. This is, however, an extrinsic effect. We note that single molecule spectroscopy of conjugated polymers [34, 45, 46] can exhibit extremely stable emission without detectable intermittencies over periods of hours [47]. Keeping in mind that the triplet lifetime of conjugated polymers such as polyfluorenes at low temperatures is of the order of seconds [48], an excursion to the triplet would render the single molecule dark for seconds. This is not observed, suggesting that the intrinsic intersystem crossing efficiency is indeed extremely low. Consequently, this method of quantifying optically or electrically induced absorptions has yielded rather conflicting results ranging from a near absence of triplets under electrical excitation [14] to a confirmation of the spin-statistical limit [14, 16, 26–31, 49].

These techniques rely on direct measurements of populations as a result of charge carrier recombination. While this is the most obvious experimental approach, the extensive spectrum of literature available suggests that there is some ambiguity in the interpretation of the results. We therefore seek to address the question of whether or not a change in the spin configuration can take place prior to the final transition from a charge transfer or polaron pair state to a molecular excitation. If a change in spin configuration cannot occur, then the implications for the ultimate quantum efficiency of an OLED are very clear: it cannot exceed the spin-statistical limit of 25% [35]. While we show this to be the case in a particular material system highly relevant to OLEDs, we note that this negative result may not be the end of the story. It appears that in a homogeneous material system charge carriers once bound cannot dissociate again and therefore maintain their spin configuration. Recent studies of photoinduced triplet absorption ($T_1 \rightarrow T_n$) in blend systems, on the other hand, do suggest that the barriers to dissociation can

be lowered if a long-lived delocalized and weakly bound exciplex state is formed [43, 50]. This may in turn affect the probability for nongeminate recombination to occur, that is, carrier dissociation followed by recombination with a new partner.

2.3
Studying Spin States using Electric Field Modulated Fluorescence and Phosphorescence

2.3.1
Electric Field Modulation of Fluorescence and Phosphorescence: Experimental Method

The idea of the present undertaking is to investigate the spin dependence of the final recombination step in a polymer based OLED, i.e., the transition from a pair of oppositely charged carriers – referred to either as a charge transfer state, radical pair or polaron pair – to a molecular excitation. In contrast to previous studies, the focus is on using a model material system for organic semiconductors which induces only a minimal perturbation in the singlet and triplet manifold of the molecule yet allows a direct visualization of both singlet and triplet states [51]. Most importantly, the experiments are to be carried out in a device geometry at room temperature in the presence of an electric field. The singlet population of an organic semiconductor is comparatively straightforward to monitor, as singlets decay radiatively and at least in the low occupation limit the number of photons emitted provides an accurate estimate of the singlet density. Triplets can be detected directly by their magnetic resonance signature in photoluminescence [52], electroluminescence [52], photocurrent [3], or photoinduced absorption spectroscopy [35]. The latter also provides an estimate of the relative triplet density on its own, i.e., in the absence of spin resonance, but is complicated by the fact that a number of species can overlap the photoinduced absorption signature [14, 42]. As in the case of singlets, the most direct and accurate measure of the triplet density is photon emission by phosphorescence [48, 53]. The problem is that this is a spin-forbidden process and is therefore not trivial to observe. The photon density can then be influenced strongly by inhomogeneities in the film and by secondary processes such as triplet–triplet annihilation.

We recently introduced a unique material system which apparently provides the best of both worlds in terms of radiative singlet *and* triplet emission [51]. As triplet deactivation is a forbidden process, these excitations have extremely long lifetimes and can therefore diffuse substantial distances through the film. It is this diffusivity which can be exploited to activate the radiative decay of triplets (phosphorescence via $T_1 \rightarrow S_0$ intersystem crossing) *without* substantially perturbing the singlet population by direct $S_1 \rightarrow T_1$ intersystem crossing. Figure 2.4 shows the chemical structure of this unique material system, a ladder-type poly(para-phenylene) with phenyl backbone substituents (PhLPPP). Its optical and optoelectronic properties are identical to those of the more commonly studied methyl-substituted LPPP
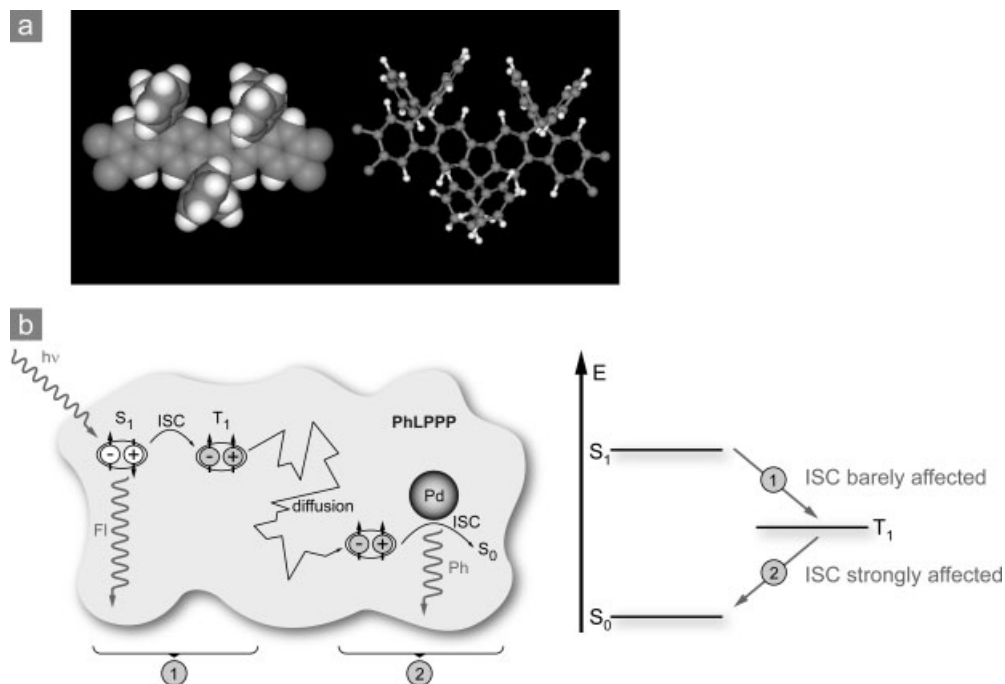
Fig. 2.4 (a) Chemical structure of the polymer system used to study singlet and triplet spin states. The ladder-type poly(para-phenylene) (PhLPPP) contains an extremely low concentration of covalently bound palladium atoms. (b) The high diffusivity and longevity of triplet excitons enables efficient triplet scavenging and rapid ($T_1{\rightarrow}S_0$) intersystem crossing with photon emission (phosphorescence), whereas the singlet population in the material is barely affected by the heavy metal atoms. Only singlets within the immediate vicinity of the Pd atom are affected, but as the diffusion length of singlets is shorter than that of triplets, this only has a minimal effect [56]. This is illustrated in the cartoon shown.

(MeLPPP), and the material can readily be used for applications as diverse as plastic lasers and single molecule spectroscopy [2, 54]. It is deposited onto a glass or indium tin oxide (ITO) covered glass substrate by means of dissolution in toluene and subsequent spin-coating to yield high quality films with typical thicknesses of 100–200 nm. The crux of the material lies in the addition of a very small number of palladium atoms, which are covalently bound to the polymer backbone during polymerization. The presence of these atoms can only be verified using highly sensitive combustion analysis, which pinpoints the concentration to around 100 ppm. This corresponds to fewer than one atom per polymer chain at the molecular weight employed or a spatial density of less than one Pd atom per cube of $15 \times 15 \times 15\,nm^3$. Nevertheless, this miniscule concentration at levels unheard of in organic synthesis is sufficient to fundamentally alter the optoelectronic properties of the material. The high degree of triplet diffusivity allows triplet excitons generated in the bulk of the material to diffuse randomly throughout the bulk over
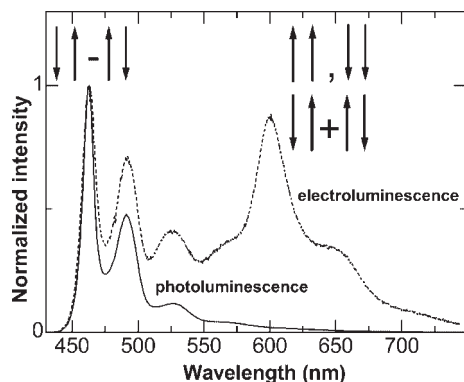
Fig. 2.5 Comparison of electroluminescence and photoluminescence spectra of the PhLPPP polymer system at room temperature. Two distinct spectral features are apparent, around 460 and around 600 nm. Whereas the high energy feature, which is associated with emission from the singlet state, is seen in both photoluminescence and electroluminescence, the red emission attributed to phosphorescence, i.e., triplet emission, only occurs upon injection of uncorrelated spin pairs in electroluminescence.

a substantial time period. The distance a triplet can diffuse is only limited by energetic disorder in the material and by slow, nonradiative recombination of the triplet, such as through phonon scattering [55, 56]. Once such a triplet exciton encounters a heavy metal atom, the strength of the spin–orbit coupling, which scales with the atomic order number as Z^4, is raised by orders of magnitude so that a mixing of the singlet and triplet manifold occurs. As back transfer to the excited singlet is impeded by the large energetic separation of the states of ~0.7 eV, the molecule relaxes back to the singlet ground state under emission of a photon. In this way the radiative decay channel of the usually dark triplets can be strongly enhanced. At the same time, the low level of metallic spin–orbit coupling centers barely affects the singlet excitons as the singlet diffusion length is lower than the triplet diffusion length due to the rapid radiative relaxation of singlets. The process is summarized in the sketch shown in Fig. 2.4: on the one hand, the heavy metal atoms barely alter the intrinsic ratio of singlet to triplet excitons [56] due to the shorter characteristic migration distance of singlets, while on the other hand they make triplets visible via the phosphorescence channel.

Figure 2.5 illustrates the simplicity and power of this approach in visualizing the two spin configurations of excitations in a conjugated polymer film. We compare the emission of the film under electrical and under optical excitation with otherwise identical conditions at room temperature. Whereas under electrical injection spin-uncorrelated charge carriers recombine, absorption of a photon leads to direct formation of a singlet exciton, which in turn has a small probability of undergoing intersystem crossing to the triplet manifold. Two main spectral features are seen, one around 460 nm and the other around 600 nm, both followed by the vibrational subbands characteristic of the coupling of the electronic

transitions to vibrational degrees of freedom of the material. In both cases the emission at 460 nm is seen. This band is attributed to the singlet exciton, which has previously been studied extensively using time resolved and single-molecule spectroscopy [57]. Under electrical excitation the second band at 600 nm appears. This emission is attributed to phosphorescence, i.e., emission from the triplet state, due to its similarity with the previously detected triplet signature under optical excitation [48, 53]. Its strength is comparable to that of the singlet emission. By comparison of the spectra we can pose an upper limit on the relative triplet density under optical and electrical excitation of a factor of 100. Although both singlets and triplets are generated by electrical injection of spin-uncorrelated electrons and holes, the vast majority of optically generated excitations are in the singlet configuration as the photon does not carry orbital angular momentum and the spin configuration of the molecule is thus conserved during the transition from the ground to the excited state.

The phosphorescence is driven by diffusion of triplets to palladium sites in the polymer film [55, 56, 58]. A small number of triplets are also generated under optical excitation due to either intrinsic or diffusion driven intersystem crossing. The intrinsic efficiency of intersystem crossing is extremely low because in ideal conjugated polymers the spin-orbit coupling will be marginal as only lightweight carbon atoms ($Z = 6$) are present. Contrary to that, in PhLPPP triplet→singlet intersystem crossing is strongly enhanced because of diffusion of triplets to palladium sites as described in detail above. As the phosphorescence is diffusion limited and not controlled by the spontaneous emission lifetime of triplets, which is relatively short close to heavy metal atoms, we observe a power law dependence of the phosphorescence intensity as a function of time. This is illustrated in Fig. 2.6 for triplets generated either optically or electrically at room temperature. The experimental method is similar in both cases. In the optical case, a short (130 fs) laser pulse excites singlets at time zero, a small fraction of which undergoes intersystem crossing to the triplet state. The phosphorescence at a time τ after excitation
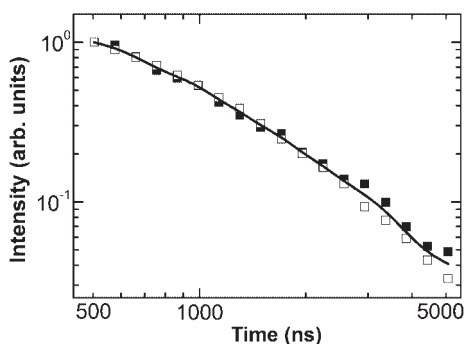
Fig. 2.6 Decay of the phosphorescence under optical (open symbols) and electrical (closed symbols) excitation at room temperature, shown on a double logarithmic scale. The line is a guide to the eye.

is recorded within detection windows of variable length (100 ns to 200 µs) by using an electrically gated image intensifier mounted in front of a charge-coupled device camera. The gate length is chosen as $\delta\tau$, typically 100 ns. For transient electroluminescence, a square voltage pulse is applied to a diode structure in forward direction. After the voltage pulse is removed, the phosphorescence is again measured in an optical gate of delay τ and width $\delta\tau$. This technique of transient electroluminescence spectroscopy is very powerful for studying delayed recombination in OLEDs and in particular the influence of trap and defect recombination [59, 60]. As determined from Fig. 2.6, the decay of the phosphorescence in both cases follows a power law with an exponent of (–1.3, showing that the decay of the triplet density under optical and electrical excitation is virtually identical. This similarity tells us that all optical or electric field modulated *optical* measurements as discussed below provide an accurate picture of the dynamics of triplet excitons generated by *electrical* injection in an OLED. Indeed, excitations generated by optical or electrical excitation are identical. Note that the power law decay of the phosphorescence can be described accurately by a diffusion model [56].

The simultaneous visualization of singlet and triplet densities in an organic semiconductor now allows us to assess the degree of spin mixing during recombination in an immediacy other methods lack. There are a number of experimental routes to addressing this question. The basic approach is to convert a singlet exciton generated optically into a meta-stable charge carrier pair, in which the radiative decay channel is deactivated [61, 62]. The radiative decay rate can then be controlled by an external electric field, as will be shown in detail. When the charge carriers finally recombine, the spin configuration of the carrier pair is directly transferred to the spin configuration of the exciton state, which can be read out as either fluorescence or phosphorescence [54]. Figure 2.7 summarizes the basic experimental strategy to measure spin conversion times in carrier pairs by modulating the recombination to excitons with an electric field. The important point to note is that an electric field applied in reverse bias, i.e., without injecting charge carriers into the diode structure, quenches (reduces) the exciton fluorescence [63]. In contrast to inorganic semiconductors, where an electric field can fully dissociate the exciton at moderate field strengths, the exciton binding energy in a conjugated polymer exceeds half an eV due to the strong Coulombic correlations and low dielectric screening [64]. Typical sizes of an exciton are in the range of a few nm. Recent studies of the electric field effect in single molecule fluorescence show clearly that it is generally not possible to dissociate or field-quench the exciton on a single chain [65]. Even in the bulk it is not possible to fully dissociate the exciton and generate free charge carriers. However, the electric field can polarize the exciton so that electron and hole no longer reside on the same molecule, creating a charge transfer state which is effectively intermolecular and lacks a radiative decay channel. This electric field induced transformation of singlet excitons to the respective dark charge transfer states is the reason for fluorescence suppression, as illustrated in Fig. 2.8(a). The dependence of the electric field quenching efficiency on the applied bias shows a parabolic functionality in panel (b), as expected for a Coulombic screening process [63]. The suppression of
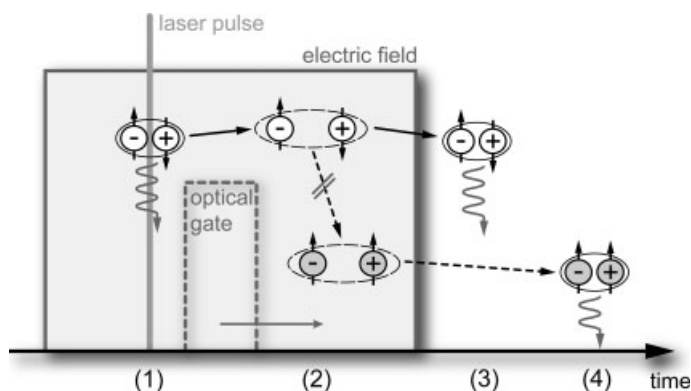
Fig. 2.7 Excitation and detection scheme for electric field modulated photoluminescence. Singlet excitons are formed by absorption of the laser pulse (1) and a certain fraction of these are dislocated in an electric field present during generation (2). An optical gate (dashed line) can be swept along the time axis to detect the amount of fluorescence and phosphorescence present at any given time. Switching off the electric field results in the dislocated, indirect exciton (which can be thought of as a charge transfer state, radical pair or polaron pair) returning to the exciton configuration (3). Note also that intersystem crossing may occur after the electrical pulse from newly generated singlet excitons, potentially modifying the radiative triplet signature (4).
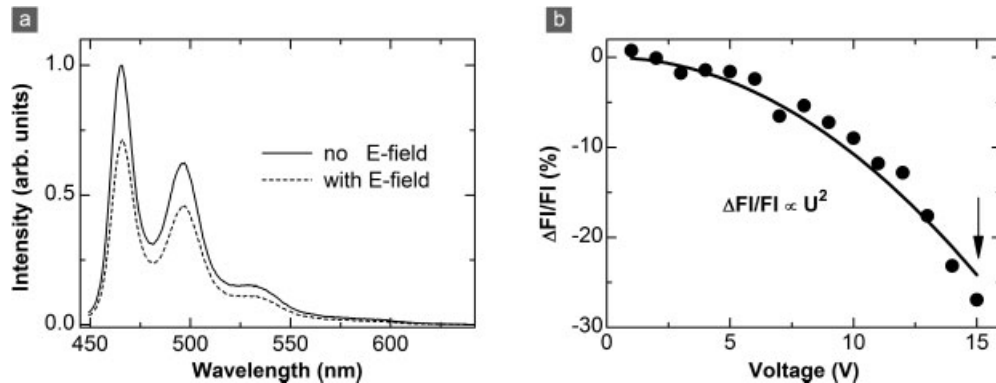
Fig. 2.8 (a) Quenching of the cw photoluminescence of a polymer film due to exciton dislocation under application of an external electric field. (b) Dependence of the quenching efficiency on the applied bias applied to a 100-nm-thick device with insulating barrier layers preventing charge injection. Fl and ΔFl refer to the fluorescence and the change in fluorescence intensity, respectively.

radiative decay does not necessarily enhance radiationless decay, as radiative recombination of a fraction of the separated carrier pairs can occur after removal of the electric field [66].

2.3.2
Estimating the Triplet Formation Rate from Transient Electroluminescence

As we outlined in the introduction, an imbalance in triplet and singlet formation rates will only affect the ultimate quantum efficiency of the device if spin mixing can occur prior to recombination, i.e., if the rate of spin-lattice relaxation exceeds the recombination rate. Thus far, only relative exciton formation cross sections have been accessible experimentally [35]. Theoretical investigations have suggested triplet formation rates of order $(100\,ns)^{-1}$, orders of magnitude lower than singlet formation rates [22]. Using our electrophosphorescent conjugated polymer along with the powerful technique of gated electroluminescence spectroscopy [59, 60], we can arrive at a straightforward estimate for an upper limit of the triplet formation time. Application of an electric field in forward bias (i.e., under injection conditions) and time resolved detection of the emission spectra allow us to estimate the time required for photon emission from the triplet state to occur.

Figure 2.9 shows the response of an OLED to an applied bias pulse resolved for both the singlet and the triplet channel. Clearly, the fluorescence sets in before the phosphorescence and the phosphorescence also lives longer. This is simply a consequence of the fact that the phosphorescence rate is limited by slow triplet diffusion to the palladium sites and not by triplet formation. This is readily seen
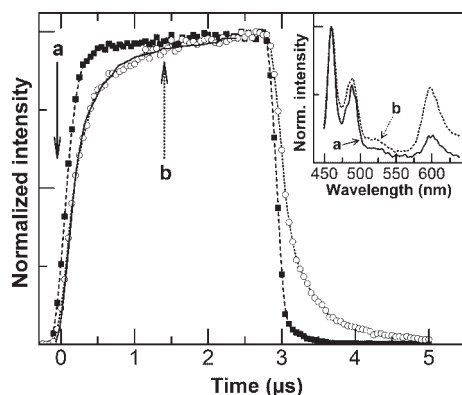
Fig. 2.9 Time resolved electroluminescence trace of a polymer LED showing singlet (closed symbols) and triplet (open symbols) emission at an applied bias of 16 V. The inset shows two representative spectra measured in a 100 ns temporal gate at the delay times indicated by arrows in the main figure. a and b mark the times in the trace at which the spectra shown in the inset were recorded. Note that the emission appears before 0 μs due to the uncertainty in the positioning of the temporal detection window (gate length 200 ns).

by superimposing the decay of the triplet signal after the voltage pulse (which is similar to the decay shown in Fig. 2.6) on the rise of the phosphorescence at the beginning of the voltage pulse. Both rise and decay overlap quite nicely proving that the triplet diffusion rate – the dominant rate for radiative triplet decay after generation of the triplets – must also be rate limiting for the onset in phosphorescence. Phosphorescence is detectable within 100 ns of application of the voltage pulse, which provides a straightforward, conservative upper estimate for the formation time of triplet excitons. Spin randomization in the precursor state would therefore have to occur on timescales substantially shorter than 100 ns to have an effect on the OLED quantum efficiency. Note that besides being limited by the diffusion of triplets through the polymer film to the palladium sites, the electroluminescence response to the voltage pulse also depends on the speed at which charge carriers can drift into the recombination zone of the OLED as well as the time required for the electric field to build up in the device, which is limited by the product of capacitance and resistance (the RC time). However, these factors should influence the build-up of the singlet and triplet channel equally. It is therefore safe to conclude that our transient electroluminescence results provide a *lower limit* for the exciton formation rate.

2.3.3
Spin Persistence in Charge Carrier Pairs Generated by an Electric Field

To investigate the possibility of spin conversion in the relevant intermediate state prior to exciton formation we resort to optical rather than electrical generation of excitations. This approach allows us to control the actual recombination time [61, 62], i.e., the time required for the conversion of a charge carrier pair into an exciton by means of an external electric field, and thus assess the magnitude of the spin-lattice relaxation time.

Figure 2.10 shows photoluminescence spectra of a polymer film sandwiched between an ITO and an aluminum electrode. As the film is only 100 nm thick, it is important to minimize quenching of excitons and the exciton intermediates – charge transfer states, polaron pairs, or radical pairs – by the electrodes. This can be achieved effectively by depositing a thin (~10 nm) layer of SiO_x between both electrodes and the polymer film. The spectra measured during application of a voltage pulse, after optical generation of the excitons by the laser pulse, show a quenching of both the singlet and the triplet in the electric field. Note that the electric field is present prior to optical generation of excitons, as sketched in the scheme in Fig. 2.7. Both fluorescence and phosphorescence are observed in the delayed luminescence due to the fact that a small number of triplet excitons are generated by optical excitation due to intersystem crossing in the excited state. The electric field suppresses the delayed recombination in both the singlet and triplet channels. As the radiative lifetime of the singlet is of order 300 ps, the delayed emission measured at 200 ns and shown in Fig. 2.10 is a consequence of delayed recombination of stored charge carrier pairs to form excitons. These carrier pairs are either generated optically upon excitation [4] or are a result of
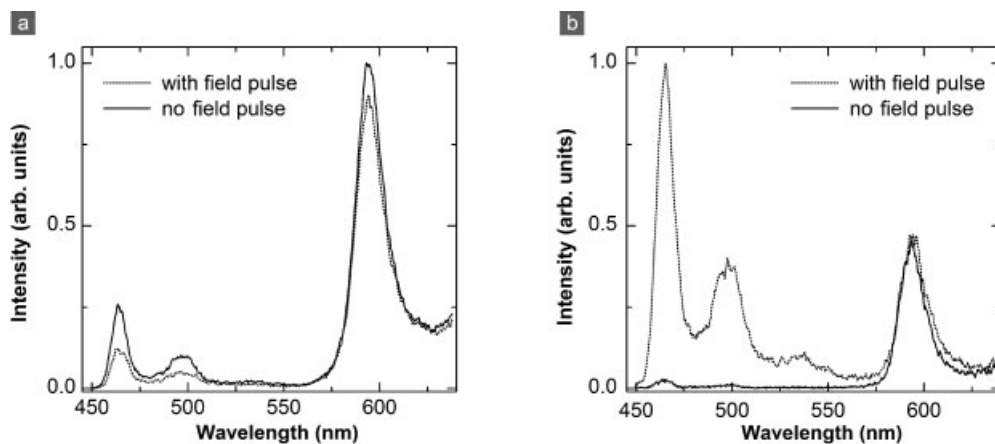
Fig. 2.10 Delayed photoluminescence spectra of a polymer film measured after excitation using gated detection, during (a) and after (b) the time window of the electric field. Both fluorescence and phosphorescence are observed in the delayed emission as a small number of triplets are photogenerated by intersystem crossing. In the time window of the voltage pulse, the field leads to a substantial suppression of the singlet emission and a small suppression of the triplet intensity. After the field window, the triplet intensity remains unchanged. The singlet intensity, in contrast, is increased by almost two orders of magnitude, as dislocated excitons can recombine again. Note that the spectra are not normalized.

field-assisted dissociation [17, 66]. There is also a possible contribution of delayed fluorescence from triplet excitons arising from triplet–triplet annihilation, but as we comment on below this is not the dominant origin of delayed fluorescence [41, 62].

The binding energy of the triplet excitons exceeds that of the singlets by over 0.7 eV, as the overall triplet energy is lowered with respect to the molecular level to level separation by the Coulombic exciton binding energy (~0.5 eV [64]) and the exchange energy. The triplet exciton is thus much less polarizable due to the covalent bonding nature of an electron and a hole. A substantially weaker field response of the triplet is therefore to be expected. However, the triplet excitons detected here are photogenerated by intersystem crossing from the singlet to the lower energy triplet manifold of the molecule. This process is not instantaneous, but clearly depends on the singlet density present. A competing channel to intersystem crossing is introduced by the field-induced quenching or dislocation of the exciton. Most of the reduction of the triplet intensity therefore arises due to the transformation of singlet excitons to charge carrier pairs and accordingly the reduction in singlet excitons available for intersystem crossing. We note that further field-induced triplet quenching could additionally occur as a consequence of interactions of triplets and meta-stable field-generated charge carrier pairs [49, 67].

The charge carrier pairs can now be stored in the electric field for tens of microseconds, i.e., orders of magnitude longer than the singlet exciton radiative lifetime. As soon as the electric field is removed, i.e., the pulse is terminated, the intermolecular charge pair can recombine again on a single molecule and form an intramolecular exciton [54, 61, 62]. Depending on the spin state of the charge carrier pair, this will lead to the generation of either a new singlet or a new triplet exciton, detectable as fluorescence or phosphorescence, respectively (see Fig. 2.3). Fig. 2.10(b) shows the photoluminescence spectra measured immediately after the voltage pulse, compared to the case of zero applied voltage. As can be seen, the triplet intensity is unchanged after the voltage pulse, irrespective of whether a bias was applied to the sample or not. In contrast, a dramatic increase by almost two orders of magnitude is observed in the singlet intensity after removal of the voltage pulse when compared to the case without a bias. The voltage pulse therefore allows us to strongly modulate the delayed emission of the singlet exciton, but not of the triplet exciton. Delayed recombination after the field pulse therefore does not occur in the triplet channel, as triplet excitons were not stored by the field. The slight quenching of the phosphorescence seen in Fig. 2.10(a) is due to reduced intersystem crossing, but not due to a conversion of triplet excitons into meta-stable charge transfer states.

Figure 2.11 summarizes the spectrally integrated delayed photoluminescence emission intensity under electric field modulation for the singlet (a) and triplet (b) channel at room temperature. The time during which the voltage pulse is applied is marked in the diagram. Note that the prompt fluorescence (cf. Fig. 2.8) is not shown in this representation, as its intensity outweighs the intensity of the delayed emission by almost two orders of magnitude. The dotted lines indicate the fluorescence and phosphorescence decay in the absence of an electric field, the solid lines the decay with an electric with an electric field pulse applied. Whereas a strong burst is observed in the singlet channel after removal of the electric field, virtually no change is seen in the triplet channel.

The fact that over 99% of the delayed recombination occurs in the singlet channel tells us two important things. Firstly, assuming that it is Coulombically bound charge carrier pairs which are stored by application of the field pulse, a spin conversion to the energetically lower lying triplet state does not take place, or else the singlet channel would be depleted with the triplet channel exhibiting a concomitant increase. Secondly, we can also exclude the possibility that the electric field pulse is able to entirely dissociate molecular excitons into completely free, uncorrelated electrons and holes. If this were the case, we would expect to arrive at a scenario comparable to the injection of entirely spin-uncorrelated free charge carriers shown in Fig. 2.5. In this case of electroluminescence (Fig. 2.5), singlet and triplet emission intensities are comparable for the recombination of free charge carriers. We can therefore conclude that during the time of exciton (or, more accurately, exciton precursor) storage of $1\,\mu s$ in this example, spin conversion is minimal. If spin-lattice relaxation were efficient, the singlet exciton precursor should relax to the lower energy state thus favoring delayed population of the triplet. This appears not to be the case. We see from this example that it is the spin-lattice relaxation time
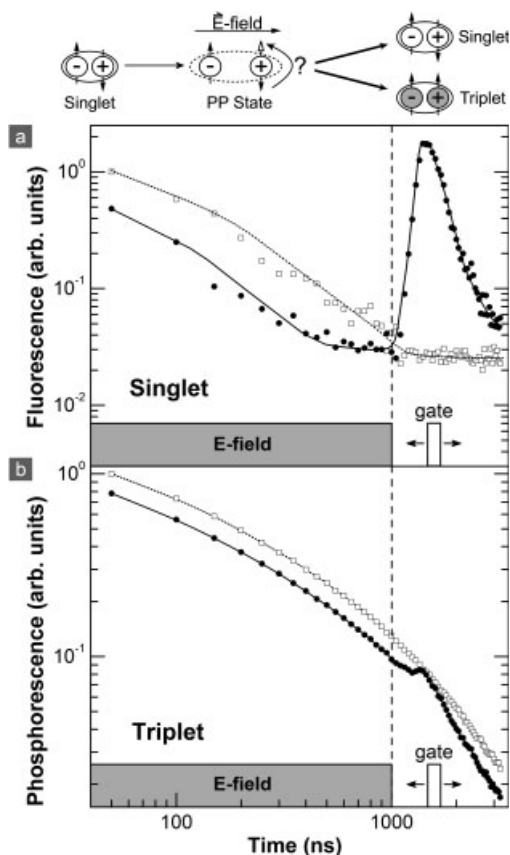
Fig. 2.11 Intensity of delayed photoluminescence emission from a polymer film under electric field modulation at room temperature, shown for the singlet (a) and triplet (b) channel. The decay in the absence of an electric field is also given (open symbols).

$1/k_{SL}$ which is relevant and not the exciton formation time $1/k_T$. Although we store the exciton precursor for over ten times the time required to form a triplet exciton ($1/k_T < 100$ ns), virtually no new triplet excitons are formed after removal of the electric field pulse. Not surprisingly, the results are independent of temperature over almost two orders of magnitude change in thermal energy [54]. This first measurement already tells us that most likely at least for the present material system under investigation as well as for structurally similar material systems, the spin-lattice relaxation rate cannot exceed the exciton formation rate, a prerequisite for high singlet-triplet ratios as discussed earlier in the text. Therefore, the ultimate quantum efficiency of an all-fluorescent PLED is limited to 25%, assuming that the intersystem crossing back transfer rate from T_1 to S_1 is small. This assumption is derived from the observation of weak spin mixing and large exchange splitting of 0.7 eV compared to the thermal energy of 0.025 eV at room temperature.
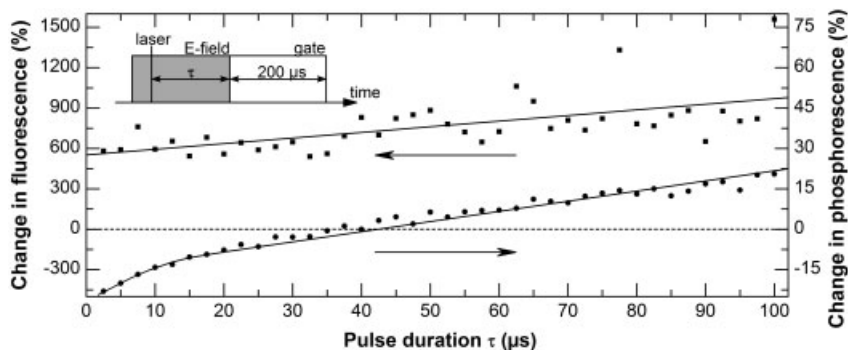
Fig. 2.12 Change in fluorescence and phosphorescence measured in a detection window of 200 μs duration immediately after turning off the electric field as a function of the electric pulse length (i.e., the storage time) at room temperature.

A small increase is observed in the triplet channel in Fig. 2.11(b) after removal of the voltage pulse. While this could be a signature of weak spin mixing, the most likely explanation is intersystem crossing of singlet excitons generated *during* the fluorescence burst. Note that this experiment basically provides a *relative* measure of perturbable singlet and triplet exciton densities which are superimposed on a background decay unaffected by the electric field (such as the neutral prompt triplet excitons). To exclude the possibility that the fact that we do not observe triplet creation in the electric field is simply a consequence of new triplets formed being masked by the residual background decay of triplets, it is important to consider the time dependence of the overshoot post field turn-off. We therefore consider the integrated decay of singlet and triplet excitons after turn-off of the voltage pulse as a function of the pulse duration. Naturally, we would expect the overall field-induced modulation of the emission to increase with increasing storage time as the background of emissive species unaffected by the field (the neutral photo-generated triplets) drops with respect to the perturbable species, i.e., the charge carrier pairs stored in the field. Note that within 100 μs the phosphorescence intensity drops by four orders of magnitude following a power law. Figure 2.12 summarizes the change in total fluorescence and phosphorescence measured in a detection window of 200 μs duration beginning immediately after the voltage pulse is switched off. Whereas the triplet modulation is of the order of a few percent and *negative* for the first 40 μs, the singlet modulation is always positive and orders of magnitude stronger. There is a weak increase in singlet and triplet modulation with storage time, as expected. We observe virtually no dependence of the modulation on temperature (300 K to 4 K), except for a tendency for the triplet modulation at room temperature to increase slightly more rapidly with storage time than at lower temperatures (not shown) [54]. This suggests that at elevated temperatures a small possibility exists to fully dissociate the charge carrier pair in the field by thermally assisted tunneling out of the mutual Coulomb well

and subsequent nongeminate recombination following spin randomization. If this mechanism does occur it is an extremely weak process. We conclude that even during 100 μs of storage of charge carrier pairs no substantial relaxation to the lower energy triplet state occurs, suggesting that spin-lattice relaxation is indeed extremely slow ($k_{SL} \ll (100 \text{ μs})^{-1}$).

In view of the strong exciton binding it appears improbable that the electric field be able to dislocate the charge carriers forming the molecular exciton over substantial distances. As mentioned above, however, the absence of a field quenching effect in single molecules shows us clearly that the field results in the formation of a meta-stable intermolecular species between different chains. The spin conservation during this process implies that the spin of the single carrier remains defined during the separation process. This can either be achieved in the presence of an external magnetic field (which provides a reference direction for the spin orientation) or by the interaction with a second particle having spin. The fact that the overall charge pair spin is maintained suggests strongly that the exchange interaction, i.e., the interactions resulting from the electron and hole that carry different spins, can have an intermolecular component (the estimated intermolecular separation for a closed film is ~4 Å [18]). It was recently proposed that polarons in LPPP can acquire intermolecular character in the solid state [68]. This observation, derived from electron spin resonance studies, is in agreement with the exceptional charge carrier mobility reported for this set of materials [69]. Intermolecular exchange may therefore be a signature of carrier delocalization between adjacent molecules.

2.3.4
Spin Persistence in Charge Carrier Pairs Generated Spontaneously

Delayed fluorescence on timescales orders of magnitude greater than the exciton lifetime is observed from polymer films even when no electric field is applied [53]. This delayed fluorescence is generally taken as a signature of charge carrier pairs formed spontaneously during or shortly after photoexcitation [4, 53, 61, 62]. As these pairs can have different spatial separations, their decay is not described by a characteristic time but rather follows a power law [62]. The closer, more strongly bound pairs decay faster than the more distant pairs. This time dependence allows us to study the field modulation of recombination of charge carrier pairs of different separations and thus of different potential levels of exchange splitting. These pairs can be thought of as being localized either on different segments of a polymer molecule or on adjacent molecules, and are effectively trapped in a local potential minimum, or else the mutual Coulombic attraction would lead to immediate recombination. Recombination occurs by tunneling through the potential well trapping the individual carrier, and leads to the formation of a molecular exciton which can then decay radiatively [61]. Application of an external bias can tilt the well confining the carrier but also modify the actual carrier wavefunction, in analogy with electric field control of the radiative rate by the quantum confined Stark effect in semiconductor nanocrystals [70]. This process is summarized in Fig. 2.13.
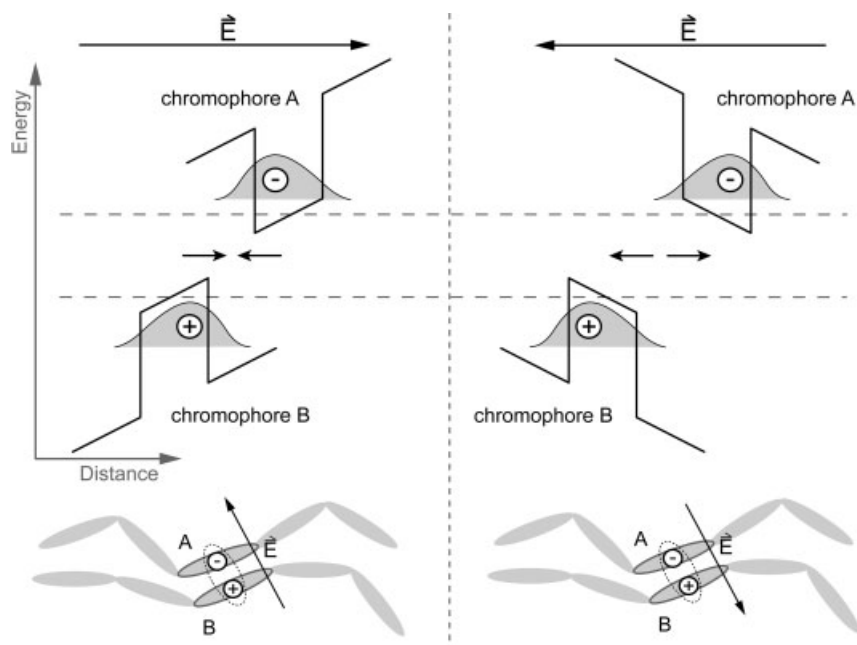
Fig. 2.13 Illustration of charge carrier pairs (indirect excitons) formed as an immediate consequence of photoexcitation. The charge carriers are trapped on different chromophores and have minimal wavefunction overlap. Delayed recombination of these pairs constitutes a contribution to the delayed emission observed from polymer films. Application of an electric field can increase and suppress delayed recombination, depending on the orientation of the pairs with respect to the applied field.

Interestingly, these optically generated meta-stable species – bound charge carrier pair precursors to exciton formation – can occur both in the singlet and in the triplet configuration, as has also previously been confirmed with electron spin resonance techniques [71]. The triplet exciton precursor – the triplet polaron pair – is of particular interest, as it is this precursor which would have to undergo a spin change to actually increase the ultimate OLED efficiency beyond the spin-statistical limit. Figure 2.14 demonstrates the presence of polarizable polaron pairs in the triplet configuration, whose recombination can be modulated by an external electric field. We show the time resolved change in phosphorescence intensity under application of an electric field pulse 1 µs after the laser pulse generated the polaron pairs optically. The phosphorescence initially shows a short increase, as some polaron pairs are pushed together in the electric field, and is quenched substantially shortly later, as the separation between polaron pairs with opposite field alignment is increased. As expected, the effect depends strongly on the magnitude of the field applied. For the three field strengths illustrated the overshoot at the onset of the field increases with the applied field, as does the magnitude of the quenching during the field pulse.
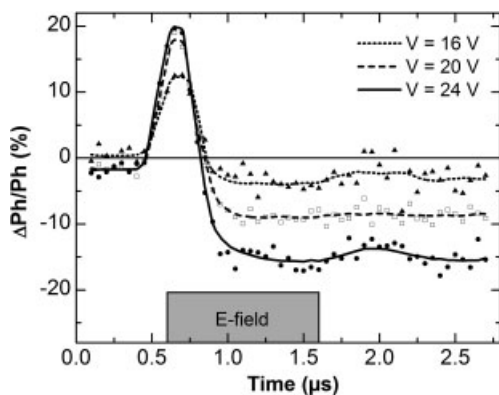
Fig. 2.14 Modulation of the phosphorescence intensity by application of an electric field pulse of different amplitudes. Turning on the field leads to an initial overshoot as charge carriers are pushed together. Both the overshoot and the subsequent quenching of the emission due to increased dislocation of the carriers increase in magnitude with increasing field strength.

Figure 2.15 shows the response of both delayed fluorescence and phosphorescence to a reverse bias pulse applied to the polymer film 1 µs after optical excitation. As in Fig. 2.14, both the phosphorescence and particularly the fluorescence initially increase under application of the field. This is because trapped charge carrier pairs of both singlet and triplet configuration can be coaxed into recombining by lowering the trapping barriers in the electric field. Subsequently, both the fluorescence and the phosphorescence decrease in intensity as the remaining trapped carriers whose dipole orientation opposes the direction of the applied field are further separated and hindered from recombining. Turning off the field leads to a brief burst in both fluorescence and phosphorescence for similar reasons as discussed above for the electrically displaced charge carrier pairs (Fig. 2.12). Naturally, the field modulation is much stronger for the singlet channel than for the triplet channel. This is a consequence of the fact that the phosphorescence arises from radiative decay of both neutral, unpolarizable triplet excitons and delayed triplet exciton formation from polarizable charge carrier pairs of triplet character. Although the electric field does not affect the neutral triplet excitons, it can modulate the recombination rate of triplet polaron pairs. As the triplet population decays by diffusion to the palladium sites in the polymer film and subsequent radiative recombination, the triplet density decreases with time following the power law discussed in Fig. 2.6. The polaron pairs, on the other hand, can be stored in the electric field for much longer times. Consequently, the overall electric field modulation amplitude of the phosphorescence increases with time as the density of polarizable triplet carrier pairs increases with respect to the density of nonpolarizable triplet excitons.
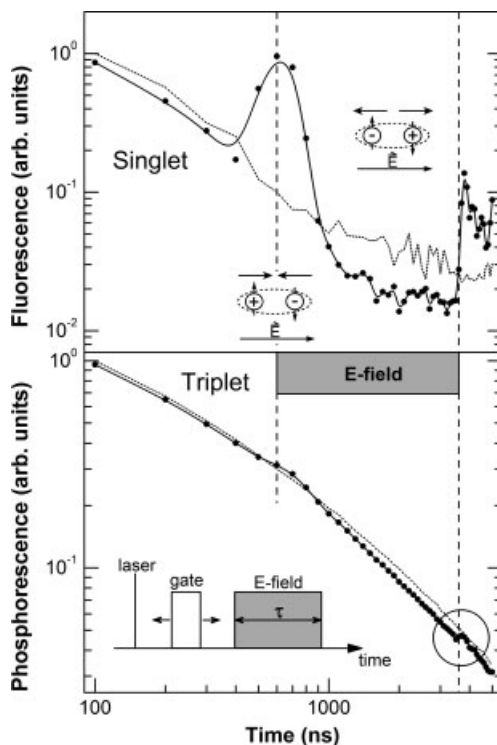
Fig. 2.15 Modulation of the delayed emission from a polymer film under application of an electric field after laser excitation at 200 K. Switching on the field leads to an initial overshoot in the emission of both singlets and triplets as charge carriers are pressed together, increasing wavefunction overlap and thus the transition probability to an emissive excitonic state. During the application of the field pulse the delayed emission intensity is reduced. After the pulse is removed, the delayed emission returns to the level observed in the absence of a field, following a small overshoot. The circle marks the region magnified in Fig. 2.16.

We note in passing that the rise in singlet emission at the onset of the voltage pulse provides conclusive evidence that triplet–triplet annihilation does not constitute the main origin of delayed fluorescence in this class of materials, which is rather controlled by microscopic charge carrier pairs. Neither singlet nor triplet excitons could exhibit a reaction in an electric field which would lead to such a rapid *increase* in delayed emission under application of an electric field. If anything, these neutral species should be quenched in a field. The highly polar charge transfer states, however, can be modified in their transition rate to the final exciton state, which gives rise to the overshoot observed. An interesting puzzle remaining is how the triplet polaron pairs are actually formed under optical excitation. Clearly, dissociation of the exciton after intersystem crossing is extremely unlikely due to the vast binding energy of the triplet. Singlet fission or annihilation effects may

play a role in the generation of these spin symmetric carrier pairs, but on the other hand appear energetically unfavorable.

Low temperature thermally stimulated luminescence measurements have previously shown that trapped polaron pairs always decay to the lowest energy state, i.e., they form a precursor for triplet rather than singlet excitons [18]. From this it was extrapolated that given sufficient thermal energy to overcome the presumed small exchange splitting, conversion of triplet to singlet exciton precursors should occur with the corresponding increase in OLED efficiency. However, the timescales involved in these prior experiments are orders of magnitude greater than those applicable to the operation of OLEDs. What the present results demonstrate is that charge carrier pairs trapped at different sites in the polymer film and hindered from recombination by an external field do not change their spin configuration, at least on the device relevant timescales. The prior thermally stimulated luminescence experiments arrived at an estimate for the exchange splitting of approx. 3 meV for the ladder-type polymer used here [18]. At 200 K (18 meV) there should therefore be more than enough thermal energy present to convert triplet polaron pairs into singlet polaron pairs, which have a much shorter lifetime and should therefore efficiently deplete the triplet polaron pair reservoir. As Fig. 2.15 shows, this is, however, not observed.

Figure 2.16 shows a blow-up of the region marked by a circle in Fig. 2.15 for different storage times τ of the polaron pairs in the electric field. The graphs display the overshoot in the phosphorescence after removal of the electric field. The longer the storage time, the stronger the overshoot. Quite the opposite would be expected if spin mixing could occur during the electric field assisted storage of
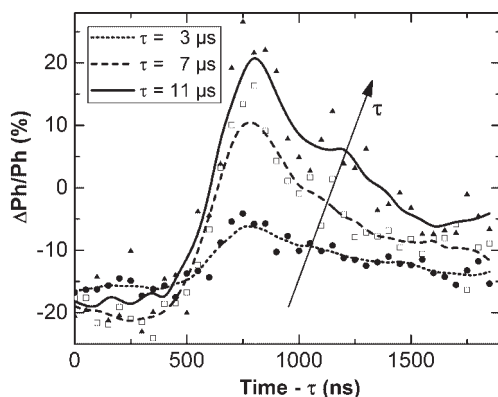
Fig. 2.16 Increase in the magnitude of the triplet emission overshoot as the pulse is removed (cf. the circled region in Fig. 2.15) for different storage times (τ as marked in Fig. 2.15) of the polaron pair. The time axis is shifted so that the axis value of 600 ns coincides with the time when the field pulse is removed in Fig. 2.15.

the exciton intermediate polaron pair. The results show that the spin configuration of the precursor state does not change during storage on timescales of µs relevant to the operation of OLEDs, and hence the triplet polaron pairs are not depleted to the benefit of singlet polaron pairs. The interpretation of the data in view of the previous model derived from the consideration of thermally stimulated luminescence [18] is that either the exchange splitting between singlet and triplet polaron pairs is much greater than previously thought [18] or spin-lattice relaxation is so weak that there is no way for the carriers constituting the precursor to exciton formation to change their spin on reasonable timescales. While we cannot distinguish between these two interpretations directly, the arguments presented above in favor of intermolecular exchange due to delocalized carrier wavefunctions can be used to support the picture of an exceptional and unexpected *intermolecular* exchange interaction in the exciton precursor state.

In this context it is also interesting to return to the magnitude of intersystem crossing. The exciton can clearly change its spin configuration in a measurable quantity within a few ns, i.e., within an order of magnitude of the radiative lifetime of the singlet, or else we would not observe optically generated triplets. Similar timescales on which the spin-orbit coupling occurs, which drives intersystem crossing, do not appear to apply to the polaron pair. We suggest that this is due to the reduced mobility of the polaron pair with respect to the singlet exciton. The polaron pair is effectively trapped and cannot migrate through the film and sample a range of Pd sites with potential fluctuations in the strength of the spin-orbit coupling.

Even if the exchange splitting were substantial in the polaron pair and this constituted the origin of the apparent spin conservation process during recombination, we would expect to see a dependence of spin conversion probability on temperature. Metal-organic phosphorescent molecules such as platinum porphyrins exhibit a striking temperature dependence of the ratio of fluorescence to phosphorescence [72]. At low temperatures, intersystem crossing, which is a purely quantum mechanical and thus temperature independent process, depletes the photoexcited singlet manifold rapidly within 50 ps [73] and gives rise to pure red emission from the triplet state. As the temperature is raised, a second narrow emission band appears in the green part of the spectrum, which is associated with emission from the singlet state. The origin of the temperature dependence of the emission, which displays an Arrhenius-type activation with a barrier corresponding to the energetic splitting between singlet and triplet (approx. 0.4 eV), lies in *reverse* ($T_1 \rightarrow S_1$!) intersystem crossing or so-called E-type delayed fluorescence. As the radiative lifetime of the singlet is much shorter than that of the triplet, even moderate thermal energy at room temperature (25 meV) can lead to substantial excitation over the exchange barrier and thus detectable singlet emission. In this case of metalorganic complexes with the strong spin-orbit coupling it is therefore indeed possible to mix singlet and triplet manifolds so that preferential emission occurs from the singlet as long as the requirement of energy conservation can be met.

Conjugated polymers, on the other hand, are typically pure hydrocarbon compounds and do not possess such an efficient spin-mixing channel through the strong spin-orbit coupling. In the absence of a spin-mixing channel thermally assisted crossing of the exchange gap cannot occur.

2.4
Summary and Outlook

We have studied the spin dependence of the final recombination step of charge carrier pairs in conjugated polymer films stabilized in an external electric field. During electrostatic storage of these pairs, conversions between the two spin manifolds of these exciton precursors appear to be highly improbable. This conclusion is further supported by the inability of strong magnetic fields of up to 8 T to induce a significant change in intensity between the singlet and triplet channels [54], in spite of a strong magnetic field effect on the fluorescence intensity [54] and the device resistance [74]. A magnetic field could either shield the hyperfine interaction in the low field limit, or else lead to a splitting of the triplet sublevels of the exciton precursor polaron pair [75]. While we were able to place an upper limit on the low field effect of spin mixing of a few percent, the absence of a systematic magnetic field dependence on the spin channels in electroluminescence at high fields demonstrates again that spin mixing within the polaron pair precursor state – in this case between the Zeeman sublevels – does not occur. In this context it is interesting to note that the Zeeman sublevels and spin mixing between them can be clearly identified spectroscopically in iridium containing small molecular complexes [76].

Recent studies of organic spin valves, diode like devices containing two spin-polarizing electrodes which only pass electrons of a given spin orientation, have shown that the spin of an electron injected from a contact into the organic semiconductor can be conserved over surprisingly long distances [6]. This single-particle spin picture should be seen in conjunction with our two-particle charge carrier pair spin picture. The absence of spin conversion in the pair state could be a signature of extremely long spin conservation times in organic semiconductors, even at room temperature. Conversion from the singlet to the triplet configuration requires conservation of both energy and angular momentum. While energy conservation can, in principle, be met by phonon emission or absorption, keeping in mind the strong degree of the electron–phonon coupling in conjugated polymers as well as the high energy (~0.2 eV) of optical phonons, spontaneous changes in angular momentum cannot occur because of the weak spin-orbit coupling. This is exactly the opposite case to inorganic semiconductor nanostructures, where the strong spin-orbit coupling can mix the spin but the absence of suitable phonons means that transitions between spin sublevels in a magnetic field are impeded because of energy conservation restrictions. Surprisingly long spin conservation times have also been observed in inorganic semiconductors, most notably in single

quantum dots coupled to a continuum of states in a bulk semiconductor [77, 78]. In this case, however, the spin persistence has been related to constraints of energy conservation due to the absence of suitable low frequency phonon modes [78]. In any case, the spin degree of freedom is an exciting parameter to use for information exchange in future generations of devices. The facility with which non-degenerate spin configurations can be read out in organic semiconductors – by considering simply the ratio between fluorescence and phosphorescence – suggests a plethora of future applications and promises to keep the field of organic electronics very lively for the coming years.

The conclusion of our studies is that for the present model material system there appears to be no suitable spin-mixing channel in the carrier recombination process and thus no route to providing preferential occupation of singlet states. Clearly, it would be beneficial to study different material systems using the same technique. Blend systems are particularly appealing for polymer-based OLEDs, and studies of photoinduced triplet absorption features have recently suggested that spin conversion can occur in meta-stable exciplex states formed at the interface between different materials [43, 50]. This could in part be due to the presence of sulfur atoms in the thiophene units of the blend structure, which give rise to the substantially stronger spin-orbit coupling because of their higher Z-value compared to carbon. Also, it is conceivable that the microscopic morphology of a polymer film strongly influences the way an exciton interacts with an electric field. Screening of the exciton by microscopic domain formation and resultant lowering of the exciton binding energy has previously been suggested in theoretical work [79]. Indeed, recent studies of the transient photocurrent and polarization anisotropy in polaron pair formation highlighted substantial differences between the model conjugated polymer systems LPPP and poly(phenylene-vinylene) (PPV) [80]. These differences were tentatively ascribed to morphological effects. Finally, a particularly intriguing aspect of the electronic structure of conjugated polymers was recently unmasked in single molecule Stark spectroscopy measurements [65]. The linear Stark effect, which is observed universally in different material systems, points toward the presence of a permanent effective dipole acting on the conjugated system. This effective dipole could introduce substantial screening effects between charge carriers constituting an exciton precursor pair. However, as such dipoles exist in different polymer systems such as LPPP and PPV, it appears safe to conclude that they cannot give rise to spin randomization by exchanging recombination partners in the precursor pair. Finally, we note that even material systems with very different properties in the ensemble exhibit near universal fluorescence signatures on the single molecule level [57]. It is therefore reasonable to assume that the intrinsic electronic structure of different material systems is actually remarkably similar, thus allowing the conclusion that the spin correlations observed in the model material system studied here actually hold for a wide variety of metal-free organic semiconductors, thereby universally limiting the achievable quantum efficiency to 25%.

References

1 M. Segal, M. A. Baldo, R. J. Holmes, S. R. Forrest, Z. G. Soos, *Phys. Rev. B* **2003**, *68*, 075211; H. Yersin, *Proc. SPIE* **2004**, *5214*, 124; H. Yersin, *Top. Curr. Chem.* **2004**, *241*, 1.

2 F. Schindler, J. Jacob, A. C. Grimsdale, U. Scherf, K. Müllen, J. M. Lupton, J. Feldmann, *Angew. Chem. Int. Ed.* **2005**, *44*, 1520.

3 E. L. Frankevich, A. A. Lymarev, I. Sokolik, F. E. Karasz, S. Blumstengel, R. H. Baughman, H. H. Hörhold, *Phys. Rev. B* **1992**, *46*, 9320.

4 M. Yan, L. J. Rothberg, F. Papadimitrakopoulos, M. E. Galvin, T. M. Miller, *Phys. Rev. Lett.* **1994**, *72*, 1104.

5 I. Žuti , J. Fabian, S. Das Sarma, *Rev. Mod. Phys.* **2004**, *76*, 323.

6 Z. H. Xiong, D. Wu, Z. V. Vardeny, J. Shi, *Nature* **2004**, *427*, 821.

7 N. C. Greenham, I. D. W. Samuel, G. R. Hayes, R. T. Phillips, Y. Kessener, S. C. Moratti, A. B. Holmes, R. H. Friend, *Chem. Phys. Lett.* **1995**, *241*, 89.

8 Y. Cao, I. D. Parker, G. Yu, C. Zhang, A. J. Heeger, *Nature* **1999**, *397*, 414.

9 J. S. Kim, P. K. H. Ho, N. C. Greenham, R. H. Friend, *J. Appl. Phys.* **2000**, *88*, 1073.

10 P. A. Hobson, S. Wedge, J. A. E. Wasey, I. Sage, W. L. Barnes, *Adv. Mater.* **2002**, *14*, 1393.

11 J. S. Wilson, A. S. Dhoot, A. Seeley, M. S. Khan, A. Köhler, R. H. Friend, *Nature* **2001**, *413*, 828.

12 M. A. Baldo, D. F. O'Brien, M. E. Thompson, S. R. Forrest, *Phys. Rev. B* **1999**, *60*, 14422.

13 M. A. Baldo, D. F. O'Brien, Y. You, A. Shoustikov, S. Sibley, M. E. Thompson, S. R. Forrest, *Nature* **1998**, *395*, 151.

14 A. S. Dhoot, N. C. Greenham, *Adv. Mater.* **2002**, *14*, 1834.

15 P. K. H. Ho, J. S. Kim, J. H. Burroughes, H. Becker, S. F. Y. Li, T. M. Brown, F. Cacialli, R. H. Friend, *Nature* **2000**, *404*, 481.

16 T. Virgili, G. Cerullo, L. Lüer, G. Lanzani, C. Gadermaier, D. D. C. Bradley, *Phys. Rev. Lett.* **2003**, *90*, 247402.

17 J. Cabanillas-Gonzalez, M. R. Antognazza, T. Virgili, G. Lanzani, C. Gadermaier, M. Sonntag, P. Strohriegl, *Phys. Rev. B* **2005**, *71*, 155207.

18 A. Kadashchuk, A. Vakhnin, I. Blonski, D. Beljonne, Z. Shuai, J. L. Brédas, V. I. Arkhipov, P. Heremans, E. V. Emelianova, H. Bässler, *Phys. Rev. Lett.* **2004**, *93*, 066803.

19 M. Wohlgenannt, K. Tandon, S. Mazumdar, S. Ramasesha, Z. V. Vardeny, *Nature* **2001**, *409*, 494.

20 M. Wohlgenannt, X. M. Jiang, Z. V. Vardeny, R. A. J. Janssen, *Phys. Rev. Lett.* **2002**, *88*, 197401.

21 W. Barford, *Phys. Rev. B* **2004**, *70*, 205204.

22 D. Beljonne, A. J. Ye, Z. Shuai, J. L. Brédas, *Adv. Funct. Mater.* **2004**, *14*, 684.

23 S. Karabunarliev, E. R. Bittner, *Phys. Rev. Lett.* **2003**, *90*, 057402.

24 K. Tandon, S. Ramasesha, S. Mazumdar, *Phys. Rev. B* **2003**, *67*, 045109.

25 Z. Shuai, D. Beljonne, R. J. Silbey, J. L. Brédas, *Phys. Rev. Lett.* **2000**, *84*, 131.

26 L. C. Lin, H. F. Meng, J. T. Shy, S. F. Horng, L. S. Yu, C. H. Chen, H. H. Liaw, C. C. Huang, K. Y. Peng, S. A. Chen, *Phys. Rev. Lett.* **2003**, *90*, 036601.

27 A. S. Dhoot, N. C. Greenham, *Phys. Rev. Lett.* **2003**, *91*, 219702.

28 R. Österbacka, *Phys. Rev. Lett.* **2003**, *91*, 219701.

29 M. Schott, *Phys. Rev. Lett.* **2004**, *92*, 059701.

30 L. C. Lin, H. F. Meng, J. T. Shy, S. F. Horng, L. S. Yu, C. H. Chen, H. H. Liaw, C. C. Huang, K. Y. Peng, S. A. Chen, *Phys. Rev. Lett.* **2003**, *91*, 219703.

31 L. C. Lin, H. F. Meng, J. T. Shy, S. F. Horng, L. S. Yu, C. H. Chen, H. H. Liaw, C. C. Huang, K. Y. Peng, S. A. Chen, *Phys. Rev. Lett.* **2004**, *92*, 059702.

32 E. L. Frankevich, *Chem. Phys.* **2004**, *297*, 315.

33 K. Becker, J. M. Lupton, J. Feldmann, S. Setayesh, A. C. Grimsdale, K. Müllen, *J. Am. Chem. Soc.* **2006**, *128*, 680.

34 J. G. Müller, M. Anni, U. Scherf, J. M. Lupton, J. Feldmann, *Phys. Rev. B* **2004**, *70*, 035205.

35 M. Wohlgenannt, Z. V. Vardeny, *J. Phys. Condens. Matter* **2003**, *15*, R83.

36 A. Köhler, J. Wilson, *Org. Electron.* **2003**, *4*, 179.

37 Ö. Mermer, G. Veeraraghavan, T. L. Francis, Y. Sheng, D. T. Nguyen, M. Wohlgenannt, A. Köhler, M. K. Al-Suti, M. S. Khan, *Phys. Rev. B* **2005**, *72*, 205202.

38 M. K. Lee, M. Segal, Z. G. Soos, J. Shinar, M. A. Baldo, *Phys. Rev. Lett.* **2005**, *94*, 137403.

39 C. G. Yang, E. Eherenfreund, Z. V. Vardeny, *Phys. Rev. Lett.* **2006**, *96*, 089701.

40 M.-K. Lee, M. Segal, Z. G. Soos, J. Shinar, M. A. Baldo, *Phys. Rev. Lett.* **2006**, *96*, 089702.

41 C. Rothe, S. M. King, A. P. Monkman, *Phys. Rev. B* **2005**, *72*, 085220.

42 A. R. Brown, K. Pichler, N. C. Greenham, D. D. C. Bradley, R. H. Friend, A. B. Holmes, *Chem. Phys. Lett.* **1993**, *210*, 61.

43 T. A. Ford, I. Avilov, D. Beljonne, N. C. Greenham, *Phys. Rev. B* **2005**, *71*, 125212.

44 S. King, C. Rothe, A. Monkman, *J. Chem. Phys.* **2004**, *121*, 10803.

45 P. F. Barbara, A. J. Gesquiere, S. J. Park, Y. J. Lee, *Acc. Chem. Res.* **2005**, *38*, 602.

46 J. G. Müller, U. Lemmer, G. Raschke, M. Anni, U. Scherf, J. M. Lupton, J. Feldmann, *Phys. Rev. Lett.* **2003**, *91*, 267403.

47 K. Becker, J. M. Lupton, *J. Am. Chem. Soc.* **2005**, *127*, 7306.

48 D. Hertel, S. Setayesh, H. G. Nothofer, U. Scherf, K. Müllen, H. Bässler, *Adv. Mater.* **2001**, *13*, 65.

49 H. H. Liao, H. F. Meng, S. F. Horng, J. T. Shy, K. Chen, C. S. Hsu, *Phys. Rev. B* **2005**, *72*, 113203.

50 T. Offermans, P. A. van Hal, S. C. J. Meskers, M. M. Koetse, R. A. J. Janssen, *Phys. Rev. B* **2005**, *72*, 045213.

51 J. M. Lupton, A. Pogantsch, T. Piok, E. J. W. List, S. Patil, U. Scherf, *Phys. Rev. Lett.* **2002**, *89*, 167401.

52 N. C. Greenham, J. Shinar, J. Partee, P. A. Lane, O. Amir, F. Lu, R. H. Friend, *Phys. Rev. B* **1996**, *53*, 13528.

53 Y. V. Romanovskii, A. Gerhard, B. Schweitzer, U. Scherf, R. I. Personov, H. Bässler, *Phys. Rev. Lett.* **2000**, *84*, 1027.

54 M. Reufer, M. J. Walter, P. G. Lagoudakis, B. Hummel, J. S. Kolb, H. G. Roskos, U. Scherf, J. M. Lupton, *Nature Mat.* **2005**, *4*, 340.

55 M. Reufer, F. Schindler, S. Patil, U. Scherf, J. M. Lupton, *Chem. Phys. Lett.* **2003**, *381*, 60.

56 M. Reufer, P. G. Lagoudakis, M. J. Walter, J. M. Lupton, J. Feldmann, U. Scherf, *Phys. Rev. B (Rapid Commun.)* **2006**, *74*, 241201. M. Reufer, J. M. Lupton, U. Scherf, *Appl. Phys. Lett.* **2006**, *89*, 141111.

57 F. Schindler, J. M. Lupton, J. Feldmann, U. Scherf, *Proc. Natl Acad. Sci. USA* **2004**, *101*, 14695.

58 M. A. Baldo, S. R. Forrest, *Phys. Rev. B* **2000**, *62*, 10958.

59 J. M. Lupton, J. Klein, *Phys. Rev. B* **2002**, *65*, 193202.

60 J. M. Lupton, J. Klein, *Chem. Phys. Lett.* **2002**, *363*, 204.

61 B. Schweitzer, V. I. Arkhipov, H. Bässler, *Chem. Phys. Lett.* **1999**, *304*, 365.

62 A. Gerhard, H. Bässler, *J. Chem. Phys.* **2002**, *117*, 7350.

63 R. Kersting, U. Lemmer, M. Deussen, H. J. Bakker, R. F. Mahrt, H. Kurz, V. I. Arkhipov, H. Bässler, E. O. Göbel, *Phys. Rev. Lett.* **1994**, *73*, 1440; V. Gulbinas, Y. Zaushitsyn, V. Sundström, D. Hertel, H. Bässler, A. Yartsev, *Phys. Rev. Lett.* **2002**, *89*, 107401.

64 S. F. Alvarado, P. F. Seidler, D. G. Lidzey, D. D. C. Bradley, *Phys. Rev. Lett.* **1998**, *81*, 001082.

65 F. Schindler, J. M. Lupton, J. Müller, J. Feldmann, U. Scherf, *Nature Mat.* **2006**, *5*, 141.

66 V. I. Arkhipov, H. Bässler, *Phys. Stat. Sol. A* **2004**, *201*, 1152.

67 J. Kalinowski, W. Stampor, J. Mezyk, M. Cocchi, D. Virgili, V. Fattori, P. Di Marco, *Phys. Rev. B* **2002**, *66*, 235321.

68 M. Wohlgenannt, X. M. Jiang, Z. V. Vardeny, *Phys. Rev. B* **2004**, *69*, 241204(R).

69 D. Hertel, U. Scherf, H. Bässler, *Adv. Mater.* **1998**, *10*, 1119.

70 J. Müller, J. M. Lupton, P. G. Lagoudakis, F. Schindler, R. Koeppe,

A. L. Rogach, J. Feldmann, D. V. Talapin, H. Weller, *Nano Lett.* **2005**, *5*, 2044.

71 V. Dyakonov, G. Rösler, M. Schwoerer, E. L. Frankevich, *Phys. Rev. B* **1997**, *56*, 3852.

72 J. Stehr, J. M. Lupton, M. Reufer, G. Raschke, T. A. Klar, J. Feldmann, *Adv. Mater.* **2004**, *16*, 2170.

73 H. Yersin, D. Donges, *Top. Curr. Chem.* **2001**, *214*, 81.

74 M. Wohlgenannt, Ö. Mermer, *Phys. Rev. B* **2005**, *71*, 165111.

75 J. Kalinowski, M. Cocchi, D. Virgili, P. Di Marco, V. Fattori, *Chem. Phys. Lett.* **2003**, *380*, 710.

76 H. Yersin, J. Strasser, *Coord. Chem. Rev.* **2000**, *208*, 331.

77 J. M. Smith, P. A. Dalgarno, R. J. Warburton, A. O. Govorov, K. Karrai, B. D. Gerardot, P. M. Petroff, *Phys. Rev. Lett.* **2005**, *94*, 197402.

78 M. Kroutvar, Y. Ducommun, D. Heiss, M. Bichler, D. Schuh, G. Abstreiter, J. J. Finley, *Nature* **2004**, *432*, 81.

79 A. Ruini, M. J. Caldas, G. Bussi, E. Molinari, *Phys. Rev. Lett.* **2002**, *88*, 206403.

80 J. G. Müller, J. M. Lupton, J. Feldmann, U. Lemmer, M. C. Scharber, N. S. Sariciftci, C. J. Brabec, U. Scherf, *Phys. Rev. B* **2005**, *72*, 195208.

3

Cyclometallated Organoiridium Complexes as Emitters in Electrophosphorescent Devices

Peter I. Djurovich and Mark E. Thompson

A brief overview is presented on cyclometallated iridium complexes that are used as phosphorescent dopants in organic light-emitting devices (OLEDs). Comparisons between devices made using either Pt(octaethylporphyrin) or Ir(phenylpyridyl)₃ as dopants are used to illustrate some parameters needed for optimal performance of electrophosphorescent OLEDs. The molecular properties responsible for the high luminescent efficiency of the Ir complexes are then described. Interactions between the triplet ligand state and the singlet and triplet metal-to-land charge transfer states are responsible for photophysical characteristics of the complexes. Examples are given of various ligand combinations used to control the phosphorescent energy and efficiency. This knowledge enables one to systematically tune the emission colors of these complexes from the near-UV to the near-infrared spectral regions.

3.1
Organic Light-Emitting Devices

The future holds tremendous opportunity for the low cost and high performance offered by organic LEDs. The term organic light-emitting device (OLED) refers to any light-emitting diode that is composed of either molecular or polymeric materials. Full-color displays that use OLEDs may eventually replace liquid-crystal displays (LCDs) in a range of mobile applications, ranging from cellular phones to laptop computers. The low power dissipation and high brightness of OLEDs make them ideal for such portable applications. OLED displays can be deposited on flexible plastic or metal foils, eliminating the fragile and heavy glass substrates used in LCDs and other flat panel displays. Moreover, OLED displays emit light without the pronounced directionality inherent in LCD viewing, all with efficiencies significantly higher than typical LCD panels. It is possible that portable and lightweight roll-up OLED displays will someday cover our walls. Another important application for OLEDs is in illumination. The high efficiencies and excellent color qualities for white OLEDs make them promising candidates for replacing conventional fluorescent and incandescent light sources.

The basic mechanism of electroluminescence involves carrier recombination, leading to formation of an electron–hole pair (exciton), which radiatively relaxes to give the observed electroluminescence. OLEDs are composed of distinct carrier transporting and emitting regions within the device, sandwiched between the anode and cathode. The exciton is formed in the emissive region of the device and becomes localized on a single molecule. A more detailed description of the process is given below; however, the mechanism as described is sufficient to illustrate the fundamental limitation of all OLEDs studied prior to the late 1990s. The hole and electron are odd electron species and thus have a spin of +1/2 or –1/2. The exciton formed by recombination of these two odd electron species can have either a singlet or triplet configuration. Simple spin statistics predicts that the ratio of singlet to triplet excitons formed in this process is 1 : 3. OLEDs studied prior to 1997 did not efficiently utilize the triplet excitons formed in this process, leading to an inherent efficiency limitation, since triplet excitons in molecular or polymeric materials are typically not emissive. Heavy metal containing phosphors (i.e., Pt and Ir complexes) were incorporated into OLEDs in the late 1990s, which efficiently harvest both singlet and triplet excitons, leading to high electroluminescence efficiencies. The development and study of these Ir- and Pt-based phosphors is the principal topic discussed in this chapter.

3.2
Phosphorescent Materials as Emitters in OLEDs

The choice of the best emitter for effective triplet harvesting in OLEDs is a critical one. Some of the earliest approaches used to exploit the triplet excitons formed in OLEDs involved either lanthanide coordination complexes [1–7] or phosphorescence from organic compounds (benzophenone [8, 9] and chrysene [10]) at low temperatures. These classes of dopant material provided limited success in triplet harvesting. While they all phosphoresce, these compounds have very long radiative lifetimes (milliseconds for lanthanide complexes and seconds for organic materials) that allow the excited state to decay from competing nonradiative processes. Moreover, the long radiative lifetimes for the lanthanide complexes and organic compounds are not well matched to the electrical characteristics of OLEDs. The time it takes for the device carrier injection, conduction, and recombination to come to steady state, such that the rate of formation of excitons within the device reaches equilibrium, is the RC time constant. Typically, OLEDs have RC time constants of 200–500 ns. While this time interval can be adjusted somewhat by device design, the value will stay in the range of hundreds of nanoseconds. The result is that phosphorescent dopants with long lifetimes will be promoted into their excited states orders of magnitude faster than they can relax [11–13]. In the meantime, the OLED will continue to generate triplet excitons, which will not be effectively trapped by the excited dopant. The net results is that these dopants are inefficient at trapping triplet excitons and do not markedly increase the OLED efficiency over the level achievable with fluorescence dopants. Only in the best
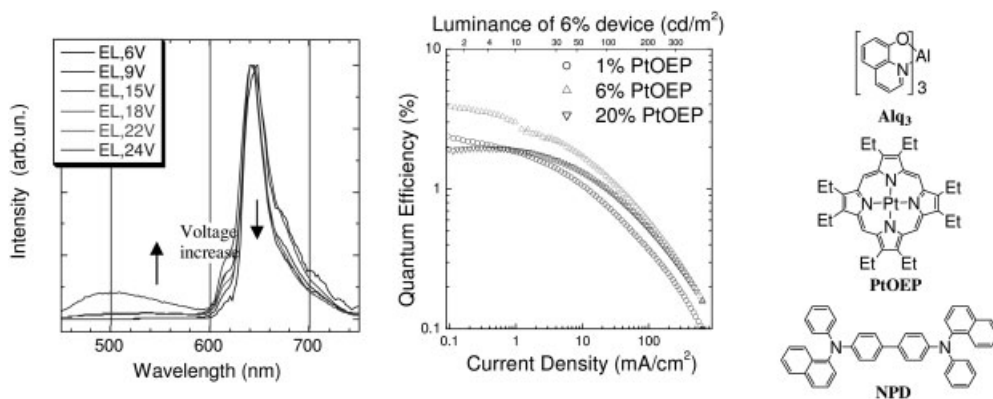
Fig. 3.1 Electroluminescence (EL) spectra of OLED with
PtOEP dopant at various potentials (left) and current–
luminance-efficiency curves with different doping levels
(center), and chemical structures of materials in the OLED.
The device structure used here was
ITO/NPD/Alq$_3$-PtOEP/Alq$_3$/Mg-Ag.

cases (lanthanide complexes) are good efficiencies achieved [14–16], while in other cases no light output is observed at room temperature (organic phosphors) [8–10].

In order to efficiently utilize the triplet excitons formed in the electroluminescent process, it is important to use phosphorescent dopants which have comparatively short radiative lifetimes and high luminance efficiencies. The first triplet emitter satisfying these criteria to be incorporated into an OLED was platinum octaethylporphyrin (PtOEP) [17]. A characteristic electroluminescence (EL) spectrum of a PtOEP-based OLED is shown in Fig. 3.1. A strong spin–orbit coupling by the central Pt atom leads to fast intersystem crossing (isc) and efficient phosphorescence at room temperature. The photoluminescent (PL) quantum yield of PtOEP is 0.5 at room temperature in both fluid solution and in a rigid, polystyrene matrix, and is >0.9 at 77 K in a frozen glass. The measured emission lifetimes at room temperature and 77 K are 90 and 131 μs, respectively [18, 19]. The high isc rate of PtOEP also provides an added benefit since any singlet exciton trapped by the dopant will be converted rapidly to a triplet, thus giving rise to only one type of emission, i.e., phosphorescence. Concurrent luminescence from both singlet and triplet excitons in the device would lead to significant line broadening and unsaturated emission.

The first OLEDs to be prepared with a PtOEP emitter utilized a two-component emissive layer within the OLED, composed of PtOEP doped into Alq$_3$ (Alq$_3$ = aluminum-tris-8-hydroxyquinolate) [17]. The optimal doping level identified in this study was 6% and gave an external quantum efficiency of 4% at low current density (Fig. 3.1). In order to evaluate the significance of the external quantum efficiencies (EQE = photon/electron) of PtOEP-based devices, it is important to

understand the optical properties of a common OLED. The EQE represents only a small fraction of the light produced within the OLED structure [20–22]. The majority of the light produced by the OLED is not emitted through the front face of the OLED, but is waveguided through the substrate or lost to absorption by the electrodes and other organic materials. Thus, the internal efficiencies of these PtOEP-based devices are actually three to five times higher than the measured external values. Therefore, PtOEP devices with a CBP host have internal efficiencies of 30%, and those with an Alq$_3$ host have internal efficiencies of over 20%. The luminance efficiencies determined for PtOEP doped into each of these host materials shows that these internal efficiencies are close to the theoretical limits, i.e., >90% of the excitons are being trapped at the dopant, and the EL efficiency is only limited by the PL efficiency of PtOEP [17].

Several platinum porphyrins other than PtOEP have also been used as phosphors in OLEDs [11, 23–27]. The basic electronic structures of these porphyrin derivatives are very similar to those of PtOEP, and the OLED properties for devices fabricated with these dopants are similar to those of the PtOEP-based devices.

3.3
Organometallic Complexes as Phosphorescent Emitters in OLEDs

Although PtOEP was the first triplet emitting complex to demonstrate high efficiency in OLEDs, Pt porphyrin-type dopants have several limitations. The luminescent color of PtOEP is deep red, and the emission energy cannot be shifted to higher values through synthetic modification without a loss in luminance efficiency. A more serious drawback, however, is the long phosphorescent lifetime of PtOEP. The long triplet lifetime of PtOEP leads to a significant roll-off in the OLED efficiency as the device current is increased. This phenomenon is illustrated for three different doping levels of PtOEP (1, 6 and 20%) in Fig. 3.1 (right). The 6% doped device is the most efficient, with an external quantum efficiency of 4% at a current density of 0.1 mA/cm^2, and drops to <2% at a current of 10 mA/cm^2. Note that all three devices show the same trend of decreasing quantum efficiencies with increasing current. The principal origin of this efficiency roll-off is a process well documented for triplet excitons, i.e., triplet–triplet (T–T) annihilation [28]. In the T–T annihilation process, two molecules in the triplet state interact, forming a singlet exciton and a ground state molecule, $T_1 + T_1 \rightarrow S_1 + S_0 \rightarrow T_1 + S_0$. The S_1 state of PtOEP rapidly intersystem crosses to the triplet; the net result is the loss of one triplet exciton. Thus, T–T annihilation is a second-order quenching process, expected to be enhanced as the number density of triplets is increased, which occurs as the current density is increased [13]. The relatively long radiative lifetime of PtOEP enables the T–T annihilation process to become competitive with radiative decay, even at moderate current densities. Additional nonradiative decay can occur from a triplet quenching by charge carriers (polarons) in the emissive layer [29, 30].
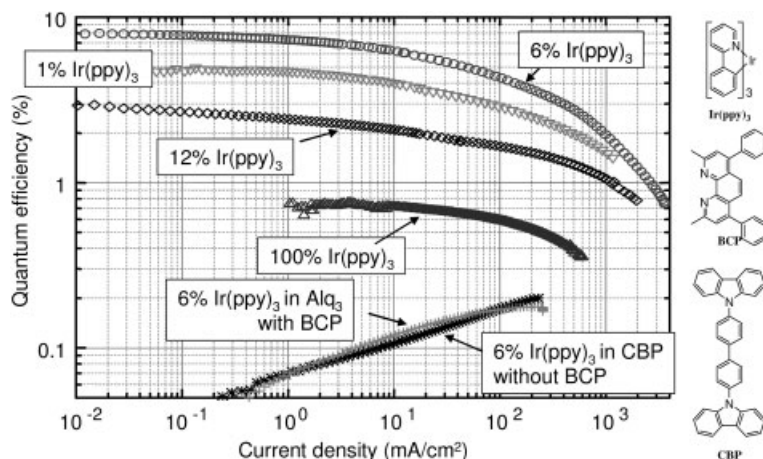
Fig. 3.2 Current-efficiency curves for various OLED structures using Ir(ppy)₃ as a dopant. The chemical structures of the materials used in the device are shown on the right.
The device structure used here was
ITO/NPD/CBP-Ir(ppy)₃/BCP/Alq₃/Mg-Ag.

The solution to the problem of these second-order quenching processes is to increase the radiative decay rate of the phosphorescent dopant, such that the triplet exciton relaxes before coming into contact with another exciton or polaron, thereby decreasing the likelihood that the excitons will undergo annihilation. An increase in the radiative rate will give an added benefit by increasing the luminescent efficiency, assuming a constant rate of nonradiative decay rate. The first example of a phosphorescent dopant with a comparatively short radiative lifetime and high luminance efficiency used in OLEDs was a cyclometallated Ir complex, *facial*-tris(2-phenylpyridinato,N,C$^{2'}$)iridium(III), *fac*-Ir(ppy)₃, see Fig. 3.2. This compound, first reported in 1985 [31], has a green emission (λ_{max} = 520 nm, triplet energy (E_T) = 2.48 eV) and a short radiative lifetime (τ_{rad} = 5 µs) in fluid solution at room temperature. The radiative decay rate is nearly two orders of magnitude larger than that of PtOEP, while the PL efficiency is similar. Recent values for the PL efficiency of *fac*-Ir(ppy)₃ have been shown to be higher than the initially reported estimates. A PL efficiency of 0.73 has been reported in toluene solution for a thoroughly degassed sample [32], and values of 0.97 were reported for samples doped into thin films at room temperature [33]. Furthermore, it has also been shown that the emission lifetime does not markedly increase upon cooling from room temperature to 100 K, consistent with the high luminescent efficiency. The first OLEDs that incorporated this Ir dopant at an optimal doping level of 6% gave external efficiencies close to 9% (internal efficiency >40%) [34], see Fig. 3.2. The roll-off in efficiency at high current densities is very low when compared to the PtOEP-based devices, as would be expected from the short radiative lifetime of Ir(ppy)₃.

When the CBP host material of the Ir(ppy)$_3$-based OLED was replaced with an electron transporting triazole host material, TAZ, the external EL efficiency increased to >15%, corresponding to an internal efficiency of >75% [35]. The improved efficiency for the TAZ-doped device is due to an increase in the host triplet energy, leading to a lower level of dopant emission quenching by the host, as observed for PtOEP-based devices (comparing Alq$_3$- and CBP-based devices) [36]. The highest efficiencies for PtOEP-doped OLEDs are achieved when the host material has a triplet energy (E_T) that is significantly higher than that of the PtOEP triplet (650 nm, $E_T = 1.91$ eV). For example, when 4,4′-di(*N*-carbazolyl)biphenyl (CBP, $E_T = 2.60$ eV) [37] is used as the host matrix for PtOEP, the EQE of the device is near 6% [36]. If the host material has a triplet energy close to that of PtOEP, such as Alq$_3$ ($E_T = 1.90$ eV) [38, 39], exciton trapping by the dopant is ineffective and the device efficiency declines to ca. 4% [36]. Similarly, devices made with host materials that also have low triplet energies, such as conjugated polymers [40, 41], lead to low EL efficiencies, often markedly less than 3% [42–44]. By optimizing the host material and device architecture (see below), OLEDs incorporating PtOEP dopants have been reported with external efficiencies as high as 9% [45].

While having a host material with a triplet energy markedly higher than the dopant is clearly beneficial, the foregoing discussion would suggest that it is required. In contrast, it is possible to achieve a reasonably high EL efficiency for a device where the dopant triplet energy is higher than the host matrix. An OLED prepared with a luminescent layer composed of a blue phosphorescent dopant *bis*(4,6-di-fluorophenyl)-pyridinato-N,C-2′)iridium(III) picolinate (FIrpic) ($\lambda_{em} = 472$ nm, $E_T = 2.6$ eV) doped into CBP gives an EQE of >5% [46]. The reason that this device emits efficiently is the disparate emission lifetimes of the triplet states of the dopant and host, i.e., 1.6 μs and 1–10 s, respectively. Although the exciton resides predominantly on the host matrix, the host triplet efficiently decays through thermal population of the dopant prior to unimolecular radiative or non-radiative decay.

3.4
Confining Triplet Excitons and Carriers in Phosphor-Doped OLEDs

Phosphorescent dopants can significantly enhance the quantum efficiencies of OLEDs; however, the devices require more complex architectures than those using fluorescence dopants. Singlet excitons have short diffusion lengths, on the order of 10–100 Å, whereas triplet states can readily diffuse >1000 Å due to their long exciton lifetimes [17, 36]. Thus, it is essential to use device configurations that confine the excitons within the luminescent layer. Triplet exciton confinement in a three-layer, double heterostructure device (anode/HTL/EML/ETL/cathode; HTL=hole transporting layer, EML=emitting layer, and ETL=electron transporting layer) is possible if the HTL and ETL have higher optical energy gaps than the phosphor, but this is not always achieved with common OLED materials. A good example was seen in devices made with PtOEP doped into CBP [36]. A single

heterostructure device (ITO/NPD/CBP:PtOEP/Alq$_3$/Mg-Ag) gave an external efficiency of 4.2%. Although it is energetically unfavorable for the PtOEP excitons to diffuse into the adjacent HTL (NPD, $E_T = 2.55$ eV) [47], that is not the case for diffusion into the ETL, where the excitons on the dopant can be quenched by energy transfer to Alq$_3$. A simple solution to this problem of exciton leakage involves inserting a material with a high triplet energy, such as bathocuproine (BCP, $E_T = 2.5$ eV) [37] between the doped CBP and the Alq$_3$ electron transporting layers (i.e., anode/NPD/CBP:PtOEP/BCP/Alq$_3$/cathode), Fig. 3.2 [36]. The added blocking layer gives a marked improvement in device performance, increasing the external efficiency to 5.6% [36]. Note that the BCP layer is also effective at blocking the migration of holes into the Alq$_3$ layer, an added benefit derived from the deep HOMO level of BCP (6.5 eV) [48]. Thus, the BCP acts as a combined hole/exciton blocking layer. An energy level diagram illustrating the relative energies of the transport, host, dopant, and blocking materials is shown in Fig. 3.3.

To act as an efficient hole blocking material, a compound must have a HOMO level with an ionization potential greater than that of both the dopant and host materials, as well as a triplet energy high enough to efficiently prevent triplet excitons from migrating out of the luminescent layer. Thus, while these materials are commonly referred to as hole blocking layers (HBLs), they must block excitons as well. In addition to having proper HOMO and triplet energies, a good HBL must have a LUMO energy similar to that of the EML materials, in order to facilitate the injection of electrons into the EML, as illustrated in Fig. 3.3. The two most common hole blocking materials in phosphorescent OLEDs are BCP [34, 35, 49, 50] and BAlq (4-biphenyloxolato aluminum(III)*bis*(2-methyl- 8-quinolinato)4-phenylphenolate) [46, 51, 52].

The need for exciton and hole blocking layers is also seen in Ir(ppy)$_3$-based OLEDs. The ordering of triplet energies for the materials is CBP > NPD > BCP > Ir(ppy)$_3$ > Alq$_3$. The triplet excitons on Ir(ppy)$_3$ will not diffuse into NPD layer, but can readily transfer into the Alq$_3$ layer if no BCP buffer layer is present. The device discussed above had a structure of anode/NPD/CBP:Ir(ppy)$_3$/BCP/Alq$_3$/cathode and gave an EQE of 9% [34]. When the BCP layer was omitted, the
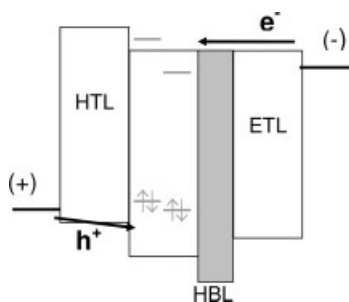
Fig. 3.3 Schematic energy level diagram for a CBP based OLED heterostructure (*i.e.* anode/NPD/doped CBP/BCP/Alq$_3$/ cathode). Ir(ppy)$_3$ (left) and PtOEP (right) energy levels are illustrated with horizontal lines.
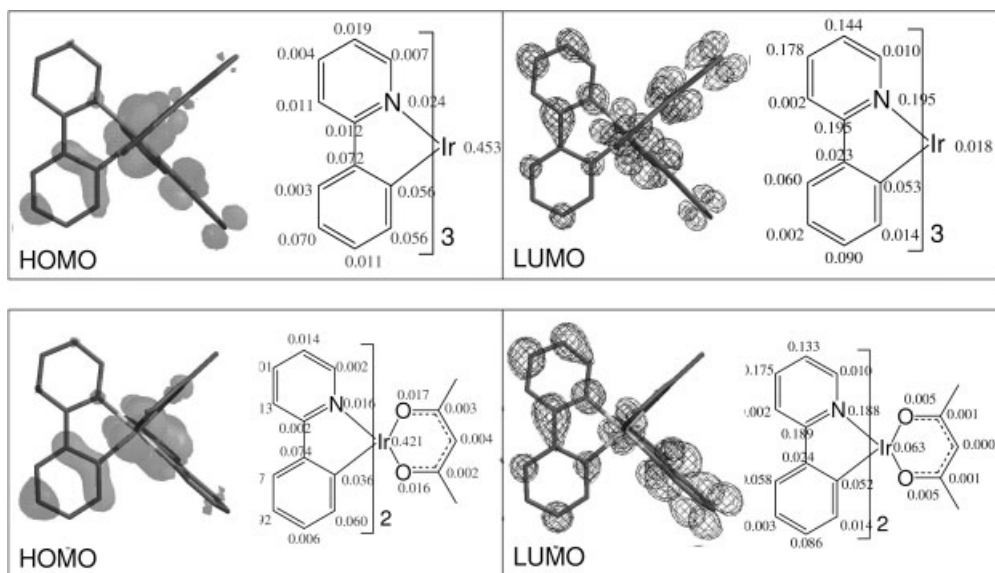
Fig. 3.4 HOMO and LUMO orbitals for Ir(ppy)$_3$ (top) and (ppy)$_2$Ir(acac) (bottom). The atomic contribution to each MO is shown on the right of the MO plot.

device efficiency dropped to 0.2%, see Fig. 3.2. The explanation given earlier for using a BCP blocking layer is that both holes and excitons must be confined within the emissive layer. While the energetic argument for exciton confinement is clear, the issue of hole blocking is less obvious. The HOMO levels of all of the materials are illustrated schematically in Fig. 3.4 for both Ir(ppy)$_3$- and PtOEP-based devices. The HOMO level for Ir(ppy)$_3$ lies above both CBP and Alq$_3$, and as such is expected to be an efficient hole trap. Thus, exciton blocking is more important than hole blocking in these Ir(ppy)$_3$-based devices.

The ability of Ir(ppy)$_3$ to act as a hole trap implies that excitons are generated during electroluminescence by direct hole–electron recombination on the dopant. In this case, an exciton is formed from a hole on the Ir dopant recombining with an electron on the CBP host (or an adjacent dopant). The triplet exciton is not transferred from the host, but formed directly on the dopant. This mechanism has a significant advantage over recombination on the host material and subsequent energy transfer to the dopant, since inefficient energy transfer from the host can be a potential loss channel [53]. The process of direct recombination by hole trapping at the dopant, can be equally applied for electron trapping at the dopant as well. A similar carrier recombination process involving a hole in the host or adjacent dopant is observed for many blue emissive organometallic phosphor-doped devices, as discussed below. In nearly all cases, direct recombination of the carriers at the dopant contributes to the high efficiencies observed for OLEDs that use phosphorescent dopants.

While the discussion thus far has focused on the need to control (prevent) hole and exciton diffusion from the emissive layer to the ETL, the same issues are relevant at the interface between the HTL and the emissive layer. If the LUMO energy of the HTL material is lower than that of the emissive layer, or the triplet energy is too low, an electron/exciton blocking layer (EBL) may be needed to prevent carrier and exciton loss at that interface. The triplet energy of the most common HTL in small molecule OLEDs, i.e., NPD, is high enough that green emissive devices do not require an electron/exciton blocking layer. However, for many blue and near-UV emitting OLEDs (*vide infra*), electron blocking layers are needed to eliminate HTL quenching of the EML and emission. An efficient electron blocking material must have a LUMO energy level and triplet energy well above those of the EML and a HOMO level close to that of the HTL.

3.5
Cyclometallated Complexes for OLEDs

3.5.1
Synthesis of Cyclometallated Ir Complexes

The successful application of $Ir(ppy)_3$ as a phosphorescent dopant has led to number of synthetic modifications of the parent complex, as well as elaboration to other metals and significantly altered organic ligands. Several of these Ir complexes will be discussed below; however, a detailed discussion of the synthetic strategies used to prepare these complexes is not given here, but the reader can find this information documented elsewhere [54].

The synthetic methods used to prepare most of these Ir complexes are shown in Scheme 3.1. A μ-dichloro bridged dimer complex with *bis*-cyclometallated Ir centers can be readily prepared from a reaction of the ligand precursor and
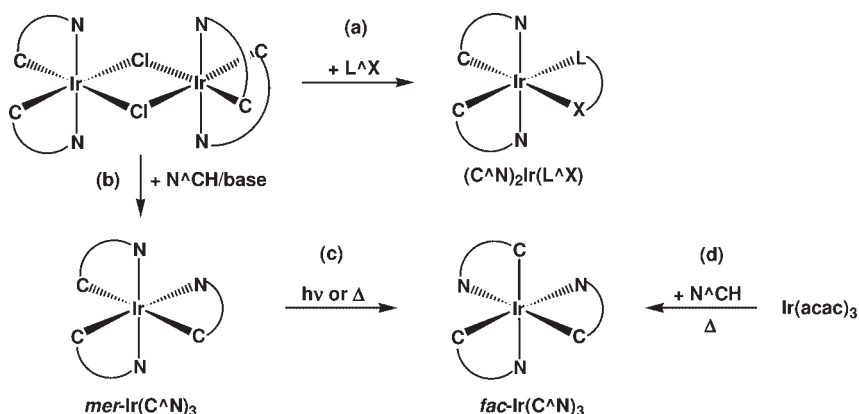
Scheme 3.1

IrCl$_3 \cdot x$H$_2$O [55, 56]. The cyclometallating ligands are illustrated by arcs, terminated with C and N atoms. The "C" atom represents an anionic moiety, such as phenyl, and the "N" atom a neutral group, such as pyridyl. Such cyclometallating ligands will be abbreviated as C^N hereafter. The chloro ligands can be subsequently replaced with a different L^X chelate (path a) which leads to a complex with a *trans-N,N* configuration of the C^N ligands. L^X ligands are chelating ligands such as β–diketonates, salicylanilides, pyrazolylborates, etc. Alternatively, a third C^N ligand can be added to form a tris-cyclometallated complex (path b). Through a careful control of reaction conditions is possible to obtain nearly pure samples of the meridional isomers of tris-cyclometallates of Ir(III), including both homoleptic (single type of C^N ligand) [57, 58] and heteroleptic tris-chelates [59–62]. Several of the isolated samples of *mer*-Ir(*C^N*)$_3$ complexes can be converted to facial forms in solution either by thermal or photochemical means (path c), indicating that the meridional isomers are the kinetically favored products. The lower thermodynamic stabilities of the meridional isomers are likely related to structural features of these complexes, i.e., the meridional configuration place strongly trans influencing aryl groups opposite each other, whereas all three aryl groups are opposite pyridyl or other neutral donor groups in the facial complexes. For some C^N ligands, typically ppy and its derivatives, the facial isomer can also be prepared directly by a thermal reaction between the ligand precursor and Ir(acac)$_3$ (acac = acetylacetonate) (path d) [63].

3.5.2
Excited States in Cyclometallated Complexes

Several research groups have used high-resolution spectroscopy to study the excited state properties of cyclometallated transition metal complexes [64–68]. This work has established that luminescence from these complexes originates from a lowest excited state that is best described as a ligand centered triplet (^{3}LC) with singlet and triplet metal-to-ligand-charge-transfer (^{1,3}MLCT) character mixed in through the spin–orbit coupling [69–71]. A schematic representation of the energy level mixing in 4d^6 and 5d^6 complexes is shown in Scheme 3.2 [65, 69].
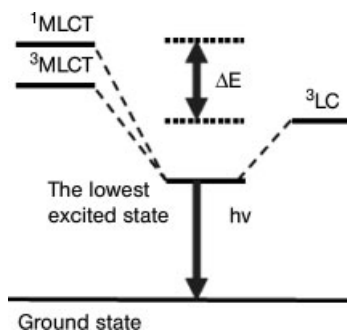
Scheme 3.2

While both ^{1}MLCT and ^{3}MLCT states are mixed with ^{3}LC states in the emissive excited state, the high oscillator strength of the ^{1}MLCT state is what provides the greatest change on the photophysical properties of the complexes. It is this ^{1}MLCT component in the excited state that gives these materials their desirable properties of high phosphorescence efficiency and comparatively short excited state lifetime. The mixing of ^{1}MLCT and ^{3}LC states can be treated by application of first-order perturbation theory [72]. The following formula is used to approximate the lowest energy excited state (Eq. (3.1)):

$$\Psi_{T_1} = \sqrt{1 - \alpha^2}\,|\,^3LC\rangle + \alpha\,|\,^1MLCT\rangle \tag{3.1}$$

where Ψ_{T_1} is the wavefunction of the lowest excited state and α is a coefficient that gives an estimate of the degree of singlet character mixed into the unperturbed triplet state (^{3}LC) [69]. The value of α can be approximated with the formula

$$\alpha = \frac{\langle\,^3LC|H_{SO}|\,^1MLCT\rangle}{\Delta E} \tag{3.2}$$

where $\langle\,^3LC|H_{so}|\,^1MLCT\rangle$ is the spin–orbital coupling matrix element, characterizing the strength of spin–orbital coupling between ^{3}LC and ^{1}MLCT, and ΔE is the energy difference between the ^{3}LC and ^{1}MLCT transitions [69]. Note that the value of α in Eq. (3.2) also includes contributions from spin–orbit coupling between the ^{1}MLCT and ^{3}MLCT states, and between the ^{3}MLCT and ^{3}LC states [73–75]. Equations (3.1) and (3.2) have been used to correlate α values with the luminescent properties of diimine and cyclometalated Rh(III) and Ir(III) complexes [64]. The mixing of ^{1}MLCT character into what is principally a ^{3}LC state has dramatic effects on the optical properties of those complexes [68, 69]. The oscillator strength and the consequent radiative decay rate of the S_0–T_1 transition in luminescent metal complexes are significantly increased when a small amount of ^{1}MLCT character is mixed into the lowest excited state. Consequently, a large decrease in the luminescence lifetimes and concomitant increase in phosphorescence efficiency occurs [69]. For example, Güdel and coworkers have estimated that the strongly luminescent complexes $[(ppy)_2Ir(bpy)]^+$ (bpy = 2,2′-bipyridine) and $[(2-thienylpyridyl)_2Ir(bpy)]^+$ have α values of 0.085 and 0.053, respectively [69]. Other phosphorescent metal complexes have smaller α values, such as $(ppy)Re(CO)_4$ (0.017) and $[(ppy)_2Rh(bpy)]^+$ (0.016) [69]. Considering the comparatively low values of α for these complexes, the excited states are still essentially triplets, even though they have singlet character mixed in. Strong spin–orbit coupling in any metal complex with a heavy atom such as Os, Ir, Pt, etc. will lead to α values sufficiently large to induce efficient intersystem crossing to the triplet manifold. The strong σ-donation from C$^-$ in a formally anionic cyclometallating ligand also stabilizes the ^{1}MLCT state and decreases the energy separation to the ^{3}LC state. This leads to a smaller ΔE term in the denominator in Eq. (3.2) that further increases the value of α. Therefore, iridium complexes with ligands cyclometallated onto heavy atoms are ideally suited to serve as phosphorescent dopants in OLEDs.

The foregoing discussion considered the lowest energy excited state for the cyclometallated complexes as being constructed from only two orbitals, ^{1}MLCT and ^{3}LC. This is a gross over simplification since the excited state is composed of multiple singlet and triplet states. A recent time-dependent density functional theory (TDDFT) study of Ir(ppy)$_3$ suggests that there are roughly 70 states with mixed singlet and triplet character within 1 eV of the lowest energy excited state [76]. However, the qualitative picture remains the same, whether two or more states are being mixed; the singlet and triplet states are effectively mixed by the strong spin–orbit coupling of the heavy metal atom in the complex, markedly enhancing the oscillator strengths of the singlet↔triplet transitions.

3.5.3
MO Analysis of Ir Cyclometallates

The model presented above for the excited states of heavy metal complexes describes the mixing of MLCT and LC states to give the emissive excited state. The mixed nature of this state can be seen in the molecular orbitals predicted for these complexes by density functional theory (DFT) methods [77]. Molecular orbital calculations have been carried out on of the heavy metal based emitters, used in OLEDs (see below). One of the first such analyses was carried out on Ir(ppy)$_3$ and (ppy)$_2$Ir(acac), at a B3LYP level with 6-31G(d,p) basis sets with an effective core potential used for the heavy atom [78]. The optimized molecular geometry from these calculations accurately reproduces the bond lengths and angles determined from X-ray crystallography of the same complexes. The HOMO and LUMO orbitals for *fac*-Ir(ppy)$_3$ and (ppy)$_2$Ir(acac) are shown in Fig. 3.4, along with schematic illustrations giving the atom-by-atom contribution to each MO. The frontier orbitals of the two iridium complexes have a similar composition of atomic orbitals. Roughly 50% of the HOMO orbitals involve metal orbitals (d_{z2} for Ir(ppy)$_3$ and d_{xy} for (ppy)$_2$Ir(acac)) [78]. The LUMO is localized on the ppy ligand, with a predominant contribution from the pyridyl ring and little metal character. The triplet states calculated for these two molecules show spin density that is localized on the C^N ligand and metal orbitals, and resembles a simple superposition of the HOMO and LUMO orbitals. TDDFT methods have been applied to the same complexes to examine the low lying singlet and triplet states. The triplet energies estimated by these methods comes very close the experimental energies, e.g., for fac-Ir(ppy)$_3$ the lowest energy triplet is predicted at 2.59 eV (479 nm) [78], whereas the triplet absorption and emission maxima fall between 470 and 515 nm [32]. The dominant orbitals involved in the singlet and triplet transitions involve charge transfer from mixed metal and ligand π orbitals to ligand π* orbitals, consistent with the description for the lowest energy excited states given above.

The acac ligand in (ppy)$_2$Ir(acac) is an ancillary ligand, not contributing substantially to either the HOMO or LUMO orbitals. The spin densities for the triplet state of (ppy)$_2$Ir(acac) correspond to 0.6 unpaired electron on Ir, and 0.7 unpaired electron on each ppy, with no spin density on the acac ligand, consistent with the ancillary nature of the acac ligand [78]. The absorption and emission spectra of

the two complexes are nearly identical, confirming that the acac ligand does not perturb the photophysical properties of the cyclometallated moiety [56]. The ability to independently vary the C^N and ancillary ligands, without strongly affecting the photophysical properties of the complex, is beneficial in designing dopants to match the ideal parameters for fabrication of high efficiency OLEDs (HOMO, LUMO, dipole moment, volatility, etc.).

Although the discussion presented here was restricted to complexes with ppy ligands, a similar MO description is found for other Ir organometallic complexes with related cyclometallating ligands; the HOMO principally comprises orbitals on the metal–aryl linkage, whereas the LUMO is ligand localized [79–85]. The case for most of the other C^N complexes of Ir mirrors that of ppy; the photophysical properties of $(C^N)_2Ir(L^X)$ and $Ir(C^N)_3$ are determined primarily by the C^N ligand so long as the L^X ligand has a higher triplet energy than the "$(C^N)_2Ir$" fragment. As seen for the ppy-based complexes discussed above, the lowest energy transitions appear to be mixtures of ^{1}MLCT and ^{3}LC states.

3.5.4
Using Ancillary Ligands to Modify the Excited State Properties

The excited state properties of many organometallic phosphors are heavily influenced by the ^{3}LC properties of the organic ligands. In order to attain a high level of thermal and chemical stability, organometallic phosphors are typically prepared with chelating L^X ligands. In a later section, tuning the phosphorescence energy by C^N modifications will be discussed in detail; however, for the purpose of the present discussion, we will consider a single C^N ligand in a heteroleptic complex, $(tpy)_2Ir(L^X)$, where tpy is N,C$^{2'}$-(2-*para*-tolylpyridyl), and the ancillary ligand, L^X, is chosen to be "nonchromophoric," i.e., to have sufficiently high singlet and triplet energies such that the excited state properties are dominated by the "$(tpy)_2Ir$" fragment (Fig. 3.5). These complexes can be used to explore the state mixing interactions depicted qualitatively in Scheme 3.2, which shows that the energy of the emissive excited state is dependent on the relative energies of the LC and MLCT states. Alteration of the ancillary ligand allows independent variation of the energies of the two states. The energy of the ^{3}LC state is expected to remain relatively constant for a related series of $(tpy)_2Ir(L^X)$ complexes, while the energy of MLCT states can be altered by varying the electron withdrawing/donating ability of the ancillary ligand [79].

Molecular orbital calculations on the $(tpy)_2Ir(L^X)$ complexes suggest that the nature of the frontier orbitals is not affected by the ancillary ligand as seen for the $(ppy)_2Ir(acac)$ complexes discussed above [79]. The HOMO remains a mixture of metal and phenyl orbitals and the LUMO is predominantly localized on the pyridyl group. The ancillary ligand is expected to affect the ground state energies by direct interaction with the metal center. This role for the ancillary ligand is confirmed by electrochemical measurements, which show that the oxidation potential is shifted by the choice of ancillary ligand, whereas the reduction potentials are relatively unperturbed [79]. The oxidation potentials of the complexes vary by over
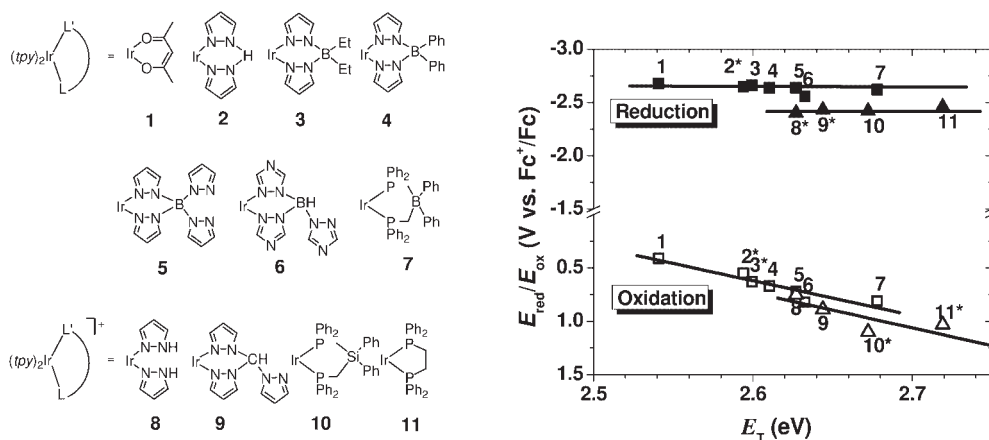
Fig. 3.5 Plot of electrochemical potentials (E_{red}, E_{ox}; Fc=ferrocene) versus emission energy, E_T, at room temperature, for a range of (tpy)2Ir(LL′) complexes. Neutral (tpy)2Ir(LL′) complexes are shown with squares and cationic (tpy)2Ir(LL′) complexes with triangles. The * symbol indicates an irreversible oxidation or reduction process; otherwise the electrochemical process is reversible or quasireversible.

400 mV for the set of ancillary ligands examined in this study, while the reduction potentials vary by less than 20 mV for the same set of complexes, Fig. 3.5. The absorption and emission spectra of the $(C^\wedge N)_2Ir(L^\wedge X)$ complexes progressively shift to higher energy, in parallel with the shift in oxidation potential. Thus, the shift in absorption and emission energy is caused by changes in the HOMO energy, while the LUMO energy is relatively unperturbed. Stabilizing the HOMO energy leads to an increase in the MLCT energy, which decreases the amount of MLCT character in the lowest energy excited state. As the MLCT energy increases, the energy of the excited state of the complex approaches that of the ^{3}LC state of the free ligand. A question then arises: at what point does the amount of MLCT character in the excited state get too low for efficient triplet emission?

The radiative rates for these complexes (Fig. 3.6) were determined from the photoluminescence quantum yields and the measured lifetimes. As the energy of emission increases, the radiative rate of emission decreases. This trend is not surprising when one considers the energy level diagram of Scheme 3.2. The increase in energy in this system is due to a decrease in the amount of MLCT character in the excited state. Since the principal source of efficient triplet emission is the mixing of MLCT character into the lowest excited state, a decreasing amount of singlet MLCT character is expected to lower the radiative decay rate. This decrease in radiative decay rate is compensated somewhat by a decrease in the nonradiative decay rate. Increasing the energy of the excited state decreases the coupling to the vibrational states that are the common source of nonradiative decay, leading to lower nonradiative decay rates [86]. For the complexes with triplet
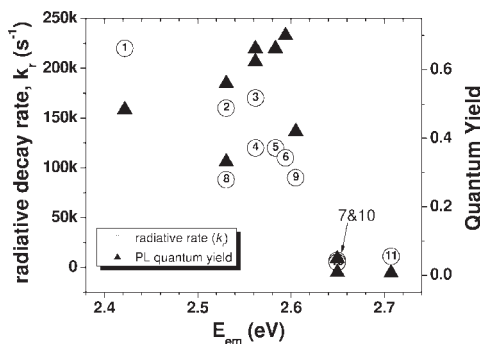
Fig. 3.6 Plot of the radiative decay rate (k_r) and relative quantum yield (QY) versus emission energy for $(tpy)_2Ir(LL')$ complexes. The ancillary ligands (LL') are numbered as in Fig. 3.5.

energies below 2.6 eV, the decrease in nonradiative decay rate is greater than the decrease in radiative decay and the PL efficiency increases. In contrast, the decrease in the radiative rate for the complexes with triplet energies greater than 2.6 eV is greater than the nonradiative rate, due to reduction in MLCT character in the excited state. The low radiative rate for these complexes leads to a significant decrease in the luminance efficiency; compounds 7, 10, and 11 give PL efficiencies <0.04, while the remaining compounds give PL efficiencies of 0.3–0.7. Changing the C^N ligand will lead to a different set energies for the complexes, but the same basic mechanism is expected: a larger energy difference between the MLCT and LC states will give less MLCT character to the excited state and thus a lower radiative rate.

3.5.5
Facial and Meridional Isomers of Tris-Cyclometallates

The homoleptic tris-cyclometallated complexes, such as *fac*-Ir(ppy)₃, represent an example of complexes with ligands having identical triplet energies. The facial isomers display photophysical characteristics than are almost indistinguishable from derivatives with acac as an ancillary ligand. However, pronounced differences exist between the facial and meridional isomers due to the marked disparity between the formally anionic phenyl ligand and neutral pyridyl ligand. The strong electron donating ability of the mutually trans phenyl groups in the meridional isomers leads to the observation that they are easier to oxidize than their facial counterparts, whereas the reduction potentials are similar between the two sets of isomers [57]. Consequently, the mer-isomers typically display emission energies that are lower than that of the facial counterparts. In addition, the luminescent quantum yields of the mer-isomers are generally lower than that of the fac-isomers. The decrease in emission efficiency comes about from an increase in the

nonradiative decay rate associated with a photo-isomerization process than occurs upon irradiation [57, 58, 61]. The photo-isomerization, while facile at room temperature in fluid solution, is suppressed when the mer-isomers are dispersed in a rigid matrix. The inhibition to isomerization when confined in a solid matrix has enabled the mer-isomers to perform nearly as well as the fac-isomers when used as dopants in OLEDs [87].

3.5.6
Ancillary Ligands with Low Triplet Energies

If the ancillary ligand has a triplet energy that is lower than that of the cyclometallated moiety, this ligand becomes directly involved in the emission process. When this ancillary ligand is another cyclometallating ligand, the emission is as intense as that from a homoleptic complex with this "ancillary" ligand [60, 88, 89]. Other examples of complexes where emission is associated with the ancillary ligand include derivatives with β-diketonate [50] or N^O chelate (N^O = picolinate, quinolinate) [83, 90] ligands. The emission in these complexes is often broad and can be relatively weak. Emission from the ancillary ligand is identified most clearly in Ir complexes that have cyclometallated ppz ligands. The high triplet energy of the $(ppz)_2Ir$ fragment makes it likely that the ancillary ligand will be the moiety with the lowest triplet energy. Emission from an ancillary ligand can be easily demonstrated in a series of cationic Ir complexes with diimine ligands. Several of these types of materials have been used to make light-emitting devices [91]. DFT calculations give some insight into the electronic structure of these heteroleptic derivatives. The discussion here will focus on the results for $(ppz)_2Ir(bpy)^+$; however, other $(C^N)_2Ir(N^N)^+$ complexes gave a similar picture for the HOMO and LUMO surfaces. The singlet HOMO, LUMO and triplet spin-density surfaces of $(ppz)_2Ir(bpy)^+$ are illustrated in Fig. 3.7. The HOMO surface is similar in appearance to that seen in $(ppy)_2Ir(acac)$ (Fig. 3.2), being principally composed of a mixture of Ir-d and phenyl-π orbitals distributed equally between the two phenyl-pyrazolyl ligands. On the other hand, the LUMO is predominantly localized on the bipyridyl ligand. The HOMO and LUMO orbitals are orthogonal to each other and thus, there is little electronic overlap between them. The spin-density surface shares the same spatial extent as the singlet HOMO and LUMO surfaces, which leads to a description of the lowest energy excited state as having metal–ligand to ligand charge transfer (MLLCT) character.

The spectra of representative Ir bisimmine complexes are shown in Fig. 3.8. Broad, featureless emission spectra are observed in fluid solution or neat solids at room temperature, with maxima ranging from 485 to 630 nm. The emission spectra exhibit large "Stokes" shifts (ca. 4000–6000 cm^{-1}) from the lowest energy absorption bands. The emission properties at room temperature are consistent with luminescence originating from a triplet MLLCT state. All three of these complexes have been used to make efficient light-emitting electrochemical cells (LECs) [91]. The EL spectra of these LEC match the PL spectra of the same materials. The external quantum efficiencies of these LECs range from 4.7 to 7.4%.
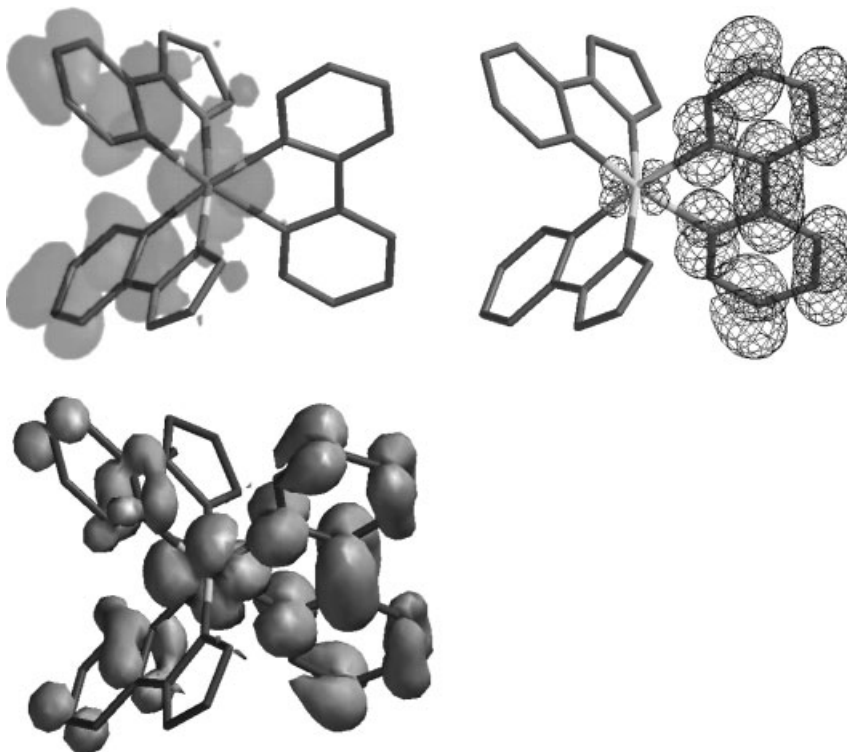
Fig. 3.7 The singlet HOMO (top left), singlet LUMO (top right) and triplet spin density (bottom) surface contour plots for the (ppz)$_2$Ir(bpy) cation obtained from DFT calculations.
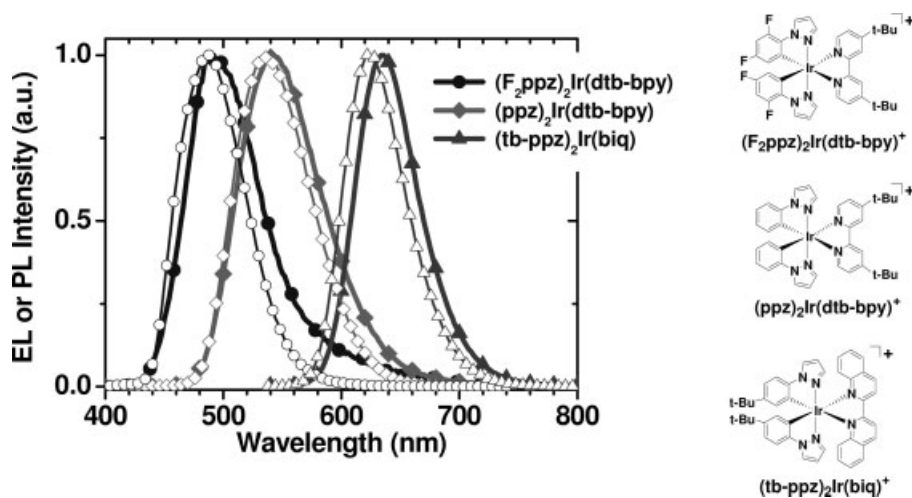
Fig. 3.8 PL (open symbols) and EL (filled symbols) spectra of Ir bisimmine complexes. PL spectra were recorded for neat thin films and EL spectra for Ir-based light-emitting electrochemical cells. The structures of the complexes are shown on the right.

3.5.7
Ligand Tuning to Achieve Green to Near-Infrared Emission

The excited state model presented in Section 5.2, built from MLCT/LC mixing, suggests another method for controlling the emission color. The first color tuning method described in Section 5.4 involved varying the energy separation between the ^{1}MLCT and ^{3}LC states by using different ancillary ligands in $(C^\wedge N)_2Ir(L^\wedge X)$ complexes. If the energy difference is decreased (ΔE in Scheme 3.2), the MLCT/LC mixing is increased, decreasing the excited state energy. Conversely, an increase in ΔE leads to an excited state with greater ^{3}LC character and thus a high excited state energy.

An alternate approach to tuning the emission color of the emitting complex involves modifying the $C^\wedge N$ ligand. This approach has been explored in some depth since the first report of efficient electrophosphorescence from $Ir(ppy)_3$-based OLEDs [34]. For the majority of the efficient phosphorescent materials, the lowest excited state is ^{3}LC-dominant; thus, the excited state energy can be varied over a wide spectral range by employing different cyclometallating ligands in the complexes. A $C^\wedge N$ ligand with a ^{3}LC state of low energy will give red-shifted absorption and emission relative to a ^{3}LC state with a higher energy. A large number of Ir and Pt complexes have been reported with different $C^\wedge N$ ligands, giving emission energies ranging from the near-UV to the near-IR. The discussion of emission energy given here will cover both photoluminescent and electroluminescent data, but will focus on EL data where possible. There is typically a good correlation between the PL and EL spectra for a given phosphor. Exceptions to this are seen when dopant aggregation or a dopant-host exciplex is observed, both leading to red-shifted emission. Aggregation effects on emission color are most pronounced in square planar Pt complexes [92, 93]. We will focus here on Ir complexes that emit from molecular states of isolated species, such that PL and EL spectra are equivalent.

Two different sets of complexes shown in Fig. 3.9 illustrate the role that substituent effects and the size of the $C^\wedge N$ π system play in determining the emission energy of cyclometallated complexes. These two sets of complexes are representative of the affects that a given change in the $C^\wedge N$ ligand will have on the emission energy. Each of the complexes in Fig. 3.9 has the same basic formula, $(C^\wedge N)_2Ir(acac)$. In all cases the ancillary ligand is acac, such that the emission energy is determined by the "$(C^\wedge N)_2Ir$" fragment. The two sets of Ir complexes involve benzazole ligands (top row) and pyridy/quinoline-arene ligands (bottom row). There is a moderate energy difference associated with interchanging O, S, and N in the benzoxazole, benzothiazole, and benzimidazole complexes (bo, bt, and bi, respectively), with a spread of roughly 30 nm between the bo and bt complexes. Theoretical modeling of these complexes is consistent with this observation. The HOMO and LUMO orbitals of an analog of $(bi)_2Ir(acac)$ are shown in Fig. 3.9 (the imidazole-N bound phenyl was removed for simplicity). The HOMO and LUMO orbitals have little orbital density on the uncoordinated heteroatoms of the benzazole ligands, so changing these heteroatoms will have a minor effect on the frontier orbitals. The small shifts that are observed likely due to the differing

C^N	EL λ_max (nm)	Ref
bo	525*	50
bt	560	50
pbi	530	90
F₂bt	530	96
obt	610	96
bon	586*	50
bsn	606	50
nbi	608	97
phbi	651	97
cbi	530	97
fbi	568	97
ppy	520	50, 98
3piq	562	99
pq	597	98
piq	630	100
niq	664	100
azp	932*	101
* photoluminescence λ_max		
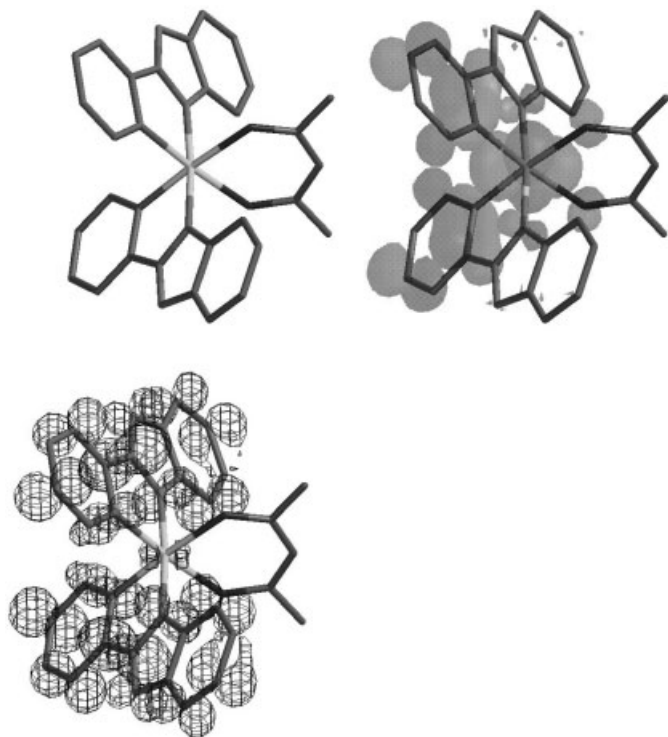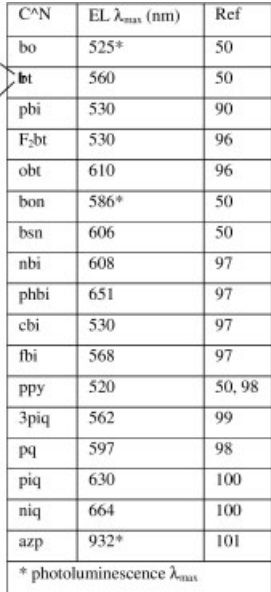
Fig. 3.9 Ligand definitions and emission energies for a series of (C^N)₂Ir(acac) complexes (top). Molecular orbitals are shown for an analog of (bi)₂Ir(acac) (middle left). The HOMO (shaded) is shown in the middle right and the LUMO (mesh) at the bottom.

electronegativities for O, N, and S, which will lead higher polarizibility and delocalization for the least electronegative heteroatom, S, in the bt derivative. The addition of electron donating and accepting groups may also affect on the emission energy of the complex. Adding an electron donating group (OMe) to the metallated phenyl gives a red shift (compare bt to obt complexes), while electron withdrawing groups (F) lead to a blue shift (compare bt to F_2bt). Similar donor and acceptor substitution based shifts in emission energy have been observed for a number of other metal complexes with ppy-based ligands as well [94, 95].

Another effective means to lower the emission energy involves expanding the size of the π-system of the C^N ligand. A comparison between complexes with benzazole ligands that have either a phenyl or naphthyl group, (*cf*, bo, bt, and bi to bon, bsn, and nbi), shows a shift of 50–80 nm occurs in species with the larger π-system. The aryl π-system is intimately involved in the frontier orbitals of these complexes and expansion with a naphthyl group leads to a marked bathochromic shift. The manner in which the π-system is expanded also affects the excited state energy. Fused rings lead to the largest red shift. The three complexes bi, nbi, and phbi give emission energies of 530, 608, and 651 nm, for phenyl, naphthyl, and phenathrenyl groups, respectively. In contrast, the addition of phenyl groups of cbi and fbi leads to a modest shift in the case of fbi and no shift for the cbi complex. A conjugated biphenyl linkage is less effective than a fused aromatic system in lowering the triplet energy, attenuating the effect of the π-system extensions in cbi and fbi.

The bottom row of compounds in Fig. 3.9 further illustrates the affects of increasing the size of the C^N ligand π-system as well as isomeric changes. All of the compounds show a marked red shift relative to the ppy analog, consistent with the expected bathochromic shift. Three different phenyl-quinoline isomers are shown, 3piq, pq, and piq. The emission energies of the Ir complexes of these three ligands are significantly different, i.e., 562, 597, and 630 nm, respectively. The variation in emission energy follows a similar trend observed for Ru complexes ligated with either 3,3′-biisoquinoline [102] or 2,2′-biquinoline [103] ligands. Replacing the phenyl group of piq with 1-napthyl gives the niq ligand, which leads to a red shift of 34 nm in the complex. Steric repulsion is expected to prevent the niq ligand from adopting a planar arrangement, attenuating the red shift caused by the naphthyl group (cf. bt and bsn). If the naphthyl and isoquinoline groups are fused, an azaperylene (azp) ligand is formed. The complex with the azp ligand gives a marked red shift, emitting at 932 nm. This emission energy is very close to the phosphorescent emission from perylene (800 nm) [104], suggesting that the excited state in this complexes is predominantly ligand centered.

OLED data are given in Table 3.1 for all of the Ir complexes discussed in this chapter. The devices chosen here have the same basic structure, i.e., anode/HTL/doped EML/HBL/ETL/cathode.

3.5.8
Near-UV Luminescent Cyclometallated Complexes

The use of electron withdrawing and donating substituents on cyclometallated ppy ligands can be used to blue shift the emission energy of $Ir(ppy)_3$-based complexes

Table 3.1 Phosphorescent OLEDs based on cyclometallated Ir emitters, with the structure anode/HTL/doped EML/HBL/ ETL/cathode. C^N ligands are shown in Fig. 3.9.

Emitter1 Ir(C^N)$_3$, (C^N)$_2$Ir(L^X)	EL λ_{max} (nm)	CIE	EQE (%)	cd/A	lm/W	Reference
Firpic	472	0.16,0.32	5.7	–	6.3	[46]
fac-Ir(ppy)$_3$	510	0.27,0.63	8.0	28	31	[34]
(ppy)$_2$Ir(acac)	520	0.31,0.64	12.3	50	38	[50]
(4′6′F$_2$bt)$_2$Ir(acac)	530	0.37,0.60	11.2	45.0	13.9	[105]
(cbi)$_2$Ir(acac)	530	0.35,0.61	12.1	44	13	[97]
(pbi)$_2$Ir(acac)	530	0.36,0.60	16.7	61	20	[97]
(bt)$_2$Ir(acac)	560	0.47,0.52	9.28	34.0	11.4	[105]
(3piq)$_2$Ir(acac)	562	0.49,0.51	7.17	23.9	9.38	[99]
mer-Ir(ppy)$_3$	564	0.42,0.50	–	15.3	5.3	[87]
(fbi)$_2$Ir(acac)	568	0.51,0.48	10.4	30	7.8	[97]
fac-Ir(pq)$_3$	589	0.56,0.43	11	33.4	11.7	]106]
(pq)$_2$Ir(acac)	597	0.61,0.38	10.3	17.6	–	[52]
(nbi)$_2$Ir(acac)	608	0.63,0.35	4.8	6.1	1.7	[97]
(obt)$_2$Ir(acac)	610	0.63,0.37	6.5	11.0	4.3	[105]
fac-Ir(piq)$_3$	620	0.68,0.32	10.3	–	8.0	[107]
(piq)$_2$Ir(acac)	630	0.68,0.32	9.21	8.22	2.34	[108]
(niq)$_2$Ir(acac)	680	0.70,0.27	0.38	0.24	–	[100]

[95, 109–112]; however, it is not possible to shift the energy of the green emissive Ir(ppy)$_3$ complex into the deep blue and near UV part of the spectrum ($\lambda_{max} < 450$ nm). This is because the emission energy of the metal complex is limited by the ^{3}LC energy of the ppy ligand itself (ppyH; $E_T = 430$ nm, 2.88 eV) [113]. One approach that was pursued to blue shift the emission relative to Ir(ppy)$_3$ involved decreasing the size of the C^N π-system, by replacing the phenyl ring with a vinyl group. Interestingly, this vinyl substitution led to a marked red shift, rather than the expected blue shift. The emission energy of the bis(2-vinylpyridyl)$_2$Ir(acac) complex was found to be 536 nm versus 515 nm for (ppy)$_2$Ir(acac) [114]. The decrease in emission energy in this case is caused by electron–electron repulsion in the triplet state, which increases with reduction in the size of the π-system, thereby lowering the triplet energy through increased singlet–triplet splitting (greater exchange energy) [28]. The same affect is seen in simple hydrocarbons, the triplet energies of vinyl substituted benzene derivatives are ca. 5 kcal/mol (0.2 eV) [115, 116] lower than that of biphenyl ($E_{0-0} = 436$ nm, 2.84 eV) [117].

An effective method to blue shift the emission energy of cyclometallated complexes markedly, relative to Ir(ppy)$_3$, involves replacing the phenyl or pyridyl functionality of ppy with other heterocyclic azole groups, such as pyrazole [118] or triazole [109, 119, 120], which have triplet energies that are significantly higher than that of pyridine [104]. One such modification involves replacing the pyridyl of ppy with a pyrazolyl group, i.e., Ir(ppz)$_3$, Scheme 3.3. The emission energy of *fac*-Ir(ppz)$_3$ ($\lambda_{max} = 414$ nm, 77 K) is significantly greater than that of *fac*-Ir(ppy)$_3$

Ir(ppz)₃   **Ir(flz)₃**   **Ir-Lappert**   **Ir(pmb)₃**   **Ir(pmi)₃**
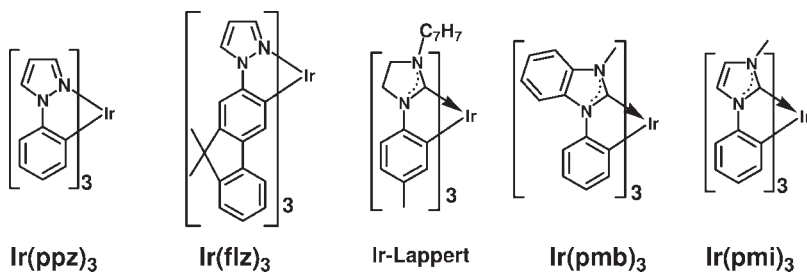
Scheme 3.3

($\lambda_{max}=494$ nm, 77 K). The photophysical properties of the Ir complexes mirror those of the ligands themselves. The triplet energy of the ppzH ligand ($E_T=380$ nm, 3.26 eV) [121] is much higher than that of ppyH (vida supra). Unfortunately, no detectable emission from *fac*-Ir(ppz)₃ is observed at room temperature, in fluid or solid solutions [57, 122]. The intensity of photoluminescence of *fac*-Ir(ppz)₃ is strongly temperature dependent, whereas the PL intensity of *fac*-Ir(ppy)₃ is invariant with temperature when dispersed in a solid matrix (at temperatures between roughly 100 K and 300 K) [33]. Weak emission from *fac*-Ir(ppz)₃ is observed in fluid solution at temperatures below 230 K, with the intensity increasing to 77 K. Thermal population of one or more higher lying nonradiative excited states prevents measurable emission from *fac*-Ir(ppz)₃ at room temperature. As the temperature is decreased, decay through the nonradiative state(s) is diminished.

To achieve efficient luminescence from cyclometallated ppz-based Ir complexes at room temperature, the nonradiative processes that thermally deactivate the excited state must be retarded or eliminated. This has been accomplished by replacing the phenyl ring of the ppz ligand with the extended π-system of a fluorenyl group, i.e., *fac*-Ir(flz)₃ (Scheme 3.3). The fluorenyl substituent lowers the ³LC energy of the complex, increasing the energy difference between the emissive triplet and nonradiative decay states. The PL efficiency of *fac*-Ir(flz)₃ at room temperature is high ($\Phi=0.38$) and the measured lifetime is 37 μs [123]. The radiative (k_r) and nonradiative (k_{nr}) decay rates estimated from the lifetime and PL efficiency are 1.0×10^4 s^{-1} and 2.0×10^4 s^{-1}, respectively. These rates are an order of magnitude lower than those reported for ppy-based tris-cyclometallated Ir complexes [114–116]. The low radiative rate for *fac*-Ir(flz)₃ is consistent with a low level of ¹MLCT character in the emissive excited state, and is due to the large separation between the ¹MLCT and ligand triplet energies.

Considerable work has focused on the thermally activated decay processes in luminescent transition metal complexes [124]. The photophysical properties of Ru(II) and Os(II) tris-diimine complexes exhibit strong temperature dependences, making them good candidates for studying this phenomenon. The temperature dependence observed for Ru(II) diimine complexes is characteristic of thermal population of ligand field (dissociative) states, whereas the Os(II) analogs have kinetic parameters more consistent with deactivation through higher energy

MLCT states [125]. The tris-cyclometallated Ir(III) complexes discussed here are isoelectronic with the Ru(II) and Os(II) tris-diimine materials, and are expected to mimic the photophysics of their Os(II) counterparts [126]. Thus, the *fac*-Ir(ppz)$_3$ complex could decay nonradiatively through higher energy nonradiative MLCT states [125]. However, the triplet energy of *fac*-Ir(ppz)$_3$ is very high (E_T = 3.0 eV, 70 kcal/mol) and comparable to the expected Ir-phenyl bond strength [127]. Therefore, thermal population to accessible ligand field states may contribute to nonradiative luminescent decay.

If the thermally accessed nonradiative state is a metal-localized, ligand field state, strengthening the metal–ligand bonds will raise its energy, since that state is largely comprised of antibonding counterparts to the metal–ligand bonding orbitals. N-heterocyclic carbene (*NHC*) ligands form strong bonds to transition metals [128], which shifts the metal–carbene antibonding orbitals to high energy, thereby decreasing or eliminating decay through the ligand field state. Specifically, the two *NHC* ligands discussed here are 1-phenyl-3-methyl-imidazolin-2-ylidene (pmi) and 1-phenyl-3-methyl-benzimidazolin-2-ylidene (pmb) (see Scheme 3.3) [123]. The carbene moiety is a neutral, two electron donor, which makes the cyclometallated ligand a bidentate monoanionic ligand (C^C: is used here as a general abbreviation for a cyclometallated carbene ligand). The first example of a tris-cyclometallated carbene complex, Ir(C^C:)$_3$, was reported in 1980 by Lappert et al. (see Ir-Lappert in Scheme 3.5) [129].

Ir(pmi)$_3$ and Ir(pmb)$_3$ have electrochemical and absorption characteristics which are very similar to those of Ir(ppz)$_3$. The data are consistent with the Ir(C^C:)$_3$ and Ir(ppz)$_3$ complexes having both low HOMO and high LUMO energies. The *fac*-isomers undergo reversible oxidation (*fac*-Ir(pmi)$_3$, $E_{1/2}^{ox}$ = 0.22 V; *fac*-Ir(pmb)$_3$, $E_{1/2}^{ox}$ = 0.48 V) and no observable reduction within the accessible solvent window. The excited state properties of the Ir(C^C:)$_3$ complexes are related to the Ir(C^N)$_3$ analogs in that both types of species emit from perturbed ^{3}LC states. The Ir(C^C:)$_3$ complexes display intense emission at 77 K in the near UV and also luminescence at room temperature in fluid solution (λ_{max} = 390 nm). The emission spectra at 77 K are highly structured and have luminescent lifetimes between 2 to 7 μs. The PL efficiencies at room temperature for the Ir(C^C:)$_3$ complexes are low (0.002 to 0.05), but markedly higher than their pyrazolyl counterparts.

Deep blue organic electrophosphorescence has been demonstrated for both *facial-* and *meridional-* isomers of Ir(pmb)$_3$ [130]. The high triplet energy of these materials necessitate the use of a wide energy gap host, *p*-bis(triphenylsilyly) benzene [131], in place of CBP. An electron blocking layer was also needed to eliminate HTL emission from this device. The highest energy electrophosphorescent transition occurs at a wavelength of λ = 389 nm for the *fac-* isomer and λ = 395 nm for the *mer-* isomer. The *fac-* and *mer-* isomers gave OLED efficiencies of 2.6% and 5.8%, respectively. Both devices gave power efficiencies of less than 2 lum/W. The relatively low power efficiencies compared to previously reported phosphor dopants reflect the limited overlap between the deep blue EL spectra of these devices and the photopic response of the human eye. The photophysical and OLED properties of related carbene complexes have also been reported [132].

3.6
Conclusion

The improvements in performance of organic light-emitting diodes since the initial report of a heterostructure device, from an efficiency of 1% [133] to an external efficiency of nearly 20% or higher [24, 134–136], are truly impressive. These devices are now performing at close to an internal efficiency of 100%. The key to these high efficiencies in these devices is the organometallic dopant, which is the ultimate source of emission in these devices. These dopants have phosphorescence efficiencies of nearly 100% in the solid state, allowing for efficient harvesting of both the singlet and triplet excitons. Organometallic complexes are ideal candidates for this application, since many phosphoresce efficiently (particularly complexes of Ir) and ligand modifications can be used to tune the emission color to span a range from the near-UV to the near-IR. In addition to applications where the ultrahigh efficiencies are important, they will be key components in white emissive devices as well, where the emission energy and the spectral linewidth are both critical components in achieving both high efficiency and white color balance. The future for phosphors based on metal complexes in organic LEDs is very bright indeed.

References

1 J. Kido, K. Nagai, Y. Ohashi, Electroluminescence in a terbium complex. *Chemistry Letters* **1990**, *19*, 657–660.

2 J. Kido, H. Hayase, K. Hongawa, K. Nagai, K. Okuyama, Bright red light-emitting organic electroluminescent devices having a europium complex as an emitter. *Applied Physics Letters* **1994**, *65*, 2124–2126.

3 G. E. Jabbour, J. F. Wang, B. Kippelen, N. Peyghambarian, Sharp red organic light-emitting devices with enhanced efficiency. *Japanese Journal of Applied Physics*, Part 2 **1999**, *38*, L1553–L1555.

4 M. D. McGehee, et al. Narrow bandwidth luminescence from blends with energy transfer from semiconducting conjugated polymers to europium complexes. *Advanced Materials* **1999**, *11*, 1349–1354.

5 W. P. Hu, M. Matsumura, M. Z. Wang, L. P. Jin, Efficient red electroluminescence from devices having multilayers of a europium complex. *Applied Physics Letters* **2000**, *77*, 4271–4273.

6 Z. R. Hong, et al. Rare earth complex as a high-efficiency emitter in an electroluminescent device. *Advanced Materials* **2001**, *13*, 1241–1245.

7 J. Kido, Y. Okamoto, Organo lanthanide metal complexes for electroluminescent materials. *Chemical Reviews* **2002**, *102*, 2357–2368.

8 S. Hoshino, H. Suzuki, Electroluminescence from triplet excited states of benzophenone. *Applied Physics Letters* **1996**, *69*, 224–226.

9 S. Hoshino, H. Suzuki, Electroluminescence from triplet excited states of benzophenone derivatives. *Molecular Crystals and Liquid Crystals Science and Technology*, Section A **1997**, *294*, 313–316.

10 S. Blumstengel, R. Dorsinville, Phosphorescent emission from polymeric light-emitting diodes doped with chrysene-d$_{12}$. *Japanese Journal of Applied Physics Part 2-Letters* **1999**, *38*, L403–L405.

11 R. C. Kwong, et al. Efficient, saturated red organic light emitting devices based on phosphorescent platinum(II) porphyrins. *Chemistry of Materials* **1999**, *11*, 3709–3713.

12 R. C. Kwong, S. Lamansky, M. E. Thompson, Organic light-emitting devices based on phosphorescent hosts and dyes. *Advanced Materials* **2000**, *12*, 1134–1138.

13 M. A. Baldo, C. Adachi, S. R. Forrest, Transient analysis of organic electrophosphorescence: II. Transient analysis of triplet-triplet annihilation. *Physical Review B* **2000**, *62*, 10967–10977.

14 P. P. Sun, J. P. Duan, H. T. Shih, C. H. Cheng, Europium complex as a highly efficient red emitter in electroluminescent devices. *Applied Physics Letters* **2002**, *81*, 792–794.

15 J. F. Fang, H. You, H. Gao, D. G. Ma, Improved efficiency by a fluorescent dye in red organic light-emitting devices based on a europium complex. *Chemical Physics Letters* **2004**, *392*, 11–16.

16 J. F. Fang, D. G. Ma, Efficient red organic light-emitting devices based on a europium complex. *Applied Physics Letters* **2003**, *83*, 4041–4043.

17 M. A. Baldo, et al. Highly efficient phosphorescent emission from organic electroluminescent devices. *Nature* **1998**, *395*, 151–154.

18 G. Ponterini, N. Serpone, M. A. Bergkamp, T. L. Netzel, Comparison of radiationless decay processes in osmium and platinum porphyrins. *Journal of the American Chemical Society* **1983**, *105*, 4639–4645.

19 D. B. Papkovsky, New oxygen sensors and their application to biosensing. *Sensors and Actuators B* **1995**, *29*, 213–218.

20 V. Bulovic, et al. Weak microcavity effects in organic light emitting devices. *Physical Reviews B* **1998**, *58*, 3730–3740.

21 G. Gu, V. Khalfin, S. R. Forrest, High-efficiency, low-drive-voltage, semitransparent stacked organic light-emitting device. *Applied Physics Letters* **1998**, *73*, 2399–2401.

22 C. Kim, P. E. Burrows, S. R. Forrest, Micropatterning of organic electronic devices by cold-welding. *Science* **2000**, *288*, 831–833.

23 J. Kavitha, et al. In search of high-performance platinum(II) phosphorescent materials for the fabrication of red electroluminescent devices. *Advanced Functional Materials* **2005**, *15*, 223–229.

24 M. Ikai, S. Tokito, Y. Sakamoto, T. Suzuki, Y. Taga, Highly efficient phosphorescence from organic light-emitting devices with an exciton-block layer. *Applied Physics Letters* **2001**, *79*, 156–158.

25 J. Kalinowski, W. Stampor, J. Szmytkowski, M. Cocchi, D. Virgili, V. Fattori, P. Di Marco, Photophysics of an electrophosphorescent platinum (II) porphyrin in solid films. *Journal of Chemical Physics* **2005**, *122*, 154710.

26 V. A. Montes, C. Perez-Bolivar, N. Agarwal, J. Shinar, P. Anzenbacher, Molecular-wire behavior of OLED materials: exciton dynamics in multichromophoric Alq3-oligofluorene-Pt(II)porphyrin triads. *Journal of the American Chemical Society* **2006**, *128*, 12436–12438.

27 L. Yanqin, et al. Multifunctional platinum porphyrin dendrimers as emitters in undoped phosphorescent based light emitting devices. *Applied Physics Letters* **2006**, *89*, 061125.

28 N. J. Turro, Modern Molecular Photochemistry (Benjamin/Cummings, Menlo Park, CA, **1978**).

29 J. Kalinowski, W. Stampor, J. Mezyk, M. Cocchi, D. Virgili, V. Fattori, P. Di Marco, Quenching effects in organic electrophosphorescence. *Physical Review B* **2002**, *66*, 235321.

30 J. Kalinowski, W. Stampor, J. Szmytkowski, D. Virgili, M. Cocchi, V. Fattori, C. Sabatini, Coexistence of dissociation and annihilation of excitons on charge carriers in organic phosphorescent emitters. *Physical Review B* **2006**, *74*, 085316.

31 K. A. King, P. J. Spellane, R. J. Watts, Excited-state properties of a triply ortho-metalated iridium(III) complex. *Journal of the American Chemical Society* **1985**, *107*, 1431–1432.

32 W. Holzer, A. Penzkofer, T. Tsuboi, Absorption and emission spectroscopic characterization of Ir(ppy)₃. *Chemical Physics* **2005**, *308*, 93–102.

33 Y. Kawamura, et al. 100% phosphorescence quantum efficiency of Ir(III) complexes in organic semiconductor films. *Applied Physics Letters* **2005**, *86*, 071104.

34 M. A. Baldo, S. Lamansky, P. E. Burrows, M. E. Thompson, S. R. Forrest, Very high-efficiency green organic light-emitting devices based on electrophosphorescence. *Applied Physics Letters* **1999**, *75*, 4–6.

35 C. Adachi, M. A. Baldo, S. R. Forrest, M. E. Thompson, High-efficiency organic electrophosphorescent devices with tris(2-phenylpyridine)iridium doped into electron-transporting materials. *Applied Physics Letters* **2000**, *77*, 904–906.

36 D. F. O'Brien, M. A. Baldo, M. E. Thompson, S. R. Forrest, Improved energy transfer in electrophosphorescent devices. *Applied Physics Letters* **1999**, *74*, 442–444.

37 M. A. Baldo, S. R. Forrest, Transient analysis of organic electrophosphorescence: I. Transient analysis of triplet energy transfer. *Physical Review B* **2000**, *62*, 10958–10966.

38 M. Colle, C. Garditz, M. Braun, The triplet state in tris-(8-hydroxyquinoline) aluminum. *Journal of Applied Physics* **2004**, *96*, 6133–6141.

39 H. D. Burrows, M. Fernandes, J. S. de Melo, A. P. Monkman, S. Navaratnam, Characterization of the triplet state of tris(8-hydroxyquinoline)aluminium(III) in benzene solution. *Journal of the American Chemical Society* **2003**, *125*, 15310–15311.

40 Y. V. Romanovskii, et al. Phosphorescence of pi-conjugated oligomers and polymers. *Physical Review Letters* **2000**, *84*, 1027–1030.

41 D. Hertel, et al. Phosphorescence in conjugated poly(para-phenylene)-derivatives. *Advanced Materials* **2001**, *13*, 65–70.

42 R. W. T. Higgins, A. P. Monkman, H. G. Nothofer, U. Scherf, Energy transfer to porphyrin derivative dopants in polymer light-emitting diodes. *Journal of Applied Physics* **2002**, *91*, 99–105.

43 V. Cleave, et al. Transfer processes in semiconducting polymer-porphyrin blends. *Advanced Materials* **2001**, *13*, 44–47.

44 X. H. Yang, D. Neher, U. Scherf, S. A. Bagnich, H. Bassler, Polymer electrophosphorescent devices utilizing a ladder-type poly(para-phenylene) host. *Journal of Applied Physics* **2003**, *93*, 4413–4419.

45 G. E. Jabbour, J. F. Wang, N. Peyghambarian, High-efficiency organic electrophophorescent devices through balance of charge injection. *Applied Physics Letters* **2002**, *80*, 2026–2028.

46 C. Adachi, et al. Endothermic energy transfer: a mechanism for generating very efficient high-energy phosphorescent emission in organic materials. *Applied Physics Letters* **2001**, *79*, 2082–2084.

47 Y. Wang, Dramatic effects of hole transport layer on the efficiency of iridium-based organic light-emitting diodes. *Applied Physics Letters* **2004**, *85*, 4848–4850.

48 I. G. Hill, A. Kahn, Organic semiconductor heterointerfaces containing bathocuproine. *Journal of Applied Physics* **1999**, *86*, 4515–4519.

49 C. Adachi, et al. High-efficiency red electrophosphorescence devices. *Applied Physics Letters* **2001**, *78*, 1622–1624.

50 S. Lamansky, et al. Highly phosphorescent bis-cyclometalated iridium complexes: synthesis, photophysical characterization, and use in organic light emitting diodes. *Journal of the American Chemical Society* **2001**, *123*, 4304–4312.

51 T. Watanabe, et al. Proceedings of SPIE 4105, 2001, 175.

52 R. C. Kwong, et al. High operational stability of electrophosphorescent devices. *Applied Physics Letters* **2002**, *81*, 162–164.

53 H. Yersin, Triplet emitters for OLED applications. Mechanisms of exciton trapping and control of emission properties. *Topics in Current Chemistry* **2004**, *241*, 1–26.

54 M. E. Thompson, P. I. Djurovich, S. Barlow, S. R. Marder, *Comprehensive*

Organometallic Chemistry, Vol. 12 (ed. O'Hare, D.) 101–194 (Elsevier, Oxford, **2007**).

55 M. Nonoyama, [Benzo[h]quinolin-10-yl-N]iridium(III) complexes. *Bulletin of the Chemical Society of Japan* **1974**, *47*, 767–768.

56 S. Lamansky, et al. Synthesis and characterization of phosphorescent cyclometalated iridium complexes. *Inorganic Chemistry* **2001**, *40*, 1704–1711.

57 A. B. Tamayo, et al. Synthesis and characterization of facial and meridional tris-cyclometalated iridium(III) complexes. *Journal of the American Chemical Society* **2003**, *125*, 7377–7387.

58 T. Karatsu, et al. Photochemical mer → fac one-way isomerization of phosphorescent material. Studies by time resolved spectroscopy for tris[2-(4′,6′-difluorophenyl)pyridine]iridium(III) in solution. *Chemistry Letters* **2003**, *32*, 886–887.

59 M. C. DeRosa, P. J. Mosher, G. P. A. Yap, K. S. Focsaneanu, R. J. Crutchley, C. E. B. Evans, Synthesis, characterization, and evaluation of [Ir(ppy)$_2$(vpy)Cl] as a polymer-bound oxygen sensor. *Inorganic Chemistry* **2003**, *42*, 4864–4872.

60 K. Dedeian, J. M. Shi, N. Shepherd, E. Forsythe, D. C. Morton, Photophysical and electrochemical properties of heteroleptic tris-cyclometalated iridium(III) complexes. *Inorganic Chemistry* **2005**, *44*, 4445–4447.

61 T. Karatsu, E. Ito, S. Yagai, A. Kitamura, Radiative and nonradiative processes of meridional and facial isomers of heteroleptic iridium-trischelete complexes. *Chemical Physics Letters* **2006**, *424*, 353–357.

62 S. Q. Huo, J. C. Deaton, M. Rajeswaran, W. C. Lenhart, Highly efficient, selective, and general method for the preparation of meridional homo- and heteroleptic tris-cyclometalated iridium complexes. *Inorganic Chemistry* **2006**, *45*, 3155–3157.

63 K. Dedeian, P. I. Djurovich, F. O. Garces, G. Carlson, R. J. Watts, A new synthetic route to the preparation of a series of strong photoreducing agents –

ac tris-ortho-metalated complexes of iridium(III) with substituted 2-phenylpyridines. *Inorganic Chemistry* **1991**, *30*, 1685–1687.

64 M. G. Colombo, H. U. Güdel, Synthesis and high-resolution optical spectroscopy of bis(2-(2-thienyl)pyridinato-C3,*N'*) (2,2′-bipyridine)iridium(III). *Inorganic Chemistry* **1993**, *32*, 3081–3087.

65 G. F. Strouse, H. U. Güdel, V. Bertolasi, V. Ferretti, Optical spectroscopy of single-crystal [Re(bpy)(CO)$_4$](PF$_6$) – mixing between charge-transfer and ligand centered excited-states. *Inorganic Chemistry* **1995**, *34*, 5578–5587.

66 H. Wiedenhofer, S. Schutzenmeier, A. Von Zelewsky, H. Yersin, Characterization of triplet sublevels by highly resolved vibrational satellite structures – application to Pt(2-thpy)$_2$. *Journal of Physical Chemistry* **1995**, *99*, 13385–13391.

67 J. Schmidt, H. Wiedenhofer, A. Von Zelewsky, H. Yersin, Time-resolved vibrational-structures of the triplet sublevel emission of Pd(2-thpy)$_2$. *Journal of Physical Chemistry* **1995**, *99*, 226–229.

68 H. Yersin, D. Donges, Low-lying electronic states and photophysical properties of organometallic Pd(II) and Pt(II) compounds. Modern research trends presented in detailed case studies. *Topics in Current Chemistry* **2001**, *214*, 81–186.

69 F. W. M. Vanhelmont, H. U. Güdel, M. Förtsch, H. B. Bürgi, Synthesis, crystal structure, high-resolution optical spectroscopy, and extended Huckel calculations for [Re(CO)$_4$(thpy)] (thpy = 2-(2-thienyl)pyridinate). Comparison with related cyclometalated complexes. *Inorganic Chemistry* **1997**, *36*, 5512–5517.

70 H. Yersin, W. Humbs, Spatial extensions of excited states of metal complexes. Tunability by chemical variation. *Inorganic Chemistry* **1999**, *38*, 5820–5831.

71 Y. Komada, S. Yamauchi, N. Hirota, Phosphorescence and zero-field optically detected magnetic-resonance studies of the lowest excited triplet-states of organometallic diimine complexes.1. [Rh(bpy)$_3$]$^{3+}$ And [Rh(phen)$_3$]$^{3+}$. *Journal of Physical Chemistry* **1986**, *90*, 6425–6430.

72 A. P. B. Lever, Inorganic Electronic Spectroscopy (Elsevier, New York, 1984).

73 T. Azumi, H. Miki, Spectroscopy of the spin sublevels of transition metal complexes. *Topics in Current Chemistry* **1997**, *191*, 1–40.

74 S. Kimachi, R. Satomi, H. Miki, K. Maeda, T. Azumi, M. Onishi, Excited-state properties of the ligand-localized ³pi-pi* state of cyclometalated ruthenium(II) complexes. *Journal of Physical Chemistry A* **1997**, *101*, 345–349.

75 H. Miki, M. Shimada, T. Azumi, J. A. Brozik, G. A. Crosby, Effect of the ligand-field strength on the radiative properties of the ligand-localized ³pi-pi* state of rhodium complexes with 1,10-phenanthroline – proposed role of dd states. *Journal of Physical Chemistry* **1993**, *97*, 11175–11179.

76 K. Nozaki, Theoretical studies on photophysical properties and mechanism of phosphorescence in [fac-Ir(2-phenylpyridine)₃]. *Journal of the Chinese Chemical Society* **2006**, *53*, 101–112.

77 A. Vlček, S. Záliš, Modeling of charge-transfer transitions and excited states in d⁶ transition metal complexes by DFT techniques. *Coordination Chemistry Reviews* **2007**, *251*, 258–287.

78 P. J. Hay, Theoretical studies of the ground and excited electronic states in cyclometalated phenylpyridine Ir(III) complexes using density functional theory. *Journal of Physical Chemistry A* **2002**, *106*, 1634–1641.

79 J. Li, et al. Synthetic control of excited-state properties in cyclometalated Ir(III) complexes using ancillary ligands. *Inorganic Chemistry* **2005**, *44*, 1713–1727.

80 T. Yutaka, et al. Syntheses and properties of emissive iridium(III) complexes with tridentate benzimidazole derivatives. *Inorganic Chemistry* **2005**, *44*, 4737–4746.

81 M. Polson, M. Ravaglia, S. Fracasso, M. Garavelli, F. Scandola, Iridium cyclometalated complexes with axial symmetry: time-dependent density functional theory investigation of trans-bis-cyclometalated complexes containing the tridentate ligand 2,6-diphenylpyridine. *Inorganic Chemistry* **2005**, *44*, 1282–1289.

82 G. C. Choi, J. E. Lee, N. G. Park, Y. S. Kim, TD-DFT studies of electronic structures in cyclometalated phenylpyrazol Ir(III) complexes: fac-Ir(ppz)₃ and Ir(ppz)₂(acac). *Molecular Crystals and Liquid Crystals* **2004**, *424*, 173–185.

83 T. H. Kwon, et al. Color tuning of cyclometalated iridium complexes through modification of phenylpyrazole derivatives and ancillary ligand based on ab initio calculations. *Organometallics* **2005**, *24*, 1578–1585.

84 W. Sotoyama, T. Satoh, H. Sato, A. Matsuura, N. Sawatari, Excited states of phosphorescent platinum(II) complexes containing NCN-coordinating tridentate ligands: spectroscopic investigations and time-dependent density functional theory calculations. *Journal of Physical Chemistry A* **2005**, *109*, 9760–9766.

85 K. Pierloot, A. Ceulemans, M. Merchan, L. Serrano-Andres, Electronic spectra of the cyclometalated complexes M(2-thienylpyridine)₂ with M = Pd, Pt: A theoretical study. *Journal of Physical Chemistry A* **2000**, *104*, 4374–4382.

86 E. M. Kober, J. V. Caspar, R. S. Lumpkin, T. J. Meyer, Application of the energy-gap law to excited-state decay of osmium(II) polypyridine complexes – calculation of relative nonradiative decay-rates from emission spectral profiles. *Journal of Physical Chemistry* **1986**, *90*, 3722–3734.

87 C. H. Yang, K. H. Fang, C. H. Chen, I. W. Sun, High efficiency mer-iridium complexes for organic light-emitting diodes. *Chemical Communications*, **2004**, 2232–2233.

88 A. Beeby, S. Bettington, I. D. W. Samuel, Z. J. Wang, Tuning the emission of cyclometalated iridium complexes by simple ligand modification. *Journal of Materials Chemistry* **2003**, *13*, 80–83.

89 M. J. Frampton, E. B. Namdas, S. C. Lo, P. L. Burn, I. D. W. Samuel, The synthesis and properties of solution processable red-emitting phosphorescent dendrimers. *Journal of Materials Chemistry* **2004**, *14*, 2881–2888.

90 Y. M. You, S. Y. Park, Inter-ligand energy transfer and related emission change in the cyclometalated heteroleptic iridium complex: facile and efficient color tuning over the whole visible range by the ancillary ligand structure. *Journal of the American Chemical Society* **2005**, *127*, 12438–12439.

91 A. B. Tamayo, et al. Cationic bis-cyclometalated iridium(III) diimine complexes and their use in efficient blue, green, and red electroluminescent devices. *Inorganic Chemistry* **2005**, *44*, 8723–8732.

92 A. K. Bansal, W. Holzer, A. Penzkofer, T. Tsuboi, Absorption and emission spectroscopic characterization of platinum-octaethyl-porphyrin (PtOEP). *Chemical Physics* **2006**, *330*, 118–129.

93 V. Adamovich, et al. High efficiency single dopant white electrophosphorescent light emitting diodes. *New Journal of Chemistry* **2002**, *26*, 1171–1178.

94 J. Brooks, et al. Synthesis and characterization of phosphorescent cyclometalated platinum complexes. *Inorganic Chemistry* **2002**, *41*, 3055–3066.

95 V. V. Grushin, et al. New, efficient electroluminescent materials based on organometallic Ir complexes. *Chemical Communications*, **2001**, 1494–1495.

96 I. R. Laskar, T. M. Chen, Tuning of wavelengths: synthesis and photophysical studies of iridium complexes and their applications in organic light emitting devices. *Chemistry of Materials* **2004**, *16*, 111–117.

97 W. S. Huang, et al. Highly phosphorescent bis-cyclometalated iridium complexes containing benzoimidazole-based ligands. *Chemistry of Materials* **2004**, *16*, 2480–2488.

98 S. Lamansky, R. C. Kwong, M. Nugent, P. I. Djurovich, M. E. Thompson, Molecularly doped polymer light emitting diodes utilizing phosphorescent Pt(II) and Ir(III) dopants. *Organic Electronics* **2001**, *2*, 53–62.

99 C. L. Li, et al. Yellow and red electrophosphors based on linkage isomers of phenylisoquinolinyliridium complexes: distinct differences in photophysical and electroluminescence properties. *Advanced Functional Materials* **2005**, *15*, 387–395.

100 C. H. Yang, C. C. Tai, I. W. Sun, Synthesis of a high-efficiency red phosphorescent emitter for organic light-emitting diodes. *Journal of Materials Chemistry* **2004**, *14*, 947–950.

101 D. Murphy, Ph.D. Thesis (University of Southern California, Los Angeles, **2004**).

102 A. Juris, F. Barigelletti, V. Balzani, P. Belser, A. Vonzelewsky, Luminescence of ruthenium(II) tris chelate complexes containing the ligands 2,2′-bipyridine and 2,2′-biisoquinoline – behavior of the Ru(bpy)$^{2+}$ and Ru(bpy)$_2^{2+}$ emitting units. *Inorganic Chemistry* **1985**, *24*, 202–206.

103 F. Barigelletti, A. Juris, V. Balzani, P. Belser, A. Vonzelewsky, Excited-state properties of complexes of the Ru(diimine)$_3^{2+}$ family. *Inorganic Chemistry* **1983**, *22*, 3335–3339.

104 S. L. Murov, I. Carmichael, G. L. Hug, Handbook of Photochemistry (Marcel Dekker, New York, **1993**).

105 W. C. Chang, A. T. Hu, J. P. Duan, D. K. Rayabarapu, C. H. Cheng, Color tunable phosphorescent light-emitting diodes based on iridium complexes with substituted 2-phenylbenzothiozoles as the cyclometalated ligands. *Journal of Organometallic Chemistry* **2004**, *689*, 4882–4888.

106 K. Saito, et al. Microwave synthesis of iridium(III) complexes: synthesis of highly efficient orange emitters in organic light-emitting devices. *Japanese Journal of Applied Physics*, Part 1 **2004**, *43*, 2733–2734.

107 A. Tsuboyama, et al. Homoleptic cyclometalated iridium complexes with highly efficient red phosphorescence and application to organic light-emitting diode. *Journal of the American Chemical Society* **2003**, *125*, 12971–12979.

108 Y. J. Su, et al. Highly efficient red electrophosphorescent devices based on iridium isoquinoline complexes:

remarkable external quantum efficiency over a wide range of current. *Advanced Materials* **2003**, *15*, 884–888.

109 P. Coppo, E. A. Plummer, L. De Cola, Tuning iridium(III) phenylpyridine complexes in the "almost blue" region. *Chemical Communications*, **2004**, 1774–1775.

110 I. R. Laskar, S. F. Hsu, T. M. Chen, Syntheses, photoluminescence and electroluminescence of some new blue-emitting phosphorescent iridium(III)-based materials. *Polyhedron* **2005**, *24*, 189–200.

111 R. Ragni, et al. Blue emitting iridium complexes: synthesis, photophysics and phosphorescent devices. *Journal of Materials Chemistry* **2006**, *16*, 1161–1170.

112 I. R. Laskar, S.-F. Hsu, T.-M. Chen, Investigating photoluminescence and electroluminescence of iridium(III)-based blue-emitting phosphors. *Polyhedron* **2006**, *25*, 1167–1176.

113 M. Maestri, D. Sandrini, V. Balzani, U. Maeder, A. Von Zelewsky, Absorption-spectra, electrochemical-behavior, luminescence spectra, and excited-state lifetimes of mixed-ligand ortho-metalated rhodium(III) complexes. *Inorganic Chemistry* **1987**, *26*, 1323–1327.

114 B. Paulose, D. K. Rayabarapu, J. P. Duan, C. H. Cheng, First examples of alkenyl pyridines as organic ligands for phosphorescent iridium complexes. *Advanced Materials* **2004**, *16*, 2003–2007.

115 T. Ni, R. A. Caldwell, L. A. Melton, The relaxed and spectroscopic energies of olefin triplets. *Journal of the American Chemical Society* **1989**, *111*, 457–464.

116 V. Ramamurthy, J. V. Caspar, D. F. Eaton, E. W. Kuo, D. R. Corbin, Heavy-atom-induced phosphorescence of aromatics and olefins included within zeolites. *Journal of the American Chemical Society* **1992**, *114*, 3882–3892.

117 H. V. Taylor, A. L. Allred, B. M. Hoffman, Electron spin resonance study of the phosphorescent states of some 4- and 4,4′-substituted biphenyls.

Journal of the American Chemical Society **1973**, *95*, 3215–3219.

118 C.-H. Yang, et al. Heteroleptic cyclometalated iridium(III) complexes displaying blue phosphorescence in solution and solid state at room temperature. *Inorganic Chemistry* **2005**, *44*, 7770–7780.

119 S. C. Lo, et al. Blue phosphorescence from iridium(III) complexes at room temperature. *Chemistry of Materials* **2006**, *18*, 5119–5129.

120 C. S. K. Mak, et al. Blue-to-green electrophosphorescence of iridium-based cyclometallated materials. *Chemical Communications*, **2005**, 4708–4710.

121 J. W. Pavlik, R. E. Connors, D. S. Burns, E. M. Kurzweil, Phototransposition chemistry of 1-phenylpyrazole – experimental a computational studies. *Journal of the American Chemical Society* **1993**, *115*, 7645–7652.

122 E. J. Nam, J. H. Kim, B. O. Kim, S. M. Kim, N. G. Park, Y. S. Kim, Y. K. Kim, Y. Ha, A synthesis and luminescence study of Ir(ppz)$_3$ for organic light-emitting devices. *Bulletin of the Chemical Society of Japan* **2004**, *77*, 751–755.

123 T. Sajoto, et al. Blue and near-UV phosphorescence from iridium complexes with cyclometalated pyrazolyl or *N*-heterocyclic carbene ligands. *Inorganic Chemistry* **2005**, *44*, 7992–8003.

124 L. S. Forster, Thermal relaxation in excited electronic states of d^3 and d^6 metal complexes. *Coordination Chemistry Reviews* **2002**, *227*, 59–92.

125 R. S. Lumpkin, E. M. Kober, L. A. Worl, Z. Murtaza, T. J. Meyer, Metal-to-ligand charge-transfer (MLCT) photochemistry – Experimental-evidence for the participation of a higher lying MLCT state in polypyridyl complexes of ruthenium(II) and osmium(II). *Journal of Physical Chemistry* **1990**, *94*, 239–243.

126 I. M. Dixon, et al. A family of luminescent coordination compounds: iridium(III) polyimine complexes. *Chemical Society Reviews* **2000**, *29*, 385–391.

127 S. P. Nolan, C. D. Hoff, P. O. Stoutland, L. J. Newman, J. M. Buchanan, R. G. Bergman, G. K. Yang, K. S. Peters, Heats

of reaction of Cp*(PMe$_3$)Ir(C$_6$H$_5$)(H), Cp*(PMe$_3$)Ir(C$_6$H$_{11}$)(H), Cp*(PMe$_3$)Ir(H)(H) with HCl, CCl$_4$, CBr$_4$, and CH$_3$I – a solution thermochemical study of the C-H insertion reaction. *Journal of the American Chemical Society* **1987**, *109*, 3143–3145.

128 D. Nemcsok, K. Wichmann, G. Frenking, The significance of pi interactions in group 11 complexes with *N*-heterocyclic carbenes. *Organometallics* **2004**, *23*, 3640–3646.

129 P. B. Hitchcock, M. F. Lappert, P. Terreros, Synthesis of homoleptic tris(organo-chelate)iridium(III) complexes by spontaneous ortho-metallation of electron-rich olefin-derived N,N′-diarylcarbene ligands and the x-ray structures of fac-[Ir[CN(C$_6$H$_4$Me-p)(CH$_2$)$_2$NC$_6$H$_3$Me-p]$_3$] and mer-[Ir[CN(C$_6$H$_4$Me-p)(CH$_2$)$_2$NC$_6$H$_3$Me-p]$_2$[CN(C$_6$H$_4$Me-p)(CH$_2$)$_2$NC$_6$H$_4$Me-p]]Cl (a product of HCl cleavage). *Journal of Organometallic Chemistry* **1982**, *239*, C26–C30.

130 R. J. Holmes, et al. Saturated deep blue organic electrophosphorescence using a fluorine-free emitter. *Applied Physics Letters* **2005**, *87*, 243507.

131 X. F. Ren, et al. Ultrahigh energy gap hosts in deep blue organic electrophosphorescent devices. *Chemistry of Materials* **2004**, *16*, 4743–4747.

132 C. Schildknecht, et al. in Organic Light-Emitting Materials and Devices, Vol. IX, p. 59370E (SPIE, San Diego, CA, USA, **2005**).

133 C. W. Tang, S. A. Vanslyke, Organic electroluminescent diodes. *Applied Physics Letters* **1987**, *51*, 913–915.

134 C. Adachi, M. A. Baldo, M. E. Thompson, S. R. Forrest, Nearly 100% internal phosphorescence efficiency in an organic light-emitting device. *Journal of Applied Physics* **2001**, *90*, 5048–5051.

135 G. F. He, et al. High-efficiency and low-voltage p-i-n electrophosphorescent organic light-emitting diodes with double-emission layers. *Applied Physics Letters* **2004**, *85*, 3911–3913.

136 K. Ono, T. Yanase, M. Ohkita, K. Saito, Synthesis and properties of 9,9′-diaryl-4,5-diazafluorenes. A new type of electron-transporting and hole-blocking material in EL device. *Chemistry Letters* **2004**, *33*, 276–277.

4

Highly Efficient Red-Phosphorescent Iridium Complexes

Akira Tsuboyama, Shinjiro Okada, and Kazunori Ueno

This chapter summarizes our recent research on molecular design, photophysics of highly efficient red-phosphorescent cyclometalated iridium complexes and subsequent organic light-emitting diodes (OLEDs) using the complex as an emitter. We designed and synthesized tris-cyclometalated iridium complexes based on the known green-phosphorescent complexes, *fac*-Ir(thpy)$_3$ and *fac*-Ir(ppy)$_3$ [thpy = 1-(thiophen-2-yl)pyridinato, ppy = 1-phenylpyridinato]. The Ir(thpy)$_3$ family (the complexes with 2-(thiophen-2-yl)pyridine derivatives) exhibits large bathochromic shifts of the phosphorescence spectra by introducing large conjugation moieties and appropriate substituents, methyl, trifluoromethyl, thiophen-2-yl. However, phosphorescence quantum yield (Φ_p) of the red-emissive complexes (phosphorescence spectrum peak (λ_{max}) > 600 nm) becomes small, caused by a significant decrease of the radiative rate constant (k_r). In contrast, the complexes with 1-arylisoquinoline ligands are found to yield marked bathochromic shifts of λ_{max} and very high Φ_p. These complexes, Ir(piq)$_3$, Ir(tiq)$_3$, and Ir(fliq)$_3$ [piq = 1-phenylisoquinolinato, tiq = 1-(thiophen-2-yl)isoquinolinato and fliq = 1-(9,9-dimethyl-9*H*-fluoren-2-yl)isoquinolinato], emit through a triplet metal-to-ligand charge transfer (^{3}MLCT) excited state, leading to approximately one order of magnitude larger k_r value than those of the Ir(thpy)$_3$ family. The complex Ir(piq)$_3$ shows pure red-phosphorescence (λ_{max} = 620 nm) with very high Φ_p (0.26) in toluene at room temperature. We further examined substituent effects on Ir(piq)$_3$ to optimize the performance as a red-emitting material for OLEDs. The emission energy and the decay kinetics of the excited state of the complexes Ir(X$_1$/X$_2$piq)$_3$ (X$_1$=4F, 4CH$_3$O, 4CH$_3$; X$_2$=5CH$_3$) were successfully tuned by the nature and position of the substituents on the ligands. We consequently obtained the highly red-phosphorescent iridium complex, Ir(4F5mpiq)$_3$ (4F5mpiq = 1-(4-fluoro-5-methylphenyl)isoquinolinato), (λ_{max} = 607 nm and Φ_p = 0.32). The OLED device using Ir(4F5mpiq)$_3$ as a red emitter shows very high electroluminescence efficiency: power efficiency = 12.4 lm/W and external quantum efficiency, η_{ex} = 15.5% at 220 cd/m^2. The CIE chromaticity coordinates were estimated to be x = 0.66, y = 0.34, which is near the National Television Standard Committee (NTSC) red specification.

4.1
Introduction

Recently, organic light-emitting diodes (OLEDs) using phosphorescent transition metal complexes as emitters have been extensively studied [1, 2]. The phosphorescent OLEDs produce highly efficient electroluminescence, which significantly exceeds the widely accepted theoretical limitation of the external quantum efficiency (η_{ex}), 5%, for conventional fluorescence-based OLEDs. In OLED devices, the excited states electrogenerated by recombination of holes and electrons provide the statistical ratio of singlet:triplet excited states of 1:3. In view of intersystem crossing from the singlet to the triplet state, the phosphorescent OLED can utilize both the singlet and triplet energy for electroluminescence. Thus, the phosphorescent OLEDs afford, in principle, four times higher η_{ex} than that of the fluorescence-based OLEDs. Phosphorescent emitters usually used in the OLEDs are 5d transition metal complexes, which include both octahedral $5d^6$ complexes [Ir(III) [1b, 2], Re(I) [3], and Os(II) [4]] and square planer $5d^8$ complexes [Pt (II)] [1a, 5]. Strong spin–orbit coupling caused by 5d metal ions incorporated in the complexes leads to efficient intersystem crossing from a singlet to a triplet excited state. The spin-forbidden nature in the radiative relaxation from the triplet state is eliminated through mixing of the singlet and triplet excited state via spin–orbit coupling, leading to high phosphorescence efficiency [6].

In 1999, Baldo *et al.* succeeded in developing an efficient green-phosphorescent OLED with η_{ex} of 8%, using the iridium complex, *fac*-Ir(ppy)$_3$ [*fac*=facial, Ir(ppy)$_3$=tris(2-phenylpyridinato-C^2,N) iridium(III)], as an emissive dopant [1b]. The tris-cyclometalated iridium complex, *fac*-Ir(ppy)$_3$, was first reported by King *et al.* in 1985 [7]. Lamansky *et al.* [2a,b] reported in 2001 that a series of bis-cyclometalated iridium complexes with β-diketonato ancillary ligands such as (ppy)$_2$Ir(acac) (acac=acetylacetonato) gave a wide range of emission colors with high phosphorescence yields comparable to those of tris-cyclometalated iridium complexes. Since these initial OLED reports, many researchers and groups have directed their attention to phosphorescent cyclometalated iridium complexes and OLEDs using the complexes as emitters [2].

The cyclometalated iridium complexes provide distinct features applicable to phosphorescent dopants used in the OLEDs [2, 8]: The general features include that (1) the complexes with suitably designed ligands give high phosphorescence quantum yields in solutions, ranging from 0.1 to 0.5, (2) the high ligand field strength of a carbon atom bonding to the iridium atom provides high emission energy, which potentially covers the whole range of visible light from blue to red, (3) cyclometalating ligands are formally monoanionic and can thus be used to prepare neutral tris-coordinated complexes, (4) the ligands afford high design freedom, and (5) the complexes are thermally and chemically stable under ambient conditions.

This chapter summarizes our recent research on molecular design of highly efficient red-phosphorescent iridium complexes suitable for OLED devices [2g,o]. We have investigated the photophysical properties and nature of the emissive excited state of a new class of iridium complexes for highly efficient red-phosphorescence.

In addition to high phosphorescence efficiency, we have examined thermal stability of the complexes for the device fabrication and stable device performance.

4.2
Issues of Red-Emissive Materials

The emission quantum yield (Φ) from an emissive excited state to a ground state is generally expressed as

$$\Phi = \frac{k_r}{k_r + k_{nr}} \tag{4.1}$$

where k_r and k_{nr} are the radiative and nonradiative rate constant, respectively. The rate constants have a strong dependence on the energy gap (ΔE) between the emissive excited state and the ground state, formulated as [9]

$$k_{nr} = \alpha \exp(-\beta \Delta E) \quad [\alpha, \beta: \text{constant}] \tag{4.2}$$

$$k_r \propto A_{mn} = \frac{(\Delta E)^3}{3\pi\varepsilon_0 c^3 \hbar^4} |M_{mn}|^2 \tag{4.3}$$

Equation (4.2) is well known as "the energy gap law," which indicates that k_{nr} increases with a decrease of ΔE. A_{mn} in Eq. (4.3) is Einstein's A coefficient and M_{mn} is the emission transition moment between the mth and nth state. It is obvious from these equations that red emission with small ΔE tends to give larger k_{nr} and smaller k_r, leading to the lower emission quantum yield, Φ. Actually, from these reasons, efficient red-emissive materials practicable for low-power-consumption OLEDs have not been developed. For obtaining an efficient red-emissive material, suppressing both an increase of k_{nr} and a decrease of k_r with a decrease of ΔE is essential.

4.3
Red-Phosphorescent Iridium Complexes

Figure 4.1 shows the iridium complexes and their abbreviation used in this study. The iridium complexes, Ir(ppy)$_3$ and Ir(thpy)$_3$, are known to provide strong green-phosphorescence [7, 10]. In this study, we designed new ligands in order to obtain highly efficient red-phosphorescent iridium complexes.

4.3.1
Lowest Excited State of Iridium Complexes

In order to qualitatively understand the nature of the phosphorescent excited state of cyclometalated iridium complexes, the results of the HOMO/LUMO calculation
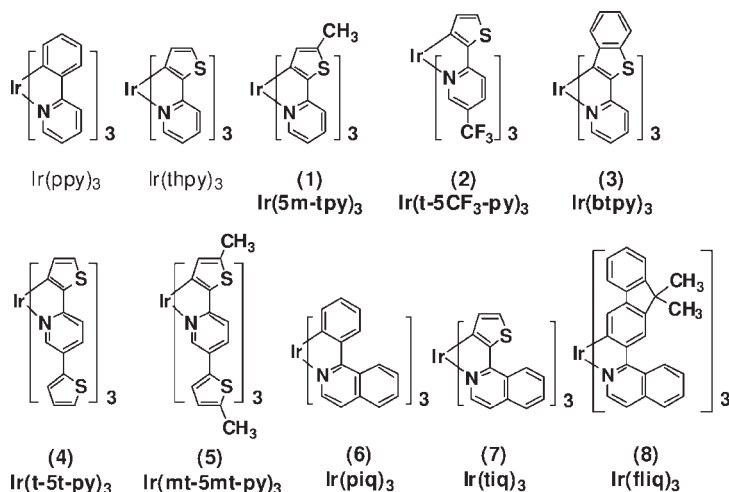
Fig. 4.1 Iridium complexes and their abbreviation used in this study.
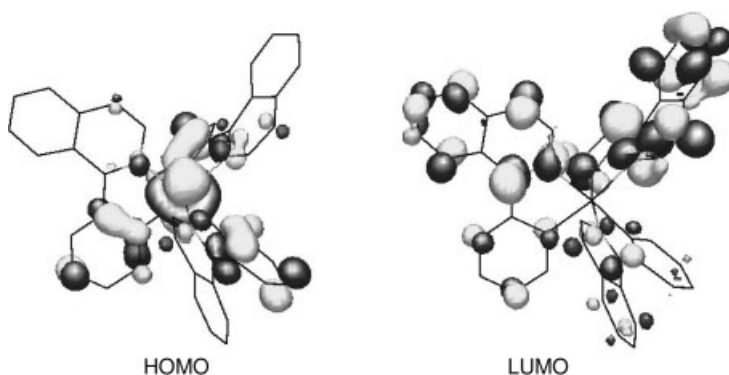
Fig. 4.2 HOMO and LUMO of Ir(piq)₃ **(6)**, calculated by the Hartree–Fock method.

[11] on Ir(piq)₃ **(6)** are shown in Fig. 4.2. The HOMO distributes over the phenyl ring and the iridium atom, while the LUMO is localized at the isoquinoline ring. Supposing that an emissive lowest excited state is formed via the LUMO←HOMO electronic transition, the excited state should be mixing of MLCT (metal-to-ligand charge transfer) [π^*(isoquinoline) $\leftarrow$ 5d orbital (Ir)] and LC (ligand-centered) π–π^* excited states.

The lowest triplet excited state, ϕ_T, responsible for phosphorescence, of the cyclometalated iridium complexes is principally expressed as [2g]

$$\phi_T = a\phi(\text{MLCT})_T + b\phi(\text{LC})_T \tag{4.4}$$

where a and b are the normalized coefficients and $\phi(\text{MLCT})_T$ and $\phi(\text{LC})_T$ are the wavefunctions of the MLCT and the ligand-centered triplet excited state, respec-

tively. Equation (4.4) implies that the phosphorescent excited state, ϕ_T, of the iridium complexes is an admixture of $\phi(MLCT)_T$ and $\phi(LC)_T$. The triplet excited state is attributed to the predominantly ^{3}MLCT excited state when $a > b$ and the predominantly $^3\pi$–π^* excited state when $a < b$. According to the previous paper [10], the phosphorescent excited states of Ir(ppy)$_3$ and Ir(thpy)$_3$ have been ascribed to the predominantly ^{3}MLCT and the predominantly $^3\pi$–π^* excited state, respectively.

In general, the k_r values of emission from the ^{3}MLCT-based excited state are two or three orders of magnitude larger than those from the $^3\pi$–π^* excited state [12]. The complex Ir(ppy)$_3$, with the predominantly ^{3}MLCT excited state, possesses especially large radiative rate constant, k_r (3×10^5 s^{-1}), relative to that of Ir(thpy)$_3$. The large k_r of Ir(ppy)$_3$ leads to high phosphorescence quantum yield (0.4) in toluene at room temperature. Thus, we focused our attention on designing metal complexes that provide red emission from an ^{3}MLCT excited state.

4.3.2
Molecular Design and Structure

The cyclometalating ligands for red-phosphorescent iridium complexes were designed and synthesized based on the following design concepts.

(1) For the iridium complexes having the emissive $^3\pi$–π^* excited state, the peak wavelength of phosphorescence is assumed to be essentially governed by the excited triplet energy of the ligand. This assumption leads to the consideration that, when the ligand L has a smaller triplet energy than thpyH, the iridium complex, Ir(L)$_3$, probably gives more red-shifted phosphorescence than Ir(thpy)$_3$. The triplet energy of the ligand should decrease with an increase in the π-conjugation system. Accordingly, we designed ligands with π-conjugation systems much larger than that of thpyH: 2,5-di(thiophene-2yl)pyridine (t-5t-pyH) and 2-benzo[b]thiophen-2-yl-pyridine (btpyH).

(2) Molecules having intramolecular donor–acceptor (DA) systems exhibit bathochromic shifts of both absorption and emission spectra. Originally, 2-thiophen-2-yl-pyridine (thpyH) itself has a DA character resulting from the interaction between an electron-rich group, thiophen, and an electron-deficient group, pyridine. Introduction of a methyl group (an electron donor) and a trifluoromethyl group (an electron acceptor) into the thiophene and pyridine moieties, respectively, is considered to enhance the DA character of the ligand. Thus, we have synthesized the following ligands: 2-(5-methyl-thiophen-2-yl)pyridine (5m-tpyH), 2,5-di(5-methyl-thiophen-2-yl)pyridine (mt-5mt-pyH), and 2-thiophen-2-yl-5-trifluoromethyl-pyridine (t-5CF$_3$-pyH).

(3) For the iridium complexes having the emissive ^{3}MLCT excited state, the HOMO level of the complex should not change unless the coordination structure significantly varies. The ^{3}MLCT energy is expected to effectively decrease when a complex has a ligand with lower LUMO level. Thus, the isoquionoline ring, more electron-accepting moiety than pyridine ring, is introduced to the ligands. Accordingly, we designed the 1-arylisoquinoline ligands: 1-phenylisoquinoline (piqH), 1-(thiophen-2-yl)isoquinoline (tiqH), and 1-(9,9-dimethyl-9 H-fluoren-2-yl)isoquinolinato (fliqH).

The complexes using the above-mentioned ligands were synthesized according to the previous paper [13], and were characterized with X-ray crystallography and ^{1}H NMR. The ^{1}H NMR spectra of all the complexes are consistent with a facial structure, which indicates that the number of coupled spins is equal to that of protons on one ligand as the three ligands are magnetically equivalent due to 3-fold symmetry [10]. The facial arrangement of the three ligands in Ir(piq)₃ (6) was confirmed by X-ray crystallography. Selected parameters of the molecular structure are listed in Table 4.1. Figure 4.3 displays the ORTEP diagram of Ir(piq)₃ (6) given

Table 4.1 Selected structural parameters for Ir(piq)₃**(6)**.

Bond lengths (Å)

Ir(1)–N(1)	2.135(5)
Ir(1)–C(15)	2.009(6)
N(1)–C(1)	1.374(8)
N(1)–C(9)	1.339(8)

Bond angles (deg)

N(1)–Ir(1)–C(15)	78.5(2)
Ir(1)–N(1)–C(1)	124.8(4)
Ir(1)–N(1)–C(9)	115.1(4)
Ir(1)–C(15)–C(10)	116.3(4)
C(1)–N(1)–C(9)	119.7(5)

Torsion angles (deg)

C(15)–Ir(1)–N(1)–C(9)	10.8(1)
N(1)–Ir(1)–C(15)–C(14)	173.2(1)
Ir(1)–N(1)–C(9)–C(8)	160.7(6)
C(3)–C(8)–C(9)–C(10)	–169.8(9)
C(8)–C(9)–C(10)–C(11)	22.9(2)
C(7)–C(8)–C(9)–N(1)	–161.2(9)
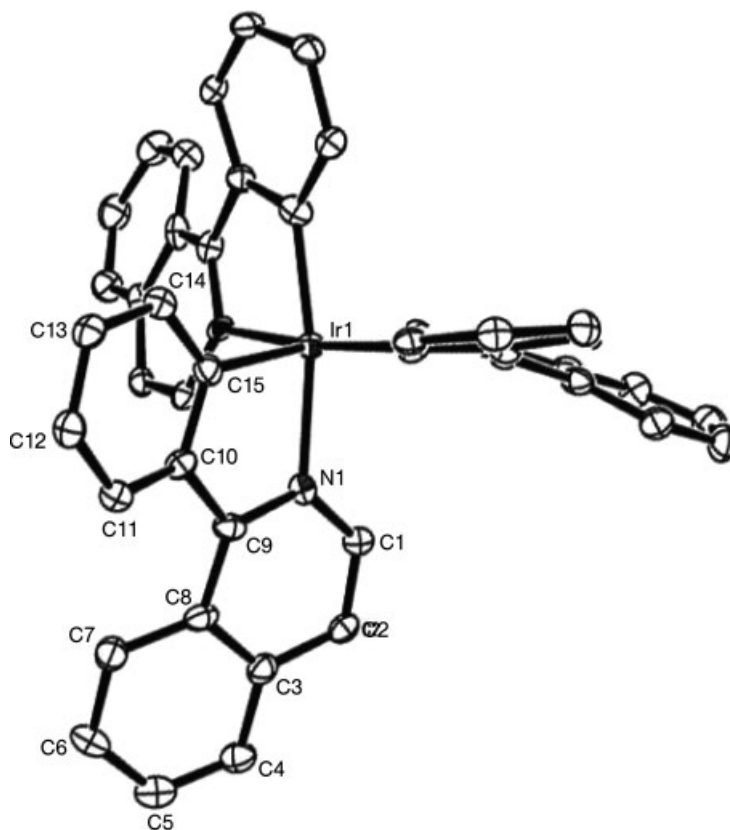
Fig. 4.3 ORTEP diagram of Ir(piq)₃ **(6)** with the thermal ellipsoids representing a 50% probability level. Hydrogen atoms are omitted for clarity.

by X-ray analysis, showing that the sterically crowded ligand results in large deformation with regard to the isoquinoline and phenyl rings. The deformation is caused by steric hindrance originating from the repulsion between two hydrogen atoms bound to the carbon atoms 7 and 11 (atom numbering is shown in Fig. 4.3). The X-ray data show not only a large dihedral angle [C(8)–C(9)–C(10)–C(11) = 23°] between the two rings, but also a strongly deformed isoquinoline ring out of the plane with a dihedral angle [C(7)–C(8)–C(9)–N(1)] of approximately 161°.

4.3.3
Phosphorescence Spectra

Table 4.2 summarizes the phosphorescence properties of the iridium complexes in toluene at room temperature. Figure 4.4(A) shows the phosphorescence spectra of Ir(thpy)₃ and of the complexes **(2)–(5)**. The lowest triplet excited (T₁) state of

Table 4.2 Phosphorescence properties of the iridium complexes.

	Ir(ppy)$_3$	Ir(thpy)	(1)	(2)	(3)	(4)	(5)	(6)	(7)	(8)
λ_{max}(nm)	514	550	558	563	596	613	627	620	644	652
τ(μs)	1.3	2.4	1.0	1.1	4.0	4.6	4.7	1.1	0.7	0.7
Φ_p	0.4	0.17	0.08	0.19	0.12	0.12	0.08	0.26	0.17	0.19
$k_r \times 10^{-5}$ (s^{-1})[a]	3.1	0.7	0.8	1.7	0.3	0.3	0.2	2.3	2.3	2.6
$k_{nr} \times 10^{-5}$ (s^{-1})[a]	4.6	3.5	9.3	7.2	2.2	1.9	2	6.6	11.2	10.9
Lowest excited state	^{3}MLCT	$^3\pi$–π*	$^3\pi$–π*	$^3\pi$–π*	$^3\pi$–π*	$^3\pi$–π*	$^3\pi$–π*	^{3}MLCT	^{3}MLCT	^{3}MLCT

All data are measured in N$_2$-saturated toluene solutions (10^{-6} M) at room temperature. λ_{max}: emission maximum peak, τ: emission lifetime Φ_p: phosphorescence quantum yield.

a k_r and k_{nr} (radiative and nonradiative rate constant) are calculated from the following equation by assuming $\Phi_{isc} = 100\%$: $\Phi_p = \Phi_{isc} \cdot k_r/(k_r + k_{nr})$, $\tau = 1 / (k_r + k_{nr})$
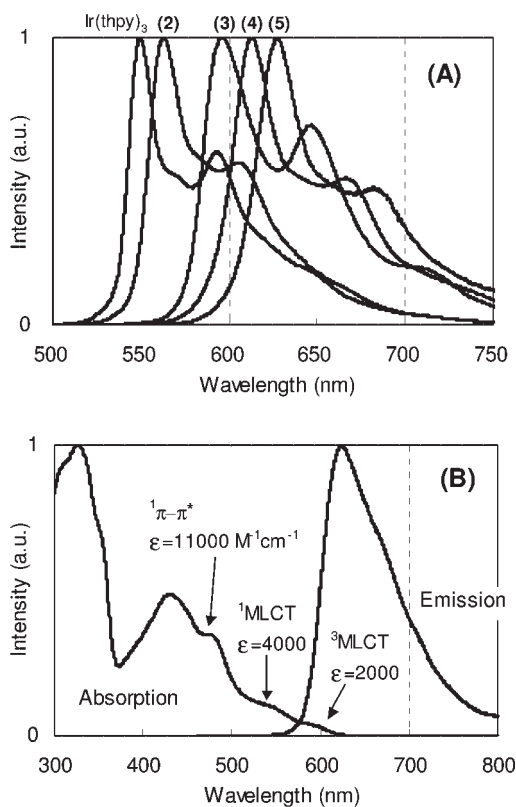
Fig. 4.4 (A) Phosphorescence spectra of Ir(thpy)$_3$ and **(2)**–**(5)**. (B) Absorption and phosphorescence spectra of Ir(piq)$_3$ **(6)** in N$_2$-saturated toluene solutions (10^{-6} M) at room temperature.

Ir(thpy)$_3$ has been assigned to the predominantly ligand-centered $^3\pi$–π^* state in terms of the distinct vibronic progression and solvent effects in the phosphorescence spectrum [2g, 10]. As the phosphorescence spectrum shapes of **(1)**–**(5)** are quite similar to that of Ir(thpy)$_3$, the phosphorescence of these complexes can also be attributed to the emission from the predominantly $^3\pi$–π^* state.

The phosphorescence spectra of the complexes with a large conjugation system, Ir(btpy)$_3$ **(3)** and Ir(t-5t-py)$_3$ **(4)**, are markedly red-shifted by 46 and 63 nm, respectively, in comparison to that of Ir(thpy)$_3$. The iridium complexes with methyl substituents, Ir(5m-tpy)$_3$ **(1)** and Ir(mt-5mt-py)$_3$ **(5)**, are also found to exhibit moderate red-shifting of the phosphorescence spectra: the phosphorescence peaks of the former and the latter are red-shifted by 8 and 14 nm, respectively, in comparison with those of the base complexes, Ir(thpy)$_3$ and Ir(t-5t-py)$_3$ **(4)**. These findings indicate that the introduction of the methyl group/s into the thienyl moiety enhances the DA character of the ligand in the Ir complexes, leading to the red shift of the phosphorescence spectra. The phosphorescence spectrum peak of the complex Ir(t-5CF$_3$-py)$_3$ **(2)** is located at the wavelength longer than that of Ir(thpy)$_3$ by 13 nm. These results lead to the conclusion that the phosphorescence spectra of the iridium complexes are red-shifted when their ligands have the large π-conjugation space and/or strong intramolecular DA interaction.

On the other hand, the phosphorescent T$_1$ states of the complexes **(6)**–**(8)** are assigned to the predominantly ^{3}MLCT excited state. Figure 4.4(B) shows the absorption and the phosphorescence spectrum of Ir(piq)$_3$ **(6)** in toluene solution at room temperature. The intense absorption band ($\varepsilon > 10^4$ M^{-1} cm^{-1}) located at 400–480 nm can be assigned to the spin-allowed $^1\pi$–$\pi^* \leftarrow$ S$_0$ transition. In addition, the weak and broad absorption bands ($\varepsilon < 4000$ M^{-1} cm^{-1}) in the wavelength region longer than 520 nm were observed. According to the previous papers, these weak absorption bands located at longer wavelengths have been assigned to the ^{1}MLCT $\leftarrow$ S$_0$ and ^{3}MLCT $\leftarrow$ S$_0$ transitions [2a, 10]. Thus, the broad absorption shoulders at 550 and 600 nm observed for the Ir(piq)$_3$ **(6)** have been ascribed to the ^{1}MLCT $\leftarrow$ S$_0$ ($\varepsilon = 4000$ M^{-1} cm^{-1}) and ^{3}MLCT $\leftarrow$ S$_0$ ($\varepsilon = 2000$ M^{-1} cm^{-1}) transitions, respectively. The phosphorescence spectrum of **(6)** does not have a distinct vibronic fine structure in contrast to those of the complexes **(1)**–**(5)**. Since emission bands from MLCT states are generally broad and featureless [2a], the phosphorescence of **(6)** can be assigned to the emission from the predominantly ^{3}MLCT excited state.

It should be noted that the complexes **(6)**–**(8)** with the aryl-isoquinoline ligand exhibit large bathochromic shifts (ca. 90 nm) compared to the base complexes, Ir(ppy)$_3$ and Ir(thpy)$_3$. The 1-arylisoquinoline ligands can effectively reduce the ^{3}MLCT excited energy of cyclometalated iridium complexes by the strong electron-accepting character of the isoquinoline moiety.

4.3.4
Phosphorescence Yield

Ir(piq)$_3$ **(6)** produces the highest phosphorescence quantum yield ($\Phi_p = 0.26$) with pure red emission ($\lambda_{max} = 620$ nm) among the red-emissive iridium complexes

(4)–(8). The ^{3}MLCT complexes **(6)–(8)** give 1.5–2 times higher Φ_p than the $^3\pi$–π^* complexes **(4)–(5)**. These high Φ_p of the ^{3}MLCT complexes are based on the large radiative rate constants, k_r, compared to those of the $^3\pi$–π^* complexes.

For ease of discussion, we divided the complexes studied here into two groups: the Ir-thiophene family, **(1)–(5)** and Ir(thpy)$_3$, and the Ir-isoquinoline family, **(6)–(8)** and Ir(ppy)$_3$. The former and the latter produce phosphorescence from the predominantly $^3\pi$–π^* and the predominantly ^{3}MLCT excited state, respectively.

Figure 4.5(A) shows the phosphorescence yield, Φ_p, versus the emission energy of phosphorescence, E_{em}. It is found that (1) Φ_p ranges from 0.08 to 0.4 and roughly tends to increase with an increase in E_{em} and (2) Φ_p of the Ir-isoquinoline family is larger than that of the Ir-thiophene family in the E_{em} region 15,000–16,500 cm^{-1}.

Figure 4.5(B) shows the plot of k_r versus E_{em}. The k_r values of the Ir-thiophene family, **(1)–(5)** and Ir(thpy)$_3$, increase with an increase in E_{em}, while those of the Ir-isoquinoline family are almost independent of E_{em}. According to the electronic transition theory, the k_r value is proportional to the square of the electric dipole transition moment, $\mathbf{M}_{T-S}$ (see Eq. (4.3)). The first-order perturbation theory gives an approximate expression for $\mathbf{M}_{T-S}$ [9b]:

$$\mathbf{M}_{T-S} = \sum_n \beta_n \left\langle {}^1\varphi_n \left| \mathbf{M} \right| {}^1\varphi_0 \right\rangle \tag{4.5}$$

where $^1\phi_n$ and $^1\phi_0$ are, respectively, the wavefunctions of the S$_n$ and the S$_0$ state, and $\mathbf{M}$ is the electric dipole vector. With the use of the spin–orbit coupling operator, $\mathbf{H}_{so}$, and the wavefunction of the lowest excited triplet state, $^3\phi_1$, β_n is formulated as
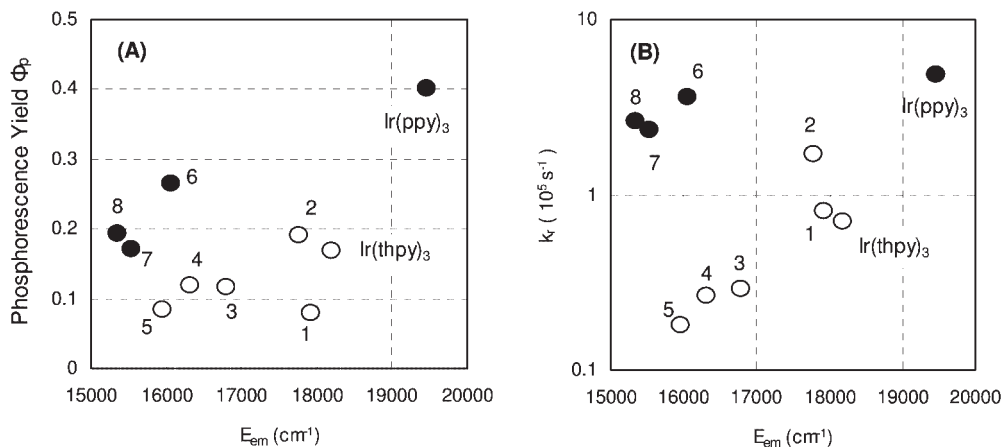
Fig. 4.5 Plots of phosphorescence yield Φ_p (A) and radiative rate constant k_r (B), obtained with the Ir-thiophene family, **(1)–(5)** (open circle), and the Ir-isoquinoline family, **(6)–(8)** (closed circle), represented as a function of the emission energy of phosphorescence, E_{em} (in reciprocal centimeters), at 298 K.

$$\beta_n = \frac{\left\langle {}^1\varphi_n \left| \boldsymbol{H}_{\text{SO}} \right| {}^3\varphi_1 \right\rangle}{{}^1E_n - {}^3E_1} \tag{4.6}$$

where ${}^1E_n$ and ${}^3E_1$ are the energies of the S_n state and the lowest excited triplet state, respectively.

Here, we assume a three-state model, S_1, T_1, and S_0. Then, Eq. (4.5) is simply expressed as

$$M_{T-S} = \frac{\left\langle {}^1\varphi_1 \left| \boldsymbol{H}_{\text{SO}} \right| {}^3\varphi_1 \right\rangle \left\langle {}^1\varphi_1 \left| \boldsymbol{M} \right| {}^1\varphi_0 \right\rangle}{{}^1E_1 - {}^3E_1} = \frac{\alpha}{{}^1E_1 - {}^3E_1} \tag{4.7}$$

Equation (4.7) predicts that, when α ($= \langle {}^1\phi_1 | \boldsymbol{H}_{SO} | {}^3\phi_1 \rangle \langle {}^1\phi_1 | \boldsymbol{M} | {}^1\phi_0 \rangle$) is approximately constant, k_r increases with a decrease in the energy difference, (${}^1E_1 - {}^3E_1$).

We find that k_r of the Ir-thiophen family increases with an increase in E_{em}. This fact is explained by assuming that the S_1 energy does not differ significantly among the complexes **(1)–(5)** and Ir(thpy)$_3$, and thus, the energy difference, (${}^1E_1 - {}^3E_1$), increases with the decrease in E_{em}. Actually, in the complexes **(1)–(5)**, spin-allowed $S_1 \leftarrow S_0$ absorption bands [$\log(\varepsilon) = \sim 4.0$] are located at 460–482 nm [2g]; however, phosphorescence ($S_0 \leftarrow T_1$) exhibits large bathochromic shifts ranging from 558 nm to 627 nm. These data provide evidence that the energy difference (${}^1E_1 - {}^3E_1$) increases with the decrease in E_{em}, and therefore, k_r increases with an increase in E_{em}.

On the other hand, the k_r values of the Ir-isoquinoline family are almost independent of E_{em}. Presumably, the energy difference (${}^1E_1 - {}^3E_1$) is approximately constant among the complexes, **(6)–(8)** and Ir(ppy)$_3$. From the absorption data of **(6)–(8)** and Ir(ppy)$_3$, the energy differences between S_1 (^{1}MLCT) and T_1 (^{3}MLCT) are found to be small, ranging from 1370 to 1520 cm^{-1} [2g]. As mentioned above, we consider that the plot of k_r versus E_{em} in Fig. 4.5(B) is qualitatively interpreted in terms of Eq. (4.7).

The red-emissive complexes of the Ir-isoquinoline family, **(6)–(8)**, give higher phosphorescence quantum yields than the complexes of the Ir-thiophene family, **(3)–(5)**. The high quantum yields of **(6)–(8)** are partly ascribed to the large k_r values, ca. 3×10^5 s^{-1}, independent of E_{em}.
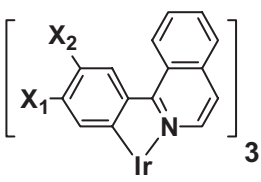
In summary, the iridium complexes with the 1-arylisoquinoline ligands shows marked red shifts of λ_{max} and very high Φ_p (0.19–0.26). These complexes are found to possess predominantly ^{3}MLCT excited states and have the k_r values one order of magnitude larger than those of the Ir-thiophene family. The complex Ir(piq)$_3$ **(6)** shows particularly high Φ_p (0.26) with pure red emission ($\lambda_{\text{max}} = 620$ nm).

4.3.5
Substituent Effects of Ir(piq)₃ (6)

Substituent effects on the photophysical properties of phosphorescent transition metal complexes have been widely investigated [13, 14]. The phosphorescence spectra and their emissive excited states were finely tuned by the nature of the

Table 4.3 Electrochemical and phosphorescence properties of the iridium complexes with the substituted ligands[a]

X$_1$=H, CH$_3$, F, CH$_3$O
X$_2$=H, CH$_3$

		(9) F H	(10) F CH$_3$	(11) CH$_3$O H	(6) H H	(12) CH$_3$ H	(13) H CH$_3$
	X_1	F	F	CH$_3$O	H	CH$_3$	H
	X_2	H	CH$_3$	H	H	H	CH$_3$
$E_{ox}{}^b$	(V)	0.67	0.54	0.43	0.45	0.44	0.32
$E_{red}{}^b$	(V)	−2.08	−2.17	−2.28	−2.18	−2.25	−[c]
λ_{max}	(nm)	598	607	610	620	621	635
Φ_p		0.4	0.32	0.28	0.26	0.30	0.21
τ	(μs)	2.43	1.65	1.81	1.12	1.29	0.97
$k_r \times 10^{-5}$	(s^{-1})	1.6	1.9	1.5	2.3	2.3	2.2
$k_{nr} \times 10^{-5}$	(s^{-1})	2.5	4.1	4.0	6.6	5.4	8.1
Hammett constant^d		0.34	0.17	0.12	−	−0.07	−0.17

a All the phosphorescence properties are observed with 428 nm excitation in N$_2$-saturated toluene solutions at room temperature. The Φ_p values measured with 428 nm excitation are different from those with 464 nm excitation described in the original paper [2o]. The difference is due to the excitation wavelength dependence of Φ_p.
b Redox potentials (E_{ox} and E_{red}) are measured in the following conditions: reference electrode, Ag/Ag$^+$; working electrode, glassy carbon; counter electrode, Pt; solution, 0.1 M n-Bu$_4$NClO$_4$ in THF solutions for E_{ox} and CH$_2$Cl$_2$ solutions for E_{red}.
c Not detected.
d Hammett constant (σ_p, σ_m) with respect to the carbon atom bonding to Ir.

ligand substituents. We tried to optimize the performance of Ir(piq)$_3$ **(6)** as a red-emissive dopant suitable for OLED devices by examining the substituent effect on the phosphorescence properties [20].

Table 4.3 shows the iridium complexes studied here and lists their electrochemical and photophysical properties, and Hammett substituent constant, σ [15]. The complexes, **(9)–(13)**, have the 1-phenylisoquinoline ligands substituted with methyl group, methoxy group, and/or fluorine atom on the phenyl ring. For the complex **(10)** with the ligand di-substituted at a *meta* and *para* position, the sum of σ_m and σ_p was used for the Hammett constant.

Tuning Redox Potential and Emission Energy   The substituents have significant influence on both electrochemical properties and phosphorescence energy. The
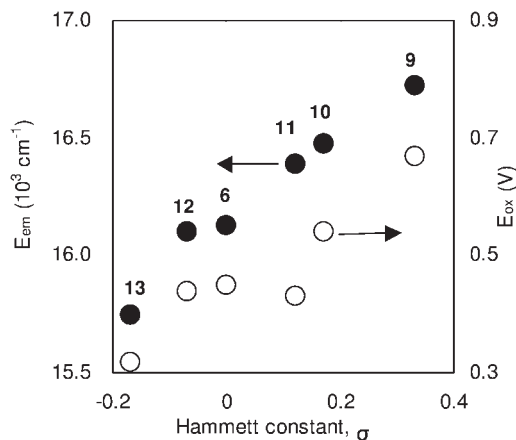
Fig. 4.6 Plots of emission energy of phosphorescence (E_{em} in reciprocal centimeters) and oxidation potential (E_{ox}) versus Hammett constant (σ).

complex with an electron-withdrawing group (F atom) shows higher E_{ox} than the complex with an electron-donating group (CH_3 and CH_3O group). On the other hand, effects of the substituents on E_{red} are relatively weak. Since the MO calculation suggests that the HOMO of Ir(piq)$_3$ **(6)** mainly distributes on the phenyl ring (see Fig. 4.2), the substituents attached to the phenyl ring are expected to have a direct effect on the electronic state of the HOMO. The oxidation potentials (E_{ox}) decrease along the following series: **(9)** (4F) > **(10)** (4F5m) > **(6)** (unsubstituted) > **(12)** (4CH$_3$) > **(13)** (5CH$_3$). This observation can be rationalized by the use of the Hammett constant, σ, which exhibits characteristics of the electronic effect of the substituents. Figure 4.6 shows the plots of E_{ox} and the emission energy of phosphorescence (E_{em}) versus the Hammett constant (σ). Electron-withdrawing substituents exhibit a positive σ value and electron-donating ones have negative values. It is found from Fig. 4.6 that (1) E_{ox} tends to increase with an increase of the electron-withdrawing character and (2) E_{em} of the complexes changes in response to E_{ox}. The clear correlation between E_{ox}/E_{em} and the Hammett constant demonstrates that the electron-donating/withdrawing character of the substituents controls the HOMO levels to change the emission energy, E_{em}. In other words, the emission color of the relevant substituted iridium complexes can be predicted and designed with the use of the Hammett constant.

Tuning the Kinetics of the Excited State Decay   Table 4.3 shows the significant change of Φ_p (0.21–0.40) and τ (0.97–2.43 µs), indicating that the nature of the substituents also affects the decay kinetics of the excited state.

The nonradiative rate constant, k_{nr}, tends to increase with a decrease of the emission energy of phosphorescence, E_{em}. Figure 4.7(A) shows a plot of nonradiative rate constant, $\ln(k_{nr})$, as a function of the emission energy, E_{em}, showing the
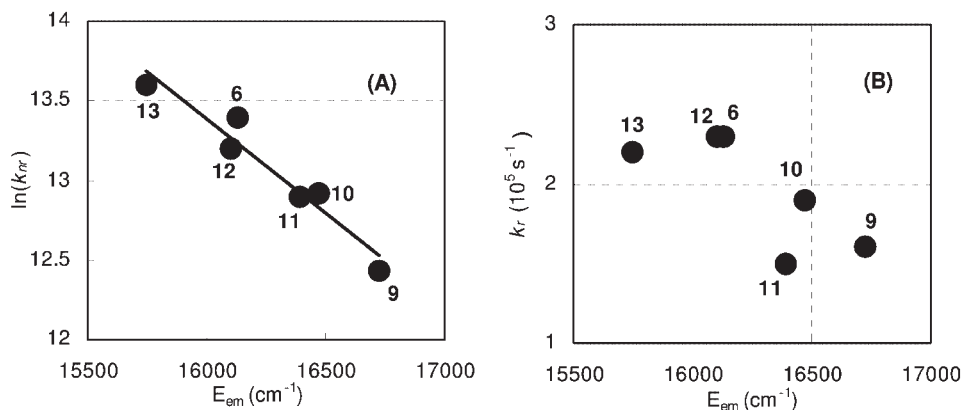
Fig. 4.7 Plots of the nonradiative rate constant, ln(k_{nr}) (A) and radiative rate constant k_r (B) as a function of the emission energy of phosphorescence, E_{em} (in reciprocal centimeters).
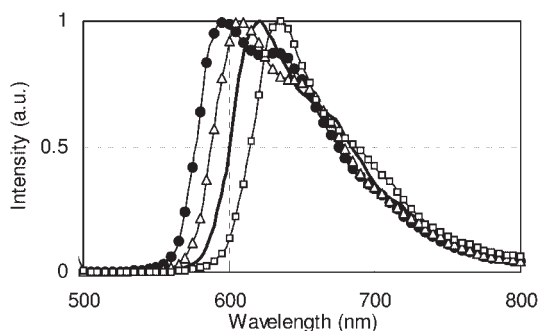
Fig. 4.8 Normalized phosphorescence spectra of **(6)** (thick line), **(9)** (closed circle), **(10)** (triangle), and **(13)** (square) in N_2-saturated toluene solutions at room temperature.

relation is in good agreement with the "energy gap law"(see Section 2). The "energy gap law" on the nonradiateive transition is based on the vibrational overlap between the excited state and the ground state, and k_{nr} is a function of an electronic coupling term and a Franck–Condon overlap integral. The linear correlation suggests that the iridium complexes with the substituted 1-phenylisoqunoline ligands possess similar vibrational and electronic components [14e].

Figure 4.7(B) shows a plot of k_r versus E_{em}. The k_r values roughly tend to increase with a decrease of E_{em}, but the E_{em} dependence of k_r is weaker relative to that of k_{nr}. In general, the energy gap (ΔE) dependence of k_r values is expressed by the Einstein A coefficient (see Eq. (4.3)). However, the k_r values of our iridium complexes have an opposite tendency against Einstein's equation. This result suggests that, by introducing the substituents, the nature of the emissive excited states of the complexes varies to some extent. Figure 4.8 reproduces the phosphorescence

spectra of the iridium complexes **(6)**, **(9)**, **(10)**, and **(13)**, showing that the phosphorescence spectrum with higher E_{em} possesses more distinct vibronic progression. As mentioned previously, phosphorescence originating from the $^3\pi$–$\pi*$ excited state generally shows characteristic vibronic progression. Thus, the phosphorescence with higher E_{em} originates from the T_1 state with a relatively larger contribution of the π–$\pi*$ character to the predominantly ^{3}MLCT excited state. In addition, a $^3\pi$–$\pi*$-based phosphorescence generally gives smaller k_r than that based on an ^{3}MLCT excited state. As a result, the phosphorescence with higher E_{em} exhibits relatively lower k_r.

From the above discussion, it follows that fluorine substituent enhances the $^3\pi$–$\pi*$ character in the predominantly ^{3}MLCT excited state. The electron-withdrawing fluorine substituent presumably changes the electronic state of the HOMO, which originally distributes over the phenyl ring and iridium atom, to increase electron density on the phenyl ring and decrease that on the iridium atom. From this point of view, it is likely that the electron density change in the ground state results in an increase of the $^3\pi$–$\pi*$ component [isoquinoline←phenyl] as well as a decrease of the ^{3}MLCT component [isoquinoline←Ir] in the excitation transition.

The phosphorescence quantum yields, Φ_p, listed in Table 4.3 have a tendency to increase with an increase of the E_{em} value. The Φ_p tendency is mainly attributed to the k_{nr}–E_{em} correlation based on the "energy gap law" (see Fig. 4.7(A)). The complexes **(9)** and **(10)** with higher E_{em}, therefore, afford higher Φ_p (0.32–0.40).

In summary, the substituents attached to the phenyl group of $Ir(piq)_3$ **(6)** can finely tune the emission energy of the complexes. We also found that the substitutions affect the contribution of the $^3\pi$–$\pi*$ state to the predominantly ^{3}MLCT excited state, leading to the effectual control of the phosphorescence quantum yield. We have consequently obtained the highly red-phosphorescent complex, $Ir(4F5mpiq)_3$ **(10)** (tris[1-(4-fluoro-5-methylphenyl)isoquinolinato-C^2,N] iridium(III)) ($\Phi_p = 0.32$ and $\lambda_{max} = 607$ nm).

4.4
OLED Device

4.4.1
Thermal Stability

A vacuum deposition method is very convenient for making OLED devices. In this fabrication process, compounds used for the devices are exposed to high temperatures (250–350 °C) when sublimed under vacuum. Thus, OLED materials should be stable even at high temperatures. When materials decompose in the deposition process, decomposition products may contaminate the OLED and cause poor device performance. Therefore, we have to carefully investigate thermal stability of the iridium complex as a phosphorescent dopant.

We measured the decomposition temperatures of the bis- and tris-cyclometalated iridium complexes [$(ppy)_2Ir(acac)$ and $Ir(ppy)_3$] and $Ir(acac)_3$ in

order to examine whether or not these complexes are suitable for making OLED devices by vacuum deposition methods. The decomposition temperature was determined from the TG/DTA curves measured under nitrogen flow. The weight reduction observed in the TG curves, accompanying exothermic reaction detected in the DTA curve, is attributed to the thermal decomposition. The 5% weight-reduction temperatures ($\Delta T_{5\%}$) of these complexes are significantly different: 413 °C for Ir(ppy)$_3$, 341 °C for (ppy)$_2$Ir(acac), and only 243 °C for Ir(acac)$_3$. These results indicate that the complexes with the acetylacetonate ligand tend to thermally decompose at relatively low temperatures. It is likely that the homoleptic cyclometalated iridium complexes are thermally more stable than the acetylacetonate complexes.

Figure 4.9 shows the TG/DTA curves of Ir(piq)$_3$ **(6)** and Ir(4F5mpiq)$_3$ **(10)**, indicating that $\Delta T_{5\%}$ of the complexes are 429 °C for **(6)** and 415 °C for **(10)**, respectively. The decomposition of the complexes began at 360–380 °C. On the other hand, the sublimation temperatures of the complexes were estimated to be 280–300 °C in a pressure of 10^{-4} Pa. The significantly lower sublimation temperatures than the decomposition temperatures of the complexes make it possible to fabricate safely stable OLED devices, because very little decomposed product can be contaminated in the emission layers of the OLEDs. In fact, the complexes can be sublimed in a vacuum chamber without thermal decomposition. We concluded that the com-
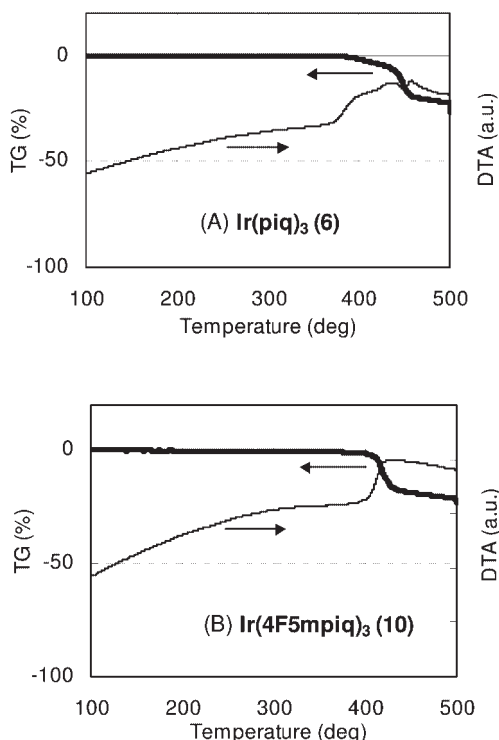
Fig. 4.9 TG/DTA curves of Ir(piq)$_3$ **(6)** (A) and Ir(4F5mpiq)$_3$ **(10)** (B)

plexes, Ir(piq)$_3$ **(6)** and Ir(4F5mpiq)$_3$ **(10)**, are the suitable red-emissive materials for OLEDs fabricated by the vacuum deposition method.

4.4.2
Red OLED using Ir(4F5mpiq)$_3$ (10)

The complex Ir(4F5mpiq)$_3$ **(10)** shows red phosphorescence with high quantum yield (Φ_p=0.32 and λ_{max}=607 nm). In our experience, OLEDs doped with iridium complexes typically exhibit an almost linear relationship between the external quantum efficiency and the phosphorescence quantum yield of the emissive dopant. Thus, the complex **(10)** is a promising candidate as a highly efficient red dopant in OLEDs.

Figure 4.10(A) shows the OLED device construction with the use of **(10)** as an emitter. The device is composed of four layers: a hole transporting layer (HTL), an emission layer (EML), an electron transporting layer (ETL), and electron injection layer (EIL). The materials used in each layer are shown in Fig. 4.10(A).

The device was fabricated by a typical vacuum deposition method. The materials for each layer were vacuum-deposited in turn on an ITO-coated glass substrate at a pressure of 10^{-4} Pa, and aluminum was deposited over the KF layer as a cathode. The emissive layer was formed by co-deposition of the phosphorescent dopant, **(10)**, and the host compound, CBP. The concentration of **(10)** in EML was 10 wt.%, which produced the optimum external quantum efficiency, η_{ex}. At concentrations more than 10 wt.%, η_{ex} tends to decrease probably due to concentration quenching.

Figures 4.10(B) and (C) show the plot of luminance versus applied voltage and the plots of power efficiency and external quantum efficiency versus luminance of the OLED. Table 4.4 summarizes the performance comparison between the devices using Ir(piq)$_3$ **(6)** and Ir(4F5mpiq)$_3$ **(10)**. The OLED device using **(10)** as an emitter shows very high efficiency, power efficiency=12.4 lm/W and external quantum efficiency, η_{ex}=15.5% at 220 cd/m^2. These electroluminescence (EL) efficiencies are significantly larger than those of the nonsubstituted iridium complex **(6)**. The CIE chromaticity coordinates are estimated to be x=0.66, y=0.34, which is near the National Standard Committee (NTSC) red specification. To the best of our knowledge, the Ir(4F5mpiq)$_3$ **(10)** device demonstrates highest published EL efficiency with red emission.

4.5
Summary

We have designed and synthesized cyclometalated iridium complexes suitable for highly efficient red OLEDs. The phosphorescence of Ir(thpy)$_3$ is shifted to red by introducing the large conjugation moieties and the donor/acceptor substituents onto the ligand. The k_r value of phosphorescence of the Ir(thpy)$_3$ family markedly decreases with a decrease in the phosphorescence energy. As a result, the
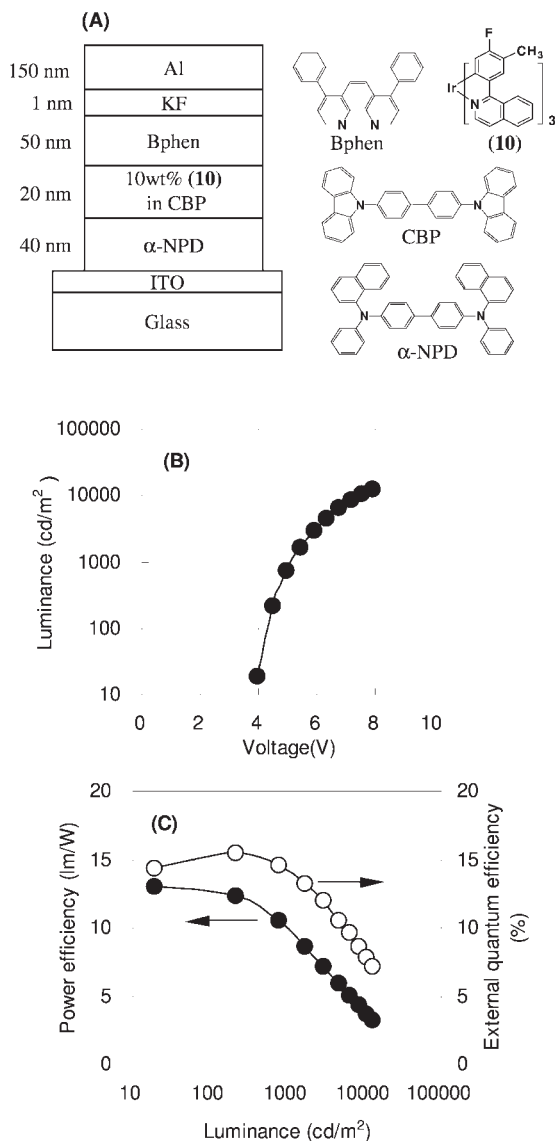
Fig. 4.10 (A) OLED construction and molecular formulae of the compounds used in each layer (Bphen: 4,7-diphenyl-[1,10]phenanthroline, CBP: 4,4-*N*,*N*-dicarbazolebiphenyl, α-NPD: 4,4′-bis-[*N*-(1-naphthyl)-*N*-phenylamino]biphenyl), (B) plot of luminance versus voltage, and (C) plots of power efficiency and external quantum efficiency versus luminance of the OLED device using **(10)** as an emissive dopant.

Table 4.4 Performance of the OLEDs using Ir(piq)$_3$**(6)** and Ir(4F5mpiq)3 **(10)** as phosphorescent dopants. The properties were measured at a luminance of 220 cd/m^2.

Dopant	Power efficiency (lm/W)	External quantum efficiency (%)	CIE coordinate (x, y)
Ir(piq)$_3$ **(6)**	7.2	10.0	0.68, 0.32
Ir(4F5mpiq)$_3$ **(10)**	12.4	15.5	0.66, 0.34

red-emissive complexes of the Ir(thpy)$_3$ family give relatively low phosphorescence quantum yield (Φ_p=0.08–0.12). On the other hand, the Ir-isoquinoline family, Ir(piq)$_3$ **(6)**, Ir(tiq)$_3$ **(7)**, and Ir(fliq)$_3$ **(8)** produces efficient pure-red emission (λ_{max} > 620 nm, Φ_p=0.17–0.26) originating from the predominantly ^{3}MLCT excited states. The substituents attached to the phenyl group of Ir(piq)$_3$ **(6)** can finely tune the emission energy of the complexes. We also found that the substitutions affect the contribution of the $^3\pi$–π^* excited state to the emissive ^{3}MLCT excited state, leading to control of the phosphorescence quantum yield. We consequently succeeded in obtaining the highly efficient red-phosphorescent complex, Ir(4F5mpiq)$_3$ **(10)** (tris[1-(4-fluoro-5-methylphenyl)isoquinolinato-C^2,N] iridium(III)) (Φ_p=0.32 and λ_{max}=607 nm). The multilayered OLED device doped with **(10)** yields very high electroluminescence efficiency (12.4 lm/W and η_{ex}=15.5% at 220 cd/m^2) as well as saturated red emission (x=0.66, y=0.34,) that satisfies the NTSC specifications.

This study was conducted by the material group of OD project in Leading-Edge Technology Development Headquarters, Canon Inc.

References

1 (a) M. A. Baldo, D. F. O'Brien, Y. You, A. Shoustikov, S. Sibley, M. E. Thompson, S. R. Forrest, *Nature*, **1998**, *395*, 151–154. (b) M. A. Baldo, S. Lamansky, P. E. Burrous, M. E. Thompson, S. R. Forrest, *Appl. Phys. Lett.*, **1999**, *75*, 4–6.

2 (a) S. Lamansky, P. Djurovich, D. Murphy, F. Abdel-Razzaq, H. Lee, C. Adachi, P. E. Burrows, S. R. Forrest, M. E. Thompson, *J. Am. Chem. Soc.*, **2001**, *123*, 4304–4312. (b) S. Lamansky, P. Djurovich, D. Murphy, R. Kwong, Abdel-Razzaq, I. Tsyba, M. Bortz, B. Mui, R. Bau, M. E. Thompson, *Inorg. Chem.*, **2001**, *40*, 1704–1711. (c) C. Adachi, M. A. Baldo, S. R. Forrest, S. Lamansky, M. E. Thompson, R. C. Kwong, *Appl. Phys. Lett.*, **2001**, *78*, 1622–1624. (d) V. V. Grushin, N. Herron, D. D. LeCloux, W. J. Marshall, V. A. Petrov, Y. Wang, *Chem Commun.*, **2001**, 1494–1495. (e) C. Adachi, M. A. Baldo, M. E. Thompson, S. R. Forrest, *J. Appl. Phys.*, **2001**, *90*, 5048–5051. (f) J. C. Ostrowski, M. R. Robinson, A. J. Heeger, G. C. Bazan, *Chem. Commun.*, **2002**, 784–785. (g) A. Tsuboyama, H. Iwawaki, M. Furugori, T. Mukaide, J. Kamatani, S. Igawa, T. Moriyama, S. Miura, T. Takiguchi, S. Okada, M. Hoshino, K. Ueno, *J. Am. Chem. Soc.*, **2003**, *125*, 12971–12979. (h) Md. K. Nazeeruddin, R. Humphry-Baker, D. Berner, S. Rivier, L. Zuppiroli, M. Graetzel, *J. Am. Chem. Soc.*, **2003**, *125*, 8790–8797. (i) A. B. Tamayo, B. D. Alleyne, P. I. Djurovich, S. Lamansky, I. Tsyba, N. N. Ho, R. Bau, M. E. Thompson, *J. Am. Chem. Soc.*, **2003**, *125*, 7377–7387. (j) T. Tsuzuki, N. Shirakawa, T. Suzuki, S. Tokito, *Adv. Mater.*, **2003**, *15*, 1455–1458. (k) Y. J. Su, H. L. Huang, C. L. Li, C. H. Chien, Y. T. Tao, P. T. Chou, S. Datta, R.

S. Liu, *Adv. Mater.*, **2003**, *15*, 884–888. (l) A. Tsuboyama, T. Takiguchi, S. Okada, M. Osawa, M. Hoshino, K. Ueno, *Dalton Trans.*, **2004**, 1115–1116. (m) B. M. J. S. Paulose, D. K. Rayabarapu, J. P. Duan, C. H. Chemg, *Adv. Mater.*, **2004**, *16*, 2003–2007. (n) T. Yutaka, S. Obara, S. Ogawa, K. Nozaki, N. Ikeda, T. Ohno, Y. Ishii, K. Sakai, M. Haga, *Inorg. Chem.*, **2005**, *44*, 4737–4746. (o) S. Okada, K. Okinaka, H. Iwawaki, M. Furugori, M. Hashimoto, T. Mukaide, J. Kamatani, S. Igawa, A. Tsuboyama, T. Takiguchi, K. Ueno, *Dalton Trans.*, **2005**, 1583–1590. (p) J. Li, P. I. Djurovich, B. D. Alleyne, M. Yousufuddin, N. N. Ho, J. C. Thomas, J. C. Peters, R. Bau, M. E. Thompson, *Inorg. Chem.*, **2005**, *44*, 1713–1727. (q) B. W. D'Andrade, R. J. Holmes, S. R. Forrest, *Adv. Mater.*, **2004**, *16*, 624–628. (r) X. Gong, D. Moses, A. J. Heeger, S. Xiao, *J. Phys. Chem. B*, **2004**, *108*, 8601–8605.

3 (a) S. Ranjan, S.-Y. Lin, K.-C. Hwang, Y. Chi, W.-L. Ching, C.-S. Liu, Y.-T. Tao, C.-H. Chien, S.-M. Peng, G.-H. Lee, *Inorg. Chem.*, **2003**, *42*, 1248–1255. (b) B. Li, M. Li, Z. Hong, W. Yu, T. Li, H. Wei, *Appl. Phys. Lett.*, **2004**, *85*, 4786–4788. (c) K. Wang, L. Huang, L. Gao, L. Jin, C. Huang, *Inorg. Chem.*, **2002**, *41*, 3353–3358. (d) F. Li, M. Zhang, G. Cheng, J. Feng, Y. Zhao, Y. Ma, S. Liu, J. Shen, *Appl. Phys. Lett.*, **2004**, *84*, 148–150.

4 (a) Y.-L. Chen, S.-W. Lee, Y. Chi, K.-C. Hwang, S. B. Kumar, Y.-H. Hu, Y.-M. Cheng, P.-T. Chou, S.-M. Peng, G.-H. Lee, S.-J. Yeh, C.-T. Chen, *Inorg. Chem.*, **2005**, *44*, 4287–4294. (b) B. Carlson, G. D. Phelan, W. Kaminsky, L. Dalton, X. Jiang, S. Liu, A. K.-Y. Jen, *J. Am. Chem. Soc.*, **2002**, *124*, 14162–14172. (c) Y.-L. Tung, P.-C. Wu, C.-S. Liu, Y. Chi, J.-K. Yu, Y.-H. Hu, P.-T. Chou, S.-M. Peng, G.-H. Lee, Y. Tao, A. J. Carty, C.-F. Shu, F.-I. Wu, *Organometallics*, **2004**, *23*, 3745–3748.

5 (a) W.-Y. Wong, Z. He, S.-K. So, K.-L. Tong, Z. Lin, *Organometallics*, **2005**, *24*, 4079–4082. (b) W. Lu, B.-X. Mi, M. C. W. Chan, Z. Hui, C.-M. Che, N. Zhu, S.-T. Lee, *J. Am. Chem. Soc.*, **2004**, *126*, 4958–4971. (c) J. Brooks, Y. Babayan, S. Lamansky, P. I. Djurovich, I. Tsyba, R. Bau, M. E. Thompson, *Inorg. Chem.*, **2002**, *41*, 3055–3066. (d) M. Cocchi, V. Fattori, C. Sabatini, P. Di Macro, M. Maestri, J. Kalinowski, *Appl. Phys. Lett.*, **2004**, *84*, 1052–1054. (e) C. Kwok, H. M. Y. Ngai, S. Chan, I. H. T. Sham, C. Che, N. Zhu, *Inorg. Chem.*, **2005**, *44*, 4442–4444. (f) J. A. G. Williams, A. Beeby, E. S. Davies, C. Wilson, *Inorg. Chem.*, **2003**, *42*, 8609–8611. (g) D. F. O'Brien, M. A. Baldo, M. E. Thompson, S. R. Forrest, *Appl. Phys. Lett.*, **1999**, *74*, 442–444.

6 (a) H. Yersin, *Top. Curr. Chem.* **2004**, *241*, 1–26. (b) W. J. Finkenzeller, H. Yersin, *Chem. Phys. Lett.*, **2003**, *377*, 299–305.

7 K. A. King, P. J. Spellane, R. J. Watts, *J. Am. Chem. Soc.*, **1985**, *107*, 1431–1432.

8 M. Maestri, V. Balzani, C. Deuschel-Cornioley, A. von Zelewsky, *Adv. Photochem.*, **1992**, *17*, 1–68.

9 (a) N. J. Turro, *Modern Molecular Photochemistry*, Benjamin/Cummings, Menlo Park, New York, **1978**. (b) J. B. Birks, *Photophysics of Aromatic Molecules*, Wiley, London, **1970**.

10 M. G. Colombo, T. C. Brunold, T. Riedener, H. U. Güdel, M. Förtsch, H. Bürgi, *Inorg. Chem.*, **1994**, *33*, 545–550.

11 M. J. Frisch, G. W. Trucks, H. B. Schlegel, G. E. Scuseria, M. A. Robb, J. R. Cheeseman, V. G. Zakrzewski, J. A. Montgomery, R. E. Stratmann, J. C. Burant, S. Dapprich, J. M. Millam, A. D. Daniels, K. N. Kudin, M. C. Strain, O. Farkas, J. Tomasi, V. Barone, M. Cossi, R. Cammi, B. Mennucci, C. Pomelli, C. Adamo, S. Clifford, J. Ochterski, G. A. Petersson, P. Y. Ayala, Q. Cui, K. Morokuma, D. K. Malick, A. D. Rabuck, K. Raghavachari, J. B. Foresman, J. Cioslowski, J. V. Ortiz, B. B. Stefanov, G. Liu, A. Liashenko, P. Piskorz, I. Komaromi, R. Gomperts, R. L. Martin, D. J. Fox, T. Keith, M. A. Al-Laham, C. Y. Peng, A. Nanayakkara, C. Gonzalez, M. Challacombe, P. M. W. Gill, B. G. Johnson, J. A. Pople, GAUSSIAN 98, Gaussian Inc., Pittsburgh, PA, **1998**.

12 (a) G. A. Crosby, *Acc. Chem. Res.*, **1975**, *8*, 231–238. (b) P. Spellane, R. J. Watts, A. Vogler, *Inorg. Chem.*, **1993**, *32*, 5633–5636.

(c) L. Sacksteder, A. P. Zipp, E. A. Brown, J. Streich, J. N. Demas, B. A. DeGraff, *Inorg. Chem.*, **1990**, *29*, 4335–4340. (d) P. J. Giordano, M. S. Wrightn, *J. Am. Chem. Soc.*, **1979**, *101*, 2888–2897. (e) S. Sprouse, K. A. King, P. J. Spellane, R. J. Watts, *J. Am. Chem. Soc.*, **1984**, *106*, 6647–6653.

13 K. Dedeian, P. I. Djurovich, F. O. Garces, G. Carlson, R. J. Watts, *Inorg. Chem.*, **1991**, *30*, 1685–1687.

14 (a) D. P. Rillema, J. K. Nagle, L. F. Barringer, T. J. Meyer, *J. Am. Chem. Soc.*, **1981**, *103*, 56–62. (b) R. J. Watts, *Inorg. Chem.*, **1981**, *20*, 2302–2306. (c) M. Maestri, N. Armaroli, V. Balzani, E. C. Constable, A. M. W. C. Thompson, *Inorg. Chem.*, **1995**, *34*, 2759–2767. (d) S. D. Cummings, R. Eisenberg, *J. Am. Chem. Soc.*, **1996**, *118*, 1949–1960.

15 (a) C. Hansch, A. Leo, S. H. Unger, K. H. Kim, D. Nikaitani, E. J. Lien, *J. Med. Chem.*, **1973**, *16*, 1207–1216. (b) C. Hansch, S. D. Rockwell, P. Y. C. Jow, A. Leo, E. E. Steller, *J. Med. Chem.*, **1977**, *20*, 304–306.

5

Pyridyl Azolate Based Luminescent Complexes: Strategic Design, Photophysics, and Applications

Yun Chi and Pi-Tai Chou

This chapter summarizes the deliberate design of the chelating C-linked 2-pyridyl azolate ligands. Attempts have been made in ligand functionalization and modification to fine-tune the photophysical properties of the associated metal complexes. Moreover, this chapter also reports the synthetic strategies, leading to a series of high emissive, boron as well as osmium, ruthenium, iridium, and platinum metal complexes, which all possess at least one 2-pyridyl azolate chromophore. Spectroscopic and dynamic measurements, in combination with theoretical analyses, have thus gain much insight into their electronically excited state properties such as the energy gap and nature of the lowest lying excited states, mechanism of intersystem crossing, and the efficiency of corresponding radiative decay and nonradiative deactivation processes. From the application point of view, efforts have been made to the exploitation of these emitting materials as dopants for preparation of high efficiency, true-blue and saturated-red polymer light-emitting diodes (PLEDs), and organic light-emitting diodes (OLEDs).

5.1
Introduction

The transition-metal complexes incorporating simple diimine ligands [1] such as 2,2′-bipyridine (bpy) and/or cyclometalated ligands [2] such as 2-phenyl pyridine (ppy) have attracted a great interest in recent years. Research work in this area was principally motivated by the use of these complexes in the study of excited-state electron and energy transfer [3] as well as the potential applications in the fabrication of chemical sensors, photovoltaics and organic light-emitting diodes (OLEDs) [4].
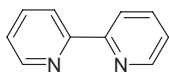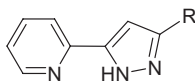
2,2'-bipyridine　　　2-pyridyl pyrazole　　　2-phenyl pyridine
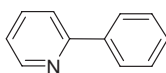
In one approach, the structural and chemical characteristics of 2-pyridyl C-linked azoles such as pyrazole are akin to those of 2,2′-bipyridine and the cyclometalated 2-phenyl pyridine ligands in which 2-pyridyl pyrazole is capable of using two of its nitrogen atoms to generate a stable metal–chelate bonding interaction [5]. Moreover, due to its strong acidity [6], the pyrazole site will readily lose a proton from the NH fragment to form a stable anionic ligand, consequently producing much stronger chelate to metal cation interaction. The strong σ-donor property of the pyrazolate, together with the π-accepting ability of the second pyridyl fragment [7], may provide a synergism of the electron delocalization so that the electron density is transferred from pyrazolate to the metal ion and back to the pyridyl side of the ligand, enhancing the metal–chelate interaction. For another comparison, although 2-phenyl pyridine and its derivatives are effective in forming similar cyclometalated complexes with late transition metal ions such as Rh(III), Ir(III), and Pt(II) [8], it was rather inert to the Ru(II) and Os(II) metal ions and particularly, to our knowledge, failed to afford any Os(II) metal complex [9]. The only exception was the formation of [OsCl(CO)(PPh₃)₂(ppy)] using bis(2-pyridyl) phenyl mercury reagent via metal exchange reaction, demonstrating the relative poor reactivity of 2-phenyl pyridine. Alternatively, due to the high acidity of the pyrazolate N–H bonding, 2-pyridyl pyrazole is expected to be more reactive and can extend the chemistry of cyclometalated ligand, giving a greater possibility in isolation of respective Ru(II) and Os(II) chelate complexes.

Moreover, the preparation of the isoelectronic transition-metal ions such as Ru(II), Os(II), and Ir(III), possessing a unique d^6-electron configuration, are found particularly attractive because of their strong metal–ligand interaction, long-lived excited states and high luminescence efficiencies, which significantly improve the likelihood of energy transfer prior to radiative or nonradiative relaxation. The strong spin–orbit coupling expected for these heavy metal ions would lead to an efficient intersystem crossing from the singlet excited state to the triplet manifold. Furthermore, mixing singlet and triplet excited-states via spin–orbit coupling, to a great extent, would remove the spin-forbidden nature of the $T_1 \rightarrow S_0$ radiative relaxation, resulting in highly intense phosphorescent emission. Based on these concepts, the aforementioned diimine, cyclometalated, or even pyridyl pyrazolate chelating ligands can form rigid molecular frameworks with these heavy transition metal ions and then give rise to the desirable absorption and efficient emission characteristics. More specifically, these chelate complexes would display intense ligand-centered ππ* absorptions plus a weak, lower energy metal-to-ligand charge transfer (MLCT) transition, while the strong emission is expected to derive from ππ*, MLCT or a mixture of both states, respectively, making them suitable to serve as ideal phosphors for the OLED applications [10].

5.2
Ligand Synthesis

At least two distinctive synthetic strategies have been employed to prepare the required C-linked pyridyl pyrazole ligands, for which the optimized reaction route

is solely dependent on their substituents on the pyrazole segment. Alkyl, fluorine substituted alkyl, and aryl substituents have been extensively employed, while the most frequently used architectures involve CF₃, methyl or *t*-butyl substituted pyrazoles such as **L1, L2,** and **L3**. The preparation of the CF₃ substituent **L1** is best executed using a hydrazine cyclization reaction with a suitably prepared pyridyl diketone intermediate, which is *in situ* obtained from the base catalyzed Claisen condensation using 2-acetyl pyridine and ethyl trifluoroacetate [11]. In contrast, preparation of alkyl substituted **L2** or **L3** is typically achieved through the condensation of methyl picolinate with acetone or pinacolone, followed by treatment with anhydrous hydrazine using the same cyclization method [12]. Other pyrazole ligands, **L4–L6**, which are useful for executing emission color tuning, are also presented in Scheme 5.1. The success of each experiment relies heavily on how the suitable starting materials in making the diketone intermediate are selected; for example, ligand **L2** can never be prepared from a treatment of 2-acetyl pyridine and ethyl acetate, followed by hydrazine cyclization. However, optimized yields for other ligand preparations often exceed 60%, based on the 2-pyridyl or 2-isoquinolyl reagent employed.
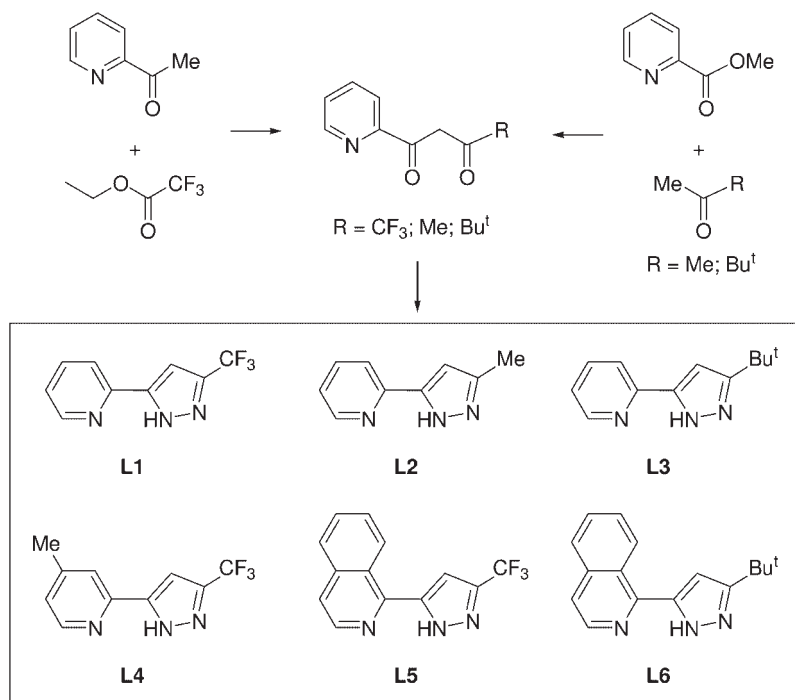
Scheme 5.1 Reaction sequence for the preparation of pyridyl pyrazole and the molecular structures of relevant ligands.

5.2.1
Ligand Modifications

Attention has also been focused on preparation of the related pyridyl C-linked pyrrole, 1,2,4-triazole, tetrazole and so forth, and in particular on the chemistry and photophysics of metal compounds in which the pyridyl pyrrolide, triazolate, and tetrazole constitute the chelating chromophore. C-linked pyridyl pyrrole may be prepared via a two-step process, which includes the prior preparation of a 1,4-dicarbonyl compound via the Stetter method using methyl vinyl ketone and the pyridyl carbaldehydes, followed by treatment of the preformed dicarbonyl compound with ammonium carbonate to give the formation of the pyrrole ring in ligand **L7** (Scheme 5.2) [13]. This pyrrole ligand will always possess a methyl group at the 2-position, which is beneficial in terms of providing steric protection. Replacement of the pyridyl group with other polyaromatic substituents such as quinolinyl and quinoxalinyl groups led to an easy functionalization, giving pyrrole ligands such as **L8** and **L9** [14]. The second method has afforded **L10** via the simultaneous dehydration following condensation of 2-aminomethylpyridine and 1,3-diketones [15]. The wide commercial availability of the diketone reagents makes this a versatile approach. We also expected that the CF_3 substituted analog **L11**, prepared from 2-aminomethylpyridine and hexafluoroacetylacetone, should serve as an excellent chelate for all metal elements due to the enhanced acidity at the pyrrolic NH site [16].

Similar to the above-mentioned pyridyl pyrazole and pyrrole analogs, the related C-linked 1,2,4-triazoles are also frequently used as chelates in preparing luminescent metal complexes, and this may be connected to their similarity in geometry as well as coordinative properties. One recent review article has summarized that
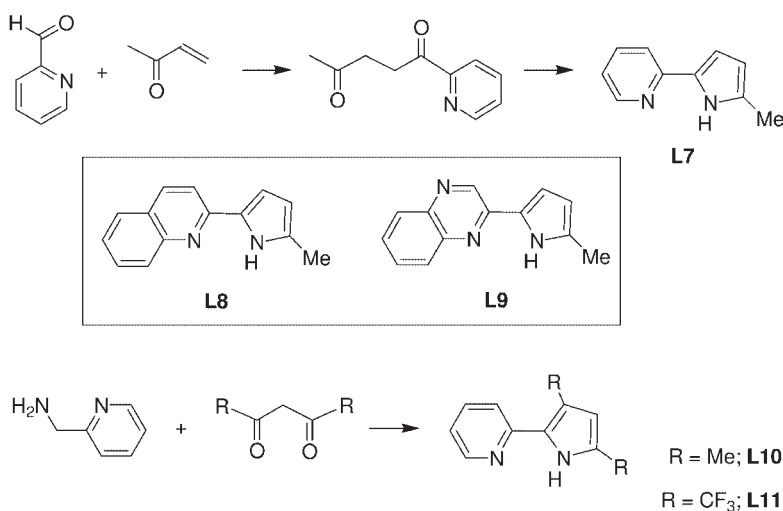
Scheme 5.2 Reaction sequence for the preparation of pyridyl pyrrole and the molecular structures of relevant ligands.

the 1,2,4-triazole ligands show a great coordination diversity, especially when the triazole segment is substituted with additional donor groups [17]. This property, combined with their strong σ donor strength, makes them very appealing for the design of new metal complexes with interesting properties. Other publications dealing with the triazolate coordination compounds can be found in a number of recent articles [18].

As shown in Scheme 5.3, the synthesis of the CF$_3$ substituted, C-linked pyridyl 1,2,4-triazole ligand **L12** was easily achieved by the condensation of 2-pyridinecarboximidamide hydrochloride with the trifluoroacetic acid hydrazide; the latter is generated by mixing ethyl trifluoroacetate and hydrazine monohydrate [19]. On the other hand, a convenient synthesis of the *t*-butyl substituted **L13** entails the direct reaction of 2-pyridinecarboxamidrazone with pivaloyl chloride in basic aqueous media, followed by dissolving of the resulting precipitate in ethylene glycol and heating of the mixture at ~210°C [20]. One fundamental character of this class of triazoles is worth mentioning. That is, due to the presence of bulky CF$_3$ or *t*-butyl group at the C-3 position of the triazole segment, formation of metal chelate tends to occur between the pyridyl site and the N-1 nitrogen atom, rather than the more congested N-4 nitrogen site due to the increased spatial interference. Thus, the substituent at the C-3 position may reduce the number of structural isomers generated during the reaction. This chemical behavior is in sharp contrast to their unsubstituted parent ligand **L14** [21]. The multicoordination capability of the triazole segment has induced formation of several isomers during reaction with the [Ru(bpy)$_2$] unit. As a consequence, effective chromatographic techniques were needed to separate these coordination isomers [22].

The last series of these bidentate ligands is the C-linked pyridyl tetrazole, such as **L15** [23]. Surprisingly, the coordination chemistry involving the tetrazoles has
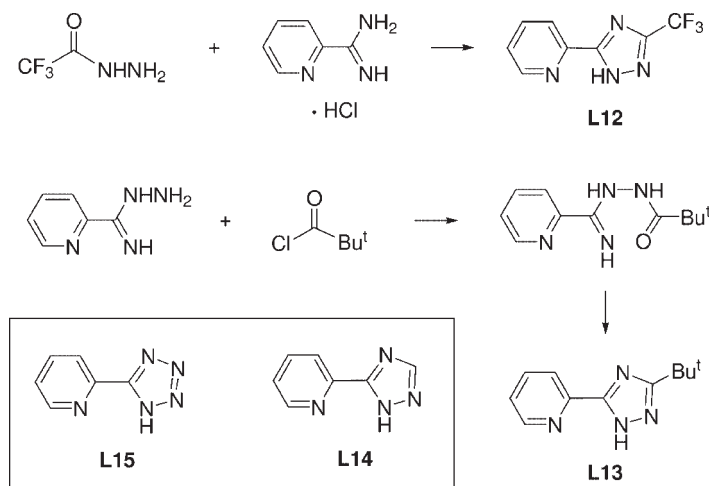
Scheme 5.3 Reaction sequence for the preparation of pyridyl triazole and the molecular structures of relevant triazole and tetrazole ligands.

received little attention in the past, despite the fact that tetrazole is the most acidic of all the azoles, with $pK_a = 4.89$, and readily deprotonates to the tetrazolate ion [24]. However, a recent report by Sharpless [25] clarified their possible explosive nature during manipulation and, in the meantime, provides an efficient preparation method employing 2-cyanopyridine and sodium azide in aqueous media. The remaining obstacle for tetrazole chelate will be the poor solubility of the tetrazolate complexes, as its multicoordination behavior may eventually afford higher nuclearity aggregates, incorporating bridging of the tetrazolate unit.

5.2.2
Fluorescent Behavior and Color Tuning

Most of the free ligands mentioned in the previous section show weak or even no fluorescence at room temperature due to the presence of a NH fragment. However, it has been reported that replacement of this proton with a metal cation would shift the emission to the visible region and significantly enhance the emission intensity [26]. The role of the metal cation is to maintain the planarity in forming the metal–chelate interaction and to provide the necessary stability without changing the HOMO/LUMO energy difference significantly [26]. The boron-containing segments were demonstrated to be a suitable candidate, as they have a high chemical and thermal stability due to the high covalency of boron–chelate bonding. Following this principle, pyridyl pyrazolate boron compounds **1** and **2** and pyrrolide boron compounds **3**, **4**, and **5** were synthesized by treatment of the free ligands with equal amounts of an appropriate BPh₃ reagent [14]. All of these complexes possess a tetrahedral geometry, as demonstrated by the single crystal X-ray diffraction studies on complexes **1** and **5**. This class of complexes displays bright luminescence with colors spanning blue to red, providing a good opportunity to shed light on the principles embedded in color tuning.
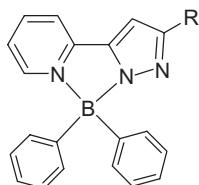
(**1**) R = CF$_3$
(**2**) R = Bu^t
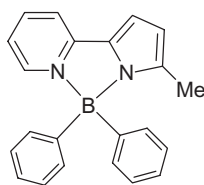
(**3**) [B(L7)Ph$_2$]
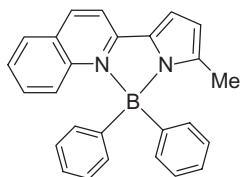
(**4**) [B(L8)Ph$_2$]
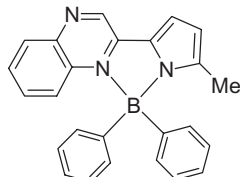
(**5**) [B(L9)Ph$_2$]

Table 5.1 Photophysical properties of pyridyl pyrazolate complexes **1–2** and pyrrolide complexes **3–5**.

Complex	Abs λ_{max} (nm)	PL λ_{max} (nm)	Φ	τ (ns)
1	320	375, 505	0.12[a]	0.53, 18.3[b]
2	340	430	0.45	9.9
3	327, 395	490 (490)[c]	0.52	11.81 (7.8)[c]
4	304, 442	510, 540 (572)[c]	0.63	8.85 (4.96)[c]
5	322, 492	572, 610 (591, 637)[c]	0.14	1.90 (1.56)[c]

a Data obtained from the integration of dual emission.
b Denotes the first and second emission signal.
c Denotes the solid-state property.

As shown in Table 5.1, the lowest energy absorption λ_{max} of these complexes follows a continuous trend ranging from 320 to 492 nm for **1–5**, and they were insensitive to the solvent polarity. The characteristic absorption band can reasonably be assigned to a ligand-centered ππ* transition. Except for **1**, which showed a complicated dual emission in the room temperature fluid state, the rest of the complexes exhibited emission with a vibronic-like progression, and the fact that the entire emission band originates from a common ground state species is ascertained by the excitation spectra throughout the monitored wavelengths of 500–700 nm. The emission decay times for compounds **2**, **3**, **4**, and **5** were measured to be 9.9, 11.8, 8.9, and 1.9 ns, respectively, which was found to be independent to the oxygen concentration (0–1 atm) [14]. This, in combination with the overlapping of the 0–0 onsets and the small amplitude of the Stokes shift (<5000 cm^{-1}), defined as the peak-to-peak frequency between absorption and emission, led us to conclude that the emission originates from the prompt ππ* fluorescence.

Both the absorption and emission of complex **2** showed significant hypsochromic shifts compared with those of the pyrrolide counterpart **3**. It is reasonable to anticipate that the highest occupied molecular orbital (HOMO) of **2** is significantly stabilized by the extra nitrogen atom of pyrazolate ligand versus the HOMO of pyrrolide complex **3**. In contrast, both absorption and emission signals underwent bathochromic shift from the series of pyrrolide complexes **3**, **4** to **5**. This systematic bathochromic shift could be rationalized by the extended π conjugation in the quinoline moiety (in e.g., **4**) as compared to pyridine (in **3**), so that the lowest unoccupied molecular orbital (LUMO) of **4** is stabilized, resulting in a smaller ππ* energy gap. Further lowering the ππ* transition can thus be achieved by introducing an additional nitrogen atom to the quinoline, forming quinoxalinyl complex **5**, in which the nitrogen atom serves as an electron-withdrawing group to the LUMO, rendering a further decrease of the ππ* energy gap.

Figure 5.1 depicts two sets of the LUMO and the HOMO mainly involved in the lower energy electronic transitions obtained using the TD-B3LYP method. The S$_1$ state has a contribution from HOMO → LUMO and LUMO+1. The results predicted that the S$_1$ state in complexes **2–4** could be well ascribed using an allowed ππ* transition located at the heterocyclic ligand of each complex. With the use of
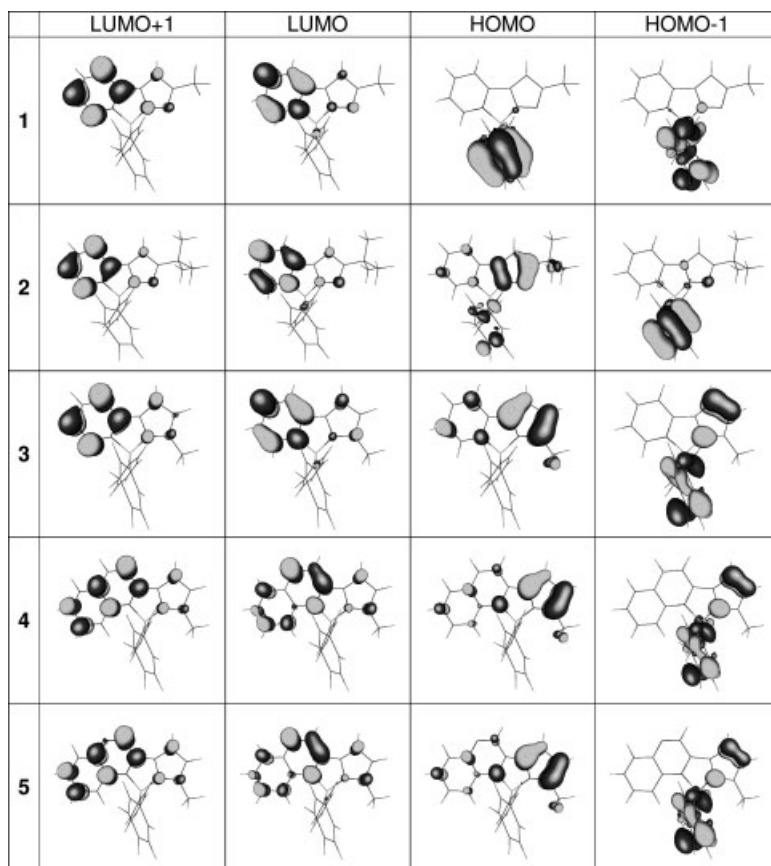
Fig. 5.1 The calcuvlated frontier orbitals for complexes **1–5**.

the TD-B3LYP method, incorporating the B3LYP/6-31+G (d′, p′) optimized geometry, the vertical (i.e., Franck–Condon) excitation energy from the ground state to the $S_1(^1\pi\pi)$ state was calculated to be 26,768 cm^{-1} (373 nm), 25,000 cm^{-1} (400 nm), 23,000 cm^{-1} (435 nm), and 21,500 cm^{-1} (465 nm) for complexes **2, 3, 4,** and **5**, respectively, which are remarkably consistent with the corresponding experimental results of 340 nm (**2**), 395 nm (**3**), 442 nm (**4**), and 492 nm (**5**). In comparison to the experimental values, the results for the energy gap are within 10% error, despite negligence of the solvation effect in the theoretical approach.

Another salient feature is regarding the $S_0 \rightarrow S_2$ transition, which mainly involves the HOMO-1 and LUMO frontier orbitals, possessing a π configuration in the phenyl substituent and a π^* pattern in the pyrrolide and pyrazolate ligand, respectively (see Fig. 5.1). Thus, one would expect that the $S_0 \rightarrow S_2$ transition may incorporate an electron transfer process from the phenyl group to the coordinated pyridyl moiety for all complexes. Certainly, due to the fast internal conversion to the S_1 state in the condense phase, i.e., Kasha's rule [27], the corresponding charge-

transfer emission would be irresolvable. Nevertheless, these results provided us a rational clue in that if the HOMO located at the pyrrolide moiety could be further stabilized by switching to the pyrazolate, the HOMO-1 originally located at the phenyl substituent might eventually be reversed and become the HOMO level. Accordingly, the lowest excited states possessing a charge transfer character with a gigantic dipolar change with respect to the ground state is expected [28]. This is apparently the case in complex **1**, in which HOMO no longer exists in the pyrazolate but rather in the phenyl site due to the addition of an electron withdrawing CF_3 group at the pyrazolate moiety (see Fig. 5.1). More importantly, such a swap between HOMO and HOMO-1 can be fine tuned. In case of replacing CF_3 by an electron donating *t*-butyl group, forming complex **2**, HOMO is taken back to the pyrazolate site. In consistence with the theoretical approach, among these complexes, **1** exhibits anomalous dual emission, in which the lower energy band originates from the photoinduced charge transfer between pyridyl and phenyl ring [28].

With respect to the OLED application, a simple EL device with a multilayer configuration ITO/NPB(40 nm)/**5**(30 nm)/BCP(10 nm)/AlQ$_3$(30 nm)/MgAg was fabricated [14]. This device shows an onset voltage of 8 V, and gives a saturated red–orange emission with peak maximum at 580 nm, and a maximum brightness of 5000 cd/m^2 at a driving voltage of 15 V. The external quantum yield is estimated to be 0.5%, showing faint potential to serve as an emitting material for fluorescent OLED applications.

5.3
Phosphorescent OLED Applications

Organometallic complexes possessing a heavy transition-metal element are crucial for the fabrication of phosphorescent organic light-emitting diodes (OLEDs) [10, 29]. The strong spin–orbit coupling effectively promotes singlet-to-triplet intersystem crossing as well as enhances the subsequent transition from the triplet excited state to the ground state, which then facilitates strong electroluminescence by harvesting both singlet and triplet excitons following the initial charge recombination. Because an internal phosphorescence quantum efficiency (η_{int}) as high as ~100% can theoretically be achieved, these heavy metal-containing emitters are superior to their fluorescent counterparts in future OLED applications. As a result, there is a continuous trend of shifting research endeavors to the heavy transition metal based emitters.

5.3.1
Osmium-Based Emitters

5.3.1.1 **Blue-Emitting Materials**
The 2-pyridyl pyrazole ligand **L1** can readily react with BPh$_3$ or fluorinated B(C$_6$F$_5$)$_3$ to form boron complex **1** or a related perfluorophenyl derivative [B(L1)(C$_6$F$_5$)$_2$], both
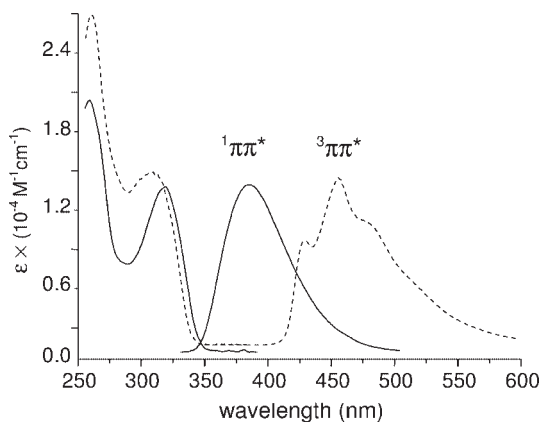
Fig. 5.2 The UV/Vis and emission spectra of [B(L1)(C$_6$F$_5$)$_2$] (solid line) and **6** (dashed line) in CH$_3$CN at RT.

of which display very high energy fluorescence in the near UV region (~380 nm) (Fig. 5.2) [28, 30]. This observation strongly suggests that the chelating pyrazole **L1** is suitable for preparation of high efficiency blue-emitting phosphorescent complexes upon linking to a third row transition metal element such as osmium. We then made use of the high reactivity of pyrazole chelate **L1**, and triazole analogs **L2** and **L3** toward carbonyl reagent Os$_3$(CO)$_{12}$ at high temperature, to prepare the required heavy metal complexes. As expected, the mononuclear products with two mutually orthogonal chelates and two *cis* CO ligands were isolated and characterized [30]. Their structural drawing is depicted below:
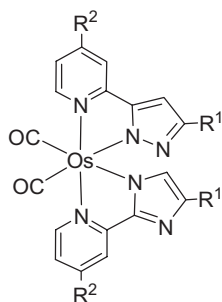
(**6**) R^1 = CF$_3$, R^2 = H
(**7**) R^1 = C$_2$F$_5$, R^2 = H
(**8**) R^1 = CF$_3$, R^2 = Me
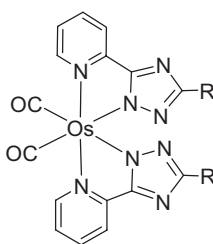
(**9**) R = Bu^t
(**11**) R = CF$_3$
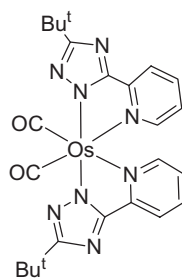
(**10**)

The corresponding photophysical data are summarized in Table 5.2, which shows the respective emission wavelengths, quantum efficiencies, and lifetimes; they are all depending on the identity of the chelate ligands and the relative ligand orientation around the central osmium atom.

Table 5.2 Photophysical properties of complexes **6–11** in degassed CH_3CN at room temperature.

Complex	Abs λ_{max} (nm)	PL λ_{max} (nm)	Q.Y. Φ	τ (μs)
6	311	430, 457, 480	0.14	18.5
7	314	430, 455, 480	0.087	13.4
8	306	428, 455, 480	0.041	6.3
9	333	455, 480, 507	0.42	39.9
10	340	460, 483, 515	0.00046	0.026
11	307	420, 446, 468	0.23	2.9

The absorption and emission spectra of osmium complex **6** are also depicted in Fig. 5.2. The dominant absorption bands in the 254–316 nm region were ascribed to the ligand-centered $\pi\pi^*$ transitions, but no absorption bands could be resolved in the region of ≥360 nm, suggesting that the possible MLCT transitions in **6** could be hidden in the UV region of the strong intraligand $\pi\pi^*$ transitions. The emission spectrum exhibits a distinct vibronic feature with λ_{max} at 430, 457, and 480 nm in CH_3CN. The fact that the entire emission band originates from a common ground state species is ascertained by the same phosphorescence excitation spectra throughout the monitored wavelengths of 420–600 nm. Furthermore, the peak-to-peak frequency between absorption and emission is as large as 9000 cm^{-1}. This observation, in combination with the lack of the 2-pyridyl pyrazolate fluorescence in the region of 370 nm and the occurrence of a lower energy structured emission profile with long excitation lifetime, leads us to propose that the emissive state of these chelate complexes should possess a very high percentage of ligand centered $^3\pi\pi^*$ character. This observation is in sharp contrast to those of the boron complex $[B(L1)(C_6F_5)_2]$, which displays a $\pi\pi^*$ fluorescence at 380 nm with Φ=0.88, while showing an essentially identical UV/Vis spectrum (Fig. 5.2).

Moreover, similar phosphorescence properties can be ascribed to complexes **7** and **8**. However, due to the relatively small radiative decay rate, the radiationless decay pathway induced by methyl (or CF_3) torsional motion may play a key role in the quenching of phosphorescence. Accordingly, among compounds **6–8**, the smallest phosphorescence quantum yield for **8** can be rationalized because of its bearing two methyl-like rotors, such as $-CH_3$ and $-CF_3$. Likewise, the phosphorescence quantum yield of **7** with C_2F_5 substituent, being smaller than that of **6** with CF_3 substituent, is plausibly due to the larger torsional degrees of freedom in the C_2F_5 group.

For the related *t*-butyl substituted triazolate complexes, two complexes with identical stoichiometry were observed for the direct treatment of **L13** with $Os_3(CO)_{12}$ [31]. Separation was achieved by using their marked differences of solubility in acetone, where the less soluble isomer **9** can be readily obtained as a crystalline solid, while isolation of the second complex **10** required repeated extraction and slow diffusion of hexane vapor into a saturated acetone solution at room temperature.
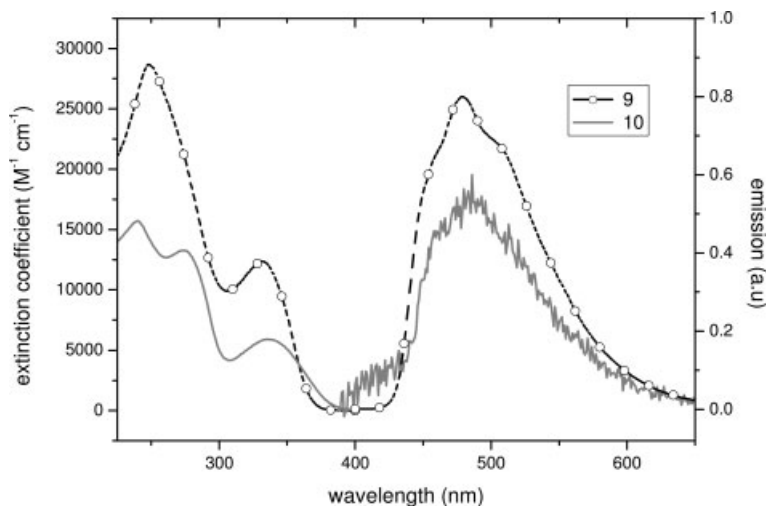
Fig. 5.3 UV/Vis absorption and emission spectra of **9** (---)
and **10** (—) in CH₃CN solution at room temperature.

Figure 5.3 shows the UV-visible absorption and emission spectra of both **9** and **10** in acetonitrile. In general, the dominant absorption band in the spectral region of 225–280 nm is attributed to the ligand-centered $\pi\pi^*$ transition of the pyridine and/or triazolate fragment. The broad, structureless band maximized at 310–334 nm can be assigned to a triazolate-to-pyridine intraligand $\pi\pi^*$ mixed with the ^{1}MLCT transition.

Their normalized emission spectra are also depicted in Fig. 5.3. Despite the diffusive ligand-centered $\pi\pi^*$ absorption band, complex **9** exhibits strong emission with a quantum yield of 0.42, for which distinct vibronic peak maxima appeared at ~455, 480, and 507 nm in degassed CH₃CN at 298 K. The luminescence intensity is linearly proportional to the increase in concentration, ruling out a possible association with any high-order aggregation. In addition, the emission is nearly solvent independent, with only a slightly hypsochromic shift from 478 nm in cyclohexane to 475 nm in CH₃CN. Thus, the possibility of the emission being associated with a large solvent dipolar relaxation can also be eliminated [32].

Remarkable differences in emission properties were observed for **10**. Although its emission profile looks quite similar to that of **9**, this complex is nearly nonemissive, showing quantum efficiency as low as 4.6×10^{-4} in degassed CH₃CN solution at 298 K. The weak phosphorescence also correlates well with the observed fast relaxation dynamics, in which the lifetime of phosphorescence for **10** was measured to be as short as 26 ns. Quenching by O₂ is negligible due to a fast nonradiative decay rate, as indicated by the nearly unchanged emission intensity and relaxation dynamics before and after the aeration.

To account for the distinctive difference in emission behavior, one possibility is that there exists certain excited states, possibly a metal-centered *dd* transition (i.e., ligand field, LF transition), which results in weakening of the metal–ligand interaction due to its antibonding character and may thus act as an activator for the overall

radiationless transition [33]. However, this possibility was ruled out, as none of the four lowest excited states, including two singlet and two triplet manifolds that were examined, possess an anticipated *dd* character. The inaccessibility of the *dd* excited state is believed to come from the strong ligand field strength of the triazolate chelates as well as the CO ligands.

On the other hand, according to the DFT calculation [34], a T_1 configuration in **10** could be reasonably attributed to a $^3\pi\pi^*$ manifold, mixed to a great extent with small amounts of the ^{3}MLCT character. Populating the T_1 excited state causes the shift of the electron density from the metal center, CO ligands and the triazolate to the pyridine moiety, resulting in a further reduction of the already weakened Os-pyridine interactions in **10**, for which the weakened bond distances have been confirmed by single crystal X-ray analysis. As a result, in **10**, the potential energy surface (PES) of T_1 might be so shallow that, under extreme conditions, a surface crossing of PES between S_0 and T_1 is possible. As shown in Fig. 5.4, upon excitation, fast S_1–T_n intersystem crossing (ISC) must take place. It is plausible that ISC proceeds from S_1 to T_2 due to their closeness in energy, followed by a fast rate of T_2 to T_1 internal conversion ($\leq 1\,ps^{-1}$). After population equilibrium, **10** can be thermally activated to certain vibrational levels close to the section of surface crossing to execute the radiationless deactivation through facile metal–ligand bond stretching. Thus, a dominant $T_1 \rightarrow S_0$ radiationless transition caused by a "loose bolt" effect might take place upon thermal activation [35].

This discovery may allow a parallel comparison with the behavior of tris-cyclometalated iridium complexes, for which isolation of two geometrical isomers has been documented in the literature [36]. Structural and spectroscopic data suggest that the facial isomers have the stronger and more evenly distributed metal–ligand bond interactions, and are highly emissive in both the fluid and solid states at room temperature. In contrast, the meridional isomers have much greater
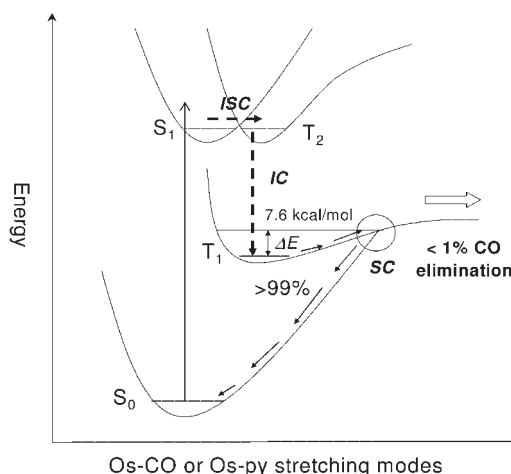
Fig. 5.4 Energy levels of the lower lying excited states and the proposed relaxation pathway for complex **10**. ISC: intersystem crossing, IC: internal conversion. SC: surface crossing.

bond length alternations caused by the differing trans influences of anionic phenyl and neutral nitrogen donors such as pyridine or N-substituted pyrazole, and are significantly less emissive under the identical conditions at room temperature. Naturally, this greater bond strength alternation of the meridional isomers then induces a similar "loose bolt" effect upon electronic excitation, which is more likely responsible for the rapid radiationless deactivation observed in this Ir(III) system.

Finally, complex **11** was obtained as the only isomer by substituting the electron donating t-butyl with an electron-withdrawing CF_3 group. The electron-withdrawing property of the CF_3 group stabilizes the HOMO of the triazolate moiety, and causes a shift of the corresponding $^3\pi\pi^*$ phosphorescence to a $\lambda_{max} = 446$ nm and $\Phi = 0.23$ as depicted in Table 5.2. However, up to this stage, none of these complexes presents opportunities for good applications for fabrication of blue phosphorescent OLEDs. To our viewpoint, this is in part attributed to the lack of suitable host materials with sufficiently large triplet energy gap.

5.3.1.2 Red-Emitting Materials

Preparation of the red-emitting Os(II) complexes requires the exploitation of the previously discussed blue-emitting complexes **6–11**. A desired synthesis was then initiated by the treatment of respective osmium complexes **6–11** with Me_3NO to eliminate the CO ligands in anhydrous diethylene glycol monoethyl ether (DGME) at 180–190°C, followed by addition of phosphine ligands [37]. A related one-pot synthetic strategy gives us the desired Os(II) complexes **12–17** in much improved (>70 %) yields, and hence has a great advantage in scaling up for the possible industrial application [38].
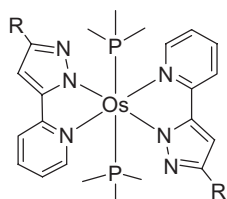
R = CF_3, P = PPh_2Me, (**12**)

R = CF_3, P = $PPhMe_2$, (**13**)
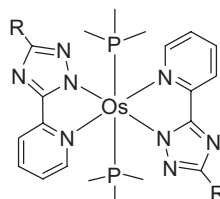
R = Bu^t, P = PPh_2Me, (**14**)

R = CF_3, P = PPh_2Me, (**15**)

R = C_3F_7, P = PPh_2Me, (**16**)

R = C_3F_7, P = $PPhMe_2$, (**17**)

Figure 5.5 shows an ORTEP diagram of **12**, for which the metal atom is located at a crystallographic center of inversion. The two chelating pyrazolate ligands establish a nearly planar OsN_4 basal arrangement, together with two PPh_2Me ligands located at the trans positions. The planar ligand arrangement is analogous to those of the porphinato ligand in metalloporphyrins such as $[Os(TTP)(PPh_3)_2]$, TTP = meso-tetraphenylporphinate, and $[Os(TPP)(CO)(Im)]$, Im = 1-methylimidazole
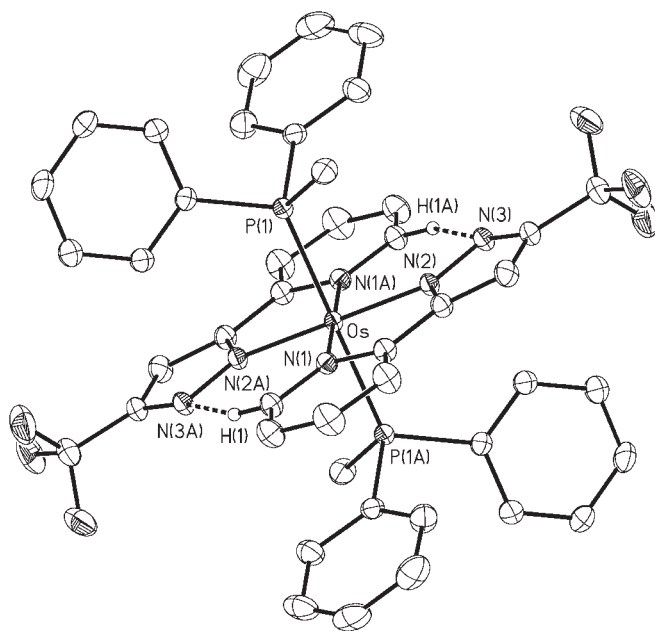
Fig. 5.5 ORTEP diagram of **12**; selected distances: Os–
P(1) = 2.3616(5), Os–N(1) = 2.090(2), Os–N(2) = 2.073(2),
N(2)–N(3) = 1.349(2), N(3)–H(1A) = 2.508 Å and angles:
N(1)–Os–N(2) = 76.48(7)°, N(1)–Os–N(2A) = 103.52(7)°.

[39]. The measured Os–N$_{(pz)}$ distances of 2.073(2) Å in **12** are slightly shorter than the respective Os–N$_{(py)}$ bonds of 2.090(2) Å; both lengths fall in the range expected for a typical N→ Os(II) dative bond. Of particular interest are the relatively weak nonbonding contacts (N3A–H1 ~2.50 Å) observed between the *ortho*-hydrogen atom of the pyridyl moiety and the N atom of the nearby pyrazolate fragment. It is speculated that this hydrogen bonding, to a certain extent, is akin to that observed in the cobaloxime complexes [40].

As indicated in Table 5.3, the UV/Vis spectra of these osmium complexes showed similar patterns, with three notable absorption maxima. The highest energy band, observed at ~400 nm, is naturally assigned to the spin-allowed $^1\pi\pi^*$ transition. The next lower energy absorption band, around 454–466 nm, can be ascribed to a spin-allowed metal-to-ligand charge transfer (^{1}MLCT) transition, while the third lowest energy band can be assigned to a state involving a mixture of both $^3\pi\pi^*$ and ^{3}MLCT characters.

For the emission spectra, in comparison to **12**, which is coordinated by two PPh$_2$Me ligands, complex **13**, bearing the PPhMe$_2$ groups, reveals a ~15 nm bathochromic shift in λ_{max} and can qualitatively be rationalized by an increase of the Os(II) d$_\pi$ energy level due to the poor π-accepting strength of the PPhMe$_2$ ligands (see Table 5.3). Based on the small variation of the emission peak wavelengths between **13** (632 nm) and **17** (629 nm), or **12** (617 nm) and **15** (617 nm), which

Table 5.3 Photophysical properties of complexes **12–17** in CH_2Cl_2 and solid state at RT.

Complex	Abs λ_{max} (nm)	PL λ_{max} (nm)	Q.Y. Φ	τ (ns)
12	405, 454, 542	617 (618)[a]	0.50 (0.21)[a]	855 (631)[a]
13	411, 456, 553	632 (655)	0.19 (0.29)	725 (610)
14	406, 466, 560	649 (670)	0.25 (0.10)	634 (440)
15	405, 457, 543	617 (631)	0.62 (0.24)	960 (180)
16	403, 457, 545	614 (618)	0.76 (0.36)	940 (580)
17	410, 465, 550	629 (634)	0.50 (0.21)	810 (910)

a   Data in parentheses are measured in solid state at RT.

possess identical phosphine ligands, we concluded that the triazolate ligand showed only a small amount of hypsochromic shift, although its π-accepting character should be considerably greater than that of the corresponding pyrazolate. On the other hand, changing the substituent on the triazolate from *t*-butyl to CF_3 and then to C_3F_7 has caused a notable blue shifting due to the increase of energy gap by lowering of both metal d_π and ligand π energy level, and is revealed by the notorious decrease of emission λ_{max} of complexes **14**, **15**, and **16**. Finally, the observed lifetimes of ca. 0.6–0.9 μs in degassed CH_2Cl_2 solution are considerably shorter than those of most reported red-emitting Ir(III) complexes, implying that the OLED devices fabricated using this class of osmium complexes could exhibit reduced triplet–triplet annihilation at higher driving voltages [41].

These Os(II) complexes were utilized for preparation of OLEDs that use polymers as the host materials, as such technologies have the potential for applications in large-area devices prepared with simple processes [37]. Preliminary EL polymer-based devices have been prepared by doping poly(*N*-vinylcarbazole) (PVK) with Os(II) complexes. For charge balance purposes, some electron-transporting materials, such as 2-(4-biphenylyl)-5-(4-*tert*-butylphenyl)-1,3,4-oxadiazole (PBD), have also been introduced to compensate for the poor electron-transporting ability of the host polymers [42]. Generally speaking, the energy transfer from PVK to the Os(II) emitters is very efficient, as supported by the lack of any PVK emission in the EL spectra. The EL with **13** reached a maximum efficiency (η_{max}) of 3.0 cd/A at 21 V with a luminance of 615 cd/m^2. Its EL λ_{max} appeared at 640 nm, showing good potential for generation of saturated red emission.

In a second study, **PF-Q**, a copolymer containing polyfluorene backbones and 2,4-diphenylquinoline (DPQ) as electrontransporting side chains, was used as host material and doped with 2.4 wt % of **13** to realize red EL [43]. Upon photoexcitation, the PL profile of the blend consists of two emission bands: one originates from the remaining emission of the **PF-Q** host, whereas the other, at about 624 nm, corresponds to the emission signal of **13**. In contrast, the host emission is quenched completely when stimulated by the EL excitation, giving red triplet emission from **13** that had Commission Internationale de L'Eclairage (CIE) color coordinates of (0.66, 0.34) at 11 V. These results suggest that both Förster energy transfer and direct charge trapping/recombination on the dopant **13** are

responsible for the observed EL. The much enhanced maximum external quantum efficiency of 6.63% (corresponding to a luminance efficiency of 8.71 cd/A) is obtained from this doped device at a current density of 47.8 mA/cm^2, together with a brightness of 4163 cd/m^2.

(**DPQ**)   (**PF-Q**)
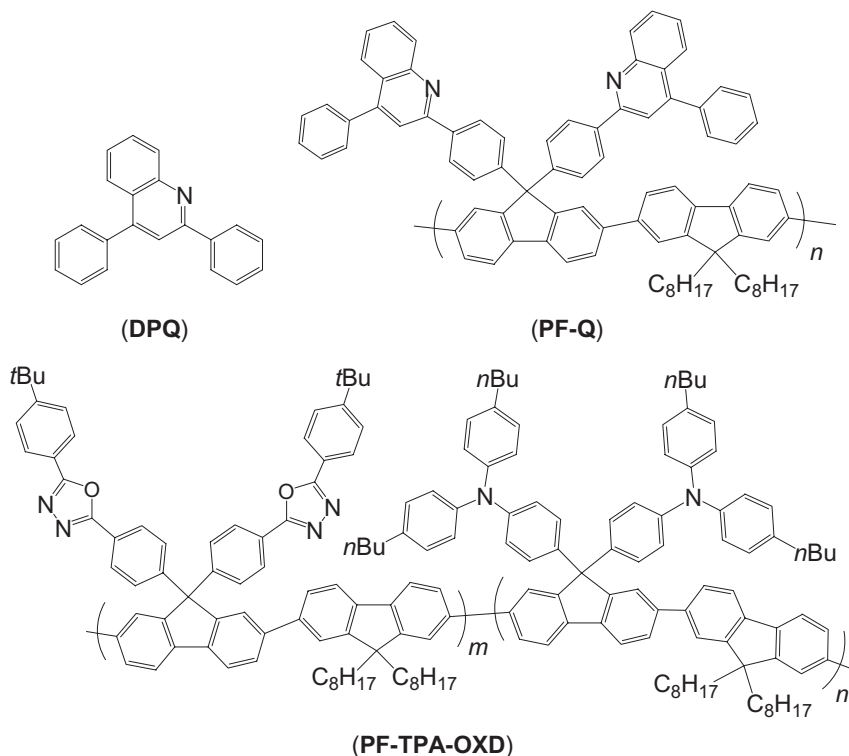
(**PF-TPA-OXD**)

In the third approach, we incorporated the osmium phosphor **13** into a tailor-made blue-emitting polyfluorene derivative **PF–TPA–OXD** [44]. This host polymer, which contains both hole- and electron-transporting side chains, is capable of facilitating charge injection and transport, and suitable for matching the dopant-host energy level to achieve the direct formation and confinement of an exciton at the dopant. This configuration leads to a reduction in the excitation of the host polymer, which in turn decreases the degree of exciton loss arising from nonradia-tive decay of the host triplet. In practice, PLED devices having the configuration ITO/poly(styrenesulfonate)-doped poly(3,4-ethylenedioxythiophene) (PEDOT) (35 nm)/polymer emitting layer (50–70 nm) and dopant **13**/TPBI (30 nm)/Mg:Ag (100 nm)/Ag (100 nm) were fabricated, keeping the optimized dopant concentra-tion of **13** being ca. 1 mol %. Again, the PL profile of this device contains two components, which are attributed to the polyfluorene emission of the **PF–TPA–OXD** host and the triplet emission of **13**, respectively; while the corresponding EL

spectra indicate an exclusively dopant emission. The dramatic difference between the PL and EL spectra reveals that the emission originates from the direct charge trapping, followed by recombination with opposite charges at the dopant sites [45]. To understand the details of the charge-transporting mechanism, the HOMO and LUMO energy of **13** were estimated using the onset potentials of the oxidations and reductions obtained using cyclic voltammetry (CV). As shown in Fig. 5.6, holes in this device can easily be injected from PEDOT (−5.2 eV) [46] into the HOMOs (−5.3 eV) of the **PF–TPA–OXD** host upon overcoming a small energy barrier (0.1 eV). For complex **13**, the estimated ionization potential of −4.5 eV is 0.8 eV above the HOMO of **PF–TPA–OXD**; therefore, holes can be trapped at the dopant site, followed by recombination of opposite charges (electrons) to form excitons [44]. For a comparison, this device reached a maximum external quantum efficiency of 8.37% with a peak brightness of 16 720 cd/m². Moreover, the highest record of η_{ext} 12.8% was achieved using a similar device configuration, employing **13** as phosphorescent dopant, **PF–TPA–OXD** as host polymer, and **PS–TPD–FTV** as hole-transporting layer [47]. **PS–TPD–TFV** is a cross-linkable polystyrene copolymer with both thermally curable triflororovinyl ether (TFV) group and hole-transporting tetraphenylenebiphenyldiamine (TPD) group as side branches.

For a comparative study, we also took advantage of the high volatility of this class of neutral complexes to prepare OLEDs using direct thermal evaporation [38]. Thus, complex **15** was selected in fabricating a series of multilayer devices of the configuration ITO/HTL(40 nm)/CBP:**15**(30 nm)/BCP(10 nm)/Alq$_3$(30 nm)/ LiF(1 nm)/Al(150 nm), where CBP, BCP and Alq$_3$ stand for 4,4′-N,N′-dicarbazolyl- 1,1′-biphenyl, 2,9-dimethyl-4,7-diphenyl-1,10-phenanthroline, and tris(8-hydroxy-
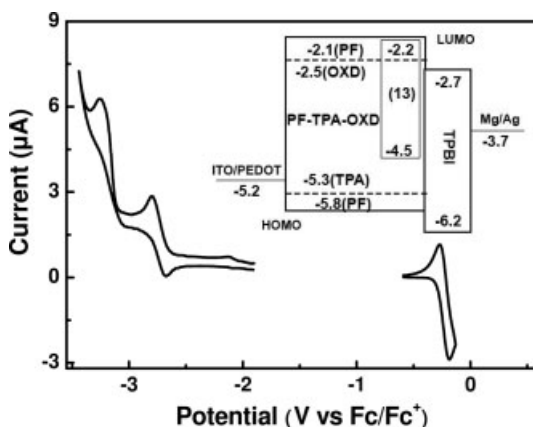
Fig. 5.6 Proposed energy level for the devices having the configuration ITO/PEDOT/**13:PF– TAP–OXD**/TPBI/MgAg and the cyclic voltammograms of **13**. Note: the ionization potential I_p and electron affinity E_a (with respect to the vacuum level) are estimated using the expressions: $I_p = (E'_{ox} + 4.8)$ and $E_a = [E'_{red} + 4.8]$ eV, in which E'_x and E'_{red} are, the onset potentials for oxidation and reduction relative to the Fc/Fc$^+$ reference, respectively.

BPAPF

BCP

CBP

NPB

LiF/Al
AlQ$_3$ (30 nm)
BCP (10 nm)
x% Os in CBP (30 nm)
NPB or BPAPF (40 nm)
ITO
Glass
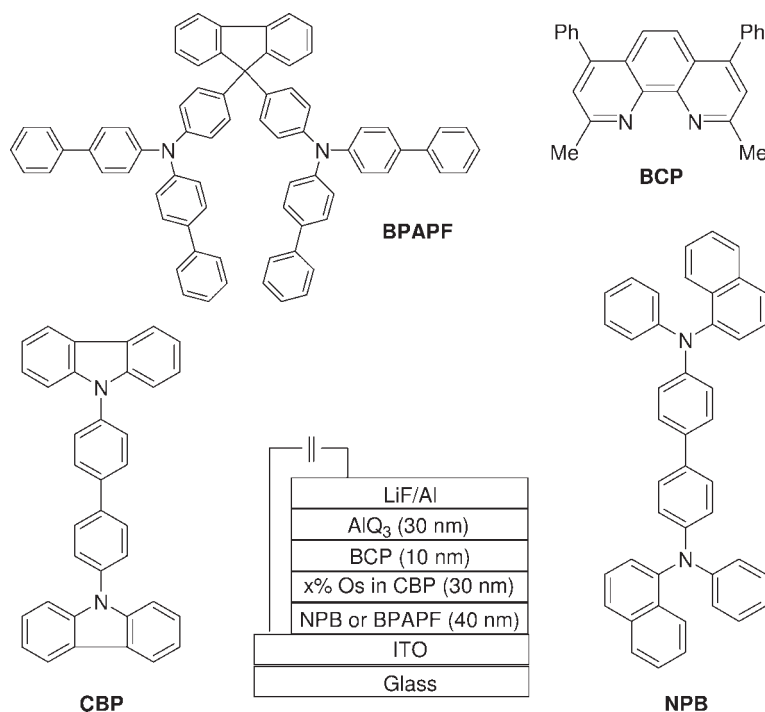
Scheme 5.4 The molecular structure of the relevant compounds used in OLED fabrication and the configuration of OLED device.

quinolinato) aluminum(III), respectively. The molecular structure of the relevant compounds used in this investigation and configuration of the OLED device are present in Scheme 5.4. Interestingly, upon changing the hole-transporting layer (HTL) from 4,49-bis[*N*-(1-naphthyl)-*N*-phenylamino]biphenyl (NPB) to 9,9-bis{4-[di-(*p*-biphenyl)aminophenyl]}fluorene (BPAPF) [48], a very high initial external quantum efficiency of ~20% and a luminous efficiency of 27.8 cd A^{-1} were obtained at 1 mA cm^{-2}. Considering the coupling out factor, this device is reaching nearly 100% internal phosphorescence efficiency [49], making them very suitable dopant emitters for phosphorescent OLED applications.

5.3.2
Ruthenium-Based Emitters

One major obstacle to the commercialization of phosphorescent OLED technologies lies in the prohibitive cost of the noble metals such as osmium, platinum, and even iridium. Thus, from a technological standpoint, there is an urgent need to develop phosphorescent emitting materials using less expensive metals such as ruthenium.

As for a rational design, it is indispensable to have nonionic, neutral Ru(II) complexes in view of suitable volatility and balanced charge mobility. Secondly, the weaker ligand field strength for the second row elements leads to the exploitation of strong bonding bidentate ligands being inevitable. Thirdly, strong field ancillary ligands such as phosphine are required to increase the energy gap of the metal-centered *dd* transition so that the radiationless deactivation can be suppressed [50]. Finally, the relatively high oxidation potential in Ru(II) requires the employment of extensively conjugated 1-isoquinolyl substituted chromophores **L5** and/or **L6** to compensate the unfavorable metal oxidation potential in generation of highly efficient, saturated red emission.

R = ᵗBu, R' = Me, (**18**)

R = ᵗBu, R' = Ph, (**19**)

R = CF₃, R' = Ph, (**20**)

R = ᵗBu, (**21**)

R = CF₃, (**22**)

R = ᵗBu, (**23**)

R = CF₃, (**24**)
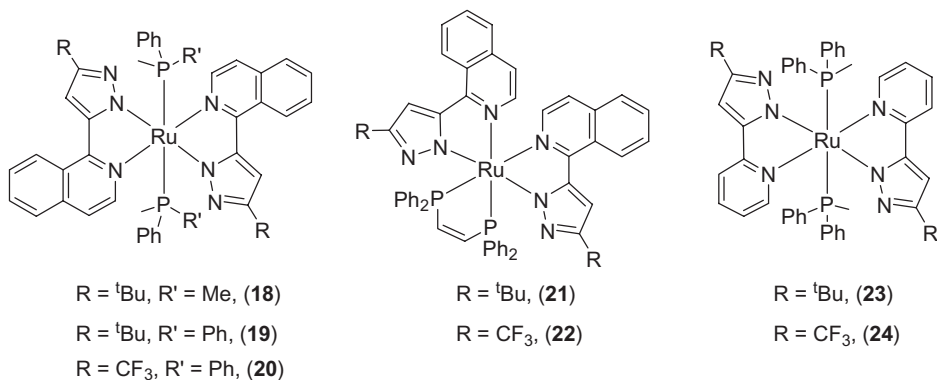
Similarly, a series of Ru(II) complexes, **18–24,** were synthesized following the synthetic scheme established for their osmium counterparts [51, 52]. The emission spectra are depicted in Fig. 5.7, while photophysical data are listed in Table 5.4. Moderate to highly intense luminescence in solid state was obtained for complexes **18–20** with λ_{max} at 709 nm, 682 nm, and 632 nm, respectively. In good agreement with the ^{3}MLCT emission, the PPh₂Me derivative **19** exhibits a ~27 nm hypsochromic shift in λ_{max} in comparison to the PPhMe₂ anchored **18**, the result of which can qualitatively be rationalized by a decrease of the Ru(II) dπ energy level due to the increase of π-accepting strength. For complex **20**, an even more notable hypsochromic shift of 50 nm was achieved. This is apparently caused by the electron-withdrawing effect of the CF₃ substituents on pyrazolate, which has a function of further lowering the electron density at both the pyrazolate moieties and the Ru(II) metal center. Upon changing the trans PPh₂Me arrangement to a dppe ligand, i.e., *cis*-1,2-bis(diphenylphosphino)ethylene, the emission underwent a further blue shift, which was revealed by emissions occurring at 609 and 559 nm for complexes **21** and **22**, respectively [52]. Moreover, the emergence of an intraligand $^3\pi\pi^*$ contribution for **22** is supported by the second emission peak at $\lambda_{max} = 581$ nm, concluded from the observation of the vibronic coupling. This is apparently caused by the better π-accepting dppe ligand, which has effectively reduced the MLCT character at the lowest energy excited states.
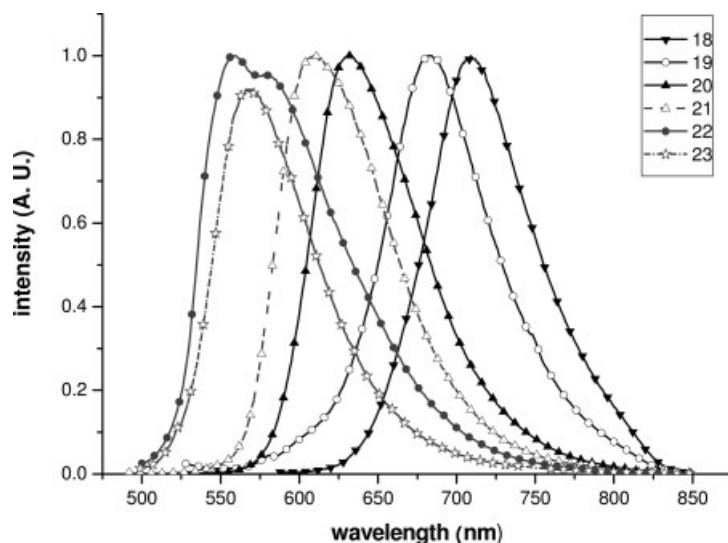
Fig. 5.7 Photoluminescence of Ru(II) phosphors as solid film at room temperature.

Table 5.4 Photophysical properties of complexes **18–24** in CH_2Cl_2 and solid state at RT.

Entry	UV/Vis absorption (nm) ($\varepsilon \times 10^3$)	PL^a λ_{max} (nm)	Φ^a	τ_{obs} (µs)
18	336 (20), 363 (14), 462 (13), ~580 (0.9, br)^b	718 (709)	– (0.02)	– (1.06)
19	332 (20), 361 (15), 455 (12), ~566 (1, br)	700 (682)	– (0.02)	– (0.64)
20	320 (25), 353 (13), 446 (17), ~523 (1, br)	636 (632)	0.01 (0.24)	0.10 (1.82)
21	316 (23), 356 (20), 368 (20), 408 (9), ~470 (4, br)	637 (609)	0.08 (0.21)	0.06 (2.1)
22	307 (22), 345 (16), 369 (18), 390 (10), ~445 (3, br)	596 (559, 581)	0.002 (0.02)	0.02 (0.56)
23	309 (19), 395 (10), 443 (1), ~493 (1, br)	– (568)	– (0.001)	– (0.16)
24	297 (22), 392 (12), ~460 (0.7, br)	–	–	–

    a   Data in parentheses are measured in solid state at RT.
    b   br is an abbreviation for broad.

To study the photophysics of reduced ligand π conjugation, replacement of the 1-isoquinolyl ligands **L5** and **L6** with less conjugated 2-pyridyl counterparts **L1** and **L3** has afforded the pyridyl complexes **23** and **24** [52]. Although **23** has a low chemical stability upon contact with chlorinated solvent in air, its solid sample gives a faint orange emission at $\lambda_{max} = 568$ nm at room temperature, a result of increasing the emission gap from that of **18** ($\lambda_{max} = 709$ nm) by reducing the π-conjugation of the ligands.

A further increase of the $S_0 \rightarrow T_1$ energy gap for **24** is expected due to the presence of electronegative CF_3 substituent on ligand **L1**, which is expected to stabilize the metal dπ orbitals by lowering its electron density. However, no emission was noted even at 77 K in solid matrices, as the pyridyl motif not only renders large structural deformation between the ground and excited states, but also increases

the possibility of the population to the upper *dd* excited states, which leads to strong radiationless deactivation. This viewpoint can be firmly supported by the TDDFT calculation. As shown by the absorption data listed in Table 5.4, complex **24** apparently possesses the highest ^{1}MLCT energy gap among all the Ru(II) complexes prepared. The results of TDDFT calculation (Fig. 5.8) on **24** show that the lowest energy triplet state involves a substantial contribution of the metal *dd* character, while the typical ^{3}MLCT state has moved up in energy and becomes the second lowest excited state [52].

As for the OLED applications, a multilayer device using 24 wt% of **20** as a dopant emitter in a CBP host and with NPB as a hole-transporting layer exhibits saturated red emission with an external quantum efficiency of 5.10%, luminous efficiency of 5.74 cd/A, and power efficiency of 2.62 lm/W, while incorporation of a thin layer of PEDOT/PSS between ITO and NPB gave an optimized result with external quantum efficiency of 7.03%, luminous efficiency of 8.02 cd/A, and power efficiency of 2.74 lm/W at 20 mA/cm^2. The nonionic nature, high emission quantum

Assignments (T$_1$) (482 nm)

HOMO → LUMO+2 (64%)

HOMO → LUMO+4 (7%)

HOMO → LUMO+12 (22%)

LUMO+12	LUMO+4
LUMO+2	HOMO
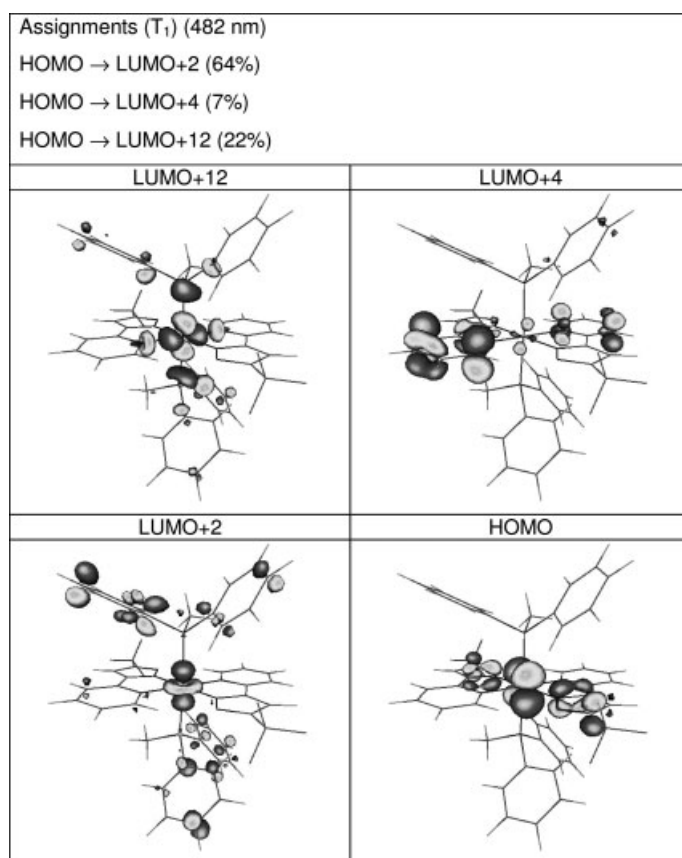
Fig. 5.8 The calculated lowest energy triplet transition and the associated frontier orbitals of **24**.

efficiency, and short radiative lifetime are believed to be key factors for this unprecedented achievement.

5.3.3
Iridium-Based Emitters

It has been reported that the replacement of one cyclometalated C^N chelate in the trisubstituted iridium complex [Ir(C^N)$_3$] with a bidentate ancillary ligand (LX) afforded heteroleptic complexes [(C^N)$_2$Ir(LX)], where C^N = cyclometalated ligand and LX = acetylacetonate (acac), *N*-methylsalicyliminate (sal), and picolinate (pic) [53]. In these iridium complexes, even though the emissions retain the main characteristics of their parent complexes [Ir(C^N)$_3$] in most cases, a minor dependence on the emission peak wavelength was also noted, which varies according to the nature of the ancillary ligand LX. For instance, the observed emission λ_{max} changes according to an order of pic < sal ~ acac, which is proportional to their electron donor strengths, resulting in a reduction of the energy gap. Accordingly, the pyrazole ligands such as **L1** and **L3** and triazole ligand such as **L12** and **L13** were utilized to serve as the third LX ligand in conducting the color tuning. As their donor strengths are expected to follow a qualitative trend of **L3** ≥ **L13** >> **L1** ≥ **L12**, it is not surprising to see that complexes with either LX ligands **L1** or **L12** display more blue-shifted emission signals. Conversely, complexes with LX = **L3** or **L13** would give rise to red-shifted emissions relative to their trisubstituted counterpart [Ir(C^N)$_3$].

5.3.3.1 Tuning the Color to Red

Cyclometalated [Ir(ppy)$_3$] and its heteroleptic analog such as [Ir(ppy)$_2$(acac)] have been extensively applied in fabricating green emitting electrochemiluminescent devices [54], while the strong emission occurring at λ_{max} ~514 nm is believed to originate from the mixed triplet states possessing both intraligand ππ* and MLCT characters [55], or with a greater contribution from MLCT [55d]. From the viewpoint of ligand chromophores, it is anticipated that the LUMO and HOMO of the ppy ligand are mainly located at the pyridyl part and the phenyl segment of the ppy ligand, respectively [34]. This is because that the phenyl group of ppy ligand carries a formal negative charge, and the pyridine is formally neutral. Accordingly, as shown in Scheme 5.5, replacement of one CH group at the pyridyl fragment by a nitrogen atom would give a pyrazine (route A) or a pyrimidine substituted ligand fragment (route B), showing a decreased LUMO energy level [56]. On the other hand, the HOMO of these ligands remain unchanged, as they are mainly located at the relatively electron rich phenyl group. Thus, after formation of the iridium metal complexes, such a hypothetical nitrogen atom substitution at the cyclometalated ligand will cause an appreciable reduction of the energy gap for the expected ^{3}ππ* and ^{3}MLCT emission. Further attachment of an extra aromatic ring into the ligand π framework, e.g., using quinoxaline to replace the hypothetical pyrazine fragment (routes A1 and A2), quinazoline to replace pyrimidine (route B1), or even using naphthalene to replace phenyl group (routes B2 and B3), should
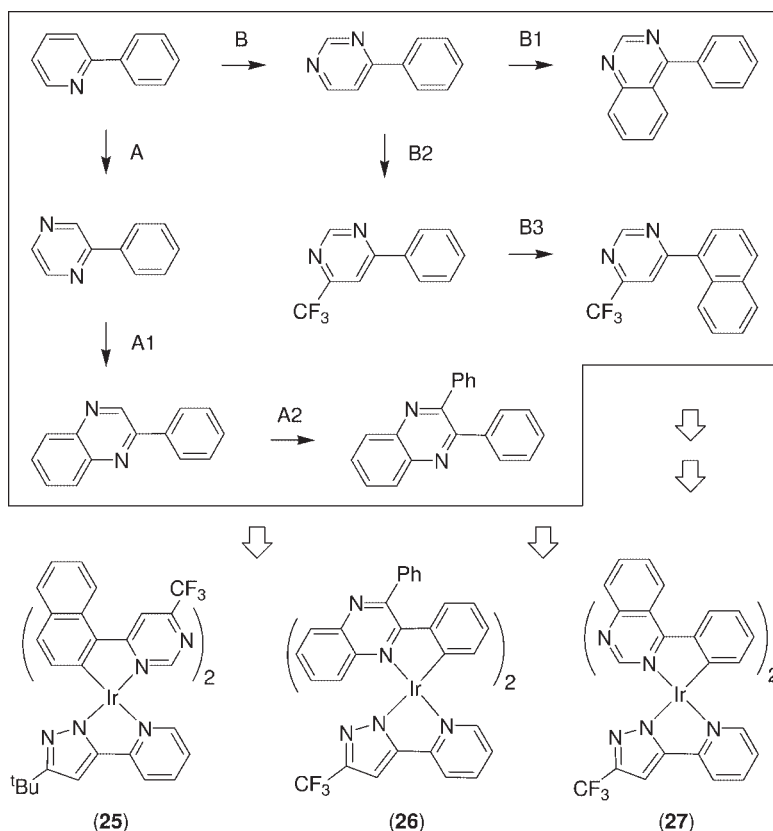
Scheme 5.5 Strategy for tuning the ligand emission to red color and the structural drawing for relevant red-emitting iridium complexes.

extend the π-conjugation, giving a further decrease of the energy gap. Therefore, continuously tuning the emission to the saturated red can be rationalized by employing these cyclometalated ligands and using pyridyl azolate as the third chelating LX ligand; see the molecular drawing for complexes **25**, **26**, and **27**.

The OLED applications were first examined using **25** doped in a tetraphenyl-diamine based hole-injection/transporting layer (HTL) and poly(BTPD-Si-PFCB) as an electron-blocking and an exciton confinement layer at the anode [57]. To realize optimum efficiency, a layer of 1,3,5-tris(*N*-phenylbenzimidazol-2,yl)benzene electron-injection/transporting layer (ETL) was also applied at the cathode for hole blocking and exciton confinement [58]. The device fabricated from a blended polymer involving 5 wt% of **25** in previously mentioned graphed copolymer **PF–TPA–OXD** gave a maximum external quantum efficiency of 7.9 % and a maximum brightness of 15800 cd/m^2, with CIE chromaticity coordinates of $x = 0.65$ and $y = 0.34$ [59]. These results are outstanding for red polymer OLEDs using iridium-based dopant in conjugated polymer.

Complex **26**, which exhibited an emission λ_{max} at 640 nm, was also utilized for the preparation of polymer OLEDs [56]. These devices consist of a multilayer configuration ITO/PEDOT:PSS/PVK-PBD (30 wt%):x wt% **26**/TPBI/Mg:Ag/Ag (100 nm), where ITO, PEDOT:PSS, PVK, PBD, TPBI, and Mg:Ag denote indium tin oxide, poly(styrenesulfonate) doped poly(3,4-ethylenedioxythiophene), poly(vinylcarbazole), 2-(4-biphenylyl)-5-(4-*tert*-butylphenyl)-1,3,4-oxadiazole, 2,2′,2″-(benzene-1,3,5-triyl)tris[1-phenyl-1*H*-benzimidazole], and magnesium: silver alloy (ca. 10:1), respectively. At the doping concentration of 1.8 wt%, the device exhibited a maximum external quantum efficiency of 3.15%, a brightness of 1751 cd/m^2 at 67.4 mA/cm^2, and a maximum brightness of 7750 cd/m^2 at 21 V. These performance data deteriorate substantially upon increasing the doping level to 5.3 wt% of **26**, which is attributed to concentration quenching and triplet–triplet annihilation. The radiative lifetimes of 4.8 μs, calculated using observed lifetimes of ca. 1.9 μs and quantum yield of 0.4 in degassed CH$_2$Cl$_2$, may serve as one major factor to account for this concentration dependence.

Preparation of OLEDs using coevaporation was also realized using the third complex **27** [60]. The multilayer devices of the configuration ITO/NPB (40 nm)/ CBP:**27** (30 nm)/BCP (10 nm)/Alq$_3$ (30 nm)/Mg:Ag were prepared, with doping concentrations varying from 7%, 14%, and 21% to a 100% neat film composition, for which the configuration was adopted from those reported by Thompson and Forrest [61]. Very bright emission was observed for all doping levels, among which the best performance was achieved using 14 wt% of **27**, exhibiting a maximum brightness of 12370 cd/m^2 and an external quantum efficiency of 8.1% at 10 V and 20 mA/cm^2, but a slightly inferior CIE value of 0.62 and 0.37. However, it is notable that, in contrast to that of a typical phosphorescent OLED, the nondoped device employing **27** also showed electroluminescence as high as 5780 cd/m^2, an external quantum efficiency of 5.5% at 10 V and a current density of 20 mA/cm^2. Reduced π–π stacking in solid state and a relatively short radiative lifetime (~1 μs) may have caused such exceptional performances.

5.3.3.2 Blue-Emitting Materials

Design and preparation of blue-emitting phosphorescent complexes have presented considerable challenges in recent years [62]. This task is far more difficult than those for preparing green and red-emitting complexes. The key lies in the selection of chelating chromophores that are suitable to form complexes as well as to have large intraligand ππ* and/or MLCT transition. To achieve the required high efficiency, a few attempts have been made through the use of strong field ancillary ligands such as CO, phosphines, and isocyanide together with cyanide with an aim to increase the HOMO–LUMO gaps and minimize radiationless decay via elevating metal-centered *dd* transitions at the same time [63]. More recently, the blue-emitting iridium complexes [(dfppy)$_2$Ir(LX)], dfppy = 2-(2,4-difluorophenyl) pyridine and LX = picolate, **FIrpic** [64], as well as [(tpy)$_2$Ir(LX)], tpy = 2-*p*-tolyl-pyridine; LX = acetylacetonato, picolate, bis(pyrazolyl)borate ligands and their analogs were also reported [65]. These results clearly demonstrate the feasibility for obtaining blue phosphorescence (Fig. 5.9).
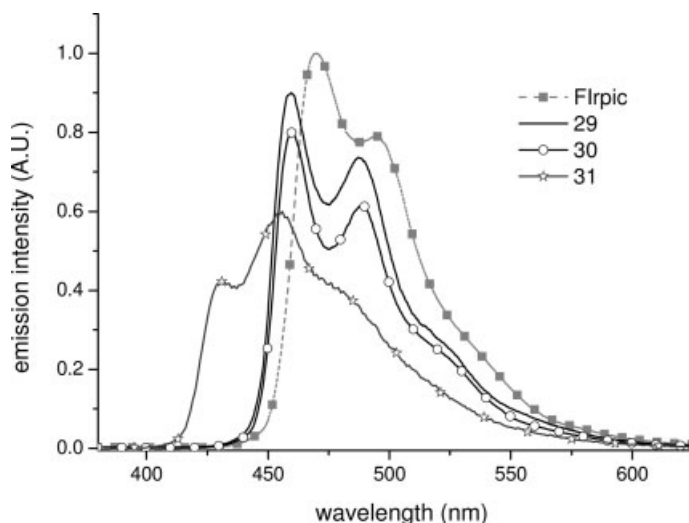
Fig. 5.9 Photoluminescence of iridium phosphors at room temperature in CH_2Cl_2.

The pyridyl azolate based ligands were found to be highly useful for such investigation. The first reported example is complex **28**, which showed an almost blue emission with the first emission λ_{max} located at 461 nm, and exhibited a hypsochromic shift of ~10 nm vs. that of **FIrpic** [66]. This notable behavior is consistent with the much greater π-accepting properties of pyridyl triazolate chelate in **28** vs. that of the picolate ligand in **FIrpic**, and further lowering the electron density at the iridium metal center. In the case of CF_3 substituted complex **29**, although the CF_3 group may exert a greater electron-withdrawing effect, it showed a slightly blue-shifted emission ($\lambda_{max} = 459$ nm) with respect to that of **28**, while replacing the triazolate with tetrazolate chelate ligand gave complex **30**, also showing the emission λ_{max} at 459 nm [67].

L^X

R = Ph, (**28**); R = CF_3, (**29**)　　(**30**)　　**FIrpic**
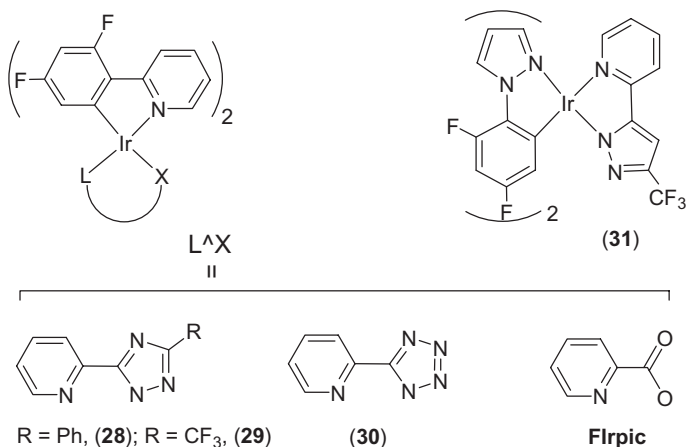
It is interesting to note that the room temperature emission of osmium complex **11**, which is attributed to the $^3\pi\pi^*$ excited state of the triazolate ligand **L12**, occurred at the much higher energy with onset at 420 nm [31]. In addition, the emission of complexes **28–30** are highly structured and the spectra are barely shifted when recorded at temperatures as low as 77 K. Based on these observations, the lowest energy excited state of **28–30** must possess a mixed $^3\pi\pi^*$ and ^{3}MLCT character that is principally localized at the cyclometalated dfppy ligand and is thus less sensitive to the change of the azolate based chelates. A recent DFT calculation on **FIrpic** showed good agreement with this delineation [68].

Moreover, Chi, Chou, and coworkers have also prepared an analogous iridium complex, **31**, in an attempt to synthesize the so-called true blue phosphors [69]. It is anticipated that the dfppz ligand will display an energy gap far greater than the typical blue radiation, which was revealed by the emission envelop of [Ir(dfppz)$_3$] starting from λ_{max} ~390 nm at 77 K, (dfppz)H = 2,4-difluorophenyl pyrazole. Thus, after attaching the pyrazole chelate **L3** to a [Ir(dfppz)$_2$] unit as the ancillary ligand in giving **31**, the ligand character of **L3** would dominate the excited state manifolds, showing the required blue phosphorescence with an additional ~30 nm blue shift compared to that of complexes **28–30**. Unfortunately, the emission quantum yield turned to a very low value ($\Phi = 0.007$) in solution, making this molecular design somewhat useless for fabricating OLEDs. The DFT calculation has again ruled out the participation of the *dd* transition in the fast deactivation process that causes low quantum yield. On the contrary, we speculate that, because the triplet states were in a high energy blue region, it would display a relatively shallow potential energy surface (PES) and may allow a fast surface crossing to the ground state. Subsequently, radiationless deactivations are executed via thermal activation to certain vibrational levels close to the section of a triplet–singlet surface through facile metal–ligand bond stretching motion. Although detailed insights into the deactivation mechanism are still pending, the experimentally extracted activation energy of 4.43 kcal/mol ($\approx$1550 cm^{-1}) of a related complex provides an estimate of the gap between the ground vibrational level of T_1 and the surface crossing section, while the pre-exponential factor of 1.25×10^{12} s^{-1} reflects the vibrational frequency of the weakly-bonding modes channeling into the major radiationless pathway.

The fabrication of OLEDs employing **29** and **30** and their electroluminescence characterization have been described, using a multilayer structure of ITO/NPB (30 nm)/mCP: **29** or **30** (30 nm, 7%)/TPBI(30 nm)/LiF (0.5 nm)/Al, where mCP = 1,3-bis(9-carbazolyl) benzene [67]. It is notable that both EL spectra exhibit three vibronic shoulders at ~460, 490, and 520 nm, which are analogous to their PL spectra. However, the device employing **30** exhibited a much more intense side band at ~490 nm that reduces the color purity, eventually shifting the CIE coordinates to 0.15, 0.24. On the other hand, the device employing **29** showed a significantly reduced emission shoulder at ~490 nm that allows the electroluminescence to appear in the deep-blue region with CIE = 0.14, 0.18. When an octyl chain is introduced at the 4-position of the pyridyl ring of **L12**, the resulting chelate ligand can be used to prepare analogous octyl substituted iridium complexes for PLEDs using PVK blends [70]. The maximum brightness is 110 cd m^{-2} at 18 V, and the luminous efficiency at 100 cd m^{-2} is 0.06 cd A^{-1}, with CIE coordinates being 0.14,

0.26. Direct charge trapping on the triplet emitter is found to be the dominant recombination process in these electrophosphorescent devices.

5.3.4
Platinum-Based Emitters

Neutral Pt(II) complexes with cyclometalating ligands, which exhibit a square planar d^8 configuration, have shown strong emissions in the fluid and solid states and have attracted a great deal of fundamental interest. Their square-planar geometry, which allows formation of dimer, excimer and even aggregate through axial coordination, results in distinctive photophysical properties when compared to the d^6 octahedral coordinated metal complexes [71]. Thus, in addition to the typical MLCT and ligand-centered $\pi\pi^*$ transition that occurred in the d^6 complexes [10c], a new type of electronic transition, denoted as metal-metal-to-ligand charge transfer (MMLCT), became possible; this type of transfer involves a charge transfer between the filled Pt–Pt antibonding orbital and a vacant, ligand-based π^* molecular orbital [72]. The pyridyl azolate based Pt(II) complexes showed no exception from such behavior, and their photophysical properties will be elaborated by systematically changing the ligand design.

These Pt(II) complexes can be obtained via treatment of the *in situ* generated pyrazolate anion with $[PtCl_2(DMSO)_2]$ in THF, or via a direct combination of the respective pyrazoles with K_2PtCl_4 in refluxing ethanol [73]. Both methods gave the anticipated products in good yields, and their structures can be seen in the structural drawings depicted below:

(32)   (33) $R_f = CF_3$, (35); C_3F_7, (36)

(34) $R_f = C_3F_7$, (37)
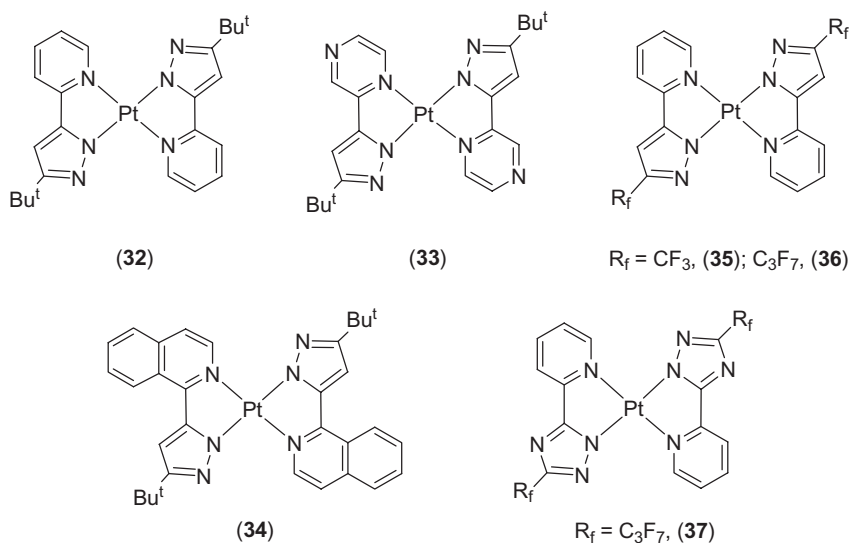
Table 5.5 summarizes the important photophysical data for complexes **32–37**. The room temperature UV-Vis and emission spectra of complexes **32–34** in THF

Table 5.5 Photophysical properties of platinum(II) complexes **32–37**.

Entry	λ_{abs}^{max} ($\varepsilon \times 10^3$, M^{-1} cm^{-1})	*PL λ_{max} (nm)*[a]	*Φ*	*τ (µs)*
32	268 (19), 320 (13), 340 (10), 416 (2.2), 442 (2.1)	494, 518[b] [489, 518, 550[b]]	0.19 [1.1×10^{-2}]	0.4 [0.4]
33	271 (23), 313 (12), 340 (12), 375 (13), 473 (2.2), 502 (2)	576, 596[b] [626]	0.82 [6×10^{-4}]	2.4 [0.03]
34	283 (31), 206 (27), 351 (30), 371 (21), 403 (5.2), 484 (4.6)	584, 632, 685[b] [593, 634, 680[b]]	0.74 [4×10^{-4}]	13 [0.04]
35	256 (24), 310 (20), 330 (12), 377 (2.9), 389 (2.5)	–[c] [595]	[0.24]	[0.3]
36	256 (23), 310 (19), 328 (12), 376 (2.9), 388 (2.5)	–[c] [552]	[0.2]	[0.3]
37	258 (22), 296 (13), 318 (12), 360 (3.5), 376 (3.2)	–[c] [544]	[0.33]	[0.3]

a   The solid state spectra are listed in square brackets.
b   Shoulder.
c   Too weak to be observed.
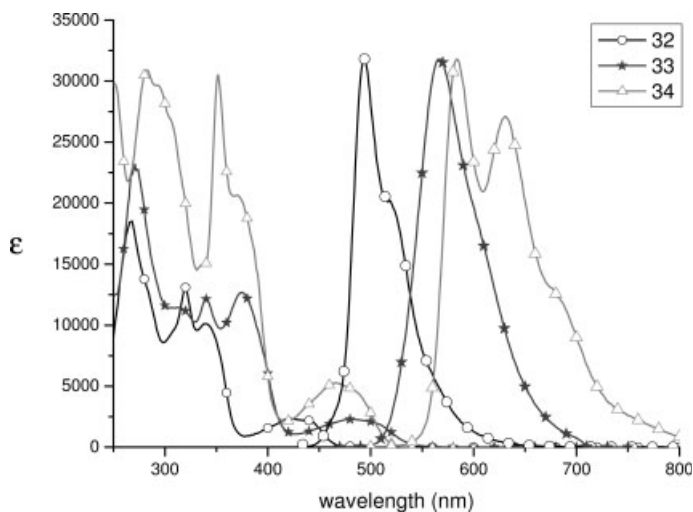
Fig. 5.10 UV-Vis absorption and emission spectra of complexes **32–34** in THF at RT.

solution are shown in Fig. 5.10. For the first two complexes **32** and **33**, the lower lying absorption bands (**32**: 416 nm; **33**: 473 nm) are assigned to the transition incorporating a state mixing singlet and triplet MLCT transitions and, to a certain extent, the intraligand $^3\pi\pi^*$ transitions. The strong singlet–triplet mixing is confirmed by the significant overlap between the UV-Vis absorption bands and the leading edge of their emission peak profile.

Moreover, the emission of the first two complexes, **32** and **33**, occurred at 494 nm ($\Phi = 0.19$; $\tau = 0.4\,\mu s$) and 576 nm ($\Phi = 0.82$; $\tau = 2.4\,\mu s$) in degassed THF, respectively. The red shift for **33** is a result of pyrazine substitution, for which the extra nitrogen atom of pyrazine lowers the ligand π^* energy level of Pt(II) metal complexes. For a further comparison, the emission of isoquinolyl complex **34** not only possesses a distinctive vibronic-like progression with peak wavelengths at 584, 632, and 685 nm, but also reveals a much larger peak–peak (absorption–emission) difference. The observed lifetime for **34** in THF ($\tau = 13\,\mu s$, $\Phi \sim 0.74$) is also substantially longer than those of **32** and **33** as well as those complexes with a ^{3}MLCT in the lowest lying manifold incorporating other Os(II), Ir(III), or Pt(II) heavy ions and with a ^{1}MLCT state in proximity. Thus, for the case of **34**, a significant amount of the ligand-centered $^3\pi\pi^*$ transitions is anticipated [74]. This can be rationalized by raising the π energy level due to the extensive π conjugation in **34**, while the progression of ~1300 cm^{-1} is akin to that corresponding to the C–C stretching modes (1270–1300 cm^{-1}) for terpyridyl Pt(II) complexes[75].

On the other hand, the solution absorption and solid-state emission spectra of the second group of Pt(II) complexes, **35–37**, are depicted in Fig. 5.11, along with the spectra of **32**, which served as the reference. It is notable that this group of complexes possesses ligands composing both 2-pyridyl and fluoroalkyl substituted azolate fragments. Significant blue shift of the MLCT absorption was noted in their UV/Vis absorption spectra. The increase in energy gap of MLCT transitions is apparently caused by either the electron withdrawing effect of CF$_3$ and C$_3$F$_7$ substituents, or the additional nitrogen atom in the case of triazolate, which induce an increase of the π^* acidity of the azolate and lower the Pt(II) metal 5d energy
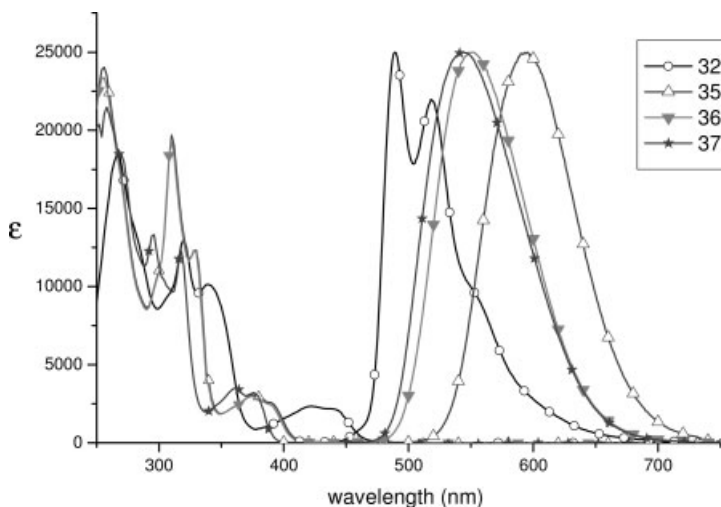
Fig. 5.11 UV-Vis absorption spectra of complexes **32** and **35–37** recorded in THF at RT and the respective solid-state emission spectra obtained from thin film samples at RT.

level. Concomitantly, the higher energy ππ* transitions, which are located at the UV region, also display a similar hypsochromic shift due to the increase of the intraligand ππ* energy gap [73].

The poor solubility of these complexes in organic solvents indicates their high tendency to form aggregation, for which the linear stacking arrangement with short Pt–Pt separation of 3.442 Å was confirmed by single crystal X-ray diffraction study on **36**. As a result, the featureless solid state emissions observed for **35–37** are assigned to the MMLCT transition [76], which is in sharp contrast to that of the emission profile of **32**, showing three distinct vibronic peaks in the solid state. Moreover, complex **35**, possessing the CF_3 substituents, exhibits a 43 nm (or 1310 cm^{-1}) bathochromic shift in emission peak λ_{max} vs. that of complex **36**, bearing C_3F_7 substituents. This result can be rationalized by an increase of the columnar ππ stacking interaction due to the decrease of steric hindrance for the CF_3 groups, as their electron withdrawing character was somewhat comparable or slightly less than that of C_3F_7. In contrast, for complex **37**, an even more notable hypsochromic shift of 51 nm (1575 cm^{-1}) was observed vs. that of **35**. This is apparently caused by the blue shift of the corresponding MLCT absorption while maintaining a similar degree of ππ stacking interaction.

As for the possible OLED application, complex **35** was tested by fabricating the typical multilayer OLED devices with doping levels varying from 7%, 20%, and 50% to 100%, using direct vacuum deposition [73]. The best device performances are achieved at ~20% of dopant concentration with an external quantum efficiency of 6.0% and a luminous efficiency of 19.7 cd/A at 20 mA/cm^2. Among other characteristics, the most interesting observation is the notable red shift in EL λ_{max} from 552 nm to 616 nm with increases in the doping concentration from 7% to 100%. As similar red-shifted EL emission was observed in the doped CBP films involving **35**, this concentration dependence is undoubtedly caused by the self-aggregation of the Pt(II) dopant within CBP host matrices.

Moreover, the achievement of high luminescence efficiency can be attributed, in part, to a rationally designed structure that greatly suppresses the aggregation effect. As a result, a rigid steric blocker such as camphor-like functionality was incorporated into the abovementioned square planar Pt(II) complexes, to reduce the solid-state aggregation and to suppress ^{3}MMLCT transitions [77]. Two Pt(II) complexes were prepared and showed unprecedented emission brightness (e.g., **38**: $\lambda_{max} = 553$ nm; $\Phi = 0.64$ and **39**: $\lambda_{max} = 635$ nm; $\Phi = 0.81$ in degassed CH_2Cl_2 at RT).

(**38**) (**39**)
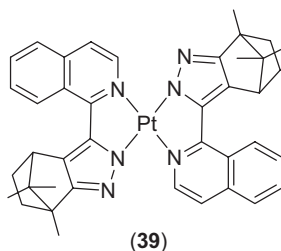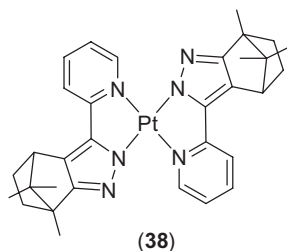
Their superior photoluminescent quantum yields are attributed to the high rigidity of camphor substituted indazole and extended π conjugation of the isoquinolinyl ligand, affording a reduction of radiationless deactivation. OLED devices fabricated using **39** as a dopant emitter have been achieved in a typical multilayer configuration of ITO/NPB/CBP:**39**/BCP/Alq$_3$/LiF/Al. At a dopant concentration of 12%, the device gave a bright red emission with λ_{max} at 612 nm and a very high external quantum efficiency of ~7% at a driving current of 20 mA. Upon increasing the doping level to 100%, electroluminescence peaked at 630 nm, with an external quantum efficiency of 3.2%, and a luminance efficiency of 3.5 cd/A, and a power efficiency of 1.52 lm/W was achieved at 20 mA [77]. The reduced red shift (18 nm) for the 100% doped device confirmed the nonexistence of aggregation for **39** in the solid state.

5.4
Concluding Remarks

The research subject of organic light-emitting diodes offers immense opportunity, for which finding the most suitable emitter remains as one of the pivotal factors. It is remarkable that the pyridyl azolate based ligands can react with a variety of metal elements, covering second row element Ru(II) and third row transition metal elements such as Os(II), Ir(III), and Pt(II), to form various neutral, stable and highly luminous coordination complexes. We also demonstrate the power of merging theoretical and experimental measures in rational design of a new series functionalized luminescent complexes. A broad spectrum of color tuning from red to blue has been achieved by derivatization of either pyridine or azolate segment as well as by variation of the electronic properties of the central metal atom via adjusting the ancillary ligands. In this chapter, we also bring out a critical issue in that the quantum efficiency, hence the radiationless deactivation process, can be qualitatively predicted via the theoretical frontier orbital analyses in combination with, e.g., X-ray structural determination. In the case of neutral Ru(II) complexes, we trust that the strategy for averting the incorporation of metal *dd* character into the lowest triplet state should be equally applicable to other systems involving second-row transition metal elements.

As for the application, we have successfully applied numerous pyridyl azolate based transition metal complexes toward making OLEDs with excellent performance. On one hand, it is possible that these pyridyl azolate based metal complexes, after full optimization, will eventually find certain industrial applications in the development of OLED devices. On the other hand, the results as well as the perspectives of our study should spark a continuous interest in the design and preparation of luminescence materials incorporating both main group and transition metal elements and for the future development of inorganic and organometallic photochemistry. For example, on the basis of a similar principle, we believe that coarse as well as fine tuning of the pyridyl azolate based complexes toward near-IR region with high luminescent efficiency is feasible, rendering their future applications in other arenas such as solar cell and near-IR imaging, etc.

References

1 (a) A. Juris, V. Balzani, F. Barigelletti, S. Campagna, P. Belser, A. Von Zelewsky, *Coord. Chem. Rev.* **1988**, *84*, 85. (b) E. C. Constable, P. J. Steel, *Coord. Chem. Rev.* **1989**, *93*, 205. (c) V. Balzani, A. Juris, *Coord. Chem. Rev.* **2001**, *211*, 97. (d) S. Serroni, S. Campagna, F. Puntoriero, C. Di Pietro, N. D. McClenaghan, F. Loiseau, *Chem. Soc. Rev.* **2001**, *30*, 367.

2 (a) M. G. Colombo, A. Hauser, H. U. Güdel, *Top. Curr. Chem.* **1994**, *171*, 143. (b) K. P. Balashev, M. V. Puzyk, V. S. Kotlyar, M. V. Kulikova, *Coord. Chem. Rev.* **1997**, *159*, 109. (c) A. Beeby, S. Bettington, I. D. W. Samuel, Z. Wang, *J. Mater. Chem.* **2003**, *13*, 80. (d) B. Ma, P. I. Djurovich, M. E. Thompson, *Coord. Chem. Rev.* **2005**, *249*, 1501.

3 (a) J. A. Treadway, B. Loeb, R. Lopez, P. A. Anderson, F. R. Keene, T. J. Meyer, *Inorg. Chem.* **1996**, *35*, 2242. (b) C. N. Fleming, K. A. Maxwell, J. M. DeSimone, T. J. Meyer, J. M. Papanikolas, *J. Am. Chem. Soc.* **2001**, *123*, 10336. (c) S. Chardon-Noblat, A. Deronzier, F. Hartl, J. Van Slageren, T. Mahabiersing, *Eur. J. Inorg. Chem.* **2001**, 613.

4 (a) E. Holder, B. M. W. Langeveld, U. S. Schubert, *Adv. Mater.* **2005**, *17*, 1109. (b) J. Brooks, Y. Babayan, S. Lamansky, P. I. Djurovich, I. Tsyba, R. Bau, M. E. Thompson, *Inorg. Chem.* **2002**, *41*, 3055.

5 (a) J. C. Jeffery, P. L. Jones, K. L. V. Mann, E. Psillakis, J. A. McCleverty, M. D. Ward, C. M. White, *Chem. Commun.* **1997**, 175. (b) A. Chadghan, J. Pons, A. Caubet, J. Casabo, J. Ros, A. Alvarez-Larena, J. F. Piniella, *Polyhedron* **2000**, *19*, 855.

6 E. M. Tjiou, A. Fruchier, V. Pellegrin, G. Tarrago, J. Heterocycl. Chem. **1989**, *26*, 893.

7 (a) R. Hage, J. G. Haasnoot, J. Reedijk, J. G. Vos, *Chemtracts: Inorg. Chem.* **1992**, *4*, 75. (b) R. Hage, J. G. Haasnoot, J. Reedijk, R. Wang, J. G. Vos, *Inorg. Chem.* **1991**, *30*, 3263.

8 (a) L. Chassot, A. Von Zelewsky, *Inorg. Chem.* **1987**, *26*, 2814. (b) J. W. Slater, D. P. Lydon, N. W. Alcock, J. P. Rourke, *Organometallics* **2001**, *20*, 4418. (c) V. V. Grushin, N. Herron, D. D. LeCloux, W. J. Marshall, V. A. Petrov, Y. Wang, *Chem. Commun.* **2001**, 1494.

9 A. M. Clark, C. E. F. Rickard, W. R. Roper, L. J. Wright, *Organometallics* **1999**, *18*, 2813.

10 (a) C. Adachi, R. C. Kwong, P. Djurovich, V. Adamovich, M. A. Baldo, M. E. Thompson, S. R. Forrest, *Appl. Phys. Lett.* **2001**, *79*, 2082. (b) H. Yersin, *Top. Curr. Chem.* **2004**, *241*, 1. (c) P.-T. Chou, Y. Chi, *Eur. J. Inorg. Chem.* **2006**, DOI: 10.1002/ejic.200600364, 3319. (d) P.-T. Chou, Y. Chi, *Chem. Eur. J.* **2007**, *13*, 380. (e) Y. Chi, P.-T. Chou, *Chem. Soc. Rev.* **2007**, *36*, 1421.

11 (a) S. P. Singh, D. Kumar, B. G. Jones, M. D. Threadgill, *J. Fluorine Chem.* **1999**, *94*, 199. (b) W. R. Thiel, J. Eppinger, *Chem. Eur. J.* **1997**, *3*, 696.

12 A. Satake, T. Nakata, *J. Am. Chem. Soc.* **1998**, *120*, 10391.

13 R. A. Jones, M. Karatza, T. N. Voro, P. U. Civcir, A. Franck, O. Ozturk, J. P. Seaman, A. P. Whitmore, D. J. Williamson, *Tetrahedron*, **1996**, *52*, 8707.

14 H.-Y. Chen, Y. Chi, C.-S. Liu, J.-K. Yu, Y.-M. Cheng, K.-S. Chen, P.-T. Chou, S.-M. Peng, G.-H. Lee, A. J. Carty, S.-J. Yeh, C.-T. Chen, *Adv. Funct. Mater.* **2005**, *15*, 567.

15 J. J. Klappa, S. A. Geers, S. J. Schmidtke, L. A. MacManus-Spencer, K. McNeill, *Dalton Trans.* **2004**, 883.

16 J. J. Klappa, A. E. Rich, K. McNeill, *Org. Lett.* **2002**, *4*, 435.

17 J. G. Haasnoot, *Coord. Chem. Rev.* **2000**, *200–202*, 131.

18 (a) R. Hage, *Coord. Chem. Rev.* **1991**, *111*, 161. (b) T. E. Keyes, C. M. O'Connor, J. G. Vos, *Chem. Commun.* **1998**, 889.

19 K. Funabiki, N. Noma, G. Kuzuya, M. Matsui, K. Shibata, *J. Chem. Res. (M)* **1999**, 1301.

20 (a) R. Hage, R. Prins, J. G. Haasnoot, J. Reedijk, J. G. Vos, *J. Chem. Soc. Dalton Trans.* **1987**, 1387. (b) P. M. Hergenrother, *J. Heterocycl. Chem.* **1969**, *6*, 965. (b) S. Kubota, M. Uda, T. Nakagawa, *J. Heterocycl. Chem.* **1975**, *12*, 855.

21 S. Fanni, T. E. Keyes, C. M. O'Connor, H. Hughes, R. Wang, J. G. Vos, *Coord. Chem. Rev.* **2000**, *208*, 77.

22 B. E. Buchanan, R. Wang, J. G. Vos, R. Hage, J. G. Haasnoot, J. Reedijk, *Inorg. Chem.* **1990**, *29*, 3263.

23 A. Facchetti, A. Abbotto, L. Beverina, S. Bradamante, P. Mariani, C. L. Stern, T. J. Marks, A. Vacca, G. A. Pagani, *Chem. Commun.* **2004**, 1770.

24 A. J. Downard, P. J. Steel, J. Steenwijk, *Aust. J. Chem.* **1995**, *48*, 1625.

25 Z. P. Demko, K. B. Sharpless, *J. Org. Chem.* **2001**, *66*, 7945.

26 S. Wang, *Coord. Chem. Rev.* **2001**, *215*, 79.

27 M. Kasha, *Disc. Faraday Soc.* **1950**, *9*, 14.

28 C.-C. Cheng, W.-S. Yu, P.-T. Chou, S.-M. Peng, G.-H. Lee, P.-C. Wu, Y.-H. Song, Y. Chi, *Chem. Commun.* **2003**, 2628.

29 (a) M. A. Baldo, D. F. O'Brien, Y. You, A. Shoustikov, S. Sibley, M. E. Thompson, S. R. Forrest, *Nature* **1998**, *395*, 151. (b) M. A. Baldo, M. E. Thompson, S. R. Forrest, *Pure Appl. Chem.* **1999**, *71*, 2095. (c) X. Gong, J. C. Ostrowski, G. C. Bazan, D. Moses, A. J. Heeger, *Appl. Phys. Lett.* **2002**, *81*, 3711.

30 P.-C. Wu, J.-K. Yu, Y.-H. Song, Y. Chi, P.-T. Chou, S.-M. Peng, G.-H. Lee, *Organometallics* **2003**, *22*, 4938.

31 J.-K. Yu, Y.-H. Hu, Y.-M. Cheng, P.-T. Chou, S.-M. Peng, G.-H. Lee, A. J. Carty, Y.-L. Tung, S.-W. Lee, Y. Chi, C.-S. Liu, *Chem. Eur. J.* **2004**, *10*, 6255.

32 B. P. Sullivan, *J. Phys. Chem.* **1989**, *93*, 24.

33 (a) A. Vogler, H. Kunkely, *Top. Curr. Chem.* **2001**, *213*, 143. (b) M. M. Glezen, A. J. Lees, *J. Am. Chem. Soc.* **1988**, *110*, 3892.

34 P. J. Hay, *J. Phys. Chem. A* **2002**, *106*, 1634.

35 N. J. Turro, *Modern Molecular Photochemistry*, **1991**, University Science Books, Mill Valley, Califorina, Chapter 6, page 170.

36 (a) A. B. Tamayo, B. D. Alleyne, P. I. Djurovich, S. Lamansky, I. Tsyba, N. N. Ho, R. Bau, M. E. Thompson, *J. Am. Chem. Soc.* **2003**, *125*, 7377. (b) T. Karatsu, T. Nakamura, S. Yagai, A.

Kitamura, K. Yamaguchi, Y. Matsushima, T. Iwata, Y. Hori, T. Hagiwara, *Chem. Lett.* **2003**, *32*, 886.

37 Y.-L. Tung, P.-C. Wu, C.-S. Liu, Y. Chi, J.-K. Yu, Y.-H. Hu, P.-T. Chou, S.-M. Peng, G.-H. Lee, Y. Tao, A. J. Carty, C.-F. Shu, F.-I. Wu, *Organometallics* **2004**, *23*, 3745.

38 Y.-L. Tung, S.-W. Lee, Y. Chi, Y.-T. Tao, C.-H. Chien, Y.-M. Cheng, P.-T. Chou, S.-M. Peng, C.-S. Liu, *J. Mater. Chem.* **2005**, *15*, 460.

39 C. M. Che, T. F. Lai, W. C. Chung, W. P. Schaefer, H. B. Gray, *Inorg. Chem.* **1987**, *26*, 3907.

40 B. D. Gupta, V. Singh, R. Yamuna, T. Barclay, W. Cordes, *Organometallics* **2003**, *22*, 2670.

41 F.-I. Wu, P.-I. Shih, C.-F. Shu, Y.-L. Tung, Y. Chi, *Macromolecules* **2005**, *38*, 9028.

42 (a) X. Yang, D. Neher, D. Hertel, T. K. Daubler, *Adv. Mater.* **2004**, *16*, 161. (b) C. Jiang, W. Yang, J. Peng, S. Xiao, Y. Cao, *Adv. Mater.* **2004**, *16*, 537.

43 H.-J. Su, F.-I. Wu, C.-F. Shu, Y.-L. Tung, Y. Chi, G.-H. Lee, *J. Polym. Sci. Part A: Polym. Chem.* **2005**, *43*, 859.

44 F.-I. Wu, P.-I. Shih, Y.-H. Tseng, G.-Y. Chen, C.-H. Chien, C.-F. Shu, Y.-L. Tung, Y. Chi, A. K.-Y. Jen, *J. Phys. Chem. B* **2005**, *109*, 14000.

45 (a) Y.-Y. Noh, C.-L. Lee, J.-J. Kim, K. Yase, *J. Chem. Phys.* **2003**, *118*, 2853. (b) M. Uchida, C. Adachi, T. Koyama, Y. Taniguchi, *J. Appl. Phys.* **1999**, *86*, 1680. (c) F.-C. Chen, S. C. Chang, G. He, S. Pyo, Y. Yang, M. Kurotaki, J. Kido, *J. Polym. Sci., Part B: Polym. Phys.* **2003**, *41*, 2681.

46 T. M. Brown, J. S. Kim, R. H. Friend, F. Cacialli, R. Daik, W. J. Feast, *Appl. Phys. Lett.* **1999**, *75*, 1679.

47 Y.-H. Niu, Y.-L. Tung, Y. Chi, C.-F. Shu, J. H. Kim, B. Chen, J. Luo, A. J. Carty, A. K.-Y. Jen, *Chem. Mater.* **2005**, *17*, 3532.

48 C.-W. Ko, Y.-T. Tao, *Synth. Met.* **2002**, *126*, 37.

49 (a) C. Adachi, M. A. Baldo, M. E. Thompson, S. R. Forrest, *J. Appl. Phys.* **2001**, *90*, 5048. (b) M. Ikai, S. Tokito, Y. Sakamoto, T. Suzuki, Y. Taga, *Appl. Phys. Lett.* **2001**, *79*, 156.

50 (a) S. Zalis, I. R. Farrell, A. Vlcek, *J. Am. Chem. Soc.* **2003**, *125*, 4580. (b) M. K.

Nazeeruddin, R. Humphry-Baker, D. Berner, S. Rivier, L. Zuppiroli, M. Graetzel, *J. Am. Chem. Soc.* **2003**, *125*, 8790.

51 Y.-L. Tung, S.-W. Lee, Y. Chi, L.-S. Chen, C.-F. Shu, F.-I. Wu, A. J. Carty, P.-T. Chou, S.-M. Peng, G.-H. Lee, *Adv. Mater.* **2005**, *17*, 1059.

52 Y.-L. Tung, L.-S. Chen, Y. Chi, P.-T. Chou, Y.-M. Cheng, E. Y. Li, G.-H. Lee, C.-F. Shu, F.-I. Wu, A. J. Carty, *Adv. Funct. Mater.* **2006**, *16*, 1615.

53 (a) S. Lamansky, P. Djurovich, D. Murphy, F. Abdel-Razzaq, H.-E. Lee, C. Adachi, P. E. Burrows, S. R. Forrest, M. E. Thompson, *J. Am. Chem. Soc.* **2001**, *123*, 4304. (b) S. Lamansky, P. Djurovich, D. Murphy, F. Abdel-Razzaq, R. Kwong, I. Tsyba, M. Bortz, B. Mui, R. Bau, M. E. Thompson, *Inorg. Chem.* **2001**, *40*, 1704.

54 (a) M. A. Baldo, S. Lamansky, P. E. Burrows, M. E. Thompson, S. R. Forrest, *Appl. Phys. Lett.* **1999**, *75*, 4. (b) T. Tsutsui, M.-J. Yang, M. Yahiro, K. Nakamura, T. Watanabe, T. Tsuji, Y. Fukuda, T. Wakimoto, S. Miyaguchi, *Jpn. J. Appl. Phys.* **1999**, *38*, L1502. (c) D. Bruce, M. M. Richter, *Anal. Chem.* **2002**, *74*, 1340.

55 (a) S. Sprouse, K. A. King, P. J. Spellane, R. J. Watts, *J. Am. Chem. Soc.* **1984**, *106*, 6647. (b) A. P. Wilde, K. A. King, R. J. Watts, *J. Phys. Chem.* **1991**, *95*, 629. (c) M. G. Colombo, T. C. Brunold, T. Riedener, H. U. Guedel, M. Fortsch, H.-B. Buergi, *Inorg. Chem.* **1994**, *33*, 545. (d) W. J. Finkenzeller, H. Yersin, *Chem. Phys. Lett.* **2003**, *377*, 299.

56 F.-M. Hwang, H.-Y. Chen, P.-S. Chen, C.-S. Liu, Y. Chi, C.-F. Shu, F.-I. Wu, P.-T. Chou, S.-M. Peng, G.-H. Lee, *Inorg. Chem.* **2005**, *44*, 1344.

57 X. Jiang, S. Liu, M. S. Liu, P. Herguth, A. K.-Y. Jen, H. Fong, M. Sarikaya, *Adv. Funct. Mater.* **2002**, *12*, 745.

58 Y. Li, M. K. Fung, Z. Xie, S.-T. Lee, L.-S. Hung, J. Shi, *Adv. Mater.* **2002**, *14*, 1317.

59 Y.-H. Niu, B. Chen, S. Liu, H. Yip, J. Bardecker, A. K.-Y. Jen, J. Kavitha, Y. Chi, C.-F. Shu, Y.-H. Tseng, C.-H. Chien, *Appl. Phys. Lett.* **2004**, *85*, 1619.

60 Y.-H. Song, S.-J. Yeh, C.-T. Chen, Y. Chi, C.-S. Liu, J.-K. Yu, Y.-H. Hu, P.-T. Chou, S.-M. Peng, G.-H. Lee, *Adv. Funct. Mater.* **2004**, *14*, 1221.

61 C. Adachi, M. A. Baldo, S. R. Forrest, M. E. Thompson, *Appl. Phys. Lett.* **2000**, *77*, 904.

62 (a) X. Ren, J. Li, R. J. Holmes, P. I. Djurovich, S. R. Forrest, M. E. Thompson, *Chem. Mater.* **2004**, *16*, 4743. (b) S. Tokito, T. Iijima, Y. Suzuri, H. Kita, T. Tsuzuki, F. Sato, *Appl. Phys. Lett.* **2003**, *83*, 569. (c) R. J. Holmes, S. R. Forrest, Y.-J. Tung, R. C. Kwong, J. J. Brown, S. Garon, M. E. Thompson, *Appl. Phys. Lett.* **2003**, *82*, 2422. (d) R. J. Holmes, B. W. D'Andrade, S. R. Forrest, X. Ren, J. Li, M. E. Thompson, *Appl. Phys. Lett.* **2003**, *83*, 3818. (e) I. Tanaka, Y. Tabata, S. Tokito, *Chem. Phys. Lett.* **2004**, *400*, 86.

63 (a) C.-L. Lee, R. R. Das, J.-J. Kim, *Chem. Mater.* **2004**, *16*, 4642. (b) M. K. Nazeeruddin, R. Humphry-Baker, D. Berner, S. Rivier, L. Zuppiroli, M. Graetzel, *J. Am. Chem. Soc.* **2003**, *125*, 8790. (c) Y.-Y. Lyu, Y. Byun, O. Kwon, E. Han, W. S. Jeon, R. R. Das, K. Char, *J. Phys. Chem. B* **2006**, *110*, 10303.

64 J. Li, P. I. Djurovich, B. D. Alleyne, I. Tsyba, N. N. Ho, R. Bau, M. E. Thompson, *Polyhedron* **2004**, *23*, 419.

65 J. Li, P. I. Djurovich, B. D. Alleyne, M. Yousufuddin, N. N. Ho, J. C. Thomas, J. C. Peters, R. Bau, M. E. Thompson, *Inorg. Chem.* **2005**, *44*, 1713.

66 P. Coppo, E. A. Plummer, L. De Cola, *Chem. Commun.* **2004**, 1774.

67 S.-J. Yeh, W.-C. Wu, C.-T. Chen, Y.-H. Song, Y. Chi, M.-H. Ho, S.-F. Hsu, C.-H. Chen, *Adv. Mater.* **2005**, *17*, 285.

68 Y. You, S. Y. Park, *J. Am. Chem. Soc.* **2005**, *127*, 12438.

69 C.-H. Yang, S.-W. Li, Y. Chi, Y.-M. Cheng, Y.-S. Yeh, P.-T. Chou, G.-H. Lee, C.-H. Wang, C.-F. Shu, *Inorg. Chem.* **2005**, *44*, 7770.

70 C. S. K. Mak, A. Hayer, S. I. Pascu, S. E. Watkins, A. B. Holmes, A. Koehler, R. H. Friend, *Chem. Commun.* **2005**, 4708.

71 B. Ma, J. Li, P. I. Djurovich, M. Yousufuddin, R. Bau, M. E. Thompson, *J. Am. Chem. Soc.* **2005**, *127*, 28.

72 S.-W. Lai, C.-M. Che, *Top. Curr. Chem.* **2004**, *241*, 27.

73 S.-Y. Chang, J. Kavitha, S.-W. Li, C.-S. Hsu, Y. Chi, Y.-S. Yeh, P.-T. Chou, G.-H. Lee, A. J. Carty, Y.-T. Tao, C.-H. Chien, *Inorg. Chem.* **2006**, *45*, 137.

74 (a) L. Sacksteder, A. P. Zipp, E. A. Brown, J. Streich, J. N. Demas, B. A. DeGraff, *Inorg. Chem.* **1990**, *29*, 4335. (b) L. Sacksteder, M. Lee, J. N. Demas, B. A. DeGraff, *J. Am. Chem. Soc.* **1993**, *115*, 8230.

75 (a) Q. Z. Yang, L. Z. Wu, Z. X. Wu, L. P. Zhang, C. H. Tung, *Inorg. Chem.* **2002**, *41*, 5653. (b) V. W. W. Yam, R. P. L. Tang, K. M. C. Wong, K. K. Cheung, *Organometallics* **2001**, *20*, 4476.

76 (a) V. H. Houlding, V. M. Miskowski, *Coord. Chem. Rev.* **1991**, *111*, 145. (b) H. Yersin, U. Riedl, *Inorg. Chem.* **1995**, *34*, 1642.

77 J. Kavitha, S.-Y. Chang, Y. Chi, J.-K. Yu, Y.-H. Hu, P.-T. Chou, S.-M. Peng, G.-H. Lee, Y.-T. Tao, C.-H. Chien, A. J. Carty, *Adv. Funct. Mater.* **2005**, *15*, 223.

6
Physical Processes in Polymer-Based Electrophosphorescent Devices

Xiao-Hui Yang, Frank Jaiser, and Dieter Neher

This book chapter is devoted to the understanding of physical processes in polymer-based phosphorescent devices. It has been recognized that doping the phosphorescent emitter into a charge-conducting matrix is necessary to spatially separate the dyes and to reduce the rate for non-radiative intermolecular decay channels. Therefore, the design of highly-efficient devices requires understanding and control of the processes leading to the excitation of the phosphorescent guest. This chapter primarily discusses mechanisms leading to electrophosphorescence in devices based on the non-conjugated host poly(vinylcarbazole) (PVK). Different transfer processes such as charge trapping, Förster and Dexter transfer are addressed. In addition, selected examples of devices with the red-emitting dye PtOEP doped into conjugated polymer hosts are presented.

6.1
Introduction

Driven by the commercial interest in the development of displays and large-area light sources, the understanding of physical processes in polymer-based light-emitting diodes (PLEDs) has significantly advanced since electroluminescence from a π-conjugated polymer was reported in 1990 [1]. Because of the complexity of the overall process leading to the emission in PLEDs, most theoretical and experimental studies focused on simple device architectures with one fluorescent polymeric component [2–6]. Despite the simplicity of fabrication of these electro-fluorescent devices, efficient blue, green and red emission from PLEDs has been reported [7, 8].

According to simple spin statistics, the recombination of uncorrelated electrons and holes in organic media forms triplet states with a 3-fold higher probability than singlet states [9]. Though this simple prediction of quantum statistics has been questioned in case of polymer-based electrofluorescent devices [10–13], only few LEDs based on single-component active polymer layers exceeded the quantum limit of 5% [14, 15]. Electrophosphorescence offers the potential to construct devices in which every injected charge leads to the emission of a photon. In the

first examples published in 1998 by Baldo et al. [16], the phosphorescent dye octa-ethyl-porphine platinum (PtEOP) was doped into a small molecule host at a low concentration. This electrophosphorescent device emitted red light with an external quantum efficiency of 4%. Shortly after this, the first polymer-based electrophosphorescent diode was published [17]. In this case, PtOEP was added at low concentration to the polymer poly[4-(*N*-4-vinylbenzyloxyethyl, *N*-methylamino)-*N*-(2,5-di-*tert*-butylphenylnaphthalimide)] PVP. Since then, the performance of small molecule and polymer-based electrophosphorescent devices has been largely improved, with high efficiencies for blue [18–20], green [21–25], red [25–27], and white [28–30] emission.

It is generally accepted that doping the phosphorescent emitter into a charge-conducting matrix is necessary to spatially separate the dyes and to reduce the rate for nonradiative intermolecular decay channels such as triplet–triplet annihilation (TTA) (see e.g., [31]). Transfer of excitation to the guest is then promoted by three processes (Fig. 6.1): (a) Förster transfer of singlet excitons generated on the matrix to the guest, (b) Dexter transfer of both singlet and triplet excitons generated on the host to the dopant, and (c) direct generation of singlet and triplet excitons on the guest by sequential trapping of charges. In the first cases, excitons are first generated on the host and then transferred to the dopant while in the latter case, the host only functions as the charge transporting matrix. Förster transfer requires a significant overlap of the emission of the matrix and the absorption of the guest. Most phosphorescent dyes used in LED applications have the most prominent absorption in the blue/deep blue wavelength region. Therefore, host materials with high-energy excited states ("wide band gap") need to be used to ensure efficient energy transfer in electrophosphorescent devices. Efficient Dexter transfer requires an overlap of the host and guest wavefunctions and that the energy of the (singlet and triplet) exciton on the host matches the exciton energy on the guest. Finally, the phosphorescent dopant itself might function as a carrier trap and recombination site if there is a significant offset between the HOMO or LUMO
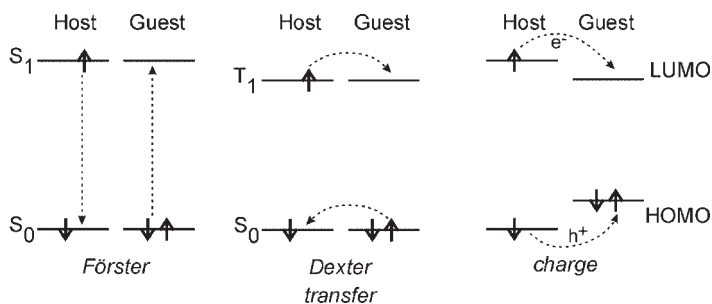
Fig. 6.1 Scheme illustrating various transfer processes from the host to the guest: Förster-type energy transfer between singlet states, Dexter-type energy transfer from the host to the guest triplet state, and electron (hole) transfer from the host LUMO (HOMO) to the guest LUMO (HOMO).

levels, respectively, of the host and the guest. Irrespective of the process leading to the excitation of the dye, confinement of the triplet exciton on the dye is only guaranteed if the T_1 energy of the guest is smaller than that of the host.

It has been shown that the singlet–triplet splitting in conjugated polymers is quite large. According to results by Monkman et al. the energy of the lowest triplet state T_1 of fully-conjugated polymers is ca. 1 eV lower than the lowest singlet excited sate S_1 [32]. Though others reported a smaller singlet–triplet splitting of ca. 0.7 eV [33, 34], these results imply that only wide-gap polymers are applicable as host materials for phosphorescent dyes. Nevertheless, a large variety of polymers with charge-transporting moieties in the side chains [17, 35, 36] or fully conjugated polymers [37–45] have been demonstrated to function as hosts in electrophosphorescent devices and more recently, copolymers with covalent binding of the phosphor have been demonstrated in efficient OLED structures [46–51].

This chapter is divided into four sections. In Section 6.2, physical mechanisms leading to the emission in devices based on the nonconjugated host poly (vinylcarbazole) (PVK) will be discussed. Different transfer processes such as charge trapping, Förster, and Dexter transfer will be addressed. The following section presents selected examples of devices with the red-emitting dye PtOEP doped into two different conjugated polymer hosts. The chapter ends with a conclusion. Note that this review does not contain a detailed discussion of the photophysical properties of the phosphors. This issue has been addressed in previous review articles [52–55].

6.2
Phosphorescent Devices Based on PVK

Polyvinylcarbazole is one of the most widely studied host polymers for electrophosphorescent diodes. Because of its high T_1 state, the polymer can host blue, green, and red phosphors. Various values have been reported for the HOMO and LUMO positions of PVK. In the following we will refer mostly to energies determined by cyclic voltammetry in solution versus the ferrocene/ferrocenium redox pair (setting the absolute energy of the ferrocene/ferrocenium redox reaction of 4.8 eV below vacuum [56]) [25]. This yields values for the absolute HOMO and LUMO energy of PVK of 5.6 eV and 2.2 eV, respectively, below vacuum. For pure PVK, hole mobilities of up to 10^{-5} cm^2/Vs have been reported [57], but the electron mobility of PVK is rather poor. Therefore, most PVK-based devices have an appropriate electron-transporting component added to the emission layer. One commonly used molecule is 2-(4-biphenylyl)-5-(4-*tert*-butylphenyl)-1,3,4-oxadiazole (PBD), [23, 36, 58–61] with the LUMO at 2.3 eV and the HOMO lower than 6 eV.

Without addition of a dye, the PVK : PBD matrix exhibits a broad emission with maximum at ca. 430 nm. This has been assigned to an exciplex, which forms rapidly after excitation of the PVK : PBD matrix [62, 63]. The quantum efficiency of this exciplex emission is ca. 10% [64]. Details about the kinetics of the excitation in the PVK : PBD blend matrix can be found in [63].

6.2.1
Charge Trapping in Devices with Ir(ppy)₃

fac-tris(2-phenylpyridine)iridium (Ir(ppy)₃) is a well-known efficient green-emitting phosphor. In fact, one of the first examples for PVK-based electrophosphorescent diodes used Ir(ppy)₃ as the phosphorescent dye [35]. Strong spin–orbit coupling induced by Ir³⁺ gives the formally spin-forbidden transition form the lowest ³MLCT to the singlet ground state a significant transition dipole strength, resulting in a short phosphorescence life time of ca. 1.5 µs in a PVK matrix. For application in solution-processed devices, various well-soluble derivatives of Ir(ppy)₃ have been tested in PVK : PBD. In the following, we will discuss the properties of devices with the dye tris(2-(4-tolyl)pyridine)iridium, Ir(mppy)₃. This dye has the emission maximum at ca. 512 nm, corresponding to a triplet energy of 2.4 eV. The HOMO and LUMO energy is at 5.0 and 2.2 eV, respectively. Thus, Ir(mppy)₃ will constitute a deep hole trap in PVK : PBD (Fig. 6.2).
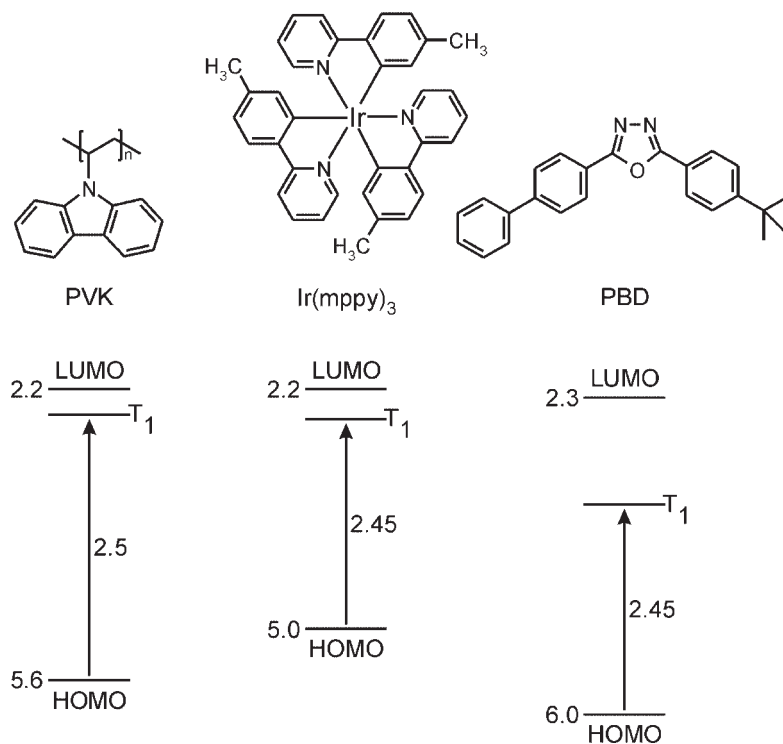
Fig. 6.2 Chemical structure of PVK, PBD, and Ir(mppy)₃, the HOMO and LUMO positions determined by cyclic voltammetry [25] and the triplet energies [50, 65]. (Note that the triplet level positions are depicted simplified as being relative to the HOMO energies).
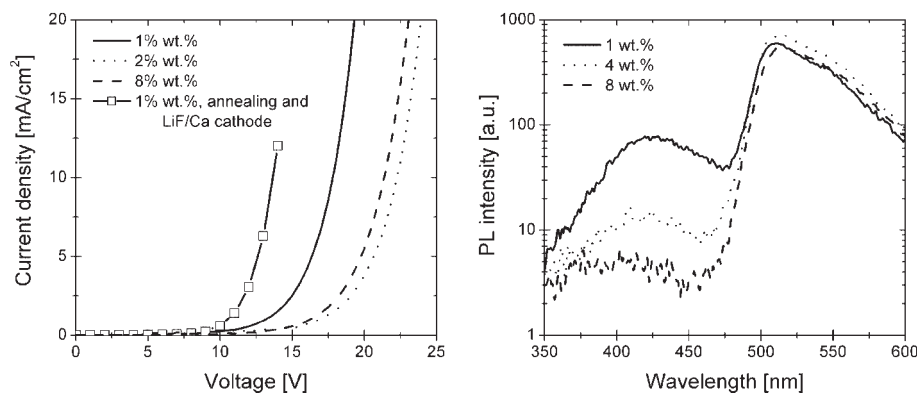
Fig. 6.3 (left) Current–voltage characteristics of single layer PVK:PBD:Ir(mppy)$_3$ electrophosphorescent devices comprising an ITO/PEDOT:PSS anode. Also shown is the characteristics of a diode with an annealed emission layer and a LiF/Ca cathode [61].

(right) PL spectra of blends of PVK:PBD:Ir(mppy)$_3$ with a phosphor concentration of 1, 4, or 8wt% relative to PVK. Excitation was at 325 nm, which almost exclusively excites the PVK:PBD host [66].

Evidence for severe carrier trapping in the Ir(mppy)$_3$ based devices with a Ca cathode comes from the comparison of current–voltage characteristics for different Ir(mppy)$_3$ concentrations. As shown in Fig. 6.3, the current–voltage curves shift to significantly higher voltages when increasing the dye concentration from 1wt% to 2wt%. Interestingly, the driving voltage decreases again when increasing the concentration further to 8wt%. This finding is consistent with reports on related blend systems [39, 65]. One possible reason is that direct jumps of holes between the Ir dyes become possible at higher concentrations, without the need for detrapping to the PVK host. Even larger shifts in voltage have been reported by X. Gong et al. for a related dye, tris[9,9-dihexyl-2-(pyridinyl-2′)fluorene iridium (Ir(DPF)$_3$) in a PVK:PBD (40wt%) matrix. In this case, the bias to drive the device at a current density of 1mA/cm^2 increased from 11 V for a Ir(DPF)$_3$ concentration of 0.05wt% to 37 V for a device with a 5wt% dye concentration.

Figure 6.3 also shows the PL spectra of PVK:PBD:Ir(mppy)$_3$ for different dye concentrations. Emission spectra were recorded with excitation at 325 nm, which almost exclusively excites the matrix. At 1wt%, one can clearly distinguish the emission from the PVK:PBD host with maximum at 425 nm and the dye emission which peaks at 510–515 nm depending on concentration. The figure shows that an Ir(mppy)$_3$ concentration of more than 4wt% is needed to fully quench the host emission. Detailed studies on a related green-emitting dye in a PVK:PBD matrix showed that the dependence of the host PL intensity on dye concentration is consistent with Förster energy transfer [67]. In contrast to this, the EL spectrum of single layer devices with a PVK:PBD:Ir(mppy)$_3$ emission layer is fully determined by the phosphorescence from the dye even at a concentration as low as 0.3wt%. For a related system, Gong et al. observed pure dye emission even for a concentra-

tion of 0.01 wt%. This finding is consistent with carrier trapping as the main mechanism for populating the dye [60, 67].

In general, the kinetics of charge trapping in a doped system is determined by both the diffusion-controlled random motion of the carriers on the host and the rate of charge transfer from the matrix to the charge-trapping dopant. Because the rate for the latter process decreases exponentially with the distance between the electron donor and electron acceptor, only the transfer from the nearest host molecule is expected to lead to the population of the trap. Therefore, for close proximity of host and guest molecules, the motion of the charges on the host toward the guest should be the rate-limiting step. Following the theoretical treatment by T.R. Waite, trapping of, e.g., holes with the density p by neutral traps (guests) of total density T should follow the kinetics [68]

$$\frac{dp}{dt} = -\kappa \left[1 + \frac{r_o}{(\pi D_p t)^{1/2}} \right] p(t)(T(t) - T^+(t)),$$

(6.1)

where $\kappa = 4\pi r_o D_p$. Here, T^+ is the density of occupied traps, D_p is the diffusion coefficient for holes, and r_o is the distance between a hole and the trap below which trapping occurs *irreversibly*. (Note that the original work by Waite considers the kinetics of diffusion-limited chemical reactions.) In the simplest case, r_o is determined by the size of the charge-trapping molecule. For steady-state conditions, Eq. (6.1) simplifies to $\frac{dp}{dt} = -\gamma_T p(t)(T(t) - T^+(t))$ with $\gamma_T = 4\pi r_o D_p$ the coefficient for carrier trapping. For carriers moving in a device with a drift velocity $v = \mu_p E$ (with μ_p being a constant hole mobility), trapping will limit the penetration depth L_T into the charge-conducting layer. In the limit of low trap occupation ($T^+ \ll T$), the penetration depth is simply given by

$$L_T^{-1} = \alpha_T = \frac{\gamma_T T}{\mu_p E} = \frac{4\pi D_p}{\mu_p E} r_o T.$$

(6.2)

Further, using Einstein relation, the drift mobility μ_p and the diffusion coefficient D_p can be related via

$$\frac{D_p}{\mu_p} = \frac{k_B \theta}{e}$$

(6.3)

where k_B is the Boltzmann constant, θ the temperature, and e the elementary charge. Combining (6.2) and (6.3) results in the simple relation

$$L_T^{-1} = \alpha_T = \frac{4\pi k_B \theta}{eE} r_o T.$$

(6.4)

For a concentration of 1 wt% Ir(mppy)$_3$ in PVK:PBD, the trap concentration T is ca. 10^{19} cm^{-3}. The trapping radius r_o can be approximated by the diameter of the phosphor, ca. 1 nm. Then, L_T is ca. 35–40 nm at a field of 10^6 V/cm at room tem-

perature. Thus, all holes should become trapped within the emission layer of a typical polymer-based OLED. However, recent theoretical and experimental investigations suggested that Einstein relation is violated in disordered semiconductors such as amorphous or semicrystalline polymers. This is because charge transport in these materials is dispersive [69, 70]. For example, investigations on PVK-based photorefractive polymers with the photoelectromotive force technique yielded a ratio of D/μ ca. three times larger than predicted by Einstein relation [70]. Thus, the free path length of holes in these highly disordered multicomponent layers might even be smaller, within the range of a few nanometers at dye concentrations larger than 1 wt%. Consequently, holes should be predominately accumulated near the anode, giving rise to a positive space charge region near the hole-injecting contact. As pointed out above, this accumulation might be responsible for the large driving voltage at high dye concentrations.

Quite surprisingly, the pronounced dependence of the bias on the phosphor concentration as displayed in Fig. 6.3 vanished almost completely after proper annealing of the emission layer and inserting a LiF interlayer between the emission layer and the Ca cathode. Since these measures are not expected to alter the hole-trapping characteristics, the reduced effect of the dye concentration on the device characteristics must be due to improved electron injection and transport. Apparently, holes trapped on the emitter close to the anode are effectively neutralized via recombination with electrons in these improved layers. Support for this model came from systematic study on PVK:PBD:Ir(mppy)$_3$ devices with different layer composition and layer thickness. Figure 6.4 summarizes the results for a fixed current density of 5 mA/cm^2. Most noticeably, we observed that the driving field decreased considerably with the increase of PBD concentration, while there was no significant correlation between the dye concentration and the driving conditions. Further, for high PBD concentrations, the electric field was almost independent of the layer thickness. Concurrently, high efficiencies were reported for the highest PBD concentrations. On the other hand, low dye concentrations turned out to be beneficial for reaching high efficiencies. Though a quantitative analysis of these results is not possible without the knowledge of all relevant kinetic parameters, a consistent picture can be drawn based on the following considerations: (a) because EL is exclusively from the dye, excitation of the phosphor must mainly occur by sequential charge trapping. (b) because the Ir phosphor does constitute a hole trap but not an electron trap, hole trapping will be mainly by neutral phosphors. (c) the free path length for hole transport changes inversely proportionally with the dye concentration. (d) electron transport is via hopping between PBD (and dye) molecules. In this model, the significant decrease in driving voltage with increasing PBD concentration is consistent with the need to transport electrons throughout the emission layer (to reach the holes trapped close to the anode).

6.2.2
Competition Between Free Carrier Recombination and Trapping

As mentioned above, the EL spectra of PVK-based devices exhibited pure dye emission even for low concentrations of the green-emitting phosphor. This result
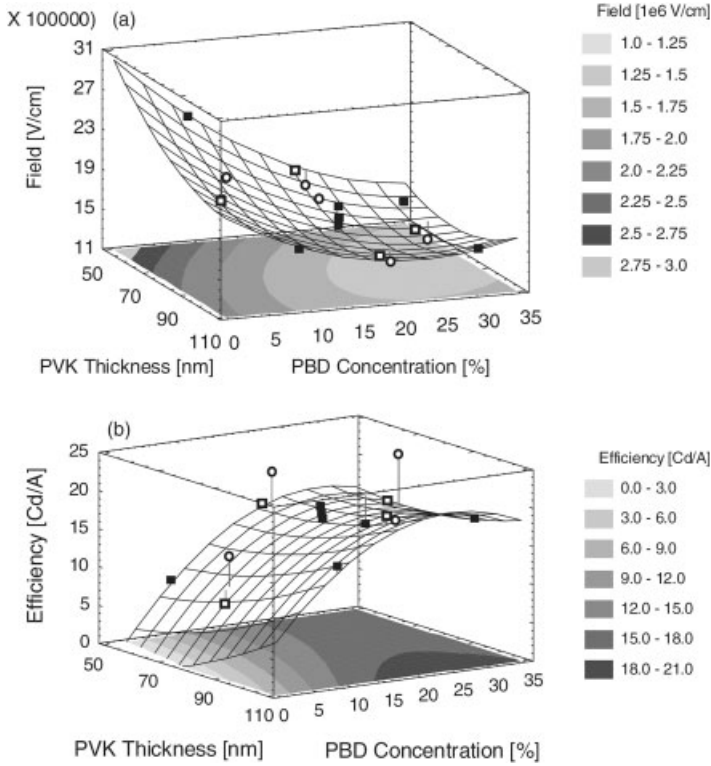
Fig. 6.4 Results of the statistical analysis of the dependence of the electric field (upper graph) and the luminance efficiency (lower graph) of PEDOT:PSS/PVK:PBD:Ir(mppy)$_3$/LiF/Ca devices on the PBD concentration, the PVK layer thickness, and the Ir(mppy)$_3$ concentration. Symbols show the experimental data measured at a constant current density of 5 mA/cm^2 for devices with Ir(mppy)$_3$ concentrations of 0.3–0.5 wt% (open circles), 2.5–4 wt% (solid squares), and 5–7 wt% (open squares). The response surface and contour plots present a multiparameter function obtained from the best fit to the experimental data, plotted for a fixed Ir(mppy)$_3$ concentration c_{Ir} of 3.5 wt% [61].

is quite surprising keeping in mind that the coefficient for recombination of oppositely charged carriers should be much larger than the coefficient for trapping on a neutral trap.

For low-mobility solids, the recombination is Langevin type, with the recombination coefficient γ_R

$$\gamma_R = 4\pi(D_p + D_e)r_C. \tag{6.5}$$

Here, $r_C = \dfrac{e^2}{4\pi\varepsilon_o\varepsilon k_B\theta}$ is the Coulomb capture radius. In other words, a free electron corresponds to a hole trap with a trapping radius equal to the Coulomb

radius. Using the Einstein relation, Eq. (6.5) can be rewritten in the form of the well-known expression for the Langevin-type recombination coefficient

$$\gamma_R = \frac{e(\mu_p + \mu_e)}{\varepsilon_o \varepsilon}.$$

In organic materials with a low dielectric constant, r_C is 18–20 nm at room temperature, much larger than the typical size of a molecule. Thus, $\gamma_R \gg \gamma_T$ and recombination of holes with free electrons should dominate over trapping on neutral molecules even at moderate charge densities.

We have recently studied the charge kinetics in a composite based on PVK, an electrically inert plasticizer (to lower the glass transition temperature) and different concentrations of the hole-trapping molecule N,N'-diphenyl-N,N'-(bis(3-methylphenyl)-[1,1-biphenyl]-4,4′-diamine (TPD, see Fig. 6.9 for structure) [71]. TPD is well suited for these investigations because it is well miscible with PVK for a wide range of concentrations. Further, the TPD HOMO level is well above that of PVK but comparable to that of Ir(ppy)₃ [72]. Mobile holes were generated in the polymer layer via photoexcitation of an appropriate sensitizer molecule (TNFM), added to the polymer matrix at low concentrations. Details about the general measurement scheme and the data analysis can be found in [73].

Figure 6.5 shows typical photocurrent transients for different concentrations of TPD. The influence of the added traps is well visible even at a concentration of 0.01% (corresponding to a trap concentration of ca. 1.2×10^{17} cm⁻³). After an initial rise the current reaches a plateau, which is determined by the equilibrium between the generation, trapping, and recombination of holes.

The experimental results could be consistently fitted with $\gamma_R = 1.6 \times 10^{-14}$ cm³/s and $\gamma_T = 0.4 \times 10^{-14}$ cm³/s. The value for γ_R is in good agreement with the result of earlier studies on other PVK-based composites [74]. Surprisingly, the recombina-
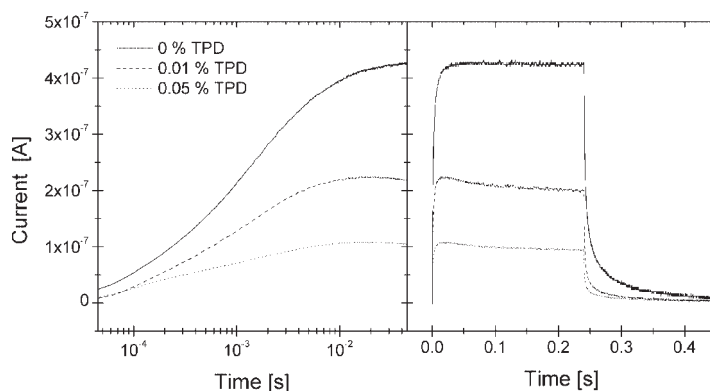
Fig. 6.5 Experimental photocurrent transients of samples of PVK without and with 0.01 wt% and 0.05 wt% TPD under single pulse illumination at (left) short and (right) long times, measured at an intensity of 10 W/cm² and electric field of 27 V/μm [71].

tion coefficient is only a factor of 4 larger than the trapping coefficient, despite the large difference between r_C and the size of a TPD molecule. Though the studied composite might not constitute an ideal model system, these results indicate that recombination in these disordered PVK composites is not consistent with Langevin-type recombination, as also suggested by reports on other PVK-based photorefractive composites [74]. The observation that the ratio between recombination and the trapping coefficient is smaller as predicted by established theories has important consequences with regard to the composition of dye-doped emission layers. Reduced recombination on the host directly implies that a smaller concentration of phosphors is needed to have emission almost exclusively from the dopant. For example, in the blend PVK:PBD:Ir(DPF)₃ mentioned earlier, the PVK:PBD emission was fully suppressed in EL for a dye concentration as small as 0.01 wt%. Undoubtedly, further investigation on the competition between trapping and recombination is needed to develop a more conclusive picture of the processes in a working electrophosphorescent device.

6.2.3
Competition between Förster Transfer and Trapping

As pointed out above, energy transfer as well as charge trapping contributes to the excitation of dyes in the PVK:PBD matrix in EL. In order to study in detail the competition between Förster-type energy transfer and charge trapping, we have analyzed the PL and EL emission properties of PVK:PBD doped with dendronized perylene diimide emitters [75]. The chemical structures of the used dyes are summarized in Fig. 6.6. Light-emitting dendrimers are a promising approach for efficient solution-processed LEDs, as the intermolecular interactions can be fine tuned via the thickness of the scaffold [76, 77]. Unlike in the figure, the polyphenyle dendrons are oriented perpendicular to the PDI plane and encase the core

PDI-M PDI-G1 PDI-G2
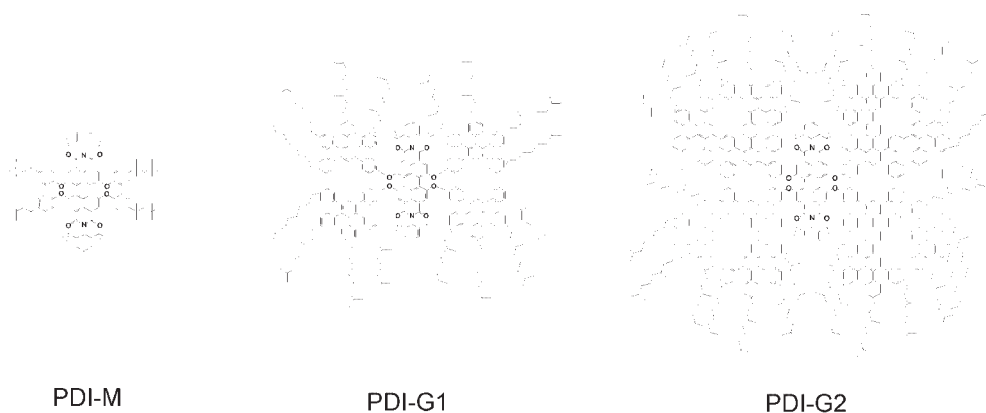
Fig. 6.6 PDIs with dendrimer shields on the bay positions. The polyphenyle dendrons form almost spherical shells around the PDI core (see Fig. 6.8).
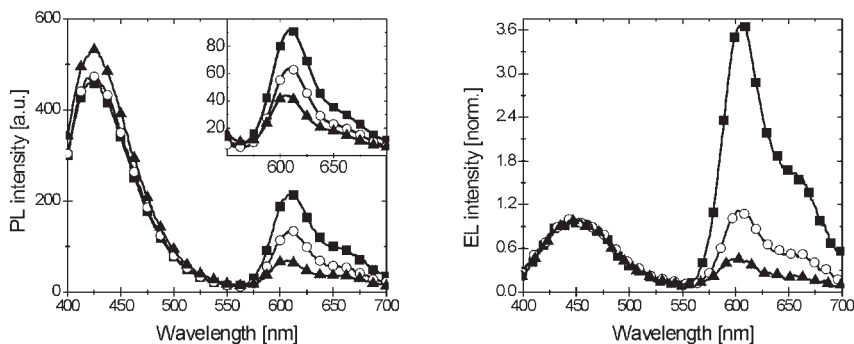
Fig. 6.7 PL spectra (left) and EL spectra (right) of PVK–PBD blended with 500 ppm of the generation one chromophore PDI-G1 (circles), the generation two chromophore PDI-G2 (triangles) and of the model PDI-M (squares). PL spectra were recorded at an excitation wavelength of 330 nm (excitation of PVK matrix). The inset shows PL spectra of the same films upon direct dendrimer excitation at 500 nm. The EL spectra were measured at an operating current density of 20 mA/cm^2 [75].

as almost spherical shells. It is expected that increasing the thickness of the shell will affect the kinetics of energy and charge transfer, thus determining the device performance.

Figure 6.7 shows the photoluminescence spectra of films containing 500 ppm of the PDI dendrimers PDI-G1 and PDI-G2 and of the model compound PDI-M, respectively, measured either upon excitation of the matrix at 330 nm or by direct dye excitation at 500 nm (inset). The concentration of guest molecules in the matrix is given in terms of dye molecules per million PVK repeating units. Upon matrix excitation, the ratio of red emission (from the dye) to blue emission (from PVK–PBD) decreases clearly with generation. (Note that the concentration of dyes in the films was rather low and light was absorbed almost entirely by the matrix).

The efficiency of Förster transfer is described in terms of the Förster transfer rate between an isolated donor and an acceptor at distance R:

$$k_F = \frac{1}{\tau}\left(\frac{R_0}{R}\right)^6.$$

(6.6)

Here, τ is the lifetime of the undisturbed host and R_0 the Förster transfer radius, which can be estimated to $R_0 = 2.5$–2.7 nm for the present system. When calculating the efficiency of Förster transfer in a blend system for a given dye concentration N_G, a common approach is to determine R via $N_G^{-1} = \frac{4\pi}{3}R^3$. In this approximation, the efficiency for Förster-type energy transfer is

$$\eta_F = \frac{1}{1 + \dfrac{1}{\left(\dfrac{4}{3}\pi N_G R_0^3\right)^2}}.$$

(6.7)

This equation has been applied successfully to describe the effect of a green-emitting phosphor on the emission properties PVK:PBD [67]. For a dye concentration of 500 ppm (corresponding to a guest concentration of ca. 1.5×10^{18} cm^{-3}) in our system, Eq. (6.7) would predict the Förster transfer efficiency to be the same for all generations, in contrast to the experimental findings. This raises the question if the commonly used approach is applicable to the energy transfer to dyes with bulky substituents.

In a homogeneous blend, host and guest molecules are statistically distributed and the spatial separation between host and guest is not a constant (for a fixed concentration). Further, the finite size of the donor and acceptor molecules will define a minimum value of R, given by the sum of the respective molecular radii R_H and R_G of the host (donor) and guest (acceptor) molecules. Following the approach by Bulovic et al. [78] we have derived the following equation for the efficiency of Förster transfer, which takes into account distribution of donor-acceptor separation in a real sample:

$$\eta_F = \frac{1}{1 + \dfrac{3M_{\text{host}}}{4\pi N_A \rho_{\text{host}} Q} \dfrac{(R_H + R_G)^3}{R_0^6}}. \tag{6.8}$$

Here, Q is the molar fraction of guest molecules in the host matrix of mass density ρ_{host} and the molar mass M_{host}. The excited host state is a PVK:PBD exciplex with an estimated radius of $R_H = 1.4$ nm. Assuming a mass density of the polymer film of about 1 g/cm^3 and $R_G = 1.1$ nm, 1.9 nm, and 2.7 nm for PDI-M, PDI-G1, and PDI-G2, respectively, Förster transfer efficiencies of 10.5%, 5.6%, and 3.5% are obtained for $Q = 500$ ppm. In other words, the Förster transfer efficiency is predicted to drop roughly by a factor of 1.7 per generation. This is in good agreement with the experimental findings on the dendrimer system, which revealed a drop of the red emission by a factor of two when going from PDI-M to PDI-G1 and from PDI-G1 to PDI-G2. (Note that the quantum efficiency of the PDI core also decreases slightly with generation.)

EL spectra of films containing 500 ppm PDI-M, PDI-G1, and PDI-G2, respectively, are also shown in Fig. 6.7. Compared to the corresponding PL spectra, the red contribution from PDI is significantly enhanced for all the three blends. At the same time, the decrease in red dye emission with generation is more pronounced. Both tendencies indicate that charge trapping on the dyes plays a major role in the excitation of the dye in EL. For structurally similar PDI dendrimers, HOMO and LUMO levels of −5.4 eV and −3.6 eV to −3.4 eV (determined by cyclovoltammetry vs. Ag/AgCl) have been measured. Apparently, the dye in the PVK:PBD matrix acts as a deep trapping site for electrons and as a weak hole trap.

We have analyzed the ratio of the red and blue emission contributions in EL, compared to that in PL, to obtain information on different contributions of Förster transfer and charge trapping for the different dendrimers in EL. Due to the small amount of dye in the system, virtually all excitons will be formed on the PVK:PBD matrix in PL experiments. Prior to reemission of a photon, a certain fraction b of

the excitation will be transferred to the dye. Thus, a fraction $(1-b)\phi_{host}$ of photons will be emitted by the matrix, and a fraction $b\phi_{guest}$ by the dye. Here, ϕ_{host} and ϕ_{guest} are the PL quantum yields of the host and the guest, respectively. Thus,

$$\left.\frac{I_{guest}}{I_{host}}\right|_{PL} = \frac{\phi_{guest}}{\phi_{host}}\frac{b}{(1-b)}. \tag{6.9}$$

In electroluminescence, almost all charges will be injected onto the PVK:PBD matrix. Due to the large difference of the respective LUMO levels, the dye is assumed to form an efficient electron trap with trapping coefficient γ. Subsequent hole trapping by the negatively charged dye (described by the coefficient γ_T) will lead to the emission of excitons from the dye. The possibility of (thermal) detrapping of electrons was excluded because of the large difference between the guest and host LUMO positions. In parallel, excitons will form on the matrix with a rate $\gamma_R n(t)p(t)$, with γ_R being the coefficient for electron–hole recombination on the matrix. Taking into account Förster transfer to the guest, the number of photons emitted per second by the host is $(1-b)\phi_{host}\gamma_R np$. On the other hand, the dye emission rate is determined by two contributions, $b\phi_{guest}\gamma_R np$ and $\phi_{guest}\gamma_T T_e^- p$. Under the assumption that only few dye molecules are populated, the following steady-state relation is obtained:

$$\left.\frac{I_{guest}}{I_{host}}\right|_{EL} - \left.\frac{I_{guest}}{I_{host}}\right|_{PL} = \frac{\gamma}{\gamma_R}\frac{\phi_{guest}}{\phi_{host}}\frac{T_e}{p(1-b)}. \tag{6.10}$$

Thus, the difference between the EL and PL emission ratios is a measure for the coefficient γ describing electron trapping on the chromophore. In the analysis of the experimental data, intensity ratios measured at a constant current density of $20\,\text{mA/cm}^2$ were compared for the same molar dye concentrations. Since the current/voltage characteristics were almost independent of generation and concentration in the range studied here, the hole density was assumed to be constant. Also, the efficiency of Förster transfer is well below unity. Using the experimentally determined intensity ratios, we concluded that the trapping coefficient decreases by a factor of about 3 for each added dendritic shell. This factor appears surprisingly small when considering the significant change in the thickness of the shell with increasing generation. (Keep in mind that the dendrons lead to an almost spherical appearance of the PDI dendrimers.)

The rate at which an electron tunnels through a rectangular barrier of thickness ℓ is proportional to $\exp(-2\beta\ell)$, with β the tunneling decay parameter in units of inverse lengths. With increasing generation, the thickness ℓ of the dendritic shell increases by $0.8\,\text{nm}$ while the electron trapping coefficient decreases by roughly a factor 3. From these results, an effective tunneling factor β of ca. $0.7\,\text{nm}^{-1}$ can be deduced. This is one order of magnitude smaller than values found for aliphatic tunneling barriers ($\beta \geq 1\,\text{Å}^{-1}$) and fully conjugated systems ($\beta = 0.2$ and $0.6\,\text{Å}^{-1}$) (see [79] for details).
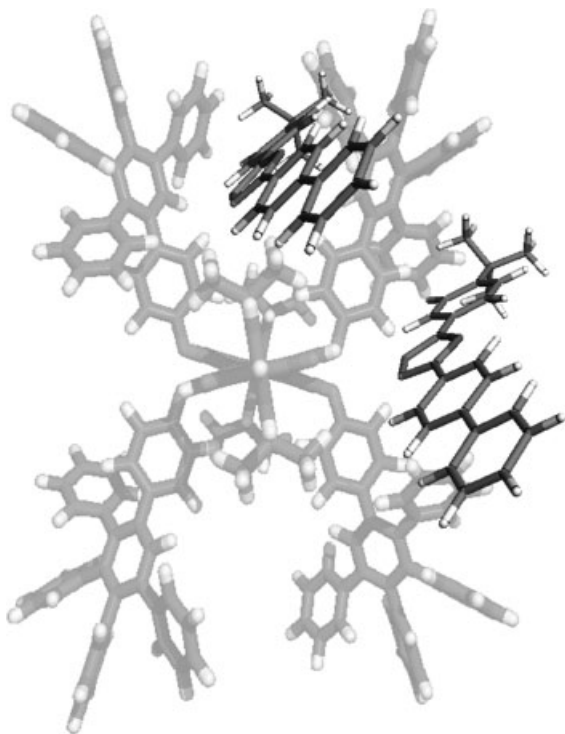
Fig. 6.8 The small molecule PBD can penetrate the dendritic shell surrounding the PDI core thus reducing the distance for electron transfer from the host (PDB) to the guest (PDI). The molecular structure of the dendrimer was optimized using quantum-chemical calculations [75].

At this point, we like to note that the dendritic shell is not completely closed. Therefore, the penetration of the shell by small molecules, e.g., PBD, might be possible. The situation is illustrated in Fig. 6.8 for the first-generation dendrimer without alkyl chains. In contrast to this, the predominant energy donor in a Förster-type transfer process from the PVK:PBD is an exciplex, which involves at least two molecular species. It can thus be expected that formation of the exciplex is not possible within the dendritic shell. In conclusion, these results show the predominance of charge carrier trapping in EL, even when a thick dendritic shell is attached to the dye. This is due to the fact that small charge-carrier transporting moieties can still penetrate the dendrons. On the other hand, the dendritic shell significantly reduces energy transfer and thus intermolecular interactions. The combination of these two effects makes dendronization a very useful approach to highly efficient electrophosphorescent devices.

One particular prediction of Eq. (6.10) is that the guest emission depends on the concentration of free holes in the device; namely an increasing hole density should decrease the red contribution. In accordance to this picture, we observed that the red emission contribution decreased continuously with increasing bias.

We have further observed that the red contribution increases (for comparable host emission intensities) when using an anode with a lower work function and thus a higher hole-injection barrier. These results show that the competition between host and guest emission is not only determined by molecular properties but also depends on the driving conditions.

6.2.3.1 Exciplex Emission

In most cases, the formation of exciplexes in phosphorescent devices constitutes an unwanted relaxation pathway, as it generally lowers the efficiency of the device and affects the color purity. On the other hand, the study of exciplex emission can be used to gain insight into the physical processes in phosphorescent diodes.

We have recently studied the properties of single-layer devices with a multi-component emission layer consisting of a PVK:PBD host, the green-emitting dye Ir(mppy)$_3$ and the hole-transporting molecule TPD [23]. TPD was added to the layer for two reasons. Firstly, utilization of PEDOT:PSS (with a work function of ca. 5.1 eV) leaves ca. 0.5 eV barrier for hole injection to PVK. It was thus expected that adding TPD at a sufficiently large concentration reduces the barrier for hole injection. Secondly, TPD was earlier shown to function as a hole-transporting moiety at high loading when doped into PVK [57]. Thus, adding TPD should allow holes to penetrate deeper into the emission layer; avoiding excitation quenching at the anode.

Interestingly, EL spectra of devices with a low Ir(mppy)$_3$ concentration in the PVK:PBD:TPD matrix exhibited an additional blue emission component. Subtracting the EL spectra with and without TPD revealed a well-resolved blue emission with maximum at ca. 460 nm (see Fig. 6.9). In order to study the origin of this emission, we measured PL spectra of several combinations of PVK, PBD, and TPD in an inert polystyrene (PS) matrix. As shown in Fig. 6.8, the spectral properties of the additional blue component agree well with the PL of a sample of the composition TPD (0.4) + PBD (0.4) + PS (0.2). This indicates a significant emission contribution from a TPD:PBD exciplex to the EL of the multicomponent samples.

Here, it is important to mention that the emission from an undoped PVK:PBD matrix was assigned to an exciplex formed between a hole on PVK and an electron on PBD [62]. The appearance of a strong TPD:PBD exciplex contribution in the PVK:PBD:TPD blend thus provides strong evidence that holes are transported almost exclusively via hopping between TPD molecules in the TPD-containing blend, while the hole density on PVK must be small. In contrast to devices with a PVK:PBD matrix, emission from the TPD:PBD exciplex clearly competes with dye emission for a Ir(mppy)$_3$ concentration of 1 wt%. This can be explained by the fact that the HOMO level offset between Ir(mppy)$_3$ and TPD is small and exciplexes form on the PVK:PBD:TPD matrix with almost the same probability as excitons form on the dye.

It was possible to fabricate devices with pure dye emission by raising the Ir(mppy)$_3$ concentration. Figure 6.9 shows EL spectra of devices of the composition PVK(0.64):PBD(0.25):TPD(0.1) and different phosphor concentrations. With 6 wt% Ir(mppy)$_3$, the exciplex contribution was fully suppressed, resulting in
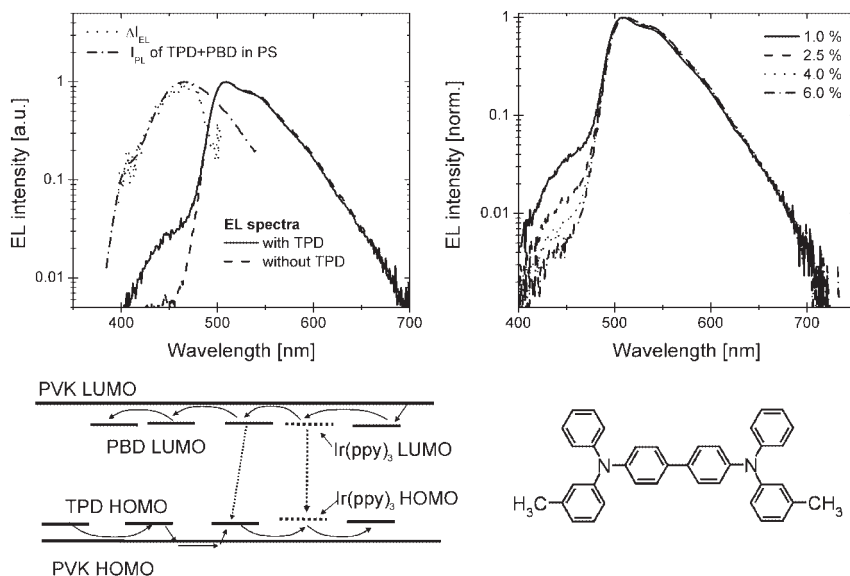
Fig. 6.9 (upper left) EL spectra of PVK:PBD:Ir(mppy)₃ without and with added TPD at a concentration of 9 wt%. The concentration of the Ir complex was 1 wt%. Also shown is the PL of a TPD:PBD blend in an inert PS matrix [23]. (upper right) EL spectra of PVK:PBD:TPD:Ir(mppy)₃ with different dye concentrations. The TPD content was ca. 8–10 wt%. (lower left) Energy scheme depicting the formation of a PBD:TPD exciplex in competition to the excitation of the dye. (lower right) Molecular structure of TPD.

green emission with a luminance efficiency (LE) of 30 cd/A and a power conversion efficiency (PE) of up to 24 lm/W. In the following this concept was also successfully applied to efficient green-emitting copolymers [50] and red-emitting devices [80].

Exciplex formation was further involved in the charge recombination in solution-processed multilayer devices [25]. These multilayer structures contained crosslinked layers of hole-transporting molecules. Details about the molecular structure and fabrication of these layers can be found elsewhere [25, 81, 82]. In the structures studied by us, one or two of these crosslinked hole-transporting layers (X-HTLs) were deposited onto ITO/PEDOT:PSS anodes, followed (after proper crosslinking) by the deposition of the PVK:PBD:Ir(mppy)₃ emission layer from solution.

Inserting a single X-HTL in a device with a 1 wt% dye concentration results in a significant decrease in current, even though the hole injection barrier to the HOMO of the PVK matrix is slightly reduced in the multilayer device (Fig. 6.10). Apparently, these devices are electron dominated and the X-HTL functions as an electron-blocking layer (the LUMO offset between PBD and the used hole-transporting molecule is ca. 0.8 eV). Surprisingly, the efficiency of these devices was very low. Also, the EL spectra of the devices with a single X-HTL layer exhibited a short-wavelength shoulder, which was not present in the device with only a
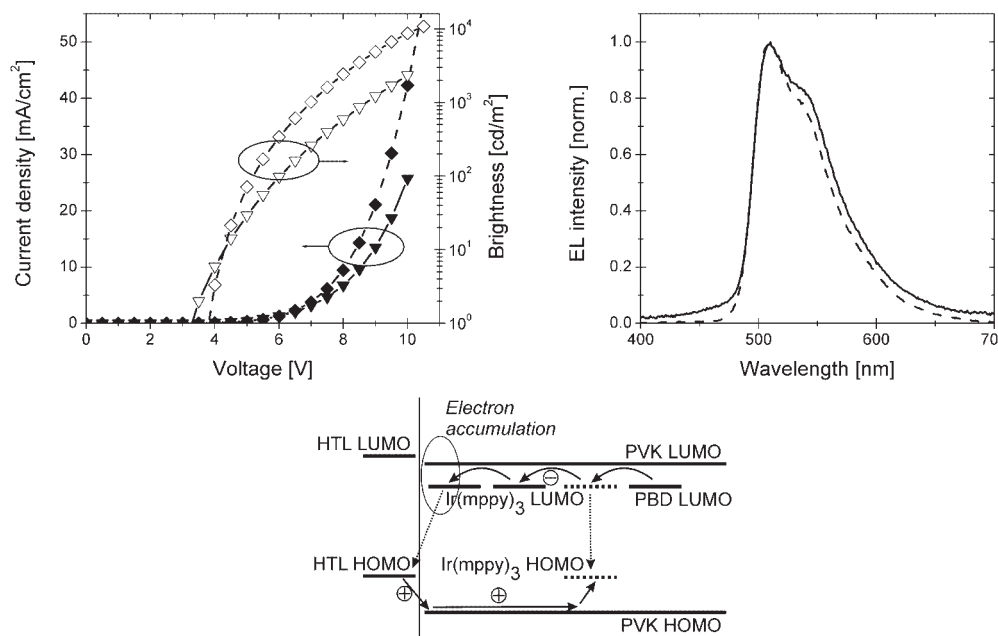
Fig. 6.10 (upper left) Current–voltage (solid symbols) and luminance–voltage (open symbols) characteristics of PVK(70):PBD(29):Ir(mppy)$_3$(1) diodes comprising a single undoped X-HTL of ca. 20 nm thickness (triangles). Also shown are the characteristics of a reference device with a PEDOT:PSS anode (diamonds). (upper right) Normalized EL spectra of devices with (solid line) and without (dashed line) a single X-HTL [25]. (lower) Energy level scheme depicting the formation of exciplexes in the multilayer structure in case of a low dye concentration.

PEDOT:PSS anode (Fig. 6.10). Based on this result and similar observations on PVK:PBD:TPD blend layers as described above, we attribute this emission to an exciplex between the hole-transporting molecules in the X-HTL and PBD in the emission layer.

The pronounced exciplex contribution in devices containing the X-HTL layer indicates that a significant fraction of electrons are accumulated at the interface to the crosslinked layer. Apparently, the PVK:PBD host in combination with a CsF/Al cathode is able to inject and transport a sufficient number of electrons to this interface. Raising the dye concentration to 6 wt% resulted in a significant enhancement of the emission intensity and the device current. At the same time, the exciplex contribution vanished completely (Fig. 6.11). We propose that in the multilayer devices with a higher phosphor content, holes are injected directly from the X-HTL into the HOMO of Ir(mppy)$_3$, followed by recombination with electrons accumulated at the interface between the emission layer and the HTL. According to the results from cyclic voltammetry, the HOMO level of the HTL almost aligns with that of Ir(mppy)$_3$, but there is a 0.4 eV energy barrier for the hole injection into the HOMO level of PVK. With a dye concentration of 6 wt%, pure green emission (color coordinates $x = 0.33$, $y = 0.60$) with a luminance efficiency of up to
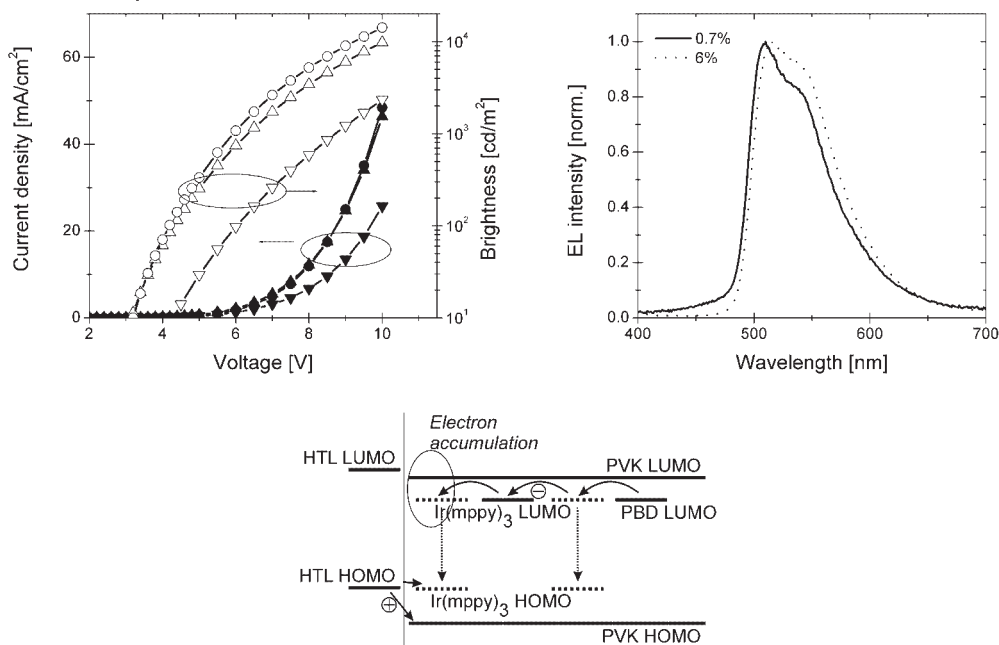
Fig. 6.11 (upper left) Current–luminance–voltage characteristics of PVK : PBD : Ir(mppy)₃ diodes comprising a single undoped X-HTL of ca. 20 nm thickness for a dye concentration of ca. 1 wt% (lower triangles) or 6 wt% (upper triangles). Also shown are the characteristics of a device with a dye content of 6 wt% and a double X-HTL structure (circles). (upper right) Normalized EL spectra of devices with a single X-HTL and a dye content of 1 wt% (solid line) or 6 wt% (dashed line) [25]. (lower) Energy level scheme depicting the excitation of the dye in the multilayer structure at a high dye concentration.

40 cd/A could be achieved. The efficiency of these devices could be further raised by inserting a second, doped X-HTL between the ITO/PEDOT : PSS anode and the undoped X-HTL. These devices emitted green light with a luminance efficiency of up to 67 cd/A, which corresponds an external quantum efficiency (EQE) of 18.8%. Given an outcoupling factor of 0.2 (assuming a refractive index $n = 1.8$ of the polymer layer), the internal quantum efficiency of the device is approaching unity. The power efficiency was maximum (ca. 65 lm/W) at a current density of 0.01 mA/cm² and decreased only gradually with increasing current density (Fig. 6.12). The concept developed for the green Ir(mppy)₃ phosphor worked equally well with the red-emitting bis(1-phenylisoquinoline)iridium(acetylacetonate) [Ir(piq)₂(acac)]. The HOMO level of Ir(piq)₂(acac) differs only slightly from that of Ir(mppy)₃, suggesting that direct injection of holes from the crosslinked HTL should be as efficient as in the green devices. In a device structure with two X-HTLs, red emission with a peak luminance efficiency of 11.7 cd/A, corresponding to an EQE of 13% and a PE of 10.7 lm/W could be achieved (Fig. 6.12). These values represent the highest efficiencies reported yet for green- and red-emitting polymer-based diodes. Apparently, electron accumulation between the emission layer and a hole-transporting layer and direct hole transfer from this hole-transporting layer to the dye
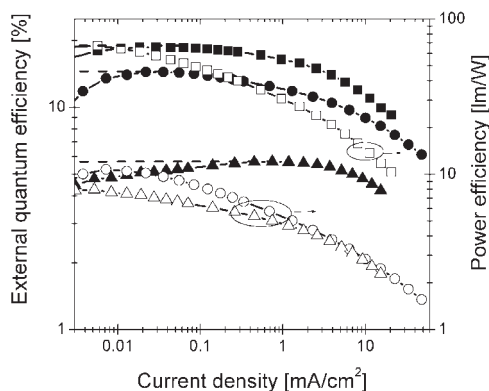
Fig. 6.12 External quantum efficiencies (solid symbols) and corresponding power efficiencies (open symbols) of devices comprising a double X-HTL structure and a green (squares), red (circles), or blue-emitting (triangles) Iridium phosphor at a concentration of 6 wt% [25].

is very favorable in view of achieving efficient emission in electrophosphorescence [21]. This conclusion has been supported by recent studies on double-layer phosphorescent diodes comprising insoluble polymer-based interlayers [83].

6.2.4
Confinement of Singlet and Triplet Excitons on the PVK : PBD Matrix

It is generally believed that a good confinement of the excitation on the emitting guest, thus avoiding back transfer to the host, is a crucial requirement for high efficiency and good color stability. A very nice and illustrative example for quenching of the triplet excited state in various Ir complexes via energy back transfer was published recently by Sudhakar et al. [84]. Accordingly, the electronic structures of the host and guest need to be carefully adjusted for efficient electroluminescence and phosphorescence. A conclusive discussion of the interrelation between the chemical structure and the triplet energy of various small molecule carbazole host materials has been published recently by Brunner et al. [85] (further details are contained in the contribution by A. van Dijken, K. Brunner, H. Börner, B.M.W. Langeveld in this volume). In these studies, efficient phosphorescence was observed only if the triplet energy of the host was equal or larger than that of the guest.

However, the above-mentioned criteria might be less crucial with respect to device performance if the exciton-accepting host possesses a long triplet lifetime. Baldo et al. and Kalinowski et al. reported rapid triplet energy exchange between Ir(ppy)$_3$ and TPD [86, 87]. This exchange was manifested by a significant increase in the lifetime of the green emission from the phosphorescent dye. For example, Fig. 6.13 shows the decay of the emission at 520 nm upon excitation with 337 nm for different concentrations of TPD in a blend with Ir(ppy)$_3$ and an inert polymeric binder. Clearly, the decay time increases considerably with increasing TPD concentration. This effect was explained by a Dexter-type energy exchange between
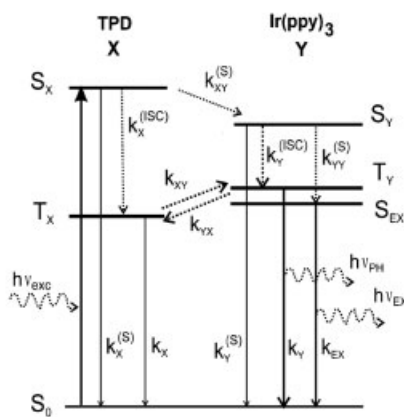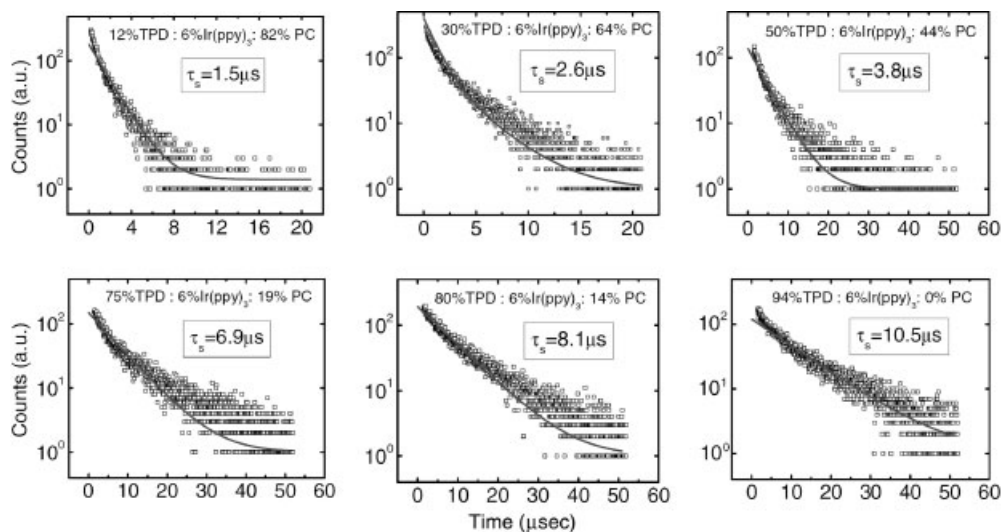
Fig. 6.13 (upper graphs) The PL transients of blends of TPD and Ir(ppy)$_3$ in an inert polycarbazole (PC) matrix for different concentrations of TPD. Excitation was with 337 nm and detection at 520 nm. The solid lines show the best monoexponatial fit of the data. (lower graph) Kinetic scheme illustrating some photophysical processes in the Ir(ppy)$_3$:TPD:PC system. The triplet exciton exchange between fluorescent TPD (*X*) and phosphorescent Ir(ppy)$_3$ (*Y*) is represented by the rates k_{XY} and k_{YX}, respectively. A hypothetical bimolecular emissive singlet excited state of Ir(ppy)$_3$ (S_{EX}) is located below the molecular triplet T_Y. It was introduced to explain a shortened decay time accompanied by slight spectral changes with increasing Ir(ppy)$_3$ concentration [87].

Ir(ppy)$_3$ and TPD (with TPD having the smaller triplet energy). No emission from TPD was observed. Since the triplet decay rate of TPD is small (due to the missing heavy-atom effect), the lifetime of the triplet exciton on TPD is sufficiently long to allow energy back transfer to Ir(ppy)$_3$. Thus, TPD was proposed to act as an effective triplet exciton reservoir rather than as a triplet quencher for Ir(ppy)$_3$. Interestingly, addition of TPD significantly increased the lifetime of the green emission, but did not alter the overall emission intensity. This example shows that the complete localization of the excitation on the phosphorescent dye is not a general requirement for efficient emission.

Triplet harvesting was observed by us when studying the emission properties of the blue-emitting phosphor bis[(4,6-difluorophenyl)-pyridinato-N,C^2] (picolinato)Ir(III) (FIrpic) in a matrix with PVK and two different electron-transporting oxadiazoles [20]. Systematic studies on single layer PLEDs comprising either PBD or 1,3-bis[(4-*tert*-butylphenyl)-1,3,4-oxidiazolyl]phenylene (OXD-7) as the electron-transporting component revealed significant differences in the device properties. Most noticeably, the efficiency of devices containing PBD was only half of that of devices with OXD-7, though the EL spectra were almost identical. Figure 6.14 shows time-resolved photoluminescence decay measurements with direct excitation of the dye at 405 nm. The phosphorescence decay of the dye in pure PVK was almost monoexponential, with a lifetime of 1.4 µs. In fact, the lifetime of the dye in PVK was found to be only slightly smaller than in an inert polymer matrix (1.7 µs). The triplet energy of PVK is still under debate and values of 2.5 eV [65, 88] or 3.0 eV [47, 89] were reported. Based on very small difference in triplet lifetime and similar decay dynamics of FIrpic in PMMA and PVK, we presume that there is little or no significant energy transfer from FIrpic to PVK.

Introducing PBD to the blend dramatically changes the luminescence decay: in addition to the initial fast decay we observed a very long lived component. In the blend with OXD-7, a long lived component was also present but with a considerably shorter lifetime. PL emission spectra measured under steady-state excitation at an excitation wavelength of 405 nm revealed a strong effect of PBD on the overall PL intensity. While the shape of the emission spectrum was virtually unaffected by addition of PBD, the PL intensity of the blend with PBD was only ca. 50% of that of the layer containing OXD-7. This ratio is comparable to the difference in EL efficiencies reported above. Apparently, the lower efficiency of the diodes containing PBD was mainly due to its influence on the triplet excited state population on the phosphor, while the balance of carrier injection and transport plays little if any role in determining the efficiencies of the devices. The triplet energy of OXD-7 (2.7 eV) [47] is comparable to that of FIrpic (2.6±0.1 eV) [90], while the triplet energy of PBD was reported to be 2.46 eV[50], ca. 0.15 eV smaller than that of FIrpic. From these values we propose that triplet energy exchange will occur between FIrpic and both PBD and OXD-7 and that both oxadiazoles will harvest triplet excitons. This interpretation is supported by the observation that the decay time of the FIrpic emission in either the PVK : PBD : FIrpic or the PVK : OXD-7 : FIpic blend is shortened upon exposure to air, while it only slightly affects the emission properties of the pure phosphor in PMMA. It is well known that
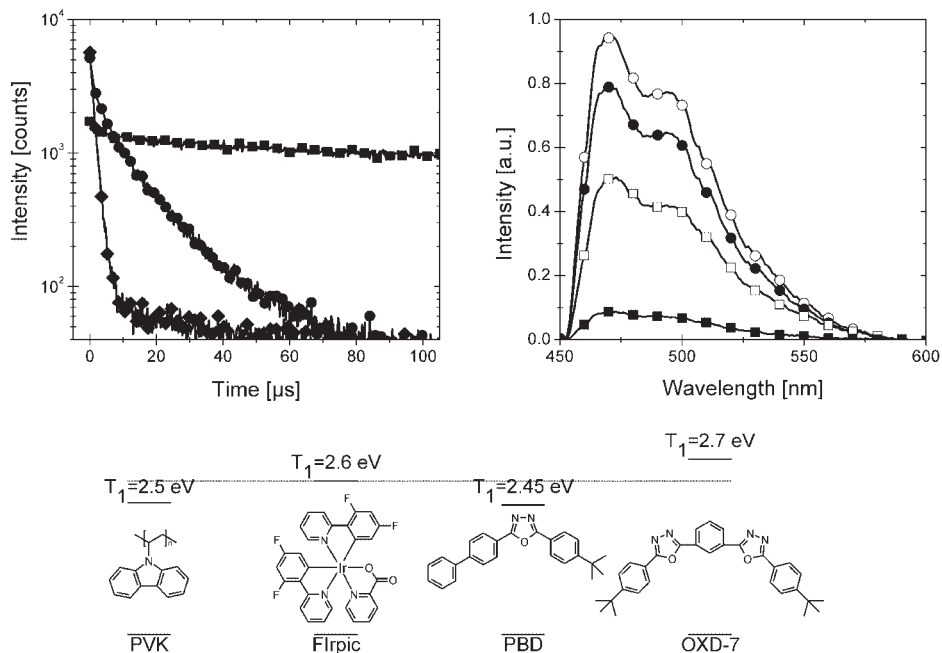
Fig. 6.14 (upper left) Phosphorescence decay of FIrpic for PVK + 3% FIrpic (diamonds); PVK + 40% PBD + 3% FIrpic (squares) and PVK + 40% OXD-7 + 3% FIrpic (circles). The excitation wavelength was 405 nm and the detection wavelength was 470 nm. (upper right) Steady-state PL measurement of PMMA + 40% PBD + 3% FIrpic (squares) and PMMA + 40% OXD-7 + 3% FIrpic (circles). Open and closed symbols denote measurements under vacuum of about 5×10^{-2} mbar and in air, respectively. (bottom) Chemical structures and triplet excited state energies of the used compounds [20].

exposure to oxygen reduces the lifetime of triplet excited states on organic molecules. The main difference between the blend with PBD or OXD-7 is that the kinetics of triplet back transfer to FIrpic is expected to be significantly slower in case of PBD, due to the larger triplet energy offset between PBD and FIrpic. Though the lifetime of the triplet excited state on PBD is not known to us, the slow decay of the blue phosphorescence in the presence of PBD suggests that triplet excitons are "stored" on this molecule for several hundreds of microseconds. This might be sufficiently long to allow nonradiative relaxation processes to compete with the back transfer to the phosphor. In accordance to this, the steady-state PL intensity of the blend with PBD was largely affected by the presence of oxygen while the effect was rather small for the OXD-7-containing blend. Note that devices with a FIrpic concentration of 5 wt% FIrpic in a PVK:OXD-7 matrix exhibited a maximum luminance efficiency of 18 cd/A (9% EQE). This shows that triplet-back transfer to the matrix is, in general, not conflicting with good device performance. On the other hand, a large density of free triplet excitons on the

matrix is expected to result in a strong and unwanted dependence of the device performance on temperature and driving conditions in such devices.

Finally, we like to note that the PVK:PBD blend has been shown to host a fluorescent dye, which had the emission maximum blue-shifted with respect to the PVK:PBD exciplex emission [91]. At a concentration of ca. 2 wt%, the EL was fully dominated by narrow emission of the blue-emitting pyrazoloquinoline dye (1,3-dimethyl-4-phenyl-1Hpyrazolo[3,4,b]quinoline, PAQ8) with maximum at 429 nm. This was explained by trapping of electrons on the fluorescent guest in competition to the formation of the PBD:PVK exciplex. Because the PVK:PBD exciplex has (by definition) no ground-state absorption, Förster-type back transfer from the dye to the host was not possible. Using this approach, deep-blue EL with CIE color coordinates of (0.15, 0.07), an external quantum efficiency of 0.91% and a power efficiency of 0.22 lm/W were realized.

6.3
Devices with PtOEP Doped into Conjugated Polymer Matrices

2,3,7,8,12,13,17,18-octaethyl-21H,23H-porphine platinum (PtOEP, see Fig. 6.15) was the first dye to be used in a polymer-based electrophosphorescent device. The absorption of this compound consists of a Soret band (at ca. 390 nm) and a Q-band (500–540 nm), while the emission peaks at ca. 650 nm. The luminescence quantum efficiency measured for the dye in a deoxygenated toluene/DMF solution at room temperature is ca. 50% [92]. The emission is largely ligand based and possesses a relatively long lifetime (83 µs in toluene/DMF solution [92]). The triplet state of PtOEP is at ca. 1.9 eV [93], HOMO and LUMO levels are at 5.3 eV and 2.8 eV, respectively. Because of its rather low triplet energy, various polymers have been tested as hosts for PtOEP in electrophosphorescent devices.

Cleave et al. have studied in detail how the electronic structure of the host affects the nature of the transfer process between a polymer host and PtOEP [37]. Figure 6.16 summarizes the chemical structures of the used compounds as well as their HOMO and LUMO positions. If the offset of the HOMO (or LUMO) levels of the host and guest was small, energy transfer dominated the excitation of the guest, while charge trapping was found to be insignificant (see e.g., PtOEP in PNP). On
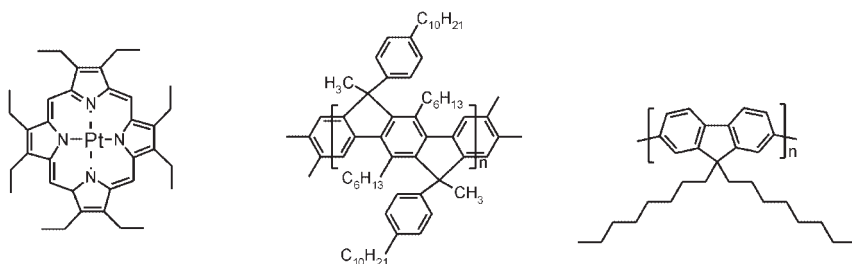
Fig. 6.15 Chemical structure of PtOEP, MeLPPP, and PFO.
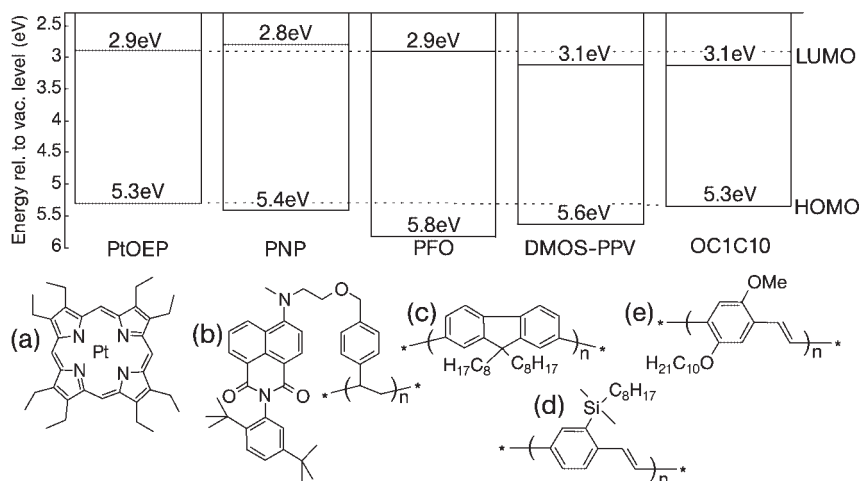
Fig. 6.16 HOMO and LUMO levels for the polymers and porphyrin studied in [37]. Oxidation potentials were determined using cyclic voltammetry, using a Ag/AgCl standard reference. LUMO levels were estimated from combination of the CV-determined HOMO energy and the optical gap for each material. The chemical structures of the materials are also shown [37].

the other hand, if a large energy offset between the energy levels of the host and guest favors charge trapping, direct recombination of charges on the dye is the dominant process (PtOEP in PFO). If both HOMO and LUMO levels are offset in the same direction, as for the DMOS–PPV blend, the triplet excited states on both the host and the guest are unstable due to charge transfer. Finally, triplet energy back transfer from the guest to the host has been observed for OC1C10-PPV doped with PtOEP.

In general, excitation of the PtOEP dye will occur in parallel via energy- and charge-transfer processes. In the following paragraphs, we like to discuss the physical processes relevant to the excitation of this dye in two conjugated polymer matrices, a ladder-type poly(para-phenylene) and poly(9,9-dialkylfluorene) (PF). Ladder-type methyl-poly(*para*-phenylene) (MeLPPP) is a well-known blue-emitting polymer. The T_1 triplet energy of MeLPPP has been reported to be ca. 2.1 eV, ca. 0.6 eV below the S_1 state (2.7 eV) [94]. The HOMO of MeLPPP is at ca. 5.5 eV [95], ca. 0.2 eV below that of PtOEP. Finally, assuming an exciton binding energy of 0.3 eV, the LUMO level of MeLPPP should be ca. 2.5 eV below vacuum. Polyfluorene is a wide gap blue-emitting polymer, which has been widely studied with respect to efficient blue-emitting diodes [96–99]. According to results from cyclic voltammetry, the HOMO and LUMO of PF in the solid state is at 2.12 eV and 5.8 eV below vacuum, respectively [100]. The T_1 is at 2.18 eV, ca. 0.75 eV below S_1 (2.92 eV) [33].
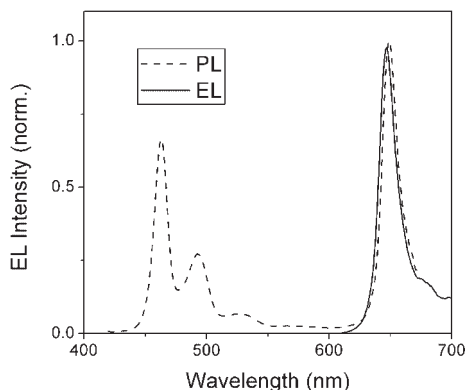
Fig. 6.17 EL spectra of a single-layer device (4 wt% PtOEP in MeLPPP between PEDOT:PSS and Ca/Al). Also shown is the PL spectrum of a layer with the same doping ratio for an excitation wavelength of 450 nm (at a maximum of the MeLPPP absorption) [44].

6.3.1
PtOEP in MeLPPP

Figure 6.17 shows the PL (excited at 450 nm) and the EL spectrum of MeLPPP doped with PtOEP at 4 wt%. In PL, emission from both the MeLPPP singlet and the PtOEP triplet excited state is observed. In contrast, the EL spectrum of a single layer device between a PEDOT:PSS anode and a Ca/Al cathode exhibits almost exclusively phosphorescence from the dye. This proves that other processes than Förster-type energy transfer are active in EL.

6.3.1.1 **Förster Transfer**
Figure 6.18 shows the prompt fluorescence of a MeLPPP layer. There is a significant overlap between the emission of MeLPPP and the Q-band of the dye. Using the absorption spectrum of PtOEP in solution and a fluorescence quantum efficiency of 0.5 for MeLPPP in the solid state, a Förster transfer radius R_0 of 3 nm is obtained. In the simple approximation of Eq. (6.7), efficient Förster transfer should occur between MeLPPP and PtOEP at dye concentrations larger than $N_{g,0} \cong 10^{19} \, \text{cm}^{-3}$ (0.015 M). As shown in Fig. 6.18, the intensity of prompt fluorescence drops considerably with increasing dye concentration and the reduction in fluorescence intensity goes along with a continuous reduction in fluorescence lifetime. Interestingly, the concentration at which the MeLPPP fluorescence intensity drops by a factor of two is almost one order of magnitude lower than $N_{g,0}$ as estimated above. This is a consequence of the fact that a conjugated polymer differs in several aspects from a typical Förster-type energy transfer system. The first and most important one relates to the spatial extent of the excited states. While Förster's theory is based upon the assumption of a spatially fixed point dipole, the excited
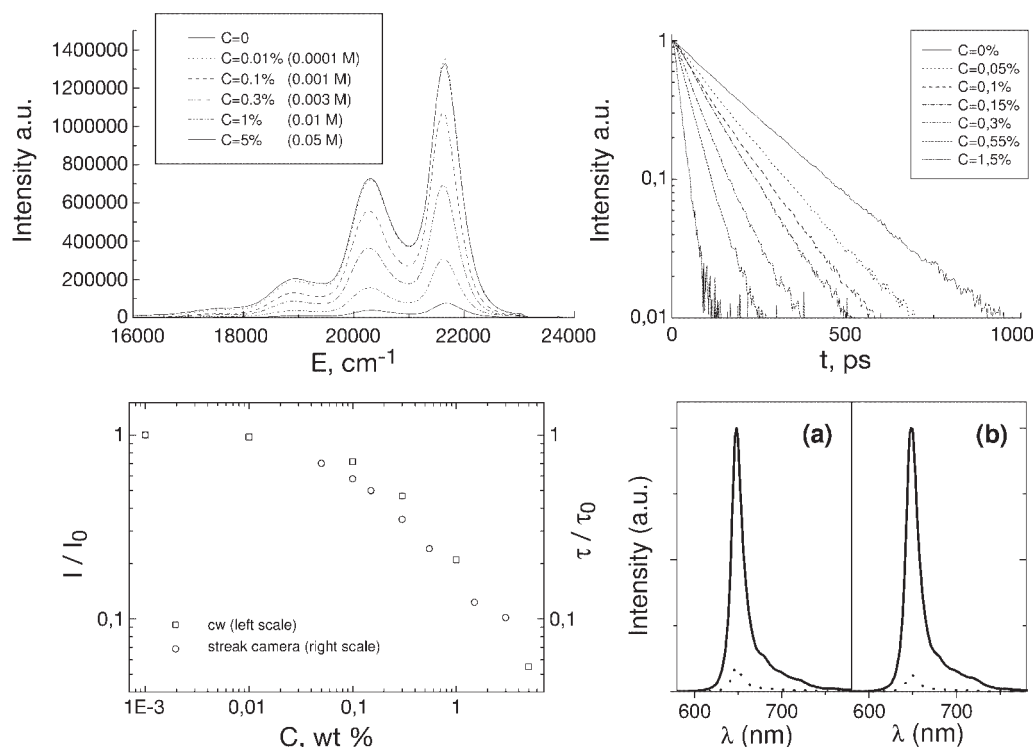
Fig. 6.18 (upper left) The prompt fluorescence spectra of the MeLPPP film with different concentrations of PtOEP at 293 K in air ($\lambda_{exc} = 430$ nm). Prompt fluorescence was recorded immediately after excitation with a gate length of 100 ns. (upper right) Decay of the prompt fluorescence of MeLPPP at different concentration of PtOEP at 293 K. (lower left) Dependence of the normalized cw intensity (left scale) and the normalized decay time (right scale) of the prompt fluorescence of MeLPPP on the PtOEP concentration at 293 K. (lower right) Phosphorescence of a sample containing 1 wt% PtOEP in LPPP. Measurements were performed at room temperature in vacuum (solid lines) or in air (dotted lines). The excitation wavelength was (a) 450 nm or (b) 536 nm [44, 103].

state of MeLPPP can be considered as that of oligomeric subunits which include 12 backbone phenylene rings of a polymer chain (5 nm). Secondary, excitations are able to migrate incoherently at room temperature [101]. This translates into an R_0 value larger than evaluated from spectral overlap. Consequently, significant Förster transfer to the dye occurs at dye concentrations as low as 10^{18} cm^{-3}. Singlet transfer from MeLPPP to PtOEP that is followed by intersystem crossing (ISC) to the dye triplet manifold should represent a dominant excitation pathway even at moderate PtOEP contents.

This observation does not rule out that dye population can occur via, first, ISC of the polymer S$_1$ state to the polymer triplet manifold followed by Dexter-energy transfer to the dye. In order to determine the efficiency of this process, we have

made use of the fact that the phosphorescence of LPPP is efficiently quenched in the presence of oxygen. Figure 6.18 compares phosphorescence spectra of LPPP doped with 1 wt% PtOEP, excited either at 450 nm via the LPPP singlet state or at 536 nm, outside the LPPP absorption but within the absorption band of the dopant. In both cases, exposure to oxygen reduces the phosphorescence intensity by a factor of ca. 10–15. At the same time, the phosphorescence lifetime is significantly shortened [102]. The fact that the influence of oxygen on the phosphorescence of the dopant is not stronger when exciting the LPPP singlet state (rather than directly the phosphor) suggests that the excitation of the dye via Dexter transfer of triplet excitons formed on the polymer by ISC is not an efficient process.

6.3.1.2 Dexter Transfer

The study of the triplet dynamics in fully conjugated polymer hosts turns out to be difficult, because intrinsic phosphorescence is hardly observed from these polymers. The main reason is the lack of spin–orbit coupling in these carbon-based conjugated polymers, resulting in low intersystem crossing rates. Consequently, the polymer triplet state is only weakly populated after photoexcitation and the quantum yield of phosphorescence is low.

An elegant approach to populate the triplet state of a conjugated polymer after excitation of its singlet has been reported by Rothe et al. [104]. The principle mechanism of this process is depicted in Fig. 6.19. A solid layer of poly(9,9-bis(2-ethylhexyl)fluorene-2,7-diyl) (PF2/6) was mixed with benzil. This molecule has a very low fluorescence quantum yield (~0), due to $n \rightarrow \pi^*$ nature of the lowest excited singlet state [105]. On the other hand, the quantum yield for ISC is very high (0.92).
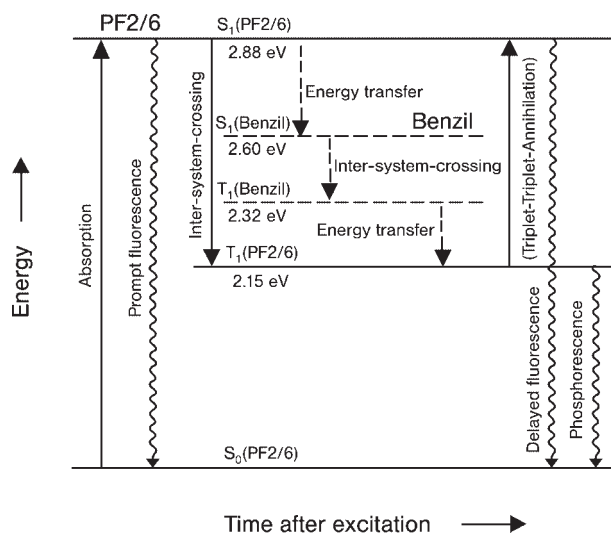
Fig. 6.19 Schematic representation of the energy levels of excited states and transfer mechanisms for PF2/6 blended with benzil [104].

Because the singlet state of PF2/6 is ca. 0.28 eV higher than that of benzil and the polymer triplet state is ca. 0.17 eV below that of benzil, this compound should act as very efficient singlet–triplet converter when blended into PF2/6. The authors further studied the photophysics of layers doped with PtOEP to provide evidence for triplet-triplet energy transfer.

Because the singlet and triplet energies of MeLPPP and PF2/6 are quite similar, this approach works equally well for MeLPPP [103]. Adding benzil to MeLPPP at a concentration of ca. 20 wt% results in drastic quenching of the prompt fluorescence of MeLPPP by a factor of more than 20. This result is quite surprising considering the weak extinction coefficient of benzil in the wavelength range of MeLPPP fluorescence (the Förster transfer radius is ca. 0.7 nm). Apparently, fluorescence quenching involves efficient diffusion of singlet excitons on the polymer host to benzil, similar to what has been reported above. Sensitized phosphorescence can be clearly seen in delayed fluorescence spectra measured upon direct excitation of the polymer at 77 K (Fig. 6.20). In addition to the distinct and strong emission at 609 nm ($16400\,cm^{-1}$) attributed to MeLPPP phosphorescence [94], the spectrum shows a broad and unstructured band. This emission has been attributed to an exciplex between benzil and MeLPPP [103].

One important advantage of this approach is that the fluorescence of the polymer host is effectively quenched by the addition of benzil. Thus, the probability for energy transfer from the polymer host to a phosphorescent dye via Förster-type singlet exciton transfer is largely reduced. In order to prove that triplet–triplet transfer takes place between the polymer host and PtOEP, a blend system with 0.001% by weight of PtOEP added to MeLPPP was studied. This amount of PtOEP does not lead to significant quenching of the polymer fluorescence. As shown in Fig. 6.20, adding 20 wt% of benzil to the MeLPPP:PtOEP layer reduced the phosphorescence intensity of PtOEP by a factor of only 3.5, while the prompt fluorescence of the polymer host decreased by a factor of 30. Since the quantum yield of fluorescence of benzil is close to zero and no strong benzil phosphorescence is observed from the MeLPPP:benzil layers, direct transfer from a singlet or triplet exciton on the benzil to the phosphorescent dye can be neglected. Further, since the fluorescence of MeLPPP is almost completely quenched upon addition of benzil, population of the dye via Förster transfer from the polymer host can be fully excluded. Thus, the main channel for populating the triplet state of PtOEP in the benzil-doped system must involve (a) the benzil-sensitized conversion of polymer singlet excitons to triplet excitons, (b) the triplet migration within the polymer matrix and (c) triplet–triplet energy transfer to the dye.

Further confirmation of this assignment comes from time-resolved phosphorescence measurements (Fig. 6.20). In both cases, fast and slow components are observed. The decay time of the fast component agrees with the intrinsic lifetime of the triplet state of PtOEP (70–100 µs). Obviously, the fast component is due to Pt-porphyrin molecules excited as a result of the singlet–singlet energy transfer from the polymer. The introduction of benzil sharply decreases this fast contribution. At the same time, there is a marked increase in the long-lived component, with a lifetime comparable to the triplet lifetime of the polymer (ca. 15 ms). This
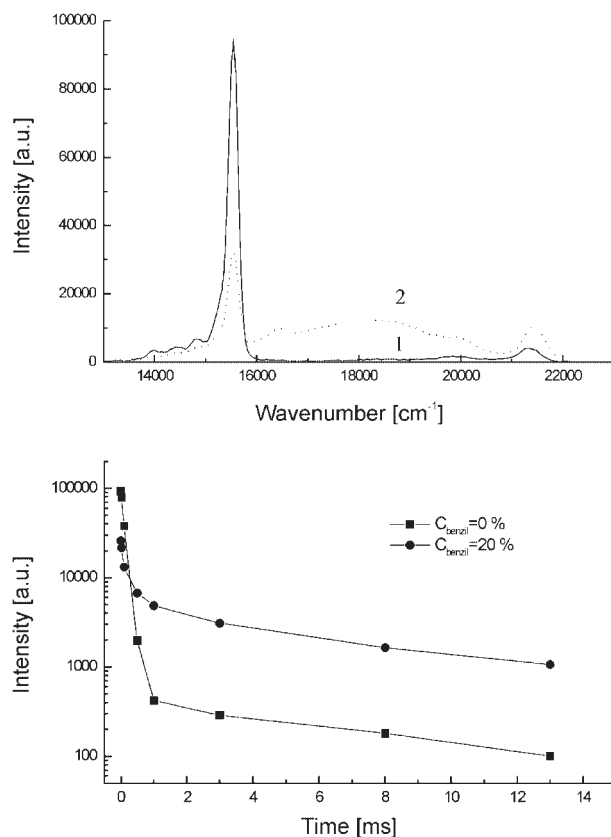
Fig. 6.20 (left) Delayed luminescence spectra of a MeLPPP film containing 0.001 wt% of PtOEP, without (1) or doped with 20 wt% of benzil (2) at 77 K (λ_{exc}=450 nm (22 222 cm^{-1})). Both spectra were recorded with a 1 μs delay after excitation and a 10 ms gate width. (right) Decay of the PtOEP phosphorescence in a MeLPPP film without and with 20 wt% of benzil at 77 K. The curves were recorded with a gate width of 10 ms (taken from [103]).

proves that the main energy donor for the PtOEP triplet state in the benzil-sensitized system is the triplet state of the polymer.

At this point we like to comment on the reduction of PtOEP emission upon addition of benzil. At a concentration of 0.001 wt% PtOEP in MeLPPP, the host fluorescence is only weakly quenched. When adding benzil at 20 wt%, efficient conversion of MeLPPP singlet excited states into triplet excitons is seen. Presuming that most of the host triplets reach the dye, a vast increase in phosphorescence intensity would be expected, in contrast to the experimental findings. Thus, triplet excitons on the host are not fully converted into dye triplet excited states. In fact, the delayed luminescence of the MeLPPP:benzil:PtOEP system reveals a significant signal from the polymer phosphorescence at 16.400 cm^{-1}. Because Dexter transfer is a short-range process, energy transfer from the polymer to the dye must

involve migration of the triplet excitons on the polymer matrix. Most π-conjugated polymers feature inhomogeneous line broadening in the corresponding optical spectra, reflecting the statistical variation of the effective conjugation lengths and, therefore, triplet energies. As a consequence, the triplet excitons on the polymer host will become immobilized with time. From a comparison of the decay time of polymer phosphorescence (originating from both mobile and immobilized triplet excitons) and delayed fluorescence (attributed to the triplet-triplet-annihilation of mobile triplet excitons in benzil-sensitized MeLPPP), immobilization in MeLPPP is expected to occur on a time scale of ca. 1 ms (at 77 K).

6.3.1.3 Electrophosphorescence

As mentioned above, the EL of single layer devices with MeLPPP doped with 4 wt% PtOEP exhibited almost no emission from the polymer host, though the PL of the same layer showed significant host fluorescence. Because the voltage for driving a certain current through the device did not change with dye concentration, direct evidence for charge capture on the dye was missing. In EL, the statistical recombination of electrons and holes should create triplet and singlet excitons in a ratio 3:1. Assuming efficient Dexter transfer from the polymer to the dye at RT, the relative guest emission in EL should be (at maximum) four times larger than in PL. In PL, the guest emission is only 1.4 times the host emission (for a dye concentration of 4 wt% and when directly exciting the host). Therefore, excitation of the dye by energy transfer via Förster and Dexter transfer should leave behind a host contribution of ca. 20%. This is not observed. We also found that devices incorporating either a hole- or an electron-blocking layer exhibited significant differences in the color coordinates. Excitation of the phosphorescent dye solely by energy transfer of excitons generated on the host would, however, not depend on whether holes or electrons are predominately accumulated at the interface to the charge-blocking layer. Thus, though Dexter transfer cannot be excluded, population of the PtOEP excited state by subsequent capture of charges is proposed to be the dominant excitation pathway in this system.

Interestingly, the best device performance was achieved in a three-layer structure, which guaranteed, on the one hand, blocking of electrons and, on the other hand, direct injection of holes from the hole-transporting layer onto the HOMO of the dye. In this case, emission from the host was fully suppressed (Fig. 6.21). Apparently, excitation of the dye via direct charge transfer (avoiding pathways involving the excitation of the host) is optimum with respect to color purity and device efficiency [44].

6.3.2
PtOEP in Polyfluorene

Because the triplet energy of PF is similar to (or even higher than) that of MeLPPP, the transfer mechanisms discussed above should be equally active in a PF : PtOEP blend. The origin of EL from a blend of PtOEP with poly(9,9-dioctylfluorene) (PFO) has been studied in detail by Lane et al. [39]. As in the MeLPPP : PtOEP system
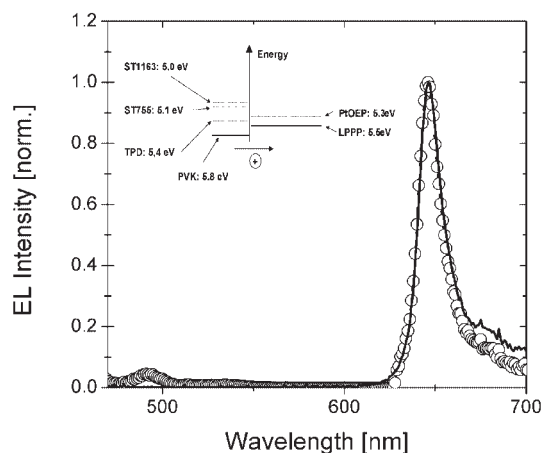
Fig. 6.21 Comparison of the EL spectra of devices consisting of a MeLPPP : PtOEP emission layer, with (solid line) or without (open symbols) a PVK : ST1163 (*N,N′*-bis (4′-(*N,N*-bis(naphta-2-yl)-amino)-biphenyle-4-yl)benzidine) hole-injecting layer. The inset shows the relative positions of the HOMO levels of the doped hole injection layer and the MeLPPP : PtOEP emission layer [44].

studied above, efficient Förster transfer occurs at concentrations larger than ca. 1 wt% (the Förster radius was calculated to 1.7 nm). As shown in Fig. 6.22, the EL of the PFO : PtOEP system was dominated by emission from the dye even at low dye concentrations. On the other hand, no evidence for Dexter transfer at room temperature was found (though triplet exciton transfer has been clearly proven at low temperatures in benzil-sensitized samples [104]). Investigations of the device properties with different dye concentrations revealed, in contrast to the MeLPPP : PtOEP system, a strong increase in driving voltage with increasing dye content. For example, the voltage to drive the LED at a current density of 5 mA/cm^2 shifted from ca. 12 V for a pure PFO layer to 33 V for a layer containing 4 wt% PtOEP. The different properties of the electrophosphorescent diodes can be well understood taking into account the deeper HOMO position of PFO compared to MeLPPP. In the former, PtOEP will constitute a ca. 0.5 eV trap and detrapping should be very slow. In addition, because of the high LUMO position of PFO, the injection of electrons from the Ca cathode should be inefficient. Rapid trapping of holes on the dye will, therefore, result in the build-up of positive space charge.

6.4
Conclusion and Outlook

In the following we will briefly discuss the relevance of the three excitation pathways discussed above with respect to device efficiency. There is no doubt that
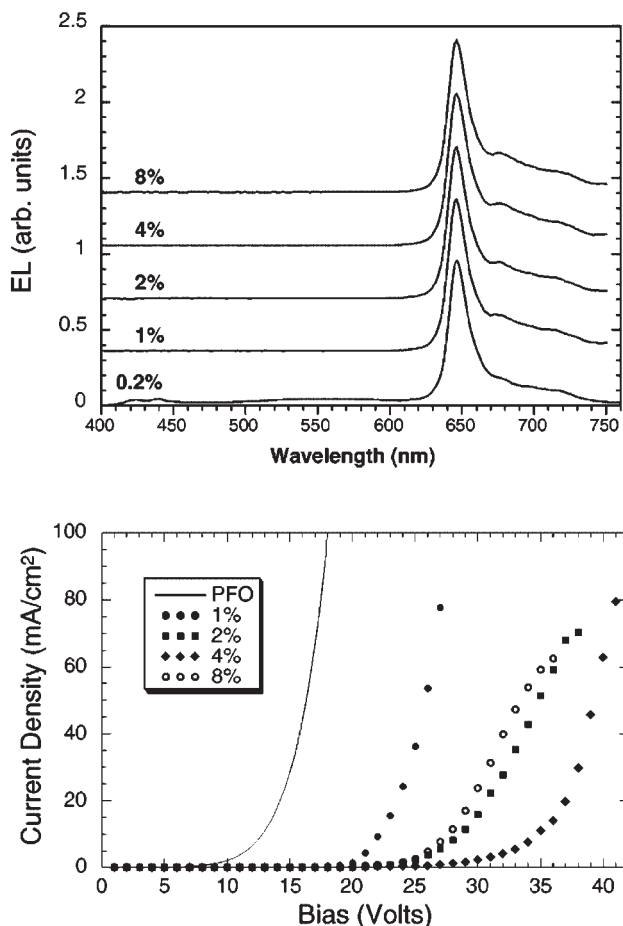
Fig. 6.22 (upper graph) Electroluminescence spectra of PFO : PtOEP LEDs for different dye concentrations. The spectra were normalized to the phosphorescence peak at 646 nm and offset for comparison. (lower graph) Current density as a function of applied bias of PFO LED and PtOEP/PFO LEDs with PtOEP concentrations of 1%, 2%, 4%, and 8% by weight [39].

Förster transfer from the singlet state of the polymer host to the singlet state of the added phosphor contributes an important pathway to the excitation of the dye. A nice example for which guest excitation was exclusively by Förster transfer is PtOEP blended into the conjugated polymer poly[2,5-bis(cholestanoxy)-1,4-phenylene vinylene)] (BCHA) [41]. This excitation pathway does not involve charge carrier trapping on the guest. Neglecting the quenching of the singlet excitons on

the host by the electric field and by charge carriers present in the device [106], Förster-type energy transfer should allow for stable color coordinates (independent of the driving conditions). This is particularly attractive with regard to color-stable white-emitting diodes. On the other hand, complete transfer of energy is generally observed only for rather high dye concentrations. With a typical Förster-transfer radius of $R_0 = 3$ nm, Eq. (6.7) predicts that a dye concentration of $N_g \cong 5 \times 10^{19}$ cm^{-3} (=4–8 wt% for a typical phosphor) is needed to transfer more than 95% of the host singlet excitons to the guest. At these concentrations, dye-dye interactions might already decrease the quantum efficiency of the system. Also, the examples summarized above showed that Eq. (6.7) is not applicable if bulky substituents on the dye set a limit to the closest approximation between the host molecules and the energy-accepting dye. Further, migration of excitons on the host alters the transfer kinetics, making absolute transfer rates rather unpredictable.

Because the statistical recombination of electrons and holes in EL favors the generation of triplet excitons on the host, Dexter-type energy transfer represents, at the first glance, an attractive excitation pathway. Triplet excitons turned out to be rather resistant to field-induced quenching processes [107]. However, we are not aware of any efficient device with predominant Dexter transfer. This is in part due to the fast localization of the triplet excitons within the inhomogeneously broadened density of states of the host. Also, the long radiative lifetime of triplet excitons on most host materials results in a relatively large probability for deactivation via nonradiative decay channels such as triplet–triplet annihilation, in particular for polymer materials. This is demonstrated in the left diagram of Fig. 6.23, where the quadratic dependence of the phosphorescence intensity on high excitation densities in the polymer contrasts with the linear dependence found for the associated monomer. TTA can result in a significant decrease in phosphorescence efficiency with increasing temperature, as illustrated in the right of Fig. 6.23. Because LEDs mostly function at room temperature (or above), the formation of triplet excitons on the host should be avoided in view of high device quantum efficiencies.

Excitation of the dye via charge trapping has been observed in most phosphor-doped polymer systems. Unfortunately, little knowledge exists about the kinetics of charge trapping in working devices at RT. The examples outlined above demonstrate that simple estimates for trapping and recombination coefficients might not be applicable for disordered multicomponent blends. Very high efficiencies in polymer-based electrophosphorescent devices have been reported for structures which allow for the direct injection of holes from an adjacent charge-transporting layer onto the dye. By using polymer interlayers with different HOMO and LUMO offsets (relative to the transport levels of the active compounds in the emission layer), we have recently demonstrated the importance of electron blocking and direct hole injection for achieving high efficiencies in polymer-based electrophosphorescent devices [83]. Ideally, holes will be exclusively transferred onto the HOMO of the dye, thus minimizing the density of triplet excitons on the host.
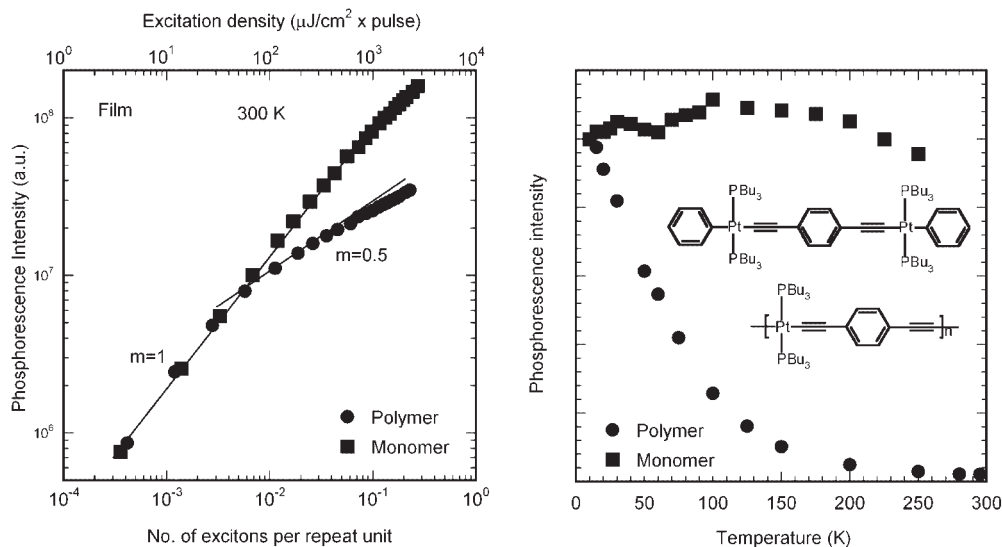
Fig. 6.23 (left) Phosphorescence intensity in dependence of excitation energy for a layer of the Pt-containing conjugated polymer Pt-TBT and the corresponding monomer. (right) Phosphorescence efficiency versus temperature for the same materials. The molecular structures are shown as an inset [108].

Acknowledgments

References

1 J. H. Burroughes, D. D. C. Bradley, A. R. Brown, R. N. Marks, K. Mackay, R. H. Friend, P. L. Burns, A. B. Holmes, *Nature* **1990**, *347*, 539–541.

2 I. D. Parker, *J. Appl. Phys.* **1994**, *75*, 1656–1666.

3 P. W. M. Blom, M. J. M. de Jong, J. J. M. Vleggaar, *Appl. Phys. Lett.* **1996**, *68*, 3308–3310.

4 B. K. Crone, P. S. Davids, I. H. Campbell, D. L. Smith, *J. Appl. Phys.* **1998**, *84*, 833–842.

5 V. I. Arkhipov, U. Wolf, H. Bässler, *Phy. Rev. B* **1999**, *59*, 7514–7520.

6 G. G. Malliaras, J. C. Scott, *J. Appl. Phys.* **1999**, *85*, 7426–7432.

7 A. Kraft, A. C. Grimsdale, A. B. Holmes, *Angew. Chem. -Int. Edit.* **1998**, *37*, 402–428.

8 R. H. Friend, R. W. Gymer, A. B. Holmes, J. H. Burroughes, R. N. Marks, C. Taliani, D. D. C. Bradley, D. A. Dos Santos, J. L. Bredas, M. Logdlund, W. R. Salaneck, *Nature*. **1999**, *397*, 121–128.

9 A. R. Brown, K. Pichler, N. C. Greenham, D. D. C. Bradley, R. H. Friend, A. B. Holmes, *Chem. Phys. Lett.* **1993**, *210*, 61–66.

10 Y. Cao, I. D. Parker, G. Yu, C. Zhang, A. J. Heeger, *Nature* **1999**, *397*, 414–417.

11 M. Wohlgenannt, K. Tandon, S. Mazumdar, S. Ramasesha, Z. V. Vardeny, *Nature* **2001**, *411*, 617–617.

12 J. S. Wilson, A. S. Dhoot, A. Seeley, M. S. Khan, A. Kohler, R. H. Friend, *Nature* **2001**, *413*, 828–831.

13 A. S. Dhoot, N. C. Greenham, *Adv. Mater.* **2002**, *14*, 1834–1837.

14 P. Herguch, X. Z. Jiang, M. S. Liu, A. K. Y. Jen, *Macromol.* **2002**, *35*, 6094–6100.

15 Q. F. Xu, J. Y. Ouyang, Y. Yang, T. Ito, J. Kido, *Appl. Phys. Lett.* **2003**, *83*, 4695–4697.

16 M. A. Baldo, D. F. O'Brien, Y. You, A. Shoustikov, S. Sibley, M. E. Thompson, S. R. Forrest, *Nature* **1998**, *395*, 151–154.

17 V. Cleave, G. Yahioglu, P. Le Barny, R. H. Friend, N. Tessler, *Adv. Mater.* **1999**, *11*, 285–288.

18 S. J. Yeh, M. F. Wu, C. T. Chen, Y. H. Song, Y. Chi, M. H. Ho, S. F. Hsu, C. H. Chen, *Adv. Mater.* **2005**, *17*, 285–289.

19 R. J. Holmes, B. W. D'Andrade, S. R. Forrest, X. Ren, J. Li, M. E. Thompson, *Appl. Phys. Lett.* **2003**, *83*, 3818–3820.

20 X. H. Yang, F. Jaiser, S. Klinger, D. Neher, *Appl. Phys. Lett.* **2006**, *88*, 021107.

21 C. Adachi, M. A. Baldo, M. E. Thompson, S. R. Forrest, *J. Appl. Phys.* **2001**, *90*, 5048–5051.

22 M. Ikai, S. Tokito, Y. Sakamoto, T. Suzuki, Y. Taga, *Appl. Phys. Lett.* **2001**, *79*, 156–158.

23 X. H. Yang, D. Neher, *Appl. Phys. Lett.* **2004**, *84*, 2476–2478.

24 T.-H. Kim, D.-H. Yoo, J. H. Park, O. O. Park, J.-W. Yu, J. K. Kim, *Appl. Phys. Lett.* **2005**, *86*, 171108–171101–171103.

25 X.-H. Yang, D. C. Müller, D. Neher, K. Meerholz, *Adv. Mater.* **2006**, *18*, 948–954.

26 A. Tsuboyama, H. Iwawaki, M. Furugori, T. Mukaide, J. Kamatani, S. Igawa, T. Moriyama, S. Miura, T. Takiguchi, S. Okada, M. Hoshino, K. Ueno, *J. Am. Chem. Soc.* **2003**, *125*, 12971–12979.

27 F. I. Wu, H. J. Su, C. F. Shu, L. Y. Luo, W. G. Diau, C. H. Cheng, J. P. Duan, G. H. Lee, *J. Mater. Chem.* **2005**, *15*, 1035–1042.

28 I. Tanaka, M. Suzuki, S. Tokito, *Jpn. J. Appl. Phys. Part 1 – Regul. Pap. Short Notes Rev. Pap.* **2003**, *42*, 2737–2740.

29 B. W. D'Andrade, R. J. Holmes, S. R. Forrest, *Adv. Mater.* **2004**, *16*, 624–628.

30 H. Kanno, R. J. Holmes, Y. Sun, S. Kena-Cohen, S. R. Forrest, *Adv. Mater.* **2006**, *18*, 339–342.

31 Y. Wang, N. Herron, V. V. Grushin, D. LeCloux, V. Petrov, *Appl. Phys. Lett.* **2001**, *79*, 449–451.

32 A. P. Monkman, H. D. Burrows, L. J. Hartwell, L. E. Horsburgh, I. Hamblett, S. Navaratnam, *Phys. Rev. Lett.* **2001**, *86*, 1358–1361.

33 D. Hertel, S. Setayesh, H. G. Nothofer, U. Scherf, K. Mullen, H. Bassler, *Adv. Mater.* **2001**, *13*, 65–70.

34 A. Köhler, J. S. Wilson, R. H. Friend, M. K. Al-Suti, M. S. Khan, A. Gerhard, H. Bassler, *J. Chem. Phys.* **2002**, *116*, 9457–9463.

35 M. J. Yang, T. Tsutsui, *Jpn. J. Appl. Phys. Part 2 – Lett.* **2000**, *39*, L828–L829.

36 S. Lamansky, R. C. Kwong, M. Nugent, P. I. Djurovich, M. E. Thompson, *Organic Electronics* **2001**, *2*, 53–62.

37 V. Cleave, G. Yahioglu, P. Le Barny, D. H. Hwang, A. B. Holmes, R. H. Friend, N. Tessler, *Adv. Mater.* **2001**, *13*, 44–47.

38 D. F. O'Brien, C. Giebeler, R. B. Fletcher, A. J. Cadby, L. C. Palilis, D. G. Lidzey, P. A. Lane, D. D. C. Bradley, W. Blau, *Synth. Met.* **2001**, *116*, 379–383.

39 P. A. Lane, L. C. Palilis, D. F. O'Brien, C. Giebeler, A. J. Cadby, D. G. Lidzey, A. J. Campbell, W. Blau, D. D. C. Bradley, *Phys. Rev. B* **2001**, *63*, 235206.

40 T.-F. Guo, S.-C. Chang, Y. Yang, R. C. Kwong, M. E. Thompson, *Organic Electronics* **2000**, *1*, 15–20.

41 L. H. Campbell, D. L. Smith, S. Tretiak, R. L. Martin, C. J. Neef, J. R. Ferraris, *Phys. Rev. B* **2002**, *65*, 085210.

42 W. G. Zhu, Y. Q. Mo, M. Yuan, W. Yang, Y. Cao, *Appl. Phys. Lett.* **2002**, *80*, 2045–2047.

43 R. W. T. Higgins, A. P. Monkman, H. G. Nothofer, U. Scherf, *J. Appl. Phys.* **2002**, *91*, 99–105.

44 X. H. Yang, D. Neher, U. Scherf, S. A. Bagnich, H. Bässler, *J. Appl. Phys.* **2003**, *93*, 4413–4419.

45 A. van Dijken, J. Bastiaansen, N. M. M. Kiggen, B. M. W. Langeveld, C. Rothe, A. Monkman, I. Bach, P. Stossel, K. Brunner, *J. Am. Chem. Soc.* **2004**, *126*, 7718–7727.

46 X. W. Chen, J. L. Liao, Y. M. Liang, M. O. Ahmed, H. E. Tseng, S. A. Chen, *J. Am. Chem. Soc.* **2003**, *125*, 636–637.

47 S. Tokito, M. Suzuki, F. Sato, M. Kamachi, K. Shirane, *Organic Electronics* **2003**, *4*, 105–111.

48 A. J. Sandee, C. K. Williams, N. R. Evans, J. E. Davies, C. E. Boothby, A. Kohler, R. H. Friend, A. B. Holmes, *J. Am. Chem. Soc.* **2004**, *126*, 7041–7048.

49 J. Liu, Q. Zhou, Y. Cheng, Y. Geng, L. Wang, D. Ma, X. Jing, F. Wang, *Adv. Mater.* **2005**, *17*, 2974–2978.

50 M. Suzuki, S. Tokito, F. Sato, T. Igarashi, K. Kondo, T. Koyama, T. Yamaguchi, *Appl. Phys. Lett.* **2005**, *86*, 103507.

51 H. Zhen, C. Luo, W. Yang, W. Song, B. Du, J. Jiang, C. Jiang, Y. Zhang, Y. Cao, *Macromol.* **2006**,

52 H. Yersin, W. Humbs, J. Strasser, *Top. Curr. Chem.*, **1997**, *191*, 153–249.

53 H. Yersin, D. Donges, *Top. Curr. Chem.*, **2001**, *214*, 81–186.

54 E. Holder, B. M. W. Langeveld, U. S. Schubert, *Adv. Mater.* **2005**, *17*, 1109–1121.

55 J. Li, P. I. Djurovich, B. D. Alleyne, M. Yousufuddin, N. N. Ho, J. C. Thomas, J. C. Peters, R. Bau, M. E. Thompson, *Inorg. Chem.* **2005**, *44*, 1713–1727.

56 J. Pommerehne, H. Vestweber, W. Guss, R. F. Mahrt, H. Bässler, M. Porsch, J. Daub, *Adv. Mater.* **1995**, *7*, 551–554.

57 D. M. Pai, J. F. Yanus, M. Stolka, *J. Phys. Chem.* **1984**, *88*, 4714–4717.

58 S. Lamansky, P. I. Djurovich, F. Abdel-Razzaq, S. Garon, D. L. Murphy, M. E. Thompson, *J. Appl. Phys.* **2002**, *92*, 1570–1575.

59 K. M. Vaeth, C. W. Tang, *J. Appl. Phys.* **2002**, *92*, 3447–3453.

60 X. Gong, M. R. Robinson, J. C. Ostrowski, D. Moses, G. C. Bazan, A. J. Heeger, *Adv. Mater.* **2002**, *14*, 581–585.

61 X. H. Yang, D. Neher, D. Hertel, T. K. Daubler, *Adv. Mater.* **2004**, *16*, 161–166.

62 X. Jiang, R. A. Register, K. A. Killeen, M. E. Thompson, F. Pschenitzka, T. R. Hebner, J. C. Sturm, *J. Appl. Phys.* **2002**, *91*, 6717–6724.

63 R. A. Negres, X. Gong, J. C. Ostrowski, G. C. Bazan, D. Moses, A. J. Heeger, *Phys. Rev. B* **2003**, *68*, 115209.

64 C. Y. Jiang, W. Yang, J. B. Peng, S. Xiao, Y. Cao, *Adv. Mater.* **2004**, *16*, 537–541.

65 Y. Y. Noh, C. L. Lee, J. J. Kim, K. Yase, *J. Chem. Phys.* **2003**, *118*, 2853–2864.

66 X. H. Yang, D. Neher, *unpublished results*.

67 X. Gong, J. C. Ostrowski, D. Moses, G. C. Bazan, A. J. Heeger, *Adv. Funct. Mater.* **2003**, *13*, 439–444.

68 T. R. Waite, *Phys. Rev.* **1957**, *1*, 463–470.

69 V. R. Nikitenko, J. M. Lupton, *J. Appl. Phys.* **2003**, *93*, 5973–5977.

70 S. Mansurova, S. Stepanov, V. Camacho-Pernas, R. Ramos-Garcia, F. Gallego-Gomez, E. Mecher, K. Meerholz, *Phys. Rev. B* **2004**, *69*, 193203.

71 L. Kulikovsky, K. Meerholz, D. Neher, *in preparation*.

72 D. Kolosov, V. Adamovich, P. Djurovich, M. E. Thompson, C. Adachi, *J. Am. Chem. Soc.* **2002**, *124*, 9945–9954.

73 L. Kulikovsky, D. Neher, E. Mecher, K. Meerholz, H. H. Horhold, O. Ostroverkhova, *Physi. Rev. B* **2004**, *69*, 125216.

74 O. Ostroverkhova, K. D. Singer, *J. Appl. Phys.* **2002**, *92*, 1727–1743.

75 J. Q. Qu, J. Y. Zhang, A. C. Grimsdale, K. Müllen, F. Jaiser, X. H. Yang, D. Neher, *Macromolecules* **2004**, *37*, 8297–8306.

76 R. Beavington, M. J. Frampton, J. M. Lupton, P. L. Burn, I. D. W. Samuel, *Adv. Funct. Mater.* **2003**, *13*, 211–218.

77 S. C. Lo, T. D. Anthopoulos, E. B. Namdas, P. L. Burn, I. D. W. Samuel, *Adv. Mater.* **2005**, *17*, 1945–1948.

78 V. Bulovic, A. Shoustikov, M. A. Baldo, E. Bose, V. G. Kozlov, M. E. Thompson, S. R. Forrest, *Chem. Phys. Lett.* **1998**, *287*, 455–460.

79 A. Salomon, D. Cahen, S. Lindsay, J. Tomfohr, V. B. Engelkes, C. D. Frisbie, *Adv. Mater.* **2003**, *15*, 1881–1890.

80 Y. Hino, H. Kajii, Y. Ohmori, *Jpn. J. Appl. Phys. Part 1* **2005**, *44*, 2790–2794.

81 C. D. Müller, T. Braig, H. Nothofer, M. Arnoldi, M. Groß, U. Scherf, O. Nuyken, K. Meerholz, *Chem. Phys. Chem.* **2000**, *1*, 207–211.

82 D. Müller, M. Gross, K. Meerholz, T. Braig, M. S. Bayerl, F. Bielefeldt, O. Nuyken, *Synth. Met.* **2000**, *111*, 31–34.

83 C.-H. Yang, F. Jaiser, B. Stiller, D. Neher, F. Galbrecht, U. Scherf, *Adv. Funct. Mater.* **2006**, *16*, 2156–2162.

84 M. Sudhakar, P. I. Djurovich, T. E. Hogen-Esch, M. E. Thompson, *J. Am. Chem. Soc.* **2003**, *125*, 7796–7797.

85 K. Brunner, A. van Dijken, H. Borner, J. Bastiaansen, N. M. M. Kiggen, B. M. W. Langeveld, *J. Am. Chem. Soc.* **2004**, *126*, 6035–6042.

86 M. A. Baldo, S. R. Forrest, *Phys. Rev. B* **2000**, *62*, 10958–10966.

87 J. Kalinowski, W. Stampor, M. Cocchi, D. Virgili, V. Fattori, P. Di Marco, *Chem. Phys.* **2004**, *297*, 39–48.

88 G. Rippen, G. Kaufmann, W. Klöpffer, *Chem. Phys.* **1980**, *52*, 165–177.

89 J. Pina, J. S. de Melo, H. D. Burrows, A. P. Monkman, S. Navaratnam, *Chem. Phys. Lett.* **2004**, *400*, 441–445.

90 C. Adachi, R. C. Kwong, P. Djurovich, V. Adamovich, M. A. Baldo, M. E. Thompson, S. R. Forrest, *Appl. Phys. Lett.* **2001**, *79*, 2082–2084.

91 B. Luszczynska, E. Dobruchowska, I. Glowacki, J. Ulanski, F. Jaiser, X. H. Yang, D. Neher, A. Danel, *J. Appl. Phys.* **2006**, *99*, 024505.

92 R. C. Kwong, S. Sibley, T. Dubovoy, M. Baldo, S. R. Forrest, M. E. Thompson, *Chem. Mat.* **1999**, *11*, 3709–3713.

93 M. A. Baldo, D. F. O'Brien, M. E. Thompson, S. R. Forrest, *Phys. Rev. B* **1999**, *60*, 14422–14428.

94 Y. V. Romanovskii, A. Gerhard, B. Schweitzer, U. Scherf, R. I. Personov, H. Bassler, *Phys. Rev. Lett.* **2000**, *84*, 1027–1030.

95 T. K. Däubler, I. Glowacki, U. Scherf, J. Ulanski, H. H. Horhold, D. Neher, *J. Appl. Phys.* **1999**, *86*, 6915–6923.

96 A. W. Grice, D. D. C. Bradley, M. T. Bernius, M. Inbasekaran, W. W. Wu, E. P. Woo, *Appl. Phys. Lett.* **1998**, *73*, 629–631.

97 D. Sainova, T. Miteva, H. G. Nothofer, U. Scherf, I. Glowacki, J. Ulanski, H. Fujikawa, D. Neher, *Appl. Phys. Lett.* **2000**, *76*, 1810–1812.

98 D. Neher, *Macromol. Rapid Commun.* **2001**, *22*, 1366–1385.

99 U. Scherf, E. J. W. List, *Adv. Mater.* **2002**, *14*, 477–487.

100 S. Janietz, D. D. C. Bradley, M. Grell, C. Giebeler, M. Inbasekaran, E. P. Woo, *Appl. Phys. Lett.* **1998**, *73*, 2453–2455.

101 E. J. W. List, C. Creely, G. Leising, N. Schulte, A. D. Schluter, U. Scherf, K. Mullen, W. Graupner, *Chem. Phys. Lett.* **2000**, *325*, 132–138.

102 S. A. Bagnich, C. Im, H. Bassler, D. Neher, U. Scherf, *Chem. Phys.* **2004**, *299*, 11–16.

103 S. A. Bagnich, H. Bässler, D. Neher, *J. Chem. Phys.* **2004**, *121*, 9178–9183.

104 C. Rothe, L. O. Palsson, A. P. Monkman, *Chem. Phys.* **2002**, *285*, 95–101.

105 A. A. Lamola, G. S. Hammond, *J. Chem. Phys.* **1965**, 43, 2129–2135.

106 M. Deussen, M. Schneidler, H. Bässler, *Synth. Met.* **1995**, *73*, 123–129.

107 C. Rothe, S. M. King, A. P. Monkman, *Phys. Rev. B* **2005**, *72*, 085220.

108 L. S. Devi, C. Dosche, M. K. Al-Suli, M. S. Khan, R. H. Friend, A. Köhler, *Manuscript in Preparation.*

7

Phosphorescent Platinum(II) Materials for OLED Applications

Hai-Feng Xiang, Siu-Wai Lai, P. T. Lai, and Chi-Ming Che

Several classes of phosphorescent platinum(II) complexes with high photoluminescence efficiency and thermal stability are examined. The tunability of photoluminescent properties through modifying the electronic and/or structural character of the auxiliary ligands is discussed. The suitability of phosphorescent platinum(II) materials as emitting dopants in organic light-emitting devices (OLEDs) and the resultant device performances are highlighted. Molecular design of phosphorescent platinum(II) dopants to improve luminous efficiency and tune electroluminescence energies is demonstrated. Device configurations as well as dopant concentrations are optimized to achieve high-performance OLEDs.

7.1
Introduction

7.1.1
Phosphorescent Materials for OLED Applications

The pursuit of high-efficiency and -brightness organic light-emitting devices (OLEDs) has prompted the development of electrophosphorescent organometallic emitters [1–3]. The involvement of heavy transition metals in these materials promotes spin–orbit coupling, which potentially harnesses both singlet (25%) and triplet (75%) excitons for electron–hole recombination from electrical excitation, leading to maximum luminous efficiency. Several accounts of iridium(III) [2] and platinum(II) [3] emitters as dopants in OLEDs have appeared and their device performances have been reported. The intense triplet excited state emission of phosphorescent compounds is an important prerequisite for fabrication of high-efficiency electroluminescent device. Ma and Che reported the first observation of electroluminescence from triplet metal-to-ligand charge transfer (^{3}MLCT) excited states of transition metal complexes, such as [Os(CN)$_2$(PPh$_3$)$_2$(Ph$_2$bpy)] (Ph$_2$bpy = 4,4′-diphenyl-2,2′-bipyridine) [4].

The diverse photoluminescent properties of platinum(II) complexes have attracted attention in OLED applications, and the remarkable variety of highly

emissive excited states [5] include (i) intraligand (IL) states (π–π*), (ii) intraligand (IL) states of "excimer" type [σ*(π) $\rightarrow$ σ(π*)], (iii) metal-to-ligand (MLCT) [Pt(5d) $\rightarrow$ π*(ligand)] excited states, (iv) oligomeric metal–metal-to-ligand charge transfer [$d\sigma$*(dz^2) $\rightarrow$ σ(π*)] (MMLCT), and (v) monomer ligand-field (LF) states. Systematic ligand modifications can alter the relative energies of the Pt d-orbitals and the π and π* orbitals of the ligands, which ultimately govern the emissive characteristics and excited-state properties of platinum(II) complexes. This can result in tunable emission energy, high photoluminescence quantum yield, and improved charge injection and transport. The application of cyclometalated platinum(II) complexes as electrophosphorescent dopants for OLEDs was also reported by Forrest and Thompson [3b, 3c, 6] and others [7–9]. Platinum(II) porphyrins have been synthesized and successfully used in organic electrophosphorescent devices [10].

One of the drawbacks of phosphorescent emitters in OLED applications is the saturation of emission sites, which are caused by excessively long lifetimes, triplet–triplet annihilation, and concentration quenching from bimolecular interactions at high doping levels [11]. The introduction of sterically hindered substituents into the auxiliary ligands can suppress self-quenching activities even at high dopant concentrations [12], and this can result in complete energy transfer between the host and dopant within devices. Moreover, ligand modifications can be customized to improve stability with regard to oxidative deterioration to afford more robust electroluminescent materials for OLEDs.

In this chapter, the structural and optical properties of several classes of platinum(II) complexes are discussed and a correlation between chemical characteristics and electroluminescent property can be established. The applications of phosphorescent platinum(II) materials as dopants in OLEDs, plus strategies to fine-tune the emission color and device performances, are presented.

7.1.2
Criteria for Complexes as OLED Emitters

The followings are the criteria for phosphorescent platinum(II) complexes as potential highly luminous and efficient electroluminescent materials: (i) high photoluminescence quantum yields, (ii) thermally, chemically, and photochemically robust, which allow tolerance to heat and vacuum deposition conditions and extends device lifetime, (iii) tunable emission energies through chemical modification of auxiliary ligands, (iv) readily prepared to achieve structurally diverse derivatives, and (v) neutral and sublimable. The ability to fulfill the above criteria was used to identify potentially suitable candidates as electrophosphorescent emitters for multicolor OLED applications.

7.2
Device Fabrication and Electroluminescence Measurements

As neutral organometallic complexes are sufficiently stable with respect to sublimation, they are suitable for vacuum deposition during OLED fabrication. However,

if complexes are thermally unstable and not sufficiently volatile, vacuum deposition cannot be used for the film formation in OLEDs. It is essential to develop systems with good filming properties, such as the immobilization of metal complexes in polymer matrices. For instance, some organometallic complexes have been doped in polymer matrices (polystyrene, PST, and poly(*N*-vinylcarbazole), PVK), resulting enhancement of the emission intensity [4]. The main nonradiative process of the ^{3}MLCT excited state is oxidative quenching by an electron acceptor. The oxidative nature of the PVK matrix stabilizes the excited state of the organometallic complexes. Efficient phosphorescent emitters doped into fluorescent host materials can harvest both singlet and triplet excitons upon electron–hole recombination from electrical excitation. The quantum efficiency of a double-layer device is invariably enhanced compared to a single-layer device. This enhancement is often due to the lowering of the effective barrier height for electron injection. The structure and concentration of the doped complex determine the charge transport properties of the PVK layer, and judicious choice of the dopant complex and its concentration should lead to higher electroluminescence (EL) efficiency.

A typical example of the device configuration used is given: glass/indium tin oxide (ITO: 30 Ω/square)/NPB (4,4′-bis[*N*-(naphthyl)-*N*-phenylamino]biphenyl, 40 nm)/complex (*x*%, 30 nm)-doped CBP (4,4′-*N*,*N*′-dicarbazole-biphenyl, 20 nm)/BCP (2,9-dimethyl-4,7-diphenyl-1,10-phenanthroline, bathocuproine, 20 nm)/Alq$_3$ (tris-(8-hydroxyquinolato)aluminum, 30 nm)/LiF (0.5 nm)/Al (100 nm). The ITO glass substrate was cleaned with detergent and deionized water, and dried in an oven for two hours. It was treated with UV ozone for 25 min before loading into a deposition chamber. The organic films of NPB, CBP/complex, BCP, and Alq$_3$ were sequentially deposited onto the ITO substrate at a pressure of around 1.0×10^{-5} mbar. The pressure during deposition of metal complex was below 9.0×10^{-6} mbar to minimize metal oxidation. The current–voltage–luminance characteristics and EL spectra were recorded with a computer-controlled DC power supply and a photometer at room temperature. The emission area of the devices is 0.1 cm^2, defined by the overlapping area of the anode and cathode. The thickness of each layer requires precise control to obtain charge balance for high-performance OLEDs.

Phosphorescent platinum(II) complexes are often strongly emissive, and the excited state can be ^{3}MLCT or ^{3}IL in nature. When the electroluminescence spectrum of a double-layer device is similar to the photoluminescence spectrum of the Pt(II) complex/PVK film, this confirms that the electroluminescence is from the Pt(II) complexes. For the ^{3}MLCT excited state of Pt(II) complexes, the π^* orbital of the chromophoric ligand is the LUMO, which should be available for trapping electrons injected from the Al cathode. The highest energy filled orbital (HOMO) comes from the Pt(II) d electrons, making it a possible site for oxidation by trapping holes injected from ITO. The recombination of trapped electrons and holes in the Pt(II) complexes results in electroluminescence from the lowest triplet MLCT excited state. When no emission from CBP or Alq$_3$ was observed from the EL, it indicates a complete energy transfer from the host exciton to the phosphor. Meanwhile, there is no exciton decay in the Alq$_3$ layer due to the hole-blocking action of the BCP layer.

7.3
Platinum(II) α-Diimine Arylacetylide Complexes

We reported the first luminescent platinum(II) acetylide complexes with aromatic diimine ligands in 1994 [13]. The [Pt(phen)(C≡CPh)₂] (phen = 1,10-phenanthroline) complex exhibits an intense emission in fluid solution at room temperature that was attributed to a ³MLCT: [Pt → π*(phen)] excited state. The incorporation of strong-field arylacetylide ligands into Pt(II) destabilizes nonradiative ligand-field (d–d) transition(s) and helps to maintain strict stereochemical integrity [14]. The excited-state properties of [Pt(α-diimine)(C≡CPh)₂] complexes can be probed by systematic ligand modification [15]. A correlation between the emission energy and electron-withdrawing property of the diimine ligand was observed for the complexes depicted in Scheme 7.1 [16]. The solution emission maxima shifted to lower energies according to the electron-withdrawing substituent(s) on the bipyridine (**1a–1c**) and phenanthroline (**2a–2c**) ligands (Fig. 7.1). The electronic effect of the α-diimine ligands alters the LUMO energy levels, which enables fine-tuning of excited-state energies. The minor blue shift of the singlet MLCT band of **3** from that of **1b** can be rationalized by the presence of the more conjugated C≡C–C≡CPh ligands. This is expected to stabilize the d_π(Pt) orbital, which results in a lowering of the HOMO level and thus an increase of the MLCT energy. The emission energies can be systematically modified over a range of $\approx 1920 \, \text{cm}^{-1}$.

The highly tunable orange–red ³MLCT emission energies of luminescent Pt(II) complexes, plus their high quantum yields, make them suitable candidates as OLED emitters. We reported the application of a series of [Pt(α-diimine)(C≡CPh)₂] complexes as electrophosphorescent emitters in single- and double-layer OLEDs [16]. Complexes **1a–1c**, or **2c** (10 wt%) and poly(*N*-vinylcarbazole) (PVK, 90 wt%) were incorporated by spin-coating into OLED devices, and the EL characteristics were examined. The EL spectra for the single-layer devices (configuration: [ITO/ PVK:**Pt**/Al]) were similar to their corresponding thin film photoluminescence (PL)
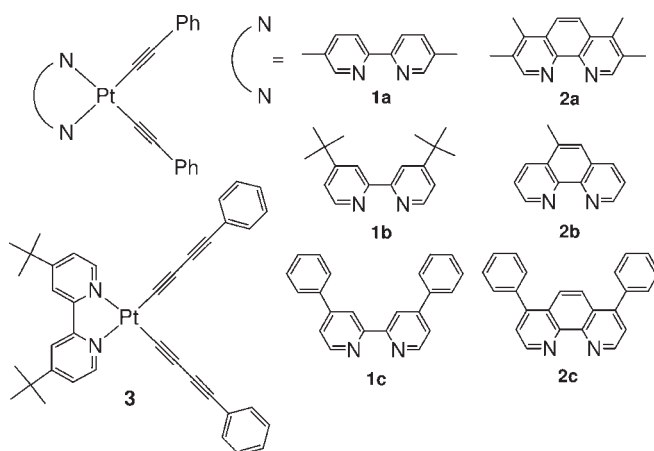
Scheme 7.1
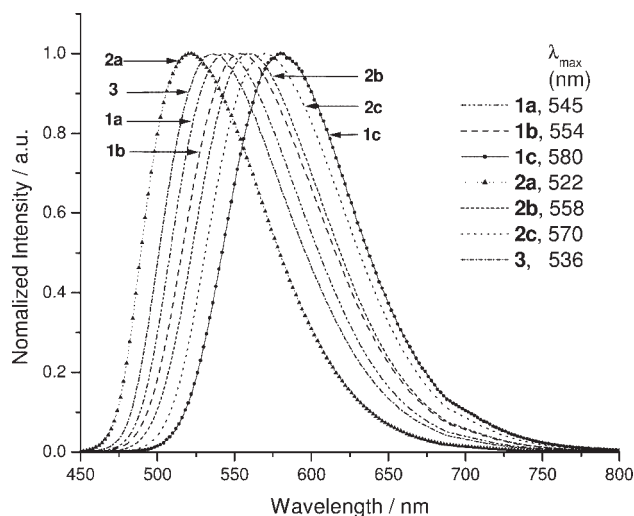
Fig. 7.1 Normalized 298 K emission spectra for **1a–1c**, **2a–2c**, and **3** in dichloromethane, illustrating the tunable range of emission energies (Reproduced with permission from [16]. Copyright 2001 Wiley-VCH).
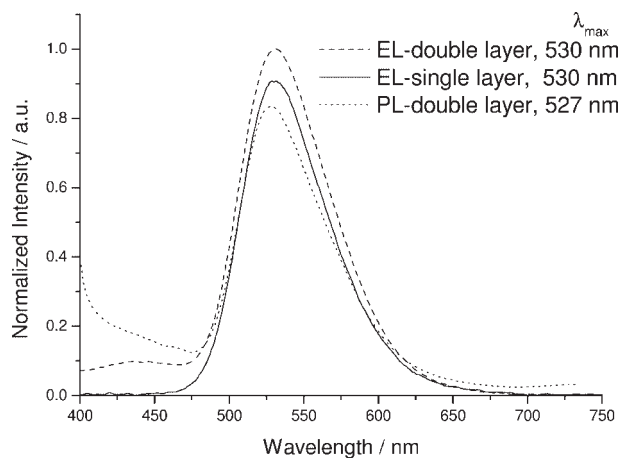
Fig. 7.2 EL and PL spectra for devices based on **1a** (Reproduced with permission from [16]. Copyright 2001 Wiley-VCH).

spectra (Fig. 7.2 for **1a**). The single-layer EL device for **1a** was superior in performance and exhibited a maximum luminance of $620 \, cd \, m^{-2}$ at driving voltage of $30 \, V$ and peak luminous efficiency of $0.10 \, lm \, W^{-1}$ at luminance of $25 \, cd \, m^{-2}$.

EL from PVK was not observed for single-layer devices, indicating efficient Förster energy transfer [17] from PVK to the Pt emitter. The PL spectra of

single-layer films of [PVK:**Pt**] were recorded and only emission bands originating from the Pt complexes were detected. Significant overlap exists between the ^{1}MLCT absorption of the Pt^{II} complexes (λ_{max} 385–411 nm) and the emission of PVK (400 nm), and this increases the likelihood for efficient singlet energy transfer.

Introducing an electron-transporting layer between the [PVK:**Pt**] layer and Al cathode in a double-layer device enhances the EL brightness and efficiency. 2-(4-Biphenyl)-5-(4-*tert*-butylphenyl)-1,3,4-oxadiazole (PBD) was selected as electron-transporting material since its LUMO level is lower than that of PVK. The lower energy barrier for electron injection between Al and PBD is expected to balance the rate of hole and electron injection into the emitter in order to achieve higher EL efficiency. In addition, PBD acts as a confinement layer to increase the distance between excitons and the cathode, at which nonradiative quenching can take place through physical and chemical interactions. The double-layer devices (configuration: [ITO/PVK:**Pt**/PBD/Al]) were found to display significant improvements in EL performance compared with the single-layer devices. The double-layer [ITO/PVK:**2c**/PBD/Al] device exhibited peak luminous efficiency of 1.33 lm W^{-1} at 23 cd m^{-2} and maximum luminance of 945 cd m^{-2} at 28 V. The *I–V–L* characteristics of the double-layer device derived from **2c** are presented in Fig. 7.3.

These highly photoluminescent bis(arylacetylide)platinum(II) diimine complexes warrant further investigations as OLED materials due to their tunable emission properties and their ability to mediate efficient energy transfer [18].
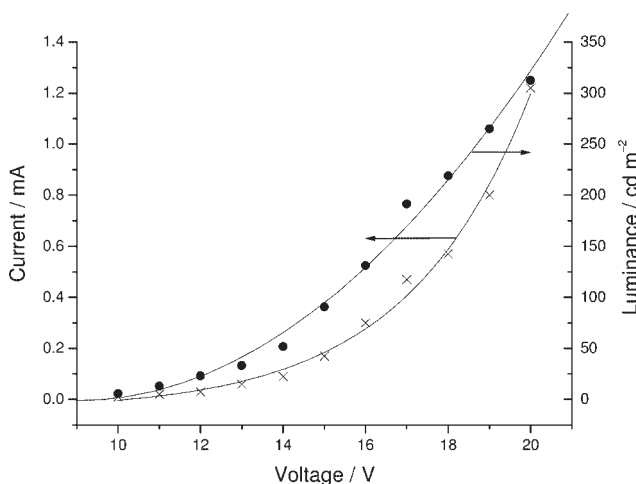
Fig. 7.3 Current–voltage and luminance–voltage plots for double-layer device of **2c** (Reproduced with permission from [16]. Copyright 2001 Wiley-VCH).

7.4
Tridentate Pt(II) Complexes

7.4.1
Cyclometalated 6-Aryl-2,2′-bipyridine Arylacetylide Pt(II) Complexes

A class of tridentate cyclometalated platinum(II) complexes bearing σ-alkynyl ancillary ligands, namely [(C^N^N)Pt(C≡C)$_n$R] (HC^N^N = 6-aryl-2,2′-bipyridine; n = 1–4; R = aryl, alkyl, or trimethylsilyl), have been studied (Scheme 7.2) [19]. Because the anionic σ-alkynyl ligand affords neutrality to these [(C^N^N)Pt(C≡C)$_n$R] complexes, they are sufficiently stable with respect to sublimation and thus are suitable for vacuum deposition during OLED fabrication. The tridentate cyclo-metalated Pt(II) complexes possess superior thermal stability when compared to bis(arylacetylide) Pt(II) complexes of aromatic diimines and other metal–alkynyl complexes that are also emissive but easily decompose during vacuum deposition [20]. Furthermore, we suggest that π-conjugation of the tridentate aromatic ligand with the Pt-acetylide moiety may impart sublimability and additional stability to these neutral materials. Thermogravimetric analysis in N_2 showed that the decom-position temperature was around 400 °C for **4**, **5**, **14**, and **15** and around 330 °C for **10** and **11** (the residual decomposition product was composed of metallic plati-num). This thermal stability is remarkable for σ-alkynylmetal complexes and especially for the butadiynyl derivative **11**.

Tridentate cyclometalated Pt(II) luminophores [Pt(C^N^N)] were utilized due to their superior emissive properties compared to the 2,2′:6′,2″-terpyridine (tpy) and (C^N^C) (HC^N^CH = 2,6-diphenylpyridine) congeners [21]. The σ-alkynyl ligand is envisaged to modulate their photophysical properties by (1) destabilizing nonradiative ligand-field transitions that are inherent to this class of complexes, and (2) modifying the properties of the triplet excited state [normally ^{3}MLCT:

R^1 = R^2 = H	
R^3 = Ph	**4**
C$_6$H$_4$-4-CH$_3$	**5**
C$_6$H$_4$-4-OCH$_3$	**6**
C$_6$H$_4$-4-Cl	**7**
C$_6$H$_4$-4-F	**8**
C$_6$H$_4$-4-NO$_2$	**9**
Si(CH$_3$)$_3$	**10**
C≡CSi(CH$_3$)$_3$	**11**
C≡C—C≡CSi(CH$_3$)$_3$	**12**
C≡C—C≡C—C≡CSi(CH$_3$)$_3$	**13**
C$_6$F$_5$	**17**
C(CH$_3$)$_3$	**18**

R^1 = R^2 = ^{t}Bu
R^3 = C$_6$F$_5$ **19**

X = S
R^4 = Ph   **14**
C$_6$H$_4$-4-CH$_3$ **15**

X = O
R^4 = Ph   **16**
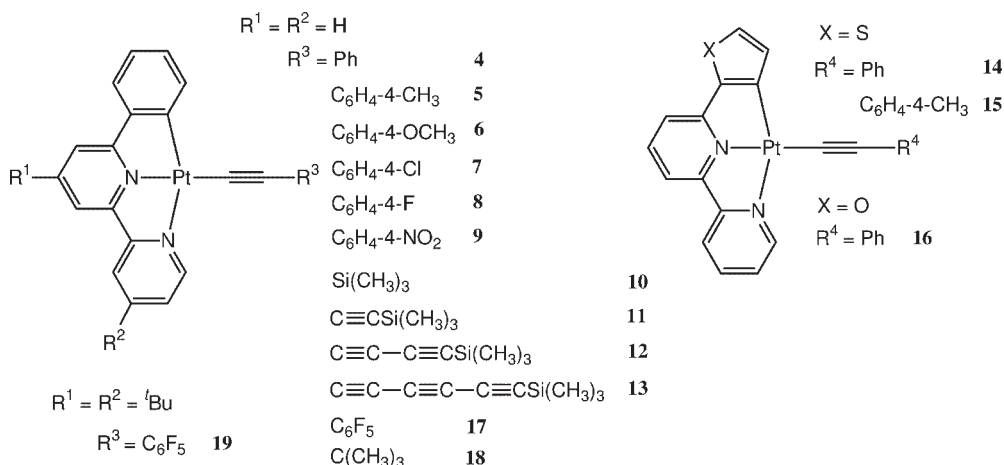
Scheme 7.2
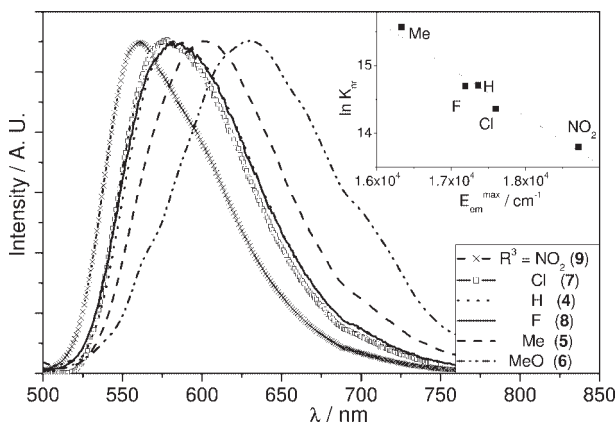
Fig. 7.4 Normalized emission spectra of **4–9** in CH$_2$Cl$_2$ solutions at 298 K (λ_{ex} = 350 nm). Inset: plot of ln k_{nr} versus emission maximum (Reproduced with permission from [19b]. Copyright 2004 American Chemical Society).

Pt → π*(cyclometalating ligand)] through π-bonding conjugation between Pt(II) and the σ-alkynyl auxiliary.

Extensive structural modification, by introducing substituents with different steric and electronic properties into both the arylacetylide and tridentate cyclometalating (C^N^N) ligands of [(C^N^N)Pt(C≡C)$_n$R] complexes, has resulted in tuning of their photophysical and luminescent characteristics. Figure 7.4 depicts that the emission maxima of this class of complexes in dichloromethane at 298 K can be tuned from 630 nm for **6** to 560 nm for **9** ($\Delta\upsilon$ = 1980 cm^{-1}) upon changing the 4-arylacetylide substituent. The electron-withdrawing group in the 4-arylacetylide ligand stabilizes the Pt-based HOMO to give blue-shifted emission, leading to tunability of the emission energies.

The effect of the π-conjugated length of the oligoyne ligands upon the emission of [(C^N^N)Pt–(C≡C)$_n$–R] has been examined. From **10** to **12**, the alkynyl ligand is homologously lengthened from trimethylsilyl-capped ethynyl to hexatriynyl. Their emission energies in CH$_2$Cl$_2$ solutions at 298 K decrease in the order: triynyl (**12**: λ_{max} 557 nm) > diynyl (**11**: λ_{max} 561 nm) > monoynyl (**10**: λ_{max} 570 nm), but the differences are minor. When the trimethylsilyl-capped oligoyne ligand is further extended to octatetraynyl (**13**), a highly structured, narrow-bandwidth emission at 298 K, with peak maxima at λ_{max} 589 and 671 nm is observed. The vibronic progression of ca. 2100 cm^{-1} signifies that the –(C≡C)$_4$– unit is involved in the electronic transition.

Modification of the tridentate (C^N^N) ligand facilitates fine-tuning of the emission energy of [(C^N^N)Pt(C≡C–R)] complexes (i.e., lower π* levels afford red-shifted emissions). The introduction of two electron-donating *tert*-butyl groups to the bipyridine moiety of the (C^N^N) ligand (R^1 = R^2 = tBu; R^3 = Ph) led to blue-shifted emissions (λ_{max} 571 nm) from λ_{max} 582 nm for **4** in CH$_2$Cl$_2$ solution at 298 K. With regards to the development of red emitters for OLED applications, the λ_{max} value in alcoholic glass at 77 K was observed to substantially red-shift when the
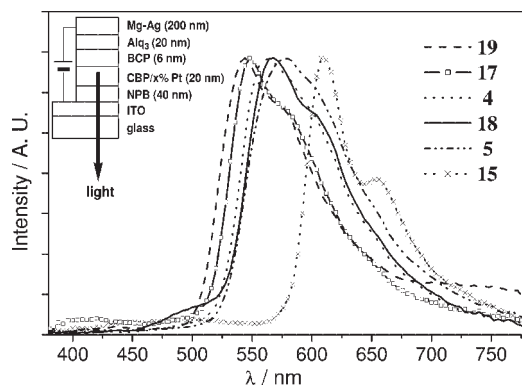
Fig. 7.5 Normalized electroluminescence spectra for **4**, **5**, **15**, **17**, **18**, and **19** (4%) operated at 10 V (Reproduced with permission from [19b]. Copyright 2004 American Chemical Society).

cyclometalating ligand was modified from C^N^N (**4**: λ_{max} 540 nm) to thienyl-(**14**: λ_{max} 595 nm) and furyl-(**16**: λ_{max} 613 nm) bipyridine for the same C≡CPh ligand. By choosing appropriate cyclometalating and σ-alkynyl ligands, the emission color of this class of platinum(II) complexes can be tuned from green–yellow to saturated red.

The intense tunable phosphorescence of these Pt(II) σ-alkynyl materials, plus their thermal stability and neutrality, render them good candidates as electrophosphorescent emitters in high-efficiency OLEDs. Selected platinum(II) complexes were doped into the emissive region of multilayer, vapor-deposited OLEDs and yellow to red electroluminescence was generated. The devices (top of Fig. 7.5) were fabricated on ITO glass using the vacuum deposition method [2c]. NPB and Alq$_3$ were used as the hole- and electron-transporting layers, respectively. BCP was used to confine excitons within the luminescent zone. Magnesium–silver alloy was applied as the cathode. The [(C^N^N)Pt(C≡C)$_n$R] materials were doped into the conductive host material, CBP, with mass ratios of 2 to 6%. The tunable electrophosphorescence energy resembled to that recorded in fluid solutions for these emitters, and the devices exhibited high luminance (approaching 10 000 cd m^{-2}) and efficiencies (up to 4.2 cd A^{-1}) with low turn-on voltages (3.6–4.5 V).

Upon stimulation of positive bias voltage above ~4 V for devices with emitter ratios of 4 and 6%, an intense orange to red electrophosphorescence was observed for **4**, **5**, **15**, **17**, **18**, and **19**. The electroluminescence data of **4**-, **5**-, **15**-, **17**-, **18**-, and **19**-doped OLEDs are listed in Table 7.1 and their EL spectra are depicted in Fig. 7.5. Blue fluorescence from the host and hole-transporting layers is negligible, implying that energy transfer from singlet to triplet excitons is complete. For **4**, **5**, **15**, and **17**, their electroluminescence maxima are independent of the doping level and applied voltage (for current density up to 600 mA cm^{-2}).

The highest luminance (9800 cd m^{-2} at 12 V; λ_{max} 548 nm; the Commission Internationale de L'Éclairage (CIE) coordinates x = 0.440, y = 0.506) and EL efficiency (3.2 cd A^{-1} (η_{ext} 1.1%) at 20 mA cm^{-2}) were achieved by using emitter **17** at 4%

Table 7.1 Electroluminescence data.

Complex	EL $\lambda_{max,}$[a] (nm) (CIE Coordinates[a] (x, y))	Turn-on voltage (V)	Doping ratio (%)	Maximum luminance (cd m^{-2})	Maximum efficiency (cd A^{-1})	Maximum η_{ext} (%)
4	564(0.480, 0.484)	3.6	2[b]	9900[e]	4.2[h]	1.6
			4	7800[d]	2.4[h]	0.9
5	580(0.508, 0.466)	4.2	4	3900[e]	1.4[g]	0.6
			6	2100[e]	0.6[g]	0.3
14	608, 656(0.549, 0.330)	4.5	2[b]	2000[e]	0.7[h]	0.6
			4	2000[e]	0.6[h]	0.5
15	612, 656(0.553, 0.305)	4.5	4	3100[f]	1.0[g]	0.8
			6	1800[e]	0.5[i]	0.7
17	548(0.440, 0.507)	4.5	2[b]	5600[f]	1.5[h]	0.3
			4	9800[e]	3.2[g]	1.1
18	567(0.480, 0.469)	4.5	5	5800[c]	1.4[g]	0.6
19	545(0.419, 0.526)	4.3	4	5500[d]	1.9[g]	0.1
			6	2090[d]	0.5[i]	0.2

a   Doping level 4%, at 10 V.
b   Weak electrofluorescence at ~ 440 nm from CBP was also observed.
c   At 10 V.
d   At 11 V.
e   At 12 V.
f   At 13 V.
g   At 20 mA cm^{-2}.
h   At 30 mA cm^{-2}.
i   At 50 mA cm^{-2}. (Reproduced with permission from [19b]. Copyright 2004 American Chemical Society)

doping level. The luminance of 7800 cd m^{-2} at 11 V and efficiency of 2.4 cd A^{-1} (η_{ext} 0.9%) at 30 mA cm^{-2} were obtained for an orange OLED (λ_{max} 564 nm; CIE coordinates $x = 0.480$, $y = 0.484$) using **4** at 4% doping level (Fig. 7.6). At 2% ratio of **4**, improved luminance (9900 cd m^{-2} at 12 V) and efficiency (4.2 cd A^{-1} (η_{ext} 1.6%) at 30 mA cm^{-2}) were observed, but weak emission from CBP at λ_{max} ca. 440 nm was also detected. For the red OLED (λ_{max} 612 (max), 656 nm; CIE coordinates $x = 0.594$, $y = 0.341$), the maximum luminance of 3100 cd m^{-2} at 12 V and efficiency of 1.0 cd A^{-1} (η_{ext} 0.8%) at 30 mA cm^{-2} were observed using 4% of **15** in CBP. Generally, higher doping ratios lead to lower efficiencies and inferior performance, apparently due to aggregate-induced quenching.

7.4.2
Pt(II) Complexes bearing 6-(2-Hydroxyphenyl)-2,2′-bipyridine Ligands

A series of robust Pt(II) emitters [(O^N^N)PtX] (HO^N^N = 6-(2-hydroxyphenyl)-2,2′-bipyridine; X = Cl, Br, I, or (C≡C(Ph)) were reported as a new class of light-emitting materials for electrophosphorescent devices (Scheme 7.3) [22]. The [(O^N^N)PtX] complexes are readily prepared, easily modified through the non-
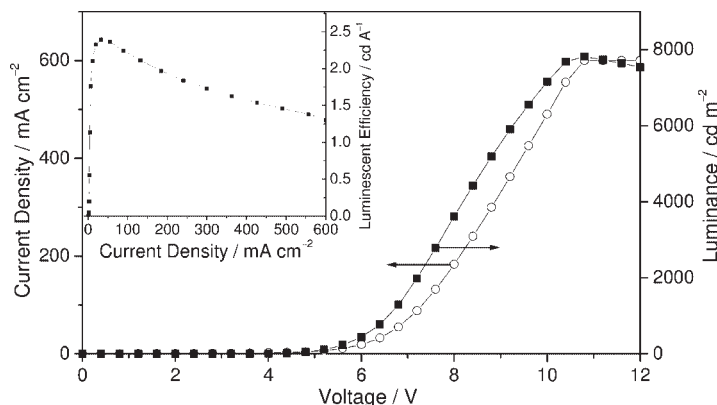
Fig. 7.6 Current density, voltage, and luminance characteristics (inset: luminescent efficiency vs. current density) for OLED using **4** as emitter at 4% doping level (Reproduced with permission from [19a]. Copyright 2002 Royal Society of Chemistry).

Z = H, Y = H	**20a**
Z = H, Y = Me	**20b**
Z = H, Y = ^{t}Bu	**20c**
Z = F, Y = H	**20d**
Z = F, Y = ^{t}Bu	**20e**
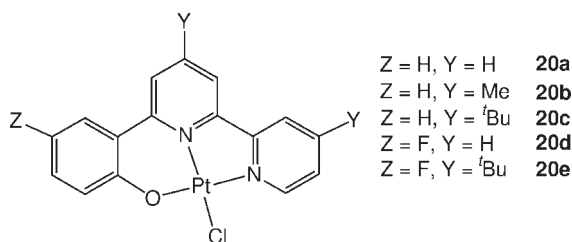
Scheme 7.3

chelated auxiliary ligand X, and exhibit high thermal stability. Thermogravimetric analysis revealed that the decomposition temperatures of **20a–20e** (388–426 °C) are comparable to those of the [(C^N^N)Pt(C≡C)$_n$R] complexes (n = 1–4; R = aryl, SiMe$_3$; T_d ≈ 400 °C) [19] and **20e** is the most stable with a decomposition temperature of 426 °C.

The intense absorption at λ_{max} ≈ 300 nm ($\varepsilon > 10^4 \, dm^3 \, mo \, l^{-1} \, cm^{-1}$) is attributed to a ligand-centered ^{1}(l → π*) (l = lone pair/phenoxide) transition, whereas the moderately intense band at 360–400 nm ($\varepsilon ≈ (0.4–0.7) \times 10^4 \, dm^3 \, mol^{-1} \, cm^{-1}$) is attributed to ^{1}[l → π*(diimine)] mixed with [Pt(d$_\pi$) → π*(diimine)] charge-transfer transitions [23]. The complexes **20a–20e** in DMF solutions show orange–red photoluminescence with peak maxima at λ_{max} = 593–618 nm, which are tentatively attributed to a triplet excited state with mixed ^{3}MLCT and ^{3}[l → π*(diimine)] parentage [24].

Devices with **20a–20e** as electrophosphorescent emitters were fabricated with the following configuration: ITO/NPB (40 nm)/CBP:**Pt** (x%, 30 nm)/BCP (20 nm)/Alq$_3$ (30 nm)/LiF (0.5 nm)/Al (100 nm). The EL energy for **20a–20e** were independent of the doping concentration, and the band shape was similar to the PL,
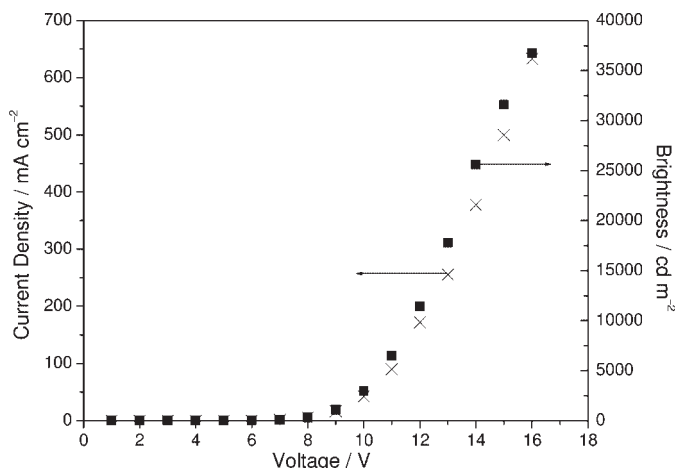
Fig. 7.7 Current density–voltage–brightness relationships for device using **20e** as dopant (Reproduced with permission from [22]. Copyright 2005 American Chemical Society).

although the EL emission was blue-shifted. The device performance followed a similar trend to those of the emission quantum yields and thermal stability of **20a–20e**. Complex **20e** afforded yellow electroluminescence with the best device performance in the series; the brightness of $1\,cd\,m^{-2}$ at low turn-on voltage (4 V), and the maximum current efficiency of $7.8\,cd\,A^{-1}$ were obtained at $89\,mA\,cm^{-2}$. The device was stable in terms of efficiency decay, and the efficiency was attained at $5.8\,cd\,A^{-1}$ when the current density increased to $633\,mA\,cm^{-2}$. The maximum luminance of $37\,000\,cd\,m^{-2}$ was achieved at 16 V (Fig. 7.7), which was higher than the yellow OLEDs using $[(C^{\wedge}N^{\wedge}N)Pt(C{\equiv}CC_6F_5)]$ (**17**) dopant (maximum luminance = $9800\,cd\,m^{-2}$, λ_{max} = 548 nm) [19b].

The $[(O^{\wedge}N^{\wedge}N)PtX]$ complexes have been found to be robust phosphorescent materials for OLEDs. The ease in preparation and structural modification warrant further investigations to optimize $[(O^{\wedge}N^{\wedge}N)PtX]$ complexes as high-performance OLED materials. For example, a class of platinum(II) complexes containing the tridentate $N^{\wedge}C^{\wedge}N$ 3,5-di(2-pyridyl)toluene ligand and a chloride/phenoxide group has also been developed as phosphors in OLEDs [25], and the resultant maximum external quantum efficiency for the phenoxide derivative was found to be 16.5%.

7.5
Tetradentate Pt(II) Complexes

7.5.1
Pt(II) Schiff Base Complexes

Platinum(II) Schiff base complexes constitute an attractive class of phosphorescent materials that are easily synthesized, thermally stable, and structurally diverse.
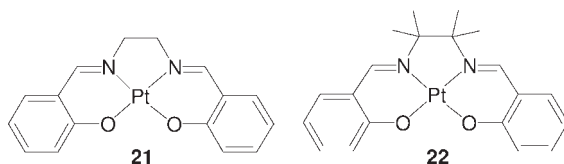
Scheme 7.4

We reported the readily prepared and sublimable Pt(II) Schiff base triplet emitters (**21** and **22**, Scheme 7.4) as OLED dopants [26]. Thermogravimetric analysis showed that **21** and **22** are stable under a nitrogen atmosphere up to 360 °C, with decomposition temperature of 406 and 382 °C respectively. In addition, **22** was observed to sublime before its decomposition temperature was reached, hence slow weight loss was detected from around 200 °C (to 95 wt%) before decomposition occurred. The reported structure for **21** revealed close intermolecular Pt–Pt distance of 3.277(1) Å [27], but in the crystal structure of **22**, no short (<3.5 Å) intermolecular Pt–Pt or π–π interaction was observed. Such contact(s) if present in the crystal structures of platinum Schiff base complexes may have direct impact upon the emissive properties of this class of complexes. The low-energy absorptions at λ > 400 nm of **21** and **22** in fluid solutions were attributed to charge transfer transition(s) involving the phenoxide lone pair (l) and the π* orbital of imine, i.e., ^{1}[l(phenoxide) → π*(imine)], mixed with ^{1}[Pt(5d) → π*(Schiff base)] MLCT character.

The sublimability, relatively short emission lifetimes (~3.5 µs in CH_3CN at 298 K, cf. > 50 µs for PtOEP [10a]) and high photoluminescent quantum efficiencies of **21** and **22** render them suitable candidates as efficient electrophosphorescent dopants. OLEDs with emitting layers comprising the host material, CBP plus **22** as dopant at different concentrations were fabricated: [ITO/NPB (40 nm)/ CBP:**22** (30 nm)/BCP (20 nm)/Alq$_3$ (30 nm)/LiF (0.5 nm)/Al (150 nm)]. These devices required low turn-on voltage of around 3 V. At the optimized dopant concentration of 4.0 wt%, EL from the dopant **22** at λ$_{max}$ 550 (sh, 590) nm was observed and the maximum external quantum efficiency (η_{ext}), luminous efficiency (η_L), power efficiency (η_P), and luminance were (current density, mA cm^{-2} in parentheses): 11% (8.5), 31 cd A^{-1} (8.5), 14 lm W^{-1} (8.5), and 23 000 cd m^{-2} (683), respectively (Fig. 7.8).

The performance of the **22**-doped OLED (4.0 wt%) at different current density is listed in Table 7.2. We note that (i) even at the high luminance of 10 000 cd m^{-2}, η_{ext}, η_L, and η_P are 4.1%, 13 cd A^{-1}, and 4.0 lm W^{-1}, respectively, and (ii) reasonable η_L was observed at very high current densities (e.g., 4.1 cd A^{-1} at 500 mA cm^{-2}). The EL spectrum for this OLED exhibited no significant change from 3 to 16 V, and the CIE coordinates at 8 V were (0.48, 0.52), which correspond to orange light.

To realize the generation of white EL, devices comprising the host material, beryllium bis(2,2′-hydroxyphenyl)pyridine (Bepp$_2$) plus **21** as dopant at different concentrations were fabricated: [ITO/NPB (50 nm)/Bepp$_2$:**21** (50 nm)/LiF (1.5 nm)/ Al (150 nm)] with four different devices A–D corresponding to 3.2, 7.7, 11.1, and 16.7 wt% of **21**, respectively (Fig. 7.9). All devices began to glow at 4–5 V and
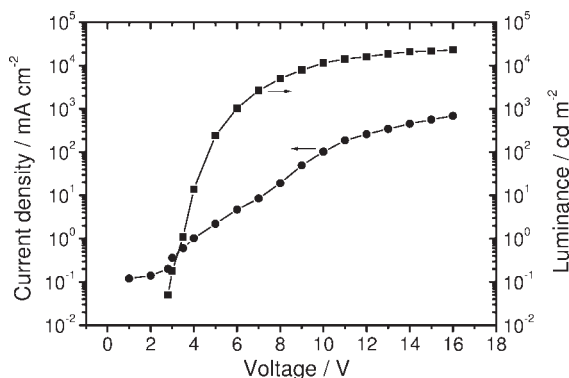
Fig. 7.8 Current density and luminance curves of **22**-doped OLED (4.0 wt%) against applied voltage (Reproduced with permission from [26]. Copyright 2004 Royal Society of Chemistry).

Table 7.2 Performance of **22**-doped OLED (4.0 wt%) at different I [a]. Reproduced with permission from [26]. Copyright 2004 Royal Society of Chemistry.

Current density(mA cm^{-2})	V (V)	L(cd m^{-2})	η_{ext}(%)	η_L(cd A^{-1})	η_P(lm W^{-1})
1	4.0	14	0.47	1.4	1.1
10	7.1	3 010	11	30	13
20	8.1	5 050	9.1	25	10
100	10.0	11 500	3.9	11	3.5
500	14.5	21 200	1.5	4.1	0.9

a Configuration: [ITO/NPB/CBP: **22**/BCP/Alq$_3$/LiF/Al].

exhibited two emission bands at λ_{max} 448 and 552 nm in the EL spectra. Device A (3.2 wt% of **21**) gave a luminous efficiency of 0.79 lm W^{-1} and luminance of 450 cd m^{-2} at 20 mA cm^{-1}. The highest achieved luminance was 3045 cd m^{-2} at 307 mA cm^{-2}. Importantly, the CIE coordinates of device A were (0.33, 0.35), which closely approach those of white light (defined as 0.33, 0.33); the white emission was produced by the EL of Bepp$_2$ (host) and **21** (dopant) in the device. Upon increasing the concentration of **21**, both the luminance and luminous efficiency were enhanced and the emission of **21** became more dominant in the EL spectra (especially in device C). However, the overall device efficiency diminished at 16.7 wt% (device D); this is consistent with aggregation of dopant molecules at sufficiently high concentrations, which could lead to intermolecular quenching.

While most examples of white OLEDs require multilayer configurations [3c, 28], we have reported that pure white EL can be achieved using a relatively simple
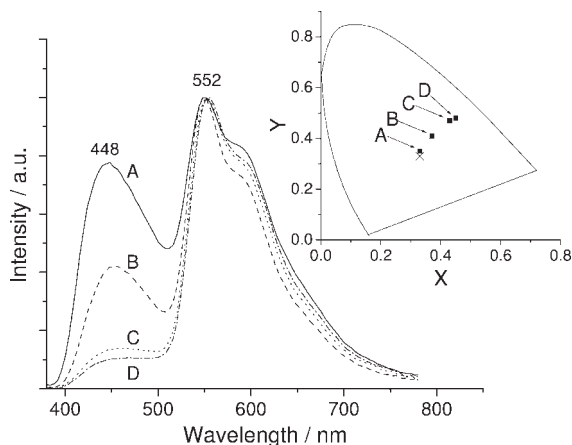
Fig. 7.9 EL spectra of devices A–D (3.2, 7.7, 11.1, and 16.7 wt% of **21** respectively) and corresponding CIE coordinates (inset, cross indicates pure white emission) (Reproduced with permission from [26]. Copyright 2004 Royal Society of Chemistry).
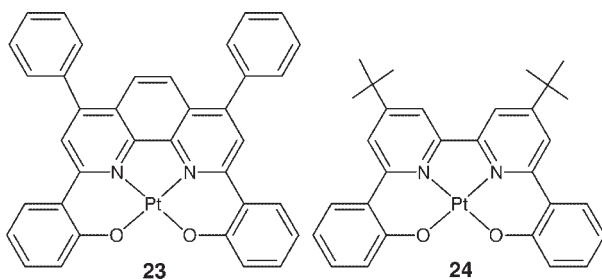
Scheme 7.5

device configuration based on high-brightness and -performance Pt(II) Schiff base dopants.

7.5.2
Pt(II) Bis(phenoxy)diimine Complexes

Phosphorescent platinum(II) complexes ligated by the tetradentate bis(phenoxy)diimine chelate N_2O_2 (diimine = 4,7-diphenyl-1,10-phenanthroline, Ph_2phen (**23**) and 4,4′-di-*tert*-butyl-2,2′-bipyridine, tBu_2bpy (**24**)) (Scheme 7.5) have been employed as new dopants in multilayer OLEDs [23a]. The N_2O_2 ligand framework is devised with chemically inert functionalities and the considerable chelate effect should confer good stability, and indeed, these neutral [Pt(N_2O_2)] complexes display high thermal stability (>400 °C in N_2).

The crystal structure of **23** consists of (head-to-tail)-interacting dimers with the $[Pt(N_2O_2)]$ planes separated by 3.462 Å and the closest Pt–Pt distance of 3.517 Å, whereas molecules of **24** are arranged into infinitely stacked planar sheets with possible π–π interactions (the interplanar distance = 3.486 Å) but no close Pt–Pt contacts (Pt–Pt 5.521 Å). Complexes **23** and **24** are highly luminescent in CH_2Cl_2 solutions at 298 K with a structureless emission at λ_{max} = 586 and 595 nm respectively, which were assigned as mixed $^3[l \rightarrow \pi^*(diimine)]$ (l = lone pair/phenoxide) and $^3[Pt(d) \rightarrow \pi^*(diimine)]$ charge-transfer states. The nature of phenyl and *tert*-butyl substituents appended to the $Pt(N_2O_2)$ moiety affect the solid-state photo- and electroluminescent properties (see below). EL devices were fabricated by incorporating **23** and **24**, which gave emitting layers with different EL properties, and the differences in brightness, color, and overall performance of devices were attributed to the effect of the diimine substituents.

The EL device structures were prepared as the following: ITO/NPB (30 nm)/**23** (or **24**) -doped (*x* wt%) $Bepp_2$ (30 nm)/LiF (0.5 nm)/Al (250 nm). The device structure was a multilayer stack deposited on ITO glass. All devices exhibited low turn-on voltages of 5–7 V and generated yellow to yellow–green EL at various voltages. In device E, at 2% ratio of **23**, only EL from $Bepp_2$ at around 450 nm was observed when driven under forward bias, suggesting ineffective host-dopant Förster energy transfer. At 10% dopant concentration level of **23** (device F), yellow EL from **23** (λ_{max} 588 nm) only was visible at low voltages but contribution from the $Bepp_2$ host became noticeable around 10 V. This is consistent with the long electrophosphorescent lifetime exhibited by **23**, which leads to saturated triplet exciton population at high voltages so that energy transfer from $Bepp_2$ excitons becomes blocked. Maximum luminance and power efficiency of 850 cd m^{-2} (at 360 mA cm^{-2}) and 0.26 lm W^{-1} (at 14 mA cm^{-2}), respectively, were achieved. While the abundance of π electrons in **23** may be beneficial for charge mobility, the favorable formation of dimeric assemblies in the crystal structure and the presence of pendant phenyl substituents can facilitate intermolecular quenching (including self-quenching) processes. This may explain the inferior brightness and efficiency of devices derived from dopant **23**.

The employment of ancillary ligands containing bulky substituents was demonstrated to be advantageous for electrophosphorescent OLEDs with regard to suppression of self-quenching activities [12] and maintenance of amorphous films [29]. Modification of the diimine moiety from Ph_2phen in **23** to $^tBu_2bpy$ in **24** resulted in substantially improved OLED performance. At 0.3% dopant level of **24**, (device G, Fig. 7.10), long-range Förster energy transfer from host excitons appeared considerably more efficient compared to **23** and two EL emission peak maxima at λ_{max} = 453 and 540 nm due to $Bepp_2$ and **24**, respectively were observed, and culminated in strong yellow–green EL (CIE 0.33, 0.47). Excellent maximum luminance (Fig. 7.11) of 9330 cd cm^{-2} (at 330 mA cm^{-2}) and power efficiency of 1.44 lm W^{-1} (at 40 mA cm^{-2}) were achieved, and this can be ascribed to the molecular structure of **24**, which may mediate effective charge transport to yield relatively balanced charge recombination within the **24**-doped $Bepp_2$ layer without promoting quenching mechanisms.
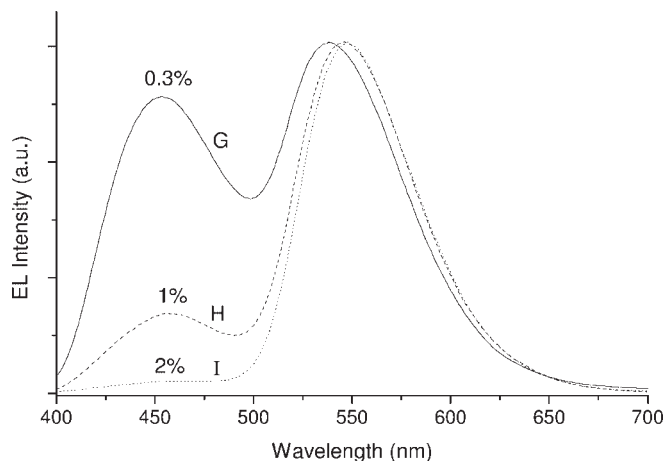
Fig. 7.10 EL spectra for devices G–I (0.3, 1, and 2 wt% of **24** respectively) (Reproduced with permission from [23a]. Copyright 2003 Wiley-VCH).
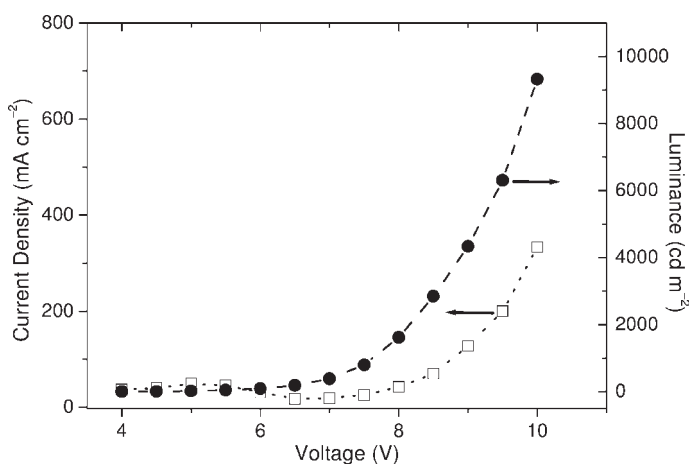
Fig. 7.11 *I–V–L* characteristics for device G: [ITO/NPB/**24**-doped (0.3%) Bepp$_2$/LiF/Al] (Reproduced with permission from [23a]. Copyright 2003 Wiley-VCH).

Upon increasing the concentration of **24** to 1% in device H (Fig. 7.10), the 550 nm emission from **24** became noticeably more intense than the Bepp$_2$ emission at 450 nm. However, this EL color adjustment (CIE 0.39, 0.54) was accompanied by detrimental device performance. For example, the maximum luminance dropped to 6200 cd m^{-2} at 390 mA cm^{-2} while the optimum efficiency fell to 0.80 lm W^{-1} at 84 mA cm^{-2}. In device I, a 2% dopant content of **24** generated yellow EL (CIE 0.42, 0.56) with minimal contribution from Bepp$_2$ emission, but the observed optimal luminance (4480 cd m^{-2} at 280 mA cm^{-2}) and power efficiency

($0.51 \, \text{lm W}^{-2}$ at $280 \, \text{mA cm}^{-2}$) were comparatively poor. This may be accredited to enhanced aggregation of dopant molecules leading to intermolecular quenching (due to continuously stacked layers in crystal lattice of **24**) or formation of crystalline domains. In summary, the overall brightness and performance of devices using dopant **24** bearing *tert*-butyl substituents at the diimine moiety is superior to those using the phenyl analog **23**.

7.5.3
Pt(II) Bis(pyrrole)diimine Complexes

Neutral phosphorescent tetradentate bis(pyrrole)diimine Pt(II) complexes (Scheme 7.6) were reported as a new class of molecular phosphorescent materials with potential applications in organic optoelectronics [30].

Complex **25** shows a yellow emission with a peak maximum at 566 nm and a shoulder at 613 nm in CH_3CN at 298 K. The concentration-dependent emissive behavior of **25** in frozen CH_3CN at 77 K has been investigated. At a concentration of $1.0 \times 10^{-6} \, \text{mol dm}^{-3}$, a vibronic yellow emission with peak maxima at 560 and 611 nm was observed. Upon increasing the complex concentration ($>10^{-3} \, \text{mol dm}^{-3}$), the higher energy yellow emission (λ_{max} 560 nm) was switched to a lower energy red emission at 610 nm. A similar red shift in emission energy at λ_{max} 610 nm was also evident for **25**-doped CBP thin film with a high dopant concentration. This was attributed to oligomer formation at high concentrations of the Pt(II) complexes [3c, 6, 21c, 31]. For **26**, no oligomer emission was observed, possibly because the tetramethylethylene moiety disfavors close intermolecular contacts. The photoluminescence of **27** occurred at a low energy with λ_{max} 680 nm, presumably due to the extended π-conjugated ligand system. Complexes **25** and **26** exhibited shorter PL lifetimes (4.2 and 3.6 μs in CH_3CN at 298 K, respectively), reasonable quantum efficiencies (9.7 and 10.5% upon excitation at 459 and 431 nm in $1 \times 10^{-6} \, \text{mol dm}^{-3}$ CH_3CN, respectively) and good thermal stability (decomposition temperature = 288 and 320 °C, respectively). Complex **27** is less suitable for OLED applications since its emission energy is close to the IR region with low quantum efficiency.

The electroluminescence spectra of **25** and **26** in the CBP host are depicted in Fig. 7.12. At a low dopant concentration (0.8 wt%), the **25**-doped OLED gave orange–red emission with a peak maximum at 580 nm and a shoulder at 620 nm. At a high dopant concentration of 6.0%, red electroluminescence from the oligomer of **25** (λ_{max} 620 nm) was detected. The CIE coordinates of (0.62, 0.38) in the **25**-doped OLED was comparable to pure red light at (0.65, 0.35). The maximum
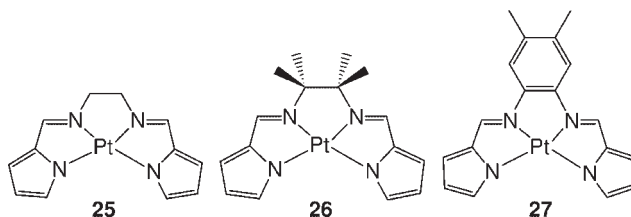
Scheme 7.6
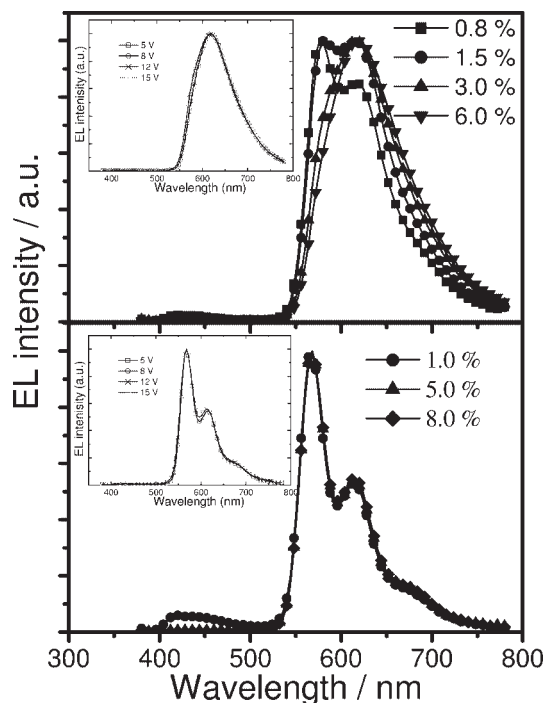
Fig. 7.12 EL spectra of **25**- (Top) and **26**-doped (Bottom) OLEDs with different dopant concentrations at applied voltage of 8 V. Inset: EL spectra of 6.0% **25**-(Top) and 5.0% **26**-doped (Bottom) OLEDs at different applied voltages. Configuration: [ITO/NPB (40 nm)/CBP:**25** or **26** (*x* wt%, 30 nm)/BCP (10 nm)/Alq₃ (30 nm)/LiF (0.5 nm)/Al (150 nm)]. (Reproduced with permission from [30]. Copyright 2005 Royal Society of Chemistry).

external quantum efficiency (η_{ext}), luminous efficiency (η_L), power efficiency (η_P), and brightness for the 6.0% **25**-doped OLED were 6.5%, 9.0 cd A^{-1}, 4.0 lm W^{-1}, and 11 100 cd m^{-2}, respectively. The EL spectra of the 6.0% **25**-doped OLED exhibited negligible change for input voltages from 4 V to 16 V.

The **26**-doped OLEDs gave an orange emission with CIE coordinates of (0.51, 0.47) and did not exhibit red-shifted electroluminescence at high dopant concentrations (Fig. 7.12). Nevertheless, 5.0% **26**-doped OLEDs displayed good performance with maximum η_{ext}, η_L, η_P, and brightness of 4.9%, 13.1 cd A^{-1}, 5.9 lm W^{-1}, and 10 120 cd m^{-2}, respectively. The EL efficiencies of **25**- and **26**-doped OLEDs decreased with increasing input current densities due to triplet–triplet annihilation, but the diminution in EL efficiency for the **25**-doped OLED was less dramatic.

7.5.4
Pt(II) Porphyrin Complexes

Applications of platinum(II) porphyrins as electrophosphorescent materials have been extensively studied [10, 32–34]. The emission of platinum(II) porphyrins is

ligand-based [35], hence, it becomes feasible to improve and customize the properties of this class of materials through modification of the porphyrinato ligand. Fluorinated porphyrins can exhibit improved stability with regard to oxidative deterioration [36]. We described that [*meso*-tetrakis(pentafluorophenyl)porphyrinato] platinum(II) (PtF$_{20}$TPP) exhibits strong red phosphorescence and high stability [37], and its application as an efficient phosphorescent dopant in saturated red OLEDs has been achieved.
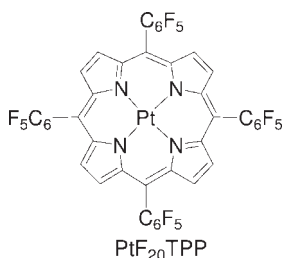
PtF$_{20}$TPP

A narrow Q(0,0) emission peak (full width at half-maximum intensity ~35 nm) at 647 nm with a weak Q(1,0) band at 710 nm is observed for PtF$_{20}$TPP in CH$_2$Cl$_2$ at room temperature. Various EL devices at different doping concentrations of the PtF$_{20}$TPP emitter were fabricated. The device structure was a multilayer stack deposited on ITO glass. In these devices, Bepp$_2$ acted as the host material, while NPB and copper phthalocyanine (CuPc) were used as the hole-transporting and buffer layers, respectively. Hence, the following EL device structures were prepared: [ITO/CuPc (15 nm)/NPB (60 nm)/Bepp$_2$:x% PtF$_{20}$TPP (50 nm)/LiF (1 nm)/ Al (200 nm)] (Devices J–M correspond to 4, 6, 8 and 12% of PtF$_{20}$TPP in Bepp$_2$, respectively). The red emission at 655 nm dominated the EL spectra and was similar to the PL spectrum of PtF$_{20}$TPP.

At low voltages (<5 V), blue fluorescence from the host was not observed for device J (4% of PtF$_{20}$TPP), implying complete energy transfer from the host exciton to PtF$_{20}$TPP. When a high driving voltage was applied, a weak blue emission at 450 nm from Bepp$_2$ became apparent and its intensity increased with the driving voltage. Clearly, saturation of the emissive PtF$_{20}$TPP sites in the Bepp$_2$–PtF$_{20}$TPP system had occurred. The weak emission located at 550 nm can be attributed to exciplex emission of Bepp$_2$ or the fluorescence of PtF$_{20}$TPP, which arises from triplet–triplet annihilation (T$_1$ + T$_1$ → S$_1$ + S$_0$) with extremely fast intersystem crossing at high current [32a]. For devices L and M (8% and 12% of PtF$_{20}$TPP, respectively), extremely weak emission from Bepp$_2$ was observed even at driving voltages greater than 8 V, and thus the EL spectra were dominated by red emission from the fluorinated dopant (Fig. 7.13).

The turn-on voltage for the PtF$_{20}$TPP-doped devices was ca. 3 V. The EL efficiency increased with the dopant concentration up to 8%, but decreased again above 8%. High concentrations of metalloporphyrin complexes often undergo intermolecular self-quenching processes. Devices J–M exhibited maximum EL
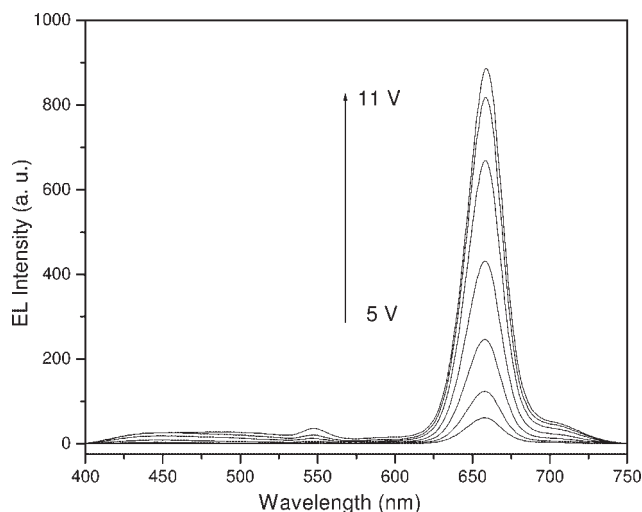
Fig. 7.13 EL spectra of device L (8% PtF$_{20}$TPP) in Bepp$_2$ at various voltages. (Reproduced with permission from [37]. Copyright 2003 Royal Society of Chemistry).

efficiencies of 0.17, 0.25, 0.90, and 0.13 lm W^{-1}, respectively. Device L (8% of PtF$_{20}$TPP) showed luminance of 8.1 cd m^{-2}, an EL efficiency of 0.015 lm W^{-1} and an operating voltage of 8.5 V at a current of 20 mA cm^{-2}, while a maximum luminance of 80 cd m^{-2} was achieved at 18 V. At 8% PtF$_{20}$TPP concentration, complete energy transfer from Bepp$_2$ to PtF$_{20}$TPP and high EL efficiency was realized. The EL efficiency of device L was 0.30 lm W^{-1} at a current density of 1.0 mA cm^{-2}, but the efficiency dropped to 0.015 lm W^{-1} at 20 mA cm^{-2}. Devices J, K, and M also showed similar EL efficiency dependence on current density, which can be rationalized as above in terms of triplet–triplet annihilation and saturation of emissive sites due to high triplet exciton population [32a, 38].

7.6
Concluding Remarks

Materials with high triplet-state photoluminescence efficiency can be used in the emitting layer of organic electroluminescent devices and offer a means to improve electroluminescence efficiency. Examples of platinum(II) chelates employed for OLED applications contain: (i) dianionic tetradentate ligands, such as N$_2$O$_2$$^{2-}$ (H$_2$N$_2$O$_2$ = bis(2′-phenol)bipyridines or -phenanthrolines) [23a], Schiff bases [26, 39], and porphyrins [10, 32–34, 37]; (ii) mono-anionic cyclometalated auxiliaries [40], for instance [(C^N)Pt(O^O)] (C^N = 2-phenylpyridyl, 2-(2′-thienyl)pyridyl or 2-(4,6-difluorophenyl)pyridyl; O^O = β-diketonato) [3b, 3c, 6, 9b, 41], and [(C^N^N)Pt(C≡C)$_n$R] (HC^N^N = 6-aryl-2,2′-bipyridine) [19]; and (iii) bidentate N–N donor ligands, such as in [Pt(iqdz)$_2$] and [Pt(pydz)$_2$] (iqdz = isoquinolinyl

indazole, pydz = pyridyl indazole) [9c, 42]. Molecular design of chromophoric ligands facilitates the manipulation of the relative energy between the metal d and ligand π* orbitals, which confers diverse color tunability upon these platinum(II) dopants. Modifications of ligands and their chelating effect can further improve the rigidity and stability of the emitters, which enhances their capabilities to withstand conditions in device fabrication and operation. Phosphorescent Pt(II) materials have been strategically and rationally designed to fulfil the criteria for high-efficiency and brightness OLED emitters. This promises further significant advances for phosphorescent Pt(II) dopants in OLED applications.

Acknowledgments

References

1 (a) M. A. Baldo, M. E. Thompson, S. R. Forrest, *Pure Appl Chem* **1999**, *71*, 2095; (b) H. Yersin, *Top Curr Chem* **2004**, *241*, 1.

2 (a) M. A. Baldo, S. Lamansky, P. E. Burrows, M. E. Thompson, S. R. Forrest, *Appl Phys Lett* **1999**, *75*, 4; (b) M. A. Baldo, M. E. Thompson, S. R. Forrest, *Nature* **2000**, *403*, 750; (c) C. Adachi, M. A. Baldo, S. R. Forrest, M. E. Thompson, *Appl Phys Lett* **2000**, *77*, 904; (d) Y. Wang, N. Herron, V. V. Grushin, D. LeCloux, V. Petrov, *Appl Phys Lett* **2001**, *79*, 449; (e) C. Adachi, R. C. Kwong, P. Djurovich, V. Adamovich, M. A. Baldo, M. E. Thompson, S. R. Forrest, *Appl Phys Lett* **2001**, *79*, 2082; (f) S. Lamansky, P. Djurovich, D. Murphy, F. Abdel-Razzaq, H. E. Lee, C. Adachi, P. E. Burrows, S. R. Forrest, M. E. Thompson, *J Am Chem Soc* **2001**, *123*, 4304; (g) C. Adachi, M. A. Baldo, M. E. Thompson, S. R. Forrest, *J Appl Phys* **2001**, *90*, 5048; (h) J. P. J. Markham, S. C. Lo, S. W. Magennis, P. L. Burn, I. D. W. Samuel, *Appl Phys Lett* **2002**, *80*, 2645; (i) Y. J. Su, H. L. Huang, C. L. Li, C. H. Chien, Y. T. Tao, P. T. Chou, S. Datta, R. S. Liu, *Adv Mater* **2003**, *15*, 884; (j) J. P. Duan, P. P. Sun, C. H. Cheng, *Adv Mater* **2003**, *15*, 224; (k) A. B. Tamayo, B. D. Alleyne, P. I. Djurovich, S. Lamansky, I. Tsyba, N. N. Ho, R. Bau, M. E. Thompson, *J Am Chem Soc* **2003**, *125*, 7377; (l) M. K. Nazeeruddin, R. Humphry-Baker, D. Berner, S. Rivier, L. Zuppiroli, M. Graetzel, *J Am Chem Soc* **2003**, *125*, 8790.

3 (a) M. E. Thompson, P. E. Burrows, S. R. Forrest, *Curr Opin Solid State Mater Sci* **1999**, *4*, 369; (b) C. Adachi, M. A. Baldo, S. R. Forrest, S. Lamansky, M. E. Thompson, R. C. Kwong, *Appl Phys Lett* **2001**, *78*, 1622; (c) B. W. D'Andrade, J. Brooks, V. Adamovich, M. E. Thompson, S. R. Forrest, *Adv Mater* **2002**, *14*, 1032.

4 Y. Ma, H. Zhang, J. Shen, C. Che, *Synth Met* **1998**, *94*, 245.

5 (a) V. M. Miskowski, V. H. Houlding, *Inorg Chem* **1989**, *28*, 1529; (b) C. M. Che, L. Y. He, C. K. Poon, T. C. W. Mak, *Inorg Chem* **1989**, *28*, 3081; (c) J. Biedermann, G. Gliemann, U. Klement, K. J. Range, M. Zabel, *Inorg Chem* **1990**, *29*, 1884; (d) H. Kunkely, A. Vogler, *J Am Chem Soc*

1990, *112*, 5625; (e) V. M. Miskowski, V. H. Houlding, *Inorg Chem* **1991**, *30*, 4446; (f) V. H. Houlding, V. M. Miskowski, *Coord Chem Rev* **1991**, *111*, 145; (g) K. T. Wan, C. M. Che, K. C. Cho, *J Chem Soc, Dalton Trans* **1991**, 1077; (h) H. Wiedenhofer, S. Schützenmeier, A. von Zelewsky, H. Yersin, *J Phys Chem* **1995**, *99*, 13385; (i) W. B. Connick, L. M. Henling, R. E. Marsh, H. B. Gray, *Inorg Chem* **1996**, *35*, 6261; (j) W. Humbs, H. Yersin, *Inorg Chim Acta* **1997** *265*, 139; (k) K. P. Balashev, M. V. Puzyk, V. S. Kotlyar, M. V. Kulikova, *Coord Chem Rev* **1997**, *159*, 109; (l) W. Paw, S. D. Cummings, M. A. Mansour, W. B. Connick, D. K. Geiger, R. Eisenberg, *Coord Chem Rev* **1998**, *171*, 125; (m) M. Hissler, J. E. McGarrah, W. B. Connick, D. K. Geiger, S. D. Cummings, R. Eisenberg, *Coord Chem Rev* **2000**, *208*, 115; (n) H. Yersin, D. Donges, W. Humbs, J. Strasser, R. Sitters, M. Glasbeek, *Inorg Chem* **2002**, *41*, 4915.

6 V. Adamovich, J. Brooks, A. Tamayo, A. M. Alexander, P. I. Djurovich, B. W. D'Andrade, C. Adachi, S. R. Forrest, M. E. Thompson, *New J Chem* **2002**, *26*, 1171.

7 M. Cocchi, V. Fattori, D. Virgili, C. Sabatini, P. Di Marco, M. Maestri, J. Kalinowski, *Appl Phys Lett* **2004**, *84*, 1052.

8 M. Cocchi, D. Virgili, C. Sabatini, V. Fattori, P. Di Marco, M. Maestri, J. Kalinowski, *Synth Met* **2004**, *147*, 253.

9 (a) Q. Liu, L. Thorne, I. Kozin, D. Song, C. Seward, M. D'Iorio, Y. Tao, S. Wang, *J Chem Soc*, Dalton Trans **2002**, 3234; (b) W. Y. Wong, Z. He, S. K. So, K. L. Tong, Z. Lin, *Organometallics* **2005**, *24*, 4079; (c) J. Kavitha, S. Y. Chang, Y. Chi, J. K. Yu, Y. H. Hu, P. T. Chou, S. M. Peng, G. H. Lee, Y. T. Tao, C. H. Chien, A. J. Carty, *Adv Funct Mater* **2005**, *15*, 223.

10 (a) M. A. Baldo, D. F. O'Brien, Y. You, A. Shoustikov, S. Sibley, M. E. Thompson, S. R. Forrest, *Nature* **1998**, *395*, 151; (b) D. F. O'Brien, M. A. Baldo, M. E. Thompson, S. R. Forrest, *Appl Phys Lett* **1999**, *74*, 442.

11 M. A. Baldo, C. Adachi, S. R. Forrest, *Phys Rev* B **2000**, *62*, 10967.

12 H. Z. Xie, M. W. Liu, O. Y. Wang, X. H. Zhang, C. S. Lee, L. S. Hung, S. T. Lee, P. F. Teng, H. L. Kwong, H. Zheng, C. M. Che, *Adv Mater* **2001**, *13*, 1245.

13 C. W. Chan, L. K. Cheng, C. M. Che, *Coord Chem Rev* **1994**, *132*, 87.

14 (a) V. M. Miskowski, V. H. Houlding, C. M. Che, Y. Wang, *Inorg Chem* **1993**, *32*, 2518; (b) J. E. Song, B. O. Kim, Y. Ha, *Mater Sci Eng* C **2004**, *24*, 191.

15 (a) W. B. Connick, D. Geiger, R. Eisenberg, *Inorg Chem* **1999**, *38*, 3264; (b) M. Hissler, W. B. Connick, D. K. Geiger, J. E. McGarrah, D. Lipa, R. J. Lachicotte, R. Eisenberg, *Inorg Chem* **2000**, *39*, 447; (c) F. Hua, S. Kinayyigit, J. R. Cable, F. N. Castellano, *Inorg Chem* **2005**, *44*, 471.

16 S. C. Chan, M. C. W. Chan, Y. Wang, C. M. Che, K. K. Cheung, N. Zhu, *Chem Eur J* **2001**, *7*, 4180.

17 (a) C. L. Lee, K. B. Lee, J. J. Kim, *Appl Phys Lett* **2000**, *77*, 2280; (b) F. C. Chen, S. C. Chang, G. He, S. Pyo, Y. Yang, M. Kurotaki, J. Kido, *J Polym Sci, Part B: Polym Phys* **2003**, *41*, 2681.

18 (a) L. Zhang, Y. H. Niu, A. K. Y. Jen, W. Lin, *Chem Commun* **2005**, 1002; (b) F. Hua, S. Kinayyigit, J. R. Cable, F. N. Castellano, *Inorg Chem* **2005**, *44*, 471.

19 (a) W. Lu, B. X. Mi, M. C. W. Chan, Z. Hui, N. Zhu, S. T. Lee, C. M. Che, *Chem Commun* **2002**, 206; (b) W. Lu, B. X. Mi, M. C. W. Chan, Z. Hui, C. M. Che, N. Zhu, S. T. Lee, *J Am Chem Soc* **2004**, *126*, 4958.

20 Y. G. Ma, W. H. Chan, X. M. Zhou, C. M. Che, *New J Chem* **1999**, *23*, 263.

21 (a) C. W. Chan, T. F. Lai, C. M. Che, S. M. Peng, *J Am Chem Soc* **1993**, *115*, 11245; (b) T. C. Cheung, K. K. Cheung, S. M. Peng, C. M. Che, *J Chem Soc*, Dalton Trans **1996**, 1645; (c) S. W. Lai, M. C. W. Chan, T. C. Cheung, S. M. Peng, C. M. Che, *Inorg Chem* **1999**, *38*, 4046; (d) S. W. Lai, M. C. W. Chan, K. K. Cheung, C. M. Che, *Organometallics* **1999**, *18*, 3327; (e) J. H. K. Yip, Suwarno, J. J. Vittal, *Inorg Chem* **2000**, *39*, 3537; (f) W. Lu, M. C. W. Chan, N. Zhu, C. M. Che, C. Li, Z. Hui, *J Am Chem Soc* **2004**, *126*, 7639; (g) S. W. Lai, C. M. Che, *Top Curr Chem* **2004**, *241*, 27.

22 C. C. Kwok, H. M. Y. Ngai, S. C. Chan, I. H. T. Sham, C. M. Che, N. Zhu, *Inorg Chem* **2005**, *44*, 4442.

23 (a) Y. Y. Lin, S. C. Chan, M. C. W. Chan, Y. J. Hou, N. Zhu, C. M. Che, Y. Liu, Y. Wang, *Chem Eur J* **2003**, *9*, 1263; (b) D. Donges, J. K. Nagel, H. Yersin, *Inorg Chem* **1997**, *36*, 3040.

24 H. Yersin, W. Finkenzeller, S. W. Lai, C. M. Che, (manuscript in preparation) has determined the amount of zero-field splitting (ZFS) for this triplet: ΔE(I–III) = 19 cm^{-1} (compound **20c**). According to this value and H. Yersin, *Top Curr Chem* **2004**, *241*, 1, this assignment can be confirmed.

25 W. Sotoyama, T. Satoh, N. Sawatari, H. Inoue, *Appl Phys Lett* **2005**, *86*, 153505.

26 C. M. Che, S. C. Chan, H. F. Xiang, M. C. W. Chan, Y. Liu, Y. Wang, *Chem Commun* **2004**, 1484.

27 W. Sawodny, U. Thewalt, E. Potthoff, R. Ohl, *Acta Crystallogr* C **1999**, *55*, 2060.

28 (a) J. Kido, M. Kimura, K. Nagai, *Science* **1995**, *267*, 1332; (b) B. W. D'Andrade, M. E. Thompson, S. R. Forrest, *Adv Mater* **2002**, *14*, 147; (c) B. W. D'Andrade, S. R. Forrest, *Adv Mater* **2004**, *16*, 1585.

29 J. C. Ostrowski, M. R. Robinson, A. J. Heeger, G. C. Bazan, *Chem Commun* **2002**, 784.

30 H. F. Xiang, S. C. Chan, K. K. Y. Wu, C. M. Che, P. T. Lai, *Chem Commun* **2005**, 1408.

31 (a) S. W. Lai, M. C. W. Chan, K. K. Cheung, C. M. Che, *Inorg Chem* **1999**, *38*, 4262; (b) S. W. Lai, H. W. Lam, W. Lu, K. K. Cheung, C. M. Che, *Organometallics* **2002**, *21*, 226.

32 (a) R. C. Kwong, S. Sibley, T. Dubovoy, M. Baldo, S. R. Forrest, M. E. Thompson, *Chem Mater* **1999**, *11*, 3709; (b) V. Cleave, G. Yahioglu, P. Le Barny, R. H. Friend, N. Tessler, *Adv Mater* **1999**, *11*, 285.

33 (a) J. Guo, K. Ye, Y. Wu, Y. Liu, Y. Wang, *Synth Met* **2003**, *137*, 1075; (b) H. F. Xiang, S. C. Yu, C. M. Che, P. T. Lai, *Appl Phys Lett* **2003**, *83*, 1518.

34 (a) M. A. Baldo, D. F. O'Brien, M. E. Thompson, S. R. Forrest, *Phys Rev B* **1999**, *60*, 14422; (b) J. M. Lupton, I. D. W. Samuel, M. J. Frampton, R. Beavington, P. L. Burn, *Adv Funct Mater* **2001**, *11*, 287.

35 (a) K. M. Smith, Porphyrins and Metalloporphyrins, Elsevier, New York **1975**; (b) J. L. Retsek, C. J. Medforth, D. J. Nurco, S. Gentemann, V. S. Chirvony, K. M. Smith, D. Holten, *J Phys Chem B* **2001**, *105*, 6396.

36 S. W. Lai, Y. J. Hou, C. M. Che, H. L. Pang, K. Y. Wong, C. K. Chang, N. Zhu, *Inorg Chem* **2004**, *43*, 3724.

37 C. M. Che, Y. J. Hou, M. C. W. Chan, J. Guo, Y. Liu, Y. Wang, *J Mater Chem* **2003**, *13*, 1362.

38 R. C. Kwong, S. Lamansky, M. E. Thompson, *Adv Mater* **2000**, *12*, 1134.

39 F. Galbrecht, X. H. Yang, B. S. Nehls, D. Neher, T. Farrell, U. Scherf, *Chem Commun* **2005**, 2378.

40 S. C. F. Kui, I. H. T. Sham, C. C. C. Cheung, C. W. Ma, B. Yan, N. Zhu, C. M. Che, W. F. Fu, *Chem Eur J* **2007**, *13*, 417.

41 (a) J. Brooks, Y. Babayan, S. Lamansky, P. I. Djurovich, I. Tsyba, R. Bau, M. E. Thompson, *Inorg Chem* **2002**, *41*, 3055; (b) A. S. Ionkin, W. J. Marshall, Y. Wang, *Organometallics* **2005**, *24*, 619.

42 S. Y. Chang, J. Kavitha, S. W. Li, C. S. Hsu, Y. Chi, Y. S. Yeh, P. T. Chou, G. H. Lee, A. J. Carty, Y. T. Tao, C. H. Chien, *Inorg Chem* **2006**, *45*, 137.

9

High-Efficiency Phosphorescent Polymer LEDs

Addy van Dijken, Klemens Brunner, Herbert Börner, and Bea M.W. Langeveld

Rational design of conjugated polymers has resulted in the preparation of carbazole-based conjugated polymers having a high triplet energy, and excellent charge-injection and charge-transporting properties. When these conjugated polymers are used as host materials for green light-emitting triplet emitters, phosphorescent polymer LEDs are obtained that combine ease of manufacture with a high efficiency. Furthermore, the concepts described in this contribution leave room to design conjugated polymers that could possibly be used as hosts for blue phosphorescent emitters, which would constitute an important step towards the realization of high-efficiency full-color or white phosphorescent pLEDs for the next generation display or lighting applications, respectively.

9.1
Introduction

Organic light-emitting diodes (OLEDs) are interesting devices for use in display and lighting applications. These devices are either based on small molecules or on polymers. Small-molecule organic light-emitting diodes (smOLEDs) are usually prepared by the consecutive vacuum evaporation of several organic layers. In the resulting multilayer device, each layer takes care of a specific function, such as charge injection, charge transport, or emission of light. By carefully tuning the properties of each of these layers, efficient devices can be obtained. Polymer light-emitting diodes (pLEDs) are prepared from solution, either by spin-coating or inkjet-printing. The ease of processing ability is a strong asset of pLEDs, but processing from solution does not lend itself easily to the construction of multilayer devices. Generally, only a double-layer device structure can be processed using solutions based on two orthogonal solvents. In practice, a layer of poly(ethylenedioxythiophene):poly(styrenesulfonic acid) (PEDOT:PSS) is often inserted between the anode and the polymer layer. When one does not want to compromise on the ease of processing from solution, for pLEDs, functions such as charge injection and/or transport, and the emission of light have to be integrated in one layer. This makes it more challenging to prepare high-efficiency pLEDs, as compared to

smOLEDs. This contribution will describe our efforts toward the preparation of high-efficiency green phosphorescent pLEDs.

9.2
The Route Toward High-Efficiency OLEDs

Especially for lighting applications, OLEDs should have high efficiencies to be able to compete with existing technologies. Higher efficiencies will result in energy savings and longer operational lifetimes. The efficiency of an OLED is the product of an internal efficiency, and an optical outcoupling efficiency. Here, we will only consider the internal efficiency, which involves the ratio of electrons to holes (in other words, the charge balance inside the device), the intrinsic quantum efficiency of the emitting species, and the fraction of excited states that can undergo radiative relaxation to the ground state. The latter contribution to the internal efficiency is closely connected to the existence of singlet and triplet excited states in organic compounds.

9.3
Singlet and Triplet Excited States

For an organic molecule in its ground state, all electrons are paired in orbitals. In the excited state two electrons are orbitally unpaired. Consequently, the ground state of an organic molecule is a singlet state, while its excited states may either be singlet or triplet states, depending on the relative orientation of the electron spin momenta. Singlet and triplet excited states that are derived from the same electron orbital configuration have a difference in energy. The triplet excited state represents a lower energy than the singlet excited state as a result of less electron–electron repulsion. A simplified state energy diagram of an organic molecule is shown in Fig. 9.1.

Radiative transitions from excited states back to the ground state are governed by selection rules. In a zero order approximation, where electronic and spin motions are strictly separated, radiative transitions between singlet and triplet states are forbidden (or better, kinetically unfavorable). For such a transition to occur, the overall spin of the system has to change, and this cannot be compen-
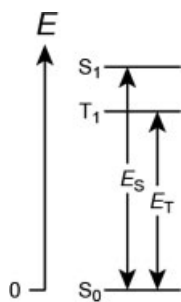
Fig. 9.1 Simplified state energy diagram of an organic molecule. S_0 denotes the ground singlet state, while S_1 and T_1 denote the first excited singlet and triplet states, respectively. The S_0–S_1 and S_0–T_1 energy differences are denoted by E_S and E_T, and are called the singlet and triplet energy of the organic molecule, respectively.

sated for by the creation of a photon. However, the interaction between an electron's spin and orbital magnetic moments, which is called spin–orbit coupling, essentially mixes singlet and triplet states, which allows transitions between them to a certain extent. The strength of this spin–orbit coupling depends on the nuclear charge, and the stronger the spin–orbit coupling the transitions between singlet and triplet states will be more allowed. In organic molecules, the spin–orbit coupling strength is weak, which means that organic molecules can only emit light from excited singlet states. In other words, organic molecules can only show fluorescence and not phosphorescence, and excited triplet states are nonradiatively deactivated at ambient temperature.

When organic molecules are electrically excited, both singlet and triplet excited states are created. Based on straightforward spin statistics, assuming equal formation cross sections for both types of excited states, the singlet:triplet ratio would be 1:3, meaning that 75% of all excited states that are formed upon the recombination of injected charge carriers is of the triplet variety. Although the exact ratio in which the two types of excited states are created has been the subject of intense discussion for some years [1–19]; it is clear that a significant part of the electrically excited states of an organic molecule are triplet excited states. As organic molecules cannot show phosphorescence, the creation of triplet excited states poses a fundamental limit on the efficiency of an OLED. Fortunately, this limitation can be relieved through the use of compounds that contain heavy atoms. As mentioned before, on a heavy atom, spin–orbit coupling is relatively strong which makes a transition between triplet and singlet levels more favorable.

9.4
Phosphorescent Emitters

A much used approach in this respect is the use of transition metal complexes as dyes. Such complexes consist of an array of ligands surrounding a central transition metal, such as ruthenium, iridium, or platinum. These complexes are also known as phosphorescent (or triplet) emitters. The radiative electronic transitions in these complexes involve charge transfer reactions between the central transition metal and the ligands. By changing the chemical nature of the ligands, the emission wavelength can be tuned. The use of transition metal complexes as dyes in OLEDs was first reported for smOLEDs using the red phosphorescent platinum complex PtOEP (see Fig. 9.2), clearly demonstrating the usefulness of such phosphorescent emitters for improving OLED efficiencies [20]. Following this publication, the green phosphorescent iridium complex $Ir(ppy)_3$ (see Fig. 9.2) was introduced as dye in a smOLED [21]. The relatively short decay time of this complex (µs timescale) prohibits saturation at high current densities, making it a promising candidate for achieving high-efficiency green OLEDs. Many publications on the use of iridium-based phosphorescent emitters have appeared over the years. The chemistry of these particular complexes has been extensively investigated and by changing the nature of the ligands, iridium-based phosphorescent emitters have been developed that cover almost the entire visible part of the

(a)

(b)   (c)   (d)
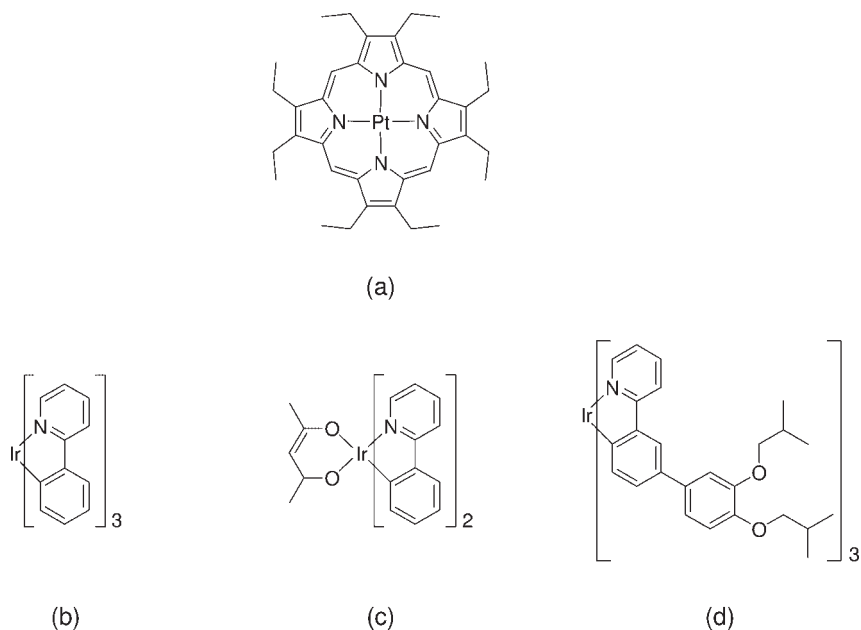
Fig. 9.2 Chemical structures of (a) 2,3,7,8,12,13,17,18-octaethyl-21H,23H-porphine platinum(II) (PtOEP), (b) tris(2-phenylpyridine)-iridium(III) (Ir(*ppy*)$_3$), (c) bis(2-phenylpyridine)-iridium(III)-acetylacetonate (Ir(*ppy*)$_2$(acac)), (d) tris[2-(2-pyridinyl-kN)(4-(3,4-bis(2-methylpropyloxy)phenyl)-phenyl)-kC]-iridium(III) (Ir-SC4).

electromagnetic spectrum [22–24]. Most of the work was focused on red and green phosphorescent emitters, culminating in the demonstration of electroluminescent organic devices with very high efficiencies [25–29]. For example, a green phosphorescent smOLED was demonstrated with an efficiency of about 48 cd/A at a luminance of 1000 cd/m^2 [28]. This device employs a stack of a hole-transporting layer, an emissive layer (doped with the green phosphorescent emitter Ir(*ppy*)$_2$(acac)), see Fig. 9.2), and an electron transport layer.

More recently, people are focusing on the use of blue phosphorescent emitters [30–33].

9.5
Host Materials for Phosphorescent Emitters

9.5.1
General Requirements

When using dyes to tune the emission color of a device, the host material should not act as a quencher of the dye emission via energy transfer from the dye to the
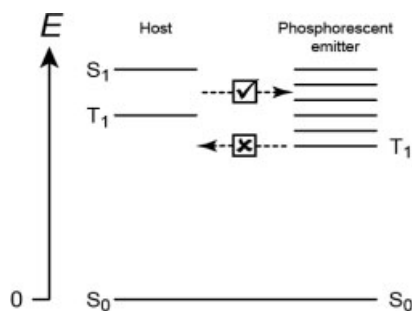
Fig. 9.3 Simplified state energy diagram for a combination of a host and a phosphorescent emitter, showing the desired situation in which the host has a higher triplet energy than the guest. The dashed horizontal arrows indicate that in this situation energy transfer can only occur from the host to the phosphorescent emitter, and not vice versa.

Table 9.1 The minimum HOMO–LUMO energy difference, singlet energy (E_S), and triplet energy (E_T) that a conjugated polymer should have for use as host in combination with a red, green, or blue phosphorescent emitter.

Color	HOMO–LUMO (eV)	E_S (eV)	E_T (eV)
Red	2.8	2.7	2.0
Green	3.4	3.2	2.5
Blue	3.7	3.4	2.7

host. When the dye is a phosphorescent emitter, its emission could be quenched by energy transfer to the triplet excited state of the host [34, 35]. To prevent this, it is required that the triplet energy of the host is higher than that of the dye (see Fig. 9.3).

This requirement poses some restrictions on materials that are to be used as hosts for phosphorescent emitters. The minimum triplet energy that a host should have for use in combination with a red, green, or blue phosphorescent emitter is summarized in Table 9.1. The triplet energy of an organic compound is correlated to its HOMO–LUMO energy difference. In a first approximation, the HOMO–LUMO energy difference is equal to the sum of the triplet energy, the singlet–triplet energy difference (also known as the exchange energy), and the exciton binding energy. The stronger the localization of the excited state is, the larger is both the exchange energy and the exciton binding energy will be. For small molecules as well as polymers, electron–electron correlation is strong and the exchange energy is relatively large. For polymers, the exchange energy is almost constant and close to 0.7 eV, while for small molecules it depends on molecular size, and varies over a wide range of values [36–42]. The exciton binding energy can be as

small as 0.1 eV, or as large as 1 eV, depending on the spatial extension of the exciton. For conjugated polymers, the exciton binding energy is usually reported to be about 0.1 eV to 0.3 eV [43–46]. Based on the above-mentioned considerations, the minimum HOMO–LUMO energy difference of a conjugated polymer required for use as a host for a red, green, or blue phosphorescent emitter can be estimated (see Table 9.1).

Well-known conjugated polymers such as poly(*p*-phenylene vinylene) (PPV) [47, 48] and polyfluorene (PF) [49–54] have triplet energies of 1.6 eV and 2.4 eV, respectively. Consequently, their application as host in phosphorescent pLEDs is limited to red (or yellow) phosphorescent emitters. In this contribution, we will focus on polymer hosts for green phosphorescent emitters. The relatively large HOMO–LUMO energy differences required for polymers to be able to host green phosphorescent emitters have important consequences. Such polymers will generally have relatively low charge carrier mobilities and low stability. Furthermore, relatively large injection barriers might be present in a device, due to mismatch between the HOMO and LUMO levels of the polymer, and the Fermi levels of the injecting contacts. For smOLEDs, the latter issue can be alleviated through the use of additional layers. The possibility of building multilayer device structures means that a staircase can be constructed to efficiently inject charge carriers from the contacts into the emissive layer. As mentioned in the introduction, multilayer device structures are very difficult to process from solution. To ensure proper injection of holes in pLEDs, the ionization potential of the polymer should be smaller than the work function of the anode. Furthermore, to ensure proper injection of electrons, the electron affinity of the polymer should be larger than the work function of the cathode. It is clear that for standard pLEDs, using a PEDOT: PSS hole injection layer with a work function of 5.0 eV, and a barium cathode with a work function of 2.0 eV, it is a challenge to find a polymer that has the right characteristics for hosting green phosphorescent emitters, and at the same time minimize charge injection barriers.

9.5.2
Carbazole-Based Host Materials

Most organic compounds with high triplet energies used in the literature as host for phosphorescent emitters are based on carbazole (see Fig. 9.4). The carbazole molecule has a triplet energy of 3.0 eV [55], and carbazole derivatives can maintain this triplet energy when the conjugation between their constituting units is minimized. Some examples of such compounds are shown in Table 9.2.

CBP and TCTA are well-known hosts for green phosphorescent emitters [21, 25, 27, 29, 56, 57], while CDBP and mCP have been used as host for blue phosphorescent emitters [31, 58, 59].

As the materials are to be used as layers in a device, just minimizing the conjugation between the constituting units is not sufficient to maintain a high triplet energy. In the solid state, the materials should form an amorphous glass to prevent a loss of triplet energy as a result of intermolecular electronic interactions. This effect is clearly illustrated when phosphorescence spectra of materials in (frozen)
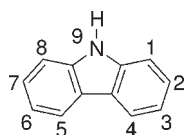
Fig. 9.4 Chemical structure of carbazole. The substitution positions are indicated by numbers.

Table 9.2 Triplet energies of several carbazole derivatives, derived from the highest energy peak of the phosphorescence spectrum measured at cryogenic temperatures on solid films of the materials.

Name	Chemical structure	E_T (eV)
CBP		2.6
TCTA		2.7
CDBP		2.8
mCP		2.9

diluted solution are compared to those of solid films. For CBP, the triplet energy of the material in diluted solution is 2.67 eV [60], while a solid film of CBP has a triplet energy of 2.56 eV [30, 59]. Similar comparisons for CDBP and mCP give energy differences of 0.2 eV [58, 59], and 0.1 eV [31, 60], respectively.

When phosphorescent emitters are used in pLEDs, the polymer of choice has been poly(9-vinylcarbazole) (PVK) [35, 61–71]. PVK has a large HOMO–LUMO

energy difference of 3.5 eV, and its emission spectrum is dominated by excimer emission bands, both in fluorescence and in phosphorescence. The excimers involve the interaction of electronically excited carbazole groups with nonexcited carbazole groups in a sandwich-like arrangement [72–74]. Nevertheless, in the solid state PVK still has a relatively high triplet energy of 2.5 eV, which is sufficient to host green phosphorescent emitters. When PVK is used as host for the green phosphorescent emitter Ir(*ppy*)₃ in a double-layer device structure, with PEDOT:PSS as hole injection layer, a device with an external quantum efficiency of about 10%, corresponding to a current efficiency of 36 cd/A, can be obtained [65]. However, the power efficiency of such devices is well below 10 lm/W, because it requires a high voltage of about 15 V to operate them. This is typical for devices based on PVK, and it is mainly due to a high barrier for the injection of holes at the interface between PEDOT:PSS and PVK, that exists because PVK has a high ionization potential of about 5.7 eV [35, 75]. Carbazole has an electron-rich conjugated system, due to the strong mesomeric effect of the nitrogen atom, and as a result, carbazole-based compounds are *p*-type conductors. Therefore, in pure PVK the conduction is due to holes only [76]. However, even when electron-transporting layers are inserted between the PVK layer and the cathode (by thermal evaporation) [61, 64, 68], or when electron-transporting compounds are mixed into the PVK layer [62, 66, 67, 71], still very low power efficiencies are obtained.

9.5.3
Tuning the Properties of Carbazole Derivatives

Nevertheless, carbazole is a promising building block for polymers that are to host green phosphorescent emitters. Investigation of the effects of different substitution patterns on the properties of carbazole derivatives reveals a method for incorporating the carbazole building block into a polymer backbone in such a way that polymers are obtained that combine a high triplet energy with a suitable ionization potential [77, 78].

It is well established that carbazole shows irreversible oxidation behavior because of the occurrence of N–N and C–C coupling reactions [79, 80]. For the carbazole radical cation, the 3, 6, and 9 positions are the reactive sites, as the 1 and 8 positions are subject to sterical hindrance. From the point of view of stability, carbazole should therefore be substituted at these positions to ensure electrochemical reversibility. This is confirmed by performing cyclic voltammetry measurements on compounds 1 to 3 as shown in Fig. 9.5. While compound 1 shows irreversible oxidation behavior, compounds 1 and 3 exhibit reversible oxidation waves [77]. In this respect, it is interesting to note that compound 4 also shows reversible oxidation behavior. Apparently for such carbazole derivatives, it is not necessary to substitute the 6 positions of the constituting carbazole molecules, as stability is already ensured by coupling them via their 3 positions.

Next to stability, the substitution pattern also influences the ionization potential of carbazole derivatives. Generally, attaching electron withdrawing substituents to conjugated molecules decreases the electron density in the π-system.
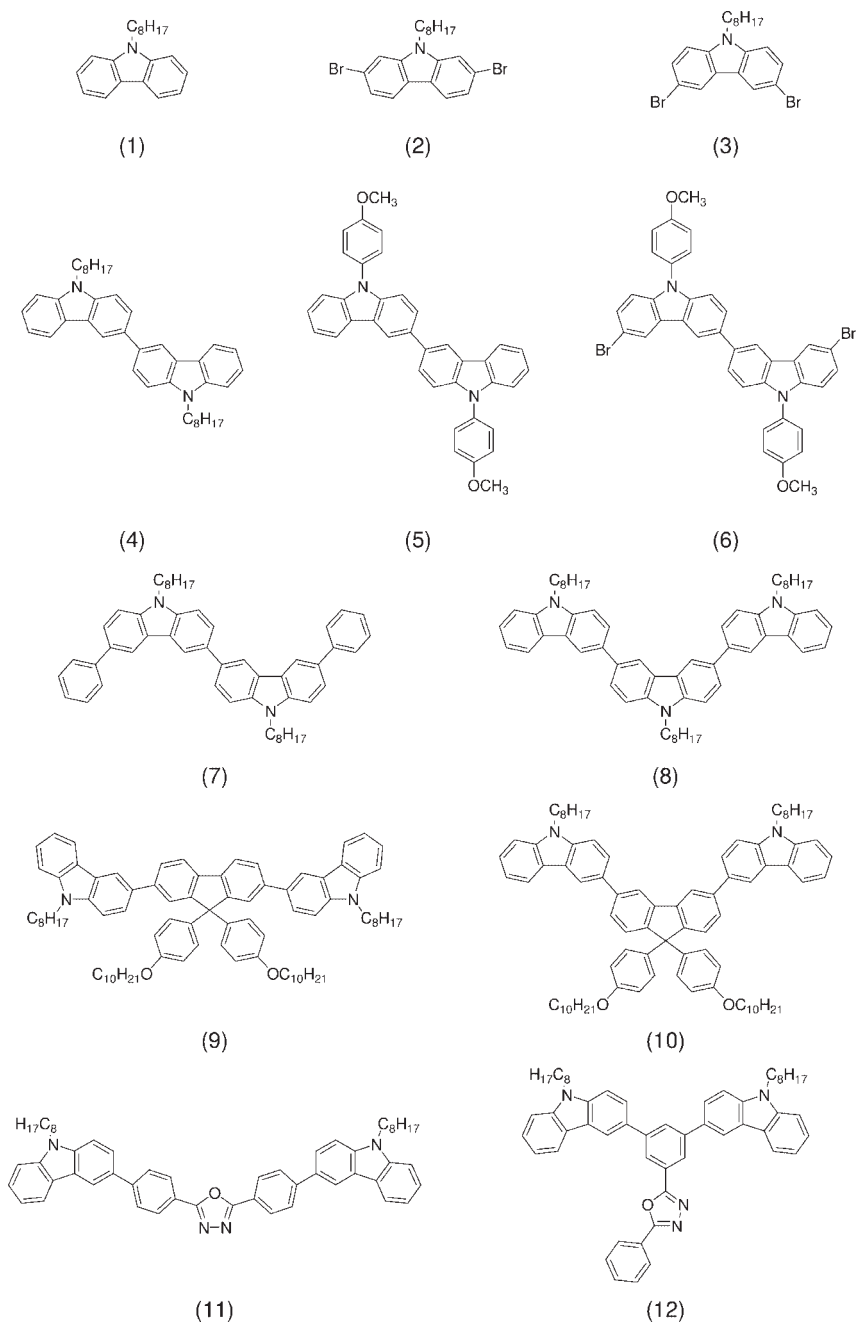
Fig. 9.5 Chemical structures of several carbazole derivatives.

Table 9.3 Ionization potentials (IP) and triplet energies (E_T) of the carbazole derivatives shown in Fig. 9.5 (the ionization potentials are derived from cyclic voltammetry measurements and the triplet energies are measured on frozen diluted solutions at cryogenic temperatures [77]).

Compound	IP (eV)	E_T (eV)
(1)	5.9	3.02
(2)	6.1	2.88
(3)	6.2	2.93
(4)	5.6	2.75
(5)	5.7	2.75
(6)	5.8	2.76
(7)	5.6	2.74
(8)	5.6	2.73
(9)	5.8	2.38
(10)	5.9	2.73
(11)	5.9	2.44
(12)	5.9	2.70

Consequently, the molecule is stabilized and the ionization potential is increased. For the carbazole molecule, it turns out that attaching electron withdrawing substituents to the 3 and 6 positions has a stronger stabilizing effect than attaching them to the 2 and 7 positions. This is because the electronic density at the 2 and 7 positions is less than at the 3 and 6 positions [79]. This is illustrated by using bromine as electron withdrawing substituent (see compounds 1 to 3 in Fig. 9.5 and Table 9.3).
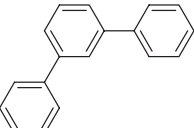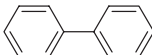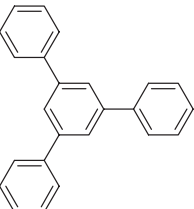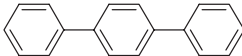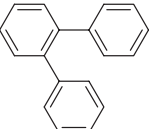
A second substitution effect is related to the 9 position of carbazole. When alkyl substituents at the 9 position are replaced by aryl substituents, the ionization potential increases (compare compounds 4 and 5). Apparently compared to aryl substituents, alkyl substituents at the 9 position increase the electron density on the carbazole ring system, making the compound easier to oxidize.

The effects on the ionization potential that these two substitution patterns have (substitution at the 3 and 6 positions, and substitution at the 9 position) are additive, as is clearly illustrated by comparing compounds 4, 5, and 6. The ionization potential of compound 4 can be increased by replacing the alkyl substituents at the 9 positions by aryl substituents. Next, the ionization potential can be increased further by attaching electron withdrawing substituents at the 6 positions of each of the two carbazole units. The above clearly shows that a method exists to tune the stability and the ionization potential of carbazole derivatives, which enables the design of carbazole-based polymers with suitable HOMO levels. To be able to design carbazole-based polymers that will be able to efficiently host green or blue phosphorescent emitters, the method should be extended with a protocol for maintaining high triplet energies. Such a protocol can also be found by studying

different substitution patterns. First, coupling two carbazole molecules via their 3 positions results in a decrease of the triplet energy from 3.02 eV to 2.75 eV. Coupling a third carbazole molecule in a similar way does not result in a further decrease of the triplet energy (compare compounds 1, 4, and 8 in Table 9.3). Second, compounds 9 and 10 both consist of two carbazole molecules connected via their 3 positions to a central fluorene derivative. However, for compound 9 the carbazoles are connected to the 2 and 7 positions of the fluorene derivative, while for compound 10 they are connected to the 3 and 6 positions. The effect on the triplet energy of the compounds is clear, as compound 9 has a triplet energy that is 0.35 eV lower than that of compound 10. The trend in triplet energy revealed by these substitution patterns is similar to that observed for polyphenyls (see Table 9.4) [55, 81, 82].

For *para*-coupled polyphenyls, the triplet excited state is delocalized along the longest molecular axis, while for *meta*-coupled polyphenyls, it is localized at every composing biphenyl structure [81, 82]. Carbazole has a higher triplet energy than biphenyl (3.02 eV versus 2.85 eV), but compound 4 has a triplet energy close to that of biphenyl. This means that the triplet excited state of compound 4 is predominantly localized on the biphenyl structure that is shared between the two carbazoles. This explains why the triplet energy decreases upon going from compound 1 to compound 4, but remains constant while going to compound 8. Furthermore, the relatively low triplet energy of compound 9 can be understood, as in this compound a chain of 4 *para*-coupled phenyl rings can be identified.

Table 9.4 Chemical structures and triplet energies (E_T) of benzene, and several polyphenyl molecules.

Chemical structure	E_T *(eV)*	*Chemical structure*	E_T *(eV)*
	3.65		2.82
	2.85		2.80
	2.55		2.67

When carbazole derivatives are to be used as host materials in electroluminescent devices, the presence of electron-transporting compounds is required to improve the charge balance, as carbazole derivatives are predominantly hole-transporting compounds. For this purpose, oxadiazole derivatives are often used [75, 83–86]. These compounds can be applied in the form of separate layers [61, 64, 68], or they can be mixed with the carbazole derivative [62, 66, 67, 71]. In the case of a pLED, it is desirable to have the electron-transporting compound copolymerized into the polymer chain. When such a copolymer is to be used as host for a phosphorescent emitter, the incorporation of the electron-transporting compound should not result in a decrease of the triplet energy. When comparing compounds 4, 11, and 12 in Fig. 9.5 and Table 9.3, the influence of two different ways of incorporating an electron-transporting compound into a carbazole derivative on the triplet energy of the resulting mixed compound can be seen. In this particular example, 2,5-diphenyl-1,3,4-oxadiazole is used as electron-transporting compound. For compound 12, the triplet energy remains at the value of that of compound 4, while for compound 11 the triplet energy has decreased considerably. This is due to an increase in the delocalization of the triplet excited state for compound 12 as compared to compound 4.

So, it is shown that a method exists to design carbazole derivatives with high triplet energies and suitable ionization potentials. Furthermore, it is shown that it is possible to incorporate other compounds (such as electron-transporting compounds) into these carbazole derivatives without influencing the triplet energy.

9.5.4
Carbazole-Based Polymers for High-Efficiency Phosphorescent pLEDs

Using the knowledge described in the previous paragraphs, carbazole-based polymers can be designed that are to be used as hosts for green phosphorescent emitters. To illustrate this, several carbazole-based polymers are shown in Fig. 9.6.

Polymers 14 and 15 are based on the homopolymer 13, but with the additional incorporation of 2,5-diphenyl-1,3,4-oxadiazole that is to fulfill the role of electron-transporting unit. The ionization potentials and triplet energies of these three carbazole-based polymers are shown in Table 9.5.

In the solid state, carbazole homopolymer 13 has a similar triplet energy as PVK. However, the ionization potential of polymer 13 is much lower than that of PVK, which ensures a lower barrier for injection of holes from an ITO/PEDOT:PSS anode. The effect of this becomes immediately clear when comparing the current–voltage characteristics devices based on either polymer 13 or PVK (see Fig. 9.7).

A device based on polymer 13 has a much higher current density at a certain applied voltage than a device based on PVK. Next, the polymers 13 to 15 have been used in pLEDs as hosts for the green phosphorescent emitter Ir-SC4 (see Fig. 9.2). For devices based on the homopolymer 13, efficiencies are shown in Fig. 9.8.

From Fig. 9.8, it is clear that when using polymer 13 as host for a green phosphorescent emitter, a poor efficiency is obtained. This is due to the fact that the

(13)

(14)

(15)
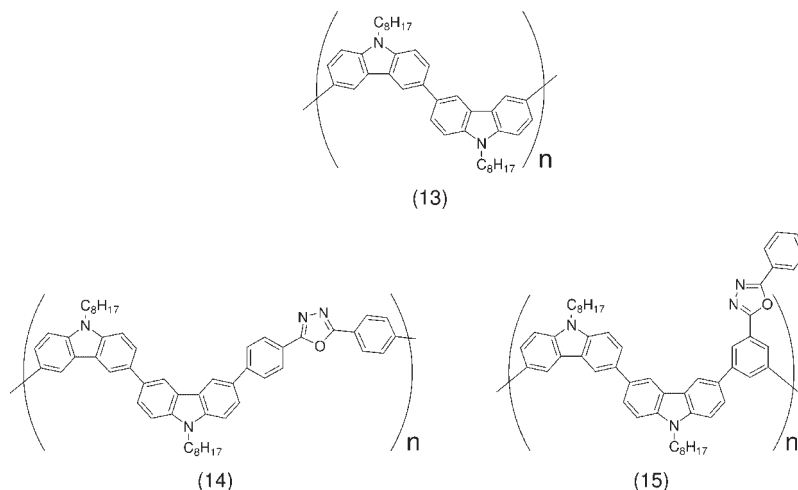
Fig. 9.6 Chemical structures of a carbazole homopolymer (13), and two carbazole-oxadiazole copolymers (14 and 15).

Table 9.5 Ionization potentials (IP) and triplet energies (E_T) of the carbazole-based polymers shown in Fig. 9.6 (the ionization potentials are derived from UPS measurements, and the triplet energies are measured on thin films of the polymers at cryogenic temperatures [78]).

Compound	IP (eV)	E_T (eV)
(13)	5.1	2.6
(14)	5.2	2.3
(15)	5.3	2.6

charge carrier distribution inside the emissive layer is out of balance, and the recombination zone is close to the Ba/Al cathode. Of course, this is the result of the fact that carbazole derivatives are predominantly hole-transporting materials. This becomes immediately clear upon inserting a hole-blocking electron-transporting layer between the polymer layer and the cathode, which results in a strong increase of the efficiency (see curve b in Fig. 9.8, where a 30-nm layer of 1,3,5-tris-(phenyl-2-benzimidazole)-benzene (TPBI) is used for this purpose [87–91]). To improve the charge balance, polymers 14 and 15 have been prepared, in which 2,5-diphenyl-1,3,4-oxadiazole has been copolymerized into the polymer chain as electron transporter. For devices based on these two copolymers, efficiencies are shown in Fig. 9.9.

From Fig. 9.9, it is clear that green phosphorescent devices based on polymer 14 have a low efficiency. This is mostly due to the low triplet energy of the polymer
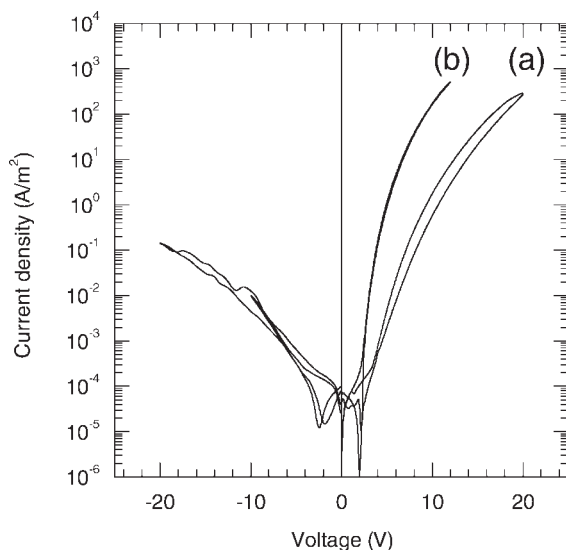
Fig. 9.7 Current density as a function of applied voltage for devices containing a 80 nm layer of PVK (a) or polymer 13 (b) sandwiched between ITO (135 nm)/PEDOT:PSS (100 nm) and Ba (5 nm)/Al (100 nm) electrodes. The hysteresis behavior of the PVK device (curve (a)) is probably due to transient charging effects.
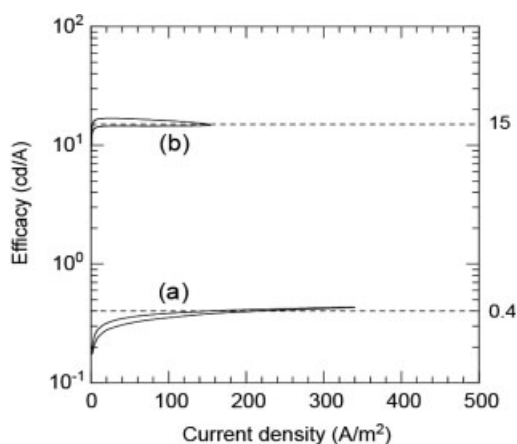
Fig. 9.8 Efficacy as a function of current density for a device containing a 80 nm layer of polymer 13 doped with Ir-SC4 sandwiched between ITO (135 nm)/PEDOT:PSS (100 nm) and Ba (5 nm)/Al (100 nm) electrodes (a). Curve (b) represents a similar device, but with an additional 30 nm layer of TPBI inserted between the polymer layer and the Ba/Al electrode.
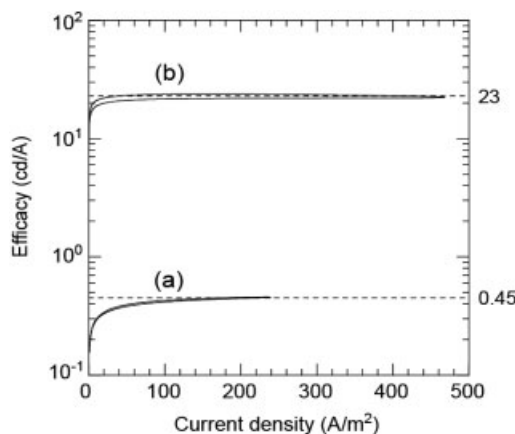
Fig. 9.9 Efficacy as a function of current density for devices containing an 80 nm layer of polymer 14 (a) or polymer 15 (b), both doped with Ir-SC4, sandwiched between ITO (135 nm)/PEDOT:PSS (100 nm) and Ba (5 nm)/Al (100 nm) electrodes.

as a result of the particular means of copolymerizing the oxadiazole electron transporter into the polymer chain. However, polymer 15 is a good host for green phosphorescent emitters, and an efficiency of 23 cd/A is obtained up to luminance levels of more than 10 000 cd/m². The high efficiency is already achieved at applied voltages below 5 V, which results in a maximum power efficiency of about 15 lm/W for this device.

9.6
Outlook

There is no reason to presume that the efficiency values reported in the previous section are the highest attainable ones for green phosphorescent pLEDs. Firstly, one could try to improve the charge balance even further, for instance, by modifying the oxadiazole comonomer, or by using electron-transporting comonomers of a different kind. Secondly, measures can be taken to improve the optical outcoupling of the pLEDs. This implies that green phosphorescent pLEDs should be able to compete with green phosphorescent smOLEDs as far as efficiencies are concerned. Recalling the large difference in complexity of these two different types of OLEDs, this is an important message indeed. Furthermore, the concepts described here leave room to design polymers that could possibly be used as hosts for blue phosphorescent emitters, which would constitute an important step towards the realization of high-efficiency full-color or white phosphorescent pLEDs for next-generation display or lighting applications, respectively.

References

1 M. A. Baldo, D. F. O'Brien, M. E. Thompson, S. R. Forrest, *Phys. Rev. B* **1999**, *60*, 14422.

2 Y. Cao, I. D. Parker, G. Yu, C. Zhang, A. J. Heeger, *Nature* **1999**, *397*, 414.

3 P. K. H. Ho, J. S. Kim, J. H. Burroughes, H. Becker, S. F. Y. Li, T. M. Brown, F. Cacialli, R. H. Friend, *Nature* **2000**, *404*, 481.

4 J. S. Kim, P. K. H. Ho, N. C. Greenham, R. H. Friend, *J. Appl. Phys.* **2000**, *88*, 1073.

5 M. N. Kobrak, E. R. Bittner, *Phys. Rev. B* **2000**, *62*, 11473.

6 T.-M. Hong, H.-F. Meng, *Phys. Rev. B* **2001**, *63*, 075206.

7 Z. Shuai, D. Beljonne, R. J. Silbey, J.-L. Brédas, *Phys. Rev. Lett.* **2000**, *84*, 131.

8 Z. Shuai, A. Ye, D. Beljonne, R. J. Silbey, J.-L. Brédas, *Synth. Met.* **2001**, *121*, 1637.

9 J. S. Wilson, A. S. Dhoot, A. J. A. B. Seeley, M. S. Khan, A. Köhler, R. H. Friend, *Nature* **2001**, *413*, 828.

10 M. Wohlgenannt, K. Tandon, S. Mazumdar, S. Ramasesha, Z. V. Vardeny, *Nature* **2001**, *409*, 494.

11 M. Wohlgenannt, X. M. Jiang, Z. V. Vardeny, R. A. J. Janssen, *Phys. Rev. Lett.* **2002**, *88*, 197401.

12 A. Ye, Z. Shuai, J.-L. Brédas, *Phys. Rev. B* **2002**, *65*.

13 A. S. Dhoot, D. S. Ginger, D. Beljonne, Z. Shuai, N. C. Greenham, *Chem. Phys. Lett.* **2002**, *360*, 195.

14 M. Segal, M. A. Baldo, R. J. Holmes, S. R. Forrest, Z. G. Soos, *Phys. Rev. B* **2003**, *68*, 075211.

15 L. C. Lin, H. F. Meng, J. T. Shy, S. F. Horng, L. S. Yu, C. H. Chen, H. H. Liaw, C. C. Huang, K. Y. Peng, S. A. Chen, *Synth. Met.* **2003**, *135–136*, 425.

16 K. Tandon, S. Ramasesha, S. Mazumdar, *Phys. Rev. B* **2003**, *67*, 045109.

17 S. Yin, L. Chen, P. Xuan, K.-Q. Chen, Z. Shuai, *J. Phys. Chem. B* **2004**, *108*, 9608.

18 D. Beljonne, A. Ye, Z. Shuai, J.-L. Brédas, *Adv. Funct. Mater.* **2004**, *14*, 684.

19 M. Reufer, M. J. Walter, P. G. Lagoudakis, A. B. Hummel, J. S. Kolb, H. G. Roskos, U. Scherf, J. M. Lupton, *Nature Materials* **2005**, *4*, 340.

20 M. A. Baldo, D. F. O'Brien, Y. You, A. Shoustikov, S. Sibley, M. E. Thompson, S. R. Forrest, *Nature* **1998**, *395*, 151.

21 M. A. Baldo, S. Lamansky, P. E. Burrows, M. E. Thompson, S. R. Forrest, *Appl. Phys. Lett.* **1999**, *75*, 4.

22 S. Lamansky, P. Djurovich, C. E. Murphy, F. Abdel-Razzaq, R. C. Kwong, I. Tsyba, M. Bortz, B. Mui, R. Bau, M. E. Thompson, *Inorg. Chem.* **2001**, *40*, 1704.

23 S. Lamansky, P. Djurovich, D. Murphy, F. Abdel-Razzaq, H. E. Lee, C. Adachi, P. E. Burrows, S. R. Forrest, M. E. Thompson, *J. Am. Chem. Soc.* **2001**, *123*, 4304.

24 A. Tsuboyama, H. Iwawaki, M. Furugori, T. Mukaide, J. Kamatani, S. Igawa, T. Moriyama, S. Miura, T. Takiguchi, S. Okada, M. Hoshino, K. Ueno, *J. Am. Chem. Soc.* **2003**, *125*, 12971.

25 T. Tsutsui, M. J. Yang, M. Yahiro, K. Nakamura, T. Watanabe, T. Tsuji, M. Fukuda, T. Wakimoto, S. Miyaguchi, *Jpn. J. Appl. Phys. Pt. 2* **1999**, *38*, L1502.

26 C. Adachi, M. A. Baldo, S. R. Forrest, M. E. Thompson, *Appl. Phys. Lett.* **2000**, *77*, 904.

27 C. Adachi, R. C. Kwong, S. R. Forrest, *Org. Electron.* **2001**, *2*, 37.

28 C. Adachi, M. A. Baldo, M. E. Thompson, S. R. Forrest, *J. Appl. Phys.* **2001**, *90*, 5048.

29 M. Ikai, S. Tokito, Y. Sakamoto, T. Suzuki, Y. Taga, *Appl. Phys. Lett.* **2001**, *79*, 156.

30 C. Adachi, R. C. Kwong, P. Djurovich, V. Adamovich, M. A. Baldo, M. E. Thompson, S. R. Forrest, *Appl. Phys. Lett.* **2001**, *79*, 2082.

31 R. J. Holmes, S. R. Forrest, Y.-J. Tung, R. C. Kwong, J. J. Brown, S. Garon, M. E. Thompson, *Appl. Phys. Lett.* **2003**, *82*, 2422.

32 R. J. Holmes, B. W. D'Andrade, S. R. Forrest, X. Ren, J. Li, M. E. Thompson, *Appl. Phys. Lett.* **2003**, *83*, 3818.

33 S.-J. Yeh, M.-F. Wu, C.-T. Chen, Y.-H. Song, Y. Chi, M.-H. Ho, S.-F. Hsu, C. H. Chen, *Adv. Mater.* **2005**, *17*, 285.

34 M. Sudhakar, P. I. Djurovich, T. E. Hogen-Esch, M. E. Thompson, *J. Am. Chem. Soc.* **2003**, *125*, 7796.

35 F.-C. Chen, S.-C. Chang, G. He, S. Pyo, Y. Yang, M. Kurotaki, J. Kido, *J. Polymer Sci. Pt. B: Polymer Phys.* **2003**, *41*, 2681.

36 Y. V. Romanovskii, A. Gerhard, B. Schweitzer, U. Scherf, R. I. Personov, H. Bässler, *Phys. Rev. Lett.* **2000**, *84*, 1027.

37 D. Hertel, S. Setayesh, H. G. Nothofer, U. Scherf, K. Müllen, H. Bässler, *Adv. Mater.* **2001**, *13*, 65.

38 A. P. Monkman, H. D. Burrows, L. J. Hartwell, L. E. Horsburgh, I. Hamblett, S. Navaratnam, *Phys. Rev. Lett.* **2001**, *86*, 1358.

39 H. Bässler, V. I. Arkhipov, E. V. Emelianova, A. Gerhard, A. Hayer, C. Im, *J. Rissler. Synth. Met.* **2003**, *135–136*, 377.

40 A. Köhler, J. S. Wilson, R. H. Friend, M. K. Al-Suti, M. S. Khan, A. Gerhard, H. Bässler, *J. Chem. Phys.* **2002**, *116*, 9457.

41 A. Köhler, D. Beljonne, *Adv. Funct. Mat.* **2004**, *14*, 1.

42 A. K. Kadashchuk, A. Vakhnin, I. Blonski, D. Beljonne, Z. Shuai, J. L. Brédas, V. I. Arkhipov, P. Heremans, E. V. Emelianova, H. Bässler, *Phys. Rev. Lett.* **2004**, *93*, 066803.

43 R. H. Friend, D. D. C. Bradley, P. D. Townsend, *J. Phys. D: Appl. Phys.* **1987**, *20*, 1367.

44 P. Gomes da Costa, E. M. Conwell, *Phys. Rev. B* **1993**, *48*, 1993.

45 J.-L. Brédas, J. Cornil, A. J. Heeger, *Adv. Mater.* **1996**, *8*, 447.

46 D. Moses, J. Wang, A. J. Heeger, N. Kirova, S. Brazovskii, *Synth. Met.* **2002**, *125*, 93.

47 J. Morgado, F. Cacialli, R. Iqbal, S. C. Moratti, A. B. Holmes, G. Yahioglu, L. R. Milgrom, R. H. Friend, *J. Mater. Chem.* **2001**, *11*, 278.

48 W. Zhu, Y. Mo, M. Yuan, W. Yang, Y. Cao, *Appl. Phys. Lett.* **2002**, *80*, 2045.

49 P. A. Lane, L. C. Palilis, D. F. O'Brien, C. Giebeler, A. J. Cadby, D. G. Lidzey, A. J. Campbell, W. Blau, D. D. C. Bradley, *Phys. Rev. B* **2001**, *63*, 235206.

50 T. F. Guo, S. C. Chang, Y. Yang, R. C. Kwong, M. E. Thompson, *Org. Electron.* **2000**, *1*, 15.

51 R. W. T. Higgins, A. P. Monkman, H. G. Nothofer, U. Scherf, *J. Appl. Phys.* **2002**, *91*, 99.

52 A. J. Campbell, D. D. C. Bradley, T. Virgili, D. G. Lidzey, H. Antoniadis, *Appl. Phys. Lett.* **2001**, *79*, 3872.

53 X. Chen, J.-L. Liao, Y. J. Liang, M. O. Ahmed, H.-E. Tseng, S.-A. Chen, *J. Am. Chem. Soc.* **2003**, *125*, 636.

54 A. J. Sandee, C. K. Williams, N. R. Evans, J. E. Davies, C. E. Boothby, A. Köhler, R. H. Friend, A. B. Holmes, *J. Am. Chem. Soc.* **2004**, *126*, 7041.

55 J. B. Birks, *Photophysics of Aromatic Compounds*; Wiley: New York, **1970**.

56 R. C. Kwong, M. R. Nugent, L. Michalski, T. Ngo, K. Rajan, Y.-J. Tung, M. S. Weaver, T. X. Zhou, M. Hack, M. E. Thompson, S. R. Forrest, J. J. Brown, *Appl. Phys. Lett.* **2002**, *81*, 162.

57 X. Zhou, D. S. Qin, M. Pfeiffer, J. Blochwitz-Nimoth, A. Werner, J. Drechsel, B. Maennig, K. Leo, M. Bold, P. Erk, H. Hartmann, *Appl. Phys. Lett.* **2002**, *81*, 4070.

58 S. Tokito, T. Iijima, Y. Suzuri, H. Kita, T. Tsuzuki, F. Sato, *Appl. Phys. Lett.* **2003**, *83*, 569.

59 I. Tanaka, Y. Tabata, S. Tokito, *Chem. Phys. Lett.* **2004**, *400*, 86.

60 T. Thoms, S. Okada, J.-P. Chen, M. Furugori, *Thin Solid Films* **2003**, *436*, 264.

61 M. J. Yang, T. Tsutsui, *Jpn. J. Appl. Phys.* **2000**, *39*, L828.

62 S. Lamansky, P. I. Djurovich, F. Abdel-Razzaq, S. Garon, D. L. Murphy, M. E. Thompson, *J. Appl. Phys.* **2002**, *92*, 1570.

63 Y. Kawamura, S. Yanagida, S. R. Forrest, *J. Appl. Phys.* **2002**, *92*, 87.

64 K. M. Vaeth, C. W. Tang, *J. Appl. Phys.* **2002**, *92*, 3447.

65 K. M. Vaeth, J. Dicillo, *J. Polymer Sci. Pt. B: Polymer Phys.* **2003**, *41*, 2715.

66 X. Gong, M. R. Robinson, J. C. Ostrowski, D. Moses, G. C. Bazan, A. J. Heeger, *Adv. Mater.* **2002**, *14*, 581.

67 X. Gong, J. C. Ostrowski, D. Moses, G. C. Bazan, A. J. Heeger, *J. Polymer Sci. Pt. B: Polymer Phys.* **2003**, *41*, 2691.

68 Z. Xie, C. Qiu, H. Chen, B. Tang, M. Wong, H.-S. Kwok, "High efficiency polymer-based electrophosphorescent organic light-emitting diode"; SID 03, **2003**.

69 X. Yang, D. Neher, D. Hertel, T. K. Däubler, *Adv. Mater.* **2004**, *16*, 161.

70 C.-L. Lee, R. R. Das, J.-J. Kim, *Chem. Mater.* **2004**, *16*, 4642.

71 J. Gao, H. You, Z.-P. Qin, J. Fang, D. Ma, X. Zhu, W. Huang, *Semicond. Sci. Technol.* **2005**, *20*, 805.

72 W. Klöpffer, *J. Chem. Phys.* **1969**, *50*, 2337.

73 G. E. Johnson, *J. Chem. Phys.* **1975**, *62*, 4697.

74 G. Rippen, G. Kaufmann, W. Klöpffer, *Chem. Phys.* **1980**, *52*, 165.

75 J. Kido, H. Shionoya, K. Nagai, *Appl. Phys. Lett.* **1995**, *67*, 2281.

76 J. V. Grazulevicius, P. Strohriegl, J. Pielichowski, K. Pielichowski, *Prog. Polym. Sci.* **2003**, *28*, 1297.

77 K. Brunner, A. van Dijken, H. Börner, J. J. A. M. Bastiaansen, N. M. M. Kiggen, B. M. W. Langeveld, *J. Am. Chem. Soc.* **2004**, *126*, 6035.

78 A. van Dijken, J. J. A. M. Bastiaansen, N. M. M. Kiggen, B. M. W. Langeveld, C. Rothe, A. Monkman, I. Bach, P. Stössel, K. Brunner, *J. Am. Chem. Soc.* **2004**, *126*, 7718.

79 J. F. Ambrose, R. F. Nelson, *J. Electrochem. Soc.* **1968**, *115*, 1159.

80 J. F. Ambrose, L. L. Carpenter, R. F. Nelson, *J. Electrochem. Soc.* **1975**, *122*, 876.

81 J. Higuchi, K. Hayashi, K. Seki, M. Yagi, K. Ishizu, M. Kohno, E. Ibuki, K. Tajima, *J. Phys. Chem. A* **2001**, *105*, 6084.

82 J. Higuchi, K. Hayashi, M. Yagi, H. Kondo, *J. Phys. Chem. A* **2002**, *106*, 8609.

83 C. C. Wu, J. C. Sturm, R. A. Register, J. Tian, E. P. Dana, M. E. Thompson, *IEEE Trans. Electron Devices* **1997**, *44*, 1269.

84 Z. Peng, Z. Bao, M. E. Galvin, *Adv. Mater.* **1998**, *10*, 680.

85 X. Jiang, R. A. Register, K. A. Killeen, M. E. Thompson, F. Pschenitzka, J. C. Sturm, *Chem. Mater.* **2000**, *12*, 2542.

86 X. Jiang, R. A. Register, K. A. Killeen, M. E. Thompson, F. Pschenitzka, T. R. Hebner, J. C. Sturm, *J. Appl. Phys.* **2002**, *91*, 6717.

87 Z. Zhang, X. Jiang, S. Xu, *Thin Solid Films* **2000**, *363*, 61.

88 Z.-L. Zhang, X.-Y. Jiang, W.-Q. Zhu, B.-X. Zhang, S.-H. Xu, *J. Phys. D: Appl. Phys.* **2001**, *34*, 3083.

89 Y. T. Tao, E. Balasubramaniam, A. Danel, P. Tomasik, *Appl. Phys. Lett.* **2000**, *77*, 933.

90 Y. T. Tao, E. Balasubramaniam, A. Danel, B. Jarosz, P. Tomasik, *Appl. Phys. Lett.* **2000**, *77*, 1575.

91 Y. T. Tao, C. H. Chuen, C. W. Ko, J. W. Peng, *Chem. Mater.* **2002**, *14*, 4256.

8

Energy-Transfer Processes between Phosphorescent Guest and Fluorescent Host Molecules in Phosphorescent OLEDs

Isao Tanaka and Shizuo Tokito

We studied the energy-transfer processes between phosphorescent guests and fluorescent hosts in phosphorescent organic light-emitting devices by using absorption and photoluminescence spectroscopy. The phosphorescence spectra were measured for various fluorescent host molecules in addition to the phosphorescent guest molecules, and their triplet excited states were characterized. We especially concentrated on the triplet energy transfer in the systems such as 4,4′-N,N'-dicarbazole-biphenyl (CBP) doped with bis[(4,6-difluorophenyl)-pyridinato-N,C$^{2'}$](picolinate) iridium (FIrpic), tris(8-hydroxyquinoline) aluminum (Alq$_3$) doped with *fac* tris(2-phenylpyridine) iridium [Ir(ppy)$_3$], and bis(2-methyl-8-quinolinato)-4-phenylphenolate aluminum (BAlq) doped with Ir(ppy)$_3$, where the triplet energy of the phosphorescent guest molecule is higher than the triplet energy of the fluorescent host molecule. Energy transfer plays an important role in the confinement of triplet energy on the phosphorescent guest, which determines emission efficiency in phosphorescent organic light-emitting devices. It is revealed that the photoluminescence behavior depends on the difference of the triplet energies between guest and host molecules.

8.1
Introduction

Organic materials have found an important application in organic light-emitting devices (OLEDs). Since the initial report of efficient electroluminescence (EL) from OLEDs by Tang and VanSlyke in 1987 [1], the OLEDs have been extensively investigated for flat panel or flexible display applications because of advantages that include their thin, lightweight structure, high luminance, low drive voltage, and variety of emission colors. Until now, efforts have mainly focused on improving the emission efficiency of the OLEDs, either by developing more efficient materials or improving device structure.

The OLEDs typically consist of thin films of molecular [1, 2] or polymeric [3] amorphous organic materials. When electrons and holes recombine within the

emitting layer in an OLED, a localized excited state with a binding energy of ~1 eV is formed. This excited state, called an "exciton," is associated with spin. Exciton spin plays an important role because it determines whether excitons can efficiently emit photons. In most molecules, the ground state is a singlet state. Since the emission of photons conserves the symmetry of the spin wavefunction, only singlet excited states decay efficiently to ground states, and thus emit photons. This radiative decay of spin-antisymmetric singlet excited states with total spin $S = 0$ is termed "fluorescence," and occurs rapidly (at a rate of $k \sim 10^9 s^{-1}$). In contrast, the radiative decay of spin-symmetric triplet excited states with $S = 1$ is termed "phosphorescence," and is much slower (e.g., $k < 10^6 s^{-1}$). In general, radiation from triplet excited states is very inefficient. However, radiative decay from triplet excited states is partially allowed if the singlet and triplet excited states are mixed. Singlet–triplet mixing and efficient phosphorescence can be achieved in molecules with strong spin–orbit coupling due to the presence of heavy metal atoms such as platinum (^{78}Pt) [4] or iridium (^{77}Ir) [5]. Since the reports by Baldo et al. [4, 5], the use of phosphorescent emitters of heavy-metal complexes such as 2,3,7,8,12,13,17,18-octaethyl-21H,23H-porphyrine platinum (PtOEP)[4] or *fac* tris(2-phenypyridine) iridium [Ir(ppy)$_3$] [5, 6] in OLEDs, called phosphorescent OLEDs, have been attracting a lot of attention because it enables dramatic improvements in device performance [7, 8].

Phosphorescent materials are usually doped as guests into host materials having high-energy triplet states at a relatively low concentration of a few percent. From the viewpoint of the confinement of triplet energy on the phosphorescent guest, which determines the triplet state emission efficiency, we need to consider the processes of energy transfer between guest and host molecules. In addition, the diffusion of triplet excitons into hole-transporting and electron-transporting layers must also be considered because triplet excitons generated by charge-carrier recombination are usually formed near these interfaces. In this article, we concentrate on energy-transfer processes between phosphorescent guest and fluorescent host molecules, and present the results of spectroscopic studies on the mechanisms of light emission in guest – host systems of phosphorescent OLEDs.

8.2
Electronic Structure and Energy Transfer in Guest–Host Systems

At first, electronic structure and energy transfer in guest–host systems in phosphorescent OLEDs are described. Figure 8.1 shows the energy-level scheme of singlet excited states (S$_1$), triplet excited states (T$_1$), and singlet ground states (S$_0$) and the energy-transfer and light-emission processes in guest–host systems of the emitting layer in phosphorescent OLEDs. In phosphorescent OLEDs, energy transfers from host donors to guest acceptors by Förster and/or Dexter mechanisms [9, 10] are utilized to tune color and improve emission efficiency. Förster energy transfer is a long range (up to ~10 nm), nonradiative, dipole–dipole coupling of donor and acceptor molecules [9–11]. Dexter energy transfer is a short
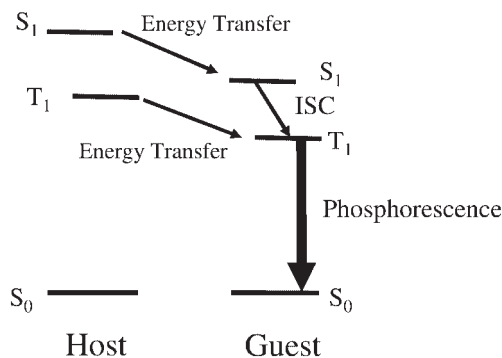
Fig. 8.1 Energy level scheme of singlet excited states (S_1), triplet excited states (T_1), and singlet ground states (S_0), and energy-transfer and light-emission processes in guest–host systems of emitting layer in phosphorescent OLEDs.

range (typically ~1 nm) process where excitons diffuse from donor to acceptor sites via intermolecular electron exchange [9, 10, 12]. In general, the recombination of electrons and holes generates triplet and singlet excited states at a ratio of 3:1 in terms of standard quantum mechanics [9, 10, 13, 14]. Thus, the nature of emission from pure singlet excitons in fluorescent organic materials limits the internal quantum efficiency (number of photons per electron) to 25%. As shown in Fig. 8.1, in the presence of singlet–singlet (S_1 to S_1) Förster and triplet–triplet (T_1 to T_1) Dexter transfers and rapid intersystem crossing (ISC) from the S_1 to the T_1, the theoretical efficiency is four times that of emission from the S_1. This results in 100% internal quantum efficiency. It was recently demonstrated that an OLED and a solid thin film based on Ir(ppy)$_3$ showed ~100% EL internal quantum efficiency [15] and ~100% photoluminescence (PL) quantum yield [16], respectively.

The triplet energy-transfer processes between guest and host molecules are shown in Fig. 8.2. In this figure, k_G and k_H are the radiative decay rates of T_1 of guest and host molecules, respectively, and the broken arrows indicate nonradiative transitions; k_{FW} and k_{BW} are the forward and backward triplet energy-transfer rates from the host to the guest, respectively. These transfer rates of k_{FW} and k_{BW} are determined by Gibb's free energy change (ΔG) and the wavefunction overlap of the molecules; also significant are k_G and k_H [17, 18]. ΔG corresponds to the difference in triplet energy between guest and host molecules. Host-to-guest triplet energy transfer is exothermic when $\Delta G < 0$, as shown in Fig. 8.2(a), and endothermic when $\Delta G > 0$, as shown in Fig. 8.2(b). In an exothermic system, such as 4,4′-N,N'-dicarbazole-biphenyl (CBP) doped with Ir(ppy)$_3$ [CBP:Ir(ppy)$_3$] with $\Delta G = -0.13$ eV, the triplet energy is strongly confined on the phosphorescent guest Ir(ppy)$_3$. The triplet state density and associated quenching losses in the CBP host are small, which leads to high emission efficiency [5, 6]. Thus, in OLEDs, a guest–host system with exothermic host-to-guest triplet energy transfer is used for the emitting layer. Conversely, an endothermic system, such as CBP doped with

(a) Exothermic

(b) Endothermic

— — ▶ Nonradiative transition
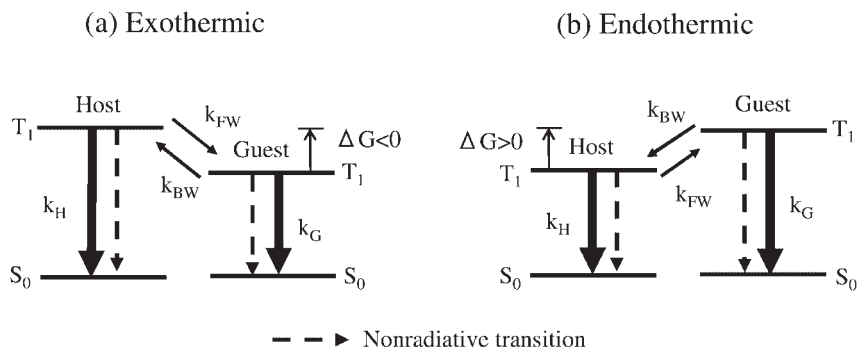
Fig. 8.2 Triplet dynamics in systems with (a) exothermic and (b) endothermic energy transfer from host to guest. Rates of forward and backward triplet energy transfer from host to guest, k_{FW} and k_{BW}, are determined by Gibb's free energy change (ΔG) and molecular overlap; also significant are the rates of decay from the guest and host triplet excited states, labeled k_G and k_H, respectively. Broken lines indicate nonradiative transitions.

bis[(4,6-difluorophenyl)-pyridinato-N,C$^{2'}$](picolinate) iridium (FIrpic) (CBP:FIrpic) with $\Delta G = +0.09$ eV, decreases the emission efficiency in OLEDs because of inefficient confinement of the triplet energy on the FIrpic molecule [19, 20]. This results in the triplet energy transfer between the guest and host molecules, which is discussed later. The triplet energy transfer, which is the subject of this study, enables us to obtain information on the triplet excited states in various host molecules.

8.3
Luminescence Properties of Phosphorescent and Fluorescent Materials

Chemical structures of blue-, green-, and red-emitting phosphorescent materials of Ir complexes are shown in Fig. 8.3(a). The EL spectra of OLEDs using these materials at room temperature are shown in Fig. 8.3(b), which is taken from [21, 22]. In these Ir complexes, mixing of singlet and triplet states leads to nearly 100% efficiency of ISC, and allows a strong radiative transition from triplet excited states to singlet ground states. Therefore, very strong phosphorescence with a relatively short radiative lifetime, of the order of microseconds, is observed without fluorescence even at room temperature. OLEDs that use FIrpic and Ir(ppy)$_3$ as phosphorescent emitters exhibit blue and green emissions, respectively. These emissions are assigned to the transition from the triplet metal-to-ligand charge transfer (^{3}MLCT) states of FIrpic[23] and Ir(ppy)$_3$ [24–26]. An OLED using bis[2-(2'-benzothienyl)pyridinato-N,C$^{3'}$](acetylacetonate) iridium [Btp$_2$Ir(acac)] exhibits a vibronic-structured red emission, which is due to the transition from the $^3\pi$–π^* ligand states [27, 28]. The triplet energies of FIrpic, Ir(ppy)$_3$, and Btp$_2$Ir(acac) are estimated from the highest energy peaks of the phosphorescence spectra to be 2.64, 2.42, and 2.00 eV, respectively.

(a)

FIrpic   Ir(ppy)₃   Btp₂Ir(acac)
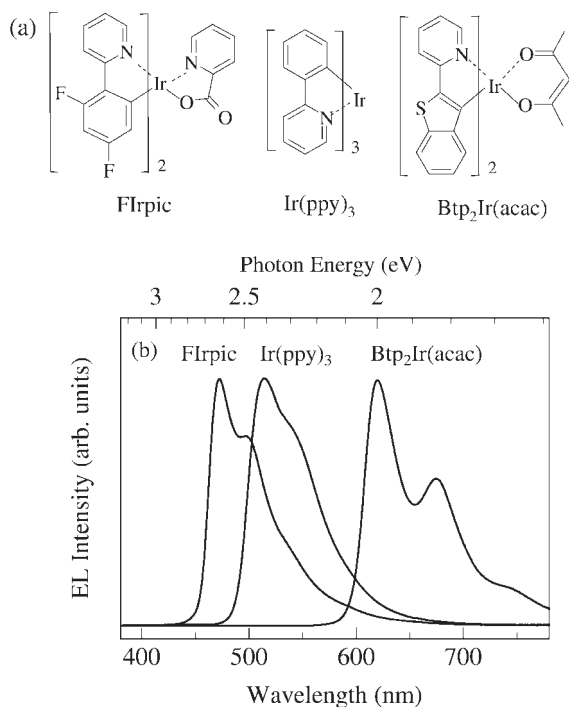
Fig. 8.3 (a) Chemical structures of typical blue-, green-, and red-emitting phosphorescent materials of Ir complexes [FIrpic, Ir(ppy)₃, and Btp₂Ir(acac)]. (b) Electroluminescence spectra of OLEDs using these materials at room temperature.

In general, it is difficult to observe phosphorescence from fluorescent materials, which are usually used as the host, because the rates of triplet radiative decay are much slower than the rates of the competing nonradiative processes. Therefore, we have to perform PL measurements at extremely low temperatures where the nonradiative processes are negligible [17]. Since it is well known that phosphorescence is affected by oxygen, a thin film (50 nm thick) deposited using high-vacuum thermal evaporation was encapsulated with a glass cap in a nitrogen atmosphere using UV-epoxy adhesive. Figure 8.4 shows the PL spectra of a neat CBP thin film held in a contact-type cryostat at 8 K. Photoexcitation was carried out using a diode-pumped passively Q-switched neodymium-doped yttrium aluminum garnet laser with a wavelength of 355 nm. The typical power density on the surface of the sample was ~1 W/cm². In conventional cw-PL measurement, strong violet fluorescence with a short lifetime, of the order of nanoseconds, is mainly observed at 376 nm. In addition, a weak structured-PL band appears at around 490 nm. This weak PL band shows a very long lifetime of about 1 s, which indicates phosphorescence from the CBP. To clearly detect the phosphorescence spectra, the phosphorescence emission was recorded by measuring the time-resolved PL spectra with a delay of 300 ms after applying pulsed excitation for 100 ms using
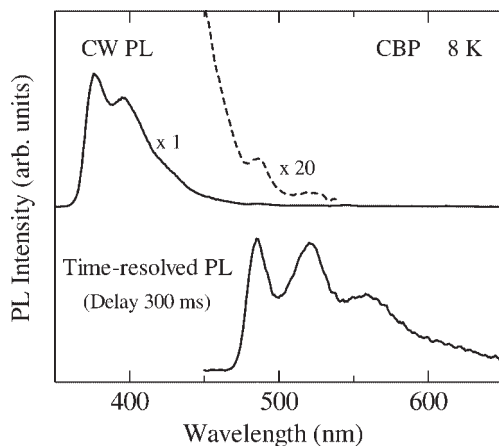
Fig. 8.4 Photoluminescence spectra at 8 K of a neat CBP thin film held in contact-type cryostat. For time-resolved photoluminescence measurements, delayed photoluminescence corresponding to phosphorescence was recorded at delay time of 300 ms after pulsed excitation for 100 ms using an electric shutter.

an electric shutter. The triplet energy of CBP was estimated from the highest energy peak of the time-resolved PL spectra to be 2.55 eV.

The chemical structure and phosphorescence spectra at 8 K of various organic materials used as hosts or carrier-transporting layers are shown in Figs. 8.5 and 8.6, respectively. These were measured using the same method as described above. The triplet energy (E_T) was estimated from the highest energy peak of the phosphorescence spectra corresponding to the 0–0 transition. These materials exhibit strong fluorescence. However, phosphorescence emission can be detected by using time-resolved PL spectroscopy at low temperatures. In some materials, for example, aluminum complexes of tris(8-hydroxyquinoline) aluminum (Alq_3) and bis(2-methyl-8-quinolinato)-4-phenylphenolate aluminum (BAlq), the phosphorescence quantum yield is extremely low because of the inefficient ISC due to the weak–heavy atom effect of a light metal such as aluminum [29]. However, by doping phosphorescent material into these aluminum complexes and utilizing triplet energy transfer, we succeeded in observing phosphorescence from aluminum complexes [30–32], as discussed later.

8.4
Energy Transfer of Blue Phosphorescent Molecules in Guest–Host Systems

As the triplet energy of phosphorescent molecules increases, it becomes more important to find appropriate host molecules with suitably high-energy triplet states. Blue emission of OLEDs is necessary for their application to full-color
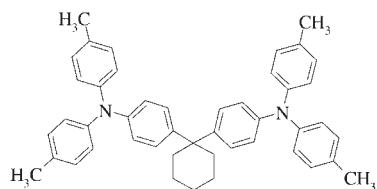
TAPC
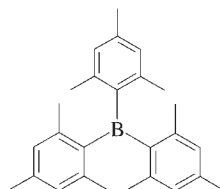
TMB
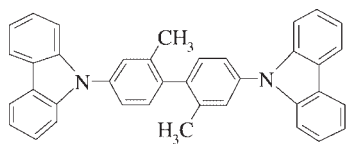
CDBP
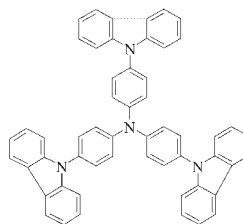
TCTA
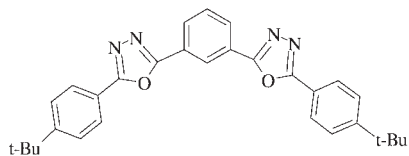
OXD-7

CBP

PBD

BCP

TPD
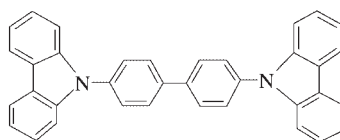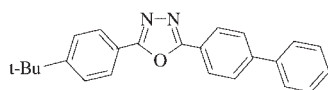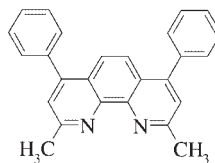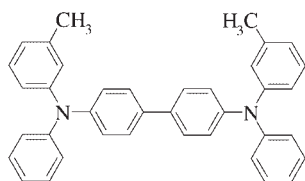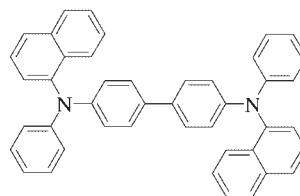
α -NPD

Fig. 8.5 Chemical structures of various organic materials used for hosts or carrier-transporting layers.
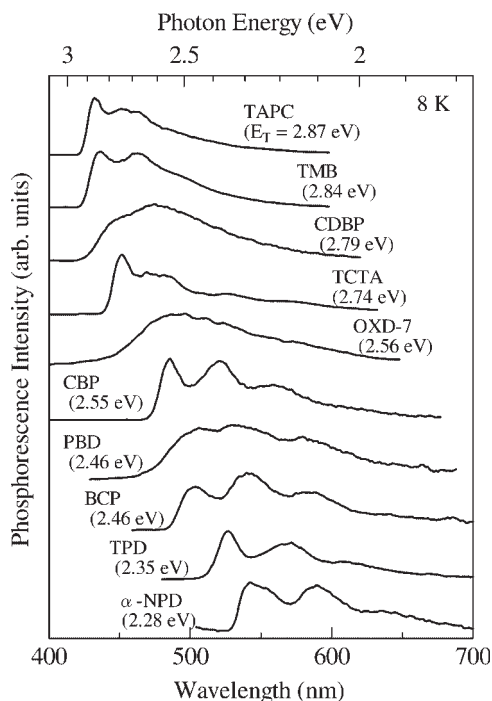
Fig. 8.6 Phosphorescence spectra at 8 K of various organic materials used as hosts or carrier-transporting layers. Phosphorescence spectra were recorded at a delay time of 300 ms after pulsed excitation with a pulse width of 100 ms using an electric shutter.

flat-panel displays. This requires both highly efficient blue-light-emitting phosphorescent materials and appropriate host materials. In this section, we concentrate on the energy transfer between blue phosphorescent molecules and host molecules, especially, the energy-dissipative processes and light-emission mechanism of FIrpic doped into two host molecules, CBP and 4,4′-bis(9-carbazolyl)-2,2′-dimethyl-biphenyl (CDBP), which have different triplet energies.

The PL spectra at 8, 80, 150, and 295 K of a 3-wt% FIrpic-doped CBP [CBP:FIrpic (3 wt%)] thin film are shown in Fig. 8.7 [33]. At 8 K, the PL intensity is weakest, and the spectral line shape is broad and complicated. As shown earlier in Figs. 8.3 and 8.4, the triplet energies were estimated to be 2.64 eV and 2.55 eV for FIrpic and CBP, respectively. Exothermic energy transfer from FIrpic to CBP would be expected to occur because the triplet energy of FIrpic guest is 90 meV higher than that of CBP host ($\Delta G = +0.09$ eV). Both phosphorescent emissions of FIrpic, with a peak of 470 nm, and CBP, with a peak of 486 nm, were observed at extremely low temperatures, as indicated by the broken and dash-dotted lines in Fig. 8.7, respectively. At temperatures above 80 K, only FIrpic phosphorescence was observed because the intensity of the CBP phosphorescence was greatly reduced.
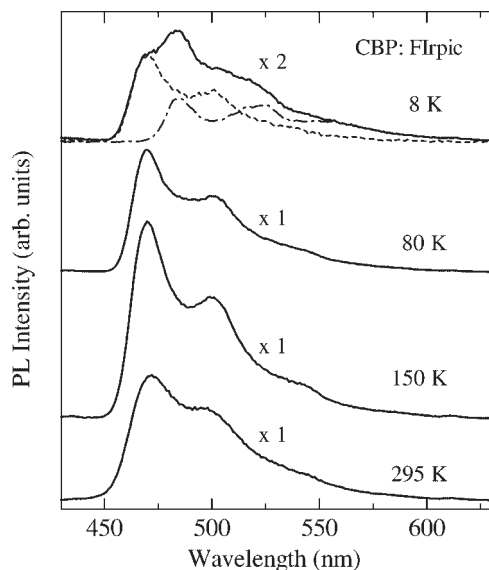
Fig. 8.7 Photoluminescence spectra at 8, 80, 150, and 295 K of 3-wt% FIrpic-doped CBP thin film. Only the photoluminescence spectrum at 8 K was magnified twice.
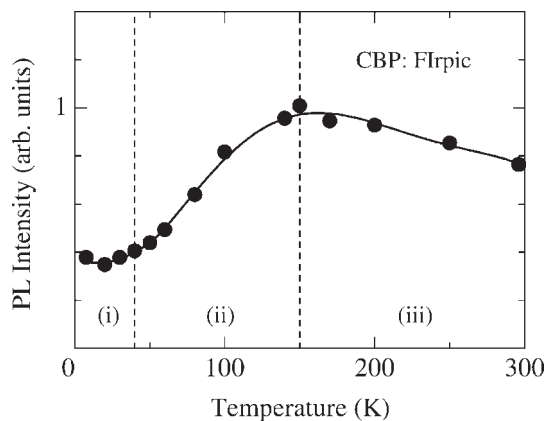
Fig. 8.8 Temperature dependence of integrated photoluminescence intensity of 3-wt% FIrpic-doped CBP thin film.

This unique temperature dependence of the phosphorescence intensity is discussed below.

The temperature dependence of the PL intensity of the CBP:FIrpic thin film is shown in Fig. 8.8 [33]. The PL intensity was evaluated by integrating the intensity over the detectable spectrum. From the viewpoint of differences in temperature
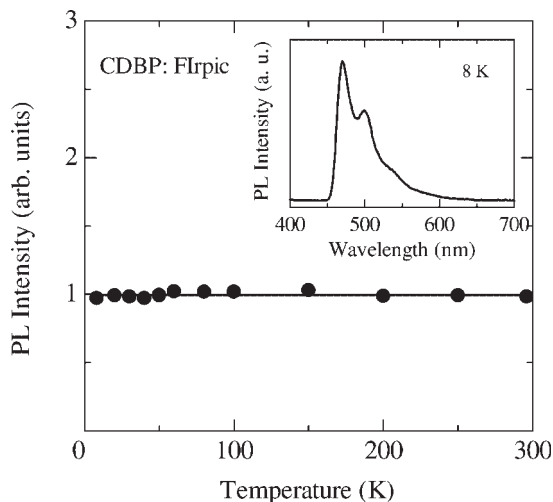
Fig. 8.9 Temperature dependence of integrated photoluminescence intensity of 3-wt% FIrpic-doped CDBP thin film. Photoluminescence spectrum at 8 K is shown in inset.

dependence, three temperature regions were identified: (i) $T < 40$ K, (ii) 40 K $< T < 150$ K, and (iii) $T > 150$ K. The intensity was weakest in temperature region (i) because of the exothermic energy transfer from FIrpic to CBP, as mentioned above. In temperature region (ii), the increase in thermal energy promoted endothermic transfer from CBP to FIrpic, resulting in an increase in FIrpic phosphorescence with a maximum intensity at 150 K. In temperature region (iii), nonradiative transitions from the CBP triplet states became more active with increasing temperature, leading to a gradual decrease in intensity. The unique temperature dependence of the phosphorescence intensity is attributed to inefficient confinement of the triplet energy on the FIrpic molecules. This PL-intensity behavior is similar to that reported for 4,4′-bis[*N*-(p-tolyl)-*N*-phenyl-amino]biphenyl (TPD) doped with Ir(ppy)₃ [TPD:Ir(ppy)₃] [34, 35], where ΔG is almost equal to that for CBP:FIrpic (about +0.1 eV).

Next, we discuss energy transfer between FIrpic and CDBP, where the triplet energy of FIrpic guest is 150 meV lower than that of CDBP host ($\Delta G = -0.15$ eV), as shown earlier in Figs. 8.3 and 8.6. The temperature dependence of the integrated PL intensity of a 3-wt% FIrpic-doped CDBP [CDBP:FIrpic (3 wt%)] thin film is shown in Fig. 8.9 [33]. The inset shows the PL spectrum at 8 K. The PL intensity did not show any dependence on temperature, similar to results for the exothermic system of CBP:Ir(ppy)₃ [34, 36, 37] and polycarbonate (PC) doped with Ir(ppy)₃ [PC:Ir(ppy)₃] [38]. PC is a stable and optically nonactivated host polymer with a high triplet energy of ~2.9 eV [39], which results in ΔG of ~−0.5 eV for the PC:Ir(ppy)₃ system. The temperature independence of the PL intensity suggests that the thermally activated nonradiative decay processes must be much weaker than the radiative decay processes, and that the phosphorescence quantum yield
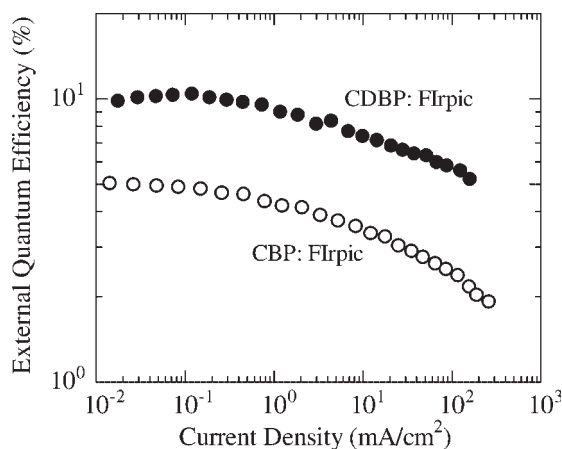
Fig. 8.10 Current density dependence of external quantum efficiency for blue OLEDs with either CBP (○) or CDBP (●) as host.

is extremely high. Therefore, blue phosphorescent OLEDs using CDBP:FIrpic as the emitting layer potentially have an external quantum efficiency as high as the theoretical limit of 20%. Time-resolved PL measurements were also performed using a streak camera. The PL lifetime increased significantly with decreasing temperature below ~50 K, similar to results for CBP:Ir(ppy)$_3$ [34, 36] and PC: Ir(ppy)$_3$ [38]. Furthermore, the temperature dependence of the phosphorescence intensity and lifetime of the CDBP:FIrpic thin film were similar to those of a PC: FIrpic thin film. These PL properties indicate excellent confinement of the triplet energy on FIrpic molecules in a CDBP host.

The external quantum efficiencies of CBP:FIrpic- and CDBP:FIrpic-based OLEDs are shown as a function of current density in Fig. 8.10 [20]. An OLED using CBP exhibited a maximum efficiency of 5.1%, which is comparable to that of ~5.7% reported in a similar device by Adachi et al. [23]. However, an OLED using CDBP was much more efficient: the maximum external quantum efficiency was 10.4% at 0.1 mA/cm^2, which was almost twice that of the OLED using CBP. In both devices, a gradual decrease in the external quantum efficiency was observed at higher current densities, which has been attributed to triplet–triplet (T–T) annihilation [40]. The improvement in efficiency can be explained in terms of the efficient confinement of triplet energy on the FIrpic molecule.

Finally, we discuss the transient PL characteristics of FIrpic-doped thin films. Figure 8.11(a) shows the PL decay profiles of CBP:FIrpic and CDBP:FIrpic thin films measured at the peak maximum at 295 K [20]. The solid lines are the results fitted by double- and mono-exponential decay models for CBP:FIrpic and CDBP: FIrpic thin films, respectively. In the CBP:FIrpic thin film, two-component decay was observed, comprising a fast decay process with a 1.3-μs lifetime and a delayed process with a 7.3-μs lifetime. As shown in the schematic energy scheme in Fig. 8.11(b), the delayed component is attributed to exothermic energy transfer from FIrpic to CBP, which has a long T$_1$ lifetime, and endothermic energy transfer from
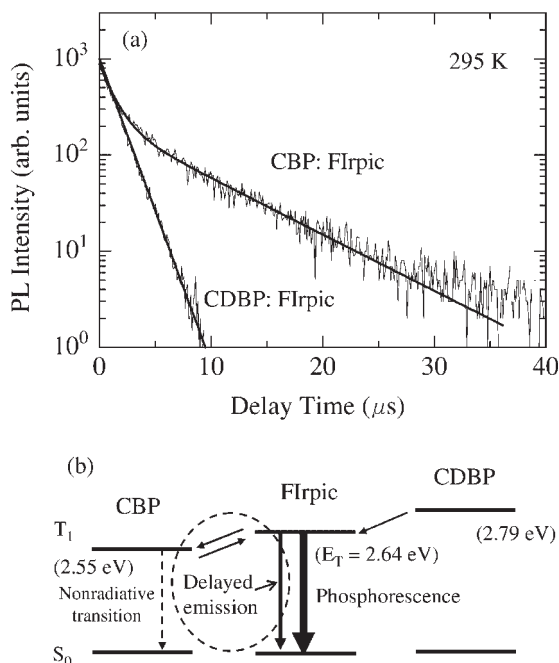
Fig. 8.11 (a) Transient photoluminescence decay profiles for CBP:FIrpic and CDBP:FIrpic thin films under the excitation at 355 nm. (b) Scheme of triplet energy levels and energy-transfer schemes for FIrpic, CBP, and CDBP.

CBP to FIrpic [16, 20, 23]. The CDBP:FIrpic thin film clearly showed a mono-exponential decay curve with a lifetime of 1.4 μs. The transient PL characteristics clearly indicate that triplet energy transfer from FIrpic to CDBP was completely suppressed and that the triplet energy of FIrpic is effectively confined in the CDBP host because FIrpic has lower triplet energy than CDBP. As shown in Fig. 8.10, very efficient phosphorescence from FIrpic was observed in the OLED. Thus, high triplet energy of the host material is an important factor in the emission efficiency of FIrpic-based blue OLEDs.

8.5
Energy Transfer Between Ir(ppy)$_3$ and Alq$_3$: Enhancement of Phosphorescence from Alq$_3$

Alq$_3$ has been used as an emitting material in OLEDs since it was first discovered to produce efficient EL [1]. The luminescence observed in Alq$_3$ is due to the radiative processes of singlet excitons formed by photoexcitation, or in the case of EL, by charge-carrier injection. The singlet excitons are ascribed to ligand-centered (LC) π–π* excited states formed in the transition of electrons from the highest

occupied molecular orbital (HOMO) mainly on the phenoxide ring to the lowest unoccupied molecular orbital (LUMO) predominantly on the nitrogen atom [41]. Several studies of singlet excitons in Alq$_3$ have already resulted in reports of the fluorescence lifetime [42–44], quantum yield [44, 45], and photocalorimetric properties [45]. However, until recently, there have only been few reports on triplet excitons because attempts to observe phosphorescence from Alq$_3$ have been unsuccessful [17, 29, 46]. The phosphorescence quantum yield of Alq$_3$ was reported to be extremely low because of the negligible ISC due to the weak–heavy atom effect of a light metal such as aluminum [29]. However, even for phosphorescent OLEDs, Alq$_3$ is still being used as the electron-transporting layer [5, 6], and is now a basic and important material for OLEDs.

Curry and Gillin [47] observed phosphorescence from Alq$_3$ as the lower energy tail of a fluorescence peak in the PL spectra. However, the observed emission was not clear enough to enable accurate evaluation of the triplet energy. In 2003, Burrows et al. [48] were the first to observe phosphorescence from Alq$_3$ in an ethyl iodide glass matrix at 77 K by promoting the ISC due to the presence of the heavy atom iodine, called external heavy atom effect [49]. They estimated the triplet energy to be 2.17 ± 0.10 eV. Cölle and coworkers observed phosphorescence from polycrystalline Alq$_3$ by using time-resolved PL spectroscopy [50], and determined the triplet energy to be 2.05 ± 0.1 eV from the delayed EL spectra of Alq$_3$-based OLEDs [51]. Furthermore, they determined that the triplet energies of the meridional and facial isomers (in α- and δ-Alq$_3$) were 2.11 ± 0.1 and 2.16 ± 0.1 eV, respectively [52, 53]. Goushi et al. [34] reported enhancement of the phosphorescence of the fluorescent molecule, 4,4′-bis[N-(1-naphthyl)-N-phenyl-amino]biphenyl (α-NPD), by doping with the phosphorescent molecule Ir(ppy)$_3$ of which the triplet energy is 0.14 eV higher than that of α-NPD ($\Delta G = +0.14$ eV). In this section, we describe the PL properties of Alq$_3$:Ir(ppy)$_3$ thin films, and characterize the triplet energy of Alq$_3$ based on the transfer of triplet energy.

The chemical structures of Alq$_3$ and Ir(ppy)$_3$ and the PL spectra of a neat Alq$_3$ thin film and Alq$_3$:Ir(ppy)$_3$ thin films at 8 K are shown in Fig. 8.12 [30]. With an increase of the Ir(ppy)$_3$ concentration, the Alq$_3$ fluorescence intensity at around 520 nm decreases remarkably. This behavior cannot be explained only by the decrease in the Alq$_3$ concentration. For the 10-wt% Ir(ppy)$_3$-doped Alq$_3$ [Alq$_3$:Ir(ppy)$_3$ (10 wt%)] thin film, a weak emission of around 610 nm appeared at the lower energy shoulder of the fluorescence peak. For the Alq$_3$:Ir(ppy)$_3$ (50 wt%) thin film, a vibronic-structured emission in the wavelength range from 600 to 800 nm becomes dominant. This strong red emission is completely different from the Ir(ppy)$_3$ phosphorescence, of which the emission peak lies around 610 nm as shown earlier in Fig. 8.3. The energy at the shortest wavelength shoulder of the PL spectra indicated by the arrows in Fig. 8.12(b) was estimated to be 2.03 eV. This energy is close to the theoretical triplet energy (2.13 eV) of Alq$_3$, which was reported by Martin et al. [54] from time-dependent density-functional calculations. It is also comparable to the triplet energy (2.0 eV) estimated by Baldo and Forrest [17], and the energies obtained from time-resolved phosphorescence measurements by Burrows et al. [48] and Cölle et al. [50–53]. Therefore, this red emission can be
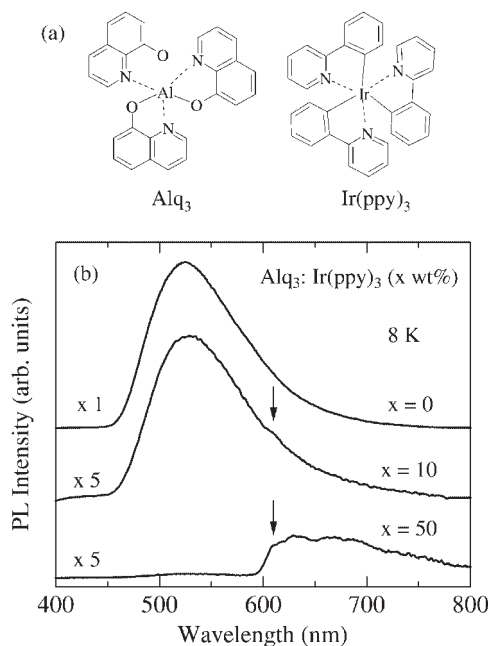
Fig. 8.12 (a) Chemical structures of Alq$_3$ and Ir(ppy)$_3$. (b) Photoluminescence spectra of neat Alq$_3$ thin film and 10-wt% and 50-wt% Ir(ppy)$_3$-doped Alq$_3$ thin films at 8 K. Arrows indicate the highest energy peak of the photoluminescence spectra corresponding to the triplet energy of Alq$_3$.

assigned to the phosphorescence from Alq$_3$ in the Alq$_3$:Ir(ppy)$_3$ thin film. It should be noted that ΔG for the Alq$_3$:Ir(ppy)$_3$ system is about +0.4 eV, which is about 4 times larger than that in endothermic CBP:FIrpic system.

The time-resolved PL spectra of the Alq$_3$:Ir(ppy)$_3$ (10 wt%) thin film with different delay times at 8 K is shown in Fig. 8.13 [30]. Immediately after pulsed photoexcitation, the Alq$_3$ fluorescence was extremely strong and dominant at around 520 nm. At a delay time of 300 μs, as shown in Fig. 8.13 (bottom), only the red phosphorescence from Alq$_3$ was observed, and its lifetime was estimated to be 5.3 ms. From an analysis of the diffusion length in Alq$_3$:PtOEP, assuming nondispersive transport, a lifetime of 25 ± 15 μs was estimated for the triplet states in Alq$_3$ at room temperature [17]. However, longer lifetimes of 8.1 ± 0.5 ms at 30 K from transient EL measurements in Alq$_3$-based OLEDs [51] and 9.3 ± 0.5 ms at 20 K from transient PL ones in amorphous thin films [52, 53] were reported. These lifetimes are comparable to the experimental results we obtained at 8 K. This suggests that there is strong temperature dependence of the phosphorescence lifetime due to triplet hopping and quenching sites at higher temperatures. With a 50-μs delay, both green and red emissions were detected. For the green emission, a PL decay profile, consisting of not only a fast component but also a slow one with weak
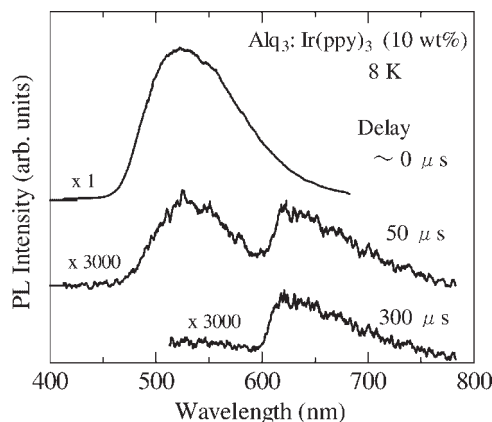
Fig. 8.13 Time-resolved photoluminescence spectra with different delay times for 10-wt% Ir(ppy)$_3$-doped Alq$_3$ thin film at 8 K. Gate time was about 1 µs.
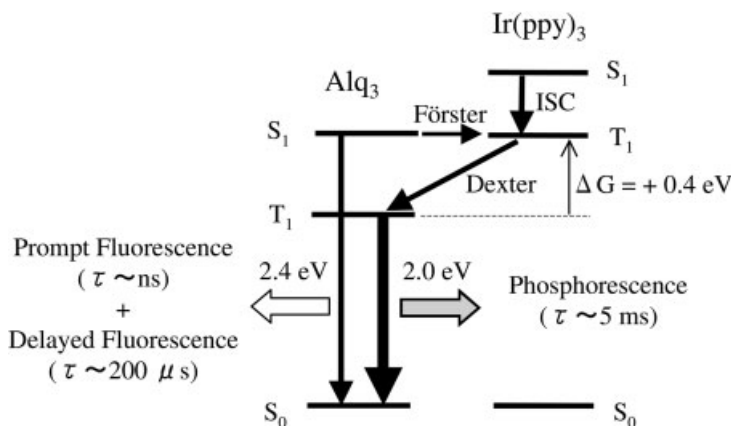
Fig. 8.14 Energy-level scheme of singlet excited state (S$_1$), triplet excited states (T$_1$), and singlet ground states (S$_0$) in Alq$_3$ and Ir(ppy)$_3$ and energy-transfer and light-emission processes.

intensity, was observed. Their lifetimes were estimated to be 12 ns and about 200 µs, respectively. The fast decay component is due to the prompt fluorescence from Alq$_3$, and the slow decay component is due to the so-called P-type of delayed fluorescence from Alq$_3$. This delayed fluorescence occurs as a result of the annihilation of two triplet excitons, T–T annihilation, and is therefore a bimolecular process [51–53, 55, 56]. Thus, this observation of delayed fluorescence is also evidence for the formation of emissive triplet excitons, as discussed later.

We now discuss the energy-transfer and light-emission mechanisms in Alq$_3$: Ir(ppy)$_3$ thin films. Figure 8.14 shows the schematic energy level scheme of the
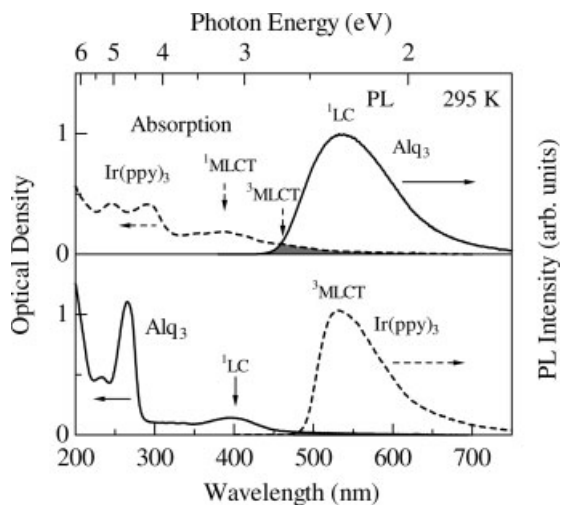
Fig. 8.15 Absorption and photoluminescence spectra of neat Alq$_3$ (solid lines) and neat Ir(ppy)$_3$ (broken lines) thin films at 295 K. Film thickness of samples was 50 nm.

S$_1$, T$_1$, and S$_0$ in Alq$_3$ and Ir(ppy)$_3$ and the light-emission processes [30, 31]. After photoexcitation, both the S$_1$ in Alq$_3$ and the S$_1$ in Ir(ppy)$_3$ are generated. Consequently, fluorescence promptly occurs from the Alq$_3$. The absorption and PL spectra of neat Alq$_3$ and neat Ir(ppy)$_3$ thin films at 295 K are shown in Fig. 8.15 [30]. The electronic transitions responsible for the Ir(ppy)$_3$ luminescence result from ^{3}MLCT states [24–26]. As shown in the gray-shaded regions of Fig. 8.15, the spectral overlap between the S$_1 \rightarrow$S$_0$ fluorescence band of the LC singlet (^{1}LC) states in Alq$_3$ and the S$_0 \rightarrow$T$_1$ absorption band of the ^{3}MLCT states in Ir(ppy)$_3$ is much larger than that between the T$_1 \rightarrow$S$_0$ phosphorescence band of the ^{3}MLCT states in Ir(ppy)$_3$ and the S$_0 \rightarrow$S$_1$ absorption band of the ^{1}LC states in Alq$_3$. This suggests that the S$_1$ in Alq$_3$ transfers to the T$_1$ in Ir(ppy)$_3$ through the long-range process of Förster energy transfer [11] by dipole–dipole coupling as shown in Fig. 8.14. On the other hand, Förster transfer from the T$_1$ in Ir(ppy)$_3$ to the S$_1$ in Alq$_3$ seems to be extremely inefficient. Furthermore, as shown in Fig. 8.15 (top), the spectral overlaps between the S$_1 \rightarrow$S$_0$ fluorescence band of the ^{1}LC states in Alq$_3$ and the S$_0 \rightarrow$S$_1$ absorption band of the ^{1}MLCT states in Ir(ppy)$_3$ are so small that Förster transfer from the S$_1$ in Alq$_3$ to the S$_1$ in Ir(ppy)$_3$ might not be active.

Here, we discuss the Förster transfer from the S$_1$ (donor) in Alq$_3$ to the T$_1$ (acceptor) in Ir(ppy)$_3$. The efficiency of the Förster transfer is usually described in terms of the Förster radius, i.e., the separation between donor and acceptor for which the probability of transfer is equal to the probability of recombination on the donor [9–11, 57]. The energy transfer rate k_{FET} is given by

$$k_{FET} = k_D(R_0 / R_{DA})^6, \tag{8.1}$$

where k_D is the radiative decay rate of the donor, R_{DA} is the donor–acceptor separation, and R_0 is the Förster transfer. The Förster radius R_0 can be calculated from the fluorescence spectrum of the donor and the absorption spectrum of the acceptor. The expected relation is [10, 57]

$$R_0^6 = \frac{9000(\ln 10)\kappa^2\varphi_D}{128\pi^5 N_A n^4}\int_0^\infty F_D(\lambda)\varepsilon_A(\lambda)\lambda^4 d\lambda, \tag{8.2}$$

where κ^2 is an orientation factor equal to 2/3 for a random donor–acceptor orientation, φ_D is the PL quantum yield of the pure donor, N_A is the Avogadro constant, n is the refractive index of the medium, λ is the wavelength, $F_D(\lambda)$ is the normalized donor fluorescence intensity, and $\varepsilon_A(\lambda)$ is the molar absorption coefficient of the acceptor. We measured the absorption spectrum of the chloroform solution of Ir(ppy)₃, and estimated R_0 to be 1.6 nm from Eq. (8.2) under the assumption that the PL quantum yield of Alq₃ is 0.20 [58]. This distance is shorter than the R_0 in the CBP:Ir(ppy)₃ system, reported as ~3 nm by Ramos–Ortiz et al. [59]. This suggests that the efficiency of the Förster transfer in an Alq₃:Ir(ppy)₃ system is lower than that in a CBP:Ir(ppy)₃ system. We also observed a shortening of the fluorescence lifetime from Alq₃ when the Ir(ppy)₃ concentration was increased. The lifetime at 8 K was estimated to be 12 and 4 ns, respectively, for the Alq₃:Ir(ppy)₃ (10 wt%) and Alq₃:Ir(ppy)₃ (50 wt%) thin films. For the neat Alq₃ thin film, the measured fluorescence lifetime was 25 ns at 8 K. Assuming that the nonradiative decay rate of the $S_1 \rightarrow S_0$ transition and the ISC decay rate of the $S_1 \rightarrow T_1$ transition are independent of the Ir(ppy)₃ concentration, the efficiency of the Förster transfer of the $S_1(\text{Alq}_3) \rightarrow T_1(\text{Ir(ppy)}_3)$ transition was estimated to be 0.52 and 0.84, respectively, for the Alq₃:Ir(ppy)₃ (10 wt%) and Alq₃:Ir(ppy)₃ (50 wt%) thin films [30]. This indicates that Förster transfer is promoted by increasing the Ir(ppy)₃ concentration, which leads to a remarkable decrease in the Alq₃ fluorescence intensity by doping with Ir(ppy)₃, as shown in Fig. 8.12.

For Ir(ppy)₃, nearly 100% conversion of the ISC from the S_1 to the T_1 occurs because of strong spin–orbit coupling. According to a report based on femtosecond time-resolved absorption measurements [60], the ISC relaxation time in Ir(ppy)₃ was very short, estimated to be 70–100 fs. The extremely efficient energy transfer from the T_1 in Ir(ppy)₃ to the T_1 in Alq₃ could explain why there is no observable phosphorescence from Ir(ppy)₃. This triplet energy transfer is ascribed to the short-range process of Dexter energy transfer [12], which requires an overlap of the molecular orbital of adjacent molecules. Time-resolved PL measurements were also performed for PC thin films co-doped with 20-wt% Alq₃ and 5-wt% Ir(ppy)₃, which were prepared by spin coating from chloroform solutions. In the PC:Alq₃,Ir(ppy)₃ thin films, not only fluorescence and phosphorescence emissions from Alq₃, but also phosphorescence emission from Ir(ppy)₃ were clearly observed. This indicates that Dexter transfer is reduced by the longer distance between Alq₃ and Ir(ppy)₃ due to the low concentrations of these molecules. Therefore, it is concluded that the phosphorescence from Alq₃ in the Alq₃:Ir(ppy)₃ thin film occurs via the two possible processes shown in Fig. 8.14: $S_1(\text{Alq}_3) \rightarrow T_1(\text{Ir(ppy)}_3) \rightarrow$

$T_1(Alq_3) \rightarrow S_0(Alq_3)$ and $S_1(Ir(ppy)_3) \rightarrow T_1(Ir(ppy)_3) \rightarrow T_1(Alq_3) \rightarrow S_0(Alq_3)$. Efficient triplet energy transfer from $Ir(ppy)_3$, in addition to Förster transfer to $Ir(ppy)_3$ and the rapid ISC in $Ir(ppy)_3$, enables us to observe the phosphorescence from Alq_3. $Ir(ppy)_3$ acts as a "triplet sensitizer" or "phosphorescent sensitizer" for Alq_3. Conversely, Alq_3 acts as a "triplet quencher" for $Ir(ppy)_3$. Baldo et al. [61] introduced the concept of triplet (phosphorescent) sensitization for improving the emission efficiency of fluorescent dye in small-molecule-based OLEDs. Recently, a triplet sensitizer was applied to polymer-based OLEDs [62] and white OLEDs [63, 64]. Even more recently, efficient triplet-sensitized photocyclization was reported for photochromic dithienylethene derivatives containing ruthenium metal units [65]. Our experimental results indicate that doping a triplet sensitizer with higher triplet energy into a fluorescent molecule is a useful method for characterizing the phosphorescence properties of an organic molecule, especially with regard to the triplet energy.

Next, we consider the mechanism of the delayed fluorescence shown in Fig. 8.13. If the energy of the S_1 is less than the sum of the energies of the colliding T_1, delayed fluorescence should occur. Since the delayed fluorescence originates from the $S_1 \rightarrow S_0$ transition, its spectral line shape is the same as that observed in cw PL measurements. This process, in which the S_1 is populated by T–T annihilation, excites one molecule in the S_1 state. This corresponding lifetime is much longer than that of the spontaneous fluorescence [51–53, 55, 56]. It can be written as

$$T_1 + T_1 \rightarrow S_0 + S_1 \rightarrow S_0 + S_0. \tag{8.3}$$

In this bimolecular process, the lifetime of the delayed fluorescence is half the value of the concomitant phosphorescence. However, the observed lifetime of the delayed fluorescence (about 200 µs) was much shorter than half the phosphorescence lifetime (5.3 ms). This significant shortening of the delayed-fluorescence lifetime, in addition to the extremely weak intensity, might be due to Förster transfer of the $S_1(Alq_3) \rightarrow T_1(Ir(ppy)_3)$ transition. Furthermore, the triplet sensitized T–T annihilation was observed as the deviation from the linearity of the phosphorescence intensity of Alq_3 to the excitation power [31].

Finally, we discuss the temperature dependence of the phosphorescence properties of Alq_3 in the Alq_3:$Ir(ppy)_3$ system. Figure 8.16 shows the PL spectra of the Alq_3:$Ir(ppy)_3$ (50 wt%) thin film at 8, 80, 150, and 295 K [30]. The PL spectra exhibited an extremely weak emission at around 520 nm due to Alq_3 fluorescence and a strong emission around 610 nm due to Alq_3 phosphorescence. Even at room temperature, the weak phosphorescence from Alq_3 could be detected using the triplet sensitizer. As shown in the inset of Fig. 8.16, the phosphorescence intensity decreased with an increase in temperature. Furthermore, we also observed strong temperature dependence of the phosphorescence lifetime, especially at temperatures above 100 K [30]. The phosphorescence lifetimes were estimated to be 3.1 ms at 100 K and 5.2 µs at 295 K, which is three-orders shorter than that at 8 K. These results indicated that the decrease in PL intensity at higher temperatures was
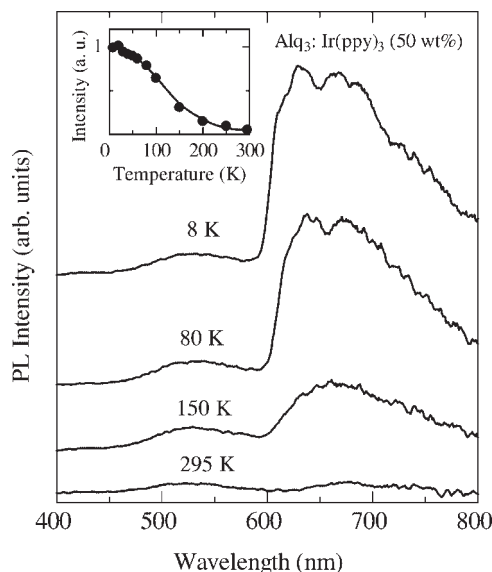
Fig. 8.16 Photoluminescence spectra of 50-wt% Ir(ppy)₃-
doped Alq₃ thin film at 8, 80, 150, and 295 K. Inset shows
temperature dependence of integrated red phosphorescence
intensity of Alq₃.

primarily due to thermally nonradiative processes, and that the temperature-dependent phosphorescence behavior of Alq_3 is quite different from that of $Ir(ppy)_3$ [34, 36, 38].

We also measured the PL spectra of the Alq_3:FIrpic and bis(2-phenylpyridinato-$N,C^{2'}$) rhodium (acetylacetonate) [$(ppy)_2Rh(acac)$] doped Alq_3 thin films to study the presence of the external heavy-atom effects. The triplet energy of FIrpic is in almost agreement with that of $(ppy)_2Rh(acac)$ (2.63 eV), and ΔG is estimated to be ~+0.6 eV. This leads to the small efficiency of the Förster transfer from the $S_1(Alq_3)$ to the T_1 of the phosphorescent material [FIrpic and $(ppy)_2Rh(acac)$]. The atomic number of core metal of FIrpic ([77]Ir) is much larger than that of $(ppy)_2Rh(acac)$ ([45]Rh). The intensities of observed phosphorescence from Alq_3 were extremely weak and of the same order between the above two thin films. This suggests that energy-transfer processes are dominant for determining the enhancement of the phosphorescence from Alq_3.

8.6
Energy Transfer Between Ir(ppy)₃ and BAlq: Observation of Thermal Equilibrium of Triplet Excited States

Recently, green phosphorescent OLEDs using $Ir(ppy)_3$ and a BAlq hole-blocking layer have achieved an external quantum efficiency of 5.6% over a half-operational
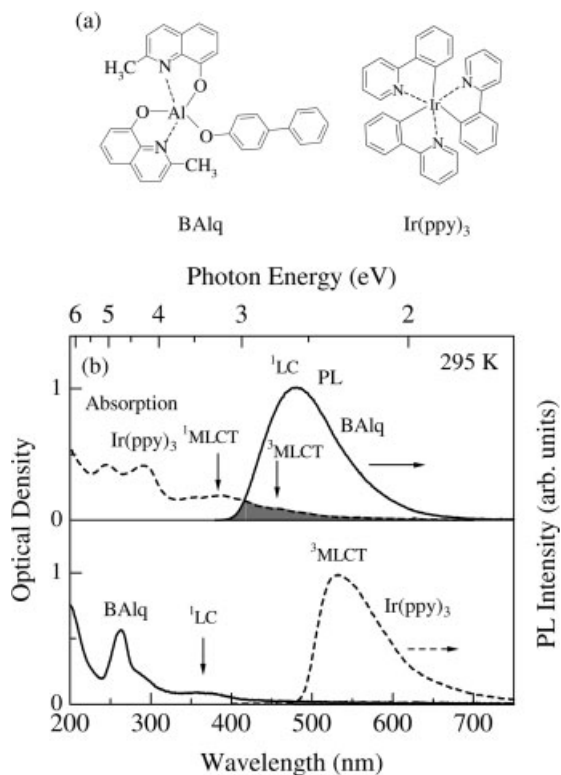
Fig. 8.17 (a) Chemical structures of BAlq and Ir(ppy)$_3$.
(b) Absorption and photoluminescence spectra of neat BAlq
(solid lines) and neat Ir(ppy)$_3$ (broken lines) thin films at
295 K. Film thickness of samples was 50 nm.

lifetime of 10 000 h at an initial luminance of 500 cd/m^2 [66]. Tsuji et al. [67]
reported that BAlq could also be utilized as a host material in OLEDs using the
red phosphorescent dopant of Btp$_2$Ir(acac), and demonstrated a prolonged opera-
tional lifetime (13 000 h) at an initial luminance of 179 cd/m^2 with an efficiency of
8.6%. Very recently, Chu et al. [68] characterized the electronic structure of BAlq
by using density functional theory (DFT) calculations, and estimated the triplet
energy to be 2.42 eV. However, there have been few reports on phosphorescence
in BAlq. In this section, we describe a study of the energy-transfer processes
between a fluorescent BAlq molecule and phosphorescent Ir(ppy)$_3$ one by charac-
terizing the PL properties of BAlq:Ir(ppy)$_3$ thin films over a wide temperature
range from 8 to 295 K.

The chemical structure of BAlq and Ir(ppy)$_3$ is shows in Fig. 8.17(a). The absorp-
tion and PL spectra of neat BAlq (solid lines) and neat Ir(ppy)$_3$ (broken lines) thin
films at 295 K are shown in Fig. 8.17(b). The fluorescence from BAlq at 480 nm is
ascribed to ^{1}LC π–π^* excited states. As shown in the gray-shaded area in Fig.
8.17(b), the spectral overlap between the fluorescence band of the ^{1}LC states in
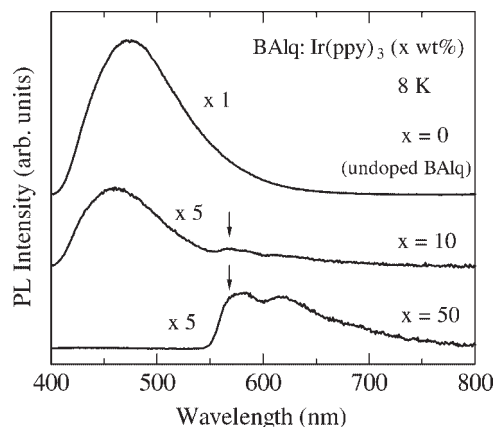
Fig. 8.18 Photoluminescence spectra of neat BAlq thin film and 10-wt% and 50-wt% Ir(ppy)₃-doped BAlq thin films at 8 K.

BAlq and the absorption band of the ^{3}MLCT states in Ir(ppy)$_3$ is much larger than that between the phosphorescence band of the ^{3}MLCT states in Ir(ppy)$_3$ and the absorption band of the ^{1}LC states in BAlq. This indicates that the S$_1$ in BAlq energetically transfers to the T$_1$ in Ir(ppy)$_3$ through Förster energy transfer. In contrast, Förster transfer from the T$_1$ in Ir(ppy)$_3$ to the S$_1$ in BAlq seems to be extremely inefficient. Furthermore, the small spectral overlap between the fluorescence band of the ^{1}LC states in BAlq and the absorption band of the ^{1}MLCT states in Ir(ppy)$_3$ suggests that Förster transfer from the S$_1$ in Alq$_3$ to the S$_1$ in Ir(ppy)$_3$ occurs only weakly.

The PL spectra of a neat BAlq thin film and BAlq:Ir(ppy)$_3$ thin films at Ir(ppy)$_3$ concentrations of 10 and 50 wt% at 8 K are shown in Fig. 8.18 [32]. The fluorescence intensity at 480 nm of the host BAlq drastically decreased as the concentration of Ir(ppy)$_3$ increased. In addition, the spectral peak blueshifted, which may result from the presence of polar Ir(ppy)$_3$. For the BAlq:Ir(ppy)$_3$ (50 wt%) thin film, the bluish green fluorescence emission from BAlq disappeared, and a vibronic-structured emission became dominant in the wavelength range from 550 to 800 nm. This yellow emission showed a rather slow transient decay, and the PL lifetime was estimated to be 16 ms at 8 K for the BAlq:Ir(ppy)$_3$ (50 wt%) thin film. This PL lifetime is much longer than the fluorescence lifetime of BAlq (39 ns at 8 K) and the phosphorescence lifetime of Ir(ppy)$_3$ (~40 μs at 8 K) [34, 36, 38]. Therefore, the yellow emission can be assigned to phosphorescence from BAlq; the triplet energy of BAlq is estimated to be 2.18 eV (shown by the arrows in Fig. 8.18) from the highest energy peak of the phosphorescence spectra. We also tried to detect phosphorescence from the neat BAlq thin film by using time-resolved PL spectroscopy at low temperatures. However, we were unable to observe any phosphorescence from the film using our measurement system. It was concluded that Ir(ppy)$_3$ has the potential to play an important role as a triplet sensitizer for BAlq, which is similar to the Alq$_3$:Ir(ppy)$_3$ system discussed earlier. Although the triplet
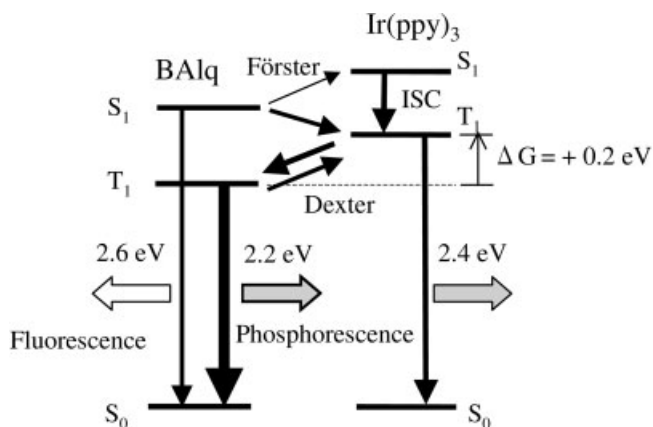
Fig. 8.19 Energy-level scheme of singlet excited (S_1), triplet excited (T_1), and singlet ground (S_0) states, and energy-transfer and light-emission processes in BAlq:Ir(ppy)$_3$ system.

energy we obtained is smaller than the theoretical value (2.42 eV) based on DFT calculations [68], it is consistent with the fact that BAlq can be utilized as a host material in red phosphorescent OLEDs using Btp$_2$Ir(acac) [67], which has a triplet energy of 2.0 eV [27, 28]. However, BAlq is not suitable for use as a host or hole-blocking material for blue and green phosphorescent OLEDs.

Next, we discuss the energy-transfer mechanism in a BAlq:Ir(ppy)$_3$ system and the reason for the enhancement of phosphorescence from BAlq. Figure 8.19 shows the energy-level scheme of the S_1, T_1, and S_0 in the BAlq:Ir(ppy)$_3$ system [32]. The S_1 in both BAlq and Ir(ppy)$_3$ is generated by photoexcitation. Fluorescence occurs in BAlq together with Förster transfers of the relatively efficient S_1(BAlq)→T_1(Ir(ppy)$_3$) transition and possibly the S_1(BAlq)→S_1(Ir(ppy)$_3$) transition. We estimated the Förster radius to be 2.4 nm from Eq. (8.2), assuming that the PL quantum yield of BAlq is 0.42 [58]. This distance is longer than the R_0 in a Alq$_3$:Ir(ppy)$_3$ system, which is 1.6 nm, indicating that the efficiency of the Förster transfer in the BAlq:Ir(ppy)$_3$ system is higher than that in the Alq$_3$:Ir(ppy)$_3$ system. This supports that the degree of fluorescence quenching in BAlq (Fig. 8.18) is larger than that in Alq$_3$ (Fig. 8.12). For Ir(ppy)$_3$, nearly 100% conversion of the rapid ISC from the S_1 to the T_1 occurs. Consequently, Dexter energy transfer of the T_1(Ir(ppy)$_3$)→T_1(BAlq) transition occurs, and phosphorescence from BAlq can be observed. This energy transfer is similar to that in the Alq$_3$:Ir(ppy)$_3$ thin films discussed earlier. Here, it should be noted that BAlq:Ir(ppy)$_3$ forms an endothermic system for the host (BAlq) to guest [Ir(ppy)$_3$] triplet energy transfer (the guest T_1 is higher than the host T_1), and that ΔG is about +0.2 eV, which is a half of that for the Alq$_3$:Ir(ppy)$_3$ system.

The PL spectra of the BAlq:Ir(ppy)$_3$ (50 wt%) thin film at several temperatures are shown in Fig. 8.20 [32]. The phosphorescence from BAlq becomes weaker and broader and redshifts with increasing temperature, primarily due to thermally
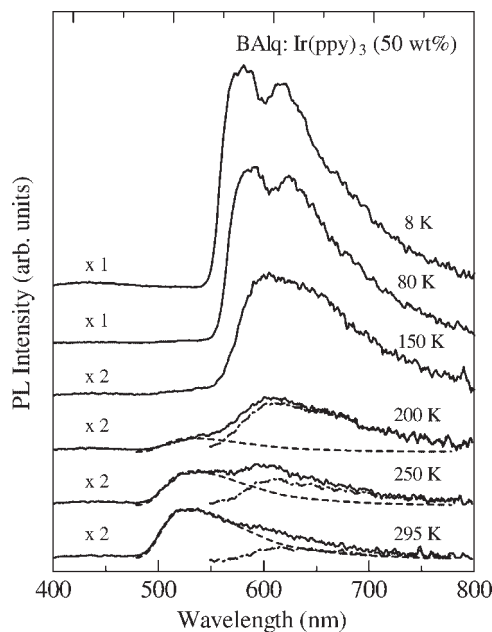
Fig. 8.20 Photoluminescence spectra of 50-wt% Ir(ppy)₃-doped BAlq thin films at a range of temperatures from 8 to 295 K.

nonradiative processes. However, if we focus on the temperature region from 200 to 295 K, we can see a change in the PL spectra. Both yellow phosphorescence from BAlq (indicated by dash-dotted lines) and green emission (indicated by broken lines) were observed. The green emission became dominant with increasing temperature, which suggests that the energy transfer is more active at higher temperatures. In an endothermic triplet–triplet emitter system, the population of the highly energetic T_1 in the guest increases with increasing temperature because of thermally promoted triplet energy transfer from the host to the guest. Moreover, the radiative decay rate of the T_1 in Ir(ppy)₃ is much faster than that of the T_1 in BAlq. Therefore, the green PL band can be assigned to phosphorescence from the T_1 in Ir(ppy)₃ which has been thermally transferred from the T_1 in BAlq.

Finally, we discuss the temperature dependence of the PL intensity of the BAlq: Ir(ppy)₃ system. Figure 8.21 shows the temperature dependence of integrated phosphorescence intensity of BAlq [I_P(BAlq)] and Ir(ppy)₃ [I_P(Ir(ppy)₃)] in the BAlq: Ir(ppy)₃ (50 wt%) thin film. The inset shows the ratio of I_P(Ir(ppy)₃) to I_P(BAlq) as function of inverse of temperature (T^{-1}) in the temperature range from 200 to 295 K. It is evident from this figure that the logarithm of the intensity ratio is proportional to T^{-1}. Therefore, we assume the following relation:

$$I_P(\text{Ir(ppy)}_3)/I_P(\text{BAlq}) \propto \exp(-E_C/k_B T), \tag{8.4}$$
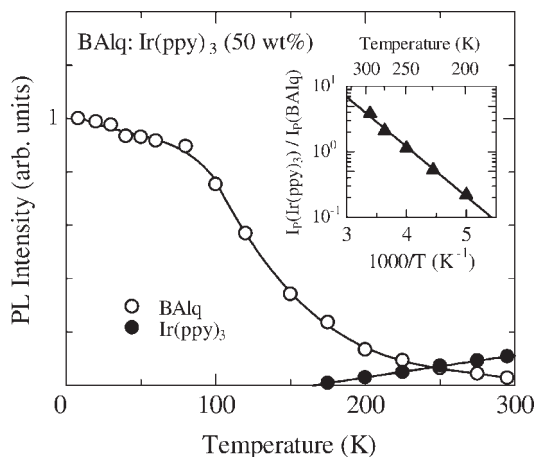
Fig. 8.21 Temperature dependence of integrated phosphorescence intensities of BAlq [○, I_P(BAlq)] and Ir(ppy)$_3$ [●, I_P(Ir(ppy)$_3$)] in 50-wt% Ir(ppy)$_3$-doped BAlq thin film. Inset shows ratio (▲) of I_P(Ir(ppy)$_3$) to I_P(BAlq) as function of inverse of temperature (T^{-1}) at a range of temperatures from 200 to 295 K.

where E_C is the characteristic energy of the temperature dependence and k_B is the Boltzmann constant. The solid line indicates the result of least squares fitting. E_C is estimated from the slope of the solid line to be 0.16 eV, and is comparable to ΔG corresponding to the difference in the triplet energy between Ir(ppy)$_3$ and BAlq (~+0.2 eV). We also observed similar PL behavior for a BAlq:Ir(ppy)$_3$ (75 wt%) thin film; E_C was estimated to be 0.16 eV. In general, PL intensities are functions of the density of the excited states and radiative decay rate [69]. The almost agreement of E_C and ΔG suggests that the radiative decay rates do not depend on temperature, and that the T$_1$ in BAlq is in thermal equilibrium with the T$_1$ in Ir(ppy)$_3$ at temperatures above ~200 K. Furthermore, ΔG for a BAlq:Ir(ppy)$_3$ system is larger than that for a CBP:FIrpic system (ΔG=+0.09 eV) [16, 19, 20, 23, 33] or TPD:Ir(ppy)$_3$ system (+0.07 eV) [34, 35, 70, 71], but smaller than that in the Alq:Ir(ppy)$_3$ system (~+0.4 eV) [30, 31]. The difference in ΔG for an endothermic triplet–triplet system supports that the temperature at which the emission from the phosphorescent guest is dominant in the BAlq:Ir(ppy)$_3$ system is higher than that in the CBP:FIrpic system (above ~80 K) [33], and that the emission from the phosphorescent guest does not appear even at room temperature in an Alq$_3$:Ir(ppy)$_3$ system [30].

8.7
Conclusion

We studied energy-transfer processes between phosphorescent guests and fluorescent hosts. Energy transfer plays an important role in the confinement of triplet

energy on the phosphorescent guest, which determines emission efficiency in OLEDs. In the CBP:FIrpic thin film, where the triplet energy of FIrpic is 0.09 eV higher than that of CBP ($\Delta G = +0.09$ eV), both exothermic triplet energy transfer from FIrpic to CBP and endothermic triplet energy transfer from CBP and FIrpic were observed as the unique temperature dependence of the PL intensity in addition to a complicated decay process. The phosphorescence intensity of the CDBP:FIrpic thin film, in which the triplet energy of FIrpic is 0.15 eV lower than that of CDBP ($\Delta G = -0.15$ eV), showed no temperature dependence. This suggests that the triplet energy was efficiently confined on the FIrpic molecules in the CDBP host, and that CDBP is an efficient host molecule for blue phosphorescent FIrpic. As a result, the external quantum efficiency of an OLED based on CDBP:FIrpic is twice as high as that of an OLED based on CBP:FIrpic. We also observed enhancement of the phosphorescence from Alq_3 and BAlq in Alq_3:Ir(ppy)$_3$ ($\Delta G \sim +0.4$ eV) and BAlq:Ir(ppy)$_3$ ($\Delta G \sim +0.2$ eV) thin films. The triplet energies (phosphorescence lifetimes) were accurately determined to be 2.03 eV (5.3 ms) for Alq_3 and 2.18 eV (16 ms) for BAlq. We demonstrated that the energy transfer between Alq_3 or BAlq and Ir(ppy)$_3$ enables us to characterize the phosphorescence properties of Alq_3 or BAlq, and that Ir(ppy)$_3$ plays an important role as a triplet sensitizer for Alq_3 and BAlq. From these spectroscopic studies, it was revealed that the energy-transfer processes and the associated PL behaviors are mainly determined by the difference in the triplet energy between the guest and host molecules.

This work will be helpful in the development of new phosphorescent guest molecules, host molecules, and guest–host systems for highly efficient OLEDs.

Acknowledgments

References

1 C. W. Tang, S. A. VanSlyke, *Appl. Phys. Lett.* **1987**, *51*, 913.

2 C. Adachi, S. Tokito, T. Tsutsui, S. Saito, *Jpn. J. Appl. Phys.* **1988**, *27*, L269.

3 J. H. Burroughes, D. D. C. Bradley, A. R. Brown, R. N. Marks, K. Mackay, R. H. Friend, P. L. Burns, A. B. Holmes, *Nature* **1990**, *347*, 539.

4 M. A. Baldo, D. F. O' Brien, Y. You, A. Shoustikov, S. Sibley, M. E. Thompson, S. R. Forrest, *Nature* **1998**, *395*, 151.

5 M. A. Baldo, S. Lamansky, P. E. Burrows, M. E. Thompson, S. R. Forrest, *Appl. Phys. Lett.* **1999**, *75*, 4.

6 T. Tsutsui, M. J. Yang, M. Yahiro, K. Nakamura, T. Watanabe, T. Tsuji, Y. Fukuda, T. Wakimoto, S. Miyaguchi, *Jpn. J. Appl. Phys.* **1999**, *38*, L1502.

7 L. S. Hung, C. H. Chen, *Mater. Sci. Eng. R* **2002**, *39*, 143.

8 E. Holder, B. M. W. Langeveld, U. S. Schubert, *Adv. Mater.* **2005**, *17*, 1109.

9 N. J. Turro, *Modern Molecular Photochemistry* (University Science Books, New York, **1991**).

10 J. R. Lakowicz, *Principles of Fluorescence Spectroscopy* (Second Edition, Plenum, New York, **1999**).

11 T. Förster, *Discuss Faraday Soc.* **1959**, *27*, 7.

12 D. L. Dexter, *J. Chem. Phys.* **1953**, *21*, 836.

13 R. C. Hughes, Z. G. Soos, *J. Chem. Phys.* **1975**, *63*, 1122.

14 M. A. Baldo, D. F. O'Brien, M. E. Thompson, S. R. Forrest, *Phys. Rev. B* **1999**, *60*, 14422.

15 M. Ikai, S. Tokito, Y. Sakamoto, T. Suzuki, Y. Taga, *Appl. Phys. Lett.* **2001**, *79*, 156.

16 Y. Kawamura, K. Goushi, J. Brooks, J. J. Brown, H. Sasabe, C. Adachi, *Appl. Phys. Lett.* **2005**, *86*, 071104.

17 M. A. Baldo, S. R. Forrest, *Phys. Rev. B* **2000**, *62*, 10958.

18 M. Baldo, M. Segal, *Phys. Status Solidi A* **2004**, *201*, 1205.

19 R. J. Holmes, S. R. Forrest, Y. J. Tung, R. C. Kwong, J. J. Brown, S. Garon, M. E. Thompson, *Appl. Phys. Lett.* **2003**, *82*, 2422.

20 S. Tokito, T. Iijima, Y. Suzuri, H. Kita, T. Tsuzuki, F. Sato, *Appl. Phys. Lett.* **2003**, *83*, 569.

21 I. Tanaka, M. Suzuki, S. Tokito, *Jpn. J. Appl. Phys.* **2003**, *42*, 2737.

22 I. Tanaka, S. Tokito, *Jpn. J. Appl. Phys.* **2004**, *43*, 7733.

23 C. Adachi, R. C. Kwong, P. Djurovich, V. Adamovich, M. A. Baldo, M. E. Thompson, S. R. Forrest, *Appl. Phys. Lett.* **2001**, *79*, 2082.

24 K. A. King, P. J. Spellane, R. J. Watts, *J. Am. Chem. Soc.* **1985**, *107*, 1431.

25 W. J. Finkenzeller, H. Yersin, *Chem. Phys. Lett.* **2003**, *377*, 299.

26 A. Tsuboyama, H. Iwawaki, M. Furugori, T. Mukaide, J. Kamatani, S. Igawa, T. Moriyama, S. Miura, T. Takiguchi, S. Okada, M. Hoshino, K. Ueno, *J. Am. Chem. Soc.* **2003**, *125*, 12971.

27 C. Adachi, M. A. Baldo, S. R. Forrest, S. Lamansky, M. E. Thompson, R. C. Kwong, *Appl. Phys. Lett.* **2001**, *78*, 1622.

28 S. Lamansky, P. Djurovich, D. Murphy, F. Abdel-Razzaq, H. E. Lee, C. Adachi, P. E. Burrows, S. R. Forrest, M. E. Thomson, *J. Am. Chem. Soc.* **2001**, *123*, 4304.

29 R. Ballardini, G. Varani, M. T. Indelli, F. Scandola, *Inorg. Chem.* **1986**, *25*, 3858.

30 I. Tanaka, Y. Tabata, S. Tokito, *Phys. Rev.* **2005**, *B71*, 205207.

31 I. Tanaka, S. Tokito, *J. Appl. Phys.* **2005**, *97*, 113532.

32 I. Tanaka, Y. Tabata, S. Tokito, *J. Appl. Phys.* **2006**, *99*, 073501.

33 I. Tanaka, Y. Tabata, S. Tokito, *Chem. Phys. Lett.* **2004**, *400*, 86.

34 K. Goushi, R. Kwong, J. J. Brown, H. Sasabe, C. Adachi, *J. Appl. Phys.* **2004**, *95*, 7798.

35 T. Tsuboi, N. Aljaroudi, *Phys. Rev. B* **2005**, *72*, 125109.

36 K. Goushi, Y. Kawamura, H. Sasabe, C. Adachi, *Jpn. J. Appl. Phys.* **2004**, *43*, L937.

37 I. Tanaka, S. Tokito, *Appl. Phys. Lett.* **2005**, *87*, 173509.

38 I. Tanaka, Y. Tabata, S. Tokito, *Jpn. J. Appl. Phys.* **2004**, *43*, L1601.

39 S. Pankasem, J. Kuczynski, J. K. Thomas, *Macromolecules* **1994**, *27*, 3773.

40 M. A. Baldo, C. Adachi, S. R. Forrest, *Phys. Rev.* **2000**, *B62*, 10967.

41 A. Curioni, M. Boero, W. Andreoni, *Chem. Phys. Lett.* **1998**, *294*, 263.

42 R. Priestley, A. D. Walser, R. Dorsinville, *Opt. Commun.* **1998**, *158*, 93.

43 K. C. Tang, P. W. Cheng, V. Chien, C. P. Cheng, P. Y. Cheng, I. C. Chen, *J. Chin. Chem. Soc.* **2000**, *47*, 875.

44 V. V. N. R. Kishore, K. L. Narasimhan, N. Periasamy, *Phys. Chem. Chem. Phys.* **2003**, *5*, 1386.

45 I. Akai, K. Harai, K. Kouno, T. Karasawa, *J. Lumin.* **2004**, *108*, 11.

46 M. Braun, J. Gmeiner, M. Tzolov, M. Coelle, F. D. Meyer, W. Milius, H. Hillebrecht, O. Wendland, J. U. von Schütz, W. Brütting, *J. Chem. Phys.* **2001**, *114*, 9625.

47 R. J. Curry, W. P. Gillin, *J. Appl. Phys.* **2000**, *88*, 781.

48 H. D. Burrows, M. Fernandes, J. S. de Melo, A. P. Monkman, S. Navaratnam, *J. Am. Chem. Soc.* **2003**, *125*, 15310.

49 S. S. Jayanthi, P. Ramamurthy, *J. Phys. Chem.* **1998**, *A102*, 511.

50 M. Cölle, W. Brütting, *Phys. Status Solidi* **2004**, *A201*, 1095.

51 M. Cölle, C. Gärditz, *Appl. Phys. Lett.* **2004**, *84*, 3160.

52 M. Cölle, C. Gärditz, M. Braun, *J. Appl. Phys.* **2004**, *96*, 6133.

53 M. Cölle, C. Gärditz, *J. Lumin.* **2004**, *110*, 200.

54 R. L. Martin, J. D. Kress, I. H. Campbell, D. L. Smith, *Phys. Rev.* **2000**, *B61*, 15804.

55 C. A. Parker, C. G. Hatchard, *Proc. Roy. Soc.* **1962**, *A269*, 574.

56 J. B. Birks, G. F. Moore, I. H. Munro, *Spectrochim. Acta* **1966**, *22*, 323.

57 B. P. Lyons, A. P. Monkman, *Phys. Rev.* **2005**, *B71*, 235201.

58 Y. Kawamura, H. Sasabe, C. Adachi, *Jpn. J. Appl. Phys.* **2004**, *43*, 7729.

59 G. Ramos-Ortiz, Y. Oki, B. Domercq, B. Kippelen, *Phys. Chem. Chem. Phys.* **2002**, *4*, 4109.

60 K. C. Tang, K. L. Liu, I. C. Chen, *Chem. Phys. Lett.* **2004**, *386*, 437.

61 M. A. Baldo, M. E. Thompson, S. R. Forrest, *Nature* **2000**, *403*, 750.

62 G. He, S. C. Chang, F. C. Chen, Y. Li, Y. Yang, *Appl. Phys. Lett.* **2002**, *81*, 1509.

63 G. Cheng, F. Li, Y. Duan, J. Feng, S. Liu, S. Qiu, D. Lin, Y. Ma, S. T. Lee, *Appl. Phys. Lett.* **2003**, *82*, 4224.

64 G. Lei, L. Wang, Y. Qiu, *Appl. Phys. Lett.* **2004**, *85*, 5403.

65 R. T. F. Jukes, V. Adamo, F. Hartl, P. Belser, L. D. Cola, *Inorg. Chem.* **2004**, *43*, 2779.

66 R. C. Kwong, M. R. Nugent, L. Michalski, T. Ngo, K. Rajan, Y. J. Tung, M. S. Weaver, T. X. Zhou, M. Hack, M. E. Thompson, S. R. Forrest, J. J. Brown, *Appl. Phys. Lett.* **2002**, *81*, 162.

67 T. Tsuji, S. Kawami, S. Miyaguchi, T. Naijo, T. Yuki, S. Matsuo, H. Miyazaki, *Society for Information Display 2004 International Symposium (SID 04) Digest of Technical Papers*, Vol. **35**, p. 900.

68 T. Y. Chu, Y. S. Wu, J. F. Chen, C. H. Chen, *Chem. Phys. Lett.* **2005**, *404*, 121.

69 M. Nakayama, I. Tanaka, I. Kimura, H. Nishimura, *Jpn. J. Appl. Phys.* **1990**, *29*, 41.

70 J. Kalinowski, W. Stampor, M. Cocchi, D. Virgili, V. Fattori, P. Di Marco, *Chem. Phys.* **2004**, *297*, 39.

71 J. Kalinowski, J. Mezyk, F. Meinardi, R. Tubino, M. Cocchi, D. Virgili, *J. Appl. Phys.* **2005**, *98*, 063532.

10
Electroluminescence from Metal-Containing Polymers and Metal Complexes with Functional Ligands

Chris Shuk Kwan Mak, and Wai Kin Chan

The applications of metal-containing polymers and molecular metal complexes with functional ligands in light-emitting devices are presented. Discussion will be focused on ruthenium and rhenium complexes with multifunctional ligands. For the molecular complexes, the ligands are capable of transporting both electron and hole carriers, and the metal centers are responsible for light emission. The physical properties of the complexes can be fine tuned by varying the structures of the ligands. For the polymers, the metal complexes can be incorporated into the polymer on the main chain or side chain. Good quality polymer thin films can be obtained by simple solution processing methods. Some of the polymers exhibit modest hole and electron carrier mobilities, which are dependent on the metal complex content in the polymers. The design approach enjoys the advantages of incorporating both charge-transporting ligands and light-emitting metal complex in a single molecule.

10.1
Introduction

An organic light-emitting diode (OLED) is a solid-state electric-to-luminous energy conversion device comprising a layer or a series of thin organic films sandwiched between two electrodes. The electroluminescence (EL) originates from the radiative decay of an exciton, which is generated from electron and hole recombination in the emissive layer. The thickness of all the combined active layers is only of the order of 100 nm. It has been a subject of extensive research of academic interests and has recently made its debut in commercial applications for flat panel display and solid-state lighting. Numerous potential advantages, such as thin profile, high brightness, power efficiency, wide viewing angle, etc., are leading OLEDs, an attractive alternative to LCDs. The first electroluminescence observed from organic substances was reported for anthracene single crystals in the 1960s [1]. These devices suffered from a high driving voltage and a short lifetime. Tang and VanSlyke of Kodak reported the unprecedented electroluminescent properties of tris(8-hydroxy-quinoline) aluminum (Alq$_3$) in the heterostructure bilayered OLED device in the

late 80s [2]. Since then, the design and synthesis of new electroluminescent materials has received unabated attention. Shortly afterward, the Cambridge group developed the first polymer-based OLED [3]. This important breakthrough has opened up the opportunity of fabricating low cost, large area panel displays. Within two decades, the device efficiency and lifetime have been improved at an astonishing pace by the evaluation of novel light-emitting materials and device architectures.

10.2
Traditional Materials Used in OLEDs

10.2.1
Molecular Materials

The electro-active materials used in OLEDs can be broadly classified into two main categories: small molecules and polymers. Most of the early examples of materials for OLEDs were based on pure organic systems or complexes of main group metallic elements. Guest–host systems were employed for the small molecule devices in order to maximize the device performance [4]. In addition, the driving voltage can be lowered by efficient charge transport from the host (matrix) to the guest (dopant) molecules and the stability of the device can also be increased [5–11]. The combination of the guest–host system in the emissive layer is crucial because it is essential to enhance the trapping of excitons by the guest emitters and to minimize the emission quenching by the guest molecules [12–15]. Detailed discussions on using organometallic complexes as guest molecules in OLEDs will be given in the later sections.

10.2.2
Polymeric Materials

Organic polymers are classically defined as electric insulators and colloquially known as "plastics." They have been widely used because of their excellent mechanical, chemical, and electrically insulating properties. After the breakthrough in the 1970s', organic π-conjugated polymers were found to be promising candidates for electrical conductors [16, 17]. Light has been shedding on the development of polymer-based optoelectronics, since the importance of this research area has been recognized by awarding the Nobel Prize to MacDiarmid, Heeger, and Shirakawa in 2000 for their discovery and contribution in conducting polymers. Research and development on light-emitting polymers have grown rapidly as a result of the feasibility of tailor making their chemical and physical properties to meet the demands of new applications. Although the OLEDs based on small phosphorescent molecules exhibit high efficiencies, the materials have to be deposited as thin film by the complex and expensive techniques, in which the device fabrication condition requires high vacuum and control temperature. In contrast, light-emitting conjugated polymers can be readily deposited from solution as thin films over large areas by spin coating, doctor blade technique, or ink-jet printing. The size of the device
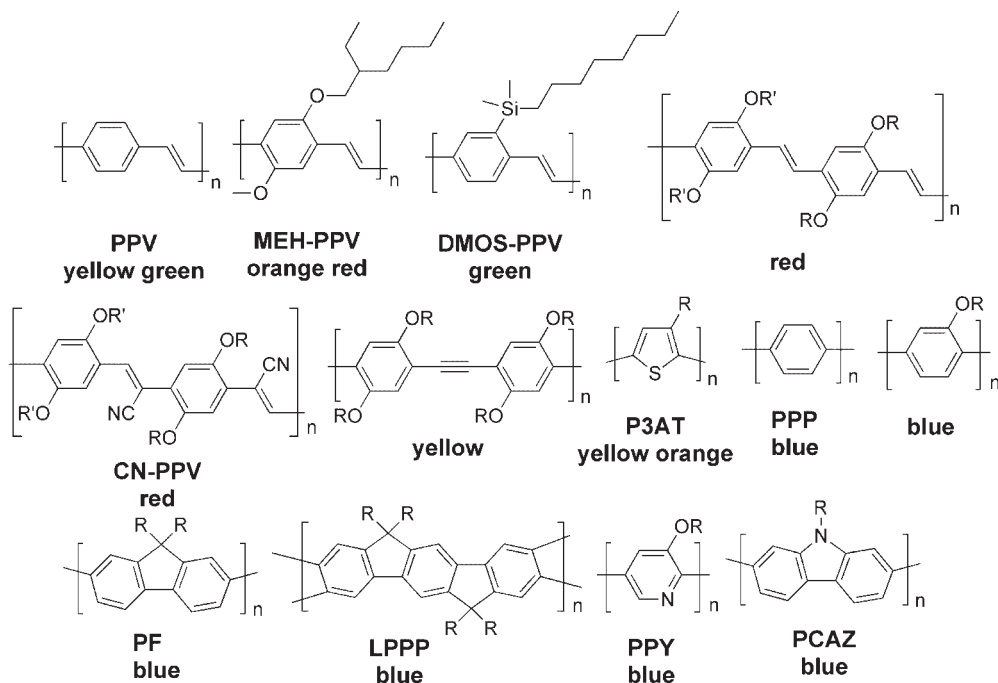
Fig. 10.1 Examples of some organic light-emitting polymers.

is virtually unlimited and the large area two-dimensional multilayer device can be manufactured by roll-to-roll coating technologies. Therefore, conjugated polymers are the promising materials for LED or other photovoltaic devices, as they can provide an easier and cheaper way for the device fabrication. The discovery of electroluminescence from conjugated polymer by Friend and Holmes in 1990 [3] has provided a new impetus toward the intensive development of the polymer-based OLEDs. Different emission colors from organic polymers are now accessible throughout the visible spectrum with readily tunable properties such as thermal stability, HOMO–LUMO separation energy, and emission monochromaticity (Fig. 10.1) [18]. The first example of polymer-based EL was observed with the yellowish green light-emitting poly (p-phenylene vinylene) (PPV). However, this polymer is intractable and insoluble, and a precursor polymer synthetic route needs to be adopted to rectify the dilemma [19]. Subsequently, research in this area was focused on the development of process-like conjugated polymers. Several groups have reported soluble derivates of PPV synthesized by copolymerization of monomers that are soluble, or modifying the substituents on the polymer backbone [20–22]. Despite the processing ability of the polymers, the electrical properties of PPV, such as HOMO/LUMO levels, charge mobility, and electron affinity, etc., can also be fine tuned in order to optimize the device performance [23–28]. Derivatives of PPV are good emitting materials in the green to red region. However, efficient blue light-emitting polymers are still sparse. Early studies on the polymers with high

emission energy were mainly focused on the violet–blue emitting poly(*p*-phenylene) [29]. Nevertheless, the polymer suffered from poor solubility. Although the introduction of solubilizing groups has improved the processing ability, reduction in photoluminescent quantum yield (PLQY) arisen from the undesired blue shift of the emission color to the violet region due to twisting of the polymer backbone. Another blue-emitting polymer polyfluorene has brought up substantial interest due to their impressively high PLQY, high thermal stability, and excellent solubility in common organic solvents [30–32]. The homopolymer, copolymers, and their derivatives are the most promising light-emitting polymers for red–green–blue (RGB) display applications [33]. The best performing polyfluorene-based polymer light-emitting diode (PLED) was reported to have external quantum efficiencies (η_{ext}) of 2, 6, and 3%, and power conversion efficiency (PCE) of 3.4, 20, and 1.2 lm W^{-1} for blue, green, and red colors, respectively [34, 35]. The device operating lifetime of more than 20 000 h is needed for most of the applications. Although this has been achieved for the green and red devices, the lifetime of the blue devices is still a challenge. In 2005, Cambridge Display Technology (CDT) announced the latest development of high efficiency, low driving voltage, and a blue PLED with lifetime over 100 000 h at 100 cd m^{-2}. This important breakthrough has brought full color PLED displays to be realized.

10.3
Development of Phosphorescent Materials for OLEDS

Efficient light emission process cannot be achieved in most of the pure organic materials because only spin-conserved transitions (25% quantum efficiency according to spin statistics) are allowed due to the spin selection rule. The majority of excitons formed in the OLEDs are in triplet state (75%) and the energy formed from this state will be dissipated as heat or vibrational energy. As a consequence, the EL quantum efficiency is severely limited. Therefore, in the past 10 years, research in OLED materials has been focused on the development of materials that emit light from the triplet excited state. By utilizing such "phosphorescent" molecules, the luminescence efficiency of molecules can exceed the theoretical limit of 25% imposed on the singlet emission. Excellent and comprehensive discussions on the mechanisms of utilizing triplet emitters in OLEDs have been delivered in several literatures [36, 37].

Phosphorescent light-emitting materials are mainly divided into two main categories: molecular and polymeric materials. Molecular metal complexes have well-defined structures. They can usually be obtained in highly pure form and can be processed by thermal evaporation method. For polymeric materials, the structures of the molecules are not well-defined due to the polydispersity of the polymer molecules. In addition, intrinsic defects may also be present in the molecules. However, polymeric materials usually have higher mechanical strength and can form free standing films. They can also be processed conveniently by solution methods such as spin coating, drop casting, ink-jet printing, or spraying techniques.

10.3.1
Small Molecules – Pure Organic Dyes and Organometallic Complexes

In the literature, molecular phosphorescent complexes are mainly based on lanthanide metals and some heavy transition metals. Lanthanide compounds usually exhibit sharp emission bands and excellent monochromaticity, which result from the intra *f–f* transitions. Terbium and europium complexes [39–43] are the commonly used phosphors in OLEDs. Some examples are shown in Fig. 10.2. Other lanthanide ions such as thulium, neodymium, etc., were also employed as blue or infrared emitters in OLEDs [38]. Different types of ligands have been used to vary the HOMO/LUMO energy levels and improve the charge-transporting properties and stabilities of the materials. The device efficiency, lifetime, and turn-on voltage can be optimized considerably with suitable metal–ligand combination [44].

Another important type of molecular phosphorescent complexes are based on transition metal complexes such as Ru, Os, Re, Pt, Ir, or Au. These complexes were frequently employed as phosphors because their excited lifetimes are mostly in the microsecond regime and the PLQY are generally high in contrast to lanthanide compounds. The investigation of triplet emitters as active materials in OLEDs has spurred the worldwide interest since the internal quantum efficiency can be raised from 25% to near 100% [45, 46]. Transition metal complexes based on neutral platinum [47–49] and iridium complexes are the well-developed phosphors and have attracted considerable attention in photonic applications due to their excellent quantum efficiencies. Their emission energies can be fine tuned over
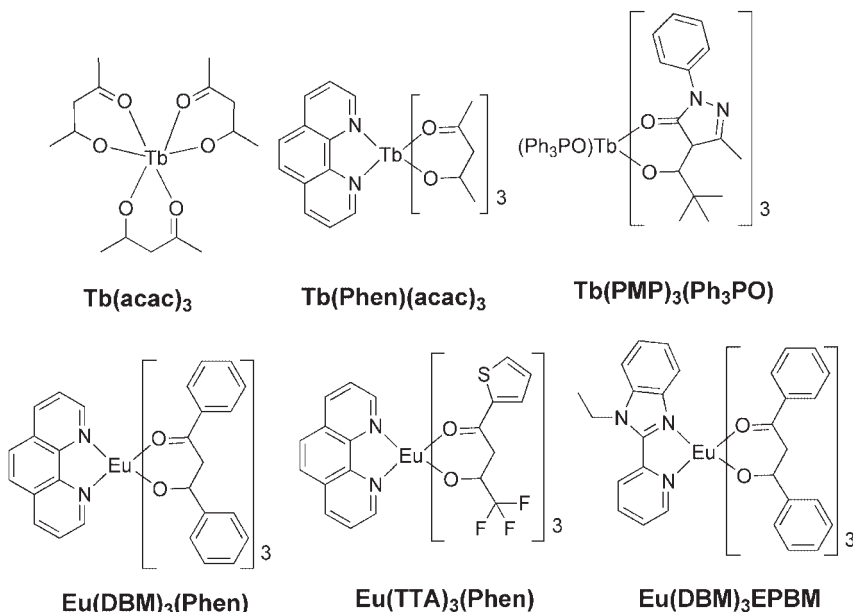
Fig. 10.2 Examples of some light-emitting rare earth metal complexes.

the visible spectrum by changing a whole set of chelating ligands or simply by manipulating the substituents on the ancillary ligands [50–60]. Highly efficient phosphorescent OLEDs have been demonstrated by multilayer device architecture [46, 61–63]. Recently, the PCE of the Ir(ppy)$_3$ based phosphorescent OLEDs has been reached to nearly 80 lm W^{-1} by employing p–i–n structure and double-emission layer device configurations [64, 65].

10.3.2
Polymeric Materials

Similar to pure organic small molecules, only singlet transitions are allowed and decay radiatively in conjugated polymers. Phosphorescent (or triplet) emitters are introduced as dopant into polymer to boost the electroluminescent quantum efficiency reaching to that of small molecule phosphorescent device. The phosphorescent dyes can be diluted into the polymer matrix either by blending or covalently linked on to the polymer backbone or as pendants. Efficient phosphorescent OLED devices usually comprise of charge transport materials as host matrix in the emissive layer. Substantial studies have been focused on blending phosphorescent emitter with polymer host. Poly(N-vinylcarbazole) (PVK) is a nonconjugated polymer containing hole-transporting carbazole as the side groups. The hole-transporting/electron-blocking properties, excellent film forming properties, temperature durability, and wide large HOMO–LUMO separation make PVK an attractive polymer host for phosphorescent dopants. Efficient phosphorescent device based on Ir complex dispersed into PVK matrix, with η_{ext} of 7.5% and PCE of 5.4 lm W^{-1} at 14 V [66] has been demonstrated. The η_{ext} and power conversion efficiency of the PVK–Ir complex based devices have been further increased with the addition of electron-transporting material 2-(4-biphenylyl)-5-(4-*tert*-butylphenyl)-1,3,4-oxadiazole (PBD) in the emissive layer [67, 68]. Conjugated polymers with high emission energy, for example, poly(p-phenylene) based polymers [69], polyfluorene [70–72] and polycarbazole [73, 74], were used as host materials for phosphorescent emitters. The triplet state of the polymer host should be higher than that of the phosphorescent emitter in order to achieve efficient electroluminescence. Until now, green to red phosphorescent emitters are restricted to be used in these conjugated polymer systems. The device efficiency dropped dramatically once the triplet energy of the emitter is higher than that of the polymer host. The PL and EL properties of a series of Ir complexes with different triplet energies (from green to red) doped in PVK ($T_1 = 2.5$ eV) and polyfluorene ($T_1 = 2.1$ eV) hosts have been examined. The relative position of the triplet energy levels of the host and guest may affect the device performance significantly [75–77]. Remarkable device performances of the devices fabricated from phosphorescent polymers based on PVK and iridium complex emitters exhibited maximum $\eta_{ext} = 6.9$, 11, and 6.6% for red, green, and blue PLEDs, respectively [78]. Schanze *et al.* have studied the photophysical and EL properties of a series of d^6 transition metal complex containing poly/oligo(aryleneethynylene). The origins of the EL feature either ^{3}MLCT or $^3\pi$–π state [79–81]. More recently, the synthesis of well-defined oligo/polyfluo-

rene containing Ir triplet emitters was demonstrated [82]. The fluorene building blocks conjugatively extended from the two cyclometallated ligands on the Ir metal center. Although substantial efforts have been put on red and green phosphorescent polymers, the design and synthesis of efficient electrophosphorescent high-energy emitters is still a big challenge in the field of optoelectronics.

The present contribution will emphasize on the material design, properties, and characterizations of molecular metal complexes and metal-containing polymers for light-emitting devices. Discussion will be focused on some functionalized ruthenium and rhenium diimine-based molecular and polymeric materials. It has been well known that the photophysical properties of metal complexes can be fine tuned by varying the structure of the ligands on the metal center. On the other hand, the ligands may also play an important role as the charge-transporting units in the electroluminescence process. In order to optimize the performance of OLED, enhancing the charge-transporting ability of the materials is as important as improving the quantum efficiency of the emitters. In the past few years, there have been several examples devoted to the investigation of functional metal complexes that can serve as both charge-transporting species and light emitters. Many of these examples are based on polypyridyl complexes of rhenium and ruthenium, which are emissive transition metal complexes with d^6 electronic configurations. The design, synthesis, and applications of these metal complexes will be presented and discussed in the following sections.

10.4
Ruthenium Containing Polymers

10.4.1
Photophysics of Ruthenium Complexes

The chemistry and photophysics of Ru(bpy)$_3{}^{2+}$ type complexes have been extensively studied [83–85]. Ruthenium(II) complex has a $4d^6$ electronic configuration that usually exhibits an octahedral geometry. The ground state configuration under strong field environment is $(t_{2g})^6$. Electrons can be promoted to different excited states upon photo excitation. The polypyridyl *N*-donor ligands are usually strong σ-donor with the orbitals localized on the nitrogen atoms. In addition, they are also π-donor and π*-acceptor ligands with the orbitals localized on the aromatic rings. A simplified molecular orbital diagram for these types of complexes is shown in Fig. 10.3. The promotion of an electron from the $d\pi_M$ metal orbital to the $\pi_L{}^*$ ligand orbitals results in the metal-to-ligand charge transfer (MLCT) excited states. Similarly, the transition of electrons from the π_M to σ^*_M and from the πL to π^* orbitals results in the metal-centered (MC) and ligand-centered (LC) excited states, respectively. The energy levels of the MLCT, MC, and LC excited states are dependent on the properties of both the metal center and ligands. Therefore, with the same metal center, it is possible to vary the photophysical properties of the complexes by modifying the structures of the ligands. In most of the Ru(II) com-
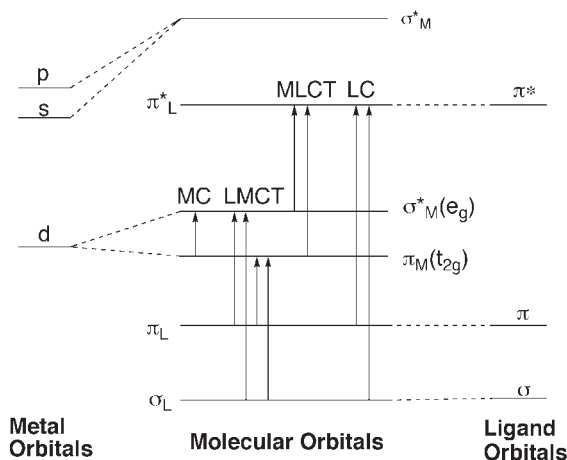
Fig. 10.3 Schematic diagram of the molecular orbitals of $Ru(bpy)_3^{2+}$ complex.

plexes, the lowest excited state is a ^{3}MLCT state, which is also responsible for several interesting luminescence and photo-redox activities. In general, the lifetime of the triplet MLCT excited states is in the order of ms to µs.

Ruthenium(II) polypyridyl complexes also exhibit interesting electrochemical properties. Several reversible redox processes can be observed. Oxidation of these complexes involves a metal-centered oxidation that produces Ru(III) species. Such process is relatively inert to the properties of the ligand concerned. On the other hand, the reduction may involve either metal-centered or ligand-centered orbital. The commonly observed reduction is a ligand-based process. The reduction process may take up more than one electron and its properties are largely dependent on the nature of the ligand.

Tris(2,2′-bipyridyl) ruthenium(II) complex $Ru(bpy)_3^{2+}$ is the most extensively studied ruthenium diimine complex. The LC, MC, and MLCT transitions are observed at ca. 280, 340, and 450 nm, respectively [84]. Upon photoexcitation, this complex will emit from the MLCT excited states and the luminescence lifetime and intensity are temperature dependent. A wide variety of molecular $Ru(bpy)_3^{2+}$ complexes have been used as photosensitizers, emission sensitizers, and photo-oxidants. Other than the bidentate 2,2′-bipyridine ligand, ruthenium complexes chelated with tridentate nitrogen donor ligands, such as 2,2′:6′,2″-terpyridine (tpy), have also drawn tremendous attention in the application of photosensitizers [86]. Terpyridine is a well-known ligand to form a variety of stable and robust complexes with various d^6 transition metals such as Ru and Os. In terms of photophysical properties, $Ru(tpy)_2^{2+}$ type complexes demonstrate similar properties as $Ru(bpy)_3^{2+}$ that they both exhibit lowest excited states with MLCT character. In addition, it is possible to build supramolecular model compounds by linking different $Ru(tpy)_2^{2+}$ complexes at the 4″ positions. These compounds exhibit linear geometry and are useful in the investigation of detailed photophysical properties. For example, dyads or triads based on $Os(tpy)_2^{2+}$, $Ru(tpy)_2^{2+}$, or heterodinuclear complexes have been reported [86].

10.4.2
Examples of Ruthenium Complex Containing Polymers

2,2′-Bipyridine and its derivatives are known to be good ligands for a variety of transition metal ions. An extensive review on polymers based on bipyridine ligand can be found in literature [87]. Ruthenium(II) complexes with this ligand are of particular interest due to their remarkable photophysical and electrochemical properties. Numerous research efforts have been focused on metal containing polymers with this type of complex in the early studies. In general, ruthenium complex containing polymers can be prepared by two different methods: (1) by physically doping the ruthenium complex into a suitable polymer matrix; or (2) by incorporating the complex as part of the polymer molecule. The first approach is relatively simple, but phase separation of the complex with the polymer is always an important factor to be considered. For the second approach (functional polymer approach), the ruthenium complex can be prepared as monomer, which is then subsequently polymerized via a suitable polymerization reaction. Due to the good chemical stability of most of the ruthenium complexes based on 2,2′-bipyridine or other diimine bidentate ligands, many different polymerization methods, such as condensation [88, 89], radical chain reaction [90], palladium catalyzed coupling [91, 92], or atom transfer living polymerization [93], etc., can be used. On the other hand, it is also possible to prepare ruthenium containing polymer by firstly synthesizing the polymer functionalized with 2,2′-bipyridyl ligands, which is then subjected to metal coordination reaction. This approach is synthetically more facile because fewer steps are involved in the monomer synthesis. However, it will be more difficult to control the metal content in the resulting polymers. Ruthenium complexes can be incorporated either onto the saturated or conjugated polymer main chains. For nonconjugated polymers, most of the early works were focused on the studies of luminescence and electrochemical properties of the polymers. In 1982, the synthesis of the water-soluble *p*-aminostyrene-*N*-vinylpyrrolidone copolymer **1** (Fig. 10.4) incorporated with $Ru(bpy)_3^{2+}$ complex was reported [90]. The ruthenium complex content in the copolymer was quite low (<10%). The luminescence from the ruthenium moiety was quenched in aqueous solutions by various quenchers such as $Fe(CN)_6^{4-}$, $Co(phen)_3^{2+}$, and Cu^{2+} ions. The quenching effect was also enhanced by the presence of polyanion such as poly(*p*-styrenesulfonate). In another report, the syntheses of different polyamides or polyesters incorporated with $Ru(bpy)_3^{2+}$ complex were demonstrated [94]. The polyamides based on 2,2′-bipyridine-4,4′dicarboxylate were synthesized by the condensation reaction between 2,2′-bipyridine-4,4′-dicarbonyl chloride and 1,6-diaminohexane. Ruthenium complex was incorporated to the polymer main chain after the polymerization reaction. The presence of ruthenium was confirmed by the change in UV-vis absorption spectra before and after metallation.

Most of the examples of ruthenium containing polymers are based on conjugated polymer systems. Polypyrroles that contain $Ru(bpy)_3^{2+}$ complex derivatives with different combinations of the ligands **2–4** were synthesized by electrochemical polymerization, which is shown in Fig. 10.4 [95]. The polypyrroles obtained showed the elimination of conductivity at high positive potential, but the electro-
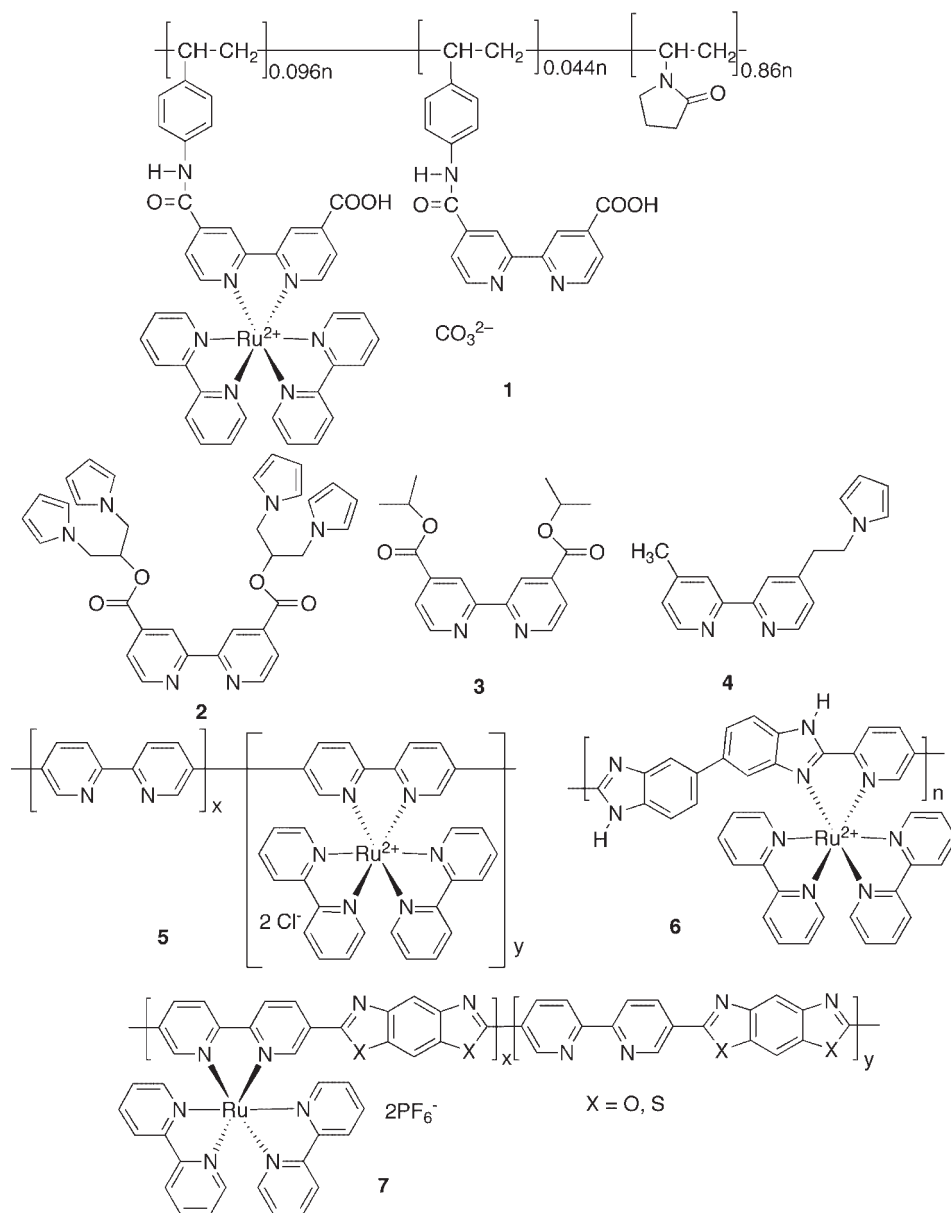
Fig. 10.4 Examples of ruthenium containing polymers.

activity of ruthenium complexes was retained. In 1992, Yamamoto *et al.* reported the metal complexation of poly(2,2′-bipyridine-5,5′-diyl) **5** [96]. The polymer formed electrochemically active complexes with ruthenium and nickel. Electron exchange between ruthenium complexes through the polymer main chain was observed

from the corresponding cyclic voltammogram. A similar electron transfer process between ruthenium centers on the main chain was also observed in the benzimidazole based polymer (polymer **6**) [97]. Some highly rigid bipyridine containing heterocyclic polymers (**7**) with poly(benzobisoxazole) and poly(benzobisthiazole) main chains were synthesized by Chan *et al.* [98]. The metal-free polymers exhibit lyotropic mesophases in methane sulfonic acid and they also have one of the highest thermal stabilities reported in the literature (decomposition temperature = 691°C under N_2). After complexation with ruthenium, the electrochemical and charge carrier mobilities were studied in detailed. Hole and electron carrier mobilities of the polymers were in the order of 10^{-5} cm^2 V^{-1} s^{-1}. It was suggested that the ruthenium complexes can play the role as charge-transporting species. Copolymer **8** composed of regular tetrathiophene and 2,2′-bipyridine were reported by Trouillet (Fig. 10.5) [99]. The resulting polymer is highly soluble in common organic solvents, which allowed them to be characterized by various spectroscopic and electrochemical methods. Polymer **9** with aliphatic imine main chain was also synthesized by the polymerization between 4,4′-diamino-2,2′-bipyridine and glyoxal, which was followed by metallation [100]. In these polymers, the electronic interaction between the conjugated main chain and the ruthenium complexes was observed. The electrochemical data of some of the polymers discussed above are summarized in Table 10.1. Other than performing polymerization on the polymer main chain, ruthenium complex polymers can also be synthesized by the metal coordination reaction. Rehahn *et al.* demonstrated the high molecular weight polymer **10** synthesized by the coordination reaction between tetrapyridophenazine and the ruthenium monomer $[Ru(bpy)Cl_3]_x$ [101]. The solution properties of the polymers obtained were thoroughly studied.

In addition to the linear polymers, dendritic polymers can also be obtained from $Ru(bpy)_3{}^{2+}$ complexes, as each ruthenium center can be coordinated by three bidentate ligands. Campagna *et al.* synthesized various ruthenium containing polymers by the "complexes-as-metals" and "complexes-as-ligands" strategies [102]. Dendrimers with 4, 10, and 22 metal ions were obtained, and an example of dendrimer **11** that contains 10 ruthenium metal centers is shown in Fig. 10.5. These polymers exhibit very intense absorption for the MLCT transition ($\varepsilon >$ 10 000 M^{-1} cm^{-1}), and the interactions between neighboring metal complex units were observed from electrochemical results.

10.4.3
Ruthenium Complexes for Light-Emitting Devices

Since $Ru(bpy)_3{}^{2+}$ type complexes exhibit interesting electrochemical and luminescence properties, they are promising candidates as the light-emitting materials in OLEDs. Some examples of ruthenium complexes that were used for OLED applications are shown in Fig. 10.6, and the device performances are summarized in Table 10.2. In these devices, the ruthenium complexes can be deposited as a single emitting layer or doped into a charge transport or inert polymer matrix. The first solid-state electroluminescent device based on Ru(II) complex (**12a**) has been
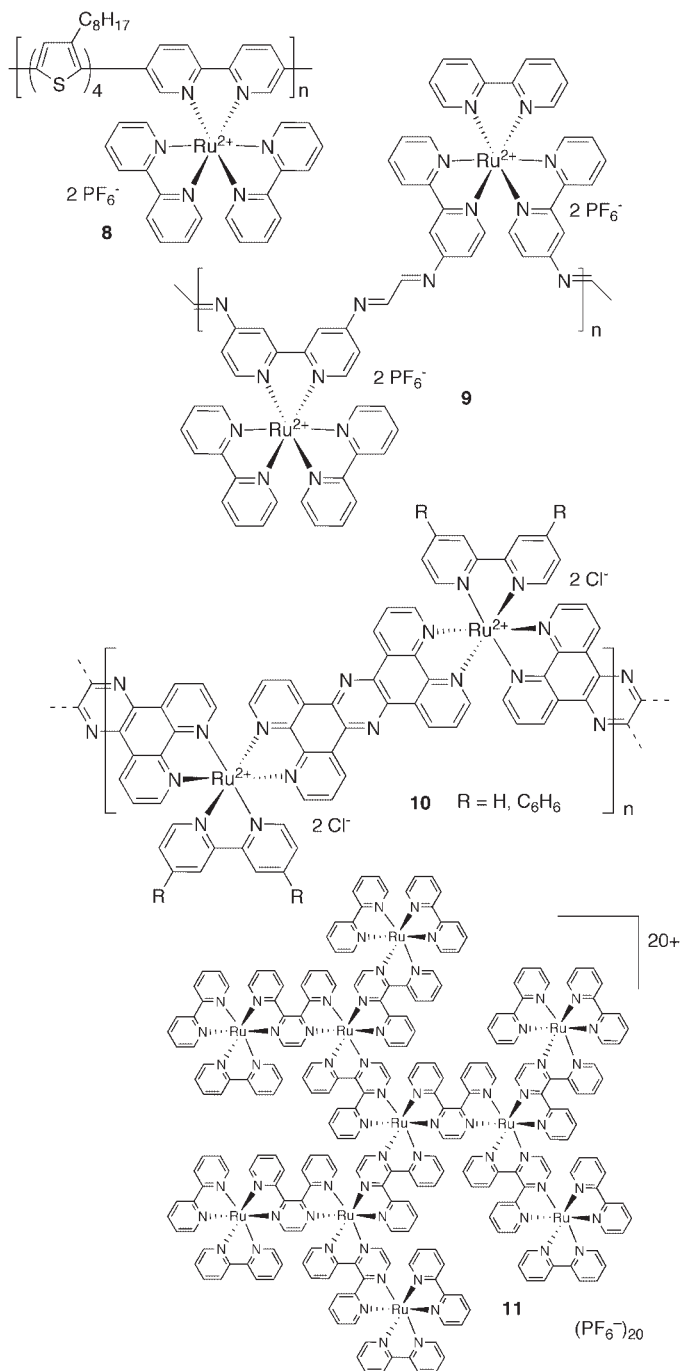
Fig. 10.5 Examples of ruthenium containing polymers.

Table 10.1 Electrochemical and spectroscopic properties of some ruthenium containing polymers (structures of the polymers are shown in Figs. 10.4 and 10.5).

Polymer	λ_{max}, abs	λ_{em}, PL (nm)	λ_{em}, EL (nm)	$E_{red}^{1/2}$ (V)	$E_{ox}^{1/2}$ (V)	Ref.
1	460	610[b]	a	a	a	90
Poly[Ru(bpy)$_2$(**2**)]	a	a	a	−1.25[c]	1.05[c]	95
Poly[Ru(bpy)(**2**)$_2$]	a	a	a	−1.20[c]	1.195[c]	95
Poly[Ru(**3**)(**2**)$_2$]	a	a	a	−1.14[c]	1.26[c]	95
Poly[Ru(**4**)$_3$]	a	a	a	−1.70[c]	0.86[c]	95
5	a	a	a	−1.1[b,c]	0.8[b,c]	96
8	475	a	a	−1.34, −1.60, −2.04, 2.14[c]	0.64, 0.78, 1.05[c]	99
9	465	666	a	−0.83, −1.49, −1.66[d]	0.99[d]	100
10	460[b]	a	a	a	a	101
11	541	809	a	−0.73, −1.22[d]	1.53[d]	102

a   Not reported
b   Approximate value
c   vs. Ag/Ag⁺
d   vs. SCE

12a: R = —⟨benzene⟩—SO₃Na

12b: R = H

12c: R = —⟨benzene⟩

13a: R₁ = ⟍—OH

13b: R₁ = R₂ = H

13c: R₁ = (C=O)—OH ; R₂ = H

13d: R₁ = R₂ = (C=O)—OH

13e: R₁ = COOC₁₂H₂₅ ; R₂ = H
13f: R₁ = R₂ = *tert*-butyl
13g: R₁ = (CH₂)₈CH₃ ; R₂ = *tert*-butyl
13h: R₁ = (CH₂)₄CH₃ ; R₂ = H
13i: R₁ = R₂ = methyl
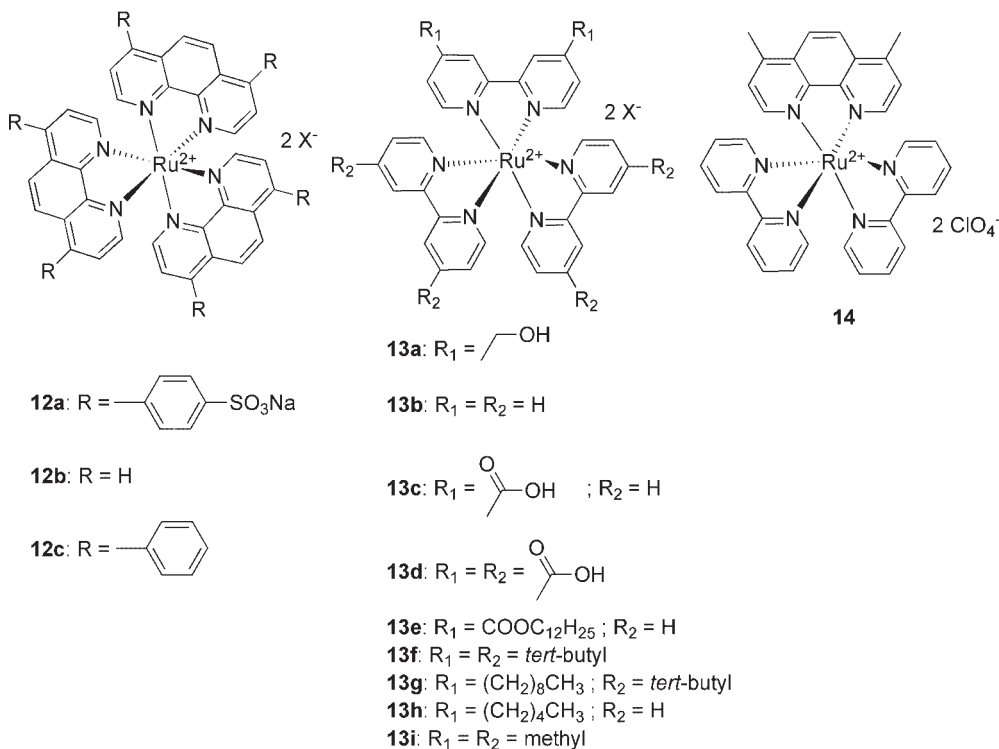
Fig. 10.6 Examples of some ruthenium complexes for electroluminescent applications.

Table 10.2 Summary of EL performance of devices fabricated from ruthenium complexes (structures of the complexes are shown in Fig. 10.6).

Complex	Device configuration	λ_{max} Abs (nm)	λ_{max} EL (nm)	Turn-on voltage V_{on} (V)	Maximum luminance (cd m^{-2})	External quantum efficiency η_{ext} (%)	Ref.
12a	ITO/(PPV/SPS)$_5$/ (PPV/PMA)$_{20}$/**12a**/Al	470	628	2.5–3.5	110	0.05	103
12a	ITO/PEO:**12a**:LiCF$_3$SO$_3$/Al	470	628	2.5–3.0	100	0.02	104
12b	ITO/**12b**/Au	447	589	–	–	0.25	106
12c	ITO/PVK:**12c**/PBD/Alq$_3$/LiF/Al	460	612	11.0	500	–	116
12c	ITO/PVK:**12c**/PBD/Alq$_3$/LiF/Al	460	612	10.0	500	–	117
12c	ITO/PVK:PBD:**12c**/Alq$_3$/BCP/ Alq$_3$/LiF/Al	–	–	9.0–10.0	3400	–	115
13a	ITO/**13a**/Al	–	630	–	1000	1.0	104
13b	ITO/**13b**/Al	–	630	–	–	0.4	105
13b	ITO/**13b**/Ga:In	455	660	2.3	3500	1.4	108
13b	ITO/**13b**/Al	–	–	3.0	1000	1.45	112
13b	ITO/PMMA:**13b**/Al	–	–	2.6	400	3.0	112
13b	ITO/Au/**13b**/Ga:In	455	660	2.3	5000	–	109
13b	ITO/PMMA:**13b**/Ag	–	630	–	–	2.7	113
13b	ITO/**13b**/Au	451	605	–	–	0.5	106
13b	ITO/Alq$_3$/**13b**/Ga:In	–	630	2.0	–	6.4	111
13c, d	ITO/**13c** or **13d**/Al	–	690	–	600	0.4	105
13f	ITO/PMMA:**13f**/Ag	–	630	–	–	4.1	113
13f	ITO/**13f**/Au	459	610	–	–	0.75	106
13f	ITO/**13f**/Au	–	–	5.0	–	0.6	106
13g	ITO/PMMA:**13g**/Ag	–	630	–	–	5.5	113
13h	ITO/**13h**/Au	454	612	–	–	0.5	106
13i	ITO/**13i**/Au	454	609	–	–	0.25	106
14	ITO/PVK:**14**/BCP/Alq$_3$/Al	460	620	8.0	95	0.14	114

demonstrated by Rubner *et al.* in 1996 [103]. Subsequently, other devices that utilized different tris-chelated Ru(II) diimine complexes (**12a**, **13a,b,c,d**) were fabricated by spin-coating [103–105] technique. The device performances were generally poor in the early studies, with maximum luminance around a few hundred cd m^{-2} and low η_{ext} (0.05%). Nevertheless, high efficiency and low driving voltage devices with this type of materials can be envisioned by modifying the molecular structure or the device architecture. The luminance was increased to 1000 cd m^{-2} at 5 V with η_{ext} ~1% by using the hydroxymethylated and esterifed derivatives of Ru(bpy)$_3^{2+}$ complex [105]. Bernhard *et al.* investigated the influence of bipyridine ligands with various aliphatic substituents on the device performance. Maximum η_{ext} (0.75%) was obtained from the device with [Ru(dtb-bpy)$_3$]$^{2+}$(PF$_6^-$)$_2$ [106, 107] (complex **13f**).

Guo and Bard introduced a Ga:In eutectic cathode in the Ru(bpy)$_3$$^{2+}$ based devices. These single-layer devices exhibited η_{ext} ranged from 0.4 to 3.4% [108–110]. By inserting a layer of Alq$_3$ at the anode interface, the emitting zone was shifted to the new interface between Alq$_3$ and Ru(bpy)$_3$$^{2+}$. The device with the configuration ITO/Alq$_3$/Ru(bpy)$_3$(ClO$_4$)$_2$/Ga:In showed high η_{ext} and power efficiency of 6.4% and 5.3 lm W^{-1}, respectively [111].

The ruthenium(II) complexes can be diluted into the polymer matrix either by blending with a polymer host in order to reduce the effect of concentration quenching. Single-layer devices of ruthenium complexes (**13b,f**) in various polymer blends (PMMA, polycarbonate or polystyrene) were examined by Rudmann and Rubner [112]. The PMMA blends with Ag as cathode exhibited η_{ext} ranged from 2.5 to 3.0%. Later, new derivatives of the Ru complex **13g** were studies with this optimized device configuration (ITO/**13g**:PMMA/Ag) [113]. The devices showed excellent stability under pulsed driving voltage with maximum η_{ext}=5.5%, which reminds the highest value reported for ruthenium polymer-based OLEDs to date. Hole-transporting polymer, PVK, was also employed as the polymer host for the ruthenium complexes **12c** and **14** [114–117]. High luminance efficiency (8.6 cd A^{-1}) and power efficiency (2.1 lm W^{-1}) were obtained by introducing charge-transporting layers in the devices [116, 117].

10.4.4
Complexes Based on Multifunctional Ligands
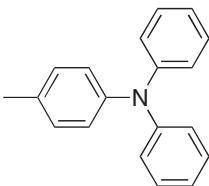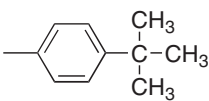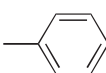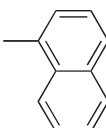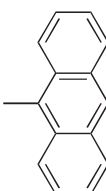
There were several attempts in synthesizing multifunctional light-emitting complexes with charge-transporting units attached to the ligands. Organic light-emitting molecules that contained both hole-transporting triphenylamine and electron-transporting 1,3,4-oxadiazole moieties were synthesized [118]. These compounds emitted blue–green light in the range between 450 and 490 nm. In another paper, Chan *et al.* reported a series of rhenium and ruthenium complexes that contain triphenylamine and oxadiazole moieties [119]. They were synthesized easily by a one-step reaction between the 2,2′-bipyridine dicarbonyl chloride and the corresponding aromatic tetrazoles (Scheme 10.1). Complexes with symmetrical ligand (**15a–e**) and asymmetrical structures (**16a–e**) were reported [119, 120]. The properties of these complexes are summarized in Table 10.3. In general, ligands with more extended conjugated structures have lower transition energies. All these complexes exhibit an intense absorption at ca. 410–478 nm and an emission band at ca. 670–720 nm originated from the MLCT transitions. The neutral rhenium complex can be doped into a polycarbonate (PC) host with the concentration up to 40 wt% without observing phase separation. For the ruthenium complexes, they were doped into poly(vinyl alcohol) (PVA). It was suggested that the complexes could play the roles as hole- and electron-transporting units as well as light emitters. The charge carrier mobilities and EL properties of some of the complexes doped in different polymer hosts are shown in Table 10.4. The rhenium complexes showed higher carrier mobilities than those of the ruthenium
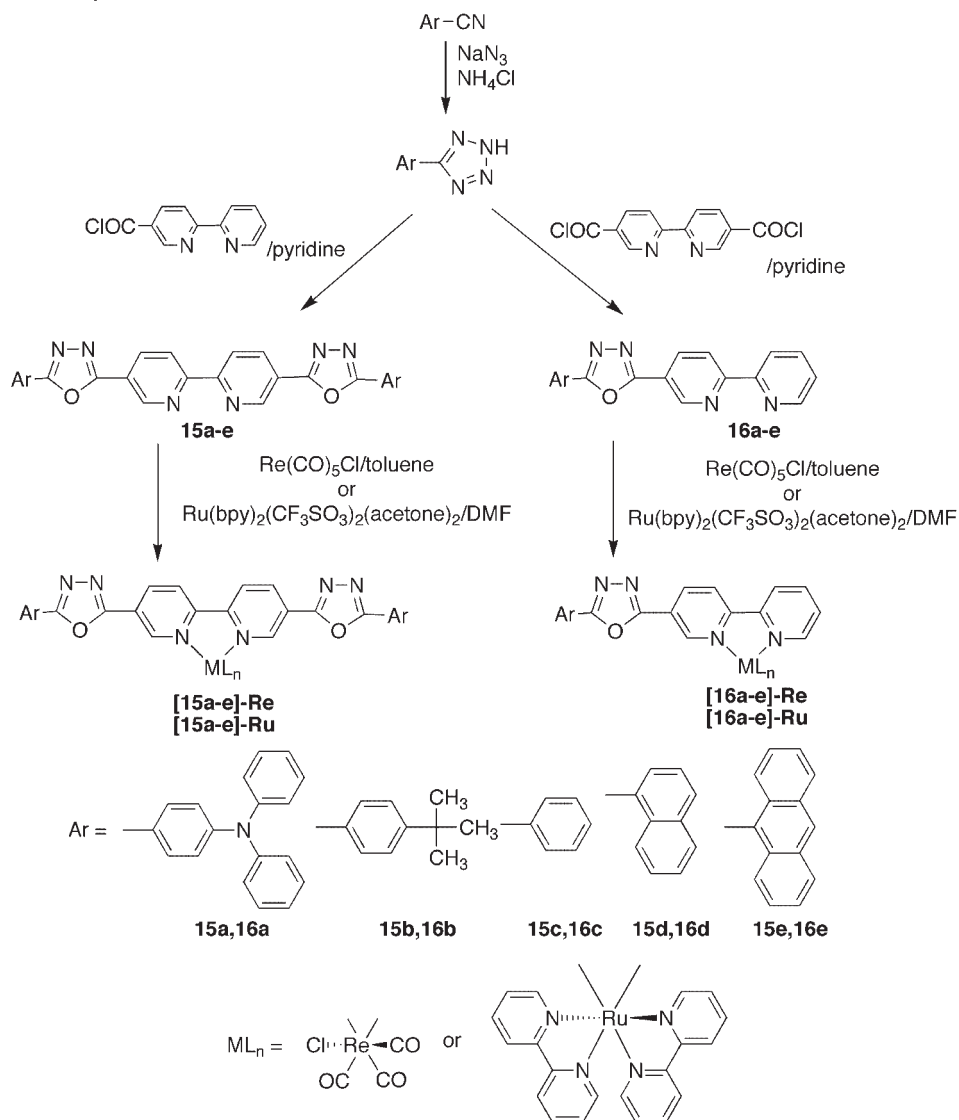
Scheme 10.1 Synthesis of multifunctional rhenium and ruthenium complexes.

complexes with the same ligand. Complex **15a–Re** exhibits a symmetric structure and has the highest carrier mobilities among all the complexes, which is probably due to the presence of two triphenylamine and oxadiazole moieties per ligand. In addition, other complexes based on ligand **15a** exhibit higher mobilities than those of **15b**. After doping the complexes into a suitable polymer matrix, the resulting composites were fabricated into single-layer light emitting devices with the structure ITO/complex:polymer/Al. The EL spectra of **15a–Re** and **15b–Re** are shown

Table 10.3 Properties of multifunctional light emitting rhenium and ruthenium complexes (structures of the complexes are shown in Scheme 10.1).

Complex	Ar	Decomposition temperature (°C)	λ_{max} Abs (nm)[a]	λ_{max} EL (nm)[a]
15a–Re		368	478	675
15a–Ru		378	440	680
16a–Re		308	444	694
16a–Ru		326	412	710
15b–Re		347	475	682
15b–Ru		363	440	722
16b–Re		318	442	700
16b–Ru		356	450	723
15c–Re		352	458	711
15c–Ru		351	438	722
16c–Re		349	422	675
16c–Ru		388	446	693
15d–Re		361	415	682
15d–Ru		356	432	722
16d–Re		322	410	675
15e–Re		333	442	726
15e–Ru		342	425	713

a   Absorption maximum measured in CHCl$_3$ solution (for Re complexes) or CH$_3$CN solution (for Ru complexes). Only the energy of the MLCT absorption band is given.

Table 10.4 Electroluminescence and charge transport properties of multifunctional rhenium and ruthenium complexes (structures of the complexes are shown in Scheme 10.1).

Complex	Polymer host[a]	λ_{max}, EL (nm)	Turn-on voltage V_{on} (V)	External quantum efficiency η_{ext} (%)	Maximum luminance (cd m^{-2})	Hole carrier mobility←μ_h (10^{-4} cm^2 V^{-1} s^{-1})[b]	Electron carrier mobility←μ_e (10^{-4} cm^2 V^{-1} s^{-1})[b]
15a–Re	PC	678	4	0.1	730	4.1	7.1
15a–Ru	PVA	665	5	0.1	650	3.4	5.8
16a–Re	PC	665	6	0.08	350	2.9	6.1
16a–Ru	PVA	700	5	0.07	130	2.6	4.6
15b–Re	PC	674	6	0.06	175	3.2	5.8
15b–Ru	PVA	710	5	0.04	160	2.5	4.2
16b–Re	PC	680	6	0.05	180	2.8	4.9
16b–Ru	PVA	720	7	0.03	190	2.3	3.6

a   PC=polycarbonate; PVA=poly(vinyl alcohol).
b   Measured at externally applied electric field E=40 kV cm^{-1}.
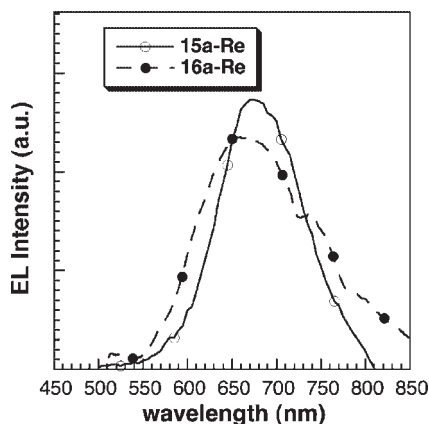
Fig. 10.7 Electroluminescence spectra of complexes **15a–Re** and **16a–Re**.

in Fig. 10.7. All the rhenium complexes exhibit similar EL spectra with an emission band centered at ca. 670 nm. The current–voltage characteristics of the devices also follow closely to those of the luminescence–voltage characteristics, which implies equally efficient charge injection and transport processes. The device based on **15a–Re** also exhibits the best device performance with the lowest turn-on voltage of 4 V. The external quantum efficiency and luminance were measured to be 0.1% and 730 cd m^{-2}. This can be explained in terms of its relatively lower hole injection barrier than that of complex **15b–Re**.

10.4.5
Ruthenium Containing Polymers for Light-Emitting Devices

10.4.5.1 EL Devices Based on Ruthenium Complex Containing Nonconjugated Polymers

Besides blending the ruthenium complexes with polymer host, another approach to reduce the concentration quenching of ruthenium complex in the thin film is to copolymerize the complex with another monomer. This method eliminates the problem of phase separation of metal complex from the polymer matrix, as both complex and polymer are covalently attached together. Rubner *et al.* reported the electroluminescent properties of polyester **17** with ruthenium complexes covalently linked onto the main chain [121, 122]. Thin film devices of ruthenium complex containing polyester and poly(acrylic acid) (PAA) were fabricated by using layer-by-layer deposition technique [121–123]. In each deposition cycle, a polymer bilayer that contained cationic polyester **17** and the anionic PAA was formed. The polymer molecules were held to each other by electrostatic force. The thickness of each (**17**/PAA) bilayer was controlled by varying the pH of the polymer solutions. The η_{ext} of the spin-coated devices and of the layer-by-layer devices were 0.08 and 1%, respectively. Devices with η_{ext} as high as 3% was obtained with optimized polymer thickness.

Detailed studies on a series of polyamides (**18a–e**) that contain 2,2′-bipyridine-4,4′-dicarboxylate and 2,2′-bipyridine-5,5′-dicarboxylate were reported [89]. The thermotropic and lyotropic liquid crystalline properties of the metal-free polymers were fully investigated. Only those polymers with low ruthenium content after complexation exhibited lyotropic mesophases, and the clearing temperatures decreased compared to the metal-free polymers. These polymers were also synthesized by another approach in which the ruthenium complex monomer was copolymerized with various diamines. No decomposition of the complex was observed during the course of the polymerization reaction. The photoconductivity and charge-transporting properties of the polymers were also studied. The hole and electron carrier mobilities of the polymers were in the order of 10^{-8} cm^2 V^{-1} s^{-1}, which subsequently increased by 2-3 orders of magnitudes after the incorporation of ruthenium complexes.

In a more recent paper, Malliaras *et al.* reported the electroluminescence properties of ruthenium containing dendrimers [124]. Five generations of polyamidoamine-based dendrimers with 4, 8, 16, 32, and 64 Ru(bpy)$_3$ complexes on the periphery were synthesized. The structure of dendrimer **19** with 8 Ru complexes is shown in Fig. 10.8. EL devices with ITO and gold electrodes were fabricated. The devices were found to behave similar to those based on Ru(bpy)$_3^{2+}$ films. The EL efficiency showed a monotonic decrease with the dendrimer generation. It was attributed to the decrease in the electronic carrier mobility and the increase in self-quenching, as the number of dendrimer generation was increased. It was suggested that the self-quenching is dependent on the precise dendrimer configuration, which was not discussed in detail in the paper.

10.4.5.2 Multifunctional Ruthenium Complex Containing Conjugated Polymers

The performance of organic light-emitting devices has been limited due to the relatively poor charge carrier mobilities; especially the transport of electrons. In nonconjugated polymers, charge transport is predominantly given by hopping of charges between different charge carriers (e.g., the ruthenium complex), and the polymer main chain is not involved in the process. Therefore, incorporation of charge transport moieties on polymer main chain may further enhance the charge carrier mobilities of the polymers. It was found that hole and electron carrier mobilities in some ruthenium terpyridyl complex containing polymers were dependent on the metal complex content. The carrier mobilities were measured to be of the order of 10^{-5} cm^2 V^{-1} s^{-1} [125]. There were also examples of improving the electron carrier mobility of polymers by incorporation of aromatic oxadiazole or triazole moieties into the light-emitting polymer. The devices fabricated from these oxadiazole containing polymers exhibited improved performance due to improved charge injection and carrier mobilities [126–128]. The design strategy is shown in Fig. 10.9. The enhancement in charge mobility was attributed to the redox behavior of the ruthenium complexes, which can function as hole and electron carrier. Similar behavior was observed in other ruthenium containing polymers with modest charge carrier mobilities [125]. Because of these interesting results, multifunctional ruthenium containing conjugated polymers (**22a–f, 23a–c**) were synthesized, and their structures are shown in Fig. 10.10 [91, 92]. The design
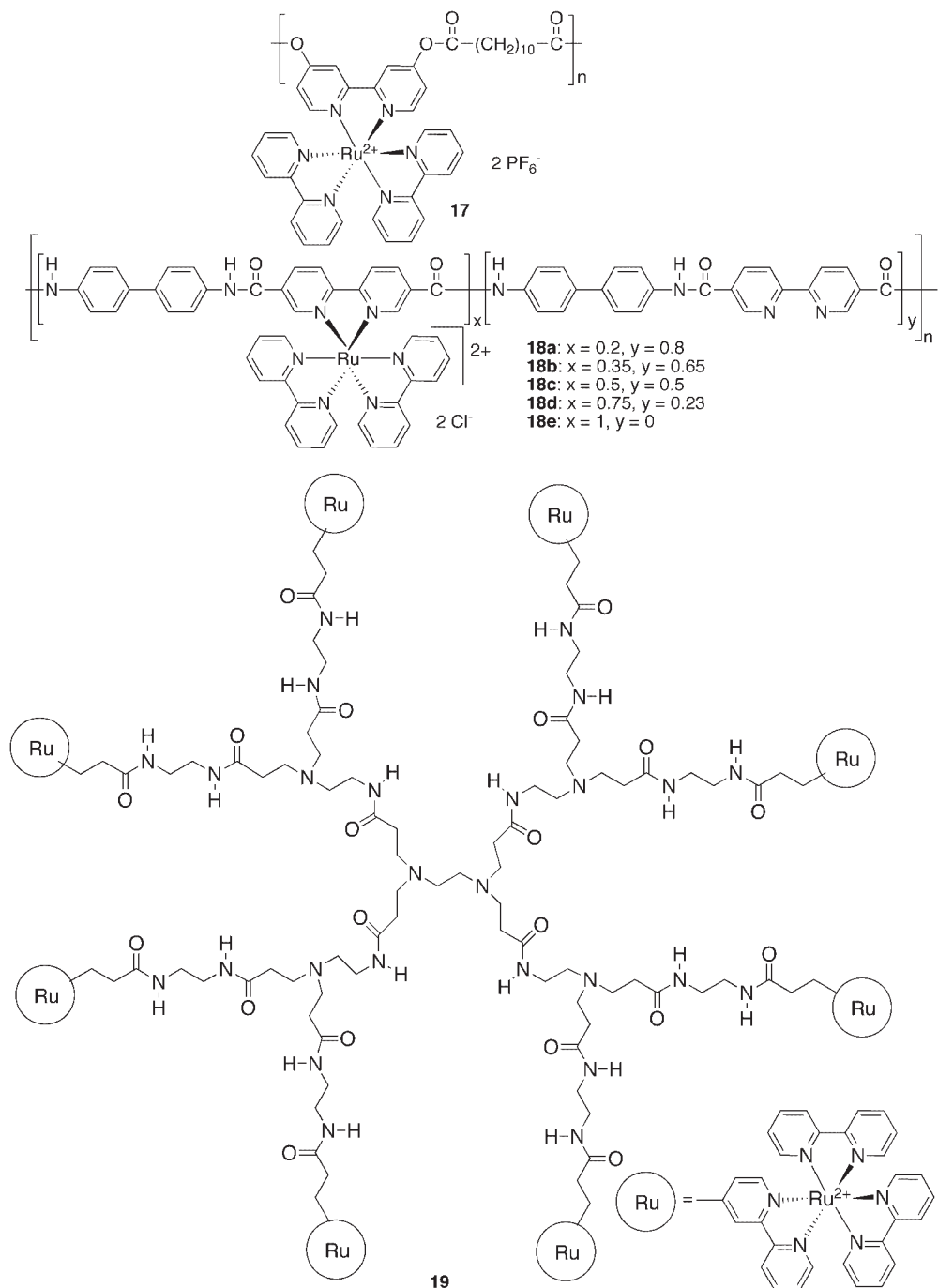
Fig. 10.8 Examples of ruthenium containing polyester, polyamides, and dendrimer (with 8 Ru(bpy)$_3^{2+}$ centers) for electroluminescent applications.
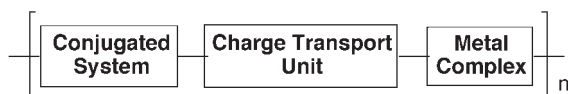
Fig. 10.9 Design of multifunctional metal containing polymers.

20: 5,5'-disubstituted bipyridine
21: 4,4'-disubstituted bipyridine

22a: x = 0.1, y = 0.9
22b: x = 0.25, y = 0.75
22c: x = 0.35, y = 0.65
22d: x = 0.5, y = 0.5
22e: x = 0.65, y = 0.35
22f: x = 1, y = 0

23a: x = 0.25, y = 0.75
23b: x = 0.5, y = 0.5
23c: x = 1, y = 0

24a: x = 0.1, y = 0.9
24b: x = 0.2, y = 0.8
24c: x = 0.3, y = 0.7
24d: x = 0.4, y = 0.6
24e: x = 0.5, y = 0.5
24f: x = 0.6, y = 0.4
24g: x = 1, y = 0

25a: x = 0.1, y = 0.9
25b: x = 0.2, y = 0.8
25c: x = 0.3, y = 0.7
25d: x = 0.5, y = 0.5
25e: x = 0.7, y = 0.3
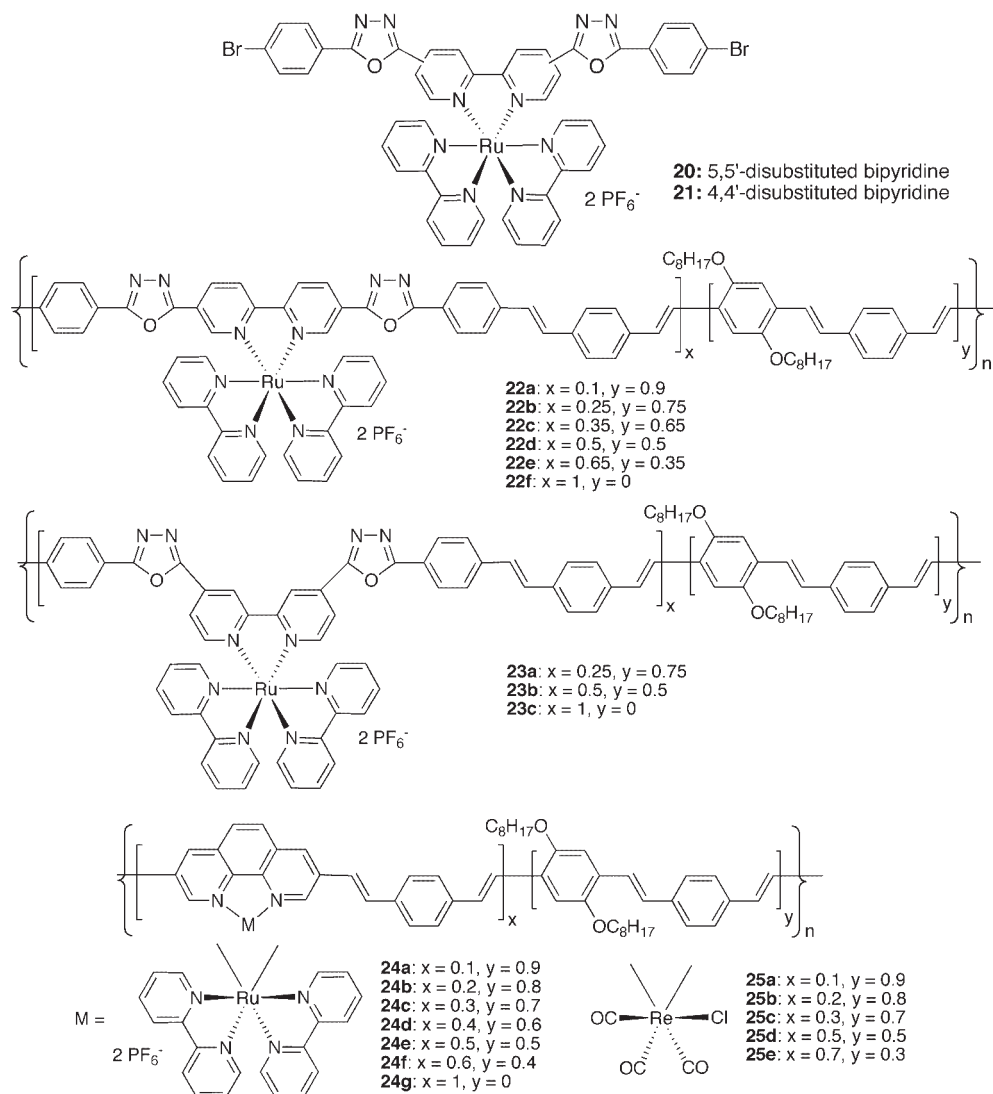
Fig. 10.10 Ruthenium and rhenium containing polymers with oxadiazole or phenanthroline moieties on the main chain.

strategy was to incorporate both charge-transporting units and light-emitting metal complexes on the same polymer chain. The key monomers are complexes **20** and **21**, which contain two aromatic oxadiazole units and a Ru(bpy)$_3^{2+}$ complex moiety. Both 2,2′-bipyridine-5,5′-diyl and 2,2′-bipyridine-4,4′-diyl ruthenium complexes were prepared. These monomers were copolymerized with 1,4-dibromo-2,5-dioctoxybenzene and 1,4-divinylbenzene in different ratio by palladium catalyzed Heck Coupling reaction. All the polymers were obtained in good to excellent yield. In order to investigate the effect of metal content to the photophysical properties, copolymers with various ruthenium contents (from 10 to 100% per repeating unit) were prepared. A series of conjugated polymers based on 1,10-phenanthroline (Phen) ligand were also synthesized. In this system, the Phen containing polymer was incorporated with ruthenium (polymers **24a–g**) or chlorotricarbonyl rhenium (polymers **25a–e**) metal center in different ratios, and the latter ones are neutral complexes which have higher solubility in some nonpolar organic solvents.

The photophysical properties of the polymers are summarized in Table 10.5. The electronic absorption spectra of polymers **22b, d, f** are shown in Fig. 10.11. All these polymers exhibit an intense absorption band in the region between 410 and 450 nm, which is assigned to the π–π* absorption by the conjugated polymer main chain. When the ruthenium complex content increases, the absorption peak shows a bathochromic shift (low energy shift). This may be due to the lowering of the energy of the π* orbital of the oxadiazole moieties on the main chain. The absorption due to the MLCT (d–π*) absorption of the ruthenium complex can be found at ca. 500 nm. For polymers with lower metal content, the MLCT absorption was overwhelmed by the extension of the π–π* absorption tail. When the metal content increases, the MLCT absorption band was observed as a shoulder at the lower energy end of the π–π* transition.

The transport of charges in molecularly doped organic polymers has been investigated in the development of materials for xerography [129]. The investigation of transient photocurrents was originally developed for organic single crystals and inorganic materials, which are characterized by nondispersive charge transport properties. However, due to the highly disordered nature in organic materials, the transport of charges is described by the disordered theory [130]. The charge carrier mobilities of the polymers were measured by the time-of-flight experiment in which the transient photocurrent generated by a pulsed laser was monitored with an oscilloscope. From this photocurrent pulse, the carrier mobility of the polymer can be deduced. Typical transient photocurrent profiles for dispersive and nondispersive charge transport processes are shown in Fig. 10.12, and the transient photocurrent of ruthenium containing polymer **22a** is also shown as reference. In this polymer, the transient photocurrent showed a featureless decay, indicating that the charge transport was highly dispersive (non-Gaussian carrier distribution) in nature. In such cases, the transit time t_T is defined by the intercept of the tangents approximating the current pulse at early and late times in the log I vs log t plot. The drift mobility μ was calculated according to the equation $\mu = L/t_T/E$, where L is the film thickness and E is the external electric field strength.

Table 10.5 Properties of ruthenium and rhenium containing polymers with oxadiazole or phenanthroline moieties on the main chain (structure of the polymers are shown in Fig. 10.10).

Polymer	Ru content per repeating unit	Decomposition temperature (°C)	Hole carrier mobility μ_h $(10^{-4}\ cm^2\ V^{-1}\ s^{-1})^a$	Electron carrier mobility μ_e $(10^{-4}\ cm^2\ V^{-1}\ s^{-1})^a$
22a	0.1	434	0.47	0.50
22b	0.25	416	0.55	0.57
22c	0.35	412	1.8	3.1
22d	0.5	402	1.5	3.6
22e	0.65	401	4.9	7.9
22f	1	424	5.1	8.3
23a	0.25	399	0.21	0.3
23b	0.5	394	0.45	1.5
23c	1	387	0.64	3.2
24a	0.1	392	0.8	2.1
24b	0.2	383	1.3	2.8
24c	0.3	372	1.3	3.0
24d	0.4	371	1.5	3.3
24e	0.5	383	1.8	3.8
24f	0.6	382	2.4	4.6
24g	1	392	3.1	6.5
25a	0.1	408	0.4	1.2
25b	0.2	403	1.0	1.9
25c	0.3	410	1.1	2.4
25d	0.5	415	1.4	2.7
25e	0.7	407	2.1	4.0

a Measured at $E=40\,kV\ cm^{-1}$.
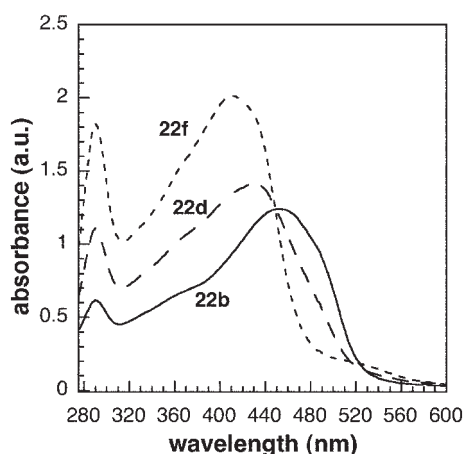
Fig. 10.11 Electronic absorption spectra of polymers **22b**, **22d**, and **22f** (Adapted from [92]).
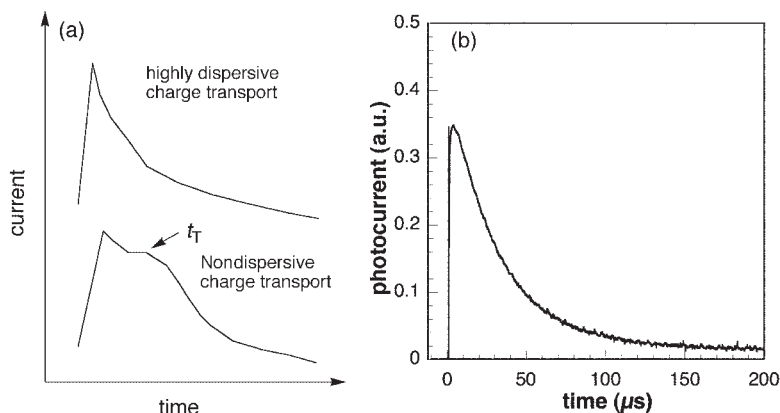
Fig. 10.12 (a) Schematic diagrams showing the difference in transient photocurrent profile for dispersive and nondispersive charge transport. (b) Transient photocurrent profile observed in the time-of-flight experiment for polymer **22a**.

Carrier mobilities of rhenium and ruthenium containing polymers are listed in Table 10.5. It can be seen clearly that both the hole and electron carrier mobilities are dependent on the metal complex content, and they are of the order of 10^{-4} to 10^{-5} cm^2 V^{-1} s^{-1}. In general, these values are higher than the carrier mobilities of some PPV derivatives [131, 132], polycarbonate doped with oxadiazoles [133], or aromatic amines [129, 134–136]. Polymers with 5,5′-disubstituted 2,2′-bipyridine (polymers **22a–f**) exhibit slightly higher carrier mobilities than those of the 4,4′-disubstituted analogues (**23a–c**), and the measured electron mobilities are slightly higher than those of hole mobilities. It was suggested that the enhancement in electron drift mobilities was possible due to the presence of oxadiazole moieties in the polymer main chain. The temperature dependent electron carrier mobilties were also studied. A plot of electron carrier mobilities for polymers **22d,f** as a function of temperature is shown in Fig. 10.13. Since the transport of charges is a thermally activated process, the activation energy can be calculated from the Arrhenius plot. From the figure, both polymers exhibit similar activation barriers under different electric field strengths, which are approximately 0.1–0.2 eV. For the polymers based on ruthenium or rhenium Phen complexes (**24a–g**), they exhibit similar hole and electron mobilities as polymers **22a–f**, and the mobilities are also dependent on the metal content.

Electroluminescent properties of these polymers were studied by the fabrication of single layer light-emitting devices ITO/polymer/Al. The performances of some of the devices fabricated are summarized in Table 10.6. The turn-on voltages of these devices are in the range between 6 and 8 V, and the external quantum efficiencies are in the order of 10^{-1}%. The emission properties were dependent on the metal content in the polymers. The PL and EL spectra of polymers **22d,f**, which have different ruthenium complex contents, are shown in Fig. 10.14. In the PL and EL spectra of polymer **22d**, the emission was dominated by the π*–π emission
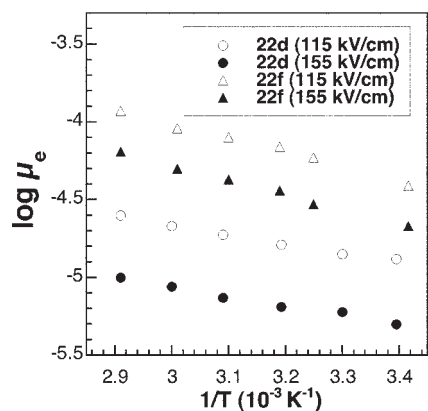
Fig. 10.13 Plot of electron carrier mobility for polymers **22d** and **22f** as a function of temperature under different externally applied electric fields (Adapted from [92]).

Table 10.6 Electroluminescence performance of single-layered light emitting devices ITO/polymer/Al fabricated from polymers **22**–**25** (structures of the polymers are shown in Fig. 10.10).

Polymer	Turn-on voltage (V)	λ_{max} EL (nm)	Maximum luminance (cd m^{-2})	External quantum efficiency (%)
22d	8	590, 690[a]	180	0.08
22e	6	710	220	0.1
22f	6	710	300	0.1
23a	6	600, 700[a]	100	0.05
23b	6	690	150	0.07
24b	6.5	570, 710[a]	90	0.15
24e	7	710	110	0.17
25b	7.5	570, 695[a]	100	0.2
25e	7	700	130	0.21

a   The emission band appeared as a shoulder.

at 590 nm originated from the polymer main chain. The emission from the MLCT states of the Ru complex only appears as a shoulder at ca. 650–700 nm, which is due to the low metal content in the polymer. For polymer **22f**, the PL and EL spectra were dominated by the metal complex emission centered at 710 nm. No emission from the π-conjugated main chain could be observed. The low lying triplet emissive state of the Ru complex sufficiently quenched the singlet emission from the polymer main chain via Förster/Dexter energy transfer processes or direct charge trapping. When the metal content (the quencher) was increased, the
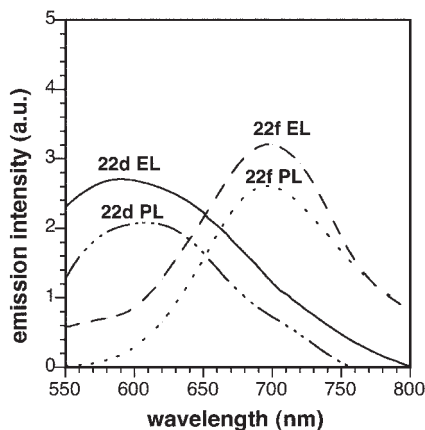
Fig. 10.14 Photoluminescence and electroluminescence spectra of polymers **22d** and **22f** (Adapted from [92]).

quenching effect becomes more prominent. The maximum luminance was measured in the device fabricated from polymer **22f** ($300 \, cd \, m^{-2}$). The Phen-based ruthenium and rhenium containing polymers exhibit slightly higher external quantum efficiency and lower maximum luminance than the oxadiazole based metal containing polymers. By using this material design approach, the emission color of this series of polymers can be fine tuned by controlling the metal content in the polymer backbone.

Energy transfer processes were also observed in another series of multifunctional metal containing polymers with ruthenium dipyridophenanzine (dppz) complexes incorporated [137]. Aromatic conjugated polymers based on nitrogen heterocyclics compounds usually behave as n-type materials. Starburst molecules with quinoxaline moieties were shown to exhibit electron mobility of the order of $10^{-4} \, cm^2 \, V^{-1} \, s^{-1}$ [138]. The structures of the ruthenium polymers **26b–e** with dppz moieties are shown in Fig. 10.15. The metal-free dppz containing polymer **26a** was also synthesized for comparison. The rhenium containing polymers **27a–f** were synthesized by similar approach as abovementioned. Polymers **26b–e** are all soluble in polar solvents such as NMP, DMF, and DMSO due to the presence of the ionic groups on the main chain. Thin optical films of high quality can be fabricated by spin coating or solution casting methods. However, the rhenium containing polymers **27a–f** are only soluble in *m*-cresol and slightly soluble in 1,1,2,2-tetrachloroethane, which are both nonvolatile solvents. The thin films obtained from *m*-cresol solution showed very poor film quality. Therefore, most of the physical measurements were carried out in solution phase, and the EL characterizations were mainly carried out for the ruthenium containing polymers. The PL spectra of **27a–f** are shown in Fig. 10.16. Polymer **27a** exhibits a main chain emission centered at 550 nm, and the emission from the Re dppz complex is observed as a shoulder at ca. 680 nm. The intensity of the main chain emission decreased together with the increase in relative emission intensity from the
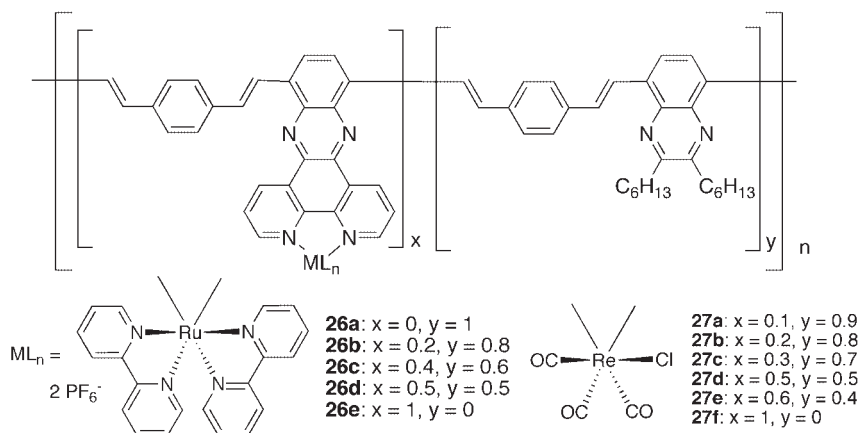
Fig. 10.15 Rhenium and ruthenium containing conjugated polymers with dipyridophenanzine ligand on the main chain.
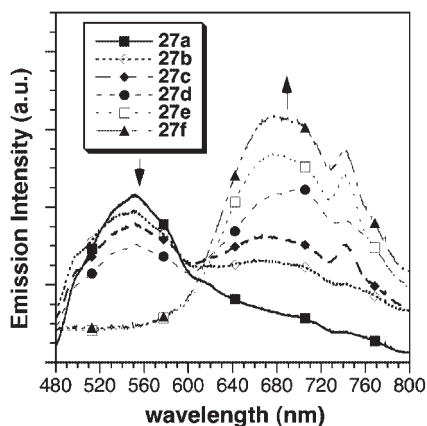
Fig. 10.16 Photoluminescence spectra of polymers **27a–f** (see Fig. 10.15) with different rhenium complex contents. The arrows indicate the trend of increasing the rhenium complex content (Adapted from [137] – Reproduced by permission of The Royal Society of Chemistry).

rhenium complex, when the Re complex content increased. No main chain emission can be observed from polymer **27f**. Similar to the previous series of polymers, it was attributed to the energy transfer from the $\pi\pi^*$ states of the main chain to the lower energy MLCT states of the metal complexes.

For the ruthenium containing polymers **26b–e**, the hole and electron carrier mobilities of the polymers were in the range between 10^{-4} and 10^{-5} cm^2 V^{-1} s^{-1} and the values are summarized in Table 10.7. The charge carrier mobilties were found to increase with the metal content. In addition, the electron carrier mobilities were

Table 10.7 Hole and electron carrier mobilities of polymers
26a–e measured at $E=40\,kV\,cm^{-1}$ (structures of the polymers
are shown in Fig. 10.15).

Polymer	Ru content per repeating unit	μ_h ($10^{-4}\,cm^2\,V^{-1}\,s^{-1}$)	μ_e ($10^{-4}\,cm^2\,V^{-1}\,s^{-1}$)
26a	0	0.55	0.85
26b	0.2	0.46	1.2
26c	0.4	0.89	1.6
26d	0.5	0.87	1.7
26e	1	3.2	4.0
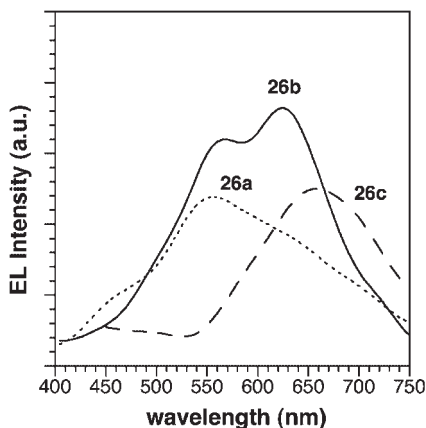
Fig. 10.17 Electroluminescence spectra of polymers **26a, 26d,**
and **26e** (Adapted from [137] – Reproduced by permission of
The Royal Society of Chemistry).

higher than the hole carrier mobilities for the polymers with the same metal content. The result indicates that the dppz moieties may function as a better electron transport unit. All these results strongly support the importance of the nature of the metal complex toward the charge-transporting processes in these polymers. The PL of the main chain and metal complex are observed at 570 and 680 nm, respectively, and their relative intensities are dependent on the metal complex content. The EL spectra from the device with the configuration ITO/polymer/Al resemble to the PL spectra (Fig. 10.17), indicating that the emissive excited states are from the same origin. The turn-on voltage of these devices was measured to be approximately 10 V.

10.4.5.3 Conjugated Polymers with Pendant Metal Complexes

An example of light emitting conjugated polymers with metal complex as pendant is shown in Fig. 10.18. Polymers **27a** and **27b** with different ruthenium contents were synthesized from the Heck coupling reaction between divinylbenzene and the corresponding aromatic di-iodide incorporated with ruthenium complex [139].
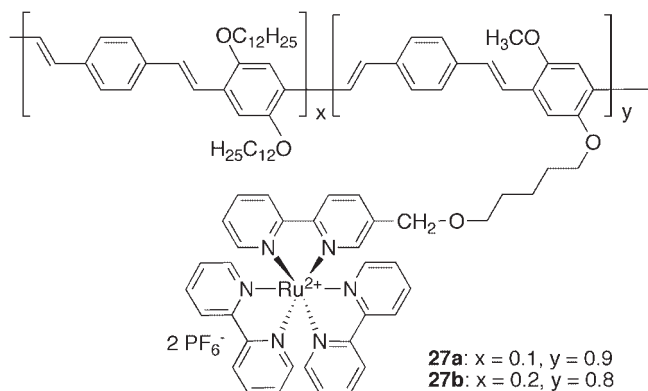
Fig. 10.18 PPV incorporated with $Ru(bpy)_3^{2+}$ complexes at the side chain.
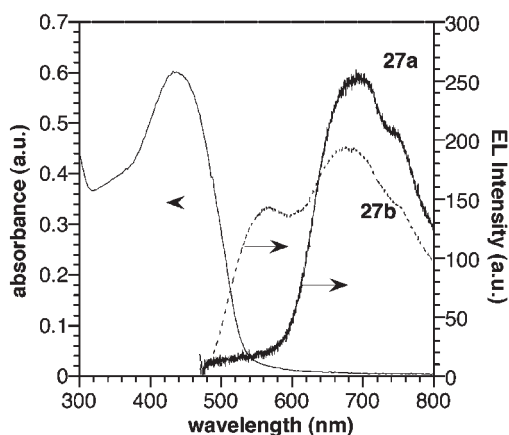
Fig. 10.19 UV-vis absorption spectrum of polymer 27b and electroluminescence spectra of polymers 27a and 27b.

In the UV-vis absorption spectrum of polymer 27b (Fig. 10.19), the peak of the π–π* transition was observed at 440 nm, but the Ru complex MLCT absorption only appeared as a very small shoulder at ca. 500–520 nm. Despite the low metal content in the polymer, the PL spectrum was dominated by the emission from the Ru complex MLCT states at 640 nm. The emission due to the main chain only appeared as a shoulder at 560 nm. This is also an indication of quenching of the main chain emission by the metal complex. The EL spectra of polymers 27a and 27b are shown in Fig. 10.19. Polymer 27a (with 10% Ru) showed the emission from both main chain and pendant Ru complex, which resulted in a yellow emission from the device. On the other hand, polymer 27b was dominated by the red emission, entirely from the Ru complex. The results suggested that the desired emission color can be easily adjusted from the metal containing polymers with the metal complex either conjugatively linked onto the polymer backbone or attached as a pendant.

10.5
Summary

It has been shown that metal containing polymers are also promising candidates as key materials in light-emitting devices. Emission properties of the devices can be modified simply by varying the metal center of the complex, the structure of the chelating ligands, or the metal content in the polymer. In most of the examples of metal containing polymers, light emissions are originated from the triplet excited states, which reveals that the device efficiency can be approached to that of small molecular electrophosphorescent materials and with superior processing ability for device fabrication. The metal complex can be incorporated on the polymer backbone or as a pendant. The different material architectures provide large versatility in tailor-making promising materials with desired properties via various types of polymerization reactions for monomers with different functionalities. The electronic properties of these two types of metal containing polymers can be fine tuned and the emission can be obtained spanning from UV to IR. In contrast to the currently developed PLEDs materials based on platinum or iridium, most of the ruthenium polymers presented in this chapter are by no means considered to be highly efficient light-emitting materials, since the intrinsic electronic properties are different and the device configurations for the ruthenium-based device still have room for improvement. Nevertheless, they demonstrated unique electrochemical and electronic properties which have drawn the attention of researchers for further development in this area. Bearing numerous merits of metal containing polymers, high efficiency OLEDs based on this type of material are expected to play an important role in the display industry. In addition to serving as light emitters, metal complexes can also play a role as sensitizers and charge transport units. Electronic interactions between metal complexes and the polymer main chain may result in interesting photophysical properties. It is of fundamental importance to understand these processes. There have been examples of employing ruthenium containing polymers as the photosensitizing materials in polymer-based photovoltaic cells [140]. Polymer **22f** was fabricated into photovoltaic cells by sandwiching the polymer between ITO and C_{60}/Al electrodes, in which the fullerene functioned as the electron accepting layer [92]. The power conversion efficiency was measured to be 0.5%. In a more recent example, photovoltaic cells composed of ruthenium terpyridyl complex containing PPV and sulfonated polyaniline were fabricated by the layer-by-layer deposition technique [141]. The advantage of this thin film formation method is that the thickness of the polymer multilayer can be easily and accurately controlled by varying the number of deposition cycles in the fabrication process. The controlled film-forming process and well-defined film morphology are essential in optimizing the device performance. More examples of metal containing multifunctional polymers as the electroactive materials for various photonic and electronic applications can be envisaged in the near future.

References

1 M. Pope, H. Kallmann, P. Magnante, *J. Chem. Phys.* **1963**, *38*, 2042.

2 C. W. Tang, S. A. Vanslyke, *Appl. Phys. Lett.* **1987**, *51*, 913.

3 J. H. Burroughes, D. D. C. Bradley, A. R. Brown, R. N. Marks, K. Mackay, R. H. Friend, P. L. Burn, A. B. Holmes, *Nature* **1990**, *347*, 539.

4 C. W. Tang, S. A. Vanslyke, C. H. Chen, *J. Appl. Phys.* **1989**, *65*, 3610.

5 Y. Qiu, Y. D. Gao, L. D. Wang, P. Wei, L. Duan, D. Q. Zhang, G. F. Dong, *Appl. Phys. Lett.* **2002**, *81*, 3540.

6 Y. Hamada, N. Matsusue, H. Kanno, H. Fujii, T. Tsujioka, H. Takahashi, *Jpn. J. Appl. Phys. 2* **2001**, *40*, L753.

7 T. Tsujioka, Y. Hamada, H. Takahashi, *Jpn. J. Appl. Phys. 1* **2000**, *39*, 3463.

8 Y. Hamada, H. Kanno, T. Tsujioka, H. Takahashi, T. Usuki, *Appl. Phys. Lett.* **1999**, *75*, 1682.

9 W. B. Gao, K. X. Yang, H. Y. Liu, J. Feng, J. Y. Hou, S. Y. Liu, *Synth. Met.* **2003**, *137*, 1529.

10 S. A. Swanson, G. M. Wallraff, J. P. Chen, W. J. Zhang, L. D. Bozano, K. R. Carter, J. R. Salem, R. Villa, J. C. Scott, *Chem. Mater.* **2003**, *15*, 2305.

11 C. W. Ko, Y. T. Tao, J. T. Lin, K. R. J. Thomas, *Chem. Mater.* **2002**, *14*, 357.

12 A. Hepp, G. Uirich, R. Schmechel, H. von Seggern, R. Ziessel, *Synth. Met.* **2004**, *146*, 11.

13 S. E. Shaheen, B. Kippelen, N. Peyghambarian, J. F. Wang, J. D. Anderson, E. A. Mash, P. A. Lee, N. R. Armstrong, Y. Kawabe, *J. Appl. Phys.* **1999**, *85*, 7939.

14 V. Bulovic, A. Shoustikov, M. A. Baldo, E. Bose, V. G. Kozlov, M. E. Thompson, S. R. Forrest, *Chem. Phys. Lett.* **1998**, *287*, 455.

15 F. Nuesch, D. Berner, E. Tutis, M. Schaer, C. Q. Ma, X. S. Wang, B. W. Zhang, F. Niiesch, *Adv. Funct. Mater.* **2005**, *15*, 323.

16 H. Shirakawa, E. J. Louis, A. G. MacDiarmid, C. K. Chiang, A. J. Heeger, *J. Chem. Soc. Chem. Commun.* **1977**, 578.

17 C. K. Chiang, C. R. Fincher, Y. W. Park, A. J. Heeger, H. Shirakawa, E. J. Louis, S. C. Gau, A. G. MacDiarmid, *Phys. Rev. Lett.* **1977**, *39*, 1098.

18 A. Kraft, A. C. Grimsdale, A. B. Holmes, *Chem. Int. Ed.* **1998**, *37*, 402.

19 P. L. Burn, D. D. C. Bradley, A. R. Brown, R. H. Friend, A. B. Holmes, *Synth. Met.* **1991**, *41*, 261.

20 S. Hoger, J. J. Mcnamara, S. Schricker, F. Wudl, *Chem. Mater.* **1994**, *6*, 171.

21 D. H. Hwang, S. T. Kim, H. K. Shim, A. B. Holmes, S. C. Moratti, R. H. Friend, *J. Chem. Soc. Chem. Commun.* **1996**, 2241.

22 Z. N. Bao, Y. M. Chen, R. B. Cai, L. P. Yu, *Macromolecules* **1993**, *26*, 5281.

23 A. C. Grimsdale, F. Cacialli, J. Gruner, X. C. Li, A. B. Holmes, S. C. Moratti, R. H. Friend, *Synth. Met.* **1996**, *76*, 165.

24 P. L. Burn, A. Kraft, D. R. Baigent, D. D. C. Bradley, A. R. Brown, R. H. Friend, R. W. Gymer, A. B. Holmes, R. W. Jackson, *J. Am. Chem. Soc.* **1993**, *115*, 10117.

25 P. L. Burn, A. B. Holmes, A. Kraft, D. D. C. Bradley, A. R. Brown, R. H. Friend, *J. Chem. Soc. Chem. Commun.* **1992**, 32.

26 P. L. Burn, A. B. Holmes, A. Kraft, D. D. C. Bradley, A. R. Brown, R. H. Friend, R. W. Gymer, *Nature* **1992**, *356*, 47.

27 N. C. Greenham, S. C. Moratti, D. D. C. Bradley, R. H. Friend, A. B. Holmes, *Nature* **1993**, *365*, 628.

28 A. Kraft, P. L. Burn, A. B. Holmes, D. D. C. Bradley, A. R. Brown, R. H. Friend, R. W. Gymer, *Synth. Met.* **1993**, *55*, 936.

29 G. Grem, G. Leditzky, B. Ullrich, G. Leising, *Synth. Met.* **1992**, *51*, 383.

30 M. Leclerc, *J. Polym. Sci. Pol. Chem.* **2001**, *39*, 2867.

31 I. D. Rees, K. L. Robinson, A. B. Holmes, C. R. Towns, R. O'Dell, *MRS Bull.* **2002**, *27*, 451.

32 U. Scherf, E. J. W. List, *Adv. Mater.* **2002**, *14*, 477.

33 W. S. Wu, M. Inbasekaran, M. Hudack, D. Welsh, W. L. Yu, Y. Cheng, C. Wang, S. Kram, M. Tacey, M. Bernius, R. Fletcher, K. Kiszka, S. Munger, J. O'Brien, *Microelectron. J.* **2004**, *35*, 343.

34 I. S. Millard, *Synth. Met.* **2000**, *111*, 119.

35 A. Cirpan, L. M. Ding, F. E. Karasz, *Synth. Met.* **2005**, *150*, 195.

36 M. A. Baldo, M. E. Thompson, S. R. Forrest, *Nature* **2000**, *403*, 750.

37 H. Yersin, *Top. Curr. Chem.* **2004**, *241*, 1.

38 J. Kido, Y. Okamoto, *Chem. Rev.* **2002**, *102*, 2357.

39 J. Kido, K. Nagai, Y. Ohashi, *Chem. Lett.* **1990**, 657.

40 J. Kido, K. Nagai, Y. Okamoto, T. Skotheim, *Chem. Lett.* **1991**, 1267.

41 J. Kido, K. Nagai, Y. Okamoto, *J. Alloy Compd.* **1993**, *192*, 30.

42 V. Christou, O. V. Salata, T. Q. Ly, S. Capecchi, N. J. Bailey, A. Cowley, A. M. Chippindale, *Synth. Met.* **2000**, *111*, 7.

43 S. Capecchi, O. Renault, D. G. Moon, M. Halim, M. Etchells, P. J. Dobson, O. V. Salata, V. Christou, *Adv. Mater.* **2000**, *12*, 1591.

44 Z. Q. Bian, C. H. Huang, "Progress in Electroluminscence Based on Lanthanide Complexes" chapter 12 this volume.

45 M. A. Baldo, D. F. O'Brien, Y. You, A. Shoustikov, S. Sibley, M. E. Thompson, S. R. Forrest, *Nature* **1998**, *395*, 151.

46 M. A. Baldo, S. Lamansky, P. E. Burrows, M. E. Thompson, S. R. Forrest, *Appl. Phys. Lett.* **1999**, *75*, 4.

47 R. C. Kwong, S. Sibley, T. Dubovoy, M. A. Baldo, S. R. Forrest, M. E. Thompson, *Chem. Mater.* **1999**, *11*, 3709.

48 D. F. O'Brien, M. A. Baldo, M. E. Thompson, S. R. Forrest, *Appl. Phys. Lett.* **1999**, *74*, 442.

49 C. Adachi, M. A. Baldo, S. R. Forrest, S. Lamansky, M. E. Thompson, R. C. Kwong, *Appl. Phys. Lett.* **2001**, *78*, 1622.

50 J. Brooks, Y. Babayan, S. Lamansky, P. I. Djurovich, I. Tsyba, R. Bau, M. E. Thompson, *Inorg. Chem.* **2002**, *41*, 3055.

51 S. Lamansky, P. Djurovich, D. Murphy, F. Abdel-Razzaq, H. E. Lee, C. Adachi, P. E. Burrows, S. R. Forrest, M. E. Thompson, *J. Am. Chem. Soc.* **2001**, *123*, 4304.

52 S. Lamansky, P. Djurovich, D. Murphy, F. Abdel-Razzaq, R. C. Kwong, I. Tsyba, M. Bortz, B. Mui, R. Bau, M. E. Thompson, *Inorg. Chem.* **2001**, *40*, 1704.

53 A. B. Tamayo, B. D. Alleyne, P. Djurovich, S. Lamansky, I. Tsyba, N. N. Ho, R. Bau, M. E. Thompson, *J. Am. Chem. Soc.* **2003**, *125*, 7377.

54 J. Li, P. Djurovich, B. D. Alleyne, I. Tsyba, N. N. Ho, R. Bau, M. E. Thompson, *Polyhedron* **2004**, *23*, 419.

55 P. Coppo, E. A. Plummer, L. De Cola, *J. Chem. Soc. Chem. Commun.* **2004**, 1774.

56 J. C. Ostrowski, M. R. Robinson, A. J. Heeger, G. C. Bazan, *J. Chem. Soc. Chem. Commun.* **2002**, 784.

57 X. Gong, J. C. Ostrowski, G. C. Bazan, D. Moses, A. J. Heeger, *Appl. Phys. Lett.* **2002**, *81*, 3711.

58 X. Gong, M. R. Robinson, J. C. Ostrowski, D. Moses, G. C. Bazan, A. J. Heeger, *Adv. Mater.* **2002**, *14*, 581.

59 Y. J. Su, H. L. Huang, C. L. Li, C. H. Chien, Y. T. Tao, P. T. Chou, S. Datta, R. S. Liu, *Adv. Mater.* **2003**, *15*, 884.

60 C. S. K. Mak, A. Hayer, S. I. Pascu, S. E. Watkins, A. B. Holmes, A. Köhler, R. H. Friend, *J. Chem. Soc. Chem. Commun.* **2005**, 4708.

61 C. Adachi, M. A. Baldo, S. R. Forrest, M. E. Thompson, *Appl. Phys. Lett.* **2000**, *77*, 904.

62 C. Adachi, M. A. Baldo, M. E. Thompson, S. R. Forrest, *Appl. Phys. Lett.* **2001**, *90*, 5048.

63 M. Ikai, S. Tokito, G. Sakamoto, T. Suzuki, Y. Taga, *Appl. Phys. Lett.* **2001**, *79*, 156.

64 R. D. Xia, G. Heliotis, D. D. C. Bradley, *Synth. Met.* **2004**, *140*, 117.

65 G. He, M. Pfeiffer, K. Leo, M. Hofmann, J. Birnstock, R. Pudzich, J. Salbeck, *Appl. Phys. Lett.* **2004**, *85*, 3911.

66 M.-J. Yang, T. Tsutsui, *Jpn. J. Appl. Phys.* **2000**, *39*, 828.

67 K. M. Vaeth, C. W. Tang, *J. Appl. Phys.* **2002**, *92*, 3447.

68 X. Yang, D. Neher, D. Hertel, T. K. Däubler, *Adv. Mater.* **2004**, *16*, 161.

69 W. Zhu, Y. Mo, M. Yuan, W. Yang, Y. Cao, *Appl. Phys. Lett.* **2002**, *80*, 2045.

70 D. F. O'Brien, C. Giebeler, R. B. Fletcher, J. Cadlby, L. C. Palilis, D. G. Lidzey, P. A. Lane, D. D. C. Bradley, W. Blau, *Synth. Met.* **2001**, *116*, 379.

71 P. A. Lane, L. C. Palilis, D. F. O'Brien, C. Giebeler, A. J. Cadby, D. G. Lidzey, A. J. Campbell, W. Blau, D. D. C. Bradley, *Phys. Rev. B* **2001**, 63.

72 T. F. Guo, S. C. Chang, Y. Yang, R. C. Kwong, M. E. Thompson, *Org. Electron.* **2000**, *1*, 15.

73 K. Brunner, A. van Dijken, H. Borner, J. J. A. M. Bastiaansen, N. M. M. Kiggen, B. M. W. Langeveld, *J. Am. Chem. Soc.* **2004**, *126*, 6035.

74 A. van Dijken, J. J. A. M. Bastiaansen, N. M. M. Kiggen, B. M. W. Langeveld, C. Rothe, A. Monkman, I. Bach, P. Stossel, K. Brunner, *J. Am. Chem. Soc.* **2004**, *126*, 7718.

75 F. C. Chen, S. C. Chang, G. He, S. Pyo, Y. Yang, M. Kurotaki, J. Kido, *J. Polym. Sci. Pol. Phys.* **2003**, *41*, 2681.

76 X. Gong, J. Ostrowski, D. Moses, G. C. Bazan, A. J. Heeger, *J. Polym. Sci. Pol. Phys.* **2003**, *41*, 2691.

77 F. C. Chen, G. F. He, Y. Yang, *Appl. Phys. Lett.* **2003**, *82*, 1006.

78 S. Tokito, M. Suzuki, F. Sato, *Thin Solid Films* **2003**, *445*, 353.

79 K. A. Walters, K. D. Ley, C. S. P. Cavalaheiro, S. E. Miller, D. Gosztola, M. R. Wasielewski, A. P. Bussandri, H. van Willigen, K. S. Schanze, *J. Am. Chem. Soc.* **2001**, *123*, 8329.

80 K. D. Glusac, S. Jiang, K. S. Schanze, *J. Chem. Soc. Chem. Commun.* **2002**, 2504.

81 G. B. Cunningham, Y. Li, S. Liu, K. S. Schanze, *J. Phys. Chem. B* **2003**, *107*, 12569.

82 A. J. Sandee, C. K. Williams, N. R. Evans, J. E. Davies, C. E. Boothby, A. Köhler, R. H. Friend, A. B. Holmes, *J. Am. Chem. Soc.* **2004**, *126*, 7041.

83 K. Kalyanasundaram, *Coord. Chem. Rev.* **1982**, *46*, 159.

84 A. Juris, V. Balzani, F. Barigelletti, S. Campagna, P. Belser, A. Von Zelewsky, *Coord. Chem. Rev.* **1988**, *84*, 85.

85 H. Yersin, W. Humbs, J. Strasser, *Top. Curr. Chem.* **1997**, *191*, 153.

86 J.-P. Sauvage, J.-P. Collin, J.-C. Chambron, S. Guillerez, C. Coudret, *Chem. Rev.* **1994**, *94*, 993.

87 C. Kaes, A. Katz, M. W. Hosseini, *Chem. Rev.* **2000**, *100*, 3553.

88 J.-K. Lee, D. Yoo, M. F. Rubner, *Chem. Mater.* **1997**, *9*, 1710.

89 S. C. Yu, S. J. Hou, W. K. Chan, *Macromolecules* **2000**, *33*, 3259.

90 Y. Kurimura, N. Shinozaki, F. Ito, Y. Uratani, K. Shigehara, E. Tsuchida, M. Kaneko, A. Yamada, *Bull. Chem. Soc. Jpn.* **1982**, *55*, 380.

91 P. K. Ng, X. Gong, W. T. Wong, W. K. Chan, *Macromol. Rapid Commun.* **1997**, *18*, 1009.

92 P. K. Ng, X. Gong, S. H. Chan, L. S. M. Lam, W. K. Chan, *Chem. Eur. J.* **2001**, *7*, 4358.

93 X. F. Wu, C. L. Fraser, *Macromolecules* **2000**, *33*, 4053.

94 K. Yagi, M. De Loudres Rivera-Castro, *Inorg. Chim. Acta.* **1987**, *131*, 273.

95 S. Cosnier, A. Deronzier, J. F. Roland, *J. Electroanal. Chem.* **1990**, *285*, 133.

96 T. Yamamoto, Y. Yoneda, T. Maruyama, *J. Chem. Soc. Chem. Commun.* **1992**, 1652.

97 C. G. Cameron, P. G. Pickup, *J. Chem. Soc. Chem. Commun.* **1997**, 303.

98 S. C. Yu, X. Gong, W. K. Chan, *Macromolecules* **1998**, *31*, 5639.

99 L. Trouillet, A. De Nicola, S. Guillerez, *Chem. Mater.* **2000**, *12*, 1611.

100 S. C. Rasmussen, D. W. Thompspn, V. Singh, J. Petersen, *Inorg. Chem.* **1996**, *35*, 3449.

101 S. Kelch, M. Rehahn, *Macromolecules* **1997**, *30*, 6185.

102 S. Campagna, G. Denti, S. Serroni, A. Juris, M. Venturi, V. Ricevuto, V. Balzani, *Chem. Eur. J.* **1995**, *1*, 211.

103 J. K. Lee, D. S. Yoo, E. S. Handy, M. F. Rubner, *Appl. Phys. Lett.* **1996**, *69*, 1686.

104 C. H. Lyons, E. D. Abbas, J. K. Lee, M. F. Rubner, *J. Am. Chem. Soc.* **1998**, *120*, 12100.

105 E. S. Handy, A. J. Pal, M. F. Rubner, *J. Am. Chem. Soc.* **1999**, *121*, 3525.

106 S. Bernhard, J. A. Barron, P. L. Houston, H. D. Abruna, J. L. Ruglovksy, X. C. Gao, G. G. Malliaras, *J. Am. Chem. Soc.* **2002**, *124*, 13624.

107 D. A. Bernards, T. Biegala, Z. A. Samuels, J. D. Slinker, G. G. Malliaras, S. Flores-Torres, H. D. Abruna, J. A. Rogers, *Appl. Phys. Lett.* **2004**, *84*, 3675.

108 F. G. Gao, A. J. Bard, *J. Am. Chem. Soc.* **2000**, *122*, 7426.

109 F. G. Gao, A. J. Bard, *Chem. Mater.* **2002**, *14*, 3465.

110 C. Y. Liu, A. J. Bard, *J. Am. Chem. Soc.* **2002**, *124*, 4190.

111 C. Y. Liu, A. J. Bard, *Appl. Phys. Lett.* **2005**, *87*, 061110.

112 H. Rudmann, M. F. Rubner, *J. Appl. Phys.* **2001**, *90*, 4338.

113 H. Rudmann, S. Shimada, M. F. Rubner, *J. Am. Chem. Soc.* **2002**, *124*, 4918.

114 J. H. Yang, K. C. Gordon, *Chem. Phys. Lett.* **2003**, *372*, 577.

115 J. Yang, K. C. Gordon, *Synth. Met.* **2005**, *152*, 213.

116 H. Xia, C. B. Zhang, S. Qiu, P. Lu, J. Y. Zhang, Y. G. Ma, *Appl. Phys. Lett.* **2004**, *84*, 290.

117 H. Xia, C. B. Zhang, X. D. Liu, S. Qiu, P. Lu, F. Z. Shen, J. Y. Zhang, Y. G. Ma, *J. Phys. Chem. B* **2004**, *108*, 3185.

118 N. Tamato, C. Adachi, K. Nagai, *Chem. Mater.* **1997**, *9*, 1077.

119 X. Gong, P. K. Ng, W. K. Chan, *Adv. Mater.* **1998**, *10*, 1337.

120 P. K. Ng, PhD Thesis, The University of Hong Kong (Hong Kong), **1999**.

121 J. K. Lee, D. Yoo, M. F. Rubner, *Chem. Mater.* **1997**, *9*, 1710.

122 A. P. Wu, J. Lee, M. F. Rubner, *Thin Solid Films* **1998**, *329*, 663.

123 A. Wu, D. Yoo, J. K. Lee, M. F. Rubner, *J. Am. Chem. Soc.* **1999**, *121*, 4883.

124 J. A. Barron, S. Bernhard, P. L. Houston, H. D. Abruna, J. L. Ruglovsky, G. G. Malliaras, *J. Phys. Chem. A* **2003**, *107*, 8130.

125 W. K. Chan, X. Gong, W. Y. Ng, *Appl. Phys. Lett.* **1997**, *71*, 2919.

126 Y. Yang, Q. Pei, *Adv. Mater.* **1995**, *7*, 559.

127 Z. Peng, Z. Bao, M. E. Galvin, *Adv. Mater.* **1998**, *10*, 680.

128 B. Schulz, M. Bruma, L. Brehmer, *Adv. Mater.* **1997**, *9*, 601.

129 P. M. Borsenberger, D. S. Weiss, *Organic Photoreceptors For Xerography*, Marcel Dekker, New York, **1998**.

130 M. Van der Auweraer, F. C. De Schryver, P. M. Borsenberger, H. Bässler, *Adv. Mater.* **1994**, *6*, 199.

131 P. M. Borsenberger, L. Pautmeier, H. Bässler, *J. Chem. Phys.* **1991**, *94*, 5447.

132 A. Y. Kryukov, A. C. Saidov, A. V. Vannikov, *Thin Solid Films* **1992**, *209*, 84.

133 H. Tokuhisa, M. Era, T. Tsutsui, S. Saito, *Appl. Phys. Lett.* **1995**, *66*, 3433.

134 P. M. Borsenberger, W. Mey, Chowdry, *J. Appl. Phys.* **1978**, *49*, 273.

135 P. M. Borsenberger, *J. Appl. Phys.* **1990**, *68*, 6253.

136 G. Pfister, *Phys. Rev. B* **1977**, *16*, 3676.

137 W. K. Chan, P. K. Ng, X. Gong, S. J. Hou, *J. Mater. Chem.* **1999**, *9*, 2103.

138 M. Redecker, D. D. C. Bradley, M. Jandke, P. Strohriegi, *Appl. Phys. Lett.* **1999**, *75*, 109.

139 C. T. Wong, W. K. Chan, *Adv. Mater.* **1999**, *11*, 455.

140 W. K. Chan, C. S. Hui, K. Y. K. Man, K. W. Cheng, H. L. Wong, N. Zhu, A. B. Djurisic, *Coord. Chem. Rev.* **2005**, *249*, 1351.

141 K. Y. K. Man, H. L. Wong, W. K. Chan, C. Y. Kwong, A. B. Djurisic, *Chem. Mater.* **2004**, *16*, 365.

11

Molecular Engineering of Iridium Complexes and their Application in Organic Light Emitting Devices

Mohammad K. Nazeeruddin, Cedric Klein, Michael Grätzel, Libero Zuppiroli, and Detlef Berner

Iridium (III) cyclometalated complexes exhibit exceptional photophysical properties useful for Organic Light-Emitting Diode (OLED) applications. In this chapter, we report a study of neutral, cationic and anionic Ir(III) complexes, and describe a strategy to tune the phosphorescence wavelength and emission quantum yields by selective ligand functionalization. A typical light-emitting electrochemical cell, and multi-layer device architecture containing triplet emitters with the effect of doping concentration on the transport characteristics is described.

11.1
Introduction

Iridium(III) cyclometalated complexes are attracting widespread interest because of their unique photophysical properties and applications in organic light-emitting diodes (OLEDs). Several groups have extensively used neutral iridium cyclometalated complexes in OLEDs and obtained up to 19% external quantum efficiency [1–4], which require a multilayered structure for charge injection, transport, and light emission. In these devices, neutral iridium complexes are used, which can be evaporated under vacuum [5]. Another type of organic light-emitting device is the light-emitting electrochemical cell (LEC), which makes use of ionic charges to facilitate electronic charge injection from the electrodes into the organic or inorganic molecular semiconductor, eliminating the need for extra layers [6–11]. This is a promising alternative to OLED, particularly for large-area lighting applications [11]. In these cells, the use of ionic complexes facilitates electronic charge injection into the light-emitting film [7, 12–15].

   The main requirement for OLEDs and LECs is that the phosphorescent emitter should have sharp color and exhibit very high phosphorescent quantum yields. Modification of iridium complexes by modulating ligands for tuning of phosphorescence wavelength from blue to red is attractive for both fundamental research and practical applications. The goal of this chapter is to elucidate phosphorescent color tuning characteristics of iridium complexes, to discuss the corresponding

OLED device architecture in which they are used as dopants, the related charge transport features, and the quantum efficiency.

The photophysical and photochemical properties of 4d and 5d metal complexes using polypyridyl ligands have been thoroughly investigated during the last three decades. The main thrust behind these studies is to understand the energy and electron transfer processes in the excited states and to apply this knowledge to potential practical applications such as dye-sensitized solar cells, organic light-emitting diodes, and light-emitting electrochemical cells. The electrochemical, photophysical, ground, and the excited state properties of these complexes play an important role for charge transfer dynamics at the interfaces.

For organic light-emitting diodes and light-emitting electrochemical cells, phosphorescent iridium complexes are one of the key components. The choice of iridium metal is of special interest for a number of reasons: (i) because of its quasioctahedral geometry, one can introduce specific ligands in a controlled manner; (ii) the photophysical and the electrochemical properties of iridium complexes can be tuned in a predictable way; (iii) the iridium metal possess stable and accessible oxidation and reduction states; (iv) tris-orthometallated iridium complexes are known to have the highest triplet quantum yields.

The periodic chart of the elements is fascinating for chemists working with metals, for example, iridium metal is in the group VIII B, which lies below cobalt and rhodium metals. Although, cobalt is an inexpensive and abundant metal, the photophysical and electrochemical properties of its complexes are difficult to tune in an expected fashion. The other notable disadvantage of the cobalt metal is its small ligand field splitting compared to rhodium and iridium. On the other hand, iridium being in the third row of the transition metal ions has a stronger ligand field splitting compared to cobalt and rhodium. Moreover, the spin orbit coupling in iridium complexes leads to enhanced conversion of singlet state into triplet state population resulting in augmented quantum yields. In the following section, we will briefly discuss the ligand field splitting of octahedral d^6 complexes.

11.1.1
Ligand Field Splitting

The five d orbitals d_{xy}, d_{xz}, d_{yz}, $d_{x^2-y^2}$, and d_{z^2}, of free transition metal ions, in the gas phase, are degenerated in energy. Though, it is oversimplified, one can view the formation of a complex between metal ion and ligands as an electrostatic attraction between positively charged metal and negatively charged ions or the negative ends of the dipoles of neutral ligands. The approach of the negative or neutral ligands toward a charged metal repels electrons residing in d orbitals and raises their energies both with respect to those residing on the ligands and the metal. In an octahedral ligand field, these five degenerate d orbitals split into degenerate t_{2g} (d_{xy}, d_{xz}, d_{yz},) and e_g ($d_{x^2-y^2}$, and d_{z^2}) set of orbitals. The energy gap between these sets of degenerated orbitals is called ligand field splitting (Δ_{Oh}). The ligand field splitting value increases by about 40% as one moves from the first row (3d) to the second (4d) and third (5d) row transition metal ions. A schematic rep-
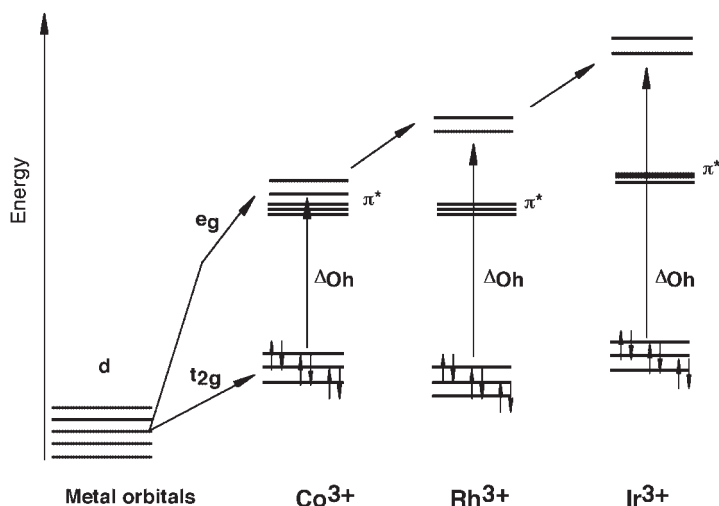
Fig. 11.1 A d-orbital splitting pattern for Co^{3+}, Rh^{3+}, and Ir^{3+} in an octahedral field. The relative e_g levels with respect to t_{2g} and ligand $\pi*$ orbitals are shown arbitrarily.

resentation for splitting of d orbitals and the position of ligand orbitals in an octahedral complex is shown in Fig. 11.1.

11.1.2
Photophysical Properties

The photophysics of polypyridyl complexes of iridium can be understood with the aid of an energy diagram shown in Fig. 11.2. In these complexes, there are three possible types of excited states: (a) metal-centered (MC) excited states, which are due to promotion of an electron from t_{2g} to e_g orbitals; (b) ligand-centered (LC) states that are $\pi-\pi*$ transitions; (c) metal-to-ligand charge transfer states (MLCT). An electron transition from metal t_{2g} orbitals to empty ligand orbitals without spin change is allowed, which is called singlet–singlet absorption. The allowed transitions are identified by large extinction coefficient. The transitions with spin change are called singlet–triplet absorption, which are forbidden and associated with small extinction coefficient. However, the excited singlet state may involve in spin flip, resulting in an excited triplet state that is called intersystem crossing (ISC). The radiative process of a singlet and triplet excited state to a singlet ground state is termed as fluorescence and phosphorescence, respectively. The excited singlet states associated with ligand-centered (LC) $\pi-\pi*$ and metal-to-ligand charge transfer transitions (MLCT) converts into triplet excited states efficiently in iridium complexes due to spin–orbit coupling resulting enhanced phosphorescence quantum yields. For the cyclometalated iridium complexes, the wavefunction of the excited triplet state, responsible for phosphorescence is principally expressed as combination of the ligand-centered and the MLCT excited triplet state. However,
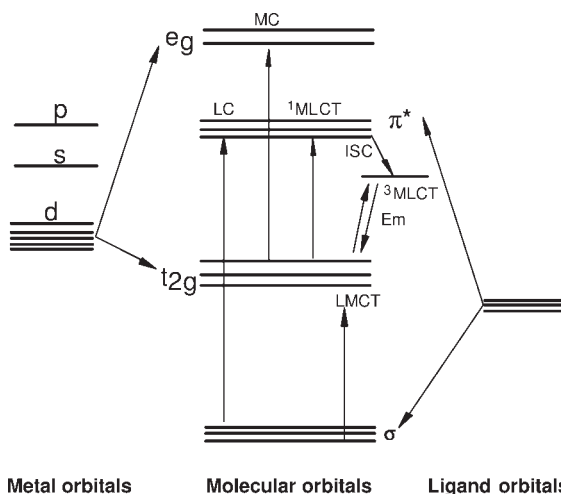
Fig. 11.2 Schematic and simplified molecular orbital diagram for an octahedral d^6 metal complex involving 2-phenylpyridine (C_3 symmetry) type ligands in which various possible transitions are indicated.

not all the complexes are highly luminescent because of the different deactivation pathways, and the discussion is beyond the scope of this chapter.
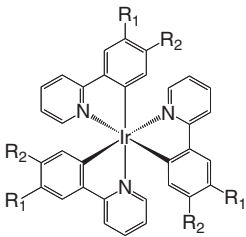
11.2
Phosphorescent Iridium Complexes

11.2.1
Tuning of Phosphorescence Colors in Neutral Iridium Complexes

Neutral iridium complexes were obtained by orthometalation reaction with ligands, which contain a benzene ring attached to a functional group containing a donor atom such as 2-phenylpyridine (ppy) and benzo[h]-quinoline (bzq) [16]. The coordination of ppy and bzq ligands to metal is analogous to that found in 2,2′-bipyridine except nitrogen is replaced by carbon anion [17]. In a typical example, three 2-phenylpyridine ligands coordinate around iridium(III) resulting in a neutral complex, in which the phenyl group carries a formal negative charge due to loss of proton and subsequent orthometalation to iridium metal. The highest occupied molecular orbital (HOMO's) in tris-phenylpyridine iridium(III) [Ir(ppy)$_3$] is principally composed of orbitals of the phenyl ring and the metal d orbitals. The pyridine is formally neutral and the major contributor to the lowest unoccupied molecular orbital (LUMO) in [Ir(ppy)$_3$] complex [18].

The absorption spectra of [Ir(ppy)$_3$] display strong ligand-to-ligand (LC, π–π*) and metal-to-ligand charge transfer (MLCT) transitions in the UV and the visible region, respectively. The MLCT transitions bands are lower in energy compared to the ligand-centered π–π* transitions. The excited triplet state shows strong

Table 11.1 Emission, lifetime, and electrochemical data of complexes **1–8**.

1 : R_1=H ; R_2=H
2 : R_1=H ; R_2=CH_3
3 : R_1=H ; R_2=C_3H_7
4 : R_1=H ; R_2=tBu
5 : R_1=H ; R_2=F
6 : R_1=H ; R_2=CF_3
7 : R_1=H ; R_2=OCH_3
8 : R_1=OCH_3 ; R_2=H

Complex	Emission. λ_{max} (nm)	Lifetime τ (µs)	$E^{1/2}_{ox}$ V vs. saturated calomel electrode (SCE)
1	494	1.9	0.77
2	493	1.9	0.70
3	496	1.9	0.67
4	497	1.9	0.66
5	468	2.0	0.97
6	494	2.2	1.08
7	481	2.2	0.75
8	539	2.9	0.55
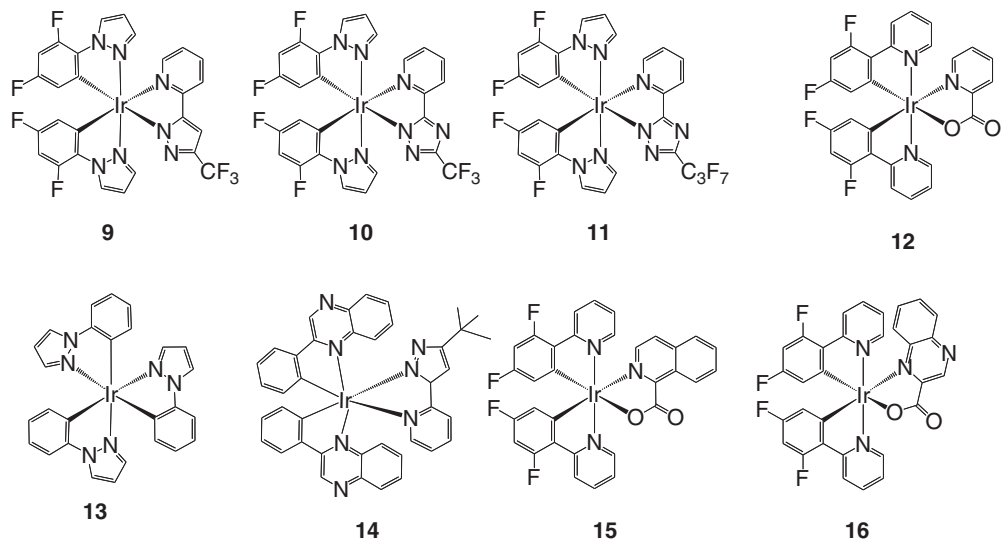
phosphorescence in the green region at around 515 nm, with an excited state lifetime of 2 µs [19].

In order to tune the phosphorescence color of [Ir(ppy)$_3$], Watts et al., synthesized several substituted 2-phenylpyridine-based neutral iridium complexes [19–21]. Table 11.1 shows the list of complexes, which show strong phosphorescence from a ^{3}MLCT excited state, and the phosphorescence lifetime of these complexes is in the range of 2–3 µs in nitrogen-saturated acetonitrile at room temperature [20]. The photophysical and electrochemical data (see Table 11.1) demonstrate the influence of ligands bearing electron-withdrawing and the electron-donating substituents. It is interesting to note the difference between the complexes **7** and **8** (Table 11.1), which is simply the effect of position of electron-donating substitution on the phenyl ring. In complex **8**, the electron-donating group is substituted at 3-position of phenyl ring that destabilizes the HOMO by 0.2 V when compared to the complex **7** in which the electron-donating group is substituted at 4-position. The HOMO of a 2-phenylpyridine cyclometallated iridium complex is located primarily on the phenyl groups, therefore incorporation of electron-donating substituent in the positions *para* to the iridium–carbon bond decreases the emission energy due to *mesomeric* (oxygen lone pair donation to the aromatic π orbitals) effect. From the electrochemical data of the complexes shown in Table 11.1, it is evident that the less positive oxidation potential values result from ligands with electron-donating substituents and more positive oxidation potential values result from ligands with electron-withdrawing substituents.

In these complexes, the photophysical properties are very similar to the phenylpyridine-based iridium complexes because of substitution of electron-donating or electron-withdrawing groups on the phenyl ring. This is not surprising because the substitution of donor or acceptor groups tunes both the highest occupied molecular orbitals (HOMO) and the lowest unoccupied molecular orbitals (LUMO) levels of the metal complex in parallel, leading to marginal changes in the photophysical properties.

In mixed ligand complexes **9–12**, shown in Table 11.2 the HOMO levels have stabilized significantly compared to the tris-phenylpyridine iridium(III) complex leading to blue shifts of the emission maxima, which is also apparent from the

Table 11.2 Absorption, emission and electrochemical properties of the iridium complexes **9–16**.

Complex	Absorption, λ_{max} (nm)	Emission λ_{max} (nm) at 298 K	Electrochemical data V vs. ferrocene (Fc)		Lifetime (μs)
			$E^{1/2}_{ox}$	$E^{1/2}_{red}$	
9	295, 349	455	0.98	−2.72	0.040
10	300, 349	457	1.11	−2.72	0.008
11	302, 348	455	1.11	−2.53	0.009
12	–	468	1.00	−1.9	–
13	321	444	0.41	−3.20	–
14	359, 469	649	0.77	−1.71	1.9
15	–	581	–	−1.2	–
16	–	666	1.00	−1.1	–

Data taken from Refs. [22, 23, 26, 30].

electrochemical data [22, 23]. On the other hand, the blue shift of the emission maxima in complex **13** is due to destabilization of LUMO's of the 1-phenylpyrazolyl ligand. Several other groups have developed heteroleptic iridium complexes (see Table 11.2) in which the LUMO levels were stabilized (see Table 11.2 for $E^{1/2}_{red}$ values of complexes **14–16**) compared to tris-phenylpyridine iridium(III) complex leading to phosphorescent color maxima from green to red [24–29]. Therefore, the compounds in Table 11.2 provide an exciting opportunity to tune the emission spectral properties from blue to red, by simply selecting appropriate donor/acceptor ligands compared to the tris-homoleptic complexes of the type shown in Table 11.1.

11.2.2
Tuning of Phosphorescence Colors in Cationic Iridium Complexes
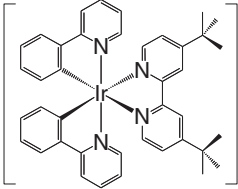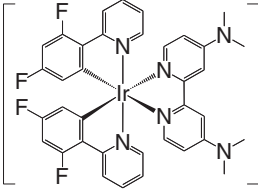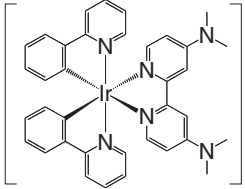
The tuning aspect of the MLCT transitions in cationic iridium complexes is illustrated by considering the following complexes: [Ir(2-phenylpyridine)$_2$(4,4'-*tert*-butyl-2,2'-bipyridine)]PF$_6$ (**17**), [Ir(2,4-difluorophenylpyridine)$_2$(4,4'-dimethylamino-2,2'-bipyridine)](PF$_6$) (**18**), and [Ir(2-phenylpyridine)$_2$(4,4'-dimethylamino-2,2'-bipyridine)](PF$_6$) (**19**). These complexes were synthesized in a low boiling solvent dichloromethane by reacting the corresponding dichloro-bridged iridium(III) dimer with 4,4'-*tert*-butyl-2,2'-bipyridine or 4,4'-dimethylamino-2,2'-bipyridine ligands (see Table 11.3) [31].

The cyclic voltammogram of complex **19** (Fig. 11.3) measured in acetonitrile containing 0.1 M tetrabutylammonium hexafluorophosphate with 100 mV scan rate shows a reversible wave at 0.72 V vs. Fc due to oxidation of iridium(III/IV), which is cathodically shifted by 210 mV compared to the complex **17** due to the donor strength of 4,4'-dimethylamino-2,2'-bipyridine [7, 31]. The three reversible reduction waves at −2.17 and −2.61, and −2.87 V vs. Fc (only two waves are shown in Fig. 11.3) are assigned to the reduction of 4,4'-dimethylamino-2,2'-bipyridine and the two 2-phenylpyridine ligands, respectively. It is interesting to note that the ligand-based reduction potential of **19** is significantly shifted cathodically (390 mV) compared to the complex **17** demonstrating that the destabilization of LUMO orbitals of 4,4'-dimethylamino-2,2'-bipyridine offsets more than the destabilization of iridium HOMO orbitals caused by donor 4,4'-dimethylamino-2,2'-bipyridine ligand, ensuing an increase in a gap between the HOMO and the LUMO of **19** compared to the HOMO–LUMO gap of complex **17**.

The cyclic voltammogram of complex **18** shows a reversible couple at 1.0 V vs. Fc due to oxidation of iridium(III/IV), and two reversible reduction waves at −2.13 and −2.49 V vs. Fc are due to 4,4'-dimethylamino-2,2'-bipyridine and 2-(2,4-difluorophenyl)pyridine ligand, respectively. The HOMO orbitals in **18** are stabilized upon insertion of fluoride substituents on the phenyl pyridine ligands, thus ensuing an increase between HOMO and LUMO gap of **18** compared to HOMO and LUMO gap of **17** and **19** (Table 11.3) [32].

UV-Vis absorption spectra of the complexes **17**, **18**, and the **19** in dichloromethane solution at 298 K display bands in the UV and the visible region due to

Table 11.3 Absorption, emission, and electrochemical properties of iridium cationic complexes **17**, **18**, and **19**.

Complex	Absorption, λ (nm)[a] (ε/10^4 M^{-1} cm^{-1})	Emission at 298 K[b]	Electrochemical data V vs. Fc[c]		Lifetime[d] (μs)
			$E^{1/2}_{ox}$	$E^{1/2}_{red}$	
17		581[e]	0.88[e]	−1.83[e]	0.557[e]
18	266 (8.27); 316 (2.89): 344 (2.20); 376 (1.45); 410 (0.41); 444 (0.14)	463, 493	1.0	−2.13 −2.49 −2.77	4.11 ± 0.02
19	268 (5.62); 290 (3.49): 356 (0.95); 376 (0.85); 444 (0.19)	491, 520	0.72	−2.17 −2.61 −2.87	2.43 ± 0.02

a   Absorption data were measured in CH2Cl2 solution.
b   Emission data were collected at 298 K by exciting at 380 nm.
c   Electrochemical measurements were carried out in acetonitrile solution and the potentials are V vs.
    ferrocinium/ferrocene (Fc).
d   Liftetime data are collected in degassed solutions.
e   Data taken from Ref. [7].

intraligand (π–π*) and metal-to-ligand charge transfer transitions (MLCT), respectively (Fig. 11.4 and Table 11.3) [33]. When excited at 298 K within the π–π* or MLCT absorption bands, complex **18** shows emission maxima at 463 and 493 nm due to the 4,4′-dimethylamino-2,2′-bipyridine ligand that increases the gap between LUMO of 4,4′-dimethylamino-2,2′-bipyridine and HOMO of iridium resulting in a blue shift of the emission maxima compared to the **17** [7, 19].

It is worth to note that the argon-degassed dichloromethane solution of the **18** and **19** shows bright luminescence in a lighted room, and displays unusual phosphorescence quantum yields of 80 ± 10% in the solution at room temperature. The emission spectral profile is independent of excitation wavelength and emission of **18** and **19** decayed as a single exponential with lifetimes of 2 and 4 μs in CH_2Cl_2 solution, respectively [34].

The electronic structure of these complexes-based DFT calculations, together with plots of selected molecular orbitals are shown in Fig. 11.5. The highest occupied molecular orbital (HOMO) in these complexes is an antibonding combination of Ir(t_{2g}) and ppy(π) orbitals, and is calculated at −5.50 and −5.66 eV for **18** and **17**,
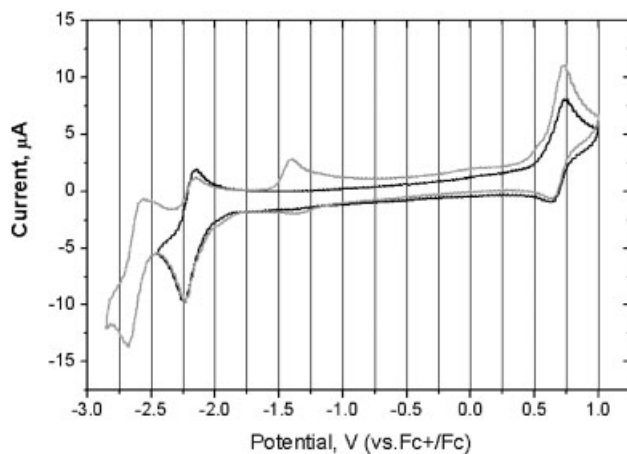
Fig. 11.3 Cyclic voltammogram of complex **19** measured in acetonitrile in presence of 0.1 M tetrabutyl ammonium hexafluorophosphate supporting electrolyte with 100 mV scan speed. The black line shows scanning between –2.4 and 1 V, and the grey line between –2.8 and 1 V, the observed irreversible new wave at around –1.35 V is due to unknown product that is formed while scanning more negatively.
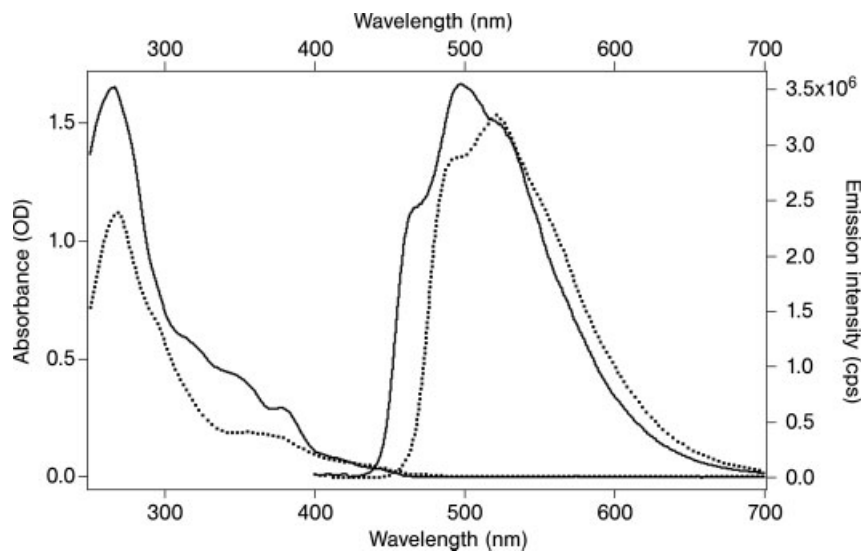
Fig. 11.4 Absorption and emission spectra of **18** (solid line) and **19** (dashed line) in dichloromethane solution at 298 K.
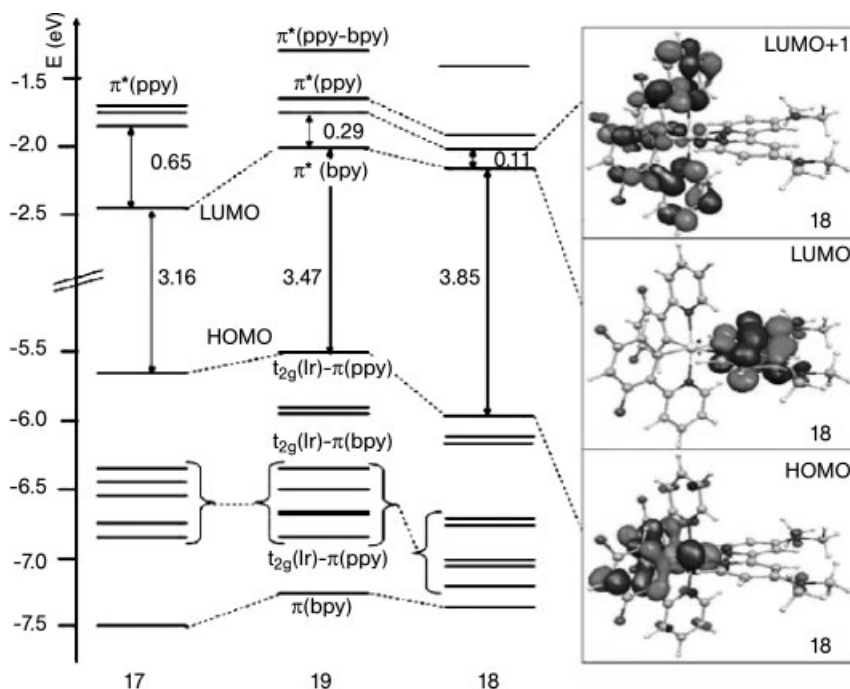
Fig. 11.5 Energy and character of the frontier molecular orbitals of **17**, **19**, and **18** complexes. Also shown are isodensity plots of selected molecular orbitals.

respectively [32]. The lowest unoccupied molecular orbitals (LUMO) of both complexes is a π* orbital localized on the 4,4′-dimethylamino-2,2′-bipyridine ligand and is calculated at −2.49 and −2.3 eV for **17** and **18**, respectively. At higher energy, the LUMO is followed by an almost degenerate couple of phenylpyridine π* orbitals, whose energies approach that of the 4,4′-dimethylamino-2,2′-bipyridine π* LUMO while going from **17**, **19** to **18**.

11.2.3
Tuning of Phosphorescence Colors in Anionic Iridium Complexes

The tuning aspects of phosphorescence colors in anionic iridium complexes are illustrated using the following representative complexes. The $(C_4H_9)_4N[Ir(2-phenylpyridine)_2(CN)_2]$ (**20**), $(C_4H_9)_4N[Ir(2-phenyl)-4-dimethylaminopyridine)_2(CN)_2]$ (**21**), $(C_4H_9)_4N[Ir(2-(2,4-difluorophenyl)-pyridine)_2(CN)_2]$ (**22**), $(C_4H_9)_4N[Ir(2-(2,4-difluorophenyl)-4-dimethylaminopyridine)_2(CN)_2]$ (**23**), and $(C_4H_9)_4N[Ir(2-(3,5-difluorophenyl)-4-dimethylaminopyridine)_2(CN)_2]$ (**24**) [35]. All these complexes were conveniently synthesized in a low boiling dichloromethane by reacting the dichloro-bridged iridium(III) dimer with tetrabutylammonium cyanide. The crystal structure of complex **20** shows that the cyanide ligands are coordinating through the carbon atom and adopt a *cis* configuration (Fig. 11.6).
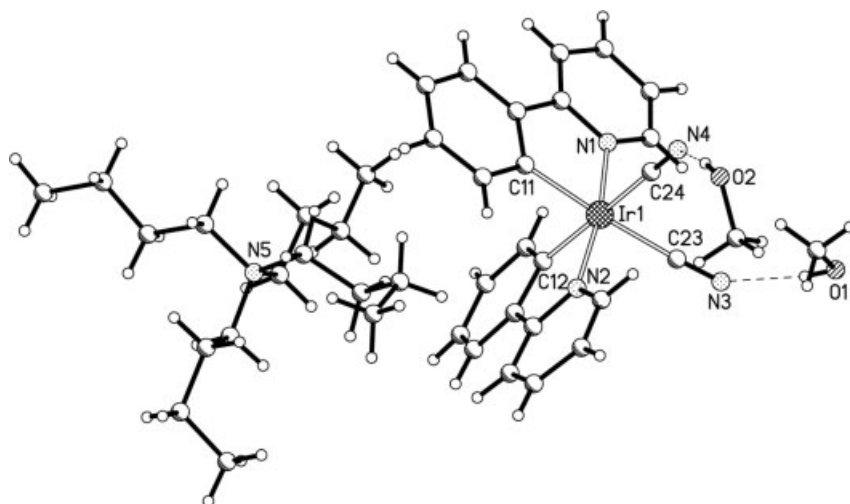
Fig. 11.6 Crystal structure of $(C_4H_9)_4N[Ir(2-phenylpyridine)_2(CN)_2]$ **20**.

Table 11.4 shows a comparison of photophysical and electrochemical properties of the complexes **20–24**, which were measured in dichloromethane solution at 298 K. When these complexes excited within the $\tilde{\pi} - \pi^*$ and MLCT absorption bands, they show emission maxima in the blue and yellow regions of the visible spectra. The air-equilibrated dichloromethane solutions exhibit shorter luminescence lifetimes (70–90 ns) compared to the degassed solutions (1–3 µs). It is apparent from the photoluminescence data, which were obtained by exciting at 380 nm, that the complexes **20–24** show a color range from brilliant blue to yellow, unravelling tuning aspect of the HOMO and the LUMO levels.

The LUMO levels complex of **21** are destabilized by incorporating dimethylamino group on the 4-position of pyridine and in complex **22**, the HOMO levels are stabilized by insertion of fluoride substituents on the phenyl ring of the 2-phenylpyridine ligand. However, in complex **23** both aspects, i.e., destabilization of the LUMO orbitals by incorporating dimethylamino group on the 4-position of pyridine together with stabilization of HOMO orbitals by insertion of fluoride substituents on the phenyl of 2-phenylpyridine ligand, lead to an increase of the HOMO–LUMO gap accompanied by a blue shift of the emission spectra. Figure 11.7 shows a representative absorption and emission spectra of the complex **23** measured in dichloromethane solution at 298 K. The complex displays bands in the UV and the visible region due to intra-ligand (π–π*) and metal-to-ligand charge transfer transitions (MLCT), respectively [33, 35]. When excited within the π–π* and MLCT absorption bands at 298 K, complex **23** shows emission maxima at 450 and 473 nm, due to the 2,4-difluorophenyl-4-dimethylaminopyridine ligand that increases the HOMO–LUMO gap, resulting in a blue shift of the emission maxima compared to the complexes **21** and **22**.

Table 11.4 Structures, absorption, emission, quantum yields, lifetime, and electrochemical data of complexes **20**, **21**, **22**, **23**, and **24** measured at 298 K in dichloromethane solution.

Bu_4N

20

Bu_4N

21

Bu_4N

22

Bu_4N

23

Bu_4N

24
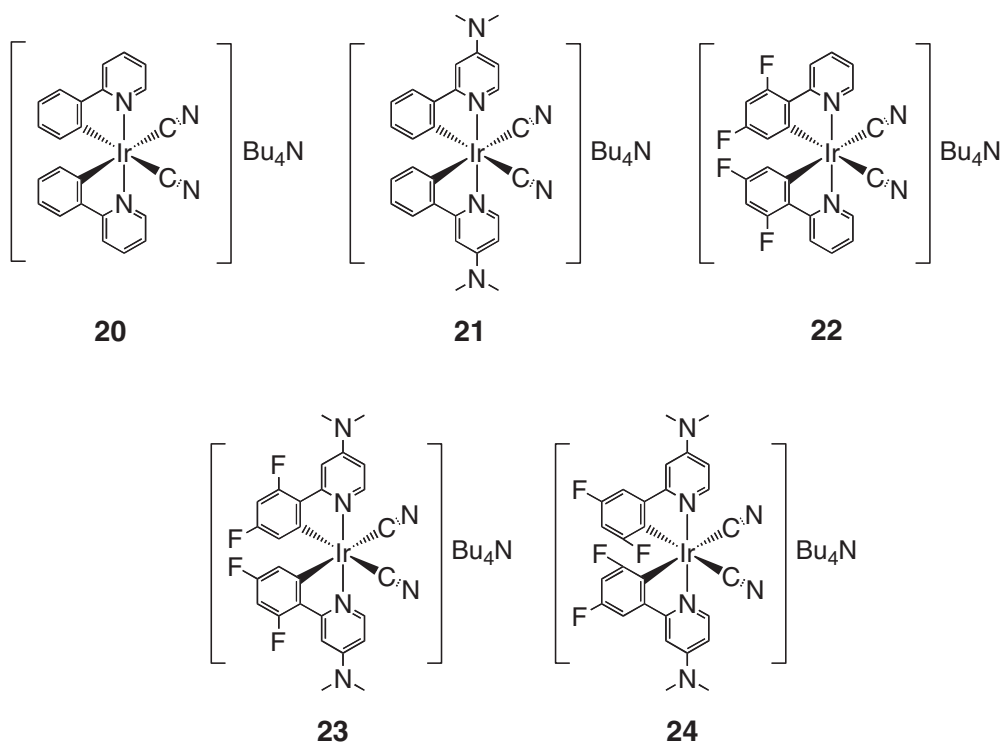
Complex	Absorption, λ (nm) (ε/10⁴ M⁻¹ cm⁻¹)	Emission at 298 K[a]	Lifetime (μs)	Electrochemical data V vs. Fc	
				$E^{1/2}_{ox}$	$E^{1/2}_{red}$
20	260 (41.7), 337 (0.85), 384 (0.58), 433 sh (0.61)	470, 502	3.3	0.55	−2.69
21	272 (3.79), 302 sh (2.21), 3.32 (1.07), 354 (0.89), 380 (0.59)	465, 488	2.0	0.33	−3.0
22	254 (6.04), 290 (2.79), 362 (0.78), 390 (0.38)	460, 485	3.3	0.96	−2.6
23	266 (2.83), 290 (2.63), 302 (2.38), 338 (1.32), 360 (1.08)	451, 471	1.4	0.58	−2.98
24	268 (5.25), 288 (4.20), 302sh (3.22), 356 (1.52), 378 (0.95)	468, 492	3.0	0.53	−2.8

a   The emission spectra were obtained from de-gassed solutions by exciting into the lowest MLCT band.
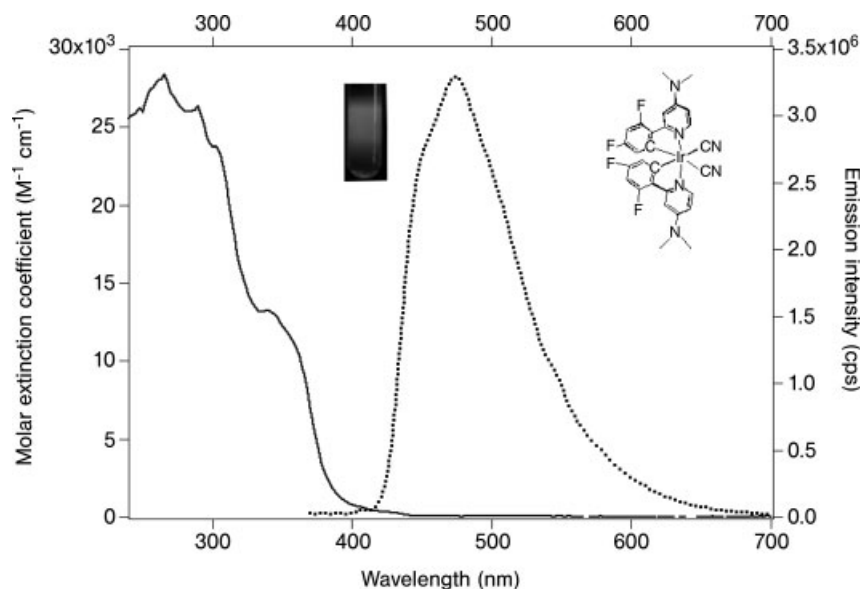
Fig. 11.7 Absorption (solid line) and emission (dashed line) spectra of complex **23** in dichloromethane solution at 298 K. The inserts show a photo of the **23** solution, exhibiting very strong blue emission upon excitation at 380 nm and the chemical structure of **23**.

The difference between complexes **23** and **24** is only that the position of the fluoride atoms on the phenyl ring of the 2-phenylpyridine ligand, which are at 2,4-position in the former and 3,5-position in the later. The complex **24** emission maxima is significantly red shifted compared to the complex **23**, demonstrating the influence of position of the substituents on photophysical properties. One possible explanation for this astonishing spectral shift of the complex **24** compared to the complex **23** is that the fluorides in the 3,5-position act as electron-releasing groups, destabilizing the metal HOMO orbitals thereby decreasing the HOMO–LUMO gap. In complex **23**, fluorides are in 2,4-positions and act as electron-withdrawing groups, resulting in stabilization of HOMO orbitals thereby increasing the HOMO–LUMO gap.

11.2.3.1 Phosphorescent Color Shift in Anionic Iridium Complexes by Tuning of HOMO Levels

Figure 11.8 shows schematically the concept of HOMO level tuning in iridium pseudohalogen complexes of the type TBA[Ir(ppy)$_2$(CN)$_2$] (**20**), TBA[Ir(ppy)$_2$(NCS)$_2$] (**25**), and TBA[Ir(ppy)$_2$(NCO)$_2$] (**26**). These complexes were conveniently synthesized under inert atmosphere by reaction between the dichloro-bridged iridium dimer [Ir(ppy)$_2$(Cl)]$_2$ in dichloromethane solvent with an excess of pseudohalogen ligand such as tetrabutylammonium cyanide, tetrabutylammonium thiocyanate or tetrabutylammonium isocyanate, respectively with over 70% yields [4].
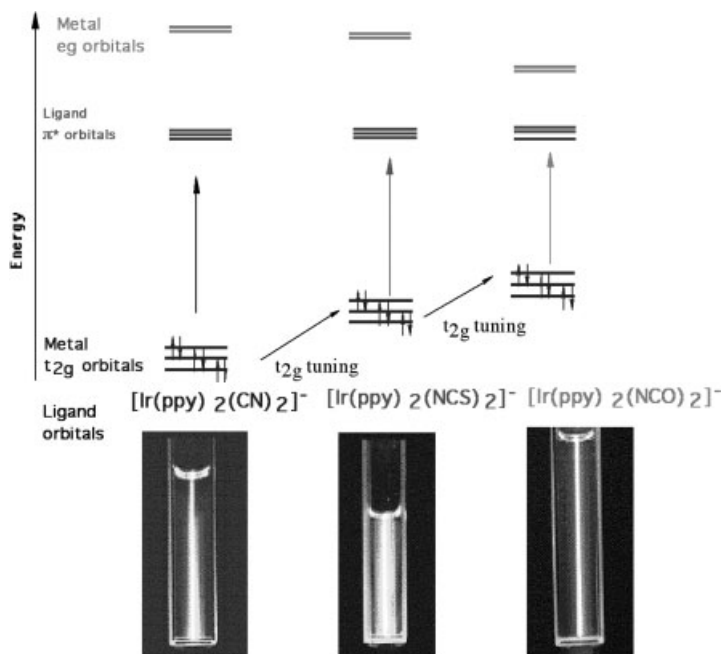
Fig. 11.8 Schematic drawing of HOMO and LUMO orbitals for complexes **20**, **25**, and **26** and their phosphorescence properties, which were obtained by exciting at 415.4 nm using a krypton ion laser.

The cyclic voltammogram of **20**, **25**, and **26** shows a quasireversible oxidation potentials at 0.91, 0.45, and 0.18 V vs. ferrocene, respectively. Changes in electron-donating or withdrawing nature of the ancillary ligands can result in a variation of electronic properties at the metal center. It is interesting to compare these three complexes that contain cyanide, thiocyanate, and isocyanate ligands. The 0.73 V anodic shift in oxidation potential of the **20** compared to the complex **26** shows the extent of π back bonding to the cyanide ligand from iridium(III) center. The enormous enhancement in π back bonding leads to significant blue shift of the emission maxima of the complex **20** compared to the complexes **25** and **26**.

The absorption spectra of these complexes display bands in the UV and the visible region due to intra-ligand (π–π^*) and metal-to-ligand charge transfer transitions (MLCT), respectively [33]. The MLCT band in **20** (463 nm), significantly blue shifted compared to the **25** (478 nm) and **26** (494 nm) indicating the extent of π-acceptor strength of CN^- ligand compared to the NCS^- and NCO^- ligands. The spectral shifts are consistent with electrochemical data of these complexes. Hay in his paper has analyzed the spectral properties of iridium(III) phenylpyridine complexes using density functional theory (DFT), in which the low-lying transitions are categorized as metal-to-ligand charge transfer transitions and the high-energy bands at above 280 nm are assigned to the intra-ligand π–π^* transition of

Table 11.5 Emission, lifetime, and quantum yields data of complexes **20**, **25**, and **26** measured at 298 K in CH_2Cl_2.

Complex	Abs. λ_{max} nm, ($\varepsilon/10^3\,M^{-1}\,cm^{-1}$)	[a]Em. λ_{max} (nm)	Em. $\emptyset_f$	Lifetime τ (μs)	$E^{1/2}_{ox}$ V vs. Fc
20	463 (0.21), 384 (0.58), 337 (0.85), 260 (41.7)	470, 502	0.94	3.1	0.91
25	476 (0.65), 400 (3.4), 355 (5.3), 335 (6.7), 266 (38.9)	506, 520	0.97	1.4	0.45
26	497 (1.26), 464 (2.36), 408 (3.41), 384 (4.22), 347 (6.62), 276 (35.1)	538, 560	0.99	0.8	0.18

a The emission spectra were obtained from degassed solutions by exciting into the lowest MLCT band.

2-phenylpyridine [18]. Argon-degassed solution of complexes **20**, **25**, and **26** when excited within the π–π* and MLCT absorption band at 298 K, show emission maxima at 470, 506, and 538 nm, respectively with longer lifetimes (0.8–3.4 μs) (Table 11.5).

11.2.4
Controlling Quantum Yields in Iridium Complexes

Orthometallated iridium complexes are known to have the highest triplet emission quantum yields due to several factors [36, 37]: (a) Iridium has a large d-orbital splitting compared to other metals in the group. (b) Strong ligand field strength of the phenylpyridine anionic ligand, increases the d-orbital splitting, leading to an enlarged gap between the e_g orbitals of Ir and the LUMO of the ligand. (c) Close-lying π–π* and MLCT transitions, which together with the heavy atom effect enhances the spin–orbit coupling. However, the mixed ligand cationic iridium complexes show appreciably lower quantum yields compared to the tris-orthometallated iridium complexes because of the lower LUMO orbitals of the 2,2′-bipyridine ligand [7, 19, 38]. One strategy to increase the quantum yields of Ir complexes is to introduce F and/or CF_3 substituents. This results in a stabilization of both the HOMO and the LUMO. Since the HOMO stabilization is larger than that of the LUMO, it leads to an increase in the gap between HOMO–LUMO [39]. Another strategy however is to decrease the gap between the lowest π* orbitals of the 2-phenylpyridine ligand and the 2,2′-bipyridine ligand by introducing donor substituents such as dimethylamino groups at the 4,4′-positions of 2,2′-bipyridine, which are known to have a strong destabilization effect on the LUMO (see complexes **18** and **19**). In such type of complexes, the π–π* and MLCT states associated with the 2-phenylpyridine and 4,4′-dimethylamino-2,2′-bipyridine ligands are expected to be located closely together, which enhances the excited state decay through radiative pathways.

The quantum yield of complexes **18** and **19** measured using recrystallized quinine sulphate in 1N H_2SO_4 and the widely referred complex $Ru(bpy)_3(PF_6)_2$ as quantum yield standards. The data obtained using both the standards are in excellent agreement and indeed show yields remarkably high, i.e., 80%.

The quantum yields of iridium complexes can also be modulated by introducing ligands having strong ligand field stabilization energy such as NCS^- and CN^-. In these complexes, the gap between the metal e_g and the ligand LUMO orbitals increases resulting in a decay of the excited charge transfer states through radiative pathways [4].

11.3
Application of Iridium Complexes in Organic Light-Emitting Devices (OLEDs)

Doping of the emitting layer of OLED devices with well-selected dye molecules is an established way to improve the OLED performances. To clarify, in the context of this article, we understand by doping not the introduction of additional charges as in the classical semiconductor sense but rather the introduction of dye molecules with appropriate energy levels for color tuning. Besides this aspect, doping also leads to a change of the transport characteristics and to a considerable increase of the lifetime and the quantum efficiency.

A longtime back people thought that the luminescent dyes, used since the discovery by Tang et al., are theoretically limited to an internal conversion efficiency of 25% [40]. This factor arrives from quantum mechanics, where 75% of the charge wavefunctions are of the nonemissive triplet case and only 25% are of the singlet case, allowing radiative recombination. Taken into account that only one-fifth of the created photons can leave the device, the external quantum efficiency was limited to 5% [41]. But in contrary to this, the family of so-called phosphorescent dyes (triplet emitters) permits the opening of an additional radiative recombination channel and harvesting of up to nearly 100% of the exited states to photon creation. Responsible for this is the presence of heavy metal atoms such as Pt or Ir [42] leading to a strong spin–orbit coupling. The common way of device realization is to mix small concentration of a highly phosphorescent guest into a host material with suitable charge transport abilities. Taking into account an unchanged out-coupling factor of one-fifth, the theoretical external quantum efficiency for the triplet dyes jumps up to 20%. The first time electrophosphorescence was shown by Hoshino et al., by mixing benzophenone into a poly(methylmethacrylate) host [43], but the quantum efficiency was still low. Meanwhile quantum efficiencies up to the theoretical limits are reported in the literature [42].

Typical dye doping concentrations of singlet and triplet emitters are very different. For singlet emitters, the efficient doping ratio is often limited to the range from an half percent to two percent, as for examples, 1.3% for Rubrene in Alq_3 [44] or 0.7% for DEQ in Alq_3 [45]. For triplet emitter dyes, doping ratios until 10% or far above are possible without remarkable loss in quantum efficiency [46]. Increased doping concentrations of triplet emitters are desirable to prevent or

reduce saturation effect at increased current densities due to long lifetimes of the excited states [47]. But high doping concentrations are accompanied by side effects. To have the dye molecules with appropriate behavior inside the matrix is one point; the other point is that the dye molecule should also be able to localize the exciton. In principle, three techniques are discussed to get the exciton on the dye dopant: (1) endothermic energy transfer [48] (2) exothermic energy transfer [49], and (3) charge trapping as it applies for heavily doped systems and for blue phosphorescent devices [47].

Another aspect is that large energy gap matrices are desired to suppress both the electron and energy transfer pathways from the emissive dopant back to the host material [50]. Pai et al. observed the transition from hole hopping between host molecules to trap-controlled tunnelling transport as a function of doping concentration [51]. At concentrations of the additive below 2 wt%, the transport is dominated by the slow release of charges from the dye sites acting as charge traps. For concentrations above 2 wt%, hopping occurs via trap and host sites. As the trap concentration is further increased, the transport by tunnelling via the additive sites gets dominant.

The long lifetime of the triplet excitons enables them theoretically to diffuse significant distances. To reduce this, typical diode architectures including phosphorescent emitters require at least one more auxiliary layer, such as hole-blocking layer, compared to fluorescent emitter containing diode, and the energy levels of the host should be significantly higher to localize the excitons on the dopant [47]. This approach will be discussed in the following part in more detail.

11.3.1
Standard OLED Device Architecture

A typical multilayer device architecture containing triplet emitters is described in the following and a sketch of the resulting energy level scheme is shown in Fig. 11.9. ITO (indium-tin-oxide) coated glass substrate used as anode was precleaned with some standard procedure like successive ethanol, acetone, and soap ultrasonic treatments. On the top, a 10 nm thick CuPc (copper phthalocyanine) hole injection layer is deposited. Next a 40 nm thick hole transport layer of α-NPD (*N*,*N*′-diphenyl-*N*,*N*′-bis(*1*-naphthyl)-1,1′biphenyl-*4*,*4*″diamine) is evaporated, followed by a 20 nm layer of the wide energygap matrix of BCP (4,4′-bis(carbazol-9-yl)-biphenyl) coevaporated with a constant rate of a phosphorent emitter molecule. For hole blocking and resulting charge confinement in the emitting matrix-layer, a 5 nm layer of BCP (2,9-dimethyl-4.7-diphenyl-phenatroline) can be useful for quantum efficiency improvement. Finally, 30–40 nm thick Alq$_3$ (tris(*8-hydroxyquinolato*) *aluminum*) electron transport layer is deposited to improve the out-coupling efficiency [52] and to reduce exciton quenching by the metallic cathode [42]. For performance improvement, the organics should be purified and thermally evaporated at a rate of 1.0 Å/s at a base pressure lower than 10^{-6} mbar. A well working cathode for such architecture consists of a 0.8 nm LiF layer deposited right after the ETL in combination with 100 nm thick Al layer. To decrease
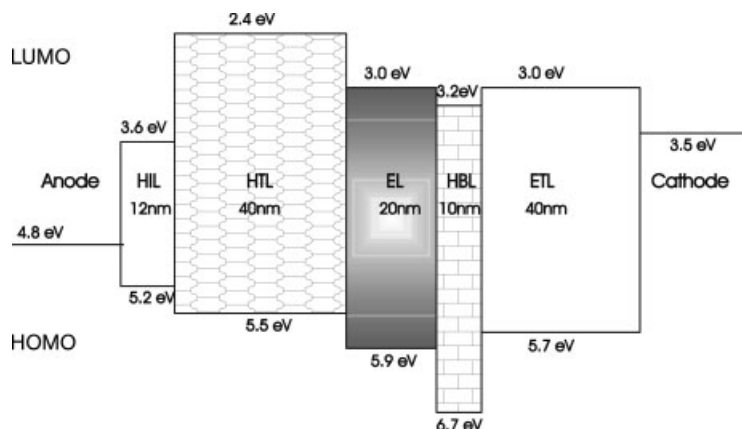
Fig. 11.9 Typical electrophosphorescent multilayer device architecture composed of a hole injection layer (HIL), a hole transport layer (HTL), an emission layer (EL), a hole-blocking layer (HBL), and finally an electron-transporting layer (ETL). The HOMOs and LUMOs of the corresponding molecules are shown [4]. The vacuum level is assumed to be constant.

contamination effects and impurity layers, the whole fabrication should be done without breaking the vacuum. The active area of engineering segments is in the range of 4 to 10 mm^2.

To show the effect of doping concentration on the transport characteristics, it is instructive to have a look on doping ratio dependent current–voltage [$I(V)$] characteristics. Therefore, the presented standard device architecture doped with different ratios of the phosphorent emitter molecule [acetylacetonato-(bis(2-phenylpyridine)iridium(III)], labeled as complex **27**, is used as a model case. Figure 11.10 shows the different current–voltage [$I(V)$] characteristics for complex **27** doped in CBP-host for doping concentrations ranging from zero to 12 mol%. The voltage region below ≈2.5–3 V is characterized by a single carrier type transport and the exact value depends on the doping concentration. Above this threshold voltage, a steep increase in the diode current corresponding to two-carrier injection is observed, which leads to light generation. The lower current threshold field (U_{th1}) here defined as the voltage for a current of 1 μA/cm^2, decreases monotonously from 3.5 V for the undoped case to 2.9 V for maximum doping of 12 mol% (see Table 11.6). This indicates that the dye molecules seem to improve carrier injection into the emission layer. The energy barrier for holes at the α-NPD/CBP interface is 0.43 eV (HOMO–HOMO barrier). However, the energy barrier from α-NPD to complex **27** is negligible, i.e., less than 0.1 eV [HOMO's of α-NPD = 5.53 eV, CBP = 5.96 eV, and of complex **27** = 5.6 eV] [4]. For higher doping concentrations, this injection and transport mechanism is even improved. The energy barriers for the electrons are less important for all organic/organic interfaces (≤0.2 eV).

As the doping concentration increases, the edge in the $I(V)$ curve at around 1×10^{-4} A/cm^2 gets more pronounced. This edge marks the transition between the
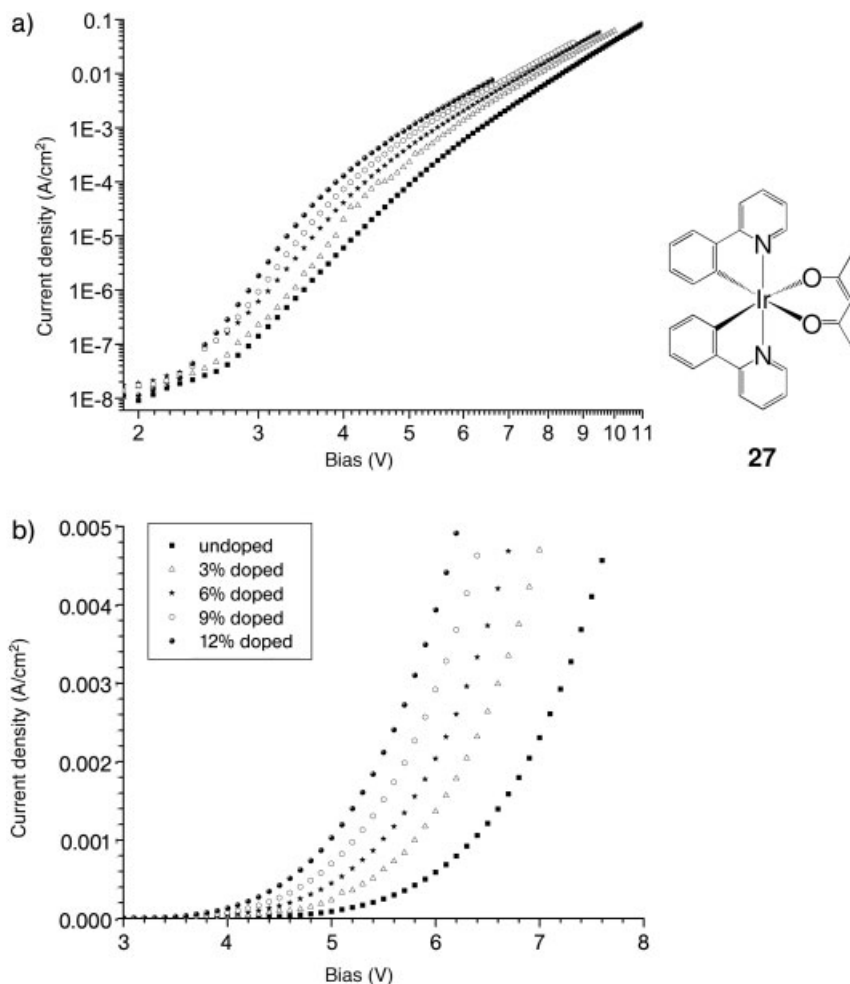
Fig. 11.10 (a) Current versus voltage characteristics for different doping concentrations of phosphorescent dye **27** in a CBP matrix. The steepness increases with increasing dopant concentration. (b) The characteristics are similar to Fig. 11.10(a) but on linear scales.

two kinds of transport behavior as the applied electric field increases. At the lower current side of the edge ($J < 10^{-4}$ A/cm^2), an increase of the steepness of the $I(V)$ characteristic for increasing doping ratio is seen. For better interpretation a power-law ($I \sim V^x$, $x = x_1$ as the index for current densities in the injection limited regime below the edge 10^{-4} A/cm^2 and $x = x_2$ as the index for current in the space charge limited current densities regime above the edge 10^{-4} A/cm^2, respectively), is fitted of the $I(V)$ characteristics, the results are summarized in Table 11.6. This increase of the exponent x_1 can be interpreted as injection improvement at the α-NPD/

Table 11.6 Current versus voltage $I(V)$ characteristics as a function of the doping concentration of complex **27** in a CBP matrix (given are the threshold voltages corresponding to the two characteristic current densities of $1\,\mu A/cm^2$ and $0.1\,A/cm^2$).

Doping rate	U_{th1} $(1\,\mu A/cm^2)$	Exponent x_1: $3\times10^{-8}\text{--}1\times10^{-4}A/cm^2$	U_{th2} $(0.1\,A/cm^2)$	Exponent x_2 J $>1\times10^{-4}A/cm^2$
Undoped	3.5	12.7	11.1	8.0
3%	3.35	13.4	10.5	7.5
6%	3.1	14.7	10.0	7.4
9%	3.0	16.1	9.75	7.0
12%	2.9	16.9	9.4	6.8

emission layer (complex **27** doped) interface, which can therefore be considered as the transport-limiting factor in the measured current range. Also, the upper current threshold field (U_{th2}) defined as the voltage for a current of $100\,mA/cm^2$, decreases monotonously from 11.1 V for the undoped case to 9.4 V for the maximum doping of 12 mol%. But in contrary to this, the power-law exponent x_2 of the current (voltage) curve above the current edge decreases slightly indicating a small deterioration of the total charge transport behavior in this current (voltage) range. Such a change can arise from dopant induced increase in the trap density accompanied by a lowering of the mobility and resulting in an increase of space charges screening the applied electric field [53].

Furthermore, by direct charge injection from the adjacent hole and electron transport layers onto the phosphor molecule doped into the wide energy-gap matrix, exciton formation occurs directly on the dopant. In other words, in this image, it is not the efficiency of the energy transfer from the host to the dye dopant, it is rather in the sense of easier injection of the holes onto the dopant where they "only" have to wait for the electron. As already pointed out, it is a function of dye concentration if the charge jumps from dye to dye or if it is energetically favorable for the charge to detrap by jumping from the dye to the host. A phenomenological description of the exciton creation on the dye molecule was given by Yersin [54].

In the case that the dye doping leads to a strong electron mobility reduction, the recombination zone distribution can split into two separated emission zones resulting in color changes. The first part takes place in the doped area located at the α-NPD/doped layer interface with the emission color of the dopant and the second part around the doped/undoped layer interface [55]. The recombination part outside the doped area in the pure Alq_3 electron transport layer leads to the typical green emission at a wavelength of 530 nm. In such a case, it might be helpful to introduce a hole-blocking layer (HBL) into the device architecture to reconfine the recombination zone inside the doped part to have only the emission color of the dopant. Figure 11.11 presents an illustration of the low and high voltage cases of the impact on the voltage-dependent recombination zone distribu-
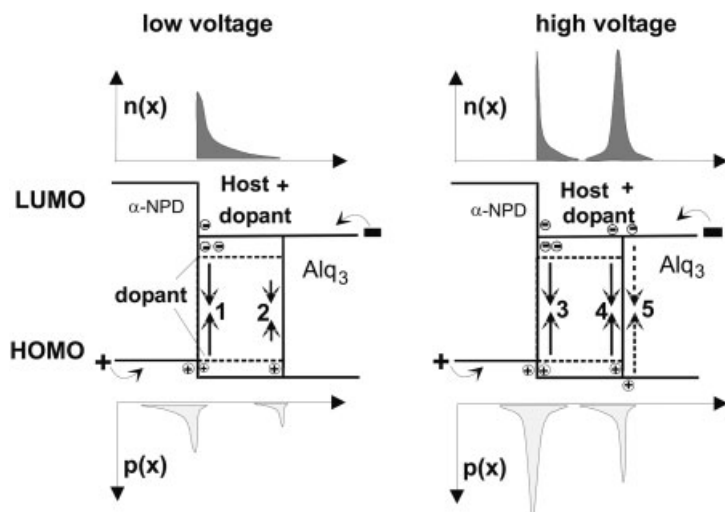
Fig. 11.11 Recombination zone distribution of partially doped diodes for the low and high voltage case. In the doped part, reduced hole and electron mobility is assumed. $p(x)$ and $n(x)$ are the charge density distributions and the arrows mark the resulting recombination zones which lead to light generation. Dotted arrows indicate color emission from the matrix, while line arrows indicate color emission from the dopant. We see that for higher voltages/respective higher current density, the recombination zone splits into two parts whereas that part of the emission zone, which moves outside the doped part, is responsible for the color change.

tion due to strongly decreased electron mobility inside the emission layer by dye doping.

Alq$_3$ used as the standard matrix material for luminescent dyes cannot be used for complex **27** because the energy gap is too small to allow for an effective energy transport from dye to dye without charge de-trapping. On the other side, also the energy transfer rate from the host to the dye via Förster transfer is not efficient between Alq$_3$ and complex **27** [56]. Because by this mechanism the transfer rate is proportional to the overlap of the emission spectra of the host and the absorption of the dye, which is negligible in the considered case.

Figure 11.12(c) shows the variation of the quantum efficiency as a function of the doping concentration. We see a slightly variation for concentrations between 3 and 12% with its maximum at 9% and 13.2% of external quantum efficiency. Only for comparison, for the undoped CBP layer, the quantum efficiency is only 0.94%. This corresponds to an improvement of around one and half orders of magnitude. Still more impressive is the improvement for the power efficiency, which increases from 0.65 lm/Watt for the undoped case (not presented) up to 37 lm/Watt for the 9% doped case, which represents an improvement factor of 56. These values are close to the values cited in the recent literature [3]. However, they are lower than the best values achieved with triplet emitters in TAZ host [57]. A reason could be that the very low TAZ HOMO level of −6.6 eV favors direct

(a)

(b)

(c)
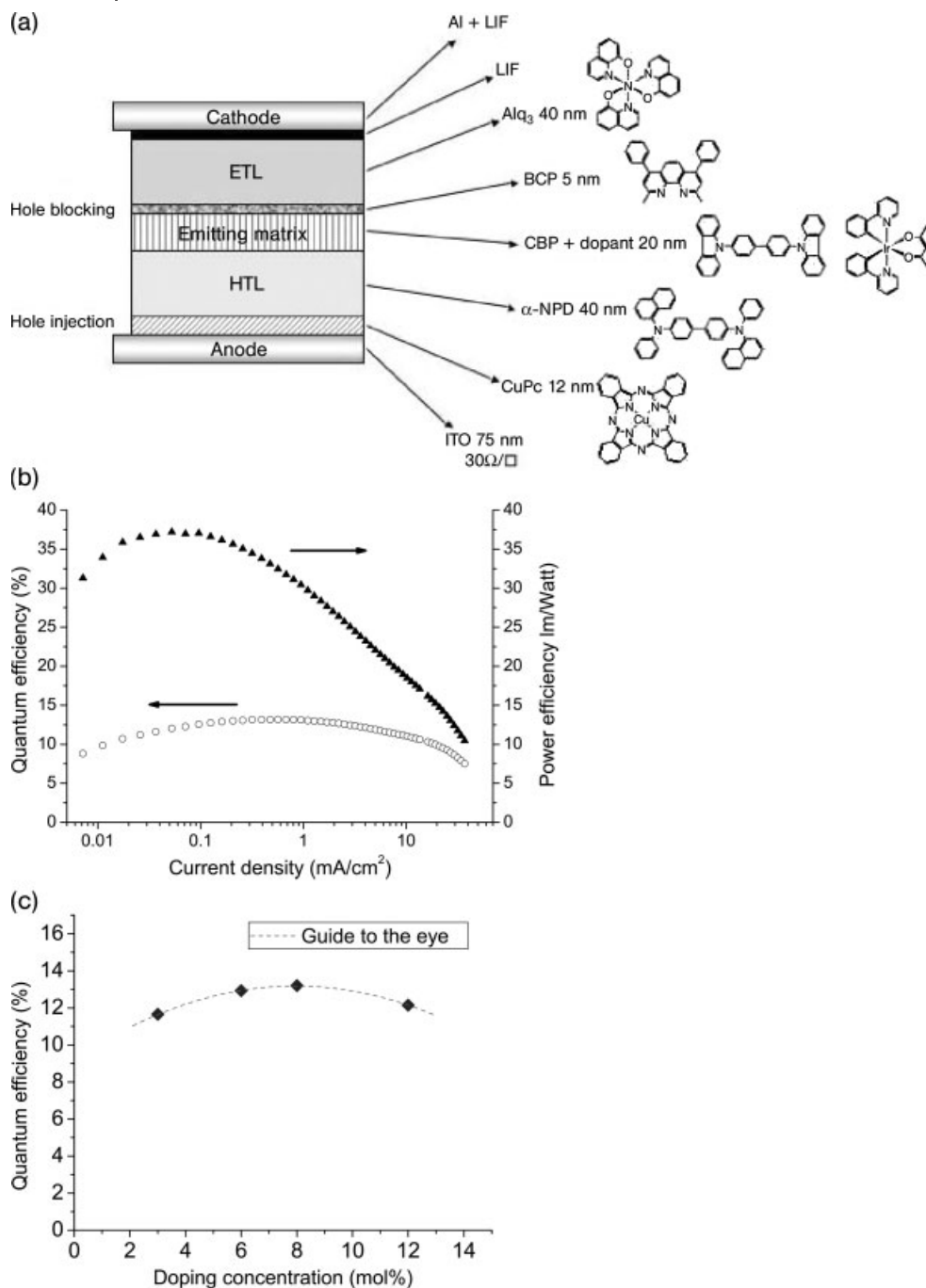
Fig. 11.12 (a) Schematic representation of cross-section of the OLED device; (b) External quantum and power efficiencies versus current, and (c) External quantum efficiency as a function of the doping concentration is presented.

injection and transport at the dopant level and therefore, the exciton escaping rate from the dopant to the host becomes negligible. This impressive value of quantum efficiency is based on a well-balanced charge ratio inside the emission layer without any leaking current, neither to the anode nor to the cathode side. Other experiments by Berner et al. [55] have shown how to get nearly equalized charge balance by using ITO/CuPc on the anode side and LiF/Al on the cathode side, taken into account the hole-blocking capabilities of BCP and the electron-blocking capabilities of α-NPD [58–61].

A nondesirable characteristic of phosphorescent dye doped OLED is that the maximum of the external quantum efficiency (QE) is located at low voltages around typically 5 V and that for higher voltages a strong decrease in the QE is seen. This kind of decrease is discussed as arising from triplet–triplet annihilation effects [62, 63].

For the 6 mol% doped device, the number of dopant molecules inside the doped volume can be calculated with the hypothesis of homogeneous distribution of the molecules. With 12 μs of the averaged lifetime of the excited state of complex **27** and the additional assumption of homogeneous distribution of excited molecules, the upper level of the average distance in the volume between excited molecules as a function of the current density can be estimated. Thereby the charge density distribution was admitted to the half of the doped zone, which is a reasonable assumption as it was demonstrated by model calculations [55]. This effective distance is directly related to the current dependent quantum efficiency $\eta_{(I)}$ of the device. Figure 11.13 shows the normalized quantum efficiency relative to its maximum η_{max}–$\eta_{(I)}$ over the effective distance of excited phosphor molecules. The minimum of the curve around 20 nm shows us the interaction distance at which triplet–triplet annihilation gets important. The fact that the recombination zone is
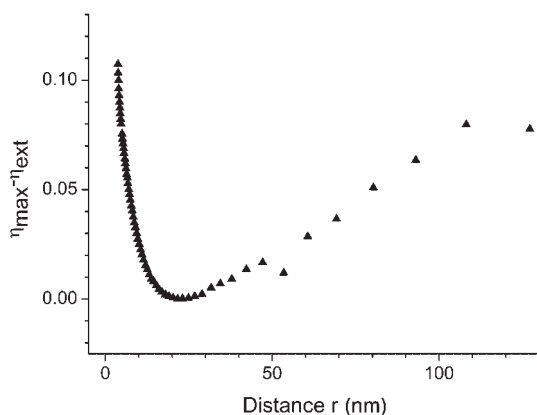
Fig. 11.13 Normalized quantum efficiency relative to its maximum η_{max}–$\eta_{(I)}$ over the effective distance between excited phosphor molecules. The minimum shows the effective distance whereas the T–T annihilation becomes efficient.

even more localized to the interface for high current densities, this distance can be taken only as an upper limit.

The quantum efficiency distribution of complex **27** doped devices as a function of the current density and concentrations is shown in Fig. 11.14. We see that the peak of maximal quantum efficiency increases to higher current density values with increasing doping concentrations. This can be explained by a larger recombination zone distribution for higher concentrations and therefore larger effective distance between excited molecules.

Table 11.7 gives a summary of the operating conditions for the discussed devices as a function of current density and doping concentration. With increasing doping concentration, the voltage to achieve a defined brightness decreases. This reflects the change of the $I(V)$ characteristic with only a slightly change of the quantum efficiency.
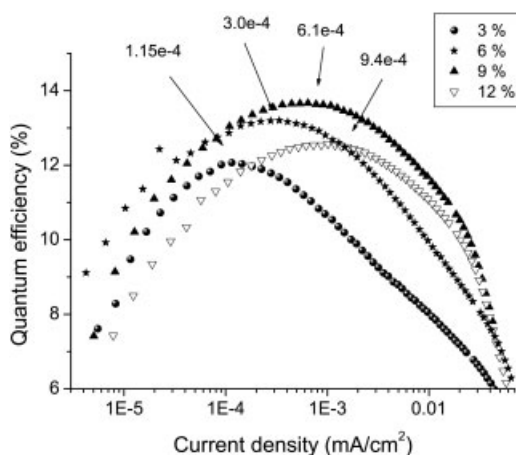
Fig. 11.14 Quantum efficiency distribution as a function of the current density for the 3, 6, 9, and 12 mol% doped devices. The numbers give the current densities in mA/cm², where the maximum of concentration dependent quantum efficiency is located.

Table 11.7 Summary of operating conditions of complex 27 in a CBP matrix.

Doping rate	Bias at 100 cd/m² (V)	Bias at 1000 cd/m² (V)	Bias at 10 000 cd/m² (V)
Undoped	8.1	10.9	–
3%	5.2	6.9	~10.1
6%	4.7	6.2	~9.5
9%	4.4	5.8	8.7
12%	4.4	5.8	8.7
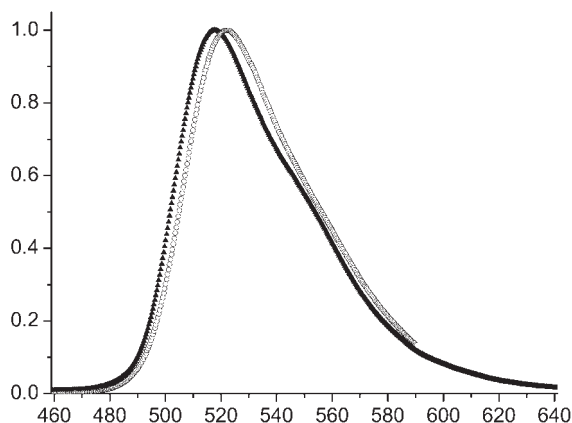
Fig. 11.15 Electrophosphorescence of the complex **27** in a CBP matrix for the 3% (black line) and 12% (grey line) doped cases are shown.

Figure 11.15 shows the electrophosphorescence spectra of complex **27** for 3% and 12% doped in CBP. A slightly red shift for increasing doping concentration is seen, but the emission spectra were independent for current densities up to 150 mA/cm². Such a red shift as a function of the doping concentration was also seen for DCM2, however with much bigger effect [64]. The red shift was attributed to a polarization effect of the molecule introduced from the matrix [64]. The emission spectra of Fig. 11.15 correspond exactly to the emission peak, which is found from solution phosphorescence spectra of the complex **27**. No emission peak contribution of the α-NPD layer, of the host layer, which are located in the blue between 440 nm and 480 nm, or of the exciplexes are visible. In the model case, the line width (FWHM) of the triplet emitter is only 52 nm in comparison to the line width of 83 nm of undoped Alq_3 emission, which leads to more saturated color, which is necessary for high performance color displays.

11.3.2
Light-Emitting Electrochemical Cell (LEC) Device Architecture

Another type of organic light-emitting device is the light-emitting electrochemical cell (LEC), which makes use of ionic charges to facilitate electronic charge injection from the electrodes into the organic molecular semiconductor, eliminating the need for extra layers [6–11]. This is a promising alternative to an OLED, particularly for large-area lighting applications [11, 65–67]. In these cells, thicker organic active layers can be used, while keeping the operating voltage low. Further, one does not need a low work function metal electrode. Recently, cationic Ir complexes **17**, **18**, and **19** were incorporated in LECs leading to green [15] and blue–green [39, 68] electroluminescence.
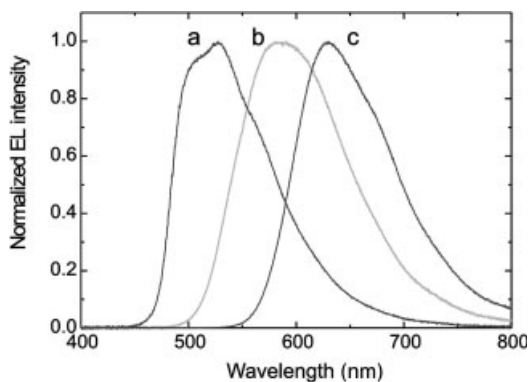
Fig. 11.16 Electroluminescence spectra of ITO/EL layer/Ag devices, where the EL layer consists of [Ir(ppy)$_2$(dma-bpy)]PF$_6$, (a), [Ir(ppy)$_2$(bpy)]PF$_6$ + PMMA (b), and [Ru(bpy)$_3$](PF$_6$)$_2$ + PMMA (c).

To investigate the electroluminescence properties of the cationic complex **19** [Ir(2-phenylpyridine)$_2$(4,4′-dimethylamino-2,2′-bipyridine)]PF$_6$, light–emitting electrochemical cells (LECs) were fabricated in a nitrogen atmosphere glovebox [11]. They consisted of a 100 nm spin-coated layer of pristine **19**, sandwiched between an ITO and an evaporated Ag electrode [31].

It is well known that solid-state LECs exhibit a significant response time since electroluminescence can only occur after the ionic double layers have been built up at the electrode interfaces [8, 11]. Since in this case, only the PF$_6^-$ anion is mobile, the double layers are formed by accumulation and depletion of PF$_6^-$ at the anode and cathode, respectively. The LEC device with **19** started to emit blue–green light at a bias of 5 V after several minutes. The electroluminescence spectrum, as shown in Fig. 11.16 trace a, is very similar to the photoluminescence spectrum recorded for a spin-coated film on glass and of a solution of the complex. For comparison, the electroluminescence spectra recorded for similar devices with [Ir(ppy)$_2$(bpy)]PF$_6$ (trace b, yellow emission) and [Ru(bpy)$_3$](PF$_6$)$_2$ (trace c, orange/red emission) as active material are also shown [11]. The fact that blue–green emission is obtained with an Ag cathode at a voltage as low as 2.5 V indicates the power of the LEC behavior.

Acknowledgments

References

1 C. Adachi, M. A. Baldo, M. E. Thompson, S. R. Forrest, *J. Appl. Phys.* **2001**, *90*, 5048.

2 S. Lamansky, P. Djurovich, D. Murray, F. Abdel-Razzaq, H.-E. Lee, C. Adachi, P. E. Burrows, S. R. Forrest, M. E. Thompson, *J. Am. Chem. Soc.* **2001**, *123*, 4304.

3 M. Ikai, S. Tokito, Y. Sakamoto, T. Suzuki, Y. Taga, *Appl. Phys. Lett.* **2001**, *79*, 156.

4 M. K. Nazeeruddin, R. Humphry-Baker, *J. Am. Chem. Soc.* **2003**, *125*, 8790.

5 C. Adachi, T. Tsutsui, S. Saito, *Optoelectron., Devices Technol.* **1991**, *6*, 25.

6 Q. Pei, G. Yu, C. Zhang, Y. Yang, A. J. Heeger, *Science* **1995**, *269*, 1086.

7 J. D. Slinker, A. A. Gorodetsky, M. S. Lowry, J. Wang, S. Parker, R. Rohl, S. Bernhard, G. G. Malliaras, *J. Am. Chem. Soc.* **2004**, *126*, 2763.

8 J. Slinker, D. Bernards, P. L. Houston, H. D. Abruna, S. Bernhard, G. G. Malliaras, *Chem. Commun.* **2003**, 2392.

9 H. Rudmann, S. Shimida, M. F. Rubner, *J. Am. Chem. Soc.* **2002**, *124*, 4918.

10 S. Bernhard, J. A. Barron, P. L. Houston, H. D. Abruna, J. L. Ruglovksy, X. Gao, G. G. Malliaras, *J. Am. Chem. Soc.* **2002**, *124*, 13624.

11 R. T. Wegh, E. J. Meijer, E. A. Plummer, L. De Cola, K. Brunner, A. van Dijken, J. W. Hofstraat, *Proc. SPIE* **2004**, *5519*, 48.

12 E. S. Handy, A. J. Pal, M. F. Rubner, *J. Am. Chem. Soc.* **1999**, *121*, 3525.

13 F. G. Gao, A. J. Bard, *J. Am. Chem. Soc.* **2000**, *122*, 7426.

14 M. S. Lowry, W. R. Hudson, J. R. A. Pascal, S. Bernhard, *J. Am. Chem. Soc.* **2005**, *126*, 14129.

15 J. D. Slinker, C. Y. Koh, G. G. Malliaras, M. S. Lowry, S. Bernhard, *Appl. Phys. Lett.* **2005**, *86*, 173506.

16 A. Juris, V. Balzani, F. Barigelletti, S. Campagna, P. Belser, A. von Zelewsky, *Coord. Chem. Rev.* **1988**, *84*, 85.

17 M. Nonoyama, *Bull. Chem. SOC. Jpn.* **1975**, *47*, 767.

18 P. J. Hay, *J. Phys. Chem. B* **2002**, *106*, 1634.

19 K. A. King, R. J. Watts, *J. Am. Chem. Soc.* **1987**, *109*, 1589.

20 K. Dedeian, P. I. Djurovich, F. O. Garces, C. Carlson, R. J. Watts, *Inorg. Chem.* **1991**, *30*, 1685.

21 S. Sprouse, K. A. King, P. J. Spellane, R. J. Watts, *J. Am. Chem. Soc.* **1984**, 6647.

22 C. H. Yang, S. W. Li, Y. Chi, Y. M. Cheng, Y. S. Yeh, P. T. Chou, G. H. Lee, C. H. Wang, C. F. Shu, *Inorg. Chem.* **2005**, *44*, 7770.

23 T. Sajoto, P. I. Djurovich, A. Tamayo, M. Yousufuddin, R. Bau, M. E. Thompson, R. H. Holmes, S. R. Forrest, *Inorg. Chem.* **2005**, *44*, 7992.

24 A. Tsuboyama, H. Iwawaki, M. Furugori, T. Mukaide, J. Kamatani, S. Igawa, T. Moriyama, S. Miura, T. Takiguchi, S. Okada, M. Hoshino, K. Ueno, *J. Am. Chem. Soc.* **2003**, *125*, 12971.

25 Y. You, S. Y. Park, *J. Am. Chem. Soc.* **2005**, *127*, 12438.

26 Y. You, S. Y. Park, *J. Am. Chem. Soc.* **2005**, *127*, 12438.

27 S.-J. Yeh, M.-F. Wu, C.-T. Chen, Y.-H. Song, Y. Chi, M.-H. Ho, S.-F. Hsu, C.-H. Chen, *Adv. Mater.* **2005**, *17*, 285.

28 F. M. Hwang, H. Y. Chen, P. S. Chen, C. S. Liu, Y. Chi, C. F. Shu, F. L. Wu, P. T. Chou, S. M. Peng, G. H. Lee, *Inorg. Chem.* **2005**, *44*, 1344.

29 I. R. Laskar, S. F. Hsu, T. M. Chen, *Polyhedron* **2005**, *24*, 189.

30 J. Li, P. I. Djurovich, B. D. Alleyne, M. Yousufuddin, N. N. Ho, J. C. Thomas, J. C. Peters, R. Bau, M. E. Thompson, *Inorg. Chem.* **2005**, *44*, 1713.

31 C. Klein, M. K. Nazeeruddin, S. Fantacci, Q. Wang, S. M. Zakeeruddin, F. De Angelis, J. M. Moser, K. Kalyanasundaram, H. J. Bolink, M. Graetzel, *Chem. Int. Ed.* **2006**, *communicated*.

32 M. K. Nazeeruddin, R. T. Wegh, S. Fantacci, C. Klein, Q. Wang, F. De Angelis, M. Graetzel, *J. Am. Chem. Soc.* **2006**, *communicated*.

33 B. Schmid, F. O. Garces, R. J. Watts, *Inorg. Chem.* **1994**, *33*, 9.

34 K. Ichimura, T. Kobayashi, K. A. King, R. J. Watts, *J. Phys. Chem.* **1987**, *91*, 6104.

35 C. Klein, M. K. Nazeeruddin, S. Fantacci, F. De Angelis, K. Kalyanasundaram, M. Graetzel, *Inorg. Chem.* **2006**, communicated.

36 Y. Ohsawa, S. Sprouse, K. A. King, M. K. DeArmond, K. W. Hanck, R. J. Watts, *J. Phys. Chem.* **1987**, *91*, 1047.

37 F. O. Garces, K. A. King, R. J. Watts, *Inorg. Chem.* **1988**, *27*, 3464.

38 C.-H. Yang, S.-W. Li, Y. Chi, Y.-M. Cheng, Y.-S. Yeh, P.-T. Chou, G.-H. Lee, *Inorg. Chem.* **2005**, *44*, 7770.

39 M. S. Lowry, J. I. Goldsmith, J. D. Slinker, R. Rohl, R. A. Pascal, G. G. Malliaras, S. Bernhard, *Chem. Mater.* **2005**, *17*, 5712.

40 C. W. T. a. S. A. VanSlyke, *Appl. Phys. Lett.* **1987**, *51*, 913.

41 J. S. Kim, P. K. H. Ho, N. C. Greenham, R. H. Friend, *J. Appl. Phys.* **2000**, *88*, 1073.

42 M. A. Baldo, C. Adachi, S. R. Forrest, *Phys. Rev. B* **2000**, *62*, 10967.

43 S. Hoshino, H. Suzuki, *Appl. Phys. Lett.* **1996**, *69*, 224.

44 H. Mattoussi, H. Murata, C. D. Merritt, Z. H. Kafafi, *SPIE Proc.* **1998**, *3476*, 49.

45 H. Murata, C. D. Merritt, H. Mattoussi, Z. H. Kafafi, *SPIE Proc.* **1998**, *3476*, 88.

46 V. Bulovi, A. Shoustikov, M. A. Baldo, E. Bose, V. G. Kozlov, M. E. Thompson, S. R. Forrest, *Chem. Phys. Lett.* **1998**, *287*, 455.

47 M. A. Baldo, S. R. Forrest, M. E. Thompson, edited by Zakya H. Kafafi, Organic Electroluminescence, Taylor & Francis Group, CRS Press, **2005**.

48 J. Kalinowski, W. Stampor, M. Cocchi, D. Virgili, V. Fattori, P. Marco, *Chem. Phys.* **2004**, *39*, 297.

49 V. Cleave, G. Yahioglu, P. Le Barny, R. Friend, N. Tessler, *Adv. Mater.* **1999**, *11*, 285.

50 X. Ren, J. Li, R. J. Holmes, P. I. Djurovich, S. R. Forrest, M. E. Thompson, *Chem. Mater.* **2004**, *16*, 4743.

51 D. M. Pai, J. F. Yanus, M. Stolka, *J. Phys. Chem.* **1984**, *88*, 4714.

52 W. Riess, T. A. Beierlein, H. Riel, *Physics of Organic Semiconductors*, Chapter 18, edited by W. Brütting (Wiley-VCH, Weinheim, ISBN 3-527-40550-X)), pp. 511–527.

53 S. C. Jain, W. Geens, A. Mehra, V. Kumar, T. Aernouts, *J. Appl. Phys.* **2001**, *89*, 3804.

54 H. Yersin, *Top. Curr. Chem.* **2004**, *241*, 1.

55 D. Berner, H. Houili, W. Leo, L. Zuppiroli, *Phys. Stat. Sol. (a)* **2005**, *9*, 202.

56 N. J. Turo, *Modern Molecular Photochemistry*, University Science Books, Mill Valley, CA, **1991**.

57 C. Adachi, M. A. Baldo, S. R. Forrest, M. E. Thompson, *Appl. Phys. Lett.* **2000**, *77*.

58 B. Masenelli, D. Berner, M. N. Bussac, L. Zuppiroli, *Appl. Phys. Lett.* **2001**, *79*, 4438.

59 E. Tutis, M. N. Bussac, B. Masenelli, M. Carrard, L. Zuppiroli, *J. Appl. Phys.* **2001**, *89*, 430.

60 J. B. Masenelli, E. Tutis, M. N. Bussac, L. Zuppiroli, *Synth. Met.* **2001**, *122*, 141.

61 J. B. Masenelli, E. Tutis, M. N. Bussac, L. Zuppiroli, *Synth. Met.* **2000**, *121*, 1513.

62 D. Hertel, Y. V. Romanovskii, B. Schweitzer, U. Scherf, H. J. Bässler, *Synth. Met.* **2001**, *116*, 139.

63 H. Murata, C. D. Merritt, Z. H. Kafafi, *J. Selected Topics Quantum Electron.* **1998**, *4*, 119.

64 V. Bulovis, A. Shoustikov, M. A. Baldo, E. Bose, V. G. Kozlov, M. E. Thompson, S. R. Forrest, *Chem. Phys. Lett.* **1998**, *287*, 455.

65 E. Holder, B. M. W. Langeveld, U. S. Schubert, *Adv. Mater.* **2005**, *17*, 1109.

66 Q. Pei, Y. C. Zhang, Y. Yang, A. J. Heeger, *Science*, **1995**, *269*, 1086.

67 B. S. Chuah, D. H. Hwang, S. M. Chang, J. E. Davies, S. C. Moratti, X. C. Li, A. B. Holmes, J. C. De Mello, N. Tessler, R. H. Friend, *Proc. SPIE* **1997**, *132*, 3148.

68 M. K. Nazeeruddin, R. T. Wegh, Z. Zhou, C. Klein, Q. Wang, S. Fantacci, F. De Angelis, M. Grätzel, *Inorg. Chem.* **2006**, *45*, 9245.

12
Progress in Electroluminescence Based on Lanthanide Complexes

Zu-Qiang Bian and Chun-Hui Huang*

Electroluminescent devices based on lanthanide complexes are of considerable interest because their emission originates from the electronic transitions of the central ions that give sharp narrow spectral characteristic and potentially high emission quantum efficiency. After a brief overview of the device construction and operating principles, a review is given to recent progress in lanthanide complexes based luminophores, especially, Eu and Tb complexes which are being developed for improving the color properties of electroluminescent displays. It is concluded that incorporation of functional groups (electron or/and hole-transporting groups) into ligands on lanthanide complexes is a special kind of "doping" technique which is an efficient strategy with general significance to promote the performance of the materials for organic light-emitting diodes (OLEDs).

12.1
Introduction

The rapid development in the electroluminescence (EL) of organic materials has attracted much attention for their promising applications in optoelectronics and low cost flat panel display technology [1–6]. While designing light-emitting materials for OLEDs, three main issues must be addressed: emission color, emission efficiency, and lifetime. Although OLEDs studies have demonstrated considerable progress, it is still difficult to optimize simultaneously, the color, efficiency, and lifetime of the conjugated organic polymers or small molecules which are widely used for luminescent materials. It is especially difficult to obtain pure emission colors from conjugated polymers or small organic molecules because their emission spectra usually have a full width at half maximum (FWHM) of 50–100 nm or even wider. Filtering out part of the emission can give pure color OLEDs, however, these OLEDs are inefficient because only a part of their emission is utilized.

In contrast to organic chromophores, luminescent lanthanide complexes are believed to be promising candidates to solve this problem. The spectroscopic properties of some lanthanide ions are ideal for use in full color display as known

from inorganic luminescent materials in cathode ray and projection television tubes. Luminescent lanthanide complexes belong to a special class of emitters, exhibiting the following important advantages.

(1) *Sharp emission band.* Lanthanide complexes are characterized by efficient intramolecular energy transfer from the excited singlet state (S1) to the triplet state (T1) of the ligand, and then to the excited 4f states of central lanthanide metal ion. When they relax from the excited state to the ground state of lanthanide ions, the corresponding emission will take place. The sharp spectroscopic bands, usually less than 10 nm in FWHM, originate from the f–f transitions. Compared to that of polymers or organic small molecules, the emission bands from lanthanide complexes are much narrower.

(2) *Potentially high internal quantum efficiency.* EL efficiencies of fluorescent materials are limited to 25% excitons formed because about 75% of the excited states formed by electron–hole recombination in the EL process populate the triplet state, which will decay nonradiatively. In contrast, in lanthanide complexes, the lanthanide ions are excited via intramolecular energy transfer from the triplet excited states of the ligands and the relaxation from the singlet to the triplet states of the ligands also occurs through intersystem crossing. Therefore, the energy of both singlet and triplet excitons formed by electron–hole recombination can be utilized for emission. Although the intersystem crossing efficiency is not 100%, the lanthanide complex EL efficiency could at least exceed those of commonly used fluorescent materials to a large extent.

(3) *Facile ligand modification.* In order to improve the chemical and physical properties of the emitting materials, such as vapor phase deposition, solubility, stability, or carrier transporting properties, modification of the ligands is necessary. Since the 4f shells of trivalent lanthanide ions are well shielded by the filled 5s and 5p orbitals, the 4f energy levels are only weakly perturbed by the environment outside the lanthanide ions. Therefore, the modification does not result in high emission wavelength shift.

According to the emission properties, lanthanide complexes can be divided into four groups [7].

(1) Sm^{3+} ($4f^5$), Eu^{3+} ($4f^6$), Tb^{3+} ($4f^8$), and Dy^{3+} ($4f^9$): For these ions, the emissions originating from the transition of 4f electrons from the lowest excited states to the ground states fall into the visible light region, and the probabilities for these transitions are relatively high. Therefore, the strong emissions can be observed by human eyes.

(2) Pr^{3+} ($4f^2$), Nd^{3+} ($4f^3$), Ho^{3+} ($4f^{10}$), Er^{3+} ($4f^{11}$), Tm^{3+} ($4f^{12}$), and Yb^{3+} ($4f^{13}$): For these ions, the energy levels between the lowest excited state and the ground state are very close to each other. Therefore, emission often occurs in the infrared region. However, their intensities are weaker by several magnitudes compared to that of the visible emission mentioned above because nonradiative transitions occur easily.

(3) Eu^{2+} ($4f^7$), Yb^{2+} ($4f^{14}$), Sm^{2+} ($4f^6$), and Ce^{3+} ($4f^1$): The oxidation states of these ions are lower than those of the ordinary lanthanide ions. The radiation originating from d–f transitions in these ions often result in a broader emission band.

(4) Sc^{3+} ($4f^0$), Y^{3+} ($4f^0$), La^{3+} ($4f^0$), Gd^{3+} ($4f^7$), and Lu^{3+} ($4f^{14}$): The 4f electronic configurations of these ions belong to "empty," "half filled," or "all filled" configurations. Therefore, f–f transition emission cannot occur with the exception of gadolinium complexes which emit in ultraviolet light region. This class of ions cannot give emission in the visible region. However, complexes with these ions can emit light under certain conditions. For example, some complexes do have emission in the visible region when suitable ligands are coordinated to these lanthanide ions. They are classified as ligand emission complexes.

Based on the outlines mentioned above, one can see, in principle, that all lanthanide complexes can be photoluminescent and thus electroluminescence is possible. Indeed, electroluminescent devices with most of the lanthanide complexes (except Pm, Sc, and Ce complexes) have been reported and some of them have been reviewed [8].

12.2
The Device Construction and Operating Principles

Electroluminescence is the phenomenon in which electrical energy is converted to luminous energy [6]. In the early 1960s, electroluminescence from organic crystals was first observed for anthracene [9]. Since the efficiencies of the resulting devices were very low and the lifetimes were short, the electroluminescence was not widely attractive until 1987 when Tang and Van Slyke [10] succeeded in developing an OLED with a luminance over $1000 \, cd/m^2$, which is high enough for practical applications, at an operating voltage below 10 V. Another fundamental piece of work contributing to the evolution of OLEDs was a publication in 1990 by the Cambridge group [11], in which the observation of EL from devices based on the conjugated polymer poly (*p*-phenylenevinylene) (PPV) was reported. The simplicity of manufacture together with the possibility to fabricate flexible, large area, extremely thin full-color displays generated a sudden surge of interest in this research field. As a result, organic electroluminescence has now reached the point where commercialization of small, pixel-addressed displays becomes possible [6].

The basic structure of organic light-emitting diodes is depicted in Fig. 12.1. A typical heterostructure (i.e., more than one layer of organic films) OLED consists of a hole-transporting layer (HTL), an emitting material layer (EML), and an
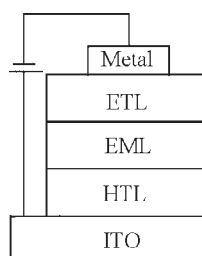
Fig. 12.1 The basic structure of OLEDs.
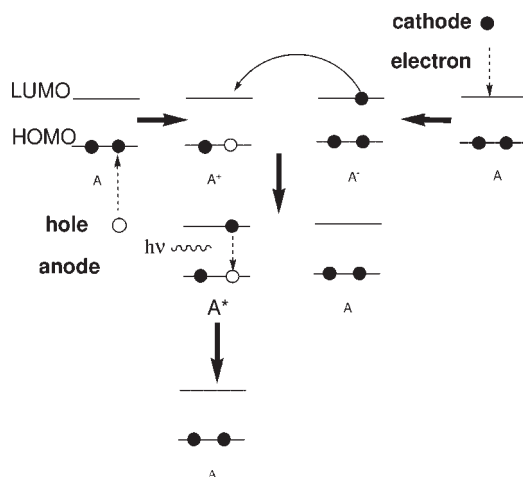
Fig. 12.2 The formation of excitons.

electron-transporting layer (ETL) sandwiched between two electrodes. An indium tin oxide (ITO)-coated glass substrate is usually used as the anode since one of the electrodes needs to be transparent in order to observe light emission from the organic layer. Metals with low work functions such as Al, Mg, Ca, or their alloys are used as cathode in order to guarantee efficient electron injection. Organic layers are deposited mainly by thermal evaporation or spin coating from solutions for small molecule or polymeric materials, respectively. Metal layers are usually made by thermal evaporation. All layers should be chemically stable, especially under the device operating conditions, and resistant to oxidation or photo-oxidation.

When an external voltage is applied to the electrodes, charge carriers, i.e., holes, from the anode and electrons from the cathode are injected into the organic layer beyond a specific threshold voltage depending on the organic material applied. In the presence of the applied electric field, the charge carriers move toward the opposite electrode through the active layer until they meet each other. Electron transport will occur through the lowest unoccupied molecular orbital (LUMO). Holes are transported through the highest occupied molecular orbital (HOMO). The efficiency of electron and hole transporting is determined by the mobilities of the charge carriers in the organic layers. When holes and electrons combine, they can form excitons. In suitable cases, as required for OLEDs, this leads to a population of excited states of the emitter materials which subsequently emits light through the transparent electrode (Fig. 12.2). Details of the mechanism of exciton formation and population processes of excited emitter states can be found in Ref. [12]. To date, the most practical and commercially used electron-transporting material is tris (8-hydroxyquinolinato) aluminum (AlQ) with its molecular structure shown in Fig. 12.3 (1). There are several hole-transporting materials which are preferred. Among them, *N,N'*-diphenyl-*N, N'*-bis(3-methylphenyl)-1,1'-biphenyl-4, 4'-diamine (TPD) and *N,N'*-diphenyl-*N,N'*-bis(1-naphthyl)-1,1'-diphenyl-4,4'-diamine (NPB) have been studied and used extensively (Fig. 12.3 (3, 4)). Since the
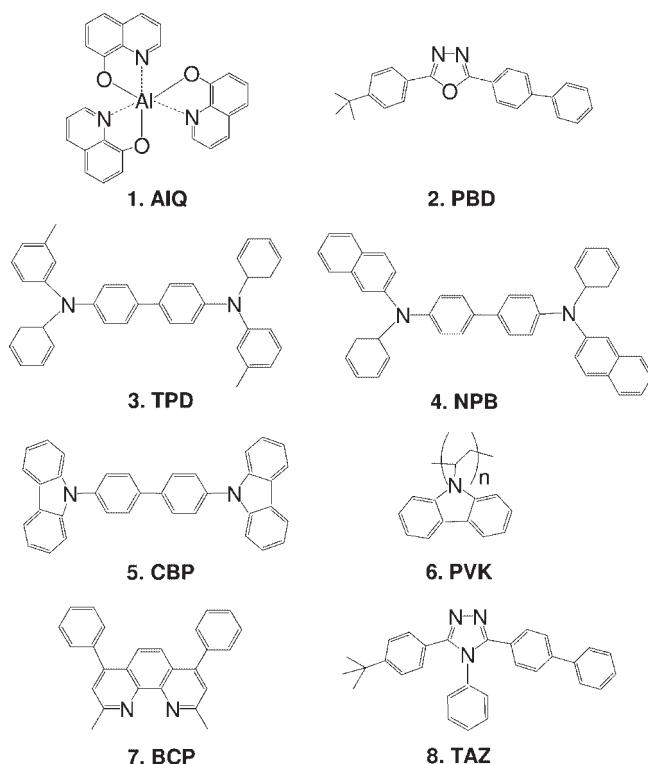
Fig. 12.3 Structures of some electron-transporting materials (1, 2), hole-transporting materials (3 to 6) and hole-blocking materials (7, 8).

electron mobility in organic materials is generally several orders of magnitude lower than the hole mobility, an electron-conducting hole-blocking layer such as 2,9-dimethyl-4,7-diphenyl-1,10- phenanthroline (BCP) or 3-(4-biphenylyl)-4-phenyl-5-(4-*tert*-butyl-phenyl)-1,2,4- triazole (TAZ) shown in Fig. 12.3 (7, 8), is often added between the layer of luminescent materials and the electron-transporting layer or the metallic electrode to balance the charge injection and transport rates. Then the recombination of electrons and holes is confined in the emitting layer and consequently a high electroluminescent efficiency can be obtained.

From the above discussion, it is obvious that a good emitting material needs to achieve several basic requirements. First, it should be an efficient luminophor and a good charge transporter. Second, it must be capable of undergoing efficient charge transfer to an electrode. Moreover, it must be thermally stable for small molecular materials to form a film by thermal evaporation in vacuum. Many lanthanide complexes are highly luminescent, however, only a few of them can simultaneously satisfy these requirements for EL applications. Therefore, further development should be focused on exploring new lanthanide complexes that satisfy the requirements listed above for EL applications.

12.3

The Red Electroluminescence Based on Europium Complexes

As shown in Fig. 12.4, the emissions based on europium ion peak at about 580, 592, 612, 652, and 703 nm, correspond to the f–f electronic transitions of $^5D_0 \rightarrow ^7F_0$ (usually strongly forbidden), $^5D_0 \rightarrow ^7F_1$, $^5D_0 \rightarrow ^7F_2$, $^5D_0 \rightarrow ^7F_3$, and $^5D_0 \rightarrow ^7F_4$, respectively. Among these, the 612 nm emission from the $^5D_0 \rightarrow ^7F_2$ electronic dipole transition is dominant and the monochromaticity (defined by the intensity ratio of $^5D_0 \rightarrow ^7F_2$ to $^5D_0 \rightarrow ^7F_1$ transitions) is usually larger than 10. Therefore, a pure saturated red emission can be observed when the europium complexes are used as emitters.

The first europium complex used for fabricating an OLED was tris (thienyltrifluoroacetonato) europium (Eu(TTA)$_3$) [14], which was molecularly dispersed in a hole-transporting poly(methylphenylsilane) (PMPS). Luminescence started at 12 V, and a maximum intensity of 0.3 cd/m^2 at 18 V was achieved when the device was operated in a continuous dc mode (biased ITO positive) with the configuration of ITO/PMPS-Eu(TTA)$_3$/PBD/Mg/Ag (PBD, structure shown in Fig. 12.3 (2), 2-(4-biphenyl)-5-(4-*tert*-butylphenyl)-1,3,4-oxadiazole, used as electron-transporting layer). Following that observation, much attention was paid to this field. However, the results have not been as satisfactory as expected. Figure 12.5 shows some examples of different Eu^{3+} complexes.

Later, the importance of the neutral ligands and their modification for improving the performance of lanthanide complexes used in fabrication of OLEDs was noticed, and a doping technique was also introduced into the field. As a result, electroluminescence performance has made a significant progress in the past few years.

For comparison, a summary of some typical performance data for Eu-based OLEDs reported in literature is listed in Table 12.1 and the structures of the complexes **13**, **14**, **15**, **16**, and **23** are shown in Fig. 12.6.
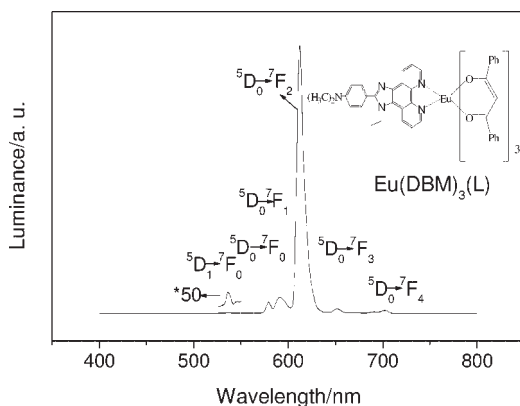
Fig. 12.4 The luminescent spectrum of an europium complex Eu(DBM)$_3$(L) [13]. (Reprinted with permission from Ref. [13], copyright 2002, Elsevier).

9. Eu(TTA)₃[14]
0.3 cd/m²

10. Eu(DFP)₃(Phen) [15]
34.3 cd/m², 0.0196 lm/w

11. En(MDFP)₃(Phen) [16]
32 cd/m², 0.043 lm/w

12. Eu(TTA)₂(PMBBP)(Phen) [17]
6 cd/m²
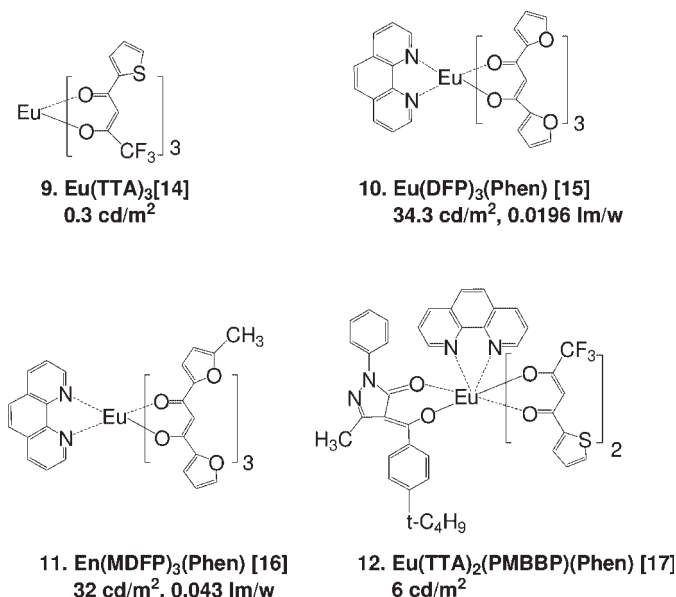
Fig. 12.5 The structures of some europium complexes used as emitters.

Table 12.1 Summary of some typical performance data for Eu-based OLEDs in the literature.

Emitter layer	*η_{ext} (%); I (mA cm^{-2})*	*L (cd m^{-2}); V (V)*	*η_p (Lm W^{-1}); I (mA m^{-2})*	*Ref.*
Eu(TTA)₃(Phen)(13)	–; –	7; 16	–; –	18
Eu(TTA)₃(Phen)/CBP(1%)	1.4; 0.4	505; 12.0	–; –	19
Eu(DBM)₃(Phen)(14)	–; –	50; 15.0	–; –	20
Eu(DBM)₃(Phen)/PBD(1:3, mol:mol)	–; –	460; 16.0	–; –	21
Eu(DBM)₃(Bath)(15)	–; –	400; 15.0	–; –	22
Eu(DBM)₃(Bath)/TPD(3/1)	1.0; 0.6	820; 18.0	1.0; 0.6	23
Eu(DBM)₃(Bath)/TPD(1/2)	4.6; 0.01	–; –	–; –	24
Eu(TTA)₃(TmPhen)(16):CBP(1%)	4.3; 0.1	800; 24.5	1.6; 0.1	25
Eu(TTA)₃(DPPz)(23)/CBP(4.5%)	2.1; 1.23	1670; 13.6	2.1; 1.23	31

η_{ext}, I: the external quantum efficiency (η_{ext}) under a given current density (I)
L, V: the maximum brightness (L) under a given driving voltage (V)
η_p, I: the power efficiency (η_p) under a given current density (I)

The most commonly used anion ligands of europium complexes for EL are TTA or DBM (see Fig. 12.6). A neutral ligand with well-matched triplet energy level would greatly help the photoluminescence and electroluminescence in ternary europium complexes. For example, T. Sano et al. used the (Eu(TTA)₃(Phen)) complex as emitter, TPD and AlQ as the hole-transporting material and electron-transporting material, respectively, and obtained a maximum luminance of 7 cd/m² from a device with the configuration ITO/TPD/Eu(TTA)₃(Phen)/AlQ/

13. Eu(TTA)$_3$(Phen) [18,19]   **14. Eu(DBM)$_3$(Phen) [20,21]**   **15. Eu(DBM)$_3$(Bath) [22-24]**

16. Eu(TTA)$_3$(TmPhen) [25]   **17. Eu(DBM)$_3$(DPIP) [26]**   **18. Eu(DBM)$_3$(CPIP) [27]**

19. Eu(DBM)$_3$(Phencarz) [28]   **20. Eu(DBM)$_3$(EAIP) [13, 29]**

21. Eu(TTA)$_3$(PyPhen): R=H [31]
22. Eu(TTA)$_3$(MMP) R=CH$_3$ [31]

23. Eu(TTA)$_3$(DPPz): R1,R2=H [30]
24. Eu(TTA)$_3$(MDPz): R1=CH$_3$, R2=H [31]
25. Eu(TTA)$_3$(DDPz): R1, R2=CH$_3$ [31]

26. Eu(TTA)$_3$(BDPz) [31]   **27. Eu(DBM)$_3$(EPBM) [32]**

28. Eu(TTA)$_3$(bipyNO) [33]   **29. Eu(DBM)$_3$(TPPO) [34, 35]**   **30. Eu(DBM)$_3$(OXD-PyBM) [36]**
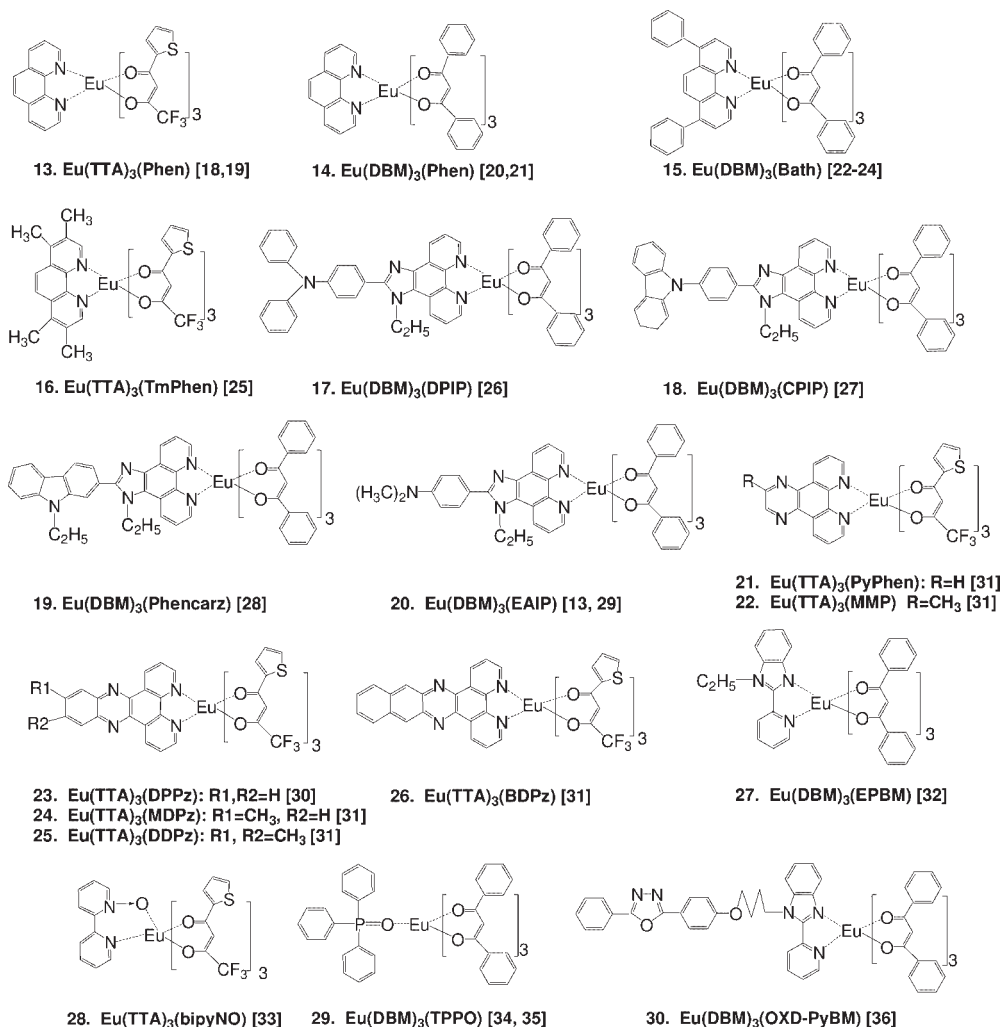
Fig. 12.6 Modifications of the neutral ligands of europium complexes used in OLEDs.

MgIn [18]. The ligand Phen acts to saturate the coordination number of the europium ion and also to improve the Eu^{3+} phosphorescence emission intensity, volatility and stability of the complex. Thus, using Eu(TTA)$_3$(Phen) as the emitting material provides an order of magnitude improvement in performance over the device based on the complex Eu(TTA)$_3$ in which the maximum brightness for Eu(TTA)$_3$ was only 0.3 cd/m^2 [14].

Doping is a useful technique for optimizing the device performance. Proper host materials not only can improve the film formation properties and the thermal stability of the film, but also improve the luminescence efficiency through improvement of energy transfer from host material to the guest materials. Tris-

(dibenzoylmethanato)(1, 10-phenanthroline) europium(III), Eu(DBM)$_3$(Phen), is a good luminescent material. However, using it as an emitter in a device with a structure of ITO/CuPc (5 nm)/α-NPD (35 nm)/Eu(DBM)$_3$(Phen) (20 nm)/BCP (15 nm)/AlQ (25 nm)/LiF/Al gave only a maximum brightness of 50 cd/m^2 at 15 V [20]. This result may be due to the poor charge-transporting properties of the complex. Doping the europium complex in charge-transporting materials such as NPB or PBD is a helpful method to obtain better device performance. Doping Eu(DBM)$_3$(Phen) into NPB host, the maximum brightness of 200 cd/m^2 at 15 V was attained with the device configuration of ITO/CuPc (5 nm)/α-NPB (35 nm)/ NPB:Eu(DBM)$_3$(Phen) (20% : 80%) (20 nm)/BCP (15 nm)/AlQ (25 nm)/LiF/Al [20]. Doping Eu(DBM)$_3$(Phen) into PBD host, a device with the structure ITO/TPD (40 nm)/Eu(DBM)$_3$(Phen):PBD (1 : 3, mol : mol) (30 nm)/AlQ (30 nm)/Mg: Ag gave a maximum brightness of 460 cd/m^2 at 16 V [21]. The same trend could also be observed with the Eu(DBM)$_3$(Bath) and Eu(DBM)$_3$(Bath):TPD systems. After Eu(DBM)$_3$(Bath) was doped into a hole-transporting material TPD, the maximum brightness increased from 400 cd/m^2 at 15 V to 820 cd/m^2 at 18 V with a similar device configuration [22, 23].

Sun et al. reported the synthesis of an europium complex Eu(TTA)$_3$(DPPz) (Fig. 12.6, compound **23**) [30], as a red emitter in electroluminescent devices. One such device with the configuration ITO/TPD (50 nm)/Eu(TTA)$_3$(DPPz):CBP (4.5%, 30 nm)/BCP (30 nm)/AlQ (25 nm)/Mg$_{0.9}$Ag$_{0.1}$/Ag exhibited an external quantum efficiency of 2.1%, current efficiency 4.4 cd/A, power efficiency 2.1 lm/W, and brightness 1670 cd/m^2. Several electroluminescent devices using Eu(TTA)$_3$(L) (L stands for a substituted phenanthroline) (see Fig. 12.6 compounds **21** to **26**) as dopant emitters were also fabricated and tested. Some of these devices exhibited behaviors among the best reported devices incorporated a europium complex as the red emitter [31].

However, doping usually leads to the potential danger of phase separation during device operation. Recently, the anionic or neutral ligands have been modified either by changing the framework or by introducing charge-transporting group into these ligands. Figure 12.6 summarizes several examples (see Fig. 12.6 compounds **15** to **30**).

Liang et al. [36] reported an oxadiazole functionalized europium complex Eu(DBM)$_3$(OXD-PyBM) (see Fig. 12.6 compound **30**), with the aim of realizing highly efficient red light emission. DBM (dibenzoylmethane) was chosen as the anionic ligand due to its relatively high PL efficiency. 2-(2-Pyridyl)-benzimidazole (PyBM) was included as the neutral ligand since it was thought to enhance the electron-transporting property of the material, in addition to saturate the coordination number of the europium ion and improve the volatility and stability of the europium complex. An oxadiazole moiety was introduced to the PyBM ligand through a flexible spacer for improving the electron-transporting property and the solubility of the resulting complex. Pure red emission at 612 nm for the simple double-layer device with structure ITO/TPD (40 nm)/Eu(DBM)$_3$(OXD-PyBM) (50 nm)/LiF (1 nm)/Al (200 nm) was observed with the maximum brightness of 322 cd/m^2, the luminous efficiency of 1.9 cd/A, and the quantum efficiency of 1.7%.

Our recent results also proved that modification of the ligand is an efficient strategy to improve device performance. For example, a device ITO/TPD (20 nm)/ Eu(DBM)$_3$(Phen) (40 nm)/BCP (20 nm)/AlQ (40 nm)/Mg: Ag gave a maximum brightness of 156 cd/m^2 at 16 V and a power efficiency 0.35 lm/W at 7 V, 0.20 cd/m^2. When the Phen was replaced by Phencarz (Fig. 12.6 compound **19**) in the europium complex, the highest power efficiency of 2.7 lm/W at 5 V and 0.5 cd/ m^2, and the luminance exceeding 2000 cd/m^2 at 20 V were obtained from a device with a similar configuration of ITO/TPD (20 nm)/Eu(DBM)$_3$(Phencarz) (40 nm)/ BCP(20 nm)/AlQ (40 nm)/Mg$_{0.9}$Ag$_{0.1}$ (200 nm)/Ag (80 nm) [28]. The excellent result was believed to derive from the improvement of the hole-transporting property owing to the introduction of the carbazyl group.

In fact, modification of ligand not only improves the charge transporting property but also enhances the thermal stability and photoluminescence of complexes, and thus greatly improves the electroluminescence performance. Table 12.2 shows the effects of the modified Phen neutral ligands (Fig. 12.7) on PL efficiencies, thermal properties and EL efficiencies of OLEDs based on the europium complexes [37].

Comparing Eu(DBM)$_3$(L3) with Eu(DBM)$_3$(L1), the maximum brightness is more than two orders of magnitude larger with the same device configuration ITO/TPD (50 nm)/Eu(DBM)$_3$(LN) (*N* = 1 to 3) (50 nm)/Mg: Ag (200 nm)/Ag (100 nm) (Table 12.2).

Another effective way is to modify the anionic ligands. Figure 12.8 shows some examples in this respect.

Table 12.2 EL performance comparison of rare earth complexes with different neutral ligands.

Complex	Neutral ligand	Decomposition temperature (°C)	Solid fluorescence	Maximum brightness cd/m^2, (V)
31	L1	358	1	3.7 (17 V)
32	L2	381	5.3	197 (20 V)
33	L3	408	5.2	561 (16 V)

31. Eu(DBM)$_3$(L1)   **32. Eu(DBM)$_3$(L2)**   **33. Eu(DBM)$_3$(L3)**
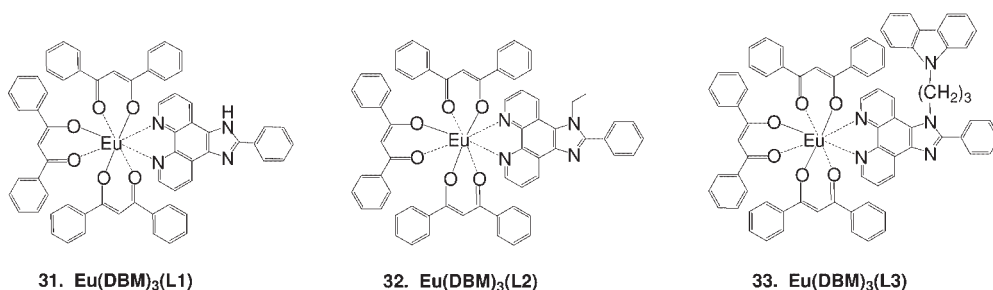
Fig. 12.7 The three-ternary europium complexes with different neutral modified Phen ligands [37].

34. Eu(NDBM)₃(Phen) [38]   **35.** Eu(DTP)₃(Bath) [39]   **36.** Eu(DCNP)(DBM)₂(Phen) [40]

37. Eu(c-DBM)₃(Bath) [41]   **38.** Eu(DBM)₂(c-DBM)(Bath) [41]   **39.** Eu(DBM)(c-DBM)(o-DBM)(Bath) [41]

40. Eu(DBM)₂(c1-DBM)(Bath) [41]   **41.** Eu(DBM)(c1-DBM)(o-DBM)(Bath) [41]   **42.** Eu(LX)₃(TPPO)(H₂O), X = 1-3 [42]
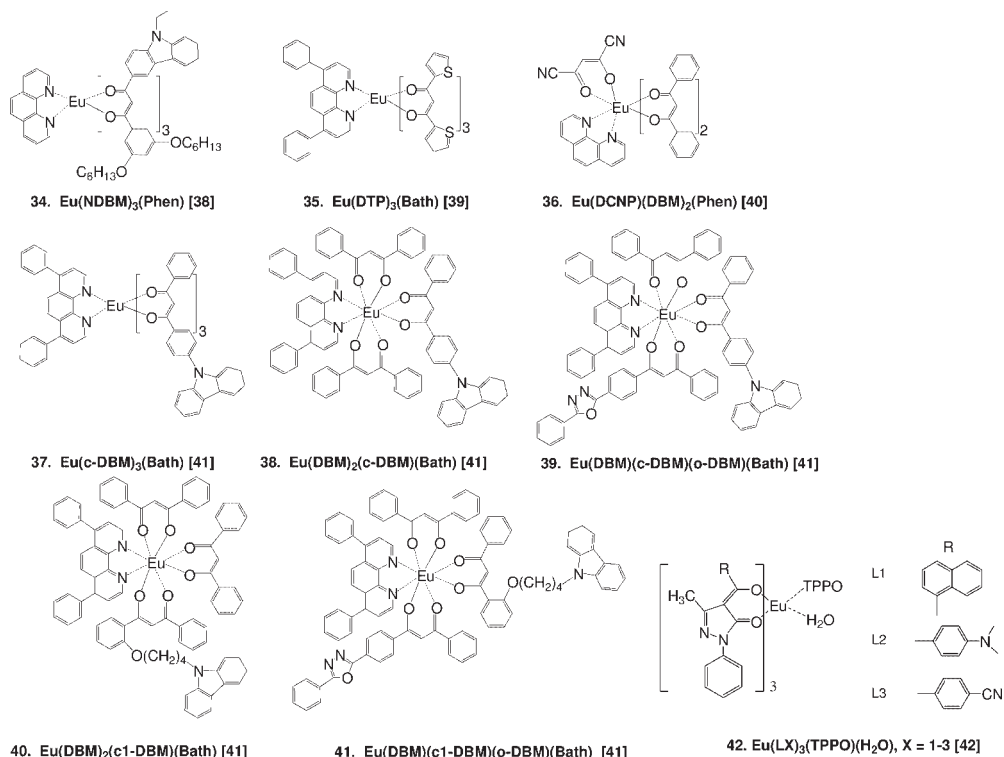
Fig. 12.8 Modified diketones incorporated in the europium complexes used in OLEDs.

In 2000, a europium complex with a modified DBM β-diketone was reported by Bazan and coworkers [38]. In the europium complex, the phenanthroline ligand acts as the electron-transporting medium and the carbazyl group attached to a β-diketone is used for the hole-transporting functional group. Furthermore, the hexyloxyl groups substituted on the phenyl prevent the complex from crystallizing and allow the formation of transparent clear films directly from the solution. In the single layer device ITO/Eu(NDBM)₃(Phen) (compound **34**)/Ca, the light output was $9 \, cd/m^2$ with an external EL quantum efficiency of 0.08%. By introducing the layer of polyvinylcarbazole (PVK) as a hole injection and electron blocking layer, the efficiency of the device ITO/PVK/Eu(NDBM)₃(Phen)/Ca was improved considerably ($50 \, cd/m^2$ at $15 \, mA \, cm^{-2}$) with an external EL quantum efficiency of 0.3%.

In 2001, a new mixed ligand europium complex Eu(DCNP)(DBM)₂(Phen) (compound **36**) for electroluminescence was reported [40]. Two devices based on this complex were fabricated by the doping technique with vacuum deposition at a pressure of about 10^{-6} torr. The configurations of the two devices were ITO/TPD (50 nm)/Eu(DCNP)(DBM)₂(Phen):PBD (10 wt%, 10 nm)/TAZ (25 nm)/AlQ (30 nm)/Mg:Ag (10:1) (200 nm) (device 1) and ITO/TPD

(50 nm)/Eu(DCNP)(DBM)$_2$(Phen):CBP(10 wt%, 20 nm)/BCP (15 nm)/AlQ (30 nm)/Mg:Ag(10 : 1)(200 nm) (device 2). Both devices resulted in the characteristic emission of the Eu^{3+} ion. Device 1 exhibited an external quantum efficiency η_{ext} of 3.5%, power efficiency η_{pw} 2.0 lm/W (10 cd/m^2, 0.17 mA/cm^2), η_{ext}1.6%, and η_{pw} 0.69 lm/W (84 cd/m^2, 2.9 mA/cm^2); while the efficiency of device 2 was about one order of magnitude lower than that of device 1 in the relatively low current density region. The efficiency was comparable with that of device 1 in the higher current density region. The maximum luminance of device 2 reached 924 cd/m^2 at 380 mA/cm^2. The good performance of device 1 in the low current density region may owe to relatively balanceable charge transportation at the emitting layer.

We synthesized several modified β-diketones and their corresponding complexes for study in electroluminescent devices [41] (compounds **37** to **41**). The complexes were designed with an effort to combine the electron-transporting group and the hole-transporting group into one molecule. The functional groups could be introduced to the β-diketone, directly (compounds **37** to **39**) or through an alkoxy chain (compound **41**). In order to adjust the recombination zone to be fairly confined in the emitting layer, the β-diketone bearing different functional groups can be used to coordinate with the central ion individually (compounds **37**, **38**, and **40**) or simultaneously (compounds **39** and **41**). For example, when Eu(c-DBM)$_3$(Bath) was used as emitting material to fabricate a device with the configuration ITO/TPD/Eu(c-DBM)$_3$(Bath)/BCP/AlQ/Mg$_{0.9}$Ag$_{0.1}$/Ag, green light at 520 nm can be observed although BCP was used as the hole-blocking layer. This result indicates that Eu(c-DBM)$_3$(Bath) acts as a hole-transporting property leading to the recombination of excitons only in the AlQ layer. To adjust the carrier-transporting properties and make the recombination zone confined to the emitting layer, a new mixed ligand complex Eu(DBM)$_2$(c-DBM)(Bath) (compound **38**) was synthesized by replacing c-DBM partly with DBM. A device with the configuration ITO/TPD(30 nm)/Eu(DBM)$_2$(c-DBM)(Bath) : PBD(1 : 1 molar ratio, 40 nm)/PBD(30 nm)/Mg$_{0.9}$Ag$_{0.1}$(200 nm)/Ag(100 nm) was fabricated leading to better performance. A maximum Eu^{3+} characteristic emission was found to be 2797 cd/m^2 (0.27 lm/W, 14 V).

Recently, an international patent application for improved electroluminescent device configurations based on europium complexes as emitting materials was published [43]. This type of device has a first layer of a electroluminescent metal complex or organometallic complex in which the central ion could be Sm(III), Eu(III), Tb(III), or Dy(III) etc. and a layer of a second organometallic complex in which the central ion could be Yb(III), Lu(III), Gd(III), or Ce(III) etc. The bandgap of the second complex is larger than that of the metal in the first electroluminescent complex. However, the maximum brightness of this kind of device is not so encouraging.

Another international patent application for a class of binary metal complexes with a general formula $(L_\alpha)_nM_1M_2(L_p)$ was also published recently [44]. In $(L_\alpha)_nM_1M_2(L_p)$, L_p is a neutral ligand, M_1 is a rare earth element, or an actinide, M_2 is a nonrare earth metal, L_α is an organic ligand and n is the combined valence state of M_1 and M_2. For example, using the binary metal complex (shown in Fig.
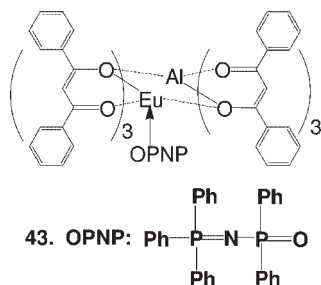
Fig. 12.9 The molecular structure of EuAl(DBM)$_6$(OPNP).
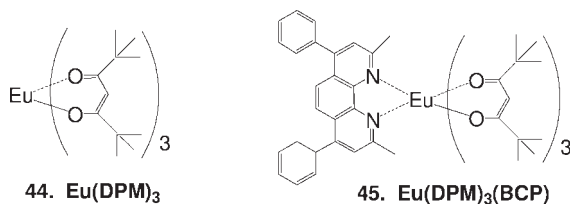
Fig. 12.10 The structure of Eu(DPM)$_3$ and Eu(DPM)$_3$(BCP).

12.9) as emitting material, a device with a configuration ITO/CuPc (2.2 nm)/α-NPB (18.3 nm)/EuAl(DBM)$_6$(OPNP) (55.0 nm)/BCP (6.0 nm)/AlQ (12.0 nm)/LiF (0.9 nm)/Al (500 nm) gave the brightness of 528 cd/m^2 at 21 V in which the current efficiency was 0.132 cd/A and electroluminescent efficiency was 0.088 lm/W.

Although the maximum brightness and the external quantum efficiency of Eu(III) complex-based devices reported gradual increase, europium complexes have been known to show partial or complete decomposition during the vacuum thermal evaporation. This is partly due to the high molecular weight (MW 1000) of Eu complexes, which does not allow vacuum sublimation of the complex smoothly. Another reason originates from the fact that some of the Eu complexes lack volatility for their electronically polarized structure, and consequently they suffer from decomposition before sublimation due to the high sublimation temperature. For example, Eu(DBM)$_3$Phen can be evaporated smoothly in vacuum, however, Eu(DBM)$_3$ decomposes before sublimation.

To solve this problem, Adachi and coworkers [45] synthesized Eu(DPM)$_3$:BCP by co-deposition of Eu(DPM)$_3$ and BCP (see Fig. 12.10). They introduced BCP as a neutral ligand to the complex because it can transport electrons and block holes and has satisfactory electron mobility (~ 10^{-4} cm^2 v^{-1} s^{-1}) [46]. They selected HDPM as anionic ligand due to Eu(DPM)$_3$ has a relatively smaller molecular weight of 701.8 and three bulky nonpolar *t*-buty1 groups that completely surround the Eu^{3+} ion, and weaken the interactions between adjacent Eu(DPM)$_3$, consequently making Eu(DPM)$_3$ enable to sublime easily. Data show that an external quantum efficiency of ~1.0% and a maximum luminescence of 2123 cd/m^2 were obtained
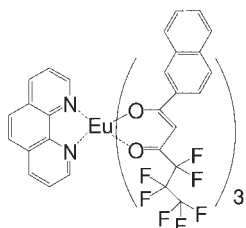
46. Eu(HFNH)₃(phen)

Fig. 12.11 The structure of Eu(HFNH)$_3$(phen).

with a device configuration of ITO (100 nm)/TAP (50 nm)/Eu(DPM)$_3$: BCP (molar ratio = 1 : 1) (20 nm)/BCP (10 nm)/AlQ (30 nm)/MgAg (100 nm)/Ag.

Encouraged by the results that fluorinated substitutes in ligands increase, the volatility of the complex, and thus facilitate thin film fabrication, Zhang et al. [47] synthesized a new complex Eu(HFNH)$_3$(phen) (Fig. 12.11). The device based on the complex with the structure ITO/TPD (50 nm)/the complex: CBP (10%, 40 nm)/ BCP (20 nm)/AlQ (30 nm)/LiF (1 nm)/Al (200 nm) exhibited the maximum brightness of 957 cd/m^2, current efficiency of 4.14 cd/A, and power efficiency of 2.28 lm/W with a pure red Eu^{3+} ion emission. Especially, at the high brightness of 200 cd/m^2, the device still has a high current efficiency of 2.15 cd/A.

12.4
The Green Electroluminescence Based on Terbium Complexes

Although AlQ has been studied extensively as a green emitting material, terbium complexes are still of great interest in the field of electroluminescence (EL) because they have many distinct advantages as mentioned above (see Section 12.1).

The photoluminescence emission based on the terbium ion peaks at 491, 549, 582, and 618 nm correspond to the f–f electronic transition of $^5D_4 \rightarrow ^7F_6$, $^5D_4 \rightarrow ^7F_5$, $^5D_4 \rightarrow ^7F_4$, and $^5D_4 \rightarrow ^7F_3$, respectively (Fig. 12.12). Among them, $^5D_4 \rightarrow ^7F_5$ is dominant. Therefore, a bright green emission can be observed when terbium complexes are used as emission materials.

Kido et al. first reported an electroluminescent device using a terbium complex, Tb(acac)$_3$, as an emitter in early 1990 [49]. Although the maximum brightness was only 7 cd/m^2 at 20 V, it opened an area for green emission materials using lanthanide complexes for electroluminescence.

Compared to europium complexes, terbium complexes reported for electroluminescence are relatively rare [48–58]. They can be summarized mainly into two aspects: terbium carboxylates and β-diketone complexes.

Terbium carboxylates not only have good luminescence but also exhibit good ultraviolet absorption. However, they are difficult to use as emission materials in OLEDs due to their multicoordination mode and consequent formation of inorganic polymers with poor solubility or volatility. Since the carboxylates have been
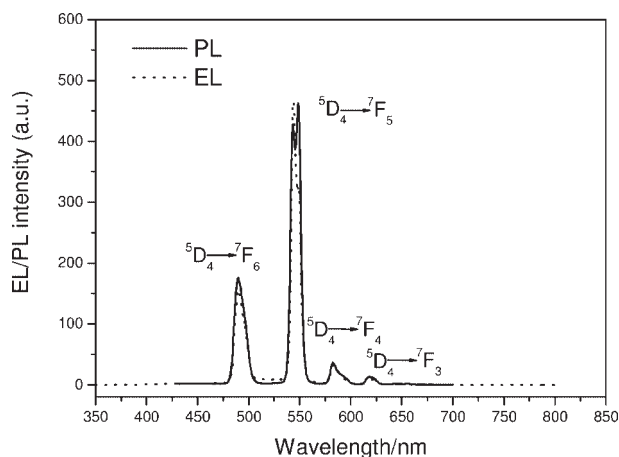
Fig. 12.12 The luminescent spectrum of a terbium complex Tb(eb-PMP)₃(TPPO) [48]. (Reprinted with permission from Ref. [48], copyright 2003, American Chemistry Society)
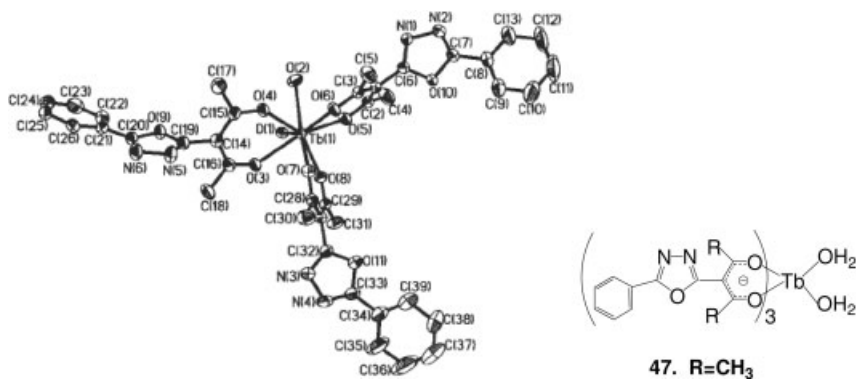
Fig. 12.13 The molecular structure and the molecular formula of the oxadiazole-functionalized Tb (III) β-diketonate (complex 47). (Reprinted with permission from Ref. [53], copyright 2001, American Chemistry Society)

reviewed by Kido [8], we will focus on the newly developed β-diketonate terbium complexes in this article.

In 2001, Zheng and coworkers reported an oxadiazole-functionalized terbium(III) β-diketonate as shown in Fig. 12.13. Using this complex to fabricate a device with the configuration of ITO/PVK:PBD, the Tb complex/AIPOP/C$_S$F/Al, a bright green emission was observed. At 15 V, the light output reached 100 cd/m² with an external EL efficiency of 1.1% and 550 cd/m² with an efficiency of 0.6% at 20 V. But starting from 19 V, a broad peak appeared at about 430 nm which is attributable to exciplex formation between PVK and the Tb complex [53].
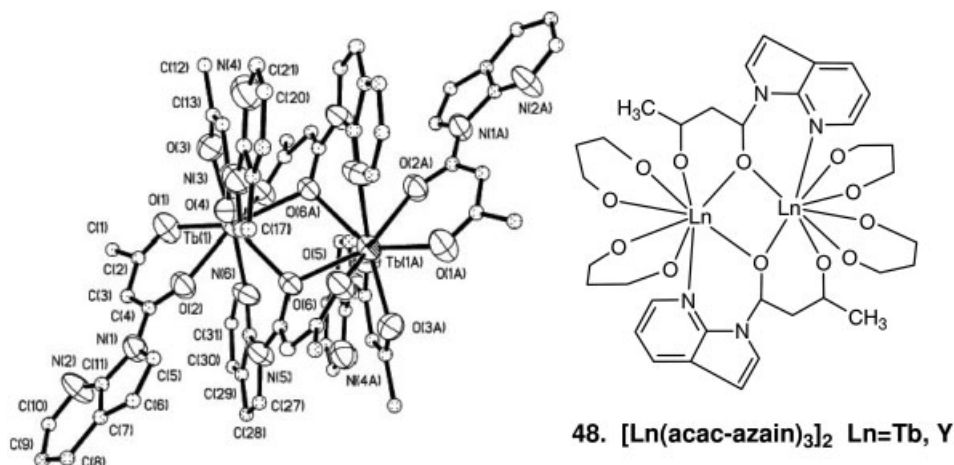
Fig. 12.14 The molecular structure and the simplified structural formula of [Tb(acac-azain)$_3$]$_2$. (Reprinted with permission from Ref. [54], copyright 2002, American Chemistry Society)

In 2002, Wang and coworkers reported a binuclear luminescent terbium complex with formula [Tb(acac-azain)$_3$]$_2$ as shown in Fig. 12.14 [54]. Due to the high molecular weight of the compound, it cannot be sublimed in vacuum and so cannot be used as an emitter in OLEDs by vacuum deposition. Using PVK as the host/hole transport layer and PBD as the electron transport layer, a double layer device with configuration ITO/PVK: [Tb(acac-azain)$_3$]$_2$ (20%, 50 nm)/PBD (30 nm)/ LiF (1.5 nm)/Al (150 nm) was fabricated. Characteristic Tb(III) emission bands were observed which matched the PL of the compound (Fig. 12.15). A weak emission band at 400 nm generated from PVK was also observed. The turn-on voltage was 11 V and the highest efficiency of 0.65 cd/A for the double-layered device was achieved at 13 V and 1.72 mA/cm^2.

In 1998, the first example of electroluminescent devices using a terbium pyrazolonate complex, tris(1-phenyl-3-methyl-4-isobutyl-5-pyrazolone)-bis(triphenylphosphine oxide) terbium (Tb(ip-PMP)$_3$(TPPO)$_2$) (Fig. 12.16 compound **49**), as emitter was reported by our group [55]. With a configuration ITO/TPD/Tb(ip-PMP)$_3$(TPPO)$_2$/AlQ/Al, the device gave a maximum brightness of 920 cd/m^2 at a drive voltage of 18 V and a luminous efficiency of 0.51 lm/W at a current density of 0.70 mA/cm^2. Two years later, Christou and coworkers [56] prepared OLEDs based on modifying the above system with the device configuration of ITO/MTDATH/TPD/Tb(tb-PMP)$_3$(TPPO)/TAZ/Al. A maximum brightness of 2000 cd/m^2 with a luminescence efficiency of 2.63 lm/W was observed. They thought that the device current is apparently hole limited for Tb(tb-PMP)$_3$(TPPO) (Fig. 12.16 compound **52**). However, when appropriate transport layers MTDATH and TAZ were used, charge recombination was moved away from the electrode/ phosphor interface to the transport/phosphor interface, which was rationalized in
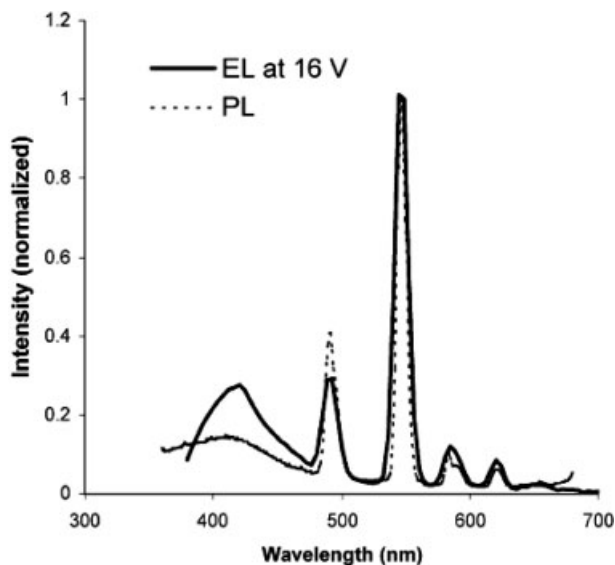
Fig. 12.15 PL of [Tb(acac-azain)$_3$]$_2$ in PVK and EL of the double layer device. (Reprinted with permission from Ref. [54], copyright 2002, American Chemistry Society).
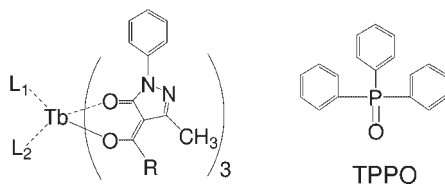
49. L1=TPPO, L2=TPPO,   R=–CH(CH$_3$)$_2$,   Tb(ip-PMP)$_3$(TPPO)$_2$ [55]
50. L1=CH$_3$CH$_2$OH, L2=H$_2$O, R=–CH(CH$_3$)$_2$, Tb(ip-PMP)$_3$(CH$_3$CH$_2$OH)(H$_2$O) [57]
51, L1=TPPO,   R=–CH(C$_2$H$_5$)$_2$, Tb(eb-PMP)$_3$(TPPO) [48,57]
52. L1=TPPO,   R=–C(CH$_3$)$_3$,   Tb(tb-PMP)$_3$(TPPO) [56]
53. L1=TPPO,   R=–CH$_2$C(CH$_3$)$_3$, Tb(tba-PMP)$_3$(TPPO) [58]
54. L1=H$_2$O,   R=CH$_2$C(CH$_3$)$_3$, Tb(tba-PMP)$_3$(H$_2$O) [58]
55. L1=Phen,   R=–CH$_2$C(CH$_3$)$_3$, Tb(tba-PMP)$_3$(Phen) [58]

Fig. 12.16 Structures of some terbium pyrazolonate complexes.

terms of an energy level diagram (see Fig. 12.17) in which the HOMO of the phosphor was placed at 6.4 eV.

After a systematic study on the terbium pyrazolonate complexes, we demonstrated that Tb(ip-PMP)$_3$(TPPO)$_2$ (compound **49)** had very good electron-
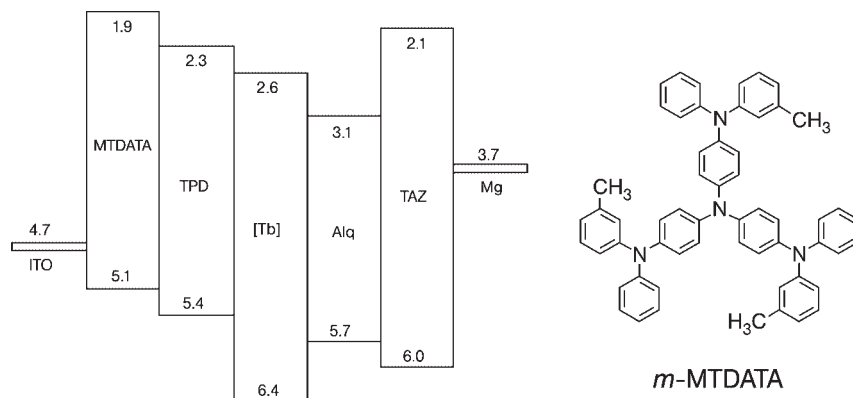
Fig. 12.17 Proposed energy level diagram of the HOMO and LUMO energies of the materials used to prepare OLEDs based on Tb(tb-PMP)$_3$(TPPO) [56]. (Reprinted with permission from Ref. [56], copyright 2000, John Wiley).
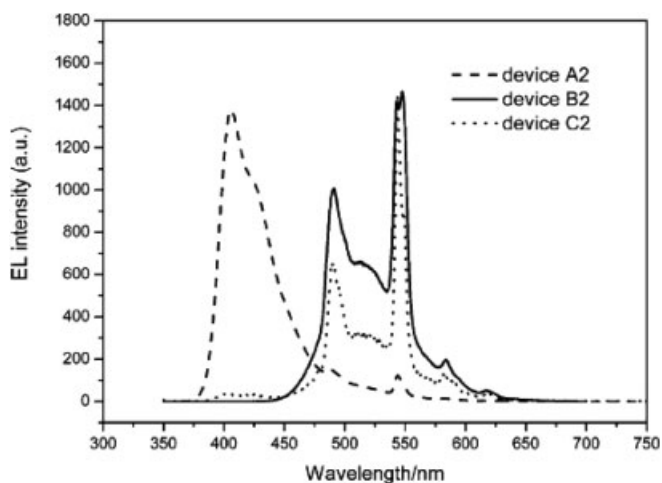
Fig. 12.18 EL spectra of devices with the same configuration ITO/TPD (20 nm)/Tb-complex (50 nm)/AlQ (30 nm)/Mg$_{0.9}$Ag$_{0.1}$ (200 nm)/Ag (80 nm) using complexes 49 (A2), 50 (B2) and 51 (C2) as emitter with applied voltage 10 V [57]. (Reprinted with permission from Ref. [57], copyright 2003, American Chemistry Society).

transporting properties and the recombination zone was confined mainly in the TPD layer, while Tb(ip-PMP)$_3$(H$_2$O)(EtOH) (compound **50**) only showed a hole-transporting property and the recombination zone was confined mainly in the AlQ layer (Fig. 12.18). To adjust the carrier-transporting properties and make the recombination zone easily confined in terbium complex layer, we synthesized a new terbium complex tris[1-phenyl-3-methyl-4-(2-ethylbutyryl)-5-pyrazolone]

(triphenylphosphine oxide) terbium, (Tb(eb-PMP)$_3$(TPPO)), (compound **51**) by modifying the ligand [48, 57]. Since the coordination number of lanthanide complexes is changeable, the goal of the modification was to increase the steric hindrance of the β-diketonate and to fashion the environment which has no room suitable for two TPPO to coordinate with the central Tb^{3+} ions.

The results revealed that holes and electrons were more easily confined to this complex by constructing a proper device configuration. To prevent the hole from entering the AlQ layer, a 20 nm hole-blocking material, BCP was inserted between complex **51** and AlQ in the device with configuration ITO/TPD (20 nm)/complex **51** (50 nm)/BCP (20 nm)/AlQ (30 nm)/Mg$_{0.9}$Ag$_{0.1}$ (200 nm)/Ag (80 nm). At an applied voltage of 18 V, the light output reached 8800 cd/m^2, and a peak external quantum and power efficiency of 21 cd/A and 9.4 lm/W were achieved at 7 V, 87 cd/m^2 (see Fig. 12.19). Moreover, a performance with peak power efficiency of 11.3 lm/W at 7 V and brightness higher than 12 000 cd/m^2 at 18 V was achieved from a device with configuration ITO/NPB (10 nm)/Tb(eb-PMP)$_3$(TPPO) (50 nm)/ BCP (20 nm)/AlQ(40 nm)/Mg$_{0.9}$Ag$_{0.1}$ (200 nm)/Ag (800 nm).

Our results also proved that the neutral ligands used in these terbium complexes strongly affected their photoluminescence and electroluminescence performances. Recently, three terbium complexes Tb(tba-PMP)$_3$(TPPO), Tb(tba-PMP)$_3$(H$_2$O), and Tb(tba-PMP)$_3$(Phen) (compounds **53** to **55**) with different neutral ligands were synthesized and how the neutral ligand affects the mechanism of luminescence was studied in detail [58]. Experiments revealed that the neutral ligands TPPO and Phen strongly affect the PL intensities of the terbium complexes. The integral emission intensity is quite different from each other with a ratio of Tb(tba-PMP)$_3$(TPPO) : Tb(tba-PMP)(H$_2$O) : Tb(tDa-PMP)(Phen) = 2.1 : 1.3 : 1 (Fig. 12.20).
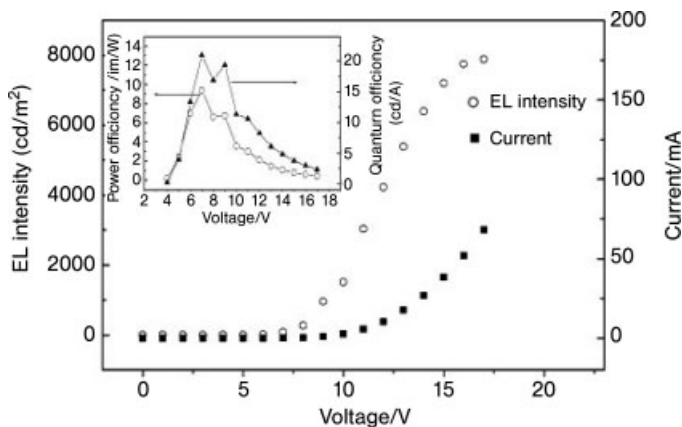
Fig. 12.19 Current–voltage (■), luminance–voltage (○), and external quantum and power efficiency (inset) curves of device ITO/TPD(20 nm)/Tb(eb-PMP)$_3$(TPPO)(50 nm)/BCP(20 nm)/ AlQ(30 nm)/Mg$_{0.9}$Ag$_{0.1}$(200 nm)/Ag(800 nm) [57]. (Reprinted with permission from Ref. [57], copyright 2003 American Chemistry Society).
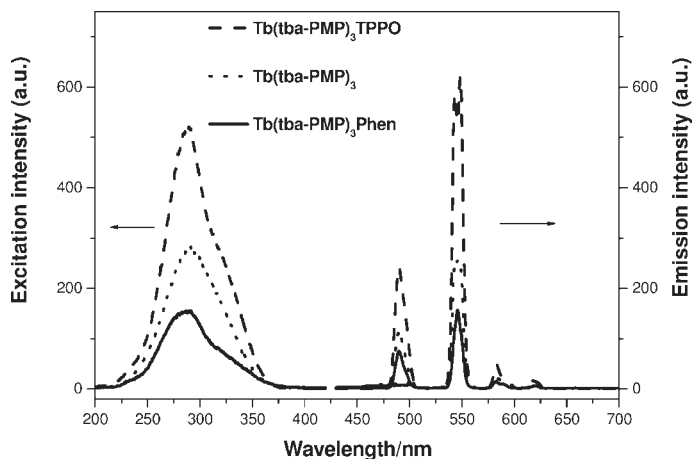
Fig. 12.20 Photoluminescence spectra (λ_{ex} = 285 nm; λ_{em} = 545 nm) of Tb(tba-PMP)$_3$(TPPO), Tb(tba-PMP)$_3$(H$_2$O), and Tb(tba-PMP)$_3$(Phen) measured from their 80 nm vacuum evaporated films on quartz substrates. (Reprinted with permission from Ref. [58], copyright 2004, American Chemistry Society).

Table 12.3 The singlet and triplet state energy levels of the ligands [58].

Complexes	Singlet energy level (eV)	Triplet energy level (eV)
Gd(tba-PMP)$_3$(H$_2$O)(EtOH)	3.81	2.51
Gd(TPPO)$_2$(NO$_3$)$_3$	4.51	2.35
Gd(Phen)$_2$(NO$_3$)$_3$	3.87	2.09

Obviously, this difference originated from the different coordination environments caused by the varying neutral ligand. Compared to the complex Tb(tba-PMP)$_3$(H$_2$O) without a neutral ligand (H$_2$O was lost during the vacuum deposition), TPPO strengthened the PL intensity of the complex Tb(tba-PMP)$_3$(TPPO). On the other hand, Phen decreased the PL intensity of the complex Tb(tba-PMP)$_3$(Phen). The results indicated that this is caused by the different excited energy levels between tba-PMP, TPPO, and Phen, which were obtained from their phosphorescence spectra measured with their corresponding gadolinium complexes Gd(tba-PMP)$_3$(H$_2$O)(EtOH), Gd(TPPO)$_2$(NO$_3$)$_3$ and Gd(Phen)$_2$(NO$_3$)$_3$, as shown in Table 12.3.

From Fig. 12.21, we can see that compared to complex **54**, the excitation energy absorbed by TPPO can be efficiently transferred either to tba-PMP and then to the central ion Tb^{3+}, or transferred directly to Tb^{3+} ion since TPPO's excited singlet and triplet energy levels match with the excited states of tba-PMP and the $^5D_4$ energy level of Tb^{3+}, and consequently enhance the PL intensity of complex **53**.
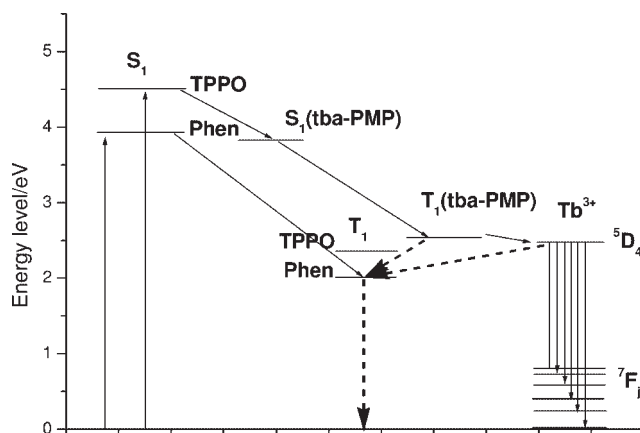
Fig. 12.21 Schematic energy level diagram and the energy transfer processes. S_1: first excited singlet state, T_1: first excited triplet state. (Reprinted with permission from Ref. [58], copyright 2004, American Chemistry Society)

On the contrary, back energy transfer occurred between Phen and tba-PMP or Tb^{3+} since the triplet energy level of Phen is lower than that of tba-PMP and also the $^5D_4$ energy level of Tb^{3+} as well. Terbium complex electroluminescence (EL) also greatly depended on its PL intensity. The performances of the complexes **53**, **54**, and **55** achieved were $9540\,cd/m^2$, $7.2\,lm/W$, $3230\,cd/m^2$, $1.17\,lm/W$, and $690\,cd/m^2$, $0.13\,lm/W$, respectively, with power efficiency ratio of complex **53** : complex **54** : complex **55** = 55 : 9 : 1, which was greatly increased compared to their PL intensity ratio of complex **53** : complex **54** : complex **55** = 2.1 : 1.3 : 1.

12.5
The Near Infrared Electroluminescence Based on Neodymium, Erbium, or Ytterbium Complexes

Comparing to those lanthanide elements which have strong emission in visible region, the research on the PL or EL of the elements which have emission in the near infrared region, such as Nd, Er, Pr, Yb, Ho, and Tm is relatively rare. This is due to their much lower emission quantum efficiency ($\varphi_{PL} \sim 10^{-4}$–$10^{-6}$), which originates from the fact that the deactivation process often occurs through the nonradiative relaxation. However recently, increasing attentions have been attracted due to their electronic and optical applications, in particular for optical communication [59–63], biological and sensor applications [64]. Obviously, the reports on electroluminescence are even less compared to that on photoluminescence. In this respect, research efforts are often paid to the following attempts: (1) design of ligand with large steric hindrance or other method to avoid the relaxation of energy via resonance vibration [65]; (2) adjustment of the triplet energy level of the ligand to match the lowest unoccupied orbital of the central ion [66–68]; (3) improvement

of the energy transfer by using hetero-bimetallic compound or introduction of the functional group into the emitting molecule or blending the electronic conductive material directly with the emitting material such as conductive polymer etc., promoting the transport of the electrons and holes [69, 70].

Gillin and Curry [71] fabricated an Er-containing OLED in which the Er-tris(8-hydroxyquinoline) complex was used as the emitting material. All of the organic layers and the cathode were fabricated by vacuum deposition. Characteristic Er emission at 1.53 µm due to the $^4I_{13/2}$ to $^4I_{15/2}$ intra-atomic electron transition was obtained from the device ITO/TPD/ErQ/Al. The radiative lifetime of the excited state $^4I_{13/2}$ was measured to be ~230 ms. By incorporating Nd^{3+} into the same chelate, emissions at 0.900 ($^4F_{3/2} \rightarrow {}^4I_{9/2}$), 1.06 ($^4F_{3/2} \rightarrow {}^4I_{11/2}$), and 1.32 µm ($^4F_{3/2} \rightarrow {}^4I_{13/2}$) have been demonstrated and similarly emission at 0.98 µm from $^2F_{5/2} \rightarrow {}^2F_{7/2}$ of Yb(III) ion in Yb-tris(8-hydroxyquinoline) has been obtained, as shown in Fig. 12.22.

Yanagida and coworkers reported an OLED based on Nd(DBM)$_3$Bath. In the device, Nd(DBM)$_3$Bath was the emitting material; TPD and AlQ were used as the hole- and electron-transporting materials. Sharp near-infrared emission bands corresponding to f–f transitions of the Nd ion were obtained (Fig. 12.23). However, the device was found to be degradated during the measurement [72].

Li et al. [73] demonstrated very good electron injection ability of a Yb complex, Yb(DBM)$_3$Bath. Using it as an electron-transporting and emitting material, TPD as a hole-transporting layer, the EL device with the structure of ITO/TPD (40 nm)/Yb(DBM)$_3$Bath:TPD (weight ratio approx. 1:1, 40 nm)/Yb(DBM)$_3$Bath (80 nm)/Ag:Mg (150 nm) was made and an intense emission corresponding to the $^2F_{5/2} \rightarrow {}^2F_{7/2}$ electronic transition of the trivalent Yb ion was observed. Threshold values
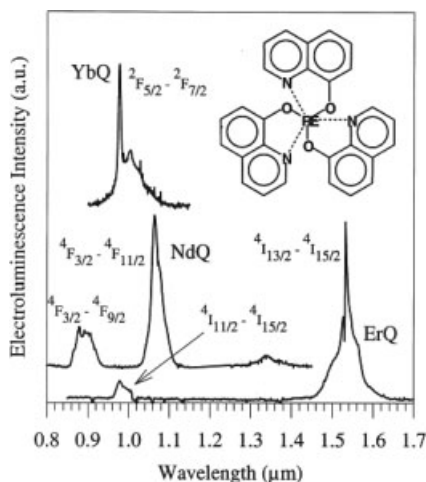
Fig. 12.22 The electroluminescence spectra obtained from RE tris(8-hydroxyquinoline) (REQ, RE = Nd, Er, or Yb) based OLEDs. (Reprinted with permission from Ref. [71], copyright 2001, Elsevier Science)
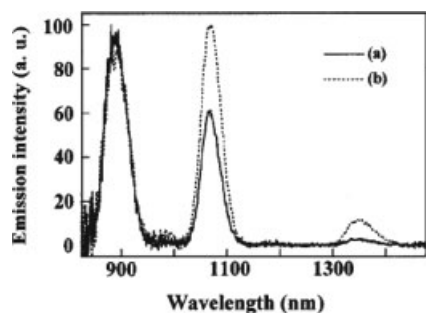
Fig. 12.23 Emission spectra in the near-IR region; (a) EL spectrum of ITO/TPD/Nd(DBM)₃Bath/AlQ/Mg:Ag device at the applied voltage of 19 V, (b) PL spectrum of deposited film of Nd(DBM)₃Bath. Thickness of deposited film for PL was 2000 Å and excited by 390 nm light [72]. (Reprinted with permission from Ref. [72], copyright 1999, American Institute of Physics)

of drive voltage and current density for the observation of IR emission from Yb³⁺ ion were 4.5 V and 1.6 mA/cm², respectively. IR emission was obtained under a low drive voltage (below 10 V).

Although initial studies on infrared luminescence from OLEDs mostly focused on small molecular weight emitters, some researchers were interested in the development of conjugated polymer-based active layers recently, as these tend to suffer less from recrystallization problems, and are therefore more promising candidates for achieving a better diode durability.

Sun and coworkers reported the PL and EL properties of an erbium complexes [74], tris(acetylacetonato)(1,10-phenanthroline)erbium [Er(acac)₃(Phen)]. To fabricate the EL devices from the compound, PVK was employed as a host polymer. The thin films of PVK doped with Er(acac)₃(Phen) were prepared by spin coating from PVK:Er(acac)₃(Phen) (10:8 by weight) dichloroethane solution. They demonstrated sharp 1.54 μm infrared emission at room temperature from the EL devices with the structure of ITO/PVK:Er(acac)₃(Phen)/Al:Li/Ag.

Schanze et al. [65] found that when poly[2-methoxy-5-(2′-ethylhexyloxy)-1,4-phenylene vinylene] (MEH-PPV) was used as a host with Ln(TPP)acac, (Ln = lanthanide, TPP = 5,10,15,20-tetraphenylporphyrinate, acac = acetoacetonate) as a dopant (Fig. 12.24), the visible PL and EL of the host were quenched, and replaced by the near-IR emission characteristic of the lanthanide complex.

They also reported the photoluminescent and electroluminescent properties of near-infrared emitting lanthanide monoporphyrinate complexes, Ln(TPP)L (L = hydridotris(1-pyrazolyl)-borate (Tp) or (cyclopentadienyl)tris(diethylphosphinito) cobaltate(I) L(OEt)) blended into conjugated and nonconjugated polymer hosts (Fig. 12.25). A blue emitting alkoxysubstituted poly(P-phenylene) (PPP-OR11) was used as the conjugated polymer host and nonconjugated hosts included polystyrene, poly(methyl methacrylate), poly(N-butyl methacrylate), and poly(bisphenol A-carbonate) [75]. Complete quenching of the PPP-OR11 host fluorescence (i.e.,
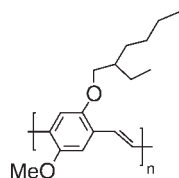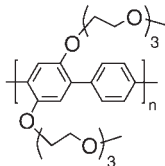
56. MEH-PPV   **57. PPP-OR11**   **58. Ln=Yb^{3+} or Er^{3+}**
Ln(TPP)acac
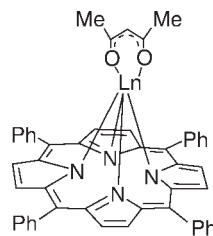
Fig. 12.24 Chemical structures of MEH-PPV, PPP-OR11 and
Ln(TPP)acac [65]. (Reprinted with permission from Ref. [65],
copyright 2001, American Institute of Physics)
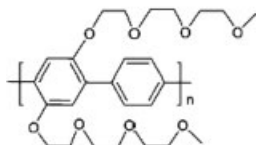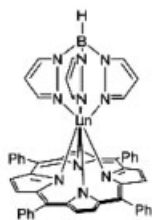
59. PPP-OR11   **60. Ln(TPP)Tp**   **61. Ln(TPP)L(OEt)**
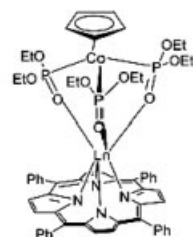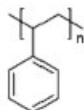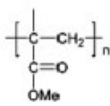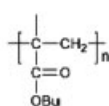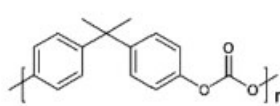
62. PS   **63. PMMA**   **64. PBMA**   **65. PC**

Fig. 12.25 Chemical structures of Ln(TPP)Tp, Ln(TPP)L(OEt)
(Ln is Yb, Er, Nd, or Ho), PPP-OR11, polystyrene (PS),
poly(bisphenenol-*A*-carbonate) (PC), poly(methyl
methacrylate) (PMMA), and poly(*N*-butyl methacrylate)
(PBMA). (Reprinted with permission from Ref. [75], copyright
2004, American Chemistry Society)

>95%) was observed at 5 mol % of Ln(TPP)Tp, and host quenching was accompa-
nied by sensitization of near-infrared emission from the lanthanide complex.
OLEDs fabricated with PPP–OR11 exhibited turn-on voltages of approximately 4 V,
whereas nonconjugated polymer devices had higher turn-on voltages (ca. 8 V),
independent of the polymer used. Comparable external electroluminescence (EL)
efficiencies in the order of 10^{-4} were observed from both the conjugated and non-
conjugated polymer host devices. They suggested that hole transport was domi-
nated by the Ln(TPP)L material, and carrier transport was believed to occur via
a site-to-site hopping mechanism. They further confirmed that the porphyrin
complex was active as a charge-transporting material by the characterization of the

66. PPP-R10

67. PPP-OR11

68. Yb(DBM)₃(phen)

70. Yb(TPP)L(OEt)

69. Yb(DNM)₃(phen)
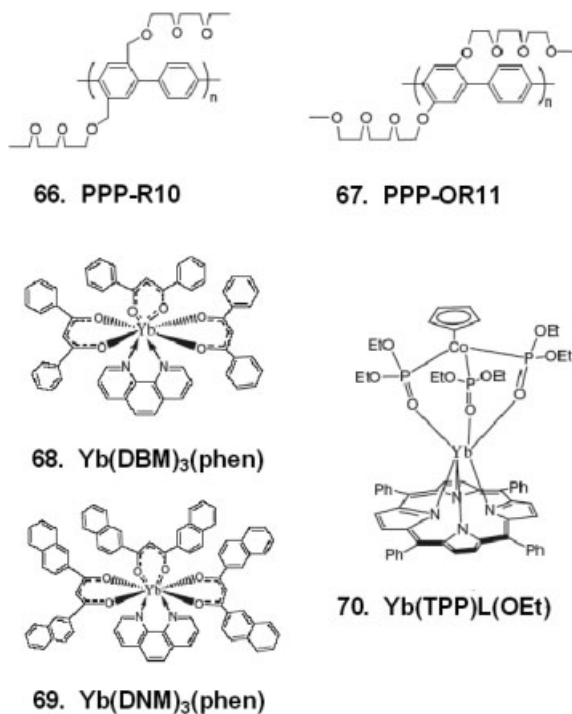
Fig. 12.26 The chemical structures of PPP-R10, PPP-OR11, and the Yb complexes [77]. (Reprinted with permission from Ref. [77], copyright 2003, John Wiley)

electroluminescence spectra and a series of near-infrared emitting electroluminescent devices in which the active material consisted of a series of LnTPP complexes dispersed in polystyrene (PS) as a host matrix [76].

Schanze et al. blended Yb(DNM)₃(Phen) (DNM = dinaphthoylmethane) with PPP–OR11 (see Fig. 12.26) to fabricate near-infrared emitting EL devises which showed enhanced near-IR output at 977 nm when compared to those fabricated with Yb(DBM)₃(Phen)/PPP–OR11 blends. The maximum near-IR external efficiencies of the devices with Yb(DBM)₃(Phen) and Yb(DNM)₃(Phen) were 7×10^{-5} (at 6 V and at 0.81 mA/mm²) and 4×10^{-4} (at 7 V, and 0.74 mA/mm²), respectively. The better results highlighted the importance of spectral overlap on the efficiency of energy transfer from the host to the Yb complex [77].

12.6
The Ligand Emission Electroluminescence Based on Yttrium, Lanthanum, Gadolinium, or Lutetium Complexes

It is well known that Y^{3+} and La^{3+} have $4f^0$ electronic configuration and usually their complexes do not emit in visible light region. In 2001, we reported a first EL device based on tris(1-phenyl-3-methyl-4-isobutyryl-5-pyrazolone) (2,2′-dipyridyl)

71. RE(ip-PMP)₃(TPPO)₂   **72. RE(ip-PMP)₃(Bipy)**   **73. RE(ip-PMP)₃(Phen)**
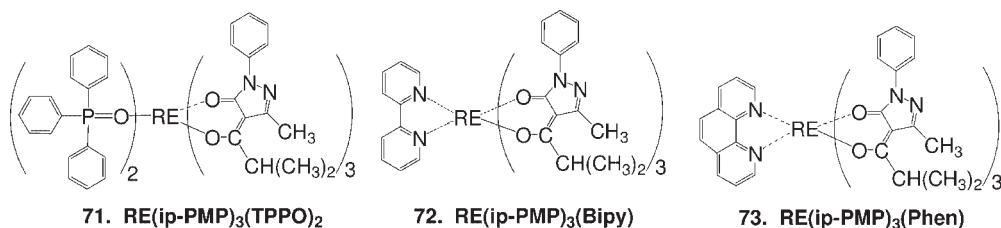
Fig. 12.27 General chemical structural formulas of RE(ip-PMP)$_3$(TPPO)$_2$, RE(ip-PMP)$_3$(Bipy), and RE(ip-PMP)$_3$(Phen) (RE^{3+} = Y^{3+}, La^{3+}, Gd^{3+}, and Lu^{3+}).
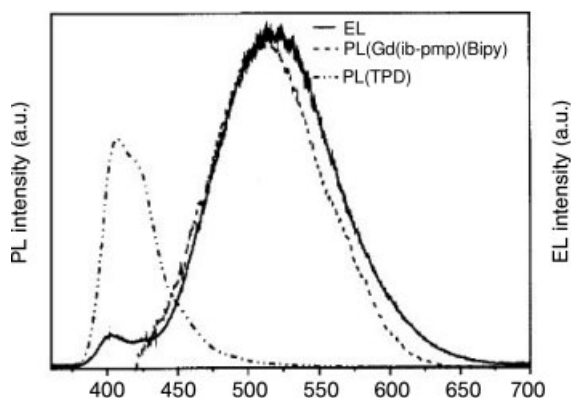
Fig. 12.28 PL (Left axis) of TPD and Gd(ip-PMP)$_3$(Bipy) (λ_{ex}=280 nm) and EL (Right axis) of the device ITO/TPD(40 nm)/Gd(ip-PMP)$_3$(Bipy) (80 nm)/Mg:Ag(200 nm)/Ag(100 nm) at 10 V [80].

yttrium [Y(ip-PMP)$_3$(Bipy)] (Fig. 12.27 compound **72**) which can emit blue photoluminescence emission peaking at 452 nm and belongs to ligand emitting complex [78]. The device with the configuration of ITO/PVK (40 nm)/Y(ip-PMP)$_3$(Bipy) (80 nm)/Mg:Ag (200 nm)/Ag (100 nm) emitted bright green light peaking at 502 nm instead of blue light, which was attributed to the exciplex formation at the solid interface between the PVK and the complex. The device exhibited a maximum luminance of 177 cd/m^2. Similar exciplex emission located at 522 nm was also observed from the device ITO/TPD(40 nm)/La(ip-PMP)$_3$(Bipy) (80 nm)/Mg:Ag(200 nm)/Ag(100 nm) [79].

Interestingly, the EL device based on Gd(ip-PMP)$_3$(Bipy) [80] with the same ligands ip-PMP and Bipy does not present such an exciplex' emission. As shown in Fig. 12.28, the central peak of EL at 516 nm, with a shoulder peak at 420 nm originated from TPD, is identical to the PL spectrum of Gd(ip-PMP)$_3$(bipy) and exciplex formation was not found from the EL spectrum of the device ITO/TPD (40 nm)/Gd(ip-PMP)$_3$(Bipy) (80 nm)/Mg:Ag (200 nm)/Ag (100 nm). The reason may be that the spin-orbit perturbation of the electronic levels of the ligand, predominantly

induced by the paramagnetic Gd^{3+} ion, gives rise to the longer lifetime excited state of Gd(ip-PMP)$_3$(Bipy), which is not for the benefit of the formation of exciplex.

Lu^{3+} has $4f^{14}$ electronic configuration and no f–f transition is observed. We reported a series of devices based on three ternary lutetium complexes Lu(ip-PMP)$_3$(TPPO)$_2$, Lu(ip-PMP)$_3$Bipy, and Lu(ip-PMP)$_3$Phen (Fig. 12.27). Similar to the gadolinium complexes, no exciplex' emission was obtained from the device based on Lu(ip-PMP)$_3$(TPPO)$_2$, the reason is due to the nonplanar configuration of ligand TPPO. It is known that the formation of an exciplex is a result of the charge transfer between a donor excited state and an accepter ground state at the interface, which often occurs between planar molecules. Neutral ligand Bipy became plane after it was coordinated to Lu^{3+} and made Lu(ip-PMP)$_3$(Bipy) easily form exciplex. The same phenomenon was observed from the complex Lu(ip-PMP)$_3$(Phen). When a positive voltage was applied to the ITO electrode of the device ITO/TPD(40 nm)/Lu(ip-PMP)$_3$(TPPO)$_2$ (40 nm)/Mg$_{0.9}$Ag$_{0.1}$, blue light originated from this complex was observed, while the same configuration devices using the other two complexes as emitting materials exhibited green light peaking at 512 nm, which is contributed by exciplex formed at the interface of TPD and the corresponding lutetium complex [81].

12.7
Conclusion

In a word, considerable progress has been achieved with OLEDs by utilizing complexes with lanthanide ions such as Eu and Tb as the emitting materials. However, the quantum efficiencies of most of these lanthanide complexes are unfortunately still low and the lifetimes of these devices are unsatisfied. This may be due to the inefficiency of the energy transfer, poor stability of the lanthanide complexes under the fabrication and the operation of the devices. Thus, in order to obtain effective OLEDs using lanthanide-based compounds, we should design ligands which have more efficient energy transfer to the lanthanide metal ions. Furthermore, the host materials must be effective for energy transfer. For the practical application of lanthanide complexes in OLEDs, further development should also be focused on obtaining lower cost, more easily fabricated, and better chemically and thermally stabilized lanthanide complexes. Recent results revealed that incorporating functional groups (electron or/and hole transporting groups) into lanthanide complex ligands is a special kind of "doping" technique, which is an efficient and useful strategy to improve the performance of these materials for OLEDs.

References

1 D. Y. Kim, H. N. Cho, C. Y. Kim, *Prog. Polym. Sci.*, **2000**, *25*, 1089.

2 P. W. M. Blom, M. C. J. M. Vissenberg, *Mater. Sci. Eng. R*, **2000**, *27*, 53.

3 C. H. Chen, J. Shi, *Coord. Chem. Rev.*, **1998**, *171*, 161.

4 J. L. Segura, *Acta Polym.*, **1998**, *49*, 319.

5 U. Mitschke, P. Bauerle, *J. Mater. Chem.*, **2000**, *10*, 1471.

6 L. S. Huang, C. H. Chen, *Mater. Sci. Eng. R*, **2002**, *39*, 143.

7 C. H. Huang, *Rare Earth Coordination Chemistry*, Science Press, P. R. China, **1997**.

8 J. Kido, Y. Okamoto, *Chem. Rev.*, **2002**, *102*, 2357.

9 M. Pope, H. P. Kallmann, P. Magnante, *J. Chem. Phys.*, **1963**, *38*, 2042.

10 C. W. Tang, S. A. VanSlyke, *Appl. Phys. Lett.*, **1987**, *51*, 913.

11 J. H. Burroughes, C. A. Jones, R. H. Friend, *Nature*, **1990**, *335*, 137.

12 H. Yersin, *Top. Curr. Chem.*, **2004**, *24*, 1.

13 Z. Q. Bian, K. Z. Wang, L. P. Jin, *Polyhedron*, **2002**, *21*, 313.

14 J. Kido, K. Nagai, Y. Okamoto, *Chem. Lett.*, **1991**, *235*, 1267.

15 K. Okada, M. Uekawa, Y. F. Wang, T. F. Chen, T. Nakaya, *Chem. Lett.*, **1998**, 801.

16 K. Okada, Y. F. Wang, T. Nakaya, *Synth. Met.*, **1998**, *97*, 113.

17 W. G. Zhu, Q. Jiang, Z. Y. Lu, X. Q. Wei, M. G. Xie, D. C. Zou, T. Tsutsui, *Synth. Met.*, **2000**, *111–112*, 445.

18 T. Sano, M. Fujita, T. Fujii, Y. Hamada, K. Shibata, K. Kuroki, *Jpn. J. Appl. Phys.*, **1995**, *34*, 1883.

19 C. Adachi, M. A. Baldo, S. R. Forrest, *J. Appl. Phys.*, **2000**, *87*, 8049.

20 H. Heil, J. Steiger, R. Schmechel, H. Von Seggern, *J. Appl. Phys.*, **2001**, *90*, 5357.

21 J. Kido; H. Hayase, K. Honggawa; K. Nagai, K. Okuyama, *Appl. Phys. Lett.*, **1994**, *65*, 2124.

22 C. L. Liang, Z. R. Hong, X. Y. Liu, D. X. Zhao, D. Zhao, W. L. Li, J. B. Peng, J. Q. Yu, C. S. Lee, S. T. Lee, *Thin Solid Film*, **2000**, *14*, 359.

23 C. L. Liang, D. Zhao, Z. R. Hong, D. X. Zhao, X. Y. Liu, W. L. Li, J. B. Peng,
J. Q. Yu, C. S. Lee, S. T. Lee, *Appl. Phys. Lett.*, **2000**, *76*, 67.

24 Z. R. Hong, C. J. Liang, R. G. Li, W. L. Li, D. Zhao, D. Fan, D. Y. Wang, B. Chu, F. X. Zang, L. S. Hong, S. T. Lee, *Adv. Mater.*, **2001**, *13*, 1241.

25 J. F. Fang, D. G. Ma, *Appl. Phys. Lett.*, **2003**, *83*, 4041.

26 M. Sun, H. Xin, K. Z. Wang, Y. A. Zhang, L. P. Jin, C. H. Huang, *Chem. Commun.*, **2003**, 702.

27 M. Guan, Z. Q. Bian, F. Y. Li, H. Xin, C. H. Huang, *New J. Chem.*, **2003**, *27*, 1731.

28 H. Xin, F. Y. Li, M. Guan, C. H. Huang, M. Sun, K. Z. Wang, Y. A. Zhang, L. P. Jin, *J. Appl. Phys.*, **2003**, *94*, 4729.

29 Z. Q. Bian, D. Q. Gao, C. Y. Sun, K. Z. Wang, L. P. Jin, C. H. Huang, *Chem. Res. Chinese U*, **2002**, *18*, 466.

30 P. P. Sun, J. P. Duan, H. T. Shih, C. H. Cheng, *Appl. Phys. Lett.*, **2002**, *29*, 792.

31 P. P. Sun, J. P. Duan, J. J. Lih, C. H. Cheng, *Adv. Funct. Mater.*, **2003**, *13*, 683.

32 L. Huang, K. Z. Wang, C. H. Huang, *J. Mater. Chem.*, **2001**, *11*, 790.

33 X. H. Zhu, L. H. Wang, J. Ru, W. Huang, J. F. Fang, D. G. Ma, *J. Mater. Chem.*, **2004**, *14*, 2732–2734.

34 W. P. Hu, M. Matsumura, M. Z. Wang, L. P. Jin, *Appl. Phys. Lett.*, **2000**, *77*, 4271.

35 W. P. Hu, M. Matsumura, M. Z. Wang, L. P. Jin, *Jpn. J. Appl. Phys.*, **2000**, *39*, 6445.

36 F. S. Liang, Q. G. Zhou, Y. X. Cheng, L. X. Wang, *Chem. Mater.*, **2003**, *15*, 935.

37 Z. Q. Bian, D. Q. Gao, M. Guan, H. Xin, F. Y. Li, C. H. Huang, *Science in China (Series B)*, **2004**, *34*, 113.

38 M. R. Robinson, M. B. O'Regan, G. C. Bazan, *Chem. Comm.*, **2000**, 1645.

39 K. Okada, Y. F. Wang, T. M. Chen, M. Kitamura, T. Nakaya, H. Inoue, *J. Mater. Chem.*, **1999**, *9*, 3023.

40 M. Noto, K. Irie, M. Era, *Chem. Lett.*, **2001**, 320.

41 C. H. Huang, Z. Q. Bian, M. Guan, F. Y. Li, H. Xin, *China Patent*, Appl. 03142611.5 **2003**.

42 M. Shi, F. Y. Li, T. Yi, D. Q. Zhang, H. M. Hu, C. H. Huang, *Inorg. Chem.*, **2005**, *44*, 8929–8936.

43 Elam-t Limited, *PCT Int.*, Appl. GB2003, 005663 **2003**.

44 P. Kathirgamanathan, S. Ravichandran, S, Surendrakumar, *U.S. Patent, Appl.* 10/475, 627 **2001**.

45 T. Oyamada, Y. Kawamura, T. Koyama, H. Sasabe, C. Adachi, *Adv. Mater.*, **2004**, *16*, 1082.

46 S. Naka, H. Okada, H. Onnagawa, T. Tsutsui, *Appl. Phys. Lett.*, **2000**, *76*, 197.

47 J. B. Yu, L. Zhou, H. J. Zhang, Y. X. Zheng, H. R. Li, R. P. Deng, Z. P. Peng, Z. F. Li, *Inorg. Chem.*, **2005**, *44*, 1611–1618.

48 H. Xin, F. Y. Li, M. Shi, Z. Q. Bian, C. H. Huang, *J. Am. Chem. Soc.*, **2003**, *125*, 7166.

49 J. Kido, K. Nagai, Y. Ohashi, *Chem. Lett.*, **1990**, 657.

50 B. Li, D. G. Ma, H. J. Zhang, X. J. Zhao, J. Z. Ni, *Thin Solid Films*, **1998**, *325*, 259.

51 Q. Lin, L. Fu, Y. Liang, Y. Zheng, J. Lin, H. Zhang, *J. Rare Earths*, **2003**, *21*, 19.

52 W. L. Li, J. Q. Yu, G. Sun, Z. R. Hong, Y. Yu, Y. Zhao, J. B. Peng, T. Tsutsui, *Synth. Met.*, **1997**, *91*, 263.

53 J. F. Wang, R. Y. Wang, J. Yang, Z. P. Zheng, M. D. Carducci, T. Cayou, N. Peyghambarian, G. E. Jabbour, *J. Am. Chem. Soc.*, **2001**, *123*, 6179.

54 R. Y. Wang, D. T. Song, C. Seward, Y. Tao, S. N. Wang, *Inorg. Chem.*, **2002**, *41*, 5187.

55 X. C. Gao, H. Cao, C. H. Huang, B. G. Li, *Appl. Phys. Lett.*, **1998**, *72*, 2217.

56 S. Capecchi, O. Renault, D. G. Moon, M. Halim, M. Etchells, P. J. Dobson, O. V. Salata, V. Christou, *Adv. Mater.*, **2000**, *12*, 1591.

57 H. Xin, M. Shi, X. M. Zhang, F. Y. Li, Z. Q. Bian, C. H. Huang, K. Ibrahim, F. Q. Liu, *Chem. Mater.*, **2003**, *15*, 3728.

58 H. Xin, M. Shi, X. C. Gao, Y. Y. Huang, Z. L. Gong, D. B. Nie, H. Cao, Z. Q. Bian, F. Y. Li, C. H. Huang, *J. Phys. Chem. B*, **2004**, *108*, 10796.

59 R. Reisfeld, C. K. Jrgensen, *Lasers and Excited States of Rare Earths*, Springer, Heidelberg, **1997**.

60 T. J. Foley, B. S. Harrison, A. S. Knefely, K. A. Abboud, J. R. Reynolds, K. S. Schanze, J. M. Boncella, *Inorg. Chem.*, **2003**, *42*, 5023.

61 R. J. Mears, S. R. Baker, *Opt. Quantum Electron.*, **1992**, *24*, 517.

62 E. Desurvire, *Phys. Today*, **1994**, *47*, 20.

63 K. Kuriki, Y. Koike, Y. Okamoto, *Chem. Rev.*, **2002**, *102*, 2347.

64 M. H. V. Werts, R. H. Woudenberg, P. G. Emmerink, R. van. Gassel, J. W. Hofstraat, J. W. Verhoeven, *Chem. Int. Ed.*, **2000**, *39*, 4542.

65 B. S. Harrison, T. J. Foley, M. Bouguettaya, J. M. Boncella, J. R. Reynolds, K. S. Schanze, J. Shim, P. H. Holloway, G. Padmanaban, S. Ramakrishnan, *Appl. Phys Lett.*, **2001**, *79*, 3770.

66 D. Imbert, M. Cantuel, J. C. G. Bünzli, G. Bernardinelli, C. Piguet, *J. Am. Chem. Soc.*, **2003**, *125*, 15698.

67 J. Zhang, P. D. Badger, S. J. Geib, S. Petoud, *Chem. Int. Ed.*, **2005**, *44*, 2508.

68 H. Wang, G. Qian, M. Wang, J. Zhang, Y. Luo, *J. Phys. Chem. B*, **2004**, *108*, 8084.

69 S. Torelli, D. Imbert, M. Cantuel, G. Bernardinelli, S. Delahaye, A. Hauser, J. C. G. Bünzli, C. Piguet, *Chem. Eur. J.*, **2005**, *11*, 3228.

70 N. M. Shavaleev, L. P. Moorcraft, S. J. A. Pope, Z. R. Bell, S. Faulkner, M. D. Ward, *Chem. Commun.*, **2003**, 1134.

71 R. J. Curry, W. P. Gillin, *Curr. Opin. Solid State Mater. Sci.*, **2001**, *5/6*, 481.

72 Y. Kawamura, Y. Wada, Y. Hasegawa, M. Iwamuro, T. Kitamura, S. Yanagida, *Appl. Phys. Lett.*, **1999**, *74*, 3245.

73 Z. R. Hong, C. J. Liang, R. G. Li, D. Zhao, D. Fan, W. L. Li, *Thin Solid Films*, **2001**, *391*, 122.

74 R. G. Sun, Y. Z. Wang, B. Q. Zheng, H. J. Zhang, A. J. Epstein, *J. Appl. Phys.*, **2000**, *87*, 7589.

75 B. S. Harrison, T. J. Foley, A. S. Knefely, J. K. Mwaura, G. B. Cunnigham, T. S. Kang, M. Bouguettaya, J. M. Bonceua, J. R. Reynolds, K. S. Schanze, *Chem. Mater.* **2004**, *16*, 2938.

76 A. S. Knefely, J. M. Boncella, J. R. Reyolds, K. S. Schnaze, *Adv. Mater.*, **2003**, *15*, 1093.

77 T. S. Kang, B. S. Harrison, M. Bouguettaya, T. J. Foley, J. M. Boncella, K. S. Schanze, J. R. Reynolds, *Adv. Func. Mater.* **2003**, *13*, 205.

78 D. Q. Gao, Y. Y. Huang, C. H. Huang, F. Y. Li, L. Huang, *Chem. Phys. Lett.*, **2001**, *350*, 206.

79 D. Q. Gao, Z. Q. Bian, Y. Y. Huang, C. H. Huang, K. Ibrahim, F. Q. Liu, *Chem. Res. Chinese U.*, **2004**, *20*, 790.

80 D. Q. Gao, M. Guan, H. Xin, Z. Q. Bian, C. H. Huang, *J. Rare Earths*, **2004**, *22*, 206.

81 H. Xin, M. Shi, F. Y. Li, M. Guan, D. Q. Gao, C. H. Huang, K. Ibrahim, F. Q. Liu, *New J. Chem.*, **2003**, *27*, 1485.

Index